N° d'ordre : H 658

Université Lille1
Sciences et Technologies

Université Lille 1 Sciences et Technologies

Mémoire

pour obtenir

l'Habilitation à Diriger des Recherches

Présenté par

Denis DUFLOT

Étude *ab initio* de molécules en phase gazeuse : double ionisation, spectroscopies en couches de valence et de cœur

Soutenue publiquement le 11 juin 2009 devant le jury composé de :

Directeur :		
M. Jean-Pierre Flament,	**Directeur de recherche CNRS,**	**Université Lille 1**
Rapporteurs :		
M. Xavier Assfeld,	**Professeur,**	**Université Henri Poincaré (Nancy 1)**
M. Florent-Xavier Gadéa,	**Directeur de recherche CNRS,**	**Université Paul Sabatier (Toulouse 3)**
M. Jacques Liévin,	**Professeur,**	**Université Libre de Bruxelles**
Membres :		
M. Jean-François Paul,	**Professeur,**	**Université Lille 1**
M. Jacques Delwiche,	**Professeur émérite,**	**Université de Liège**

"To explain all nature is too difficult a task for any one man or even for any one age. 'Tis much better to do a little with certainty, and leave the rest for others that come after you, than to explain all things."

Isaac Newton

Remerciements

Je tiens à remercier chaleureusement l'ensemble des (nombreuses) personnes qui m'ont aidé et/ou accompagné dans la réalisation des travaux présentés ici, en particulier :

- Le Professeur Jean-Michel Robbe, qui m'a initié aux méthodes de la chimie quantique, ainsi que le Dr Jean-Pierre Flament, dont les connaissances en chimie et programmation ont joué un rôle essentiel dans l'obtention des résultats présentés ici.

- L'ensemble des membres, permanents et étudiants, de l'équipe « Physico-Chimie Moléculaire Théorique » du PhLAM, pour l'ambiance qui règne au sein de notre groupe.

- Les étudiants que j'ai encadrés : V. Antzoulatos, Dr N. Chabert, S. Zeggari, K. Sidhoum, et M. Zuhair.

- Last but not least, les collègues expérimentateurs, grands pourvoyeurs de nouvelles données à interpréter : J. Delwiche et M.-J. Hubin-Franskin, que je remercie pour leur accueil à Liège, ainsi que plus récemment les groupes de N. J. Mason et P. Limão-Vieira.

Enfin, merci aux membres du jury d'avoir bien voulu accepter de juger ce travail.

SOMMAIRE

Sommaire

Sommaire

Introduction générale

Introduction générale

Ce mémoire présente les travaux de recherche que j'ai effectués depuis 1995 au Laboratoire de Dynamique Moléculaire et Photonique, devenu en 1998 partie intégrante du Laboratoire de Physique des Lasers, Atomes et Molécules (PhLAM) de l'Université des Sciences et Technologies de Lille, au sein de l'équipe actuellement dénommée " Physico-Chimie Moléculaire Théorique ". Ces travaux impliquent l'application des méthodes de la chimie quantique à l'étude des états électroniques excités de molécules en phase gazeuse. Ils peuvent être regroupés en trois grands thèmes, qui sont par ordre chronologique :

a) Structure et processus de fragmentation de molécules doublement ionisées (dications)

b) Spectroscopie en couches internes

c) Spectroscopie en couches de valence (UV et ionisation)

Le premier thème se situait dans le prolongement direct de ma thèse, tandis que le second a été initié lors de mon séjour post-doctoral au laboratoire de Spectroscopie d'Électrons Diffusés de l'université de Liège. Enfin, le troisième sujet a pris de l'importance depuis quelques années suite à des discussions avec divers groupes d'expérimentateurs. C'est d'ailleurs l'une des caractéristiques des articles présentés ici vu que la plupart d'entre eux présentent des études combinées expérimentales et théoriques. Le premier thème était supporté par la communauté européenne dans le cadre du programme SCIENCE. Pour ce qui est des deux derniers, ils entrent dans le cadre de programmes de type COST, sous l'égide de l'European Science Foundation : "RADAM" (Radiation Damage in Biomolecular Systems, 2004-2007) avait pour but d'étudier au niveau microscopique l'impact des rayonnements ionisants (α, β, γ, et X) sur la matière biologique, avec entre autres objectifs d'essayer de résoudre l'énigme de la nocivité des faibles doses. Deux autres programmes, en ont pris la suite, avec des thématiques légèrement différentes : "EIPAM" (Electron Induced Processing At the Molecular Level, 2004-2009) et "ECCL" (Electron Controlled Chemical Lithography, en cours de lancement).

Après quelques hésitations, j'ai choisi de présenter ces sujets dans un ordre légèrement différent. Ce manuscrit se compose en effet de trois chapitres. Le premier décrit les travaux sur les dications, qui impliquaient surtout des recherches de géométries d'équilibre, puis d'états de transitions menant vers les produits de fragmentation. De ce point de vue, les méthodes sont identiques à celles largement employées pour l'étude de la réactivité des molécules neutres. Le second chapitre porte quant à lui sur la spectroscopie en couche de valence (UV et visible). Dans ce cas, il s'agit essentiellement de calculer les états électroniques excités verticalement à la géométrie d'équilibre de l'état fondamental, en essayant de trouver quelle méthode *ab initio* est la plus appropriée à la taille du système. Les problèmes que cela peut poser se retrouvent aussi dans le chapitre trois, qui traite cette fois de spectroscopie par excitation d'un électron interne (couche K), avec les complications qui en découlent tant au niveau théorique qu'expérimental.

Ces trois chapitres présentent souvent des points communs entre eux, qui justifieraient un autre ordre de présentation. Ainsi le programme CIPSI utilisé dans le chapitre un joue un rôle vital dans le troisième alors qu'il n'apparaît pas dans le chapitre deux. D'un point de vue expérimental, l'utilisation du rayonnement synchrotron apparaît dans les trois chapitres, même si les spectres présentés dans le chapitre trois ont la plupart du temps été obtenus par une technique différente, la spectroscopie de perte d'énergie d'électrons.

En ce qui concerne le contenu de ce mémoire, j'ai longtemps médité sur le texte officiel décrivant l'habilitation à diriger des recherches. Les exemples que j'ai pu consulter montrent une grande disparité non seulement en fonction de la thématique mais aussi de l'université, sans parler du fait que l'épaisseur recommandée du document semble augmenter au fil du temps. Finalement, et en l'absence d'instructions détaillées dans notre université, le présent texte reflète une vision personnelle : outre une présentation du contexte des articles publiés, d'un bilan et des perspectives de mon activité de recherche, mon objectif est que ce mémoire puisse servir de point de départ pour un étudiant de master, en particulier s'il n'est pas anglophone. C'est la raison pour laquelle j'ai inclus quelques rappels sur des notions plus ou moins bien connues, ainsi qu'une liste des principaux acronymes utilisés. Cela m'a amené, au cours de l'année écoulé, à lire ou relire un grand nombre d'articles et de chapitres de livres qui sont référencés ici. Même en se limitant aux molécules en phase gazeuse, la croissance exponentielle du nombre d'articles interdit d'être exhaustif, surtout pour les deux premiers chapitres. Le chapitre trois, qui constitue mon thème de recherche principal, est aussi le plus long car j'y ai détaillé la méthode de calcul que nous avons mise au point, Jean-Pierre Flament et moi, en raison de son caractère non-standard. Cette méthode est notamment comparée à d'autres utilisées dans la littérature. D'autres développements portent sur des points qui semblent souvent tenus pour acquis sans justification (pourquoi peut-on calculer des spectres obtenus par impact d'électrons comme s'il s'agissait de photoabsorption?) ou font l'objet de vifs débats depuis des décennies (l'excitation d'une orbitale 1s est-elle localisée ou délocalisée dans les molécules de hautes symétrie?).

Un autre aspect qui est discuté est de faire des comparaisons avec les travaux publiés *après* la publication de mes propres articles, en montrant les progrès accomplis tant au niveau expérimental que théorique. A plusieurs reprises aussi, il est arrivé que les auteurs d'articles récents n'avaient apparemment pas connaissance de nos travaux. Inversement, en deux occasions au moins, nous n'avons pas pu publier certains calculs car d'autres l'ont fait juste avant nous. Tout ceci justifie la présence d'un paragraphe "commentaires" après chaque article, lesquels sont regroupés en annexe à la fin du document. Comme je doute fort que qui que ce soit lise en détail l'ensemble des articles présentés ici, ces commentaires sont normalement censés être compréhensibles après avoir regardé les figures, les tableaux et/ou les conclusions des articles. A un autre niveau de lecture, on peut aussi se contenter des articles les plus marquants, à savoir 1 pour le premier chapitre, 5, 7 et 8 pour le second, 11, 12, 17 et 18 pour le troisième.

Enfin, pour terminer cette introduction, je voudrais mettre l'accent sur une singularité : du fait de ma formation initiale, de mon poste de maître de conférences en physique - sans compter la baisse régulière des effectifs, il existe une profonde dichotomie entre mon enseignement et ma recherche. Je n'ai ainsi jamais eu l'occasion d'enseigner mes domaines de prédilection (chimie quantique, spectroscopie ni même mécanique quantique), sauf sous forme de projet. Le large spectre des matières que j'enseigne (de l'électricité à la physique stellaire) m'oblige à garder une certaine culture générale plutôt que de rester focalisé sur un domaine très étroit. *A contrario*, mon ignorance quasi-totale en chimie générale a souvent été comblée par Jean-Pierre Flament, en particulier sur la dénomination des molécules. Cet aspect de mon profil explique la difficulté rencontrée pour recruter des étudiants de DEA : les étudiants de physique passent leur chemin lorsqu'ils voient le mot chimie même suivi de quantique, alors que les étudiants de chimie ne penseraient pas à regarder les sujets des laboratoires de physique. Ce n'est d'ailleurs pas un hasard si les trois étudiants en DEA que j'ai eus venaient de l'extérieur.

CHAPITRE UN

1

Stabilité et fragmentation de molécules doublement chargées

Stabilité et fragmentation de molécules doublement chargées

Collaborations extérieures :
- J. Delwiche, R. Thissen, Liège, Belgique
- J. H. D. Eland, Oxford, Royaume-Uni

1) Introduction

Les molécules doublement chargées (encore appelées dications) ont été observées dès 1921 par J. J. Thomson [1]. Elles sont aussi fréquemment observées dans les spectres de masse de nombreuses molécules à l'échelle de la microseconde [2]). D'un point de vue théorique, Pauling avait dès 1933 [3], établi la courbe caractéristique d'un dication diatomique AB^{++}, en étudiant le cas simple de He_2^{++} (Courbes calculées avec MOLPRO [4] ;voir aussi [5,6]) :

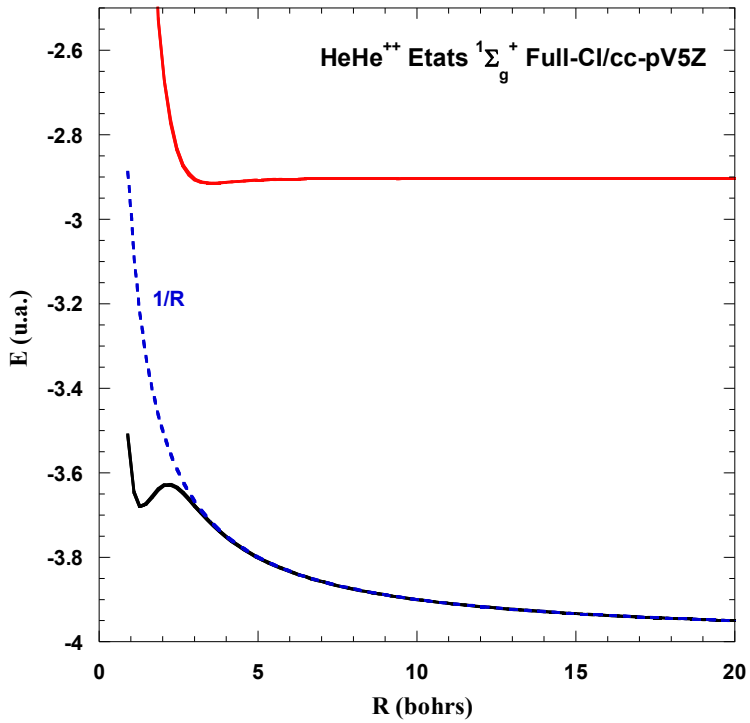

Figure 1.1. Courbes d'énergie potentielle de He_2^{++}

A grande distance, la courbe de potentiel se confond avec la répulsion coulombienne en 1/R entre les deux charges positives. A courte distance, les deux électrons créent une liaison covalente donnant lieu à un état lié de AB^{++}. Dans le cas de He_2^{++}, la distance d'équilibre de 1.33 bohrs est paradoxalement plus courte que celle de H_2.Ceci s'explique par le fait que l'énergie de liaison créée par les électrons libres est bien supérieure à la répulsion électrostatique. En utilisant une coordonnée adaptée, on peut d'ailleurs constater que la courbe de He_2^{++} est la somme de la courbe de H_2 et de la

courbe de répulsion [7]. Le raccourcissement de la longueur de liaison n'est d'ailleurs pas limité aux dications diatomiques. Ainsi, dans le 1,6-diazabicyclo[4.4.4]-tétradécane [8], la liaison N^+-N^+ vaut 1.532 Å contre 2.806 Å dans N-N, en dépit du fait que les charges positives sont localisées sur les atomes d'azote.

A une distance intermédiaire, la courbe de potentiel présente un point-selle caractéristique. L'énergie de ce point-selle détermine la durée de vie du dication, qui est donc métastable (dans la mesure où l'énergie des fragments $A^+ + B^+$ est inférieure à celle du dication [9]). Dans le cas de dications polyatomiques, cette durée de vie explique que la molécule ait le temps de changer de conformation avant que la répulsion coulombienne ne provoque la fragmentation ([10,11] et Article 1). La position du point-selle peut aussi être vue comme le croisement évité entre la courbe de potentiel de l'état se dissociant en $A^+ + B^+$ et de la dissociation en $A^{++} + B$ (par exemple), forcément moins stable, et attractive à cause d'une interaction charge-dipôle induite du type $-2\alpha/R^4$, α étant la polarisabilité de l'atome neutre B :

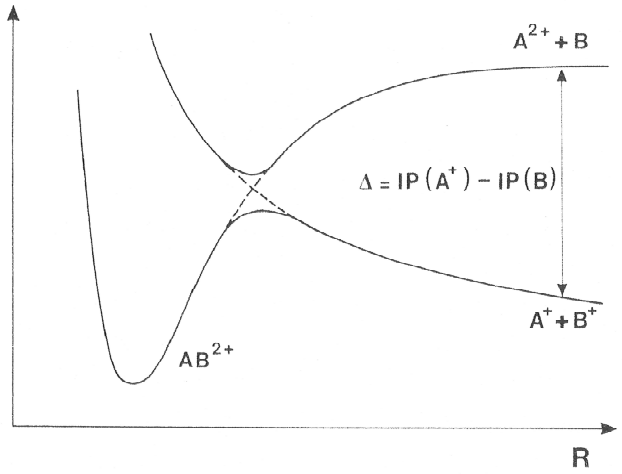

Figure 1.2. Courbes de potentiel d'un dication diatomique AB^{++} d'après [12]

La structure et la dynamique de ce type de molécules a fait l'objet d'un certain nombre d'articles de revue [13-17] couvrant les aspects à la fois théoriques et expérimentaux. Ce type d'étude a bénéficié à partir des années 1990 de la possibilité d'utiliser le rayonnement synchrotron. On peut noter que la double ionisation directe au moyen d'un seul photon est interdite pour une transition dipolaire électrique. La détection de dications est donc la signature expérimentale d'effets de corrélation électronique et illustre les limites de l'approximation mono-électronique. Expérimentalement, il existe deux méthodes distinctes pour réaliser la double ionisation d'un atome ou d'une molécule :

d) Dans la région de valence, l'énergie requise (pour des petits systèmes polyatomiques) se situé entre 25 et 40 eV. Une loi empirique [18,19] indique d'ailleurs que l'énergie de double ionisation vaut environ 2.8 fois la première énergie d'ionisation. Dans le cas de l'acétylène, la double ionisation constituait une fraction de l'absorption totale qui atteint 10% pour une énergie d'excitation de 65 eV ([10,11] et Article 1).

e) A partir de 100 eV, les dications peuvent être produits après excitation ou ionisation en couche interne (voir chapitre 3). Les couches internes possédant des énergies bien séparées, le processus est plus sélectif. Compte tenu de la durée de vie très brève de ces états, la molécule se désexcite par effet Auger qui produit là aussi un dication mais dans plusieurs états électroniques.

Les articles qui suivent constituent des exemples d'études de la stabilité et de la fragmentation de dications polyatomiques, en collaboration avec des expérimentateurs. Les méthodes de calcul utilisées comprenaient deux étapes :

- Optimisation de géométrie et calcul des fréquences harmoniques de vibration au niveau CASSCF

- Calcul de la corrélation dynamique grâce au programme CIPSI dans sa version à deux classes [20-22]

CIPSI est l'un des premiers programmes MP2 multiréférenciel. Vu que ce programme a été très largement utilisé pour les calculs présentés dans ce mémoire, rappelons-en les grandes lignes. La fonction d'onde d'ordre zéro est construite en diagonalisant l'hamiltonien sur un espace S contenant un nombre restreint de déterminants :

$$P_S H P_S \left|\Psi_m^{(0)}\right\rangle = E_m^{(MR)} \left|\Psi_m^{(0)}\right\rangle \text{ avec } P_S = \sum_{N\in S} \left|N\right\rangle\left\langle N\right|$$

Ce qui donne les fonctions d'onde d'ordre zéro pour un état m : $\left|\Psi_m^{(0)}\right\rangle = \sum_{N\in S} C_N^m \left|N\right\rangle$. Puis on calcule l'énergie de perturbation au second ordre en énergie :

$$E_m^{(2)} = \sum_{I\notin S} \frac{\left|\left\langle I\left|V\right|\Psi_m^{(0)}\right\rangle\right|^2}{E_m^0 - E_I^0}$$

Tous les calculs présenté ici ont utilisé la partition Møller-Plesset barycentrique de l'hamiltonien, ce qui signifie que les énergies E_m^0 et E_I^0 sont obtenues en utilisant l'opérateur de Fock comme hamiltonien d'ordre zéro. En pratique, la taille de l'espace S est augmentée itérativement, en incluant au fur et à mesure dans S les déterminants I de l'espace de perturbation qui ont le plus "d'influence", en particulier les quasi-dégénérescences qui se produisent lorsque $E_m^0 \approx E_I^0$. Quand on estime que l'espace S est convergé, le dernier calcul est effectué avec la version diagrammatique [21,22], plus rapide. C'est ce processus itératif, fastidieux, qui fait que CIPSI n'est maintenant plus compétitif par rapport aux techniques CASPT2 ou CASSCF/MRCI. En revanche, on peut l'utiliser pour faire une IC sur un groupe de déterminants choisi arbitrairement, une propriété qui est exploitée pour le calcul des spectres d'excitation de cœur décrits dans le chapitre trois.

2) L'acétylène C_2H_2

L'étude expérimentale de la fragmentation du dication acétylène fait partie du travail de thèse de R. Thissen [10,11], qui a aussi étudié les dications méthylamine $CH_3NH_2^{++}$ et chlorométhane CH_3Cl^{++}. La source de lumière était à l'époque le rayonnement synchrotron produit par l'anneau Super-ACO à Orsay. Les fragments chargés étaient ensuite analysés au moyen de techniques de coïncidence (PEPIPICO : Photo Electron PhotoIon PhotoIon Coincidence). Les mesures d'énergie cinétique des fragments ont été quant à elles effectuées à Oxford par J.H.D. Eland.

a) Article 1 : *Ab initio* study of the acetylene and vinylidene dications fragmentation

b) Commentaires

Dans les premières années qui ont suivi la publication de l'article précédent, il ne semble pas que le dication acétylène ait beaucoup attiré l'attention, à l'exception de l'observation de la structure vibrationnelle des états $^1\Delta_g$ et $^1\Sigma_g^+$ [23]. Tout changea en 2003 avec la publication par Osipov *et al.* [24,25] d'une mesure de la durée du réarrangement du dication acétylène-vinylidène (estimée à 60 fs), après ionisation en couche interne de l'acétylène neutre (voir chapitre 3). Depuis, plusieurs publications récentes (théoriques et expérimentales) ont été à nouveau consacrées à $C_2H_2^{++}$:

- Li et Schlegel [26] ont étudié la dynamique de fragmentation de $C_2H_2^{++}$ en recourant aux trajectoires classiques sur la surface de l'état fondamental $^3\Sigma_g^-$ calculée " on the fly " au niveau B3LYP/6-31G* pour les trois principaux processus à deux corps. Bien que 11 à 14 % des trajectoires produisaient le dication vinylidène, la fragmentation de ce dernier n'apparaissait pas, faute d'une énergie suffisante.

- Sans apparemment connaître l'existence de l'article précédent, Zyubina *et al.* [27,28] ont refait l'étude de $C_2H_2^{++}$ en utilisant diverses méthodes : B3LYP/cc-pVQZ, QCISD/cc-pVTZ, CASSCF(8,8)/6-311++G**, CASSCF(8,10)/cc-pVQZ et CASSCF(8,11)/6-311++G**. On peut s'interroger sur la nature (non précisée) de la 11ème orbitale utilisée dans le calcul CASSCF(8,11) car *a priori* l'espace actif de valence de C_2H_2 compte 10 OM (3σ, 2π, $3\sigma^*$, $2\pi^*$). De même, l'utilisation de fonctions diffuses " ++ " est probablement superflue dans le cas des dications, le nuage électronique étant plus contracté que dans la molécule neutre. Ces auteurs ont calculé les voies de dissociation de l'état triplet en plus du singulet au niveau MRCI(8,10)/cc-pVQZ//B3LYP/cc-pVQZ. Ils ont comparé leurs résultats avec les nôtres mais certaines de leurs remarques semblent difficiles à comprendre : à plusieurs reprises, ils laissent entendre que le seuil d'excitation verticale obtenu avec CIPSI (32.0 eV), plus bas que la valeur expérimentale (32.7 eV), influe sur les barrières d'activation des fragments, ce qui est inexact. De même, contrairement à ce qui est dit, nous avons bien calculé l'état de transition plié de la fragmentation en $CH^+ + CH^+$ (pour le singulet). Une autre différence est qu'apparemment, la dissociation en $C_2H^+ + H^+$ du singulet se fait de manière non-linéaire et aboutit à un C_2H^+ plié, ce qui est curieux vu que ce dernier est linéaire. Enfin, les pourcentages des fragments ont été calculés par une méthode RRKM et les résultats sont en accord qualitatif avec les mesures de Thissen *et al.* [10].

- En utilisant des méthodes de calcul poussées (CASSCF-MRCI/cc-pVQZ) et notamment en optimisant les géométries des premiers états linéaires au niveau MRCI, Kinugawa *et al.* [29] ont calculé leur structure vibrationnelle (y compris pour $C_2D_2^{++}$) et déterminé les énergies adiabatiques de double ionisation. Très récemment, l'effet Renner-Teller a été pris en compte pour le calcul de la structure vibronique de l'état fondamental [30].

- Palaudoux *et al.* [31] ont calculé (cc-pV5Z/RCCSD(T)) un nouvel état de transition, de géométrie " papillon " ou dipontée, qui est impliqué dans la dissociation $C_2H_2^{++} \rightarrow C_2 + H^+ + H^+$. Cette prédiction vient d'être confirmée expérimentalement [32]. Notons que,

cette structure, surtout connue pour être la géométrie d'équilibre de Si_2H_2 [33-35], avait déjà été calculée pour l'acétylène neutre par Halvick *et al.* [36] lors d'une analyse de la topologie de la surface d'énergie potentielle : à l'époque, au niveau MP4/6-31G**, un minimum de la surface d'énergie potentielle de forme pontée (angle de 90°, symétrie C_{2v}) avait été trouvé à 79 kcal.mol^{-1}, soit 3.4 eV au dessus de l'état fondamental de l'acétylène. L'état de transition C_2 connectant ces deux minima se trouvait à peine plus haut (80.58 kcal.mol^{-1}). Depuis, la surface d'énergie potentielle de C_2H_2 et $C_2H_2^+$ a été étudiée avec des méthodes de plus en plus poussées (cf. [37] et références citées). En particulier, il a été montré que pour ces deux molécules, l'isomérisation de l'acétylène en vinylidène passe par un minimum très peu prononcé, d'où l'existence de deux états de transition. Il est fort possible que la surface de potentiel de l'isomérisation du dication présente les mêmes propriétés.

- Osipov *et al.* [38] et Flammini *et al.* [39] ont continué l'étude expérimentale des processus de fragmentation du dication produit par cascade Auger après ionisation de cœur. S'appuyant sur le fait que l'effet Auger peuple faiblement les états triplets [40], Osipov *et al.* [38] limitent leur discussion aux singulets, contrairement à Flammini *et al.* [39] et Zyubina *et al.* [27,28]. La quantité mesurée de CH_2^+ est maximum vers 34 eV, en bon accord avec nos calculs à 32.19 eV. Notons aussi que l'asymétrie de la distribution angulaire des électrons Auger conduit Osipov *et al.* [38] à conclure à une signature expérimentale de la localisation dynamique du trou de cœur (voir discussion section 4.c du chapitre 3). Adashi *et al.* [41] arrivent aux mêmes conclusions.

- Enfin, signalons que très récemment, Hishiakawa *et al.* [42] ont étudié la dynamique de fragmentation du dication acétylène ionisé une troisième fois sous l'influence d'un champ laser très intense.

3) *Le chlorométhane CH_3Cl*

Dès 1986, Yates *et al.* [43] avaient montré au niveau Hartree-Fock que les dications du type CH_3X^{++} (X = F, Cl, SH, OH, PH_2, NH_2) étaient plus stables sous la forme CH_2XH^{++} (ylidions). Toutefois, il était possible que l'inclusion des effets de corrélation modifie l'ordre des isomères. Dans sa thèse [11], Thissen avait aussi fait l'étude des processus de fragmentation du dication méthylamine. Le résultat le plus marquant était l'apparition du fragment H_3^+ en proportion non négligeable. L'utilisation de molécules deutérées prouvait que cet ion provenait des atomes H/D liés au carbone, un effet déjà observé par Eland dans le cas de CH_3OH [44].

Vu le succès de l'étude *ab initio* de $C_2H_2^{++}$, l'étape suivante consistait à étudier des composés de plus grande taille, en commençant par le cas le plus simple : le chlorométhane, pour lequel Thissen avait aussi fait des mesures (non publiées). La taille du système permettait d'utiliser toujours les techniques CASSCF afin d'améliorer les résultats de Yates *et al.* Dans un second article, les processus de fragmentations étaient étudiés plus en détail et comparés aux résultats de Thissen (PEPICO) et à ceux de Rühl *et al.* [45] obtenus par PEPIPICO.

a) Article 2 : Stability of the CH_3Cl dication

b) Article 3 : *Ab initio* study of the chloromethane dication fragmentation

c) Commentaires

Le spectre d'excitation verticale de CH_3Cl^{++} a été remesuré par Double Transfert de Charge (DCT) et recalculé par la méthode ADC(2) en 1999 par Grant *et al.* [46]. Les auteurs n'ont pas fait la comparaison avec nos propres calculs. On peut noter que les énergies calculées étant trop basses, ils ont dû appliquer une correction de +1.2 eV pour faire coïncider les valeurs théoriques avec les mesures. Nos propres valeurs sont plus proches des mesures, mais toujours trop basses en particulier pour les triplets :

	CIPSI	ADC(2)	DCT(Singulets)	DCT(Triplets)
$^3A_2$	30.69	29.81		31.5 ± 0.2
^1E	31.64	30.76	32.3 ± 0.2	
$^1A_1$	32.15	31.32	″	
$^1A_2$	33.17	32.60	33.6 ± 0.3	
^3E	33.32	32.73		34.1 ± 0.2
$^3A_1$	33.40	32.82		″
^3E	33.47	32.89		″
$^3A_2$	34.17	33.67		35.5 ± 0.3
^1E	34.69	34.02	35.4 ± 0.3	
^1E	35.27	34.78	″	
$^1A_1$	36.17	35.65	36.5 ± 0.3	

Ce problème semble récurrent dans les calculs sur les dications et peut peut-être s'expliquer par un traitement déséquilibré des effets de corrélation entre les molécules neutres et doublement chargées : enlever deux électrons détruit de nombreuses paires et modifie profondément la corrélation électronique par rapport à l'état fondamental. D'ailleurs, les écarts relatifs entre les différents états sont bien reproduits. Il est aussi possible que l'erreur soit due à l'absence de prise en compte de l'énergie de point-zéro vibrationnelle.

La conclusion de l'article 3 indiquait qu'il serait très difficile d'étudier théoriquement les processus de fragmentation des autres membres de la famille CH_3X^{++}, parce que les méthodes du type CASSCF apparaissaient trop coûteuses. Des calculs sur la stabilité de la méthylamine avaient été commencés [47] au niveau MP2 et B3LYP dans le cadre du stage de V. Antzoulatos, étudiant en deuxième année du magistère de chimie physique à Orsay. Mais en 1999, le groupe de Olah a publié un article [48] utilisant ces mêmes méthodes (ainsi que G2) appliquées aux composés CH_3X^{++} initialement étudiés par Yates [43]. Dans le cas du chlorométhane, les auteurs se sont limités à l'abstraction d'un atome d'hydrogène (figure 1.3 page suivante).

Les structures obtenues sont très proches des nôtres si l'on excepte la **6e** que nous n'avions pas trouvée. Elle est calculée 19.9 $kcal.mol^{-1}$ (0.86 eV) au-dessus de 6b, ce qui rend le mécanisme compatible avec le seuil d'apparition de la paire CH_2Cl^{++}/H^+ trouvé à 31.0 ± 0.5 eV.

En ce qui concerne la production de H_3^+, comme indiqué dans l'article 3, nous n'avions pas trouvé de chemin menant à la production de ce fragment. Récemment, l'étude de la production de ce fragment a été poursuivie dans CH_3OH^{++} [49-52], l'emploi d'espèces deutérées confirmant qu'il provient du groupement méthyle comme dans le cas de la méthylamine. De *et al.* [51] l'ont confirmé théoriquement (au niveau UHF/6-311G(2d,1f)) en calculant une surface de potentiel à deux dimensions [R(C-H_3, R(H-H)]. *A priori*, rien n'empêcherait de reprendre les calculs au niveau CASSCF/MRCI ou CASPT2 comme nous l'avons fait pour le chlorométhane.

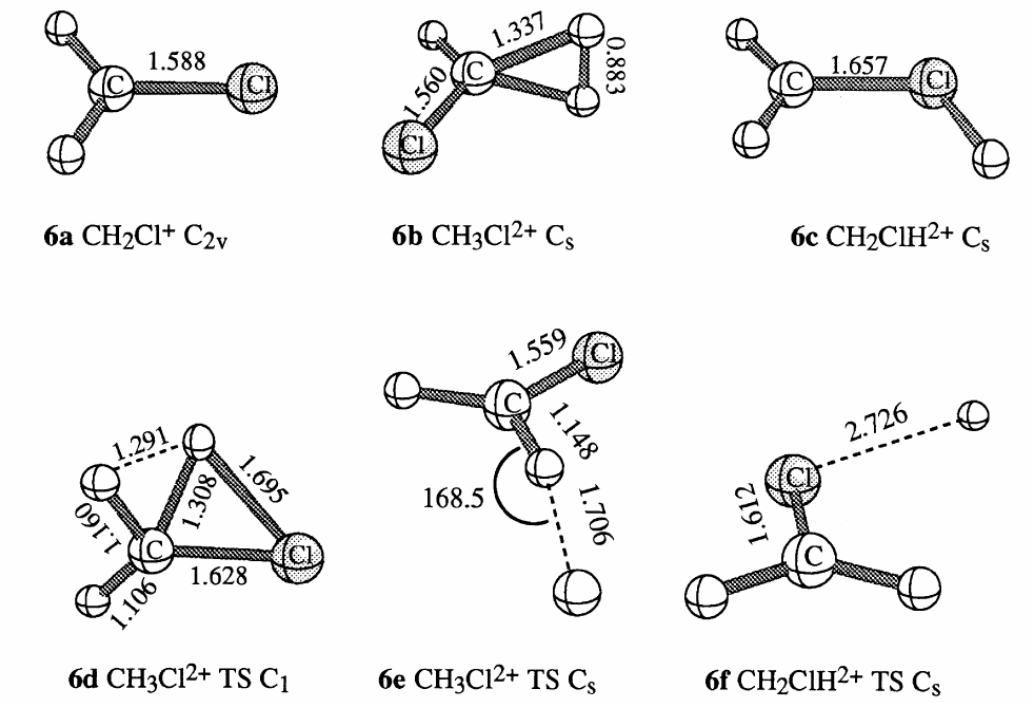

Figure 1.3. Abstraction de H de CH_3Cl^{++} d'après [48].

4) Bilan

Les calculs sur les molécules doublement chargées se sont progressivement arrêtés à partir de 1997. L'une des raisons est que j'ai consacré pratiquement tout mon temps en 1995/1996 à l'enseignement, avec en particulier le montage *ex nihilo* de nouveaux travaux pratiques. Ensuite, après le départ pour le Japon de R. Thissen — qui n'a d'ailleurs jamais publié ses mesures sur CH_3Cl^{++} et $CH_3NH_2^{++}$, les collègues de Liège se sont focalisés sur d'autres sujets, impliquant par exemple la spectroscopie par perte d'énergie d'électrons (chapitres deux et trois). L'étude de ce type de systèmes se poursuit bien évidemment [9,53], tant au niveau expérimental [54-59] qu'au niveau théorique: pour les petits systèmes, triatomiques en particulier, Hochlaf utilise les méthodes CASSCF/MRCI [30,31,60-69]. Pour des molécules plus grandes, on utilise la DFT, notamment dans le groupe de Olah [70-72].

CHAPITRE DEUX

2

Spectroscopie en couches de valence

Spectroscopie en couches de valence

Collaborations extérieures :
- J. Delwiche, M.-J. Hubin-Franskin, Liège, Belgique
- A. Giuliani, SOLEIL (Saint-Aubin), France
- S. V. Hoffmann, Åhrus, Danemark
- P. Limão-Vieira, Lisbonne, Portugal
- N. J. Mason, Milton Keynes, Royaume-Uni
- B. P. Marinkovic, Belgrade, Serbie

1) Introduction

Les articles présentés ci-dessous concernent la spectroscopie électronique de valence (excitation et/ou ionisation) de molécules dans différents contextes (atmosphérique et biologique). Il s'agissait initialement de calculs ponctuels effectués à la demande des expérimentateurs (Articles 5 et 6). Depuis 2006, cette collaboration s'est étendue à plusieurs groupes expérimentaux européens (Belgique, Danemark, Grande-Bretagne, Portugal et Serbie) dans le cadre des programmes européens COST "RADAM", "EIPAM" et plus récemment "ECCL". Les calculs *ab initio* sont en effet l'un des nombreux outils utilisés conjointement à plusieurs techniques expérimentales :

- Spectroscopie VUV à haute résolution grâce au rayonnement synchrotron (anneau ASTRID, ligne ISA, Åhrus, Danemark, opérationnel depuis 1990) [73].
- Spectroscopie HREELS (High Resolution Energy Loss Spectroscopy), brièvement décrite dans le chapitre 3, à Liège [74] ou plus récemment à Belgrade [75].
- Spectroscopie de photoélectrons, utilisant la raie HeI à 21.22 eV à Liège [76].

2) Méthodes utilisées

a) Comparaison expérience-théorie

Du point de vue théorique, le calcul du spectre électronique de molécules même de petite taille reste une tâche délicate. Une classe de molécules particulièrement étudiée de ce point de vue est constituée de systèmes cycliques aromatiques ou non (benzène, furane, pyrrole, thiophène, pyridine, pyrimidine …). Leur symétrie élevée permet d'utiliser les méthodes les plus coûteuses, i.e. multiconfigurationelles [77,78]. Toutefois, le succès obtenu est des plus variables, comme l'illustre le tableau de la page suivante, qui concerne le cas typique de la pyridine (remarquons que ce tableau est une version abrégée de celui donné par Cai *et al.* [79].

On remarque en effet qu'en fonction de la méthode et/ou de la base employées, les énergies calculées peuvent varier de plusieurs dixièmes d'eV, parfois plus (voir aussi [80]). Qui plus est, la comparaison entre théorie et expérience est souvent difficile, pour des raisons variées :

méthode	base	$^1B_1$ S_1 $n\rightarrow\pi^*$	$^1A_2$ S_3 $n\rightarrow\pi^*$	$^1B_2$ S_2 $\pi\rightarrow\pi^*$	$^3A_1$ $\pi\rightarrow\pi^*$	2^3A_1 $\pi\rightarrow\pi^*$	$^3B_1$ $n\rightarrow\pi^*$	$^3A_2$ $n\rightarrow\pi^*$	$^3B_2$ $\pi\rightarrow\pi^*$
CCSD(T)	aug-cc-pVDZ				4.44		4.54		4.85
CCSD	cc-pVDZ				4.32	4.65	4.49	5.55	4.98
CCSD	aug-cc-pVDZ				4.29		4.45		4.80
EOM-CCSD	cc-pVDZ	5.29	5.69	5.29	4.06	5.12	4.63	5.62	4.90
EOM-CCSD	aug-cc-pVDZ	5.19		5.19	4.04		4.58		4.76
CASSCF(8,11)	cc-pVDZ	5.68	6.37	5.20	4.08	5.25	5.09	6.36	5.06
CASPT2	cc-pVDZ	5.00	5.25	4.89	4.10	4.77	4.37	5.22	4.61
CASPT2	aug-cc-pVDZ	4.93		4.88	4.06		4.31		4.52
TD-B3LYP	cc-pVDZ	4.83	5.09	5.58	3.90	4.89	4.06	4.94	4.57
TD-BLYP	cc-pVDZ	4.39	4.44	5.29	4.07	4.74	3.72	4.32	4.41
SAC-CI	DZ+d+p	5.24	5.69	5.44	4.34	5.32	4.49	5.69	5.09
MRCI	DZ+d	4.50	5.36	4.76	3.95	4.93	3.87	5.43	4.98
CASPT2	ANO	4.91	5.17	4.84	4.05	4.73	4.41	5.10	4.56
STEOM-CCSD	Sadlej	4.91	5.31	4.82	3.73	4.90	4.32	5.31	4.68
Exp.		4.74	5.43?	4.99	4.1?	4.84?		5.43?	4.84?
Exp. + ZPE		4.90	5.52	5.13	4.3	4.93		5.52	4.89

- En général, les énergies de transition expérimentales sont mesurées en cherchant le maximum d'intensité de la bande, tandis que les valeurs calculées correspondent à une transition dite verticale qui ne tient pas compte de l'énergie vibrationnelle de point zéro (ZPE). Il en résulte inévitablement des erreurs sur les énergies de transitions. Si l'on fait un calcul de structure vibrationnelle, il est possible d'obtenir le maximum de la structure vibrationnelle calculée, ainsi que de déterminer la position de la transition vibrationnelle 0-0 (valeur dite adiabatique). Cette dernière est par contre difficile à déterminer expérimentalement, vu qu'elle correspond à une bande vibrationnelle de faible intensité, sans compter la possible présence de bandes chaudes (cf. Article 4).

- Bien souvent, les calculs se contentent de l'énergie de transition. Les choses s'améliorent si l'on évalue les intensités des transitions en calculant les forces d'oscillateurs, qui s'expriment dans l'approximation dipolaire électrique par :

$$f = \frac{2m_e}{3\hbar e^2}\Delta E\left|\left\langle \Psi_{exc}\left|\vec{\mu}\right|\Psi_{fond}\right\rangle\right|^2$$

Où ΔE et $\vec{\mu}$ sont respectivement l'énergie et le moment dipolaire de la transition. Ceci permet de construire un spectre théorique " bâtons ". En principe, les f calculées devraient être comparées à la surface de la raie expérimentale observée [81,82] :

$$f = \frac{2m_e}{\pi\hbar e^2}\frac{\varepsilon_0 c}{N_A}\Delta E\int\frac{\varepsilon(\Delta E)d\Delta E}{\Delta E}$$

Où $\varepsilon(\Delta E)$ est le coefficient d'extinction molaire. Mais la plupart du temps, les calculs prouvent que la bande observée contient une ou plusieurs transitions d'énergies voisines, certaines d'entre elles pouvant toutefois se révéler peu intenses.

- Idéalement, il faudrait aussi évaluer la largeur de chaque raie, autrement dit sa durée de vie. Ce paramètre étant difficile à obtenir (voir toutefois Article 4 où l'on utilise le principe de réflexion [83]), en général on se contente de représenter les transitions calculées par des raies (gaussiennes par exemple) de largeur fixe tirée de la résolution expérimentale.

b) États électroniques excités

Les techniques *ab initio* utilisées dans les articles présentés ci-dessous dépendent de la taille de la molécule étudiée, tant au niveau du nombre d'atomes que du nombre d'électrons à corréler :

- Dans le cas du chlorure de thiazyle NSCl (Article 4), la taille du système a permis d'utiliser des méthodes multiconfigurationnelles (CASSCF/MRCI(D)). Les calculs ayant été faits sur une grille, il a aussi été aisé d'obtenir des fréquences anharmoniques, plus proches de l'expérience.

- Dans le cas de composés de plus grande taille, ces méthodes sont trop coûteuses. On doit donc se restreindre à des méthodes monoconfigurationnelles, récemment revues par Dreuw et Head-Gordon [84]. Parmi elles, les méthodes du type TD-DFT [85] se sont imposées, notamment pour les systèmes les plus gros où il n'existe pas d'alternatives, et en dépit du fait que le caractère exact de la théorie ait été contesté [86,87]. Les difficultés de la TD-DFT à décrire certains types d'états (Rydberg, transfert de charge, états di-excités) sont aussi bien connues [77,84]. Toutefois, il peut arriver que les calculs TD-DFT donnent d'excellents résultats par rapport à l'expérience et aux méthodes multiconfigurationnelles. C'est par exemple le cas pour le spectre UV de l'acroléine en phase gazeuse et solvatée [88], où la fonctionnelle PBE0 [89] fournit des valeurs comparables à des calculs du type MS-CASPT2, y compris pour les états de Rydberg. C'est la raison pour laquelle la même méthode (TDDFT/PBE0/6-311++G**//PBE0/6-311G**) a été choisie pour simuler le spectre UV de l'acide acétique (Article 4). Depuis, Ciofini et Adamo [90] ont montré que la méthode TDDFT/PBE0 couplée à une base adéquate est efficace pour les excitations de Rydberg et de valence au-dessous d'une énergie ε_{HOMO} + 1 eV où ε_{HOMO} est l'énergie de la HOMO de la molécule étudiée.

- Vus les bons résultats obtenus, la même méthode a été employée dans le cas de c-C_4F_8 (Article 5), cette fois avec moins de succès. C'est pourquoi les premiers états électroniques excités ont été recalculés au niveau CCS, CC2 [91] et CCSD [92] en utilisant DALTON [93]. Malgré leur coût élevé, ces méthodes de type " Coupled Cluster " obtiennent de bons résultats [94,95]. Dans le cas de c-C_5F_8 (Article 6) et du tétrahydrofurane (Article 7), la méthode EOM-CCSD [96], avec calcul des forces d'oscillateur, implémentée dans la version 2006 de MOLPRO [4] a été préférée à DALTON, beaucoup plus lent.

c) États électroniques ionisés

Un nombre d'électrons impair (ionisation) complique encore la situation, du fait de la présence d'une couche ouverte. En plus d'un nombre plus important de configurations dans les méthodes MCSCF (Article 4), il faut choisir entre les formalismes " restricted " ou " unrestricted " dans les calculs monoconfigurationnels. Outre le fait qu'ils ne donnent que le premier potentiel d'ionisation, les calculs RCCSD et RCCSD(T) se sont révélés moins bons que la méthode OVGF [97,98] implémentée dans GAUSSIAN dans le cas de c-C_5F_8 (Article 6). La méthode MR-AQCC [99] a donné de bons résultats dans c-C_4F_8 (Article 5) mais les calculs n'ont pas convergé dans le cas de c-C_5F_8 (Article 6).

d) Structure vibrationnelle

Du point de vue théorique, le calcul des facteurs de Franck-Condon vibrationnels (FCF) n'est pas aisé pour une molécule polyatomique. En premier lieu, si le calcul des fréquences harmoniques de vibration de l'état fondamental est facile, cela n'est pas le cas pour les états excités. Dans l'idéal, il faudrait aussi avoir accès aux fréquences anharmoniques. Domcke et Cederbaum [100-102] ont trouvé une solution élégante qui permet de calculer les FCF sans avoir à calculer explicitement les fréquences de vibration de l'état électronique excité. Rappelons-en seulement les grandes lignes : on considère une transition électronique entre un état fondamental i et un état excité final f. on exprime l'hamiltonien nucléaire de l'état f par un développement limité au second ordre :

$$\hat{H}_f = \sum_s \omega_s \left(b_s^+ b_s + \frac{1}{2} \right) + \sum_s \kappa_s \left(b_s + b_s^+ \right) + \sum_{ss'} \gamma_{ss'} \left(b_s + b_s^+ \right)\left(b_{s'} + b_{s'}^+ \right) + \sum_{ss'} \tau_{ss'} \left(b_s - b_s^+ \right)\left(b_{s'} - b_{s'}^+ \right)$$

Où les indices s et s' parcourent les 3N-6 degrés de liberté nucléaires de la molécule. Les matrices κ et γ sont appelées constantes de couplage linéaire et quadratique, respectivement. La matrice τ représente la variation d'énergie cinétique des noyaux lors de l'excitation et peut s'exprimer en fonction de κ et γ. Les opérateurs de création et annihilation de bosons b_s et b_s^+ s'expriment en fonction des coordonnées normales :

$$Q_s = \frac{1}{\sqrt{2}} \left(b_s + b_s^+ \right)$$
$$\frac{\partial}{\partial Q_s} = \frac{1}{\sqrt{2}} \left(b_s - b_s^+ \right)$$

Les termes de κ et γ s'obtiennent à partir de l'énergie de transition verticale $E_{if} = E_f - E_i$ à la géométrie d'équilibre de l'état fondamental :

$$\kappa_s = \frac{1}{\sqrt{2}}\left[\frac{\partial E_{fi}}{\partial Q_s}\right]_i \qquad \gamma_{ss'} = \frac{1}{4}\left[\frac{\partial^2 E_{fi}}{\partial Q_s \partial Q_{s'}}\right]_i$$

Autrement dit, κ correspond au gradient de la surface d'énergie potentielle de l'état excité le long des modes normaux de l'état fondamental. De même, γ est la hessienne de l'état excité mais calculée à la géométrie de l'état initial. En exprimant l'hamiltonien $\hat{H}_f$ sous forme matricielle, Domcke et Cederbaum ont montré comment rendre cet hamiltonien diagonal et on trouvé des formules de récurrence permettant de calculer les FCF [100-102]. On voit l'avantage de cette méthode : il n'est pas nécessaire de connaître explicitement les fréquences de vibration de l'état excité. En pratique, le plus souvent, on fait l'approximation du couplage linéaire (γ nulle). Cela signifie concrètement que l'état électronique excité a les mêmes fréquences harmoniques de vibration que l'état fondamental mais à une géométrie différente. Dans ce cas, les facteurs de Franck-Condon obéissent à une distribution de Poisson. Évidemment, cette approximation est d'autant moins justifiée que les deux géométries sont éloignées. Cependant, Domcke et Cederbaum ont montré pour certaines molécules que l'erreur commise en négligeant γ contrebalancer les effets d'anharmonicité non pris en compte [100,101].

Le programme utilisé dans les exemples ci-après correspond à l'implémentation réalisée par J.-P. Flament dans son travail de thèse d'état en 1981 [103-105]. En 2000, il a " ressuscité " ce programme, qui a depuis subi plusieurs adaptations (passage en FORTRAN90 notamment). Les facteurs de Franck-Condon peuvent être calculés jusqu'à un degré d'excitation 8. Les bandes chaudes et les modes de combinaison (jusqu'à quatre modes excités) sont pris en compte. Il est aussi possible de calculer les couplages vibroniques en Q et Q^2, les forces rotationnelles impliquées dans le dichroïsme circulaire et il est prévu un traitement pour le cas où l'état électronique excité présente un double puits.

3) Le chlorure de thiazyle NSCl

a) Article 4 : Thiazyl chloride: an experimental and theoretical study of the valence shell HeI photoelectron spectrum

b) Commentaires

L'étude du spectre de photoélectrons de NSCl constitue l'un des chapitres de la thèse de Nicolas Chabert, soutenue en mars 2001 [106]. Un autre chapitre était consacré au spectre de photoélectrons du composé atmosphérique Cl_2O, mesuré expérimentalement un peu plus tôt [107,108]. Ces résultats n'ont pas pu être publiés suite à la parution à la mi-2000 d'une étude très sembable à la nôtre [109,110] tant du point de vue électronique que vibrationnel.

4) L'acide acétique CH_3COOH

a) Article 5 : Acetic acid electronic state spectroscopy by high-resolution vacuum ultraviolet photo-absorption, electron impact, He(I) photoelectron spectroscopy and *ab initio* calculations

b) Commentaires

Les résultats de l'article 5 montrent que la méthode TD-DFT employée conjointement avec la fonctionnelle PBE0 donne d'assez bons résultats, tout au moins pour l'interprétation des principales transitions. On peut néanmoins comparer nos valeurs à celles obtenues avec DALTON par Osted *et al.* [111] au niveau CCSD/aD(T) (CCSD avec base augmentée par des orbitales diffuses) et à celles obtenues par Leach *et al.* [112] (tableau page suivante).

On constate des différences de plusieurs dixièmes d'eV entre les deux fonctionnelles. Pour le calcul CCSD, mise à part pour la première transition purement de valence, on retrouve des différences assez significatives pour les états de Rydberg. Il est dommage que les auteurs n'aient pas calculé la transition $2\pi \rightarrow 1\pi^*$.

	TD-DFT PBE0		TD-DFT B3LYP [112]		CCSD aD(T) [111]	
$n_O \rightarrow 1\pi^*$	5.926	0.0007	5.825	0.0005	5.98	0.00032
$n_O \rightarrow 3s\sigma/\sigma^*$(O-H)	7.000	0.0495	6.669	0.0466	7.27	0.04990
$n_O \rightarrow 3p\sigma$	7.730	0.0018	7.3782	0.001	8.17	0.01931
$2\pi \rightarrow 3s\sigma/\sigma^*$(O-H)	8.906	0.0001			8.26	0.00323
$2\pi \rightarrow 1\pi^*$	8.685	0.1719	8.4283	0.1492		
$1\pi \rightarrow 1\pi^*$	10.021	0.1476				

Des calculs identiques viennent d'être faits sur d'autres acides carboxyliques dont les spectres ont été mesurés par les expérimentateurs : acide propionique CH_3-CH_2-COOH, acide butyrique CH_3-CH_2-CH_2-COOH et acide valérique CH_3-CH_2-CH_2-CH_2-COOH (travail en collaboration avec S. Canneaux du PC2A de l'USTL, soumis à PCCP). La fonctionnelle B3LYP a aussi été employée, les deux fonctionnelles ne montrant pas de différences importantes. Une nouvelle difficulté tient à la présence de plusieurs conformations d'équilibre proches en énergie (~0.1 kcal.mol^{-1}) pour les acides butyriques et valériques, en raison de la rotation des groupements COOH et CH_3. En ce qui concerne les états ioniques, seul le spectre HeI de l'acide propionique a été mesuré. Les calculs montrent notamment que la forme ionisée céto COOH est beaucoup moins stable que la forme énol COHOH. De plus, c'est la migration d'un atome d'hydrogène du groupe CH_2 central (CH_3-CH-COHOH$^+$) qui est favorisée par rapport à la migration à partir du groupement méthyle terminal (CH_2-CH_2-COHOH$^+$).

5) Le perfluorocyclobutane c-C_4F_8 et l'octafluorocyclopentène c-C_5F_8

a) Article 6 : Perfluorocyclobutane electronic state spectroscopy by high-resolution vacuum ultraviolet photoabsorption, electron impact, He I photoelectron spectroscopy, and *ab initio* calculations

b) Article 7 : Electronic state spectroscopy of c-C_5F_8 explored by photoabsorption, electron impact, photoelectron spectroscopies and *ab initio* calculations

c) Commentaires

Les deux articles précédents montrent des différences importantes entre les calculs TD-DFT et CC (CC2 pour C_4F_8 et CCSD pour C_5F_8). Pour C_5F_8, il est possible de comparer graphiquement les transitions calculées au spectre expérimental (voir figures 2.1a et b page suivante). Comme on peut le constater, le résultat est assez décevant, en particulier pour la transition $\pi \rightarrow \pi^*$ (HOMO $\rightarrow$ LUMO) qui est sous-estimée par la TD-DFT et surestimée par EOM-CCSD par plus de 0.5 eV. Un autre problème provient de la bande autour de 8.8 eV qui est bien rendue par la TD-DFT (transition HOMO $\rightarrow \sigma^*$(C-F) alors qu'elle n'existe pas dans le calcul EOM-CCSD). Il est fort possible que du fait du grand nombre d'électrons provenant des atomes de fluor, la limitation aux di-excitations d'un calcul CCSD ne soit pas suffisante. De même, la base cc-pVDZ employée est peut-être trop petite, ce choix étant dicté par la nécessité de rajouter des orbitales diffuses pour décrire les états de Rydberg. Pour le moment, le coût d'un calcul CCSD(T)/cc-pVTZ reste prohibitif. En ce qui concerne la TD-DFT, nous avons aussi testé la méthode SAOP [113,114]. Cette méthode est implémentée dans le code ADF (version 2006 du CINES) [115] et est censée corriger le mauvais comportement asymptotique de la DFT. Les calculs ont été faits avec la base AUG-TZ2P et à la géométrie PW91/TZ2P. Les transitions calculées sont représentées par des gaussiennes (FWHM de 0.1 eV). On constate que l'accord avec l'expérience est encore moins bon avec en particulier la transition $\pi \rightarrow \pi^*$ encore plus sous-estimée qu'avec PBE0 (Fig. 2.1.).

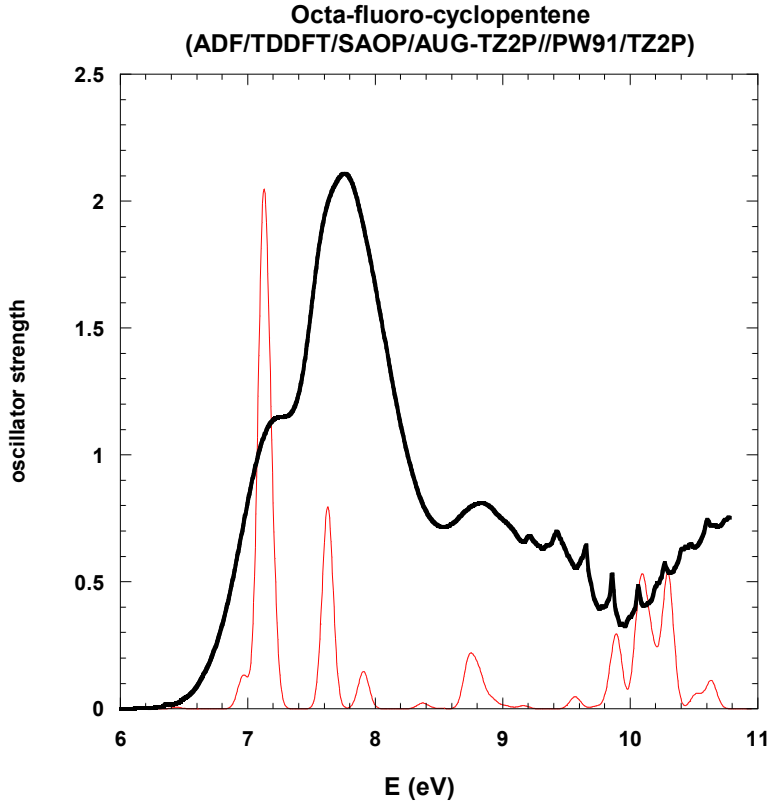

Figure 2.1. Le spectre UV de c-C_5F_8 en TD-DFT avec ADF.

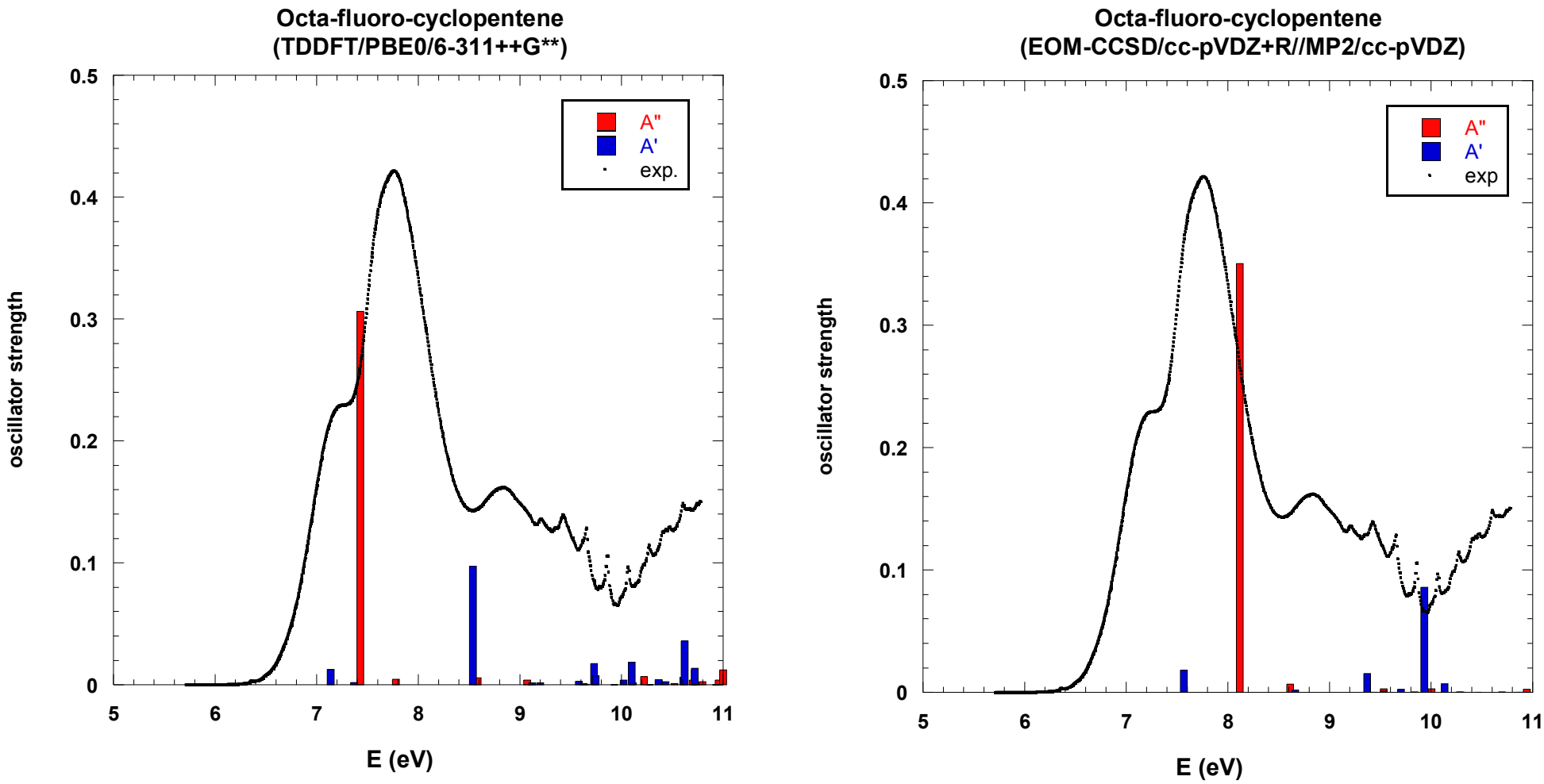

(a) (b)

Figure 2.2. Les spectres UV de c-C_5F_8 calculés en TD-DFT et EOM-CCSD comparés à l'expérience

Le texte de l'article indique aussi que le modèle de Domcke-Cederbaum a été utilisé pour déterminer l'énergie d'ionisation adiabatique de la première bande. Les calculs ont été faits en prenant en compte la matrice γ de l'ion. Les figures (montrées page suivante) n'ont finalement pas été incluses dans l'article.

Ces sont bien des spectres "bâtons" et on se rend compte du grand nombre de pics vibrationnels évalués. L'accord avec la bande observée est assez bon, mis à part pour le premier massif qui est un peu trop intense. Ceci provient du mode de "ring-puckering" qui est mal décrit par l'approximation harmonique utilisée. Une fois supprimé de la simulation, on obtient des intensités relatives proches de celles de la figure 4.b de l'article. Pour la seconde bande (fig. 2.4b), l'accord est moins bon car le spectre observé montre peu de structure fine.

6) Le tétrahydrofurane OC_4H_8

a) Article 8 : Electronic states of neutral and ionized tetrahydrofuran studied by VUV spectroscopy and *ab initio* calculations

b) Commentaires

Comme indiqué dans l'article 8, la question de la géométrie d'équilibre du THF en phase gazeuse est largement débattue, en raison de la quasi-dégénérescence des isomères C_2 et C_s, reliés par un point-selle d'ordre 2 de symétrie C_{2v}. Les calculs de l'article 8 indiquent par contre que les énergies des transitions HOMO → 3s des deux isomères diffèrent par ~0.25 eV, ce qui se traduit par deux progressions vibrationnelles distinctes dans le spectre expérimental. Notons que les énergies de transition HOMO → 3s ont été recalculées après la rédaction de l'article avec une base aug-cc-pVTZ (et à la géométrie d'équilibre MP2/aug-cc-pVTZ) :

	aug-cc-pVDZ+R	aug-cc-pVTZ+R
C_2 (^{1}B)	6.357	6.559
C_s (^{1}A')	6.608	6.812
ΔE (eV)	0.251	0.253

Les nouvelles valeurs absolues semblent légèrement surestimées par rapport à l'expérience mais l'écart est identique. En ce qui concerne les ions, il serait intéressant de confirmer les résultats cc-pVDZ en cc-pVTZ, étant donné que pour la molécule neutre ce paramètre joue beaucoup. Pour le moment, l'espace disque nécessaire au calcul MP2 n'est pas disponible.

7) Bilan

En conclusion, ce chapitre illustre toute la difficulté à reproduire correctement les spectres UV de molécules, même de petite taille. La TD-DFT a l'avantage de fournir rapidement des résultats et reste la seule solution praticable pour les très gros systèmes. En revanche, lorsqu'on peut la comparer à d'autres méthodes, on constate de grandes disparités. Qui plus est, la DFT souffre d'une maladie que Gill a qualifiée de "Hyper Parametric Disorder" [116] qui fait qu'il est de plus en

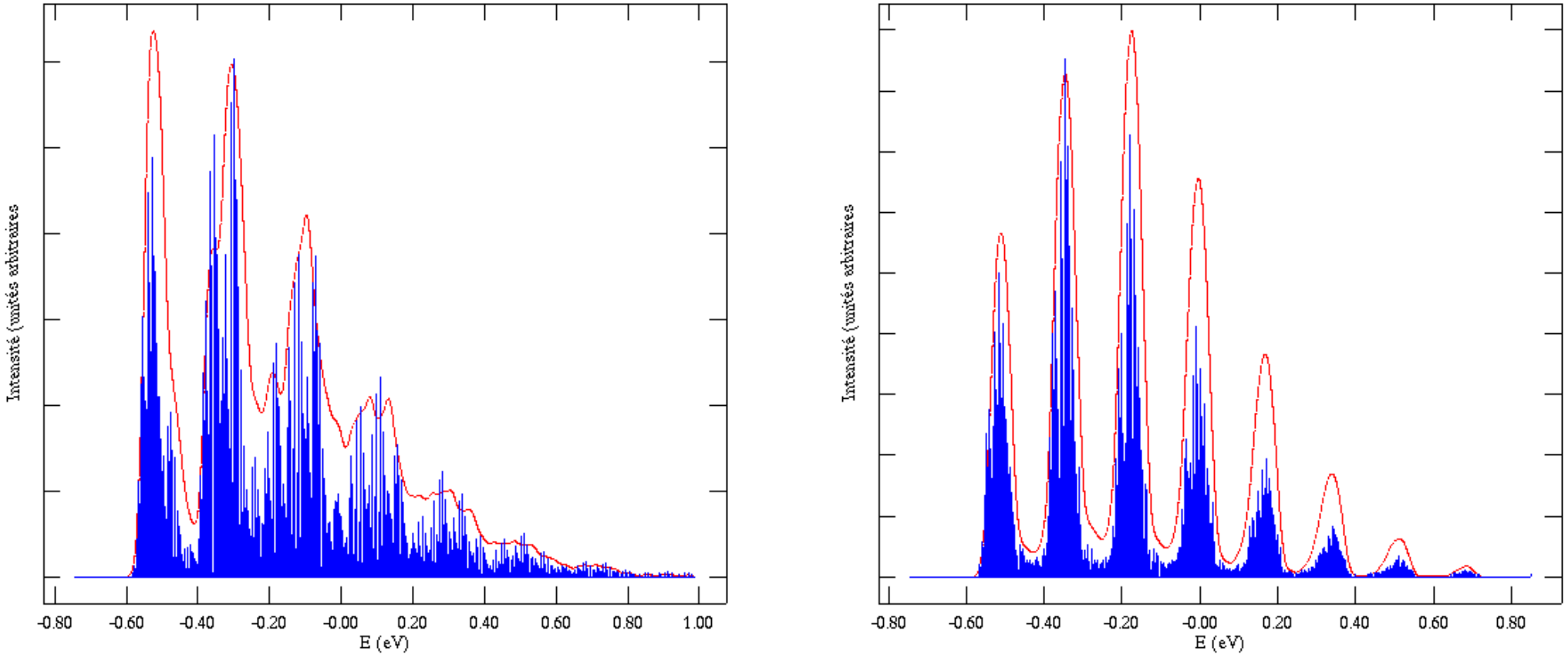

(a) (b)

Figure 2.3. Structure vibrationnelle calculée des deux premières bandes du spectre de photoélectrons de c-C_5F_8

plus difficile de choisir une fonctionnelle parmi la multitude proposée. Le choix de PBE0 pour l'acide acétique était uniquement dicté par la bonne concordance avec CASPT2 obtenue dans le cas de l'acroléine [88]. Les calculs sur d'autres acides gras ne montrent pas beaucoup de différences avec B3LYP, tant au niveau des géométries que des énergies des isomères. Mais en ce qui concerne les spectres, les énergies et forces d'oscillateurs peuvent varier assez largement.

La TD-DFT ne semble pas être utilisable non plus pour l'étude des composés fluorés. Les techniques CC ont d'ailleurs elles aussi quelques difficultés. Récemment, l'étude des spectres électroniques des fluoroéthylènes [117], calculée au niveau SAC-CI [118-123], a elle aussi révélé une grande difficulté à reproduire les transitions π - π^*. Certaines des transitions présentaient une caractère valence-Rydberg comme dans le cas bien connu de l'éthylène [124]. Néanmoins, vu l'impossibilité d'utiliser les méthodes CASSCF/MRCI ou CASPT2, elles restent la meilleure alternative.

En ce qui concerne les spectres PES, la méthode OVGF donne de bons résultats et les premières bandes observées sont parfois suffisamment séparées pour envisager un calcul vibrationnel.

CHAPITRE TROIS

3

Spectroscopie en couches internes

Spectroscopie en couches internes

Collaborations extérieures :
- A. Aouni, Fès, Maroc
- J. Delwiche, J. Heinesch, M.-J. Hubin-Franskin, Liège, Belgique
- L. F. Ferreira, Lisbonne, Portugal
- A. Giuliani, SOLEIL (Saint-Aubin), France
- G. Tourillon, Orsay, France
- I. C. Walker, Edimbourg, Royaume-Uni

1) Introduction

L'utilisation des rayons X en spectroscopie est très ancienne puisque M. Siegbahn reçut le prix Nobel de physique en 1924 pour son travail sur les raies observées dans les spectres atomiques [125]. Dans les années 1960, son fils K. Siegbahn (prix Nobel en 1981 [126]) conçut les premiers spectromètres de photoélectrons X qu'il utilisa entre autres pour l'étude des molécules. La méthode initialement appelée ESCA (Electron Spectroscopy for Chemical Analysis) [127] est maintenant connue sous le nom de XPS (X-Ray Photoelectron Spectroscopy). A l'heure actuelle, les meilleures sources de rayons X sont les anneaux synchrotron, en particulier ceux de 3^{ième} génération. Comme dans le domaine VUV (chapitres un et deux), elles n'ont pas de rivales en termes de brillance et de résolution. Elles sont utilisées pour sonder la matière tant en phase solide, que liquide et gazeuse [128], et pour l'étude des surfaces [129-131] et concerne tous les champs disciplinaires des sciences de la nature, y compris la médecine. En conséquence, il existe une multitude de techniques spectroscopiques dans ce domaine, sans compter qu'elles peuvent êtres couplées à d'autres méthodes, notamment les méthodes de coïncidence (chapitre un), ou des lasers femtosecondes [132]. Dans tout ce qui suit, on se limitera au domaine de la physico-chimie moléculaire, soit l'étude de "petites" molécules (moins de ~30 atomes), en phase gazeuse. De même, au niveau théorique, on laissera de côté les techniques basées sur le "multiple scattering" [129,133,134].

Les principaux phénomènes se produisant lorsqu'on envoie des photons X sur un système moléculaire sont schématisés dans la figure 3.1 page suivante. On peut distinguer les méthodes d'*ionisation* de cœur des méthodes d'*excitation* de cœur :

- Dans la méthode XPS (X-ray Photo-electron Spectroscopy), le photon X arrache un électron. Éventuellement, un second électron (de valence), peut être ionisé. C'est le phénomène de "shake off", qui se traduit par la présence de raies satellites dans le spectre XPS.

- Dans les méthodes du type XAS (X-ray Absorption Spectroscopy), l'électron de cœur est simplement excité dans un état lié. Là aussi, il peut y avoir une excitation concomitante d'un électron de valence ("shake up"). La molécule se trouve donc dans un état doublement excité. Comme il y a une multitude d'états excités, qui convergent vers la limite d'ionisation, on obtient un spectre constitué d'un certain nombre de raies discrètes. Ce type de spectres est appelé NEXAFS ou XANES. Il ne faut pas confondre la spectroscopie NEXAFS avec l'EXAFS, qui se produit à beaucoup plus haute énergie et qui constitue une méthode spécifique d'analyse structurale [133].

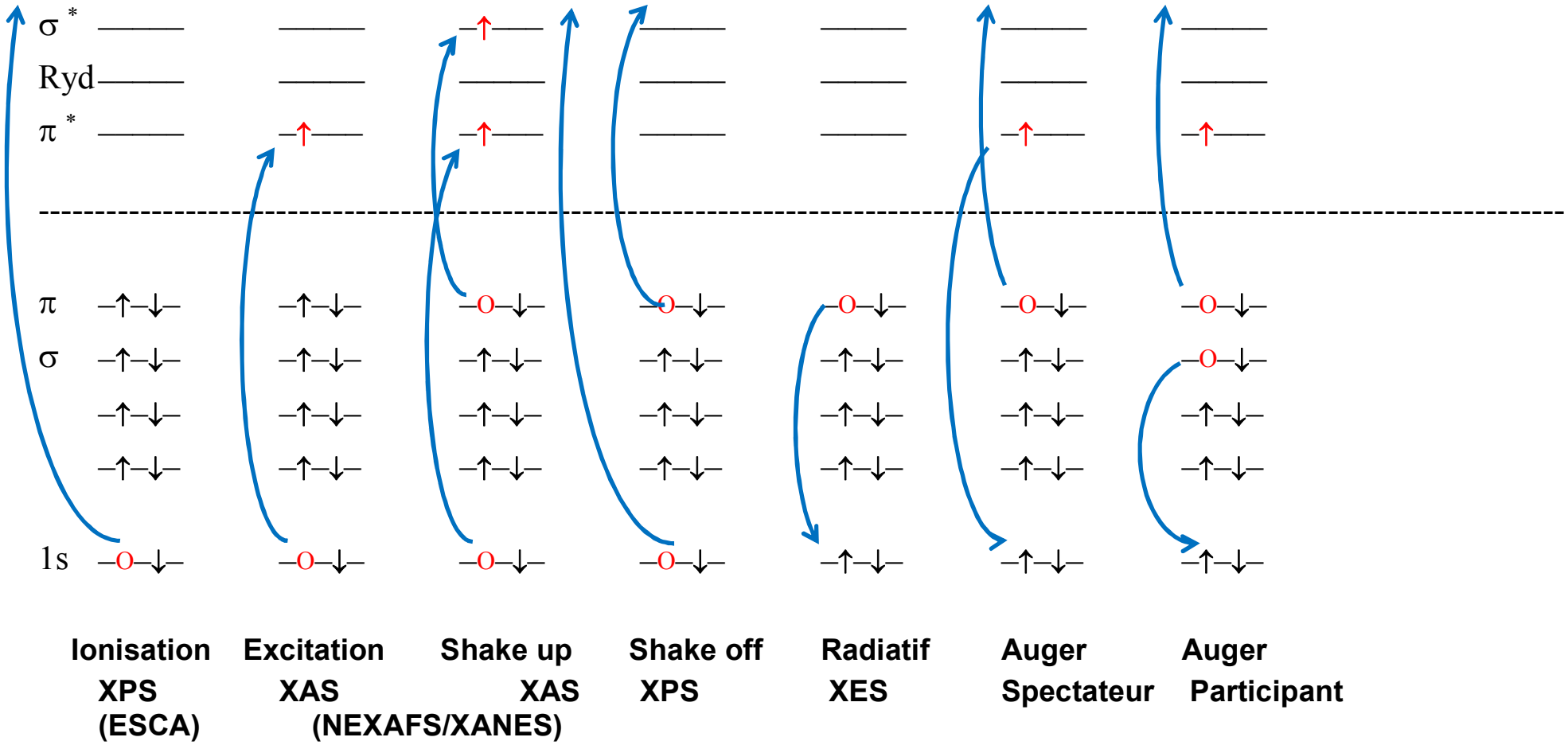

Figure 3.1. Principaux phénomènes liés à la spectroscopie d'absorption des rayons X et leurs acronymes.

Tant pour l'ionisation que pour l'excitation, la molécule finit par retomber dans son état fondamental. La désexcitation peut prendre deux formes :

- Une forme radiative qui se traduit par une fluorescence sous la forme d'un photon X (XES)
- Une forme non-radiative sous la forme d'une cascade Auger (effets Auger spectateur ou participant, Fig. 3.1).

La spectroscopie en couche interne présente un avantage majeur par rapport à la spectroscopie électronique de valence. Comme l'illustre le chapitre deux, celle-ci sonde des transitions de type HOMO → LUMO qui implique des orbitales délocalisées sur au moins deux des atomes composant la molécule. En revanche, les méthodes de type XAS excitent les orbitales les plus profondes, qui ne participent pas aux liaisons chimiques et gardent un caractère atomique[1]. Néanmoins, les énergies de transition sont légèrement différentes pour un même type d'atome en fonction de son environnement chimique, comme l'illustre l'exemple célèbre du spectre XPS du trifluoroacétate [135] :

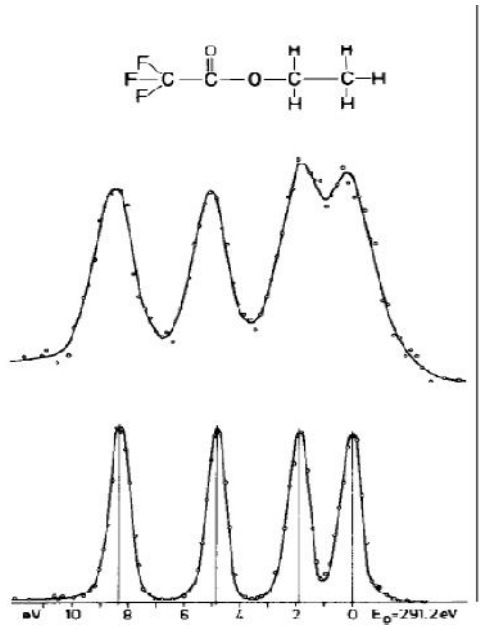

Figure 3.2. Le spectre XPS de CF_3-CO-CH_2-CH_2-H d'après [135].

On distingue quatre raies séparées correspondant aux quatre atomes de carbone différents composant la molécule. L'écart entre les transitions est appelé "chemical shift". L'une des questions auxquelles il faut répondre est de savoir à quel atome attribuer une raie. En général, les expérimentateurs s'inspirent de l'interprétation du spectre de molécules voisines mais seuls les calculs *ab initio* permettent d'apporter une réponse sans ambiguïté. Dans le cas de l'ionisation de cœur, le spectre a une structure relativement simple car il n'y a qu'un seul état ionique, même s'il peut y avoir des raies satellites. Dans le cas de l'excitation, il existe une infinité d'états excités qui convergent vers l'état ionique. Le spectre présente alors la forme caractéristique de la figure 3.3 page suivante [129].

[1] Les articles présentés dans ce chapitre concernent l'excitation des couches 1s d'atomes légers (carbone, azote, oxygène) mais les principes généraux restent valables pour des couches plus élevées d'atomes plus lourds (tels que les couches 2s et 2p pour le soufre par exemple).

Ce spectre se divise en deux zones dont la frontière est le seuil d'ionisation : en-dessous de ce seuil, on trouve des transitions discrètes alors qu'au-delà, le spectre présente un continuum auquel se superpose des bandes très larges habituellement attribuées à des "shake up" et surtout à des résonances de forme ("shape resonances") [129]. Toutefois cette interprétation est vivement contestée par Piancastelli [136]. Profitons-en pour préciser que nos calculs ne peuvent pas décrire correctement ce qui se passe au-delà du seuil d'ionisation, faute d'une représentation adéquate des états du continuum.

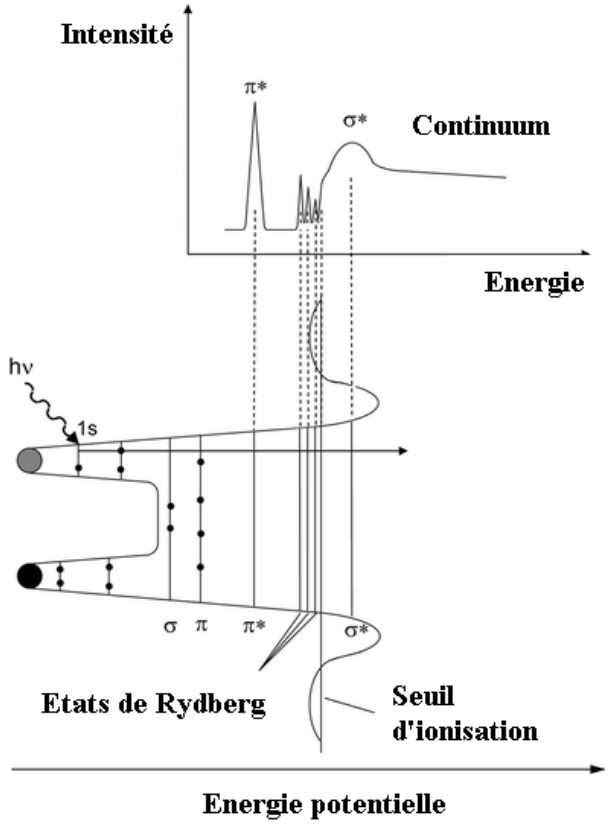

Figure 3.3. Spectre XAS typique, adapté de [137].

Avant d'expliquer comment calculer théoriquement des transitions électroniques en couches internes (qui sont de l'ordre de plusieurs centaines d'eV pour les atomes de la seconde ligne de la table périodique), il faut dire quelques mots de la seconde technique expérimentale utilisée pour mesurer des spectres d'excitation en couches internes : la méthode ISEELS. En effet, c'est cette méthode et non les rayons X, qui a été utilisée pour les spectres des articles de ce chapitre.

2) La méthode ISEELS

Dans la méthode ISEELS (Inner Shell Electron Energy Loss Spectroscopy) [138-140], un faisceau d'électrons mono-énergétique d'énergie E_i (par exemple 2 keV), est diffusé inélastiquement par un atome ou une molécule M :

$$e^-(E_i) + M(E_0) \rightarrow M^*(E_f) + e^-(E_\ell)$$

L'analyse de la perte d'énergie subie par l'électron ($E_\ell = E_0 - E_f$) ainsi que de leur distribution angulaire donne des informations spectroscopiques sur l'état excité de la molécule. En général, on exprime le résultat en fonction de la variation de quantité de mouvement $\hbar\overrightarrow{K_{0f}} = \hbar\vec{k}' - \hbar\vec{k}$ de l'électron incident correspondant à l'excitation d'un état électronique i à un état électronique f de la molécule-cible :

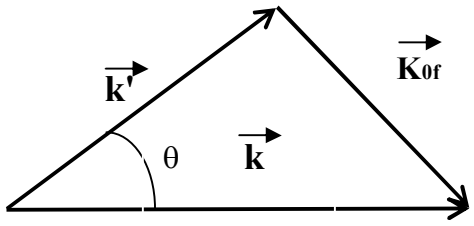

Figure 3.3. Transfert d'impulsion en ISEELS.

Si l'électron incident est suffisamment rapide, le transfert de quantité de mouvement est faible ($\overrightarrow{K_{0f}} \approx \vec{0}$, c'est-à-dire que l'angle de diffusion θ est petit) et on peut appliquer l'approximation de Born [141-143]. La section efficace différentielle de diffusion s'écrit alors [144-146] :

$$\frac{d\sigma_{0f}}{d\Omega} = 4\left(\frac{m_e e^2}{\hbar^2}\right)^2 \frac{k'}{k} K_{0f}^{-4} \left|\varepsilon_{0f}\left(\overrightarrow{K_{0f}}\right)\right|^2 \qquad \text{avec } \varepsilon_{0f}\left(\overrightarrow{K_{0f}}\right) = \left\langle f \left| \sum_n \exp\left(i\overrightarrow{K_{0f}}.\vec{\mathbf{r}}_\mathbf{n}\right) \right| 0 \right\rangle$$

Il est remarquable que cette expression est le produit de deux termes : l'élément de matrice $\varepsilon_{0f}\left(\overrightarrow{K_{0f}}\right)$, décrit la réponse à la collision des n électrons de la molécule tandis que le reste de l'expression décrit le changement subit par le mouvement de la particule incidente. Pour un échantillon en phase gazeuse, les molécules sont orientées aléatoirement. En conséquence, l'élément de matrice $\varepsilon_{0f}\left(\overrightarrow{K_{0f}}\right)$ ne dépend que de la norme de $\overrightarrow{K_{0f}}$: $\varepsilon_{0f}\left(\overrightarrow{K_{0f}}\right) = \varepsilon_{0f}\left(K_{0f}\right)$. Bethe [141] a introduit la notion de force d'oscillateur généralisée (GOS), qui s'exprime (en jauge vitesse) par :

$$f_{0f}\left(K_{0f}\right) = 2\frac{m_e}{\hbar^2}\frac{E_{0f}}{K_{0f}^2}\left|\varepsilon_{0f}\left(K_{0f}\right)\right|^2$$

E_{0f} étant l'énergie de transition. Il s'agit d'une généralisation de la notion de force d'oscillateur utilisée en absorption optique (cf. chapitre deux). On peut effectuer un développement en série de Taylor du terme exponentiel de $\varepsilon_{0f}\left(K_{0f}\right)$ [144,147]:

$$\varepsilon_{0f}\left(K_{0f}\right) = \left\langle f \left| \sum_n \sum_{m=1}^{\infty} \frac{\left(i\overrightarrow{K_{0f}}.\vec{r}_n\right)^m}{m!} \right| 0 \right\rangle = \sum_{m=1}^{\infty} \left\langle f \left| \sum_n \frac{\left(i\overrightarrow{K_{0f}}.\vec{r}_n\right)^m}{m!} \right| 0 \right\rangle = \sum_{m=1}^{\infty} \frac{\left(iK_{0f}\right)^m}{m!} \vec{u}.\left\langle f \left| \sum_n \frac{\left(\vec{r}_n\right)^m}{m!} \right| 0 \right\rangle = \sum_{m=1}^{\infty} \frac{\left(iK_{0f}\right)^m}{m!} \varepsilon_{0f,m}$$

Où $\vec{u}$ est le vecteur unitaire de $\overrightarrow{K_{0f}}$. La force d'oscillateur généralisée se met alors sous la forme [148,149] :

$$f_{0f}(K_{0f}) = 2\frac{m_e}{\hbar^2}\frac{E_{0f}}{K_{0f}^2}\left|\sum_{m=1}^{\infty}\frac{(iK_{0f})^m}{m!}\varepsilon_{0f,m}\right|^2 = 2\frac{m_e}{\hbar^2}E_{0f}\left[\varepsilon_{0f,1}^2 + \frac{K_{0f}^2}{4}\varepsilon_{0f,2}^2 - \frac{K_{0f}^2}{3}\varepsilon_{0f,1}\varepsilon_{0f,2} + \frac{K_{0f}^4}{36}\varepsilon_{0f,3}^2 + ...\right]$$

Si le transfert d'impulsion est faible $(K_{0f} \approx 0)$, on peut ne retenir que le premier terme :

$$f_{0f}^{(0)}(K_{0f}) = 2\frac{m_e}{\hbar^2}E_{0f}\varepsilon_{0f,1}^2 = 2\frac{m_e}{\hbar^2}E_{0f}\left|\vec{u}.\langle f|\sum_n \vec{r}_n|0\rangle\right|^2$$

Où l'on reconnait l'expression de la force d'oscillateur optique dans l'approximation dipolaire électrique ($\vec{u}$ représentant dans ce cas-là la polarisation du rayonnement incident) [150]. Ce résultat est le théorème limite de Lassettre [141,151] :

$$\lim_{K\to 0} f_{0f}(K_{0f}) = f_{0f}^{optique}$$

Les autres termes de $\varepsilon_{0f,m}$ correspondent aux transitions quadrupolaire électrique, dipolaire magnétique … Le théorème de Lassettre justifie le fait que les spectres ISEELS (pour des énergies incidentes élevées et aux faibles angles de diffusion) sont très semblables aux mêmes spectres obtenus en photoabsorption (voir Fig. 3, Article 5). En particulier, les transitions obéissent aux mêmes règles de sélection pour les molécules symétriques [152]. En conséquence, du point de vue *ab initio*, il n'y a pas de différences entres les spectres ISEELS et XAS, la problématique restant la même : obtenir les énergies de transitions et les forces d'oscillateur, comme illustré dans les articles de ce chapitre. En revanche, on voit qu'à plus haut transfert d'énergie (K et θ plus grands), l'intensité des termes non-dipolaires électriques est exacerbée par rapport aux dipolaires [153,154]. De plus, à faible énergie d'impact et grand angle de diffusion, il est possible d'observer des transitions interdites de spin du type singulet-triplet [155,156]. Cela se justifie par le fait que c'est le spin total du système électron-molécule qui se conserve et qu'il peut y avoir un échange entre l'électron incident et un électron de la molécule.

Même si les premières expériences de diffusions d'électrons remontent aux premières décennies du XXème siècle, le premier spectromètre ISEELS apparut en 1970 [157] et jusque dans les années 1980, la résolution était meilleure qu'avec un rayonnement synchrotron. Ce n'est plus le cas aujourd'hui, même si l'ISEELS présente encore un certain nombre d'avantages sur le synchrotron [138] en plus de la possibilité déjà mentionnée d'observer des transitions non-dipolaires : outre un coût plus faible, la résolution est constante dans la gamme d'énergie observée. Ce n'est pas le cas pour le synchrotron. Enfin, c'est grâce à l'EELS qu'il est possible de mesurer les énergies absolues qui servent de référence pour la calibration des spectres en photoabsorption [138]. Ce genre de mesures reste toutefois difficile [158-165].

3) *Le modèle du cœur équivalent*

Du point de vue *ab initio*, le calcul d'un état ionisé/excité de cœur est *a priori* impossible : si on veut faire un calcul Hartree-Fock (ou DFT), le principe variationnel implique qu'à la fin du calcul le trou se retrouve sur la HOMO de la molécule étudiée. En pratique, cela dépend de l'algorithme utilisé pour faire converger le calcul, ainsi que de la fonction d'onde d'essai initiale. En effet, le calcul variationnel converge vers le minimum local le plus proche du point de départ. Si

l'on démarre le calcul avec une fonction d'onde proche de celle décrivant l'état de cœur, le calcul peut converger sur la solution espérée.

Une autre approche possible consiste à utiliser les OM d'un calcul de l'état fondamental, puis de faire une IC convenablement choisie pour décrire l'état de cœur. Cette méthode est souvent utilisée pour calculer des états excités de valence, par exemple en EOM-CCSD (voir articles 7 à 9). Toutefois, elle ne fonctionne que dans la mesure où les OM de l'état fondamental sont (relativement) proches de celles de l'état excité. Or, comme on le verra plus loin, la densité électronique d'un état de cœur est très différente de celle de l'état fondamental. Un exemple frappant est celui d'un calcul " state-averaged " par Shirai *et al.* [166] sur l'acide acétique et l'acide formique : les erreurs sur les seuils d'ionisation O1s approchent la dizaine d'eV.

a) Présentation

Le modèle du cœur équivalent (" Equivalent Core Model ou Approximation), aussi appelé Z+1 pour des raisons explicitées ci-après, a été initialement proposé par Jolly et Hendrickson [167,168], après avoir été pressenti expérimentalement par Nakamura *et al.* [169]. Le but premier de cet article était de proposer des grandeurs thermodynamiques qui soient correctement corrélées aux énergies d'ionisation de cœur de *solides* (notamment des sels). Par la suite, ce modèle a été largement employé pour des molécules en phase gazeuse, notamment par Schwarz [170]. On part de l'hypothèse qu'après l'éjection d'un électron 1s, les électrons de valence s'adaptent à l'accroissement de la charge du cœur (défini comme étant le noyau et la couche 1s). Si l'on admet que des cœurs qui ont la même charge sont chimiquement équivalents, on peut conclure que l'accroissement de la charge du cœur d'une unité correspond au remplacement du noyau par celui de l'élément qui le suit dans la classification périodique. Par exemple, cela signifie que l'ion de cœur de l'ammoniac $N^*H_3^+$ est équivalent à l'état fondamental de la molécule OH_3^+, du point de vue de leurs électrons de valence. On voit tout de suite l'avantage au niveau *ab initio* : il est beaucoup plus aisé de calculé l'état fondamental de OH_3^+ (molécule à couches fermées) qu'un état excité de cœur de NH_3^+*.

Le modèle du cœur équivalent peut se formaliser au niveau des équations Hartree-Fock [171]. Pour cela, exprimons le " Term Value " ou TV, défini comme la différence entre l'énergie d'un état excité de cœur $1s \rightarrow i^*$ et l'énergie d'ionisation de cœur $1s \rightarrow \infty$:

$$TV(1s \rightarrow i^*) = E(1s \rightarrow \infty) - E(1s \rightarrow i^*)$$

Si l'on fait l'hypothèse que le nuage électronique de l'ion de cœur ne change pas lorsqu'on amène l'électron supplémentaire i*, le TV se réduit aux termes impliquant l'électron i* :

$$TV(1s \rightarrow i^*) = \left\langle i^* \left| \frac{-Z_E}{r_E} \right| i^* \right\rangle + J_{i^*,1s} \pm K_{i^*,1s} + \sum_{a \neq 1s} \left[2J_{i^*,a} - K_{i^*,a} \right] + \left\langle i^* \left| \frac{\Delta_{i^*}}{2} \right| i^* \right\rangle + \sum_{B \neq E} \left\langle i^* \left| \frac{-Z_B}{r_B} \right| i^* \right\rangle$$

où E désigne le noyau de l'atome excité de cœur, B les autres atomes et a les électrons des autres couches (de valence ainsi que les couches 1s qui ne sont pas excitées). Le signe vaut + pour le triplet de spin et – pour le singulet. Maintenant, on applique le modèle du cœur équivalent en remplaçant l'atome E par son suivant dans le tableau périodique, ce qui revient à ajouter un proton et un électron dans la couche 1s qui redevient complète. Dans ce cas, le TV vaut :

$$TV_{Z+1}(1s \rightarrow i^*) = \left\langle i^* \left| \frac{-(Z_E + 1)}{r_E} \right| i^* \right\rangle + 2J_{i^*,1s} - K_{i^*,1s} + \sum_{a \neq 1s} \left[2J_{i^*,a} - K_{i^*,a} \right] + \left\langle i^* \left| \frac{\Delta_{i^*}}{2} \right| i^* \right\rangle + \sum_{B \neq E} \left\langle i^* \left| \frac{-Z_B}{r_B} \right| i^* \right\rangle$$

et l'état correspondant est un doublet de spin. La différence entre ces deux TV vaut (pour le singulet) :

$$TV_{Z+1}(1s \rightarrow i^*) - TV(1s \rightarrow i^*) = \left\langle i^* \left| \frac{-1}{r_E} \right| i^* \right\rangle + J_{i^*,1s}$$

L'hypothèse du cœur équivalent repose sur l'idée que la répulsion coulombienne entre les électrons 1s et i* compense parfaitement l'attraction électrostatique entre le proton supplémentaire et l'électron i* :

$$\left\langle i^* \left| \frac{1}{r_E} \right| i^* \right\rangle = J_{i^*,1s} = \int \left| i^*(r_1) \right|^2 \frac{1}{r_{12}} \left| 1s(r_2) \right|^2 dr_1 dr_2$$

Autrement dit, à cause de la localisation de l'orbitale 1s autour du noyau a, on suppose que l'électron 1s surnuméraire écrante parfaitement le proton. Dans ce cas, on voit que le TV est identique dans la molécule excitée de cœur et dans son équivalent Z+1. En pratique, cela ne peut pas être entièrement vrai car l'intégrale d'échange $K_{i^*,1s}$ de l'atome Z+1 n'est pas rigoureusement identique à celle de l'atome excité de cœur. La valeur de $K_{i^*,1s}$ sera d'autant plus élevée que le recouvrement $\langle 1s | i^* \rangle$ sera proche de 1, c'est-à-dire que l'orbitale i* sera localisée autour de l'atome excité de cœur. A l'inverse, cette intégrale sera faible pour les états de Rydberg. Ce sera aussi le cas si Z est élevé et que l'orbitale i* pénètre peu dans le cœur : on peut ainsi prédire [171] que le modèle Z+1 devrait mieux fonctionner pour les atomes de la seconde ligne de la table périodique que pour ceux de la première ligne. Toutefois, d'autres effets, notamment de corrélation, interviennent.

La validité du modèle Z+1 peut être testée en la comparant au résultat d'un " vrai " calcul de l'état de cœur. A titre d'illustration, on a calculé la fonction d'onde de différents états électroniques du carbone et de l'azote : C(^{3}P), N^+(^{3}P), N(^{4}S) et C*(^{5}S) excité de cœur 1s $\rightarrow$ 2p. Notons que d'après le modèle Z+1, on a : C*(^{5}S) $\equiv$ N(^{4}S). Le spin élevé permet de forcer les trois orbitales 2p à rester dégénérées. Les états ^{3}P et ^{4}S ont été obtenus au moyen d'un calcul ROHF-GVB (*vide infra*). L'état ^{5}S a été obtenu au moyen d'un calcul MCSCF dans l'espace (1s, 2s, 2p). La fonction d'onde était moyennée sur les états $2s^{-1}$ et $1s^{-1}$ mais avec un poids de 100% sur le second. Afin de s'affranchir du problème du choix de la base, on a utilisée la base cc-pV5Z de Dunning [172] sous une forme totalement décontractée : 14s8p4d3f. Dans ce cas, la description de la couche s par une combinaison linéaire de 14 gaussiennes permet d'éviter la question du choix des exposants – carbone ou azote. On génère donc des orbitales naturelles atomiques ou ANO telles que définies par Almlöf et Taylor [173]. Les exposants choisis étant ceux du carbone, le calcul de l'état fondamental ^{3}P de C redonne les coefficients ANO de la base cc-pV5Z, tels qu'optimisés par Dunning. Les courbes suivantes représentent la densité de probabilité radiale pour les couches 1s, 2s et 2p (Figure 3.4. page suivante).

Pour ce qui concerne la couche 1s, il y a une nette différence entre les états fondamentaux du carbone et de l'azote C(^{3}P) et N(^{4}S). On remarque que l'orbitale 1s de l'atome excité de cœur C*(^{5}S) est un peu plus contractée que dans l'état fondamental C(^{3}P). Elle tend à se rapprocher de son analogue Z+1, l'azote N(^{4}S). Enfin, les OA 1s de N(^{4}S) et N^+(^{3}P) sont identiques, comme on s'y attend pour une ionisation de valence (Figure 3.5. page suivante).

Enfin, pour la partie externe de la couche 2s, il y a cette fois une différence nette entre l'azote neutre et l'ion N^+. Pour le carbone excité de cœur, on a toujours une situation intermédiaire entre le carbone et l'azote. Toutefois, dans la partie interne, qui se recouvre avec la 1s, le carbone C*(^{5}S) est encore plus proche de l'azote que du carbone (Figure 3.6.).

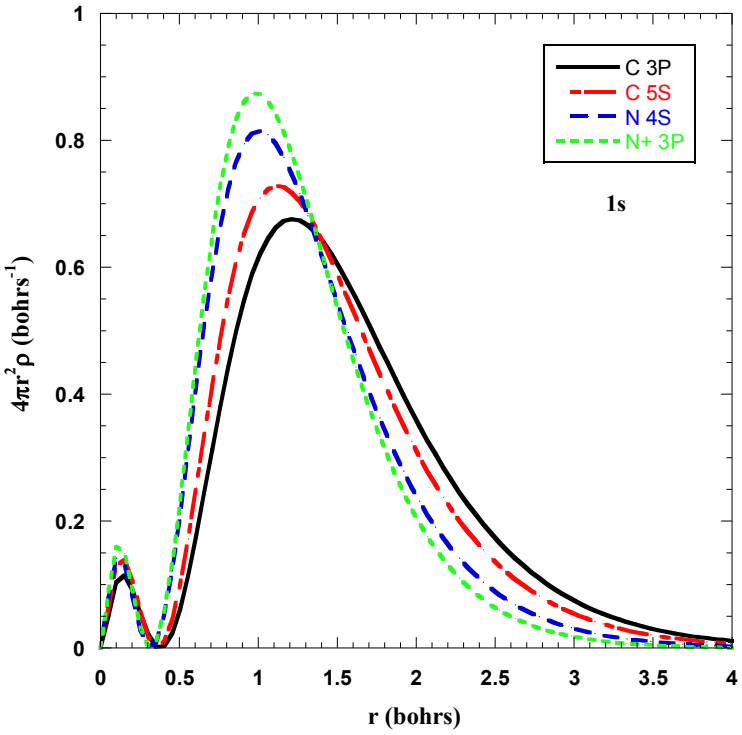

Figure 3.4. Densité de probabilité radiale : orbitales 1s.

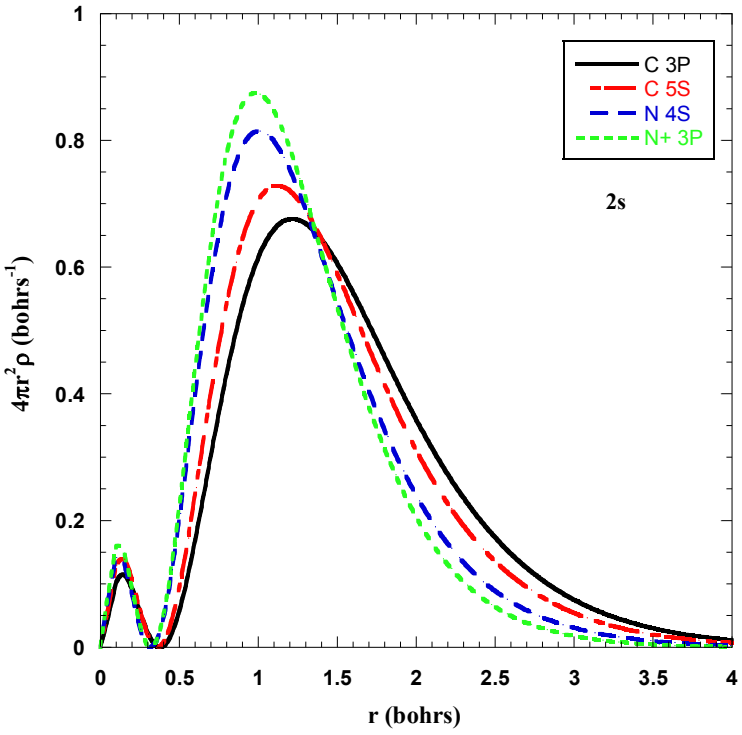

Figure 3.5. Densité de probabilité radiale : orbitales 2s.

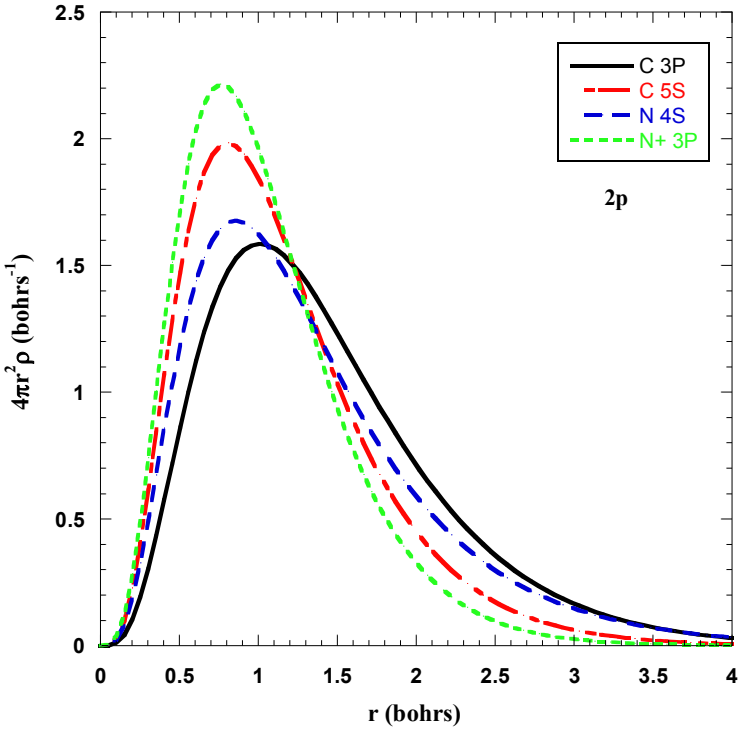

Figure 3.6. Densité de probabilité radiale : orbitales 2p.

En ce qui concerne l'orbitale 2p, la probabilité maximale pour le carbone excité de cœur se situe clairement au même niveau que l'azote et diffère notablement de la valeur de l'état fondamental de C. Ainsi, en accord avec le modèle, on peut conclure que les électrons de valence se comportent plus ou moins de la même manière dans l'atome excité de cœur que dans son analogue Z+1.

Enfin, il est remarquable que Hurley [174] avait proposé dès 1961 d'étudié des molécules doublement chargées par une méthode de type Z+1 : il s'agissait d'obtenir des fonctions d'ondes d'une molécule telle que F_2^{++} à partir de celles de la molécule isoélectronique O_2 au moyen d'un facteur de contraction (voir aussi [7]).

b) Mise en œuvre

La mise en œuvre du modèle Z+1 s'inspire des idées de Schwarz [170,175,176] et Millié [177-180]. Le but est de calculer *ab initio* les TV des différents états excités de cœur, et de les comparer aux TV expérimentaux afin d'attribuer les spectres mesurés. Remarquons que ceci n'est possible que si les énergies d'ionisation de cœur ont été aussi mesurées, par exemple en XPS, ce qui permet d'obtenir des TV expérimentaux. En première approximation, le TV vaut :

$$TV(1s \rightarrow i^*) = - \varepsilon_{i^*}$$

Où ε_{i^*} est l'énergie mono-électronique de l'orbitale virtuelle RHF i* obtenue après un calcul de l'ion cœur équivalent (EICVOM ou " Equivalent Ionic Core Virtual Orbital Model "). Il s'agit en fait du théorème de Koopmans [181] " à l'envers " : partant de l'ion de cœur, on crée l'état excité de cœur en amenant un électron sur l'orbitale d'énergie ε_{i^*}.

Comme on peut le voir dans les articles ci-après, cette approximation fonctionne assez mal, les TV calculés étant trop petits de 1 à 2 eV pour les transitions vers les OM de valence π*.

L'explication est la même que pour le théorème de Koopmans : on a négligé la perturbation que l'électron i* exerce sur les électrons de l'ion de cœur. Formellement, cette perturbation peut se diviser en deux termes [178] :

$$TV(1s \rightarrow i^*) = - \varepsilon_{i^*} + P + C$$

- *P* est un terme de repolarisation (ou relaxation) qui traduit le fait que le nuage électronique de l'ion va se déformer sous l'influence de l'électron i*.

- *C* est un terme de corrélation dû au fait que l'arrivée de l'électron i* (de valence) crée de nouvelles paires avec les électrons déjà présents. En conséquence, les mouvements des électrons, qui sont corrélés deux à deux, ne sont plus les mêmes, ce qui se traduit par une énergie supplémentaire. Notons que pour l'énergie d'ionisation de cœur, Carniato et Luo [182] ont subdivisé ce terme de corrélation en trois parties : la corrélation cœur-paire, la corrélation cœur-valence et la corrélation valence-valence. Dans le cas présent – où l'on analyse la différence entre l'ion de cœur et l'état excité de cœur – le terme *C* correspond en fait à la corrélation valence-valence entre l'électron i* et les autres. Carniato et Luo [182] ont aussi inclus une correction relativiste, qui reste assez faible pour les atomes de la première ligne de la table périodique (voir aussi les articles de Chong [183-186]). Enfin, Carniato et Luo [182] n'ont pas pris en compte une éventuelle correction vibrationnelle (voir section 3.6 plus loin).

Il est important de garder à l'esprit que termes *P* et *C* sont relativement faibles si on a pris la précaution d'utiliser les OM de l'ion de cœur. Ils seraient beaucoup plus importants si l'on utilisait les OM de l'état fondamental pour décrire les états de cœur.

En pratique, on peut montrer [187-189] que le terme *P* peut s'obtenir en faisant une IC des mono-excitations par rapport aux états excités $1s \rightarrow i^*$: on construit donc une matrice contenant les configurations du type $1s\ b \rightarrow i^*\ j^*$:

$$\Psi_{CI} = \sum_{i^*} \left[C_{i^*} + \sum_{b} \sum_{j^*} C_{bi^*} a_b a^+_{j^*} \right] a_{1s} a^+_{i^*} \Psi_{Ref}$$

où l'indice b désigne les OM occupées (en excluant toutefois les 1s des autres atomes non-excités de cœur), tandis que les indices i* et j* les OM virtuelles correspondent à l'espace CAS augmenté des orbitales diffuses de Rydberg. Ici Ψ_{Ref} désigne le déterminant RHF couches fermées de l'état fondamental mais en utilisant les OM de l'ion de cœur. Cette matrice est diagonalisée par la méthode de Davidson [190] pour trouver les fonctions propres les plus basses. Les valeurs propres donnent des TV plus proches de l'expérience (quelques dixièmes d'eV). On voit que par construction, cet espace d'IC permet de décrire les états doublement excités (" shake up "), s'ils sont présents.

Le terme *C* est quant à lui évalué par un calcul multi-références MP2, en utilisant l'espace d'IC précédemment utilisé comme fonctions d'ondes d'ordre zéro. Le calcul est effectué au moyen de la version diagrammatique [21,22] du programme CIPSI [20]. Ainsi les tri et quadri-excitations sont traitées perturbativement à l'ordre 2 en énergie.

Enfin, pour interpréter les spectres observés, il est nécessaire d'avoir une idée de l'intensité des transitions calculées. Dans le cadre du modèle Z+1, ces intensités ne peuvent pas être évaluées facilement, du fait du nombre " non physique " d'électrons dans la molécule Z+1. C'est pourquoi les intensités sont estimées en calculant le moment de transition entre l'orbitale 1s et l'orbitale i* :

$$I(1s \rightarrow i^*) \approx c_0^2 \left| \langle 1s | \vec{\nabla} | i^* \rangle \right|^2 \text{ ou } I(1s \rightarrow i^*) \approx c_0^2 \left| \langle 1s | \vec{r} | i^* \rangle \right|^2$$

où c_0^2 est le poids du déterminant 1s → i* dans la fonction d'onde. Cette approximation ne se justifie en réalité que si c_0^2 est proche de 1 (excitation mono-électronique) et n'est pas valable en particulier pour les "shake up".

c) Article 9 : Electronic excitation of gaseous pyrrole and pyrazole by inner-shell electron energy loss spectroscopy

d) Article 10 : The core excitation of pyridine and pyridazine: An electron spectroscopy and *ab initio* study

e) Article 11 : Re-analysis of the K-shell spectrum of benzene

f) Commentaires

Après la parution de l'article 10, les spectres d'excitation en couche interne de la pyridine ont été mesurés par NEXAFS avec une meilleure résolution (65 meV pour C1s et 150 meV pour N1s) [191]. Des calculs de type STEX, DFT et CI ont permis de simuler les spectres et la structure vibrationnelle a été prise en compte au moyen d'un modèle de type couplage linéaire. En particulier, on montre que les effets vibrationnels sont responsables du mauvais rapport des intensités calculées des deux pics C1s → 1π* par rapport à l'expérience :

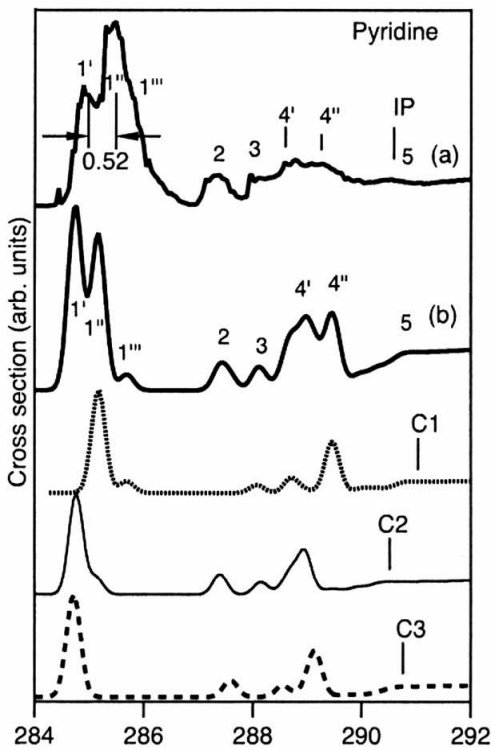

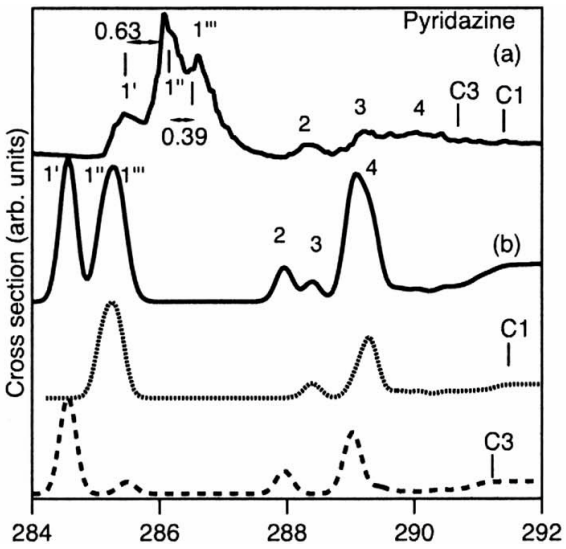

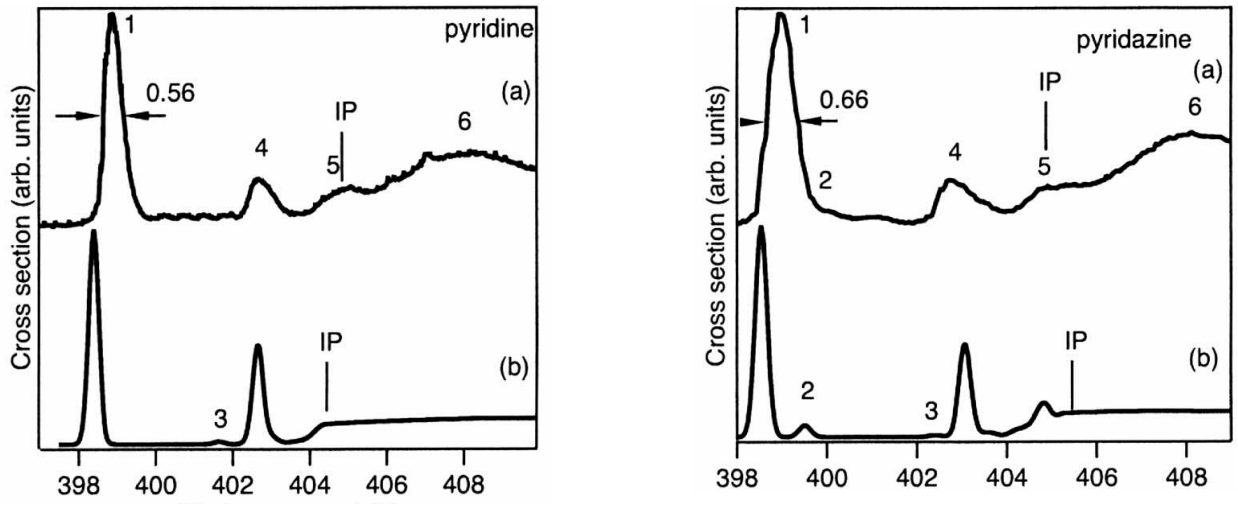

Figure 3.7. Spectres NEXAFS mesurés (en haut) et calculés de la pyridine d'après [191].

Un autre effet, que nous avions mis en évidence aussi dans le cas du benzène (tableau 6, article 11), est l'influence des orbitales de Rydberg et des di-excitations sur les énergies (et les TV) des transitions N1s $\rightarrow \pi^*$ calculées (tableau page suivante). Comme pour le benzène, on voit que l'absence d'orbitales de Rydberg dans le calcul prédit l'excitation vers l'OM $3\pi^*$ au-dessus du seuil d'ionisation. Pour les excitations $1\pi^*$ et $2\pi^*$, ce sont les di-excitations qui influent le plus. On remarque que les calculs de l'article 11, en dépit d'une taille d'IC et d'un nombre d'orbitales de Rydberg relativement limités, reproduisent assez correctement les TV et même mieux que ceux de la référence [191].

Rydberg ?	Espace Actif	Nombre d'électrons	$1\pi^*(b_1)$	$2\pi^*(a_2)$	$3\pi^*(b_1)$
Non	$3\pi/1s/3\pi^*$	6/1/1	401.68	403.52	407.80
TV			4.41	2.57	-1.71
Oui	$3\pi/1s/24\pi^*$	6/1/1	401.68	403.53	404.99
TV			4.42	2.57	1.10
Oui	$3\pi/1s/24\pi^*$	6/1/1;5/1/2	400.61	402.18	404.84
TV			5.49	3.92	1.25
TV (Article 10)			5.79	4.30	1.51
TV exp.			6.1	4.9	2.2

Plus récemment, les spectres K-shell des azabenzènes (pyridine, pyridazine, pyrimidine, pyrazine et *s*-triazine) ont été à nouveau mesurés par NEXAFS et calculés par une méthode DFT (deMon) [192]. Les énergies absolues, obtenues avec une correction relativiste de +0.3 eV pour N et + 0.2 eV pour C, ont une précision de quelques dixièmes d'eV. L'interprétation des spectres ne diffère pas sensiblement de celle présentée dans l'article 10 et dans Kolczewski *et al.* [191].

Le spectre K-shell du benzène a depuis était remesuré par rayonnement synchrotron dans plusieurs articles [193-195], le premier étant paru en même temps que l'article 11. La meilleure résolution permet de distinguer une structure fine [195] :

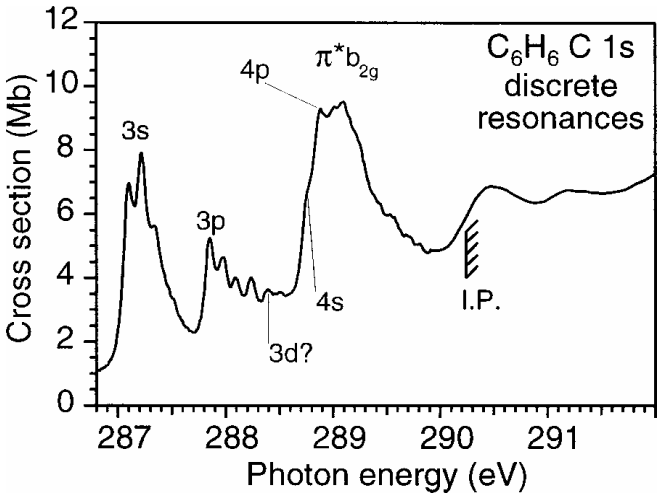

Figure 3.8. Spectre NEXAFS du benzène d'après [195].

La comparaison du spectre de C_6H_6 avec celui de C_6D_6 [194] montre que certains de ces pics sont d'origine vibrationnelle. Dans deux de ces articles [193,194], l'attribution a été faite sur la base de calculs de type DFT, notamment avec StoBe [196]. Les différences sont assez sensibles par rapport à l'article 11, notamment pour le pic à 287 eV attribué à une surprenante transition σ^*(C-C), le pic à 288 eV étant lui attribué à une transition σ^*(C-H) [193]. En ce qui concerne la bande à 289 eV, le caractère di-excité de la transition n'est pas présent dans les calculs DFT. Pour une attribution définitive, il faudrait reprendre les calculs d'IC en utilisant la méthode décrite dans la section suivante, accompagnés éventuellement de calculs de structure vibrationnelle.

g) Inconvénients du modèle du cœur équivalent

Comme le montrent les articles précédents, en particulier celui portant sur le benzène, le modèle Z+1 présente un certain nombre d'inconvénients pour les calculs d'états excités de cœur. Le principal défaut est lié à la présence d'un électron et d'un proton surnuméraires par rapport à l'état fondamental : il n'est pas possible d'obtenir les énergies d'excitation absolues mais seulement les TV. De plus, les états triplet et singulet de spin sont décrits par un même doublet (alors que des transitions vers des triplets ont été observées en ISEELS [197]). Il n'est pas non plus possible d'obtenir des intensités fiables lorsque la fonction d'onde n'est pas correctement décrite par un seul déterminant (shake up). De plus, si l'on veut s'intéresser à des excitations d'autres couches (2s, 2p, 3s, 3p …) pour des éléments plus lourds, ce modèle ne s'applique plus. On peut aussi ajouter qu'il impose *de facto* une approche localisée du trou de cœur (section 4.c). Comme il est maintenant possible de faire converger des calculs d'états de cœur, ce modèle s'avère surtout utile pour sa puissance d'interprétation, par exemple pour expliquer la géométrie des molécules excitées de cœur. Notons toutefois que le groupe de Cederbaum [198,199] a développé récemment un modèle corrigé (cECM) qui donne accès aux " vraies " énergies de cœur.

4) Méthodes ab initio *explicites*

Les méthodes " explicites " utilisent des OM issu d'un calcul comprenant un vrai trou de cœur plutôt que de recourir au modèle du cœur équivalent. Normalement, ce calcul est du type Hartree-Fock ou DFT. En particulier, pour autant que nous le sachions, il est très difficile [200], voire impossible de faire des calculs du type MCSCF/CASSCF avec un trou dans une orbitale de

cœur. En vertu du principe variationnel, le calcul converge vers un état avec le trou dans une couche de valence. Il semble qu'il soit possible de faire des calculs multi-configurationnels avec DALTON par la méthode RASSCF dans des atomes [201] ou de petites molécules telles que O_2 [202]. Dans ce dernier cas, on a fixé l'occupation des orbitales $1\sigma_g$ et $1\sigma_u$ à trois électrons mais ces orbitales sont "gelées" lors du calcul RASSCF.

a) Quelques exemples

De nombreuses méthodes ont été ou sont utilisées depuis plusieurs décennies pour calculer les énergies d'ionisation/excitation de cœur. On peut distinguer les méthodes où l'on utilise les OM issues d'un calcul de l'état fondamental (" frozen ") de celles où ce sont les OM d'un état de cœur qui sont employées (" relaxed "). Lorsque ces OM de référence sont de type Hartree-Fock, on peut utiliser pour le traitement post-Hartree-Fock les mêmes techniques que celles utilisées pour traiter les excitations de valence :

- La méthode SAC-CI [118-121], avec l'approche " frozen ", a été utilisée, par exemple, pour le calcul de l'ion de cœur de l'eau par Sankari *et al.* [203]. Elle a été maintenant adaptée [204] pour utiliser les OM de l'ion de cœur. Les méthodes Coupled Cluster du type EOM-CCSD ont aussi été utilisées ponctuellement [205]. On peut aussi utiliser les méthodes de paires telles que MCPF [206] et MCCEPA [200].

- La méthode LSCF [207] a été aussi appliquée dans le contexte de la spectroscopie de cœur [208,209]. Cette technique résout notamment le problème de la non-orthogonalité entre l'état fondamental et l'état de cœur propre aux méthodes de type " Δ " (ΔSCF, ΔKS, ΔMP2 …). Par ailleurs, il est possible de geler l'orbitale de cœur mono-occupée. Les applications concernent l'ionisation de cœur de macromolécules biologiques (dans un modèle QM/MM).

- Le programme STEX de Ågren [191,210-213] est du type " échange statique " [214] : il est basé sur une modification de l'approximation Tamm-Dancoff de la RPA, où l'on néglige le couplage des excitations provenant des couches internes d'atomes différents. Les énergies d'excitation de cœur sont obtenues à partie de celle de l'ion de cœur sans tenir compte des effets dus à l'électron supplémentaire, car on ajoute l'énergie mono-électronique calculée en résolvant une équation Hartree-Fock de l'électron de cœur. La méthode STEX permet de décrire les résonances de forme du continuum en utilisant une base étendue constituée d'un grand nombre d'orbitales diffuses. Ceci est rendu possible par l'usage de méthodes SCF directes (DSCF). La technique a été perfectionnée en remplaçant la densité électronique de l'ion par celle du premier état excité de cœur ("screened potential" [211]. La méthode STEX est maintenant disponible dans la dernière version du code DIRAC [215-217].

- Le programme GSCF3 de Kosugi [218-220] est lui aussi du type "échange statique", et utilise les IVO [214]. Par contre, il n'est pas capable de décrire le continuum. La précision de ces programmes est de l'ordre de 1 eV pour les atomes légers.

- Les méthodes de type propagateurs telles que ADC(2) [221,222] et ADC(4) [223,224] pour l'ionisation. Ces méthodes sont utilisées intensivement dans le contexte de l'excitation de cœur ([225] et références citées). Dans ce contexte, elles sont basées sur l'approximation de la séparation cœur-valence [226], c'est-à-dire que toutes les

configurations utilisées pour décrire l'état excité ont exactement une orbitale de cœur mono-occupée – c'est aussi le cas dans nos propres calculs. Il n'y a donc pas entre autres de configurations avec une orbitale de cœur complètement vide. ADC(2) a pour particularité d'être "size-consistent" et d'utiliser les OM de l'état fondamental, la relaxation s'effectuant par les mono et di-excitations. Les énergies et moments de transition des états décrits par une mono-excitation sont exacts au second ordre. Par contre, la description de la relaxation des états doublement excités ("shake up") est incomplète, puisque qu'il faudrait inclure des excitations d'ordre supérieur.

- Récemment, les méthodes basées sur la DFT se sont généralisées en spectroscopie de cœur. Les premiers articles publiés par Chong et Bureau [183-186,227-232] utilisaient deMon [233,234] et concernaient essentiellement l'ionisation de cœur. Il est maintenant possible de calculer des spectres d'excitation cœur avec ADF [235-237], le programme StoBe [196], une variante de deMon optimisée pour les spectres de cœur, ou encore plus récemment ORCA [238,239]. Grâce à l'inclusion d'une partie de la corrélation dans une fonction d'onde mono-déterminantale, ces programmes permettent de calculer facilement les spectres K-shell (ou d'autres couches) de systèmes de grande taille en un temps très court. Ils permettent aussi de traiter les phases liquides ou solides (en particulier l'eau et la glace [240-243]). De plus, les calculs peuvent être faits en utilisant l'approximation du potentiel de transition [244,245], une idée ancienne de Slater : on montre que si l'on laisse une occupation fractionnaire de ½ dans la couche excitée, les effets de relaxation sont pris en compte jusqu'au second ordre. Les résultats améliorent sensiblement les valeurs STEX [185,246]. Pour ce qui est du choix de la fonctionnelle utilisée, de nombreuses publications ont étudié la question [247-254]. Une modification spécifique de B3LYP a même été proposée [248]. Cependant, l'utilisation d'OM DFT n'est pas un bon choix si l'on a l'intention de faire des calculs d'IC par la suite.

- Les méthodes d'IC ont longtemps été illustrées par les travaux du groupe de Decleva [255-287]. La méthodologie employée était proche de la nôtre : calcul de l'ion de cœur au moyen de MELDF [288], puis calcul d'interaction de configurations avec QDPT [289]. Cette méthode ne semble plus utilisée depuis 2001 [287] et les auteurs se sont orientés vers la description du continuum au moyen de fonctions B-splines [290-295], puis l'application de la TD-DFT à l'excitation de cœur, dans ADF [296-301].

Comme pour les calculs d'excitation de valence, les méthodes TD-DFT (notamment dans ADF et StoBe) sont à l'heure actuelle employées de plus en plus fréquemment pour l'excitation de cœur, en raison de leur coût plus faible que les méthodes de type IC ou propagateurs.

b) Méthodologie choisie

La méthode de calcul que nous avons mise au point en 2001-2002 pour le calcul des spectres d'excitation de cœur s'inspire directement de la procédure utilisée précédemment avec le modèle du cœur équivalent. Une des différences tient au fait que les OM utilisées comme base commune pour la description des états de cœur sont maintenant des OM du " vrai " ion de cœur. Celles-ci sont dorénavant obtenues au niveau ROHF-GVB [302] en utilisant le programme GAMESS-US [303,304]. En général, le calcul est amorcé en utilisant les OM cœur équivalent pour accélérer la convergence. Les algorithmes DIIS [305] ou SOSCF [302] peuvent être utilisées indifféremment. L'énergie trouvée (à laquelle on soustrait évidemment l'énergie RHF de l'état fondamental) fournit directement l'énergie d'ionisation de cœur au niveau ΔSCF. Cette valeur peut d'ailleurs être raffinée au niveau MP2, en utilisant les méthodes RMP [306,307] ou ZAPT [308-310]

implémentées dans GAMESS. Il est en effet important de se rappeler qu'en présence d'une couche ouverte, il n'y a pas de forme unique de la théorie MP2 [310,311]. Pour rester cohérent avec les états excités de cœur, l'énergie de l'ion de cœur est en fait celle calculée avec CIPSI en prenant le seul déterminant ROHF comme fonction d'onde d'ordre zéro.

Comme précédemment, les énergies d'excitation de cœur 1s → i* sont donc obtenues en corrigeant l'énergie d'ionisation de cœur :

$$E(1s \rightarrow i^*) = E(1s \rightarrow \infty) + \varepsilon_{i^*} + P + C$$

Le terme de repolarisation *P* est toujours évalué en diagonalisant la matrice d'IC formée de toutes les mono-excitations par rapport aux états mono-excités de cœur, ce qui peut s'écrire :

$$\Psi_{CI} = \sum_{i^*}\left[C_{i^*} + \sum_{b} \sum_{k} C_{bk} a_b a_k^+ \right] a_{1s} a_{i^*}^+ \Psi_{Ref}$$

Où l'indice b désigne les OM occupées, l'indice k les OM virtuelles, l'indice i* les OM virtuelles correspondant aux états excités de cœur les plus bas. L'indice k balaye cette fois l'ensemble des virtuelles, compte tenu du fait qu'on a gagné un ordre de grandeur sur la taille de la matrice d'IC.

Le terme de corrélation *C* reste calculé en effectuant un calcul multi-référence MP2 sur cette matrice d'IC, utilisée comme fonction d'onde d'ordre zéro, avec cette fois-ci la dernière version du CIPSI diagrammatique [312-317]. Afin de réduire le temps de calcul, on utilise la méthode d'extrapolation proposée par Angeli *et al.* [318]. En effet, la plupart des déterminants de la matrice d'IC ont un poids très faible dans la fonction d'onde obtenue. On peut donc diviser l'espace S en deux classes (CIPSI diagrammatique à trois classes [312-317]), et n'effectuer le calcul de perturbation que sur le sous-espace appelé G contenant uniquement les déterminants " les plus importants ". En pratique, ces déterminants sont choisis si leur poids est supérieur à un seuil τ fixé arbitrairement :

- Diagonalisation de la matrice d'IC : $P_S H P_S \left|\Psi_m^{(0)}\right\rangle = E_m^{(MR)} \left|\Psi_m^{(0)}\right\rangle$ avec : $P_S = \sum_{N \in S} \left|N\right\rangle\left\langle N\right|$
- Obtention d'une fonction d'onde d'ordre zéro de l'état m, exprimée sur l'espace S :

$$\left|\Psi_m^{(0)}\right\rangle = \sum_{N \in S} C_N^m \left|N\right\rangle$$

- Sélection du sous-espace G : le déterminant $\left|N\right\rangle$ appartient à G si son poids dans la fonction d'onde de $\left|\Psi_m^{(0)}\right\rangle$ est supérieur à un seuil τ :

$$\left\{ G \subset S \;\middle|\; \left|N\right\rangle \in G \Leftrightarrow W_G^{(m)} = \sum_{N \in S} \left|C_N^m\right|^2 \geq \tau \right\}$$

Dans la méthode d'extrapolation proposée par Angeli *et al.* [318], on effectue le calcul CIPSI perturbé pour quelques valeurs décroissantes de τ, par exemple 0.999, 0.998, 0.997, 0.996, 0.995, et 0.994. On trace alors pour chaque état calculé les énergies perturbées en fonction de τ, et on extrapole les énergies correspondant à τ = 1 (c'est-à-dire G ≡ S) par une méthode de moindres carrés.

Pour illustrer cette idée, on peut prendre un exemple où le calcul complet ne prend pas trop de temps, avec un nombre restreint d'états. La courbe ci-dessous montre les énergies des états de symétrie A_2 (Rydberg 3d, 4d et 5d), du 2,5-dihydrofurane au seuil de l'oxygène :

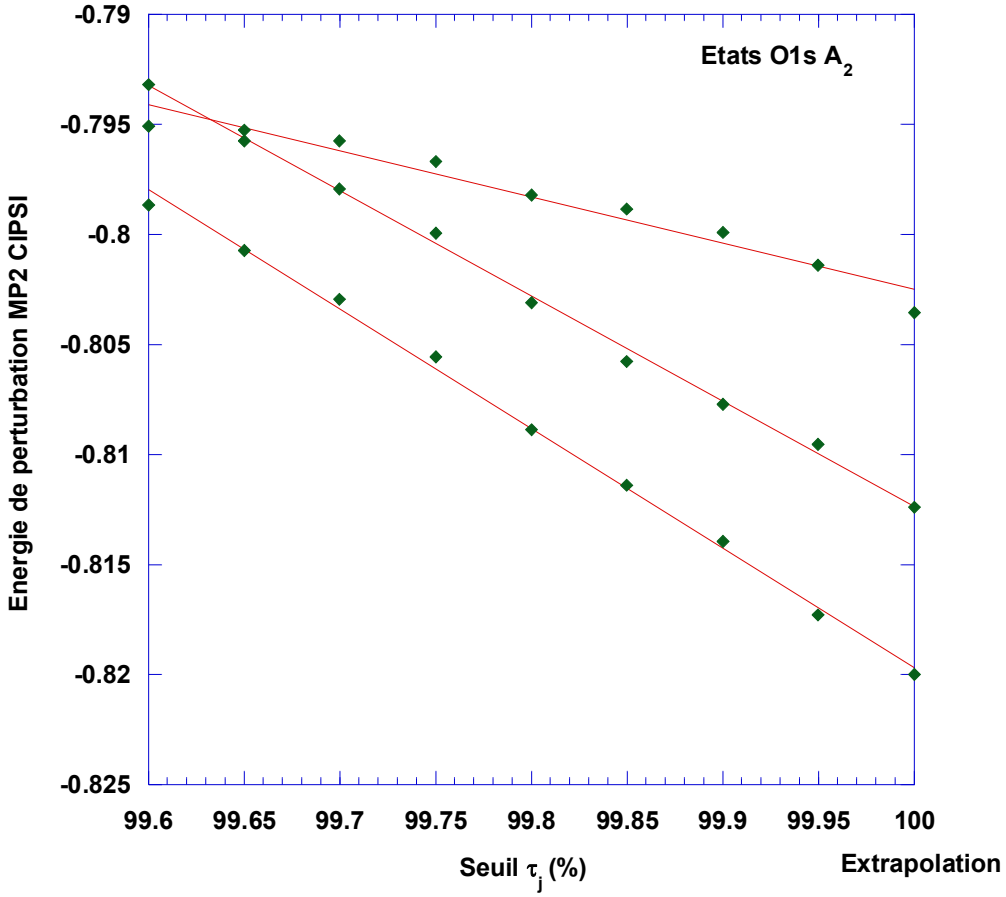

Figure 3.9. Exemple d'extrapolation par CIPSI diagrammatique.

Comme on peut le voir l'erreur commise est de l'ordre de quelques milliHartrees, soit environ 0.1 eV, ce qui est négligeable dans la gamme d'énergie étudiée. Le gain en temps de calcul se devine aisément en regardant le nombre de déterminants utilisés pour chaque valeur de τ :

τ	N	τ(Etat 1)	τ(Etat 2)	τ(Etat 3)
0.960	62	.960	.985	.963
0.965	100	.965	.985	.967
0.970	158	.970	.986	.971
0.075	238	.975	.988	.975
0.980	364	.980	.990	.980
0.985	580	.985	.992	.985
0.990	994	.990	.994	.990
0.995	1802	.995	.996	.995

Soit un total de 1802 déterminants (sur un total de 9282 soit un cinquième) qui contiennent 99.5 % des fonctions d'ondes du calcul complet. On peut aussi remarquer que 62 déterminants (soit 0.67 %) concentrent déjà 96% des fonctions d'onde.

Dans un certain nombre de cas, détaillés dans les articles qui suivent, les fonctions d'onde calculées montrent un mélange de mono et di-excitations. La question se pose alors de savoir si la transition calculée est mono-excitée ou correspond à un véritable " shake up ". En particulier, le caractère multi-configurationnel de la fonction d'onde peut être un artefact de l'IC dû à l'emploi des OM de l'ion de cœur pour décrire les états excités de cœur. Afin de trancher la question, nous utilisons la méthode des " orbitales naturelles " initialement proposée par Löwdin [319]. La présence de quatre orbitales mono-occupées signe sans ambiguïté la présence d'un état di-excité. La nature de l'état (valence et/ou Rydberg), est diagnostiquée en comparant la valeur moyenne de r^2 $\langle r^2 \rangle$ à celle de l'état fondamental.

c) Localisation *vs* délocalisation du trou de cœur

La question de la localisation du trou de cœur est très largement débattue [320], au moins depuis Snyder en 1972 [321], qui a le premier suggéré que le trou de cœur devait être localisé. Il faut distinguer le cas des molécules diatomiques homonucléaires.

- Cas des molécules diatomiques homonucléaires

Considérons l'ionisation de cœur d'une molécule possédant deux atomes lourds équivalents – le cas le plus simple étant une molécule diatomique homonucléaire telle que N_2. Dans l'état fondamental, il existe deux façons distinctes de se représenter les couches 1s :

- dans une représentation de type OM, les deux OA 1s de chacun des atomes G et D vont se combiner pour donner naissance à deux OM σ_g et σ_u quasi-dégénérées et qui respectent la symétrie du groupe $D_{\infty h}$ de la molécule :

$$\sigma_{g,u} = \frac{1}{\sqrt{2\left(1 + \langle 1s_G | 1s_D \rangle\right)}} \left(1s_G \pm 1s_D\right)$$

  Quantitativement, la valeur du recouvrement $\langle 1s_G | 1s_D \rangle$ est négligeable, au plus de l'ordre de 10^{-4} [322]. La fonction d'onde de l'état fondamental s'écrit, en négligeant les électrons de valence, $\Phi_0^d = \left|\sigma_g^2 \sigma_u^2\right|$ et on peut créer deux ions de cœur $\Phi_g^d = \left|\sigma_g^1 \sigma_u^2\right|$ et $\Phi_u^d = \left|\sigma_g^2 \sigma_u^1\right|$, qui représentent la formulation délocalisée (d) de l'ionisation de cœur. Les énergies d'ionisation de cœur diffèrent par une quantité ΔE_{gu} assez faible.

- Dans une représentation de type VB, les orbitales $1s_G$ et $1s_D$ restent localisées sur chacun des atomes G et D et on peut construire deux déterminants dégénérés :

$$\Phi_G^\ell = \left|1s_G^1 1s_D^2\right|$$
$$\Phi_D^\ell = \left|1s_G^2 1s_D^1\right|$$

Quant à la fonction d'onde de l'état fondamental, elle s'écrit : $\Phi_0^\ell = \left|1s_G^2 1s_D^2\right|$. Pour restaurer la symétrie des fonctions d'onde des ions, il est nécessaire de les combiner pour aboutir à la description localisée (ℓ) :

$$\Phi_{g,u}^{\ell} = \frac{1}{\sqrt{2\left(1 + \left\langle \Phi_G^{\ell} \middle| \Phi_D^{\ell} \right\rangle\right)}} \left(\Phi_G^{\ell} \pm \Phi_D^{\ell}\right)$$

avec pour les énergies :

$$E_{g,u}^{\ell} = \left\langle \Phi_G^{\ell} \middle| H \middle| \Phi_G^{\ell} \right\rangle \pm \frac{\left\langle \Phi_G^{\ell} \middle| H \middle| \Phi_D^{\ell} \right\rangle}{1 \pm \left\langle \Phi_G^{\ell} \middle| \Phi_D^{\ell} \right\rangle} \text{ vu que } \left\langle \Phi_G^{\ell} \middle| H \middle| \Phi_G^{\ell} \right\rangle = \left\langle \Phi_D^{\ell} \middle| H \middle| \Phi_D^{\ell} \right\rangle$$

On voit que si l'élément de couplage $\beta = \left\langle \Phi_G^{\ell} \middle| H \middle| \Phi_D^{\ell} \right\rangle$ est faible, les énergies d'ionisation de cœur sont quasi-dégénérées et ΔE_{gu} est faible.

Il est important de remarquer que les deux représentations sont strictement équivalentes. Contrairement à ce qui est souvent écrit, la création du trou de cœur n'implique pas une rupture de symétrie et la localisation du trou de cœur : les deux atomes étant indiscernables, l'état quantique est une superposition des deux situations où le trou est créé sur l'atome de gauche et sur celui de droite. En particulier l'écart ΔE_{gu} a la même valeur dans les deux représentations et il est en principe accessible à l'expérience. Cela a été confirmé dans le cas de O_2 et N_2 [323], où on a pu montrer que la symétrie d'inversion était préservée. De même, en étudiant l'effet Auger suivant l'excitation $1s \rightarrow \sigma^*$ de O_2, Björneholm *et al.* [324] ont montré qu'il est possible de distinguer les deux atomes par mesure de leur décalage Doppler : c'est la nature du processus de mesure lui-même qui brise la cohérence quantique. En fait, on obtient un état intriqué au sens de Bell et le même phénomène a été retrouvé récemment dans le cas de N_2 [325,326]. Une autre manière de briser la symétrie consiste à pouvoir distinguer les deux atomes d'azote, ce qui a été fait sur la molécule $^{14}N^{15}N$ [327].

L'origine de la croyance selon laquelle l'ionisation de cœur induit une localisation du trou dans les molécules diatomiques vient de ce que ΔE_{gu} est très petit : il a été mesuré à 0.105 eV dans C_2H_2 [328] et 0.097 eV dans N_2 [329]. Il diminue d'ailleurs dans C_2H_4 et C_2H_6 car la liaison C-C s'allonge [328]. Une autre source de confusion tient au fait qu'au niveau théorique, l'énergie calculée au niveau Hartree-Fock est plus basse si l'on utilise des orbitales localisées à la place d'orbitales délocalisées, c'est-à-dire si l'on brise la symétrie. Cela a été d'abord montré par Bagus et Schaefer dans le cas de l'ion de cœur de O_2 [330], qui ont conclu que l'électron était éjecté spécifiquement de l'un des atomes. Comme on vient de le voir, cette interprétation est incorrecte. Plus tard, il a été montré, dans le contexte de l'IC [331,332] et dans celui des méthodes de propagateurs [333], que la levée de la contrainte de symétrie implique qu'une fraction importante du terme de corrélation *C* se retrouve incorporée dans le terme de relaxation *P*. Plus précisément, dans le cas de l'IC, Denis *et al.* [331,332] ont comparé l'approche " traditionnelle " (OM délocalisées) à l'approche " excitonique " (OM localisées). L'effet dépend de la nature des excitations incluses dans l'IC :

- les excitations intra-valence ($\sigma \rightarrow \sigma^*$ et $\pi \rightarrow \pi^*$) provoquent un important abaissement de l'énergie de l'ion de cœur, représentant la polarisation gauche-droite des couches de valence créée par le trou localisé. Dans le modèle délocalisé, cet effet n'apparaît que si l'on inclut dans l'IC des di-excitations du type $\sigma\, 1s\sigma_u \rightarrow \sigma^*\, 1s\sigma_g$, ce qui correspond à un effet de corrélation.

- Pour les mono-excitations des σ/π vers les autres OM virtuelles (notamment de Rydberg), si l'OM a un caractère anti-liant, on se retrouve dans le cas précédent. Si l'OM a un

caractère pseudo-liant (σ ou π), il n'y a pas de différence entre les approches localisée et délocalisée.

- Pour les mono-excitations des paires libres n vers des OM virtuelles v situées dans la même région de l'espace, la correction est deux fois plus importante dans le modèle localisé que dans le modèle délocalisé. La partie manquante peut être récupérée au moyen de di-excitations de type n $1s\sigma_u \rightarrow$ v $1s\sigma_g$.

En résumé, on a :

OM délocalisées	→	OM localisées
Di-excitations	→	Mono-excitations
Effet de corrélation	→	Effet de repolarisation

Ceci explique pourquoi un calcul Hartree-Fock sans symétrie donne une énergie plus basse : le calcul localisé contient les mono-excitations qui décrivent la repolarisation autour du trou alors que dans un calcul avec symétrie, cet effet ne peut être décrit que par des di-excitations, absentes en Hartree-Fock. Le raisonnement ne se limite pas à l'ionisation de cœurs des molécules diatomiques, ni aux calculs Hartree-Fock vu que le phénomène se produit aussi en DFT [334]. On peut d'ailleurs remarquer que des fonctions d'onde à symétrie brisées ont aussi été utilisées pour le calcul d'états de valence [335,336] . Dans ce cas là aussi, l'énergie Hartree-Fock est plus basse, ce qui prouve bien que le problème n'est pas lié à une hypothétique localisation du trou de cœur.

En pratique, la plupart des calculs *ab initio* en spectroscopie de cœur (y compris les cas détaillés dans les articles ci-dessous) utilisent une approche localisée qui donne des énergies plus proches de l'expérience – à ceci près que l'on suppose le paramètre $\beta = \left\langle \Phi_G^\ell \middle| H \middle| \Phi_D^\ell \right\rangle$ négligeable. Les méthodes VB ont d'ailleurs été employées dans ce contexte [337,338]. En conséquence, lorsque la molécule contient des atomes chimiquement équivalents, les calculs sont faits dans un sous-groupe du groupe de symétrie réel de la molécule – même si la géométrie employée est symétrique. Une astuce simple pour obtenir des OM localisées est d'amorcer le calcul avec des OM de type Z+1 : par essence, elles sont localisées et constituent un bon point de départ du calcul. Il ne faut toutefois pas oublier qu'en réalité les deux atomes équivalents sont indiscernables et qu'en théorie, pour obtenir une fonction d'onde de cœur qui respecte la symétrie de la molécule, il faudrait combiner les OM obtenues pour chacun des atomes équivalents. Ceci ne serait pas évident, notamment dans le cas du benzène (six carbones équivalents). L'inconvénient majeur est que la réduction de la symétrie se traduit par un temps de calcul plus important.

A titre d'exemple, considérons la molécule de furane, qui comprend deux types d'atomes de carbone non-équivalents :

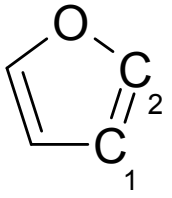

Voici les énergies ΔSCF obtenues (en eV, base TZP, géométrie RHF) dans le cas du furane dans les deux représentations :

		Koopmans	Délocalisé	Localisé	Exp.
			C_{2v}	C_s	
Ion C_1	$1s(a_1)^{-1}$	305.505	297.824	} 290.810	290.32/290.60
Ion C_1	$1s(b_2)^{-1}$	305.480	297.783		
Ion C_2	$1s(a_1)^{-1}$	307.026	300.047	} 292.066	291.81/291.59
Ion C_2	$1s(b_2)^{-1}$	307.026	300.052		
C_1	$1s(a_1) \rightarrow \pi^*(b_1)$		294.915	286.742	285.76
C_1	$1s(b_2) \rightarrow \pi^*(b_1)$	Interdite	294.870		
C_1	$1s(a_1) \rightarrow \pi^*(a_2)$	Interdite	295.823		
C_1	$1s(b_2) \rightarrow \pi^*(a_2)$		295.788		287.3
C_2	$1s(a_1) \rightarrow \pi^*(b_1)$		296.121	287.891	286.64
C_2	$1s(b_2) \rightarrow \pi^*(b_1)$	Interdite	296.124		
C_2	$1s(a_1) \rightarrow \pi^*(a_2)$	Interdite	298.704		
C_2	$1s(b_2) \rightarrow \pi^*(a_2)$		298.710		288.66

On remarque que le théorème de Koopmans (énergies mono-électroniques des orbitales 1s de l'état fondamental de la molécule), donne des valeurs trop grandes d'environ 15 eV pour l'ionisation. La levée de la contrainte de symétrie abaisse les énergies d'une dizaine d'eV, ce qui ramène les valeurs calculées à quelques dixièmes d'eV des valeurs expérimentales. On voit aussi que les deux atomes C_1 étant plus proches l'un de l'autre que les atomes C_2, ils interagissent plus d'où des différences d'énergie a_1 - b_2 plus élevées dans C_1 que dans C_2 où elles sont négligeables.

- Cas des molécules polyatomiques

Lorsqu'on a affaire à des molécules polyatomiques hautement symétriques, la localisation du trou de cœur devient possible mais par l'intermédiaire d'un effet vibronique : on parle de localisation dynamique, prédite initialement par Domcke et Cederbaum dans le cas de CO_2 [339,340]. Lorsque l'on crée un trou dans des orbitales de cœur (quasi)-dégénérées, le mouvement nucléaire crée un couplage non-adiabatique entre les états qui invalide l'approximation de Born-Oppenheimer, comme dans l'effet (pseudo)-Jahn-Teller bien connu [341-343]. Ce couplage n'est possible que via des modes de vibration non-totalement symétriques, ce qui explique que cet effet n'est pas présent dans les molécules diatomiques. Dans le cas de deux états, l'hamiltonien total sous forme localisée s'écrit sous la forme :

$$\begin{pmatrix} H_{11}^{\ell} & H_{21}^{\ell} \\ H_{12}^{\ell} & H_{22}^{\ell} \end{pmatrix}$$

et les termes hors-diagonaux dépendent de la différence d'énergie ΔE entre les deux états et de la différence entre les constantes de couplage linéaire $\delta\kappa$. Si ces paramètres sont négligeables, l'hamiltonien devient purement diagonal, ce qui signifie que le mouvement nucléaire de chacun des états (localisés) peut se traiter séparément. Ceci constitue le phénomène de localisation dynamique du trou de cœur. C'est ce qui se passe entre autres dans CO_2 [339,340,344], l'ozone [345] ou l'éthylène [346,347]. Si par contre, les deux atomes sont proches et fortement liés, le paramètre ΔE est grand et les deux états interagissent fortement : le trou reste délocalisé. Il semble que ce soit le

cas pour l'excitation O1s → σ* de SO_2 [348]. Dans l'exemple du furane cité plus haut, la localisation du trou de cœur est plus importante dans le cas de C_2 que pour C_1.

d) Le calcul des intensités de transitions

Une fois que l'on s'est affranchi du modèle du cœur équivalent, il est possible d'obtenir les intensités des transitions en calculant les forces d'oscillateur (dans l'approximation dipolaire électrique et dans la jauge longueur) :

$$f_L = \frac{2}{3}\omega\left|\left\langle \Psi_{CI} \left| \vec{\mathbf{r}} \right| \Psi_0 \right\rangle\right|^2$$

où ω est l'énergie de transition exprimée ici en unités atomiques. Il serait tout à fait possible de calculer les forces d'oscillateur dans la jauge vitesse :

$$f_V = \frac{2}{3}\frac{1}{\omega}\left|\left\langle \Psi_{CI} \left| \vec{\nabla} \right| \Psi_0 \right\rangle\right|^2$$

En vertu du théorème hyperviriel ([81], section FI18), les valeurs de f_L et f_V devraient être égales, à condition que les fonctions d'onde soient exactes. On peut d'ailleurs estimer la qualité de ces fonctions d'ondes en comparant les valeurs de f_L et f_V. Dans la plupart des articles ci-après, on s'est limité au calcul de f_L.

Le calcul de ces forces d'oscillateur pose un problème dans la mesure où les états excités de cœur sont décrits avec les OM de l'ion de cœur, alors que l'état fondamental est décrit avec ses propres orbitales obtenues au niveau RHF. Comme nous ne disposons pas d'un programme pouvant calculer les opérateurs avec des OM différentes, la fonction d'onde de l'état fondamental sera décrite elle aussi avec les OM de l'ion de cœur. Ces OM ne sont évidemment pas adaptées. Afin de compenser ce défaut, on repolarise " en sens inverse " ces OM de l'ion par une IC des mono-excitations par rapport au déterminant de l'ion. La fonction d'onde Ψ_0 de l'état fondamental s'écrit donc :

$$\Psi_0 = \sum_b \sum_k \left[C_{Ref} + C_{bk} a_b a_k^+ \right] \Psi_{Ref}$$

Pour donner une idée, le poids du C_{Ref} du déterminant RHF Ψ_{Ref} (obtenue avec les OM de l'ion de cœur mais avec l'occupation de l'état fondamental) est typiquement ≈75%. Cette astuce permet donc d'éliminer le problème de la non-orthogonalité entre les OM du fondamental et celles de l'ion. Il est aussi possible de raffiner le calcul des forces d'oscillateurs par un calcul perturbatif (au 1er ordre vu que $\vec{r}$ est un opérateur mono-électronique). Comme on peut le voir dans la figure 1 de l'article 17 ci-dessous, les différences sont minimes, pour un temps de calcul beaucoup plus long (environ 1000 fois !).

Dans certains cas (voir le 2,5-dihydrofurane et la *s*-triazine au seuil de l'azote dans les articles 15 et 16), le spectre ISEELS montre des structures mal résolues à une énergie correspondant à une transition dipolaire électrique interdite par les règles de symétrie. On peut alors penser qu'il s'agit d'une transition non-dipolaire électrique, par exemple quadrupolaire électrique ou dipolaire magnétique. Dans ce cas, il apparaît nécessaire de calculer les forces d'oscillateurs correspondantes. Après consultation d'un certain nombre de manuels de physique atomique [349,350], il semble que ces grandeurs ne sont pas utilisées parce qu'elles n'ont pas d'analogue classique : on préfère se référer aux durées de vie (ou aux coefficients d'Einstein) correspondantes. Rien n'empêche

toutefois de transposer la définition des forces d'oscillateur dipolaires électriques. Partant de l'expression de Kauzmann [351] pour le coefficient d'Einstein d'émission spontanée A_{ij}, on obtient en u.a. :

$$f_{ij}^{QE} = \frac{1}{20}\alpha^2 \Delta E^3 \left| \langle i | \vec{r} . \vec{r} | j \rangle \right|^2$$

$$f_{ij}^{DM} = \frac{1}{6}\alpha^2 \Delta E \left| \langle i | \vec{r} \wedge \vec{p} | j \rangle \right|^2$$

Il est important de se souvenir que ces expressions ne sont valables que si la force d'oscillateur dipolaire électrique est nulle (pas de termes croisés qui donneraient une expression beaucoup plus compliquée). En pratique, le calcul de f^{QE} n'a été fait que dans le cas de la s-triazine (Article 16) pour expliquer une structure absente des calculs dipolaires-électriques. La valeur trouvée s'est révélée beaucoup trop faible.

e) Le problème du choix de la base d'orbitales atomiques

Le choix d'une base d'OA adaptée est une étape cruciale de tout calcul de chimie quantique. On sait depuis longtemps que des fonctions de moment angulaire élevé sont nécessaires pour obtenir des géométries correctes et calculer la corrélation dynamique. De même, la description des états de Rydberg impose d'inclure des fonctions diffuses. Dans le cas de l'excitation/ionisation de cœur, il existe un problème supplémentaire : on peut penser que les bases usuelles, optimisées sur l'état fondamental d'un atome, ne sont pas idéales pour la description des états de cœur. Comme on l'a vu plus haut, ceci est évident si l'on se réfère au modèle du cœur équivalent : un carbone avec un trou dans l'orbitale 1s ressemble à un atome d'azote. Dans ce cas, quelle base faut-il utiliser pour le décrire, celle du carbone ou celle de l'azote ? Ce problème ne semble pas avoir souvent été évoqué dans la littérature et on se contente souvent d'utiliser des bases standard. Quelques solutions ont toutefois été proposées :

- Comme le montre le calcul test sur le carbone et l'azote ci-dessus, il suffit d'utiliser une base totalement décontractée, ce qui génère des ANO. Cette méthode peut se révéler très coûteuse lorsque la taille du système augmente. On peut réserver la décontraction à l'atome excité de cœur.

- Karlsen et Børve [352] ont proposé d'utiliser les pseudo-potentiels de Stevens et Krauss [353] et d'Huzinaga [354], modifiés pour tenir compte du fait qu'il reste un seul électron dans la couche 1s. Ils ont montré que la géométrie de l'ion de cœur du méthane ainsi calculée était comparable à celle donnée par une base tous électrons. Cette approche présente les mêmes avantages et inconvénients que le modèle Z+1, en particulier au niveau du nombre d'électrons, ce qui la rend difficile d'utilisation pour le calcul des spectres de cœur. Certains auteurs [355] utilisent les pseudo-potentiels pour décrire les atomes non-excités de cœur dans la molécule, ce qui assure automatiquement la localisation du trou de cœur .

- Chong [356,357] a proposé de modifier par un facteur d'échelle approprié les exposants de la base cc-pVTZ.

- Dans le même ordre d'idée, Carniato et Millié [358] ont obtenu par une méthode de recuit simulé au niveau UHF des bases 6-31G et TZV optimisées pour les états de cœur, l'état fondamental restant décrit par la base standard correspondante. Ces nouvelles bases donnent des énergies proches de celles obtenues avec des bases beaucoup plus grandes (cc-pCV5Z), ce qui permet de traiter des systèmes de grande taille. Dans le cas des atomes légers (Li-F) ionisés de cœur, les valeurs absolues des énergies avec ces nouvelles bases sont plus basses qu'avec la base standard : 2.5-3 eV pour la 6-31G et 0.6-0.7 eV pour la TZV. Cette différence est probablement due au fait que les bases de Pople du type N-31G sont par construction mono-dzéta pour la couche 1s, alors que la base TZV de Dunning [359-361] présente l'avantage d'être dès le départ double-dzéta.

- Si l'on veut pouvoir décrire correctement les états du continuum, les programmes STEX et StoBe utilisent une grand nombre d'orbitales très diffuses pour "paver" l'espace. Idéalement, il faudrait utiliser une base d'ondes planes, tout en gardant des gaussiennes pour la partie discrète du spectre. Pulay [362] a par exemple proposé une méthode pour calculer l'opérateur de Coulomb et l'énergie de manière précise. Dans le contexte de l'excitation de cœur, le concept a été mis en œuvre par Ianmuzzi et Hutter [363] mais essentiellement en phases liquide et solide.

En ce qui nous concerne, compte tenu du fait que le calcul des intensités de transition nous oblige à utiliser la même base pour l'état fondamental et les états de cœur, nous utilisons les bases standard telles quelles. Comme les bases " correlation-consistent " de Dunning du type cc-pVNZ [364-371] sont elles aussi par construction mono-dzéta sur l'orbitale 1s, nous préférons utiliser l'ancienne base TZV de Dunning [359-361], augmentée d'une ou deux fonctions de polarisation, ainsi qu'un ensemble d'orbitales diffuses pour la description des états de Rydberg. Pour ces dernières, les deux premiers exposants, tirés de Dunning et Hay [359], permettent d'obtenir les suivants par une méthode "even-tempered" [372].

5) Applications

a) Article 12 : Core shell excitation of 2-propenal (acrolein) at the O1s and C1s edges : An experimental and *ab initio* study

b) Article 13 : Core shell excitation of furan at the O1s and C1s edges: An experimental and *ab initio* study

c) Article 14 : *Ab initio* and experimental study of the K-shell spectra of 2,5-dihydrofuran

d) Article 15 : C1*s* and N1*s* core excitation of aniline: Experiment by electron impact and *ab initio* calculations

e) Commentaires

Les articles précédents montrent les améliorations apportées par la nouvelle méthode de calcul par rapport au modèle de cœur équivalent employé précédemment. Les énergies d'excitation de cœur sont calculées de manière absolue avec une précision de quelques dixièmes d'eV et les forces d'oscillateur sont maintenant évaluées correctement. Dans le cas de l'aniline, comme pour le benzène, l'excitation C1s $\rightarrow 3\pi^*$ présente un fort caractère di-excité. Les populations issues de l'analyse par orbitales naturelles donne des taux d'occupation autour de 1.5 et 0.5, une bonne illustration des limites de l'approximation orbitalaire et de la distinction entre transitions mono- et di-excitées.

Pour les spectres au seuil de l'oxygène du furane et du 2,5-dihydrofurane, on remarque la présence d'une bande intense relativement étroite dans la partie montante de la raie la plus large (Fig. 3, Article 13 et Fig. 2, Article 14). On remarque même une structure fine dans le cas du furane (Fig. 2, Article 13). Les calculs attribuent ces bandes à des transitions de Rydberg mais les intensités calculées sont très faibles. Le même phénomène se reproduit dans le cas du THF (travail en cours) :

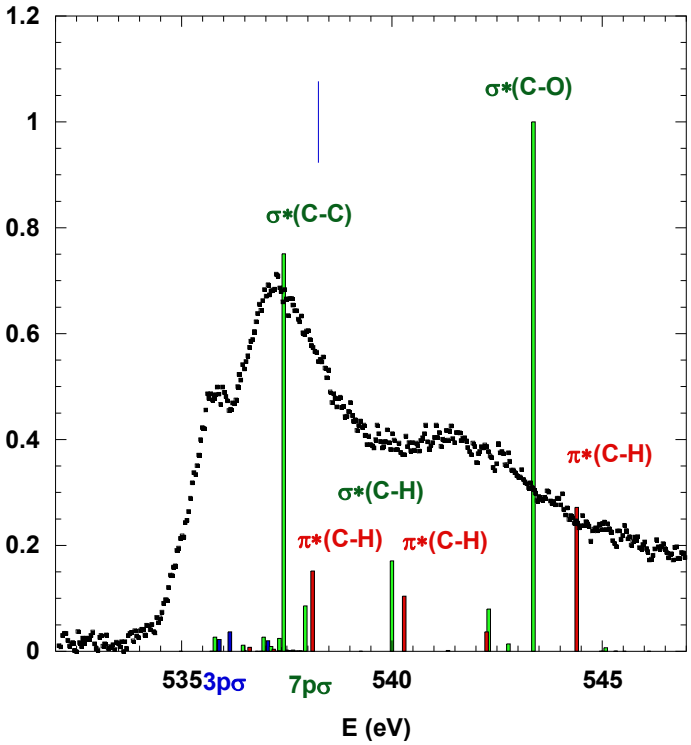

Figure 3.10. Spectres O1s mesuré et calculé du THF.

Pour le moment, il n'y a pas d'explication évidente à la mauvaise description de ces bandes par les calculs pour cette famille de molécules. Il semble exclu qui s'agisse d'une impureté dans l'expérience car l'énergie n'est pas la même dans chaque molécule :

	THF	2,5-dihydrofuran	Furane
→ A	535.89	535.72	537.57
B	537.25	537.27	539.17
C	541.49	541.15	545.3

De même, le spectre O1s du méthlyfurane mesuré à Liège (non publié), présente lui aussi une bande mal résolue autour de 538 eV. Par rapport à toutes les autres molécules étudiées, on ne voit pas non plus pour quelle raison cette bande serait mal décrite par les calculs. On peut supposer qu'il s'agit bien de transitions Rydberg dont l'intensité serait augmentée par des effets vibroniques (par exemple via le mode de "ring-puckering"). La meilleure résolution du rayonnement synchrotron permettrait peut-être de clarifier la situation.

6) La prise en compte des vibrations et la géométrie des états excités de cœur

a) Introduction

L'examen des spectres ISEELS des articles précédents montre que les raies observées ont souvent une largeur supérieure à la résolution d'appareil, même lorsque cette raie correspond à une seule transition électronique. Cette structure fut observée pour la première fois par Gelius *et al.* [373] en 1974. Ceci est dû à l'excitation vibrationnelle concomitante, qui peut être importante. Avec un rayonnement synchrotron, on peut même résoudre la structure fine vibrationnelle, en particulier en XPS pour des molécules de petite taille.

L'importance de la vibration permet en particulier d'étudier le degré de localisation du trou de cœur discuté plus haut. Même lorsque cette structure n'est pas bien résolue, il peut être intéressant de faire un calcul de facteurs de Franck-Condon pour expliquer la largeur des raies observées. Idéalement, il faudrait faire ce calcul pour chaque état électronique excité, ce qui n'est pas facile (voir cependant Article 16). Certains auteurs utilisent d'ailleurs la molécule Z+1 [374]. De plus, les différences constatées entre les énergies d'excitation de cœur calculées et le maximum d'une bande observée peuvent aussi s'expliquer par le fait que la bande vibrationnelle fondamentale 0-0 est décalée par rapport à l'énergie d'excitation verticale (souvent vers les basses énergies). Ce décalage joue un rôle dans les différences constatées entre les CEBE calculées et observées. Cette correction a été évaluée à environ 0.1 eV [375]. Toutefois, dans le cas des énergies d'ionisation de l'acide acétique (Article 18), cette correction peut atteindre 0.36 eV. Dans le cas du cyclopropane, cet effet explique pourquoi l'énergie de la transition 1s $\rightarrow$ σ^*(C-C) a une valeur calculée apparemment trop grande par rapport à l'expérience : après inclusion des effets vibrationnels, l'accord est excellent (figures 1 et 3, article 16).

Dans les molécules traitées dans les articles ci-dessous, les facteurs de Franck-Condon ont été évalués par la méthode de Domcke-Cederbaum [100-104], en se limitant au calcul de la matrice κ (approximation du couplage linéaire). Comme le remarque Hergenhan dans son article de revue [376], cette approximation est la plus fréquemment utilisée pour les molécules polyatomiques. Par contre, les effets de couplage vibronique, responsables notamment de la localisation dynamique du trou de cœur, n'ont pas été étudiés (pas de calcul avec un trou délocalisé). Ce type d'étude a été entrepris par le groupe de Cederbaum [340,377,378] mais pour un nombre limité de modes de vibration.

Dans le cas d'un état excité de cœur, la matrice κ ne peut en effet s'évaluer facilement (c'est-à-dire analytiquement) qu'au niveau ROHF-GVB. Par souci de cohérence, les fréquences harmoniques fondamentales sont donc obtenues au niveau HF, et sans appliquer de facteur correctif (" scale factor "). Elles sont donc surestimées d'environ 10% mais ceci a peu d'influence dans la mesure où la structure fine vibrationnelle est mal résolue dans les spectres ISEELS, en raison d'une trop faible résolution, et/ou à cause du recouvrement de multiples bande vibrationnelles.

Une importante excitation vibrationnelle est aussi le signe que la topologie de la surface d'énergie potentielle de l'état de cœur est très différente de celle de l'état fondamental. Ceci conduit naturellement à se poser la question de la géométrie d'équilibre des états excités/ionisés de cœur (les premières tentatives sur des molécules triatomiques datant de la fin des années 1970 [379,380]). Dans le cas de l'ionisation de cœur, les variations de géométrie se concentrent autour de l'atome où le trou est créé. Dans le cas de l'excitation de cœur, plusieurs situations sont possibles en fonction de la nature de l'orbitale cible :

- S'il s'agit d'une orbitale de Rydberg, on s'attend à ce que la géométrie soit proche de celle de l'ion de cœur. Toutefois, comme le montrent les articles présentés ici, les OM 3s et 3p ont souvent un important caractère de valence, par exemple σ*(C-H), pouvant provoquer une rupture de la liaison et la fragmentation de la molécule.
- S'il s'agit d'une orbitale purement anti-liante (σ* ou π*), il peut y avoir la même rupture si la courbe de potentiel est dissociative ou seulement une modification de la géométrie. Expérimentalement, si l'on utilise des méthodes de coïncidence couplées au rayonnement synchrotron, on doit observer les fragments caractéristiques des ruptures de liaisons. Ces ruptures sont extrêmement sélectives compte tenu de la localisation de l'excitation. Cet effet a été observé pour la première fois par Eberhardt *et al.* en 1983 pour l'excitation au seuil du carbone de l'acétone [381].

En réalité, le phénomène est plus complexe car plusieurs mécanismes entrent en compétition [382]. Pour les atomes de la première et de la seconde ligne du tableau périodique, après excitation de cœur, l'atome s'auto-ionise par effet Auger en un temps de l'ordre de 10^{-13} à 10^{-14} s. Comme on l'a vu, l'effet Auger se divise lui-même en deux types : l'Auger participant dans lequel l'électron excité de cœur subit lui-même la cascade Auger, le résultat étant un monocation de valence. Dans l'effet Auger spectateur, l'électron reste dans l'orbitale excitée initialement, tandis que les autres électrons forment un dication de valence. On obtient ainsi une méthode de production – séquentielle et non sélective – de dications (mais dans des états électroniques excités) [383]. Dans le cas de la " fragmentation ultra-rapide " de HBr (3sBr → σ*) [384], la nature dissociative de la courbe de potentiel et la faible masse de l'hydrogène provoquent la rupture avant même que la cascade Auger ait pu démarrer, ce qui se traduit par l'observation de l'effet Auger *atomique* du brome. Gadéa *et al.* [385] ont d'ailleurs suggéré qu'une molécule telle que l'acétylène pouvait s'isomériser après excitation de cœur avant que l'effet Auger ait pu démarrer, ce qui se traduirait par exemple par la présence de la paire C^+/CH_2^+. C'est ce qui été observé par Osipov *et al.* [24] mais la durée de l'isomérisation (60 fs) indique plutôt qu'il s'agissait de la fragmentation du dication de valence résultant de la cascade Auger.

Du point de vue théorique, la modélisation de l'effet Auger est difficile du fait de sa nature non-radiative [386-390]. Il est toutefois possible d'explorer la surface de potentiel d'un dication de valence (cf. chapitre un). De même, on peut optimiser la géométrie d'états excités ou ionisés de cœur. A notre connaissance, pour les molécules polyatomiques, dans le cas d'excitations du type singulet à deux couches ouvertes, seule la méthode ROHF-GVB de GAMESS-US permet de trouver analytiquement la géométrie d'équilibre et les fréquences harmoniques de l'état. Il est ensuite possible de raffiner les énergies relatives au niveau MP2 (avec CIPSI) ou en faisant une IC. Dans l'exemple du cyclopropane (Article 17), on a utilisé la méthode ORMAS (Orbital Restricted Molecular Active Space) proposée par Ivanic [391,392]. On peut aussi comparer les résultats à des calculs identiques effectués sur l'analogue Z+1 (Articles 17 et 18). Une méthodologie très similaire a été utilisée pour les états excités au seuil du carbone du formaldéhyde [393-395], le résultat le plus spectaculaire étant la prédiction d'un état di-excité thermodynamiquement stable du type C1s $n_O \rightarrow \pi^* \pi^*$. Il existe aussi quelques calculs du type MCSCF publiés, notamment sur l'acétylène [396] avec MOLCAS, ainsi que le dioxyde de carbone, l'éthylène et le benzène [378] avec DALTON.

Toutefois, on peut noter que pour éviter que le calcul ne converge vers un état de valence, l'espace actif se limite aux orbitales π, qui ont une symétrie différente de l'orbitale 1s. Dans le cas de MOLCAS [397], les optimisations de géométrie se font sur une grille.

b) Article 16 : *Ab initio* and experimental study of the K-shell spectra of *s*-triazine

c) Commentaires

Les calculs des spectres K-shell de la *s*-triazine ont été commencés par K. Sidhoum lors de son stage de DEA (année 2002-2003) [398]. Ils peuvent être comparés à des calculs (non-publiés) du type Z+1 tels que décrits dans la section 3 datant de 1999. Une fois n'est pas coutume, la base employée était la cc-pVDZ de Dunning [172] : (10s5p1d)/[3s2p1d], (4s1p)/[2s1p] + [3s3p1d] de Rydberg. Les spectres expérimentaux sont en fait ceux du groupe de Hitchcock publiés en 1993 [399] et téléchargés de sa base de données. A l'époque, en l'absence de données fiables sur les énergies d'ionisation, on a aligné l'énergie calculée de l'excitation 1s → 1π* sur le maximum de la première bande observée. En supposant que le TV calculé est correct – ce qui s'était vérifié pour d'autres molécules, on obtenait déjà des énergies d'ionisation de cœur au seuil C1s très loin des valeurs de Hitchcock, ce qui invalidait les attributions de Hitchcock :

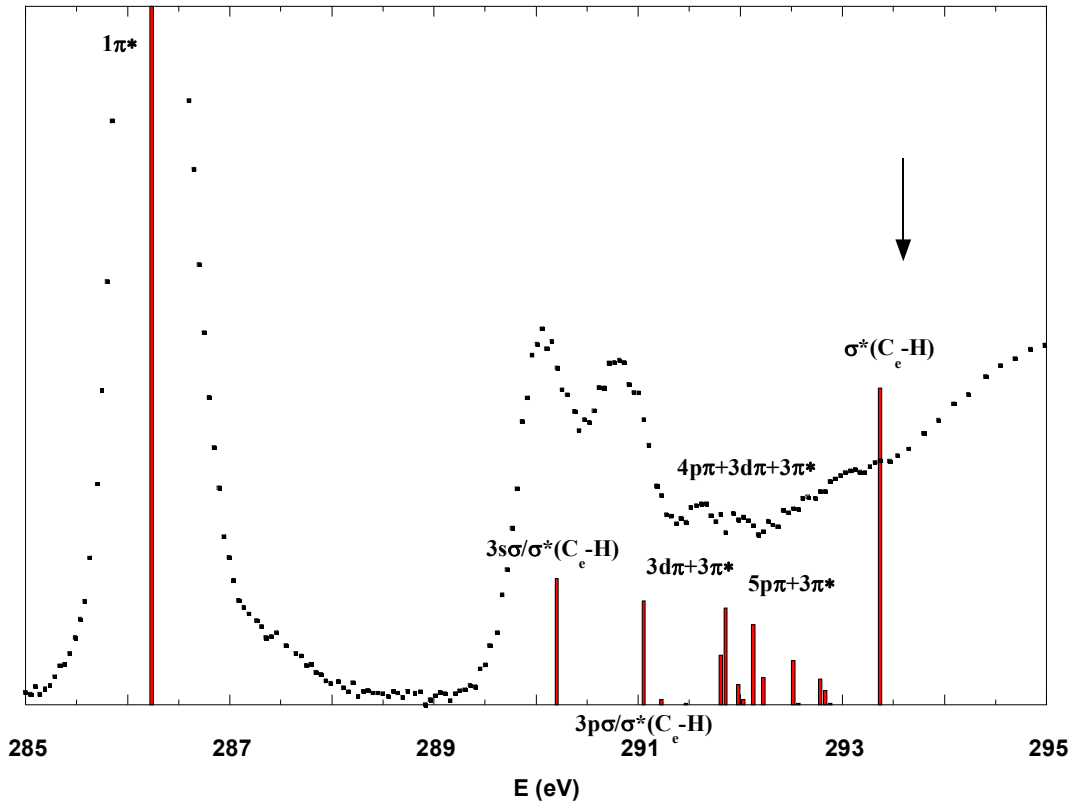

Figure 3.11. Spectres C1s de la s-triazine calculé dans l'approximation Z+1 comparé au spectre mesuré [399].

On constate un bon accord global avec les calculs publiés ultérieurement, si l'on excepte le fait que l'absence d'intensités fiables pour les transitions Rydberg/valence et/ou multi-électroniques, conduit à une large surestimation de l'intensité des bandes π*. Il est aussi

remarquable que l'on retrouve la difficulté à reproduire le TV de la bande centrée autour de 403 eV pour l'azote :

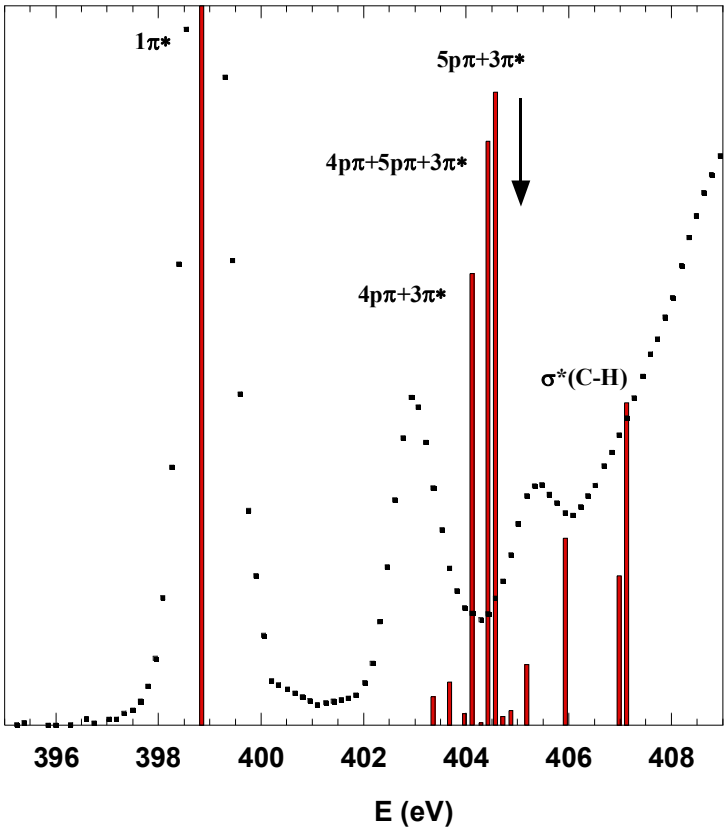

Figure 3.12. Spectres N1s de la s-triazine calculé dans l'approximation Z+1 comparé au spectre mesuré [399].

Comme indiqué plus haut, la *s*-triazine a été récemment étudiée par NEXAFS et des méthodes ΔKS avec deMon [192]. On constate que la structure vibrationnelle mieux résolue de la première bande au seuil C1s est en excellent accord avec notre simulation (figure 2 de l'article 16) :

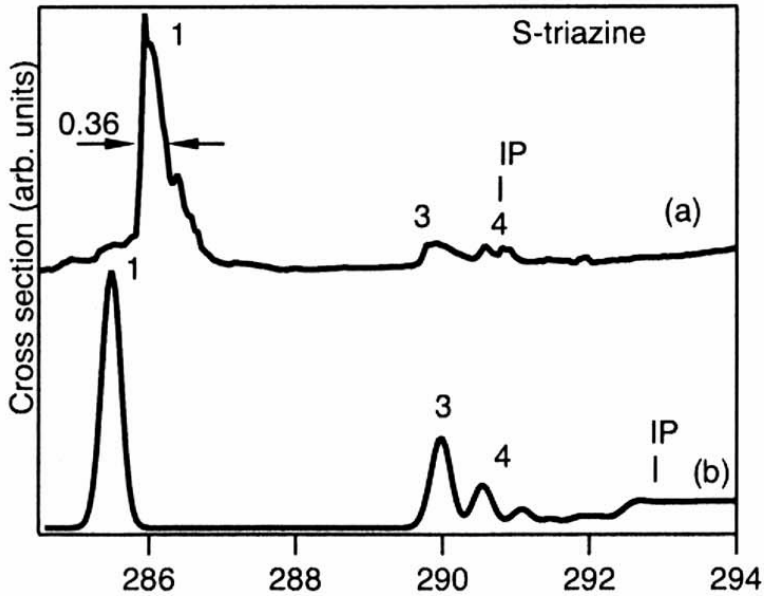

Figure 3.13. Spectres NEXAFS C1s de la s-triazine mesuré (en haut) et calculé [192].

De même, la bande 4 est maintenant résolue en deux pics comme prédit par les calculs (figure 3, article 16).

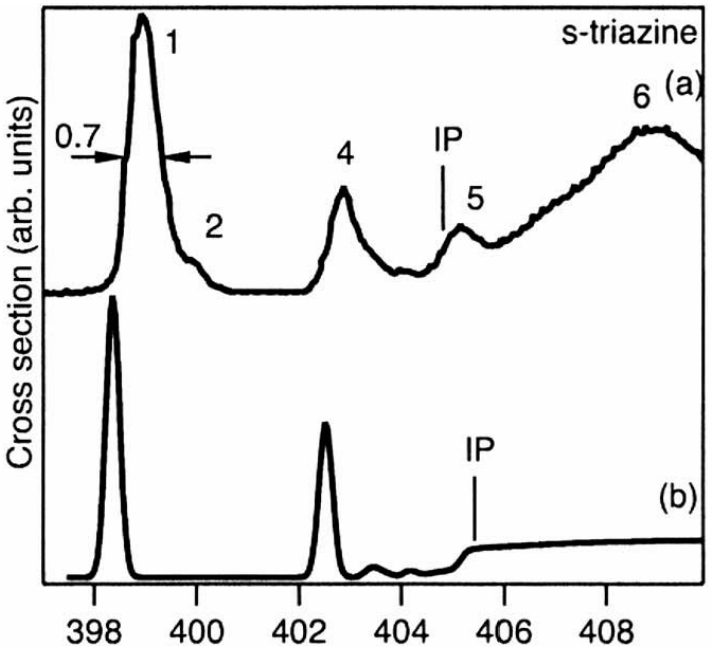

Figure 3.14. Spectres NEXAFS N1s de la s-triazine mesuré (en haut) et calculé [192].

Au seuil N1s, les calculs DFT prédisent eux aussi la transition $2\pi^*$ autour de 400 eV, c'est-à-dire au niveau de la bande 2, qui acquerrait son intensité grâce au couplage vibronique. Cette bande est aussi présente dans les spectres de la pyridazine et de la pyrimidine, où la symétrie de la molécule rend la transition autorisée. Les auteurs ont aussi suggéré que les structures observées près des seuils d'ionisation pouvaient être dues à des transitions doublement excitées, non rendues par la DFT. Comme le montrent les tableaux 4 et 6 de l'article 16, au seuil C1s, il s'agit en fait de transitions mono-électroniques σ^*, alors qu'au seuil N1s, il y a effectivement un état " shake up " très intense près du seuil.

c) Article 17 : *Ab initio* study of core excited cyclopropane

d) Article 18 : Electronic excitation of gaseous acetic acid studied by K-shell electron energy loss spectroscopy and *ab initio* calculations

e) Commentaires

L'article 17 est issu du travail initié par S. Zeggari lors de son stage de DEA pendant l'année 2001-2002 [189]. En plus du cyclopropane, Sze et Brion [400] ont aussi mesuré le spectre C1s de l'oxyde d'éthylène qui a un aspect très différent de celui du cyclopropane et semble présenter une structure fine vibrationnelle mieux résolue (travail en cours) :

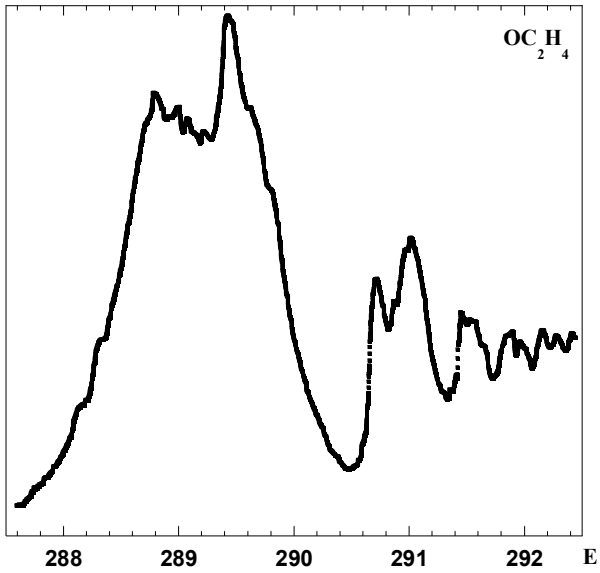

Figure 3.15. Spectree ISEELS C1s de l'oxyde d'éthylène [400]

Dans le cas de l'acide acétique au seuil C1s (Article 18), on voit que la meilleure résolution expérimentale ne révèle aucune nouvelle structure, ce que confirment (mais *a posteriori*) les calculs. En revanche, le cas de l'acide acétique montre qu'il est illusoire de vouloir par le calcul approcher à moins de 0.1 eV les valeurs XPS mesurées sans tenir compte des effets vibrationnels, par exemple en utilisant le modèle simple de Domcke-Cederbaum. En particulier, la correction ZPE semble du même ordre de grandeur que la correction relativiste qui est parfois ajoutée [182,185,401,402]. Même dans ce cas, l'accord théorie-expérience peut rester élevé comme pour l'un des deux carbones de l'acide acétique (tableau 1 de l'article 18).

7) Bilan et perspectives

Comme l'illustrent les articles présentés dans ce chapitre, la méthodologie de calcul développée permet de décrire les spectres d'excitation en couche K d'atomes légers avec une précision de quelques dixièmes d'eV. Il est illusoire de vouloir atteindre une meilleure précision, compte tenu des approximations faites, des effets négligés (relativistes par exemple) et de la difficulté de comparer spectres mesurés et calculés comme on l'a rappelé au début du chapitre deux. Comme souvent, les spectres de molécules d'une même famille montrent des analogies, mais les différences sont plus importantes qu'en spectroscopie de valence. Les exemples montrés ici illustrent bien l'effet de "chemical shift". Une famille particulière est constituée par le benzène et ses dérivés (*s*-triazine, aniline), où l'on constate la présence d'états de nature di-excitée avec des moments de transitions non-négligeables, ce qui constitue un cas unique à notre connaissance. Il faudrait donc reprendre le calcul des benzène, pyrrole, pyrazole, pyridine etc… et aussi étudier le cas de la borazine mesurée par Hitchcock [403].

Les avantages de l'IC par rapport aux méthodes monoconfigurationnelles (notamment la DFT) sont les mêmes que pour les excitations de valence : bonne description des états de Rydberg et/ou doublement excités. Par contre, elle est évidemment plus lourde à employer. Par ailleurs, l'analyse de la nature des fonctions d'onde obtenues, dans le but de trouver d'éventuels "shake up" prend beaucoup de temps et doit se faire manuellement.

A l'heure actuelle, les limites des programmes sont les suivantes : taille de la base à 256 OM, espace S de CIPSI à 500 000 déterminants de Slater pour un nombre d'états calculés de 18 (pour chaque spin). *A priori*, il est possible d'augmenter ces paramètres, d'autant que la méthode d'extrapolation du CIPSI diagrammatique permet d'obtenir un temps de calcul raisonnable en jouant

sur le seuil τ, sans réelle conséquence pour la précision des calculs. Le principal problème est que pour l'instant, les intégrales bi-électroniques sont stockées sur disque. Plus que l'espace disponible, ce sont les temps d'accès qui influent sur le coût du calcul. La méthode ORMAS de GAMESS, utilisée dans l'article 17 pour calculer l'énergie des états de cœur du cyclopropane, n'est pas une alternative pour plusieurs raisons : il n'est pas possible de sélectionner le spin, les intensités de transitions ne sont pas calculables ; de plus, le stockage de la matrice d'IC requiert beaucoup de mémoire vive.

D'autres améliorations sont possibles :

- S'il n'est pas possible de faire un calcul CASSCF, il faudrait tester la méthode GVB dans GAMESS pour les états de cœur.

- Pour le moment, les IC sont faites en utilisant les OM virtuelles de l'ion de cœur telles qu'elles sortent du calcul ROHF-GVB de GAMESS. Il est peut-être possible de les améliorer en utilisant les HAO [404] qui permettent de construire rapidement des orbitales virtuelles de valence sans passer par un calcul CASSCF [405].

- Le programme CIPSI permet d'utiliser la QDPT, une option qui ne fonctionne pas actuellement dans l'implémentation locale du programme.

- En ce qui concerne l'aspect vibrationnel, idéalement il faudrait pouvoir calculer les facteurs de Franck-Condon en utilisant les fréquences (harmoniques) des états excités, autrement dit de prendre en compte l'effet Duschinsky [406]. Des programmes existent [407,408] mais de toute manière ces calculs se limitent au calcul de la hessienne des états excités dont la symétrie diffère de celle de l'état fondamental.

Conclusion générale et perspectives

Conclusion générale et perspectives

Arrivé au terme de ce mémoire retraçant les travaux effectués depuis mon recrutement, on peut faire un retour en arrière jusqu'à mes débuts en chimie quantique – il y aura bientôt vingt ans. L'évolution dans la pratique quotidienne est frappante : mes premiers calculs ont été faits sur une station HP locale mono-processeur partagée par toute l'équipe. La seule alternative était le centre de calcul CIRCE, devenu depuis IDRIS. A cette époque, la connexion se faisait par un terminal Transpac et télécharger un fichier restait exceptionnel : le listing imprimé arrivait quelques jours après la fin du calcul par courrier postal, avec notamment le nombre d'heures consommées sur le quota total alloué. De plus, l'analyse des résultats passait par la lecture de colonnes de chiffres. A l'heure actuelle, un simple PC peut abriter un processeur suffisamment puissant pour faire des calculs de taille parfois conséquente – c'est d'ailleurs le cas pour une petite partie de ceux publiés dans les articles de ce mémoire, et afficher des structures en trois dimensions.

Une autre évolution est la floraison des codes de chimie quantique "tout-en-un" qui permettent de faire des calculs de plus en plus diversifiés. Dans mon cas, j'ai acquis une certaine dextérité à utiliser HONDO puis GAMESS, GAUSSIAN et MOLPRO et dans une moindre mesure DALTON et ADF. En revanche, je n'ai toujours pas trouvé l'occasion d'utiliser MOLCAS, Turbomole ou DIRAC, utilisés dans notre équipe. Dans le cas de CIPSI, nous sommes probablement parmi les derniers à l'utiliser. Les articles inclus ici montrent aussi que j'appartiens à la classe des "calculateurs" plutôt que des développeurs, parce que cette dernière tâche a toujours été brillamment assurée par Jean-Pierre Flament et aussi à cause d'une absence quasi-totale de formation en programmation, une lacune que je n'ai pas eu l'occasion de combler.

En ce qui concerne les perspectives, on peut retenir pour les trois thématiques abordées :

- Dans le domaine des dications, après une longue éclipse, nous avons entrepris le calcul des surfaces de potentiel du dication H_2O^{++}, suite à des contacts avec un groupe d'expérimentateurs du GANIL à Caen impliqué notamment dans RADAM. En envoyant des ions de haute énergie (MeV) sur des molécules d'eau, deutérées ou non, ceux-ci ont observé divers processus de fragmentation [409,410]. Dans le but d'interpréter les KER mesurées, B. Gervais à Caen a utilisé la surface de potentiel de l'état fondamental publiée auparavant [411,412] pour des calculs de dynamique classique. Afin d'aller plus loin, nous avons calculé les surfaces de potentiel complètes des huit plus bas états électroniques de H_2O^{++}, au niveau cc-pV5Z/CASSCF/MRCI. La petite taille du système a permis de calculer un grand nombre de points (plus de 11 000). La principale difficulté rencontrée concernait la mauvaise convergence des calculs CASSCF en certains points. Au moment où ces lignes sont écrites, les surfaces sont en cours d'ajustement à Caen, ce qui nécessite de recalculer un certain nombre de points supplémentaires. On peut aussi envisager de calculer les éléments de couplage non-adiabatique et caractériser les intersections coniques pour ensuite faire une étude dynamique quantique par des méthodes de paquets d'ondes, telles que celles employées par les dynamiciens de notre équipe.

- En ce qui concerne la spectroscopie de valence, les spectres d'autres composés d'intérêt biologique (limonène, isoprène, glycérol, alcool α-tétrahydrofurfuryle (THFA)…) sont actuellement étudiés par les expérimentateurs avec les mêmes méthodes que précédemment. Parallèlement, les calculs sont en cours. Du point de

vue théorique, la méthode de calcul choisie reste EOM-CCSD qui semble plus fiable que la TD-DFT, les méthodes CASSCF restant hors d'atteinte. Afin de réduire le coût du calcul, la base choisie est toujours du type cc-pVDZ, additionnée d'un nombre important d'orbitales diffuses placées au centre de la molécule. Il est aussi possible de réduire le nombre d'états excités calculés. Comme pour le THF, l'une des difficultés tient à la présence de plusieurs conformères très proches en énergie à la température ambiante : ainsi le limonène comporte-il 6 isomères dont 3 majoritaires [413], tandis que 5 des 126 conformations du glycérol se situent dans un intervalle de 1 $kcal.mol^{-1}$ [414]. Dans le cas du THFA, qui comme le THF est un analogue du désoxyribose, il y a 4 isomères en moins de 1 $kcal.mol^{-1}$ [415]. A chaque fois, le spectre électronique peut être vu, du moins en première approximation, comme la superposition des spectres de chaque isomère. Pour la structure vibrationnelle, le cas du THF montre qu'elle peut être bien résolue expérimentalement. Qui plus est, la ligne DESIRS de SOLEIL, où un spectromètre à transformée de Fourier est couplé au rayonnement synchrotron, promet d'atteindre une précision inégalée (pouvoir résolvant de l'ordre de 10^6 et résolution de 30 μeV). Si l'on veut simuler théoriquement les vibrations, un modèle beaucoup plus raffiné que la méthode de Domcke et Cederbaum est nécessaire : outre la forme en double puits du mode de "ring-puckering", il faudrait aussi obtenir une surface d'énergie potentielle décrivant correctement les deux isomères et le point-selle.

- Dans le domaine de l'excitation de cœur, de nouveaux composés ont été étudiés à liège (isoprène et acide propynoïque) mais à plus long terme, cette collaboration très ancienne va s'arrêter lors du départ à la retraite des collègues liégeois. Nous nous proposons donc d'utiliser l'expérience acquise sur les atomes légers pour étudier les spectres NEXAFS de composés d'actinides, qui constituent l'un des thèmes de prédilection du groupe chimie quantique, en particulier à travers le programme européen ACTINET. Comme en témoigne l'ouverture prochaine de la ligne MARS à SOLEIL, prévue pour accueillir des composés radioactifs, les différentes méthodes spectroscopiques XAS permettent d'étudier l'interaction de ligands organiques avec un atome lourd central. Par exemple, Solomon [416] a montré que l'intensité des raies dans les spectres Cl1s de composés de type MCl_4^{n-} (M = Cu, Fe, Ni …) était proportionnelle au degré de covalence de la liaison métal-ligand. Ce type d'informations est capital pour l'étude des processus de séparation des déchets nucléaires ou leur interaction avec l'environnement proche. Pour le moment, les premiers calculs, effectués sur des composés tels que UCl_6^-, $UOCl_6^-$ ou $UO_2Cl_4^{2-}$ au seuil de l'oxygène , utilisent la DFT et on se propose de la comparer à notre méthode d'IC. A cette fin, un projet de thèse en co-tutelle a été déposé, dans le cadre du programme de coopération franco-algérien TASSILI. Dans un premier temps, on se limitera aux couches 1s des atomes légers, l'étude des seuils de l'actinide nécessitant la prise en compte des effets relativistes.

Cette dernière perspective sera sans nul doute pour moi l'occasion d'explorer des domaines nouveaux, liés à l'étude des atomes les plus lourds de la classification périodique : pseudo-potentiels, effets relativistes, chimie de coordination, phases liquide voire solide. Enfin, un autre aspect, non évoqué ici, concerne la collaboration avec le sous-groupe "dynamique" de notre équipe, qui a besoin de surfaces d'énergie potentielle *ab initio*, par exemple dans le cas de la photodissociation de molécules à la surface de la glace [417], ou dans le contexte des collisions réactives telles que $Si + OH \rightarrow SiO + H$.

ACRONYMES

- a.u./u.a. atomic units/unités atomiques
- ANO Atomic Natural Orbitals
- ASTRID Århus university Storage Ring in Denmark
- CCS Coupled Cluster Single
- CCSD Coupled Cluster Single Double
- CEBE Core Electron Binding Energy
- CASSCF Complete Active Space Self-Consistent Field
- CASPT2 Complete Active Space Self-Consistent Field/Second Order Pertubation
- DCT Double Charge Transfer
- CIPSI Configuration Interaction by Perturbation Selected Iteratively
- DFT Density Functional Theory
- EICVOM Equivalent Ionic Core Virtual Orbital Model
- EOM-CCSD Equation Of Motion-Coupled Cluster Single Double
- ESCA Electron Spectroscopy for Chemical Analysis
- EXAFS Extended X-Ray Absorption Fine Structure
- FCF Franck-Condon Factors
- GAMESS General Atomic and Molecular Electronic Structure System
- GOS Generalized Oscillator Strength
- GTO Gaussian-Type Orbital
- GVB Generalized Valence Bond
- HAO Hybridized Atomic Orbitals
- HF Hartree-Fock
- HOMO Highest Occupied Molecular Orbital
- IC/CI Interaction de Configurations/Configuration Interaction
- ISEELS Inner Shell Electron Energy Loss Spectroscopy
- IVO Improved Virtual Orbitals
- KER Kinetic Energy Release
- KS Kohn-Sham
- LCAO Linear Combination of Atomic Orbitals
- LUMO Lowest Unoccupied Molecular Orbital
- MCSCF Multi-Configurational Self-Consistent Field
- MPn Perturbation en énergie de Møller-Plesset d'ordre n (n = 2, 3, 4 …)

- MRCI Multi-Reference Configuration Interaction
- NEXAFS Near Edge X-ray Absorption Fine Structure
- OA/AO Orbitales Atomiques/Atomic Orbitals
- OM/MO Orbitales Moléculaires/Molecular Orbitals
- ORMAS Orbital Restricted Molecular Active Space
- PEPICO Photo Electron PhotoIon Coincidence
- PEPIPICO Photo Electron PhotoIon PhotoIon Coincidence
- PES Photo Electron Spectroscopy
- PIPICO PhotoIon PhotoIon Coincidence
- QDPT Quasi-Degenerate Perturbation Theory
- QM/MM Quantum Mechanics/Molecular Mechanics
- RPA Random Phase Approximation
- RASSCF Restrictive Active Space Self-Consistent Field
- RHF Restricted Hartree-Fock
- ROHF Restricted Open shell Hartree-Fock
- SAC-CI Symmetry Adapted Cluster – Configuration Interaction
- SCF Self-Consistent Field (champ auto-cohérent)
- SHOMO Second Highest Occupied Molecular Orbital (≡ HOMO-1)
- SOLEIL Source Optimisée de Lumière d'Energie Intermédiaire de LURE
- STO Slater-Type Orbital
- TV Term Value
- UHF Unrestricted Hartree-Fock
- XANES X-ray Absorption Near Edge Spectroscopy
- XAS X-ray Absorption Spectroscopy
- XPS X-ray Photoelectron Spectroscopy
- ZP(V)E Zero-Point (Vibrational) Energy

Acronymes

REFERENCES

[1] J. J. Thomson, Rays of positive electricity, Cambridge University Press, Cambridge, 1921.
[2] J. R. Appling, B. E. Jones, L. E. Abbey, D. E. Bostwick, T. F. Moran, Organic Mass Spectrometry 18 (1983) 282.
[3] L. Pauling, J. Chem. Phys. 1 (1933) 56.
[4] Werner H.-J.; Knowles, P. J.; Lindh, R.; Manby, F. R.; Schütz,M.; Celani, P.; Korona, T.; Rauhut, G.; Amos, R. D.; Bernhardsson, A.;Berning, A.; Cooper, D. L.; Deegan, M. J. O.; Dobbyn, A. J.; Eckert, F.;Hampel, C.; Hetzer, G.; Lloyd, A. W.; McNicholas, S. J.; Meyer, W.; Mura,M. E.; Nicklass, A.; Palmieri, P.; Pitzer, R.; Schumann, U.; Stoll, H.; Stone, A. J.; Tarroni, R.; Thorsteinsson, T. MOLPRO: A Package of Ab Initio Programmes, version 2006.1; University College Cardiff Consultants, Ltd.: Cardiff, U.K., 2006 (http://www.molpro.net).
[5] L. Wolniewicz, J. Phys. B (1999) 2257.
[6] H. Basch, P. Aped, S. Hoz, Chem. Phys. Lett. 255 (1996) 336.
[7] J. Senekowitsch, S. O'Neil, W. Meyer, Theor. Chem. Acc. 84 (1992) 85.
[8] R. W. Alder, Acc. Chem. Res. 16 (1983) 321.
[9] D. Schroder, H. Schwarz, J. Phys. Chem. A 103 (1999) 7385.
[10] R. Thissen, J. Delwiche, J. M. Robbe, D. Duflot, J. P. Flament, J. H. D. Eland, J. Chem. Phys. 99 (1993) 6590.
[11] R. Thissen, Photo-Ionisation Double de CH_3NH_2, de C_2H_2 et de CH_3Cl à l'aide du Rayonnement Synchrotron, Université de Liège, Liège, Belgium, 1993.
[12] N. Levasseur, P. Millié, P. Archirel, B. Lévy, Chem. Phys. 153 (1991) 387.
[13] K. Lammertsma, P. v. R. Schleyer, S. H., Ang. Chem. Int. Ed. Engl. 28 (1989) 1321.
[14] D. Mathur, Physics Reports 225 (1993) 193.
[15] D. Mathur, Nuc. Inst. Meth. Phys. Res. B 99 (1995) 121.
[16] D. Mathur, Physics Reports 391 (2004) 1.
[17] V. G. Nenajdenko, N. E. Shevchenko, E. S. Balenkova, I. V. Alabugin, Chem. Rev. 103 (2003) 229.
[18] B. P. Tsai, J. H. D. Eland, Int. J. Mass Spectrom. Ion Phys. 36 (1980) 143.
[19] R. D. Molloy, A. Danielsson, L. Karlsson, J. H. D. Eland, Chem. Phys. 335 (2007) 49.
[20] B. Huron, J. P. Malrieu, P. Rancurel, J. Chem. Phys. 58 (1973) 5745.
[21] R. Cimiraglia, M. Persico, J. Comp. Chem. 8 (1987) 39.
[22] R. Cimiraglia, J. Chem. Phys. 83 (1985) 1746.
[23] O. Furuhashi, T. Kinugawa, S. Masuda, C. Yamada, S. Ohtani, Chem. Phys. Lett. 342 (2001) 625.
[24] T. Osipov, C. L. Cocke, M. H. Prior, A. Landers, T. Weber, O. Jagutzki, L. Schmidt, H. Schmidt-Böcking, R. Dörner, Phys. Rev. Lett. 90 (2003) 233002.
[25] T. Osipov, Kansas State University, Manhattan, 2003.
[26] X. Li, H. B. Schlegel, J. Phys. Chem. A 108 (2004) 468.
[27] T. S. Zyubina, Y. A. Dyakov, S. H. Lin, A. D. Bandrauk, A. M. Mebel, J. Chem. Phys. 123 (2005) 134320.
[28] A. M. Mebel, T. S. Zyubina, Y. A. Dyakov, A. D. Bandrauk, S. H. Lin, Int. J. Quantum Chem. 102 (2005) 506.
[29] T. Kinugawa, P. Lablanquie, F. Penent, J. Palaudoux, J. H. D. Eland, J. Electron Spectrosc. Related Phen. 141 (2004) 143.
[30] M. Peric, J. Palaudoux, M. Hochlaf, J. Phys. Chem. A 112 (2008) 768.
[31] J. Palaudoux, M. Hochlaf, J. Chem. Phys. 126 (2007) 044302.
[32] S. De, J. Rajput, A. Roy, P. N. Ghosh, C. P. Safvan, J. Chem. Phys. 127 (2007) 051101.
[33] B. T. Colegrove, H. F. I. Schaefer, J. Phys. Chem. 94 (1990) 5593.

[34] M. Bogey, H. Bolvin, C. Demuynck, J. L. Destombes, Phys. Rev. Lett. 66 (1991) 413
[35] G. Dolgonos, Chem. Phys. Lett. 454 (2008) 190.
[36] P. Halvick, D. Liotard, J. C. Rayez, Chem. Phys. 177 (1993) 69.
[37] S. Boyé-Péronne, D. Gauyacq, J. Liévin, J. Chem. Phys. 124 (2006) 214305.
[38] T. Osipov, T. N. Rescigno, T. Weber, S. Miyabe, T. Jahnke, A. S. Alnaser, M. P. Hertlein, O. Jagutzki, L. P. H. Schmidt, M. Schöffler, L. Foucar, S. Schössler, T. Havermeier, M. Odenweller, S. Voss, B. Feinberg, A. L. Landers, M. H. Prior, R. Dörner, C. L. Cocke, A. Belkacem, J. Phys. B (2008) 091001.
[39] R. Flammini, E. Fainelli, F. Maracci, L. Avaldi, Phys. Rev. A 77 (2008) 044701.
[40] T. Kerkau, V. Schmidt, J. Phys. B (2001) 839.
[41] J.-i. Adachi, K. Hosaka, T. Teramoto, M. Yamazaki, N. Watanabe, M. Takahashi, A. Yagishita, J. Phys. B (2007) F285.
[42] A. Hishikawa, A. Matsuda, M. Fushitani, E. J. Takahashi, Phys. Rev. Lett. 99 (2007) 258302.
[43] B. F. Yates, W. J. Bouma, L. Radom, J. Am. Chem. Soc. 108 (1986) 6545.
[44] J. H. D. Eland, B. J. Treves-Brown, Int. J. Mass Spectrom. Ion Process. 113 (1992) 167.
[45] J. Geiger, E. Ruhl, Int. J. Mass Spec. 220 (2002) 99.
[46] R. P. Grant, F. M. Harris, D. E. Parry, Int. J. Mass Spec. 192 (1999) 111.
[47] V. Antzoulatos. stage de 2e année de magistère de Chimie Physique d'Orsay, 1997.
[48] G. Rasul, G. K. Surya Prakash, G. A. Olah, J. Mol Struct. (THEOCHEM) 466 (1999) 245.
[49] M. Krishnamurthy, F. A. Rajgara, D. Mathur, J. Chem. Phys. 121 (2004) 9765.
[50] S. De, J. Rajput, A. Roy, R. Ahuja, P. N. Ghosh, C. P. Safvan, Journal of Physics: Conference Series (2007) 012005.
[51] S. De, J. Rajput, A. Roy, P. N. Ghosh, C. P. Safvan, Phys. Rev. Lett. 97 (2006) 213201.
[52] R. K. Kushawaha, B. Bapat, Chem. Phys. Lett. 463 (2008) 42.
[53] D. Schröder, Angew. Chem. Int. Ed. 43 (2004) 1329.
[54] J. Jasik, J. Roithova, J. Zabka, R. Thissen, I. Ipolyi, Z. Herman, Int. J. Mass Spec. 255-256 (2006) 150.
[55] P. Milko, J. Roithová, D. Schröder, H. Schwarz, Int. J. Mass Spec. 267 (2007) 139.
[56] C. L. Ricketts, D. Schroder, J. Roithova, H. Schwarz, R. Thissen, O. Dutuit, J. Zabka, Z. Herman, S. D. Price, PCCP 10 (2008) 5135.
[57] J. Roithova, D. Schroder, R. Berger, H. Schwarz, J. Phys. Chem. A 110 (2006) 1650.
[58] J. Roithova, D. Schroder, P. Gruene, T. Weiske, H. Schwarz, J. Phys. Chem. A 110 (2006) 2970.
[59] J. Roithova, J. Zabka, D. Ascenzi, P. Franceschi, C. L. Ricketts, D. Schroder, Chem. Phys. Lett. 423 (2006) 254.
[60] S. Taylor, J. H. D. Eland, M. Hochlaf, Chem. Phys. 330 (2006) 16.
[61] V. Sharma, B. Bapat, J. Mondal, M. Hochlaf, K. Giri, N. Sathyamurthy, J. Phys. Chem. A 111 (2007) 10205.
[62] A. B. Houria, Z. B. Lakhdar, M. Hochlaf, F. Kemp, I. R. McNab, J. Chem. Phys. 122 (2005) 054303.
[63] M. Hochlaf, A. Pilcher-Clayton, J. H. D. Eland, Chem. Phys. 309 (2005) 291.
[64] M. Hochlaf, R. I. Hall, F. Penent, J. H. D. Eland, P. Lablanquie, Chem. Phys. 234 (1998) 249.
[65] M. Hochlaf, J. H. D. Eland, PCCP 10 (2008) 5394.
[66] M. Hochlaf, F. R. Bennett, G. Chambaud, P. Rosmus, J. Phys. B 31 (1998) 2163.
[67] J. H. D. Eland, R. Feifel, M. Hochlaf, J. Chem. Phys. 128 (2008) 234303.
[68] V. Brites, J. H. D. Eland, M. Hochlaf, Chem. Phys. 346 (2008) 23.
[69] M. Hochlaf, Etude expérimentale et théorique des ions moléculaires doublement chargés formés par la double photoionisation de valence, Université Pierre et Marie Curie, Paris, 1997.

[70] G. Rasul, G. K. S. Prakash, G. A. Olah, J. Mol Struct. (THEOCHEM) 455 (1998) 101.
[71] G. H. Olah, T. Shamma, B. A., G. Rasul, G. K. Surya Prakash, J. Am. Chem. Soc. 119 (1997) 3407.
[72] G. A. Olah, G. K. S. Prakash, G. Rasul, J. Mol Struct. (THEOCHEM) 489 (1999) 209.
[73] S. Eden, P. Limao-Vieira, S. V. Hoffmann, N. J. Mason, Chemical Physics 323 (2006) 313.
[74] F. Motte-Tollet, M.-J. Hubin-Franskin, J. E. Collin, J. Chem. Phys. 97 (1992) 7314.
[75] A. R. Milosavljevic, S. Madzunkov, D. Sevic, I. Cadez, B. P. Marinkovic, J. Phys. B (2006) 609.
[76] J. Delwiche, P. Natalis, J. Momigny, J. E. Collin, Journal of Electron Spectroscopy and Related Phenomena 1 (1972) 219.
[77] L. Serrano-Andres, M. Merchan, J. Mol Struct. (THEOCHEM) 729 (2005) 99.
[78] A. Dreuw, ChemPhysChem 7 (2006) 2259.
[79] Z.-L. Cai, J. R. Reimers, J. Phys. Chem. A 104 (2000) 8389.
[80] M. Pastore, C. Angeli, R. Cimiraglia, Chem. Phys. Lett. 426 (2006) 445.
[81] P. Atkins, R. Friedman, Molecular Quantum Mechanics, Oxford University Press, Oxford, 2005.
[82] J. J. Riesz, J. B. Gilmore, R. H. McKenzie, B. J. Powell, M. R. Pederson, P. Meredith, Phys. Rev. E 76 (2007) 021915.
[83] R. Schinke, Photodissociation Dynamics, Cambridge University Press, Cambridge, 1993.
[84] A. Dreuw, M. Head-Gordon, Chem. Rev. 105 (2005) 4009.
[85] E. Runge, E. K. U. Gross, Phys. Rev. Lett. 52 (1984) 997 LP
[86] J. Schirmer, A. Dreuw, Phys. Rev. A 75 (2007) 022513.
[87] A. Holas, M. Cinal, N. H. March, Phys. Rev. A 78 (2008) 016501.
[88] F. Aquilante, V. Barone, B. O. Roos, J. Chem. Phys. 119 (2003) 12323.
[89] C. Adamo, V. Barone, J. Chem. Phys. 110 (1999) 6158.
[90] I. Ciofini, C. Adamo, J. Phys. Chem. A 111 (2007) 5549.
[91] O. Christiansen, H. Koch, P. Jorgensen, Chem. Phys. Lett. 243 (1995) 409.
[92] O. Christiansen, H. Koch, P. Jorgensen, J. Chem. Phys. 105 (1996) 1451.
[93] DALTON, a molecular electronic structure program, Release 2.0 (2005), see http://www.kjemi.uio.no/software/dalton/dalton.html.
[94] O. Christiansen, Theor. Chem. Acc. 116 (2006) 106.
[95] R. J. Bartlett, M. Musial, Rev. Mod. Phys. 79 (2007) 291.
[96] C. Hampel, K. A. Peterson, H.-J. Werner, Chem. Phys. Lett. 190 (1992) 1.
[97] J. V. Ortiz, J. Chem. Phys. 89 (1988) 6348.
[98] J. V. Ortiz, V. G. Zakrzewski, O. Dolgounircheva, in J.-L.C.a.E. Kryachko (Ed.), Conceptual Perspectives in Quantum Chemistry. Kluwer Academic, 1997, p. 465.
[99] P. G. Szalay, R. J. Bartlett, Chem. Phys. Lett. 214 (1993) 481.
[100] W. Domcke, L. S. Cederbaum, J. Chem. Phys. 64 (1976) 612.
[101] L. S. Cederbaum, W. Domcke, J. Chem. Phys. 64 (1976) 603.
[102] H. Köppel, W. Domcke , L. S. Cederbaum, Adv. Chem. Phys. 57 (1984) 59.
[103] J.-P. Flament, Application des "équations de mouvement" à la spectroscopie Université de Paris-Sud, 1981.
[104] J. P. Dognon, C. Pouchan, A. Dargelos, J. P. Flament, Chem. Phys. Lett. 109 (1984) 492.
[105] J. P. Flament, H. P. Gervais, J. Mol Struct. (THEOCHEM) 90 (1982) 351.
[106] N. Chabert, Contribution théorique à la spectroscopie de molécules triatomiques, Université des Sciences et Technologies de Lille, Lille, 2001.
[107] F. Motte-Tollet, J. Delwiche, J. Heinesch, M.-J. Hubin-Franskin, J. M. Gingell, N. C. Jones, N. J. Mason, G. Marston, Chem. Phys. Lett. 284 (1998) 452.
[108] F. Motte-Tollet, M.-P. Ska, G. M. Marston, I. C. Walker, M. R. F. Siggel, J. M. Gingell, L. Kaminski, K. Brown, N. J. Mason, Chem. Phys. Lett. 275 (1997) 298.

[109] D.-c. Wang, E. P. F. Lee, F.-t. Chau, D. K. W. Mok, J. M. Dyke, J. Phys. Chem. A 104 (2000) 4936.
[110] F.-T. Chau, J. M. Dyke, E. P. F. Lee, D. K.-W. Mok, J. Chem. Phys. 118 (2003) 4025.
[111] A. Osted, J. Kongsted, O. Christiansen, J. Phys. Chem. A 109 (2005) 1430.
[112] S. Leach, M. Schwell, S. Un, H.-W. Jochims, H. Baumgartel, Chem. Phys. 321 (2006) 159.
[113] P. R. T. Schipper, O. V. Gritsenko, S. J. A. v. Gisbergen, E. J. Baerends, J. Chem. Phys. 112 (2000) 1344.
[114] O. V. Gritsenko, P. R. T. Schipper, E. J. Baerends, Chem. Phys. Lett. 302 (1999) 199.
[115] F. M. B. G. te Velde, E. J. Baerends, C. Fonseca Guerra, S. J. A. van Gisbergen, J. G. Snijders, T. Ziegler,, J. Comp. Chem. 22 (2001) 931.
[116] P. M. W. Gill, Aust. J. Chem. 54 (2001) 661.
[117] S. Arulmozhiraja, M. Ehara, H. Nakatsuji, J. Chem. Phys. 126 (2007) 044306.
[118] H. Nakatsuji, K. Hirao, Chem. Phys. Lett. 47 (1977) 569.
[119] K. Hirao, H. Nakatsuji, Chem. Phys. Lett. 79 (1981) 292.
[120] H. Nakatsuji, Chem. Phys. Lett. 67 (1979) 329.
[121] H. Nakatsuji, Chem. Phys. Lett. 67 (1979) 334.
[122] H. Nakatsuji, Computational Chemistry - Review of Current Trends. World Scientific, Singapore, 1997, p. 62.
[123] H. Nakatsuji, K. Hirao, J. Chem. Phys. 68 (1978) 2053.
[124] R. J. Buenker, S.-K. Shih, S. D. Peyerimhoff, Chem. Phys. 36 (1979) 97.
[125] K. M. C. Siegbahn, Conférence Nobel 1924, 1925.
[126] K. Siegbahn, Electron Spectroscopy for Atoms, Molecules and Condensed Matter Conférence Nobel, 1981.
[127] K. Siegbahn, C. Nordling, G. Johansson, J. Hedman, P. F. Heden, K. Hamrin, U. Gelius, T. Bergmark, L. O. Werme, R. Manne, Y. Baer, ESCA Applied to Free Molecules, North-Holland, Amsterdam, 1969.
[128] G. Margarintondo, Elements of Synchrotron Light for Biology, Chemistry & Medical Research, Oxford University Press, Oxford, 2002.
[129] J. Stöhr, NEXAFS Spectroscopy, Springer Verlag, 1992.
[130] S. Ferrer, Y. Petroff, Surf. Sci. 500 (2002) 605.
[131] H. Wende, Rep. Prog. Phys. (2004) 2105.
[132] M. Chergui, C. Bressler, Chem. Rev. 104 (2004) 1781.
[133] J. J. Rehr, R. C. Albers, Rev. Mod. Phys. 72 (2000) 621.
[134] P. Zhu, J. Tang, S. Cao, J. Electron Spectrosc. Related Phen. 129 (2003) 27.
[135] U. Gelius, E. Basilier, S. Svensson, T. Bergmark, K. Siegbahn, J. Electron Spectrosc. Related Phen. 2 (1973) 405.
[136] M. N. Piancastelli, J. Electron Spectrosc. Related Phen. 100 (1999) 167.
[137] G. Hähner, Chem. Soc. Rev. 35 (2006) 1244.
[138] A. P. Hitchcock, J. Electron Spectrosc. Related Phen. 112 (2000) 9.
[139] A. P. Hitchcock, Phys. Scripta T31 (1990) 159.
[140] P. Rez, D. A. Muller, Annual Rev. Mat. Res. 38 (2008) 535.
[141] H. Bethe, Ann. Physik 5 (1930) 325.
[142] C. Cohen-Tannoudji, B. Diu, F. Laloë, Mécanique Quantique II, Hermann, Paris, 1973.
[143] A. Messiah, Mécanique Quantique Tome 1, Dunod, Paris, 1959.
[144] M. Inokuti, Rev. Mod. Phys. 43 (1971) 297.
[145] A. Giuliani, Furan and some selected derivatives A valence shell spectroscopic study by photon and electron impact methods, Université de Liège, Liège, 2003.
[146] H. Aouni, Spectroscopie électronique de couches internes de molécules cyanées, Liège, Liège, Belgique, 1996.
[147] E. N. Lassettre, J. Chem. Phys. 43 (1965) 4479.
[148] W. M. Huo, J. Chem. Phys. 71 (1979) 1593.

[149] K. T. Leung, J. Electron Spectrosc. Related Phen. 100 (1999) 237.
[150] G. C. Schatz, M. A. Ratner, Quantum Mechanics in Chemistry, Dover, Mineola, New York, 2002.
[151] E. N. Lassettre, A. Skerbele, M. A. Dillon, J. Chem. Phys. 50 (1969) 1829.
[152] W. A. Goddard, D. L. Huestis, D. C. Cartwright, S. Trajmar, Chem. Phys. Lett. 11 (1971) 329.
[153] V. Feyer, P. Bolognesi, M. Coreno, K. C. Prince, L. Avaldi, J. Electron Spectrosc. Related Phen. 161 (2007) 17.
[154] I. G. Eustatiu, T. Tyliszczak, A. P. Hitchcock, C. C. Turci, A. B. Rocha, C. E. Bielschowsky, Phys. Rev. A 61 (2000) 042505.
[155] A. Giuliani, M.-J. Hubin-Franskin, Chem. Phys. Lett. 348 (2001) 34.
[156] J. T. Francis, N. Kosugi, A. P. Hitchcock, J. Chem. Phys. 101 (1994) 10429.
[157] M. J. van der Wiel, T. M. El-Sherbini, C. E. Brion, Chem. Phys. Lett. 7 (1970) 161.
[158] N. D. Ugo T. Lamanna, Carla Guidotti, Giovanni P. Arrighini,, Int. J. Quant. Chem. 60 (1996) 475.
[159] A. Skerbele, E. N. Lassettre, J. Chem. Phys. 56 (1972) 845.
[160] I. G. Eustatiu, J. T. Francis, T. Tyliszczak, C. C. Turci, A. L. D. Kilcoyne, A. P. Hitchcock, Chem. Phys. 257 (2000) 235.
[161] I. G. Eustatiu, T. Tyliszczak, A. P. Hitchcock, C. C. Turci, A. B. Rocha, C. E. Bielschowsky, Phys. Rev. A 61 (2000) 425051.
[162] A. P. Hitchcock, I. G. Eustatiu, J. T. Francis, C. C. Turci, J. Electron Spectrosc. Related Phen. 88-91 (1998) 77.
[163] A. P. Hitchcock, S. Johnston, T. Tyliszczak, C. C. Turci, M. Barbatti, A. B. Rocha, C. E. Bielschowsky, J. Electron Spectrosc. Related Phen. 123 (2002) 303.
[164] X. W. Fan, K. T. Leung, J. Electron Spectrosc. Related Phen. 123 (2002) 287.
[165] R. McLaren, S. A. C. Clark, I. Ishii, A. P. Hitchcock, Phys. Rev. A 36 (1987) 1683.
[166] S. Shirai, S. Yamamoto, S.-a. Hyodo, J. Chem. Phys. 121 (2004) 7586.
[167] W. L. Jolly, D. N. Hendrickson, J. Am. Chem. Soc. 92 (1970) 1863.
[168] J. M. Hollander, W. L. Jolly, Acc. Chem. Res. 3 (1970) 193.
[169] M. Nakamura, M. Sasanuma, S. Sato, M. Watanabe, H. Yamashita, Y. Iguchi, A. Ejiri, S. Nakai, S. Yamaguchi, T. Sagawa, Y. Nakai, T. Oshio, Physical Review 178 (1969) 80
[170] W. H. E. Schwarz, Ang. Chem. Int. Ed. Engl. 13 (1974) 454.
[171] A. Koch, B. M. Nestmann, S. D. Peyerimhoff, Chem. Phys. 161 (1992) 169.
[172] T. H. Dunning Jr., J. Chem. Phys. 90 (1989) 1007.
[173] J. Almlöf, P. R. Taylor, J. Chem. Phys. 86 (1987) 4070.
[174] A. C. Hurley, V. W. Maslen, J. Chem. Phys. 34 (1961) 1919.
[175] W. H. E. Schwarz, Chem. Phys. 11 (1975) 217.
[176] K. Radler, B. Sonntag, T. C. Chang, W. H. E. Schwarz, Chem. Phys. 13 (1976) 363.
[177] C. Reynaud, S. Bodeur, J. L. Marechal, D. Bazin, P. Millié, I. Nenner, U. Rockland, H. Baumgartel, Chem. Phys. 166 (1992) 411.
[178] S. Bodeur, P. Millié, I. Nenner, Phys. Rev. A 41 (1990) 252.
[179] I. Nenner, M. J. Hubin-Franskin, J. Delwiche, P. Morin, S. Bodeur, J. Mol. Struct. 173 (1988) 269.
[180] C. Reynaud, M. A. Gaveau, P. Millié, S. Bodeur, P. Archirel, B. Lévy, I. Nenner, J. Electron Spectrosc. Related Phen. 79 (1996) 357.
[181] T. Koopmans, Physica 1 (1933) 103.
[182] S. Carniato, Y. Luo, J. Electron Spectrosc. Related Phen. 142 (2005) 163.
[183] D. P. Chong, J. Chem. Phys. 103 (1995) 1842.
[184] M. Pulfer, C.-H. Hu, D. P. Chong, Chem. Phys. 216 (1997) 91.
[185] L. Triguero, O. Plashkevych, L. G. M. Pettersson, H. Agren, J. Electron Spectrosc. Related Phen. 104 (1999) 195.

[186] Y. Takahata, D. P. Chong, Journal of Electron Spectroscopy and Related Phenomena 133 (2003) 69.
[187] A. Szabo, N. S. Ostlund, Modern Quantum Chemistry, New York, 1996, p. 5.3.1.
[188] W. H. E. Schwarz, T. C. Chang, Int. J. Quant. Chem. Symp. 10 (1976) 91.
[189] S. Zeggari, Etude ab initio du spectre d'excitation en couche interne du cyclopropane, 2002.
[190] E. R. Davidson, J. Comp. Phys. 17 (1975) 87.
[191] C. Kolczewski, R. Puttner, O. Plashkevych, H. Ågren, V. Staemmler, M. Martins, G. Snell, A. S. Schlachter, M. Sant'Anna, G. Kaindl, L. G. M. Pettersson, J. Chem. Phys. 115 (2001) 6426.
[192] G. Vall-llosera, B. Gao, A. Kivimaki, M. Coreno, J. A. Ruiz, M. de Simone, H. Ågren, E. Rachlew, J. Chem. Phys. 128 (2008) 044316.
[193] C. Kolczewski, R. Puttner, M. Martins, A. S. Schlachter, G. Snell, M. M. Sant'Anna, K. Hermann, G. Kaindl, The Journal of Chemical Physics 124 (2006) 034302.
[194] R. Püttner, C. Kolczewski, M. Martins, A. S. Schlachter, G. Snell, M. Sant'Anna, J. Viefhaus, K. Hermann, G. Kaindl, Chem. Phys. Lett. 393 (2004) 361.
[195] E. E. Rennie, B. Kempgens, H. M. Koppe, U. Hergenhahn, J. Feldhaus, B. S. Itchkawitz, A. L. D. Kilcoyne, A. Kivimaki, K. Maier, M. N. Piancastelli, M. Polcik, A. Rudel, A. M. Bradshaw, J. Chem. Phys. 113 (2000) 7362.
[196] K. Hermann, L. G. M. Pettersson, StoBe (Stockholm-Berlin), a modified version of the DFT-LCGTO program package deMon by A. St.-Amant and D. Salahub (University of Montreal), 2005.
[197] I. G. Eustatiu, T. Tyliszczak, G. Cooper, A. P. Hitchcock, C. C. Turci, A. B. Rocha, M. Barbatti, C. E. Bielschowsky, J. Electron Spectrosc. Related Phen. 156-158 (2007) 158.
[198] M. N. R. Wohlfarth, L. S. Cederbaum, J. Chem. Phys. 116 (2002) 8723.
[199] N. V. Kryzhevoi, N. V. Dobrodey, L. S. Cederbaum, J. Chem. Phys. 119 (2003) 12138.
[200] R. Fink, J. Chem. Phys. 106 (1997) 4038.
[201] S. P. Hau-Riege, Phys. Rev. A 76 (2007) 042511.
[202] E. Andersson, M. Stenrup, J. H. D. Eland, L. Hedin, M. Berglund, L. Karlsson, A. Larson, H. Ågren, J. E. Rubensson, R. Feifel, Phys. Rev. A 78 (2008) 023409.
[203] R. Sankari, M. Ehara, H. Nakatsuji, Y. Senba, K. Hosokawa, H. Yoshida, A. De Fanis, Y. Tamenori, S. Aksela, K. Ueda, Chem. Phys. Lett. 380 (2003) 647.
[204] Y. Ohtsuka, H. Nakatsuji, J. Chem. Phys. 124 (2006) 054110.
[205] M. Nooijen, R. J. Bartlett, J. Chem. Phys. 102 (1995) 6735.
[206] T. X. Carroll, K. J. Borve, L. J. Saethre, J. D. Bozek, E. Kukk, J. A. Hahne, T. D. Thomas, The Journal of Chemical Physics 116 (2002) 10221.
[207] X. Assfeld, J.-L. Rivail, Chem. Phys. Lett. 263 (1996) 100.
[208] N. Ferré, X. Assfeld, J. Chem. Phys. 117 (2002) 4119.
[209] X. A. Pierre-François Loos, Int. J. Quant. Chem. 107 (2007) 2243.
[210] H. Agren, V. Carravetta, O. Vahtras, L. G. M. Pettersson, Theor. Chem. Acc. 97 (1997) 14.
[211] V. Carravetta, O. Plashkevych, H. Ågren, Chem. Phys. 263 (2001) 231.
[212] Y. Luo, H. Ågren, M. Keil, R. Friedlein, W. R. Salaneck, Chem. Phys. Lett. 337 (2001) 176.
[213] I. Minkov, F. Gel'mukhanov, R. Friedlein, W. Osikowicz, C. Suess, G. Ohrwall, S. L. Sorensen, S. Braun, R. Murdey, W. R. Salaneck, H. Ågren, J. Chem. Phys. 121 (2004) 5733.
[214] W. J. Hunt, I. Goddard, William A., Chem. Phys. Lett. 3 (1969) 414.
[215] U. Ekstrom, P. Norman, V. Carravetta, Phys. Rev. A 73 (2006) 022501.
[216] U. Ekstrom, H. Ottosson, P. Norman, J. Phys. Chem. C 111 (2007) 13846.
[217] U. Ekstrom, P. Norman, Phys. Rev. A 74 (2006) 042722.
[218] N. Kosugi, H. Kuroda, Chem. Phys. Lett. 74 (1980) 490.
[219] N. Kosugi, J. Comp. Phys. 55 (1984) 426.
[220] N. Kosugi, Theor. Chem. Acc. 72 (1987) 149.
[221] J. Schirmer, Phys. Rev. A 26 (1982) 2395 LP

[222] A. B. Trofimov, J. Schirmer, J. Phys. B (1995) 2299.
[223] J. Schirmer, A. Thiel, J. Chem. Phys. 115 (2001) 10621.
[224] A. Thiel, J. Schirmer, H. Koppel, J. Chem. Phys. 119 (2003) 2088.
[225] O. Plekan, V. Feyer, R. Richter, M. Coreno, M. de Simone, K. C. Prince, A. B. Trofimov, E. V. Gromov, I. L. Zaytseva, J. Schirmer, Chem. Phys. 347 (2008) 360.
[226] L. S. Cederbaum, W. Domcke, J. Schirmer, Phys. Rev. A 22 (1980) 206 LP
[227] D. P. Chong, Chem. Phys. Lett. 232 (1995) 486.
[228] C.-H. Hu, D. P. Chong, Chem. Phys. Lett. 262 (1996) 729.
[229] C. Bureau, D. P. Chong, K. Endo, J. Delhalle, G. Lecayon, A. Le Moël, Nuc. Inst. Methods Phys. Res. B 131 (1997) 1.
[230] C.-H. Hu, D. P. Chong, Chem. Phys. 216 (1997) 99.
[231] D. P. Chong, C. Bureau, J. Electron Spectrosc. Related Phen. 106 (2000) 1.
[232] C. Bureau, C. Doneux, J. Charlier, J.-L. Anthoine, D. P. Chong, J. Electroanal. Chem. 502 (2001) 58.
[233] A. St-Amant, Université de Montréal, Montréal, 1991.
[234] A. St-Amant, D. R. Salahub, Chem. Phys. Lett. 169 (1990) 387.
[235] D. P. Chong, Y. Takahata, Chem. Phys. Lett. 418 (2006) 286.
[236] D. P. Chong, Chem. Phys. Lett. 441 (2007) 209.
[237] M. Casarin, P. Finetti, A. Vittadini, F. Wang, T. Ziegler, J. Phys. Chem. A 111 (2007) 5270.
[238] R. Kallol, S. DeBeer George, Edward I. Solomon, K. Wieghardt, F. Neese, Chem. Eur. J. 13 (2007) 2783.
[239] F. Neese, Orca-an ab initio, DFT and semiempirical Electronic Structure Package, Max-Planck Institut für Bioanorganische Chemie., Mülheim, 2007.
[240] U. Bergmann, D. Nordlund, P. Wernet, M. Odelius, L. G. M. Pettersson, A. Nilsson, Phys. Rev. B 76 (2007) 024202.
[241] L.-A. Naslund, D. C. Edwards, P. Wernet, U. Bergmann, H. Ogasawara, L. G. M. Pettersson, S. Myneni, A. Nilsson, J. Phys. Chem. A 109 (2005) 5995.
[242] L.-A. Naslund, J. Luning, Y. Ufuktepe, H. Ogasawara, P. Wernet, U. Bergmann, L. G. M. Pettersson, A. Nilsson, J. Phys. Chem. B 109 (2005) 13835.
[243] T. Tokushima, Y. Harada, O. Takahashi, Y. Senba, H. Ohashi, L. G. M. Pettersson, A. Nilsson, S. Shin, Chem. Phys. Lett. 460 (2008) 387.
[244] J. C. Slater, L. Per-Olov, Advances in Quantum Chemistry. Academic Press, 1972, p. 1.
[245] J. C. Slater, K. H. Johnson, Phys. Rev. B 5 (1972) 844.
[246] L. Triguero, L. G. M. Pettersson, H. Ågren, Phys. Rev. B 58 (1998) 8097.
[247] Y. Imamura, H. Nakai, Chem. Phys. Lett. 419 (2006) 297.
[248] A. Nakata, Y. Imamura, H. Nakai, J. Chem. Phys. 125 (2006) 064109.
[249] A. Nakata, Y. Imamura, T. Otsuka, H. Nakai, J. Chem. Phys. 124 (2006) 094105.
[250] Y. Imamura, H. Nakai, Int. J. Quant. Chem. 107 (2007) 23.
[251] Y. Imamura, T. Otsuka, H. Nakai, J. Comp. Chem. 28 (2007) 2067.
[252] A. Nakata, Y. Imamura, H. Nakai, J. Chem. Theory Comput. 3 (2007) 1295.
[253] H. N. Yutaka Imamura, Int. J. Quant. Chem. 107 (2007) 23.
[254] T. O. Yutaka Imamura, Hiromi Nakai,, J. Comp. Chem. 28 (2007) 2067.
[255] G. de Alti, P. Decleva, A. Lisini, Chem. Phys. 90 (1984) 231.
[256] G. De Alti, P. Decleva, A. Lisini, Chem. Phys. 93 (1985) 225.
[257] P. Decleva, A. Lisini, Chem. Phys. Lett. 120 (1985) 257.
[258] P. Decleva, A. Lisini, Chem. Phys. 97 (1985) 95.
[259] P. Decleva, A. Lisini, Chem. Phys. 106 (1986) 39.
[260] P. Decleva, A. Lisini, Chem. Phys. 112 (1987) 339.
[261] P. Decleva, G. Fronzoni, A. Lisini, Chem. Phys. 134 (1989) 307.
[262] M. Ohno, P. Decleva, Chem. Phys. 156 (1991) 309.
[263] M. Brosolo, P. Decleva, Chem. Phys. 159 (1992) 185.

[264] P. Decleva, G. Fronzoni, A. Lisini, Chem. Phys. 168 (1992) 51.
[265] P. Decleva, M. Ohno, Chem. Phys. 164 (1992) 73.
[266] P. Decleva, M. Ohno, Chem. Phys. 160 (1992) 341.
[267] P. Decleva, M. Ohno, Chem. Phys. 160 (1992) 353.
[268] A. Lisini, P. Decleva, Chem. Phys. 168 (1992) 1.
[269] A. Baldovin, G. De Alti, P. Decleva, G. Fronzoni, A. Lisini, Chem. Phys. 176 (1993) 67.
[270] M. Brosolo, P. Decleva, A. Lisini, Chem. Phys. Lett. 203 (1993) 586.
[271] G. Fronzoni, P. Decleva, A. Lisini, Chem. Phys. 174 (1993) 57.
[272] A. Lisini, M. Brosolo, P. Decleva, Chem. Phys. Lett. 209 (1993) 135.
[273] A. Lisini, P. Decleva, G. Fronzoni, Chem. Phys. 171 (1993) 159.
[274] M. Ohno, P. Decleva, Chem. Phys. 171 (1993) 9.
[275] M. Ohno, P. Decleva, Chem. Phys. 169 (1993) 173.
[276] M. Brosolo, P. Decleva, A. Lisini, Chem. Phys. 181 (1994) 85.
[277] P. Decleva, G. Fronzoni, A. Lisini, M. Stener, Chem. Phys. 186 (1994) 1.
[278] G. Fronzoni, G. De Alti, P. Decleva, A. Lisini, Chem. Phys. 195 (1995) 171.
[279] F. Guillot, C. Dézarnaud-Dandine, M. Tronc, A. Lisini, P. Decleva, G. Fronzoni, Chem. Phys. 191 (1995) 289.
[280] M. Stener, A. Lisini, P. Decleva, Chem. Phys. 191 (1995) 141.
[281] G. Fronzoni, M. Stener, A. Lisini, P. Decleva, Chem. Phys. 210 (1996) 447.
[282] F. Guillot, C. Dézarnaud-Dandine, M. Tronc, A. Modelli, A. Lisini, P. Decleva, G. Fronzoni, Chem. Phys. 205 (1996) 359.
[283] G. Fronzoni, P. Decleva, Chem. Phys. 220 (1997) 15.
[284] G. Fronzoni, P. Decleva, Chem. Phys. 237 (1998) 21.
[285] G. Fronzoni, M. Stener, P. Decleva, G. De Alti, Chem. Phys. 232 (1998) 9.
[286] G. Fronzoni, M. Stener, P. Decleva, Chem. Phys. 246 (1999) 127.
[287] S. Stranges, M. Alagia, G. Fronzoni, P. Decleva, J. Phys. Chem. A 105 (2001) 3400.
[288] E. R. Davidson, MELDF, QCPE Program 580. QCPE Bull. 9, 98., 1989.
[289] A. Lisini, P. Decleva, Int. J. Quant. Chem. 52 (1994) 549.
[290] H. Bachau, E. Cormier, P. Decleva, J. E. Hansen, F. Martin, Rep. Prog. Phys. (2001) 1815.
[291] G. Fronzoni, M. Stener, S. Furlan, P. Decleva, Chem. Phys. 273 (2001) 117.
[292] M. Stener, P. Decleva, I. Cacelli, R. Moccia, R. Montuoro, Chem. Phys. 272 (2001) 15.
[293] D. Toffoli, M. Stener, G. Fronzoni, P. Decleva, Chem. Phys. 276 (2002) 25.
[294] G. Fronzoni, M. Stener, P. Decleva, Chem. Phys. 298 (2004) 141.
[295] D. Toffoli, P. Decleva, J. Chem. Phys. 128 (2008) 234101.
[296] G. Fronzoni, M. Stener, P. Decleva, F. Wang, T. Ziegler, E. van Lenthe, E. J. Baerends, Chem. Phys. Lett. 416 (2005) 56.
[297] M. Stener, G. Fronzoni, R. De Francesco, Chem. Phys. 309 (2005) 49.
[298] M. Stener, G. Fronzoni, P. Decleva, J. Chem. Phys. 122 (2005) 234301.
[299] G. Fronzoni, R. DeFrancesco, M. Stener, M. Causa, J. Phys. Chem. B 110 (2006) 9899.
[300] M. Stener, D. Di Tommaso, G. Fronzoni, P. Decleva, I. Powis, J. Chem. Phys. 124 (2006) 024326.
[301] M. Stener, D. Toffoli, G. Fronzoni, P. Decleva, J. Chem. Phys. 124 (2006) 114306.
[302] G. Chaban, M. W. Schmidt, M. S. Gordon, Theor. Chem. Acc. 97 (1997) 88.
[303] M. W. Schmidt, K. K. Baldridge, J. A. Boatz, S. T. Elbert, M. S. Gordon, J. H. Jensen, S. Koseki, N. Matsunaga, K. A. Nguyen, S. Su, T. L. Windus, M. Dupuis, J. A. Montgomery Jr, J. Comp. Chem. 14 (1993) 1347.
[304] M. S. Gordon, M. W. Schmidt, in G.F. C.E. Dykstra, K.S. Kim, G.E .Scuseria (Ed.), Theory and Applications of Computational Chemistry, the first forty years. Elsevier, Amsterdam, 2005, p. 1167.
[305] P. Pulay, J. Comp. Chem. 3 (1982) 556.

[306] P. J. Knowles, J. S. Andrews, R. D. Amos, N. C. Handy, J. A. Pople, Chem. Phys. Lett. 186 (1991) 130.
[307] W. J. Lauderdale, J. F. Stanton, J. Gauss, J. D. Watts, R. J. Bartlett, Chem. Phys. Lett. 187 (1991) 21.
[308] T. J. Lee, A. P. Rendell, K. G. Dyall, D. Jayatilaka, J. Chem. Phys. 100 (1994) 7400.
[309] T. J. Lee, D. Jayatilaka, Chem. Phys. Lett. 201 (1993) 1.
[310] S. E. Wheeler, W. D. Allen, H. F. Schaefer, III, J. Chem. Phys. 128 (2008) 074107.
[311] T. D. Crawford, H. F. Schaefer III, T. J. Lee, J. Chem. Phys. 105 (1996) 1060.
[312] S. Evangelisti, J.-P. Daudey, J.-P. Malrieu, Chem. Phys. 75 (1983) 91.
[313] C. Angeli, R. Cimiraglia, M. Persico, A. Toniolo, Theor. Chem. Acc. 98 (1997) 57.
[314] C. Angeli, M. Persico, Theor. Chem. Acc. 98 (1997) 117.
[315] C. Angeli, R. Cimiraglia, M. Persico, Theor. Chem. Acc. 100 (1998) 324.
[316] C. Angeli, R. Cimiraglia, Theor. Chem. Acc. 105 (2001) 259.
[317] C. Angeli, R. Cimiraglia, Theor. Chem. Acc. 107 (2002) 313.
[318] C. Angeli, R. Cimiraglia, M. Persico, A. Toniolo, Theor. Chem. Acc. 98 (1997) 57.
[319] P.-O. Löwdin, Physical Review 97 (1955) 1474.
[320] R. Broer, W. C. Nieuwpoort, J. Mol Struct. (THEOCHEM) 458 (1998) 19.
[321] L. C. Snyder, J. Chem. Phys. 55 (1971) 95.
[322] N. Kosugi, Chem. Phys. 289 (2003) 117.
[323] P. Glans, P. Skytt, K. Gunnelin, J. H. Guo, J. Nordgren, J. Electron Spectrosc. Related Phen. 82 (1996) 193.
[324] O. Björneholm, M. Bässler, A. Ausmees, I. Hjelte, R. Feifel, H. Wang, C. Miron, M. N. Piancastelli, S. Svensson, S. L. Sorensen, F. Gel'mukhanov, H. Ågren, Phys. Rev. Lett. 84 (2000) 2826.
[325] M. S. Schoffler, J. Titze, N. Petridis, T. Jahnke, K. Cole, L. P. H. Schmidt, A. Czasch, D. Akoury, O. Jagutzki, J. B. Williams, N. A. Cherepkov, S. K. Semenov, C. W. McCurdy, T. N. Rescigno, C. L. Cocke, T. Osipov, S. Lee, M. H. Prior, A. Belkacem, A. L. Landers, H. Schmidt-Bocking, T. Weber, R. Dorner, Science 320 (2008) 920.
[326] K. Ueda, Science 320 (2008) 884.
[327] D. Rolles, M. Braune, S. Cvejanovic, O. Geszner, R. Hentges, S. Korica, B. Langer, T. Lischke, G. Prumper, A. Reinkoster, J. Viefhaus, B. Zimmermann, V. McKoy, U. Becker, Nature 437 (2005) 711.
[328] B. Kempgens, H. Köppel, A. Kivimäki, M. Neeb, L. S. Cederbaum, A. M. Bradshaw, Phys. Rev. Lett. 79 (1997) 3617.
[329] U. Hergenhahn, O. Kugeler, A. Rudel, E. E. Rennie, A. M. Bradshaw, J. Phys. Chem. A 105 (2001) 5704.
[330] P. S. Bagus, H. F. Schaefer III, J. Chem. Phys. 56 (1972) 224.
[331] A. Denis, J. Langlet, J. P. Malrieu, Theoret. Chim. Acta 29 (1973) 117.
[332] A. Denis, J. Langlet, J. P. Malrieu, Theoret. Chim. Acta 38 (1975) 49.
[333] L. S. Cederbaum, W. Domcke, J. Chem. Phys. 66 (1977) 5084.
[334] D. P. Chong, J. Electron Spectrosc. Related Phen. 159 (2007) 94.
[335] S. Canuto, O. Goscinski, M. Zerner, Chem. Phys. Lett. 68 (1979) 232.
[336] B. D. Dunietz, M. Head-Gordon, J. Phys. Chem. A 107 (2003) 9160.
[337] A. F. Voter, W. A. Goddard, Chem. Phys. 57 (1981) 253.
[338] E. Hollauer, M. A. C. Nascimento, J. Chem. Phys. 99 (1993) 1207.
[339] W. Domcke, L. S. Cederbaum, Chem. Phys. 25 (1977) 189.
[340] N. V. Dobrodey, H. Köppel, L. S. Cederbaum, Phys. Rev. A 60 (1999) 1988.
[341] H. Jahn, Proc. Roy. Soc. London. A 164 (1938) 117.
[342] H. Jahn, E. Teller, Proc. Roy. Soc. London. A 161 (1937) 220.
[343] R. Engelman, The Jahn–Teller Effect, Wiley, New York, 1972.

[344] A. Kivimäki, B. Kempgens, K. Maier, H. M. Köppe, M. N. Piancastelli, M. Neeb, A. M. Bradshaw, Phys. Rev. Lett. 79 (1997) 998.
[345] K. Wiesner, A. N. de Brito, S. L. Sorensen, N. Kosugi, O. Bjorneholm, J. Chem. Phys. 122 (2005) 154303.
[346] F. X. Gadea, H. Köppel, J. Schirmer, L. S. Cederbaum, K. J. Randall, A. M. Bradshaw, Y. Ma, F. Sette, C. T. Chen, Phys. Rev. Lett. 66 (1991) 883.
[347] H. Köppel, F. X. Gadea, G. Klatt, J. Schirmer, L. S. Cederbaum, J. Chem. Phys. 106 (1997) 4415.
[348] A. Lindgren, N. Kosugi, M. Gisselbrecht, A. Kivimaki, F. Burmeister, A. N. de Brito, S. L. Sorensen, J. Chem. Phys. 128 (2008) 114311.
[349] E. Biémont, Spectroscopie Atomique Instrumentation et structures atomiques, De Boeck, Bruxelles, 2006.
[350] R. D. Cowan, The Theory of Atomic Structure and Spectra, University of California Press, Berkeley and Los Angeles, 1981.
[351] W. Kauzmann, Quantum chemistry, an introduction, Academic Press, New York, 1957.
[352] T. Karlsen, K. J. Borve, J. Chem. Phys. 112 (2000) 7979.
[353] W. J. Stevens, H. Basch, M. Krauss, J. Chem. Phys. 81 (1984) 6026.
[354] S. Huzinaga, L. Seijo, Z. Barandiaran, M. Klobukowski, J. Chem. Phys. 86 (1987) 2132.
[355] K. Hermann, L. G. M. Pettersson, M. E. Casida, C. Daul, A. Goursot, A. Koester, E. Proynov, A. St Amant, D. R. Salahub, H. D. Carravetta, C. Friedrich, N. Godbout, J. Guan, C. Jamorski, M. Leboeuf, M. Leetmaa, M. Nyberg, S. Patchkovskii, L. Pedocchi, F. Sim, L. Triguero, Vela, StoBe-deMon 2006,2.2., 2006.
[356] D. P. Chong, C.-H. Hu, P. Duffy, Chem. Phys. Lett. 249 (1996) 491.
[357] G. Cavigliasso, D. P. Chong, J. Chem. Phys. 111 (1999) 9485.
[358] S. Carniato, P. Millié, J. Chem. Phys. 116 (2002) 3521.
[359] T. H. Dunning Jr., P. J. Hay, in H.F. Schaefer III (Ed.), Methods of Electronic Structure Theory. Plenum Press, New York, 1977, p. 1.
[360] T. H. Dunning Jr., J. Chem. Phys. 55 (1971) 716.
[361] T. H. Dunning Jr., J. Chem. Phys. 55 (1971) 3958.
[362] L. Fusti-Molnar, P. Pulay, J. Chem. Phys. 116 (2002) 7795.
[363] M. Iannuzzi, J. Hutter, PCCP 9 (2007) 1599.
[364] D. E. Woon, T. H. Dunning Jr., J. Chem. Phys. 98 (1993) 1358.
[365] D. E. Woon, T. H. Dunning Jr., J. Chem. Phys. 100 (1994) 2975.
[366] D. E. Woon, T. H. Dunning Jr., J. Chem. Phys. 103 (1995) 4572.
[367] A. K. Wilson, T. van Mourik, T. H. Dunning Jr., J. Mol Struct. (THEOCHEM) 388 (1996) 339.
[368] A. K. Wilson, D. E. Woon, K. A. Peterson, J. Dunning, Thom H., J. Chem. Phys. 110 (1999) 7667.
[369] K. A. Peterson, J. Dunning, Thom H., J. Chem. Phys. 117 (2002) 10548.
[370] T. H. Dunning Jr, D. E. Woon, J. Chem. Phys. 100 (1994) 2975.
[371] T. H. Dunning Jr, D. E. Woon, J. Chem. Phys. 103 (1995) 4572.
[372] R. C. Raffenetti, J. Chem. Phys. 59 (1973) 5936.
[373] U. Gelius, S. Svensson, H. Siegbahn, E. Basilier, Å. Faxälv, K. Siegbahn, Chem. Phys. Lett. 28 (1974) 1.
[374] O. Plashkevych, T. Privalov, H. Ågren, V. Carravetta, K. Ruud, Chem. Phys. 260 (2000) 11.
[375] L. Triguero, O. Plashkevych, L. G. M. Pettersson, H. Ågren, J. Electron Spectrosc. Related Phen. 104 (1999) 195.
[376] U. Hergenhahn, J. Phys. B 37 (2004) R89.
[377] H. D. Schulte, L. S. Cederbaum, J. Chem. Phys. 103 (1995) 698.
[378] P. Norman, H. Ågren, J. Mol Struct. (THEOCHEM) 401 (1997) 107.
[379] D. T. Clark, J. Müller, Chem. Phys. 23 (1977) 429.

[380] O. Goscinski, J. Müller, E. Poulain, H. Siegbahn, Chem. Phys. Lett. 55 (1978) 407.
[381] W. Eberhardt, T. K. Sham, R. Carr, S. Krummacher, M. Strongin, S. L. Weng, D. Wesner, Phys. Rev. Lett. 50 (1983) 1038 LP
[382] S. Svante, J. Phys. B (2005) S821.
[383] R. Thissen, M. Simon, M. J. Hubin-Franskin, J. Chem. Phys. 101 (1994) 7548.
[384] P. Morin, I. Nenner, Phys. Rev. Lett. 56 (1986) 1913 LP
[385] F. X. Gadéa, S. Mathieu, L. S. Cederbaum, J. Mol Struct. (THEOCHEM) 401 (1997) 15.
[386] F. Tarantelli, A. Sgamellotti, L. S. Cederbaum, in D. Mukherjee (Ed.), Applied Many-Body Methods in Spectroscopy and Electronic Structure. Plenum Press, New York 1992.
[387] R. Feifel, Y. Velkov, V. Carravetta, C. Angeli, R. Cimiraglia, P. Salek, F. Gel'mukhanov, S. L. Sorensen, M. N. Piancastelli, A. De Fanis, K. Okada, M. Kitajima, T. Tanaka, H. Tanaka, K. Ueda, J. Chem. Phys. 128 (2008) 064304.
[388] F. Tarantelli, L. S. Cederbaum, A. Sgamellotti, J. Electron Spectrosc. Related Phen. 76 (1995) 47.
[389] D. Minelli, F. Tarantelli, A. Sgamellotti, L. S. Cederbaum, J. Electron Spectrosc. Related Phen. 74 (1995) 1.
[390] F. Tarantelli, A. Sgamellotti, L. S. Cederbaum, J. Electron Spectrosc. Related Phen. 68 (1994) 297.
[391] J. Ivanic, J. Chem. Phys. 119 (2003) 9364.
[392] J. Ivanic, J. Chem. Phys. 119 (2003) 9377.
[393] A. B. Trofimov, T. E. Moskovskaya, E. V. Gromov, H. Köppel, J. Schirmer, Phys. Rev. A 64 (2001) 022504.
[394] A. B. Trofimov, E. V. Gromov, T. E. Moskovskaya, J. Schirmer, J. Chem. Phys. 113 (2000) 6716.
[395] A. B. Trofimov, E. V. Gromov, H. Koppel, J. Schirmer, K. C. Prince, R. Richter, M. D. Simone, M. Coreno, J. Phys. B (2003) 3805.
[396] K. J. Børve, L. J. Sæthre, T. D. Thomas, T. X. Carroll, N. Berrah, J. D. Bozek, E. Kukk, Phys. Rev. A 63 (2000) 012506.
[397] G. Karlström, R. Lindh, P.-Å. Malmqvist, B. O. Roos, U. Ryde, V. Veryazov, P.-O. Widmark, M. Cossi, B. Schimmelpfennig, P. Neogrady, L. Seijo, Comp. Mat. Sci. 28 (2003) 222.
[398] K. Sidhoum, Simulation ab initio de spectres d'excitation en couche interne : cas de la s-triazine, 2003.
[399] E. Apen, A. Hitchcock, J. Gland, J. Phys. Chem. 97 (1993) 6859.
[400] K. H. Sze, C. E. Brion, J. Electron Spectrosc. Related Phen. 57 (1991) 117.
[401] Y. Takahata, C. E. Wulfman, D. P. Chong, J. Mol Struct. (THEOCHEM) 863 (2008) 33.
[402] D. P. Chong, J. Electron Spectrosc. Related Phen. 148 (2005) 115.
[403] A. P. Hitchcock, D. C. Newbury, I. Ishii, J. Stohr, J. A. Horsley, R. D. Redwing, A. L. Johnson, F. Sette, J. Chem. Phys. 85 (1986) 4849.
[404] F. Illas, M. Merchan, M. Pélissier, J. P. Malrieu, Chem. Phys 107 (1986) 361.
[405] F. L. Sefyani, J. Schamps, D. Duflot, JQSRT 54 (1995) 1027.
[406] F. Duschinsky, Acta Physicochim. URSS 7 (1937) 551.
[407] F. S. Andrea Peluso, Giuseppe Del Re,, Int. J. Quant. Chem. 63 (1997) 233.
[408] Q. Peng, Y. Yi, Z. Shuai, J. Shao, J. Am. Chem. Soc. 129 (2007) 9333.
[409] S. Legendre, E. Giglio, M. Tarisien, A. Cassimi, B. Gervais, L. Adoui, J. Phys. B 38 (2005) L233.
[410] S. Legendre, Etude de l'ionisation et de la dissociation d'H2O induites par collision avec des ions multichargés rapides, Université de Caen, Caen, 2006.
[411] T. J. Van Huis, S. S. Wesolowski, Y. Yamaguchi, H. F. Schaefer III, J. Chem. Phys. 110 (1999) 11856.

[412] P. R. Bunker, O. Bludsky, P. Jensen, S. S. Wesolowski, T. J. Van Huis, Y. Yamaguchi, H. F. Schaefer, J. Mol. Spectrosc. 198 (1999) 371.
[413] B. Jansik, A. Rizzo, L. Frediani, K. Ruud, S. Coriani, J. Chem. Phys. 125 (2006) 234105.
[414] C. S. Callam, S. J. Singer, T. L. Lowary, C. M. Hadad, J. Am. Chem. Soc. 123 (2001) 11743.
[415] K. B. Borisenko, S. Samdal, I. F. Shishkov, L. V. Vilkov, J. Mol. Struct. 448 (1998) 29.
[416] E. I. Solomon, B. Hedman, K. O. Hodgson, A. Dey, R. K. Szilagyi, Coord. Chem. Rev. 249 (2005) 97.
[417] S. Woittequand, D. Duflot, M. Monnerville, B. Pouilly, C. Toubin, S. Briquez, H.-D. Meyer, J. Chem. Phys. 127 (2007) 164717.

Curriculum vitae

Etat civil

Nom : DUFLOT
Prénom : Denis
Né le 5 juillet 1968, 40 ans
Adresse : Université des Sciences et Technologies de Lille (Lille1)
Laboratoire de Physique des Lasers, Atomes et Molécules
UMR CNRS 8523 Bâtiment P5
F-59655 Villeneuve d'Ascq Cedex
France
e-mail : Denis.Duflot@univ-lille1.fr
Tél : 03 20 43 49 80
Fax : 03 20 43 40 84

Trajectoire professionnelle

Année	Fonction	Lieu
1990	DEA "Lasers, Molécules, Rayonnement Atmosphérique"	Laboratoire de Spectroscopie Moléculaire (LSM), USTL
1991-1994	Doctorant	Laboratoire de Dynamique Moléculaire et Photonique (LDMP), USTL
1994	ATER (demi-poste)	Laboratoire de Dynamique Moléculaire et Photonique (LDMP), USTL
1995	Stage post-doctoral	Laboratoire de Spectroscopie d'Électrons Diffusés, Université de Liège, Belgique
Depuis fin 1995	Maître de Conférences classe normale	Laboratoire de Dynamique Moléculaire et Photonique (LDMP) puis PhLAM, USTL

Cursus et diplômes universitaires

Année	Diplôme	Lieu
1990	Maîtrise de physique fondamentale	USTL
1991	DEA	USTL
1994	Thèse de doctorat	USTL

Thèmes de recherche

Utilisation des méthodes de la chimie quantique à l'étude des états électroniques excités de molécules en phase gazeuse. Applications :

a) Structure et processus de fragmentation de molécules doublement ionisées (dications)

b) Spectroscopie en couches internes

c) Spectroscopie en couches de valence (UV et ionisation)

Collaborations (2009)

- S. Canneaux, Physico-Chimie des Processus de Combustion et de l'Atmosphère (PC2A), USTL
- J. Delwiche, M.-J. Hubin-Franskin, Laboratoire de Spectroscopie d'Electrons Diffusés, Université de Liège, Belgique
- A. Giuliani, DISCO beamline, Synchrotron Soleil, France & CEPIA, Institut National de la Recherche Agronomique (INRA), Nantes, France
- N. Mason, Centre of Molecular and Optical Sciences, Department of Physics and Astronomy, The Open University, Milton Keynes, Royaume-Uni
- P. Limão-Vieira, Laboratório de Colisões Atómicas e Moleculares, CEFITEC, Departamento de Física, Universidade Nova de Lisboa, Caparica, Portugal
- S.V. Hoffmann, Institute for Storage Ring Facilities, University of Aarhus, Danemark
- B.P. Marinkovic, Laboratory for atomic collision processes, Institute of Physics, Belgrade, Serbie
- B. Gervais, GANIL, Caen

Encadrements

- 1997 : V. Antzoulatos, stage recherche 2ème année de Magistère de Chimie Physique d'Orsay
- 1997-2001 : N. Chabert, doctorant (20%), 1 publication
- 2001-2002 : S. Zeggari, DEA "Lasers, Molécules, Rayonnement Atmosphérique", 1 publication
- 2002-2003 : K. Sidhoum, DEA "Lasers, Molécules, Rayonnement Atmosphérique", 1 publication
- 2003-2004 : M. Zuhair, DEA "Lasers, Molécules, Rayonnement Atmosphérique"

Activités d'enseignement

Année	Fonction	Heures (TD)	Niveau	Matière
			Période pré-LMD	
1990-1991	Vacataire	8	DEUG A2	TP Thermodynamique
1991-1994	Moniteur	64	DEUG A2	TP Thermodynamique, Electronique
1994	ATER	96	DEUG A2	TP Thermodynamique, Electronique TD Thermodynamique
1995-1997	MCF	~50	DEUG MIAS1	TP Métrologie, Optique géométrique
1995-2004	MCF	~50-70	DEUG STPI1	TD/TP Mécanique, optique géométrique, électrostatique, magnétostatique
1995-2004	MCF	~80-100	DEUG STPI2	TD/TP Thermodynamique, optique ondulatoire, électromagnétisme
1995-2004	MCF	25	DEUG STPI2, Option "Génie des procédés"	TD/TP Métrologie/physique appliquée
2000-2004	MCF	25	Remise à niveau BTS/DUT entrant en DEUG STPI2	Cours/TD électrostatique, magnétostatique
			Période post-LMD	
2004-	MCF	~55	L1/S1 SVT	Cours/TD/TP Mécanique des fluides, optique géométrique
2004-	MCF	~60	L1/S2 Physique-Chimie	Cours/TD/TP Electrocinétique
2004-	MCF	~15	L2/S3 toutes filières	TP Electromagnétisme
2004-	MCF	25	L3/S6 Physique fondamentale et Sciences physiques	TD Astrophysique
2004-	MCF	12	M2 Physico-chimie du vivant	Cours : introduction aux ondes, applications en imagerie biologique/médicale

Suivi de stages/projets

Année	Niveau	Nature
	Période pré-LMD	
1995-2004	DEUG STPI1	Sujets bibliographiques (rédaction de mémoire)
1995-2004	DEUG STPI2	Sujets bibliographiques (rédaction de mémoire et exposé oral)
1995-2004	DEUG STPI2	Stages "découverte de l'entreprise" : suivi, lecture du rapport
1995-2004	MST "Mesures et contrôles" 1ère et 2ème années	Stages en contrôle qualité : suivi, lecture du rapport, soutenance orale
2000-2004	Maîtrise de physique	"Mini-stages" découverte des thèmes de recherche d'un laboratoire : introduction à la chimie quantique (soutenance orale)
	Période post-LMD	
2004-	L3/S6 Physique fondamentale et Sciences physiques	Exposés oraux d'astrophysique
2008-	M1 Physique	Stages de spectroscopie à l'Observatoire de Lille : suivi, lecture du rapport, soutenance orale

Responsabilités collectives et divers

- Responsable de l'impression et de la vente aux étudiants des cours polycopiés de l'UFR de Physique (1991-1993). Membre du bureau de l'Association des Diplômés et Étudiants de Physique (ADEP).
- Conception, achat (~150 kF), rédaction des polycopiés et mise en place de 5 séances de TP de métrologie/physique appliquée (optique ondulatoire en ondes centimétriques, méthode de zéro, pompe à chaleur, conduction thermique, régulation de température remplacé en 1997 par biprisme de Fresnel) pour l'ouverture de l'option "Génie des Procédés" du DEUG SPTI 2ème année (1995-1996; responsable unique des TP et TD de ce module jusqu'à la mise en place du LMD en 2004).
- Représentant de l'équipe à la commission "Bibliothèque" de l'UFR de physique (1997-2000).
- Création et maintenance du site internet de l'équipe (1999-2005).
- Opération Physique Itinérante : présentation d'expériences de physique dans les collèges et lycées de la région (1998-2000).
- Responsable des plannings pour les intervenants de physique en DEUG STPI1 et 2 (1998-2004).
- Responsable du TP Electrostatique en DEUG STPI1 (2001-2004).
- Responsable des TP d'Electrocinétique de Licence 1/S2 (toutes filières) : emplois du temps, gestion des salles, organisation des examens (~400 étudiants, ~25 enseignants) (depuis 2004).

- Responsable du TP Force de Laplace en Licence2/S3 (toutes filières) (depuis 2004).
- Opération RLU (Relations Lycée-Universités) : présentation de l'offre de formation de l'université dans les lycées sous forme de projection de diaporamas et/ou participation aux forums orientation/carrières organisés localement par les lycées (depuis 2001).
- Participation aux Journées Portes Ouvertes de l'université : présentation de l'offre de formation de l'UFR de physique, entretiens avec les lycéens (depuis 2004).
- Plan Académique de Formation (PAF) : initiation (3h) à l'astronomie pour les professeurs du secondaire (collèges et lycée) sur le thème "Les caractéristiques physique du Soleil" (janvier 2009).

Publications

- 25 articles publiés dans des revues à comité de lecture
- 1 acte de colloque

Communications

- 10 communications orales
- 23 communications par affiches
- 3 séminaires

LISTE DES PUBLICATIONS

- **ARTICLES**

1. R. Thissen, J. Delwiche, J-M. Robbe, D. Duflot, J-P. Flament, J. H. D. Eland : "Dissociations of the ethyne dication $C_2H_2^{++}$".
J. Chem. Phys., **99** (9), 6590-6599 (1993).

2. D. Duflot, J-M. Robbe, J-P. Flament : "*Ab initio* potential energy surfaces for $C_2H \rightarrow C_2 + H$ photodissociation".
J. Chem. Phys., **100** (2), 1236-1246 (1994).

3. D. Duflot, J-M. Robbe, J-P. Flament : "*Ab initio* study of the acetylene and vinylidene dications fragmentation".
J. Chem. Phys., **102** (1), 355-363 (1995).

4. F.L. Sefyani, J. Schamps, D. Duflot : "Theoretical study of the radiative properties of the $A^1\Pi$ - $X^1\Sigma^+$ system of the GeO molecule".
J. Quant. Spectrosc. Rad. Trans., **54** (6) 1027-1034 (1995).

5. D. Duflot, J-M. Robbe, J-P. Flament : "The stability of the CH_3Cl dication".
J. Chem. Phys., **103** (24), 10571-10579 (1995).

6. M-J. Hubin-Franskin, H. Aouni, D. Duflot, F. Motte-Tollet, C. Hannay, L. F. Ferreira, G. Tourillon : "Inner-shell excitation of monocyanoethylene, trans-dicyanoethylene, and allylcyanide by electron energy loss spectroscopy".
J. Chem. Phys., **106** (1), 35-45 (1997).

7. D. Duflot, J-M. Robbe, J-P. Flament : "*Ab initio* study of the chloromethane dication fragmentation".
Int. J. Mass Spectrom. Ion Process., **171**, 215-230 (1997).

8. D. Duflot, C. Hannay, J-P. Flament, M-J. Hubin-Franskin : "Electronic excitation of gaseous pyrrole and pyrazole by inner-shell electron energy loss spectroscopy".
J. Chem. Phys., **109** (13), 5308-5318 (1998).

9. C. Hannay, D. Duflot, J-P. Flament, M-J. Hubin-Franskin : "The core excitation of pyridine and pyridazine : an electron spectroscopy and *ab initio* study".
J. Chem. Phys., **110** (13), 5600-5610 (1999).

10. S. Kassi, D. Grée, R. Grée, D. Duflot, D. Petitprez, G. Wlodarczak : "Microwave spectrum of cyano-1-fluoro-3-but-1-ene".
J. Mol. Spectrosc., **202**, 19-23 (2000).

11. D. Duflot, J-P. Flament, J. Heinesch, M-J. Hubin-Franskin : "Re-analysis of the K-shell spectrum of benzene".
J. Electron Spectrosc. Relat. Phenom., **113**, 79-90 (2000).

12. D. Duflot, N. Chabert, J-P. Flament J-M. Robbe, I.C. Walker, J.H. Cameron, A. Giuliani, M-J. Hubin-Franskin, J. Delwiche : "Thiazyl chloride : an experimental and theoretical study of the valence HeI photoelectron spectrum".
Chem. Phys., **288** (1), 95-104 (2003).

13. D. Duflot, J.-P. Flament, I. C. Walker, J. Heinesch, M-J. Hubin-Franskin : "Core shell excitation of 2-propenal (acrolein) at the O1s and C1s edges : an experimental and *ab initio* study".
J. Chem. Phys., **118** (3), 1137-1145 (2003).

14. D. Duflot, J.-P. Flament, A. Giuliani, J. Heinesch, M-J. Hubin-Franskin : "Core shell excitation of furan at the O1s and C1s edges : an experimental and *ab initio* study".
J. Chem. Phys., **119** (17), 8946-8955 (2003).

15. D. Duflot, J.-P. Flament, A. Giuliani, J. Heinesch, M-J. Hubin-Franskin : "*Ab initio* and experimental study of the K-shell spectra of 2,5-dihydrofuran".
Chem. Phys., **310** (1-3), 67-75 (2005).

16. D. Duflot, K. Sidhoum, J.-P. Flament, A. Giuliani, J. Heinesch, M.-J. Hubin-Franskin : "*Ab initio* and experimental study of the K-shell spectra of *s*-triazine".
Eur. Phys. J. D, **35** (2), 239-248 (2005). (article invité dans : "topical issue : Electron-driven atomic and molecular processes").

17. P. Limão-Vieira, A. Giuliani, J. Delwiche, R. Parafita, R. Mota, D. Duflot, J.-.P Flament, E. Drage, P. Cahillane, N. J. Mason, S. V. Hoffmann, M.-J. Hubin-Franskin : "Acetic acid electronic state spectroscopy by high-resolution vacuum ultraviolet photo-absorption, electron impact, He(I) photoelectron spectroscopy and *ab initio* calculations".
Chem. Phys., **324** (2-3), 339-349 (2006).

18. D. Duflot, S. Zeggari, J.-P. Flament : "*Ab initio* study of core excited cyclopropane".
Chem. Phys., **327** (2-3), 518-528 (2006).

19. D. Duflot, J.-P. Flament, A. Giuliani, J. Heinesch, M. Grogna, M.-J. Hubin-Franskin : "C1*s* and N1*s* core excitation of aniline: Experiment by electron impact and *ab initio* calculations".
Phys. Rev. A, **75**, 052719 (1-12) (2007). Voir aussi : Virtual Journal of Ultrafast Science, **6**, n°6 (2007) (http://www.vjultrafast.org).

20. P. Limão-Vieira, E. Vasekova, A. Giuliani, J. M. C. Lourenço, P. M. Santos, D. Duflot, S. V. Hoffmann, N. J. Mason, J. Delwiche, M. -J. Hubin-Franskin : "Perfluorocyclobutane electronic state spectroscopy by high-resolution vacuum ultraviolet photoabsorption, electron impact, He I photoelectron spectroscopy, and *ab initio* calculations".
Phys. Rev. A **76**, 032509 (1-11) (2007).

21. S. Woittequand, D. Duflot, M. Monnerville, B. Pouilly, C. Toubin, H.-D. Meyer, S. Briquez: "Classical and quantum studies of the photodissociation of a HX (X = Cl, F) molecule adsorbed on ice".
J. Chem. Phys. **127** (16), 164717-(1-11) (2007).

22. P. Limaão-Vieira, D. Duflot, A. Giuliani, E. Vasekova, J. M. C. Lourenço, P. M. Santos, S. V. Hoffmann, N. J. Mason, J. Delwiche, M. -J. Hubin-Franskin: "Electronic State Spectroscopy of c-C_5F_8 Explored by Photoabsorption, Electron Impact, Photoelectron Spectroscopies and Ab Initio Calculations".

J. Phys. Chem. A, **112** (13), 2782 -2793, 2008.

23. A. Giuliani, P. Limão-Vieira, D. Duflot, A. R. Milosavljevic, B. P. Marinkovic, S. V. Hoffmann, N. Mason, J. Delwiche, M.-J. Hubin Franskin : " Electronic states of neutral and ionized tetrahydrofuran studied by VUV spectroscopy and *ab initio* calculations".
Eur. Phys. J. D, **51** (1), 97-108 (2008). (article invité dans : "topical issue : Bio macromolecules").

24. D. Duflot, J.-P. Flament, A. Giuliani, J. Heinesch, M.-J. Hubin-Franskin : "Electronic excitation of gaseous acetic acid studied by K-shell electron energy loss spectroscopy and *ab initio* calculations".
Int. J. Mass Spectrom., **277** (1-3), 70-78 (2009) (article invité dans : "Eugen Illenberger Honor Issue").

25. A. Vicente, R. Antunes, D. Almeida, I. J. A. Franco, S. V. Hoffmann, N. J. Mason, S. Eden, D. Duflot, S. Canneaux, J. Delwiche, M.-J. Hubin-Franskin, P. Limão-Vieira : "Propionic, butyric and valeric acids VUV spectroscopy and theoretical calculations".
Phys. Chem. Chem. Phys., sous presse.

26. B. Gervais, E. Giglio, L. Adoui, A. Cassimi, D. Duflot, M. E. Galassi : "The H_2O^{2+} potential energy surfaces dissociating into H^+/OH^+ : Theoretical analysis of the isotopic effect".
Accepté à J. Chem. Phys.

- **ACTES DE COLLOQUES**

1. H. Lavendy, J-M. Robbe, D. Duflot, J-P. Flament : "MCSCF-CI study of the isomerization reaction HCSi → HSiC"
"Physico-chimie des molécules et grains dans l'espace", Mont Saint-Odile, France, 6-10 septembre 1993, éd. I. Nenner, p. 343 (American Institute of Physics, Proceedings 312, 1994).

- **AFFICHES**

1. D. Duflot, J-M. Robbe, J-P. Flament : "Etude *ab initio* de la dissociation du dication éthyne $C_2H_2^{++}$".

Affiche présentée à la 3ème Université d'été de Physico-Chimie Théorique, La Londe Les Maures, France, 13-17 septembre 1993.
Affiche présentée au XXIème Congrès International des Chimistes Théoriciens d'expression latine, Grenoble, France, 20-24 septembre 1993.

2. H. Lavendy, J-M. Robbe, D. Duflot, J-P. Flament : "MCSCF-CI study of the isomerization reaction HCSi → HSiC".

Affiche présentée au colloque "Physico-chimie des molécules et grains dans l'espace", Mont Saint-Odile, France, 6-10 septembre 1993.

3. F.L. Sefyani, J. Schamps, D. Duflot : "Interférence quantique intrinsèque dans le spectre électronique d'émission infrarouge de Si_2 et SiC".

Affiche présentée au colloque "Journées de Spectroscopie Moléculaire (JSM)", Albi, France, 18-19 Juillet 1994.

4. D. Duflot, J-M. Robbe, J-P. Flament : "Etude *ab initio* de la fragmentation des dications acétylène et vinylidène".
Affiche présentée au colloque "Dynamique des Ions, Atomes et Molécules (DIAM3)", Albi, France, 19-21 Juillet 1994.

5. J-M. Robbe, H. Lavendy, J-P. Flament, D. Duflot : "Etude structurale des agrégats $Si_mC_p^+$ ($m+p \leq 6$) par DFT".

Affiche présentée au Symposium International "Méthodes de la Fonctionelle de Densité et leurs applications", Grenoble, France, 20-22 Mai 1997.

6. D. Duflot, J-M. Robbe, J-P. Flament : "Etude *ab initio* de la fragmentation du dication chlorométhane".

Affiche présentée au colloque "Physico-chimie des états électroniques excités", Aspet, France, 8-12 Septembre 1997.

7. D. Duflot, C. Hannay, J-P. Flament, M-J. Hubin-Franskin : "Etude théorique et expérimentale de l'excitation en couche interne du pyrrole et du pyrazole".

Affiche présentée au colloque "Journées de Spectroscopie Moléculaire (JSM3)", Reims, France, 7-8 Juillet 1998.
Affiche présentée au colloque "Dynamique des Ions, Atomes et Molécules (DIAM5)", Reims, France, 8-10 Juillet 1998.

8. V. Antzoulatos, D. Duflot, J.-M. Robbe, J.-P. Flament : "Etude *ab initio* de la stabilité et de la structure du dication méthylamine".

Affiche présentée au colloque "6ème Réunion des Chimistes Théoriciens Français", Villeneuve d'Ascq, France, 13-16 Octobre 1998.

9. D. Duflot, J-P. Flament : "Etude *ab initio* du spectre d'excitation en couche interne de la *s*-triazine".

Affiche présentée à la 6ème Université d'été de Physico-Chimie Théorique, Marly-le-Roi, France, 6-10 septembre 1999.

10. D. Duflot, J-P. Flament : "*Ab initio* study of the K-shell spectrum of *s*-triazine".

Affiche présentée au colloque "Excited States in Molecules and Solids" (ESMS99), Tarragone, Espagne, 21-24 octobre 1999.

11. M-J. Hubin-Franskin, D. Duflot, J.-P. Flament, I. C. Walker : "K-shell excitation of 2-propenal at the C1s and O1s edges by inner-shell electron energy loss spectroscopy and *ab initio* calculations".

Affiche présenté au colloque "19th International Conference on X-ray and Inner-Shell Processes", Rome, Italie, 24-28 juin 2002.
Affiche présentée au colloque "XVI Jahn-Teller Conference", Leuven, Belgique, 26 août-1er septembre 2002.
Affiche présentée au colloque "ESPA2002 : Electronic Structure : Principles and Applications", Sevilla, Espagne, 11-13 septembre 2002.

12. D. Duflot, J.-P. Flament, I. C. Walker, M-J. Hubin-Franskin : "Etude théorique et expérimentale du spectre d'excitation en couche interne du 2-propénal".

Affiche présentée au colloque "6èmes Journées Francophones des Jeunes Physico-Chimistes, Marseille, France, 3-5 juillet 2002.
Affiche présentée au colloque "8ème Réunion des Chimistes Théoriciens Francophones", Strasbourg, France, 16-20 septembre 2002.
Affiche présentée à la réunion "Journée calcul numérique intensif en chimie et en physique", Villeneuve d'Ascq, France, 6 mars 2003.

13. D. Duflot, J.-P. Flament, A. Giuliani , J. Heinesch, M-J. Hubin-Franskin : "*Ab initio* and experimental study of the K-shell spectra of furan".

Affiche présenté au colloque "XIth International Congress of Quantum Chemistry" (ICQC-XI), Bonn, Allemagne, 20-26 juillet 2003.
Affiche présentée à la 8ème Université d'été de Physico-Chimie Théorique, Ambleteuse, France, 31 août-5 septembre 2003.

14. M-J. Hubin-Franskin , J. Delwiche, D. Duflot, J.-P. Flament, S. Stranges , M. Alagia : "Revisited K-shell excitation spectrum of furan using high resolution soft X-ray photoabsorption of synchrotron radiation".

Affiche présentée au colloque "International Scientific Meeting", Mons, Belgique, 25-26 mai 2004.

15. D. Duflot, J.-P. Flament, A. Giuliani, J. Heinesch, M.-J. Hubin-Franskin : "*Ab initio* and experimental study of the K-shell spectra of 2,5-dihydrofuran".

Affiche présenté au colloque "European Conference on Atomic and Molecular Physics (ECAMP8)", Rennes, France, 6-10 juillet 2004.

16. R Mota, R Parafita, A Giuliani, M-J Hubin-Franskin, J Delwiche, D Duflot, J-P Flament, E Drage, P Cahillane, N J Mason and P Limão-Vieira : "The electronic state spectroscopy of acetic studied by VUV synchrotron radiation, electron energy loss and He(I) photoelectron spectroscopy".

Affiche présentée au colloque "RADAM Conference 2005", Postdam, Allemagne, 17-20 mars 2005.

17. R Mota, R Parafita, A Giuliani, M-J Hubin-Franskin, J Delwiche, D Duflot, J-P Flament, E Drage, P Cahillane, N J Mason and P Limão- Vieira : "Spectroscopic studies of valence, Rydberg and ionic states of acetic acid, CH_3COOH".

Affiche présentée au colloque "XXIV ICPEAC", Rosário, Argentine (2005).

18. R Mota, R Parafita, A Giuliani, M-J Hubin-Franskin, J Delwiche, D Duflot, J-P Flament, E Drage, P Cahillane, N J Mason and P Limão- Vieira : "The electronic states of acetic acid studied by photon absorption and electron impact spectroscopies".

Affiche présentée au colloque "VII Iberian Joint Meeting on Atomic and Molecular Physics", Lisbonne, Portugal (2005).

19. D. Duflot, K. Sidhoum, J.-P. Flament, A. Giuliani, J. Heinesch, M.-J. Hubin-Franskin : "Ab initio and experimental study of the K-shell spectra of *s*-triazine".

Affiche présentée au colloque "Congrès général de la Société Française de Physique et de la Belgian Physical Society", Lille, France, 29 août-2 septembre 2005.

20. D. Duflot, S. Zeggari, J.-P. Flament : "*Ab initio* study of core excited cyclopropane".

Affiche présentée au colloque "Radiation damage in biomolecules, RADAM06", Groningen, Pays-Bas, 6 juin-10 juin 2006.

21. D. Duflot, J.-P. Flament, A. Giuliani, J. Heinesch, M. Grogna" M.-J. Hubin-Franskin: "The C1s and N1s core excitation of aniline: Experiment by electron impact and *ab initio* calculations".

Affiche présentée au colloque "Radiation damage in biomolecules, RADAM07", Groningen, Pays-Bas, 19 juin-22 juin 2007.

22. M.-J. Hubin-Franskin, J. Delwiche, D. Duflot, A. Giuliani, P. M. Santos, N. J. Mason, P. Limaão-Vieira : "Resonant-enhanced vibrational excitations of c-C_5F_8 by high resolution spectroscopies and *ab initio* calculations".

Affiche présentée au colloque "Electron Controlled Chemical Lithography 2008 Meeting", 12-16 mars 2008, Lisbonne, Portugal.

23. D. Duflot, J.-P. Flament, A. Giuliani, J. Heinesch, M.-J. Hubin-Franskin: "Electronic excitation of gaseous tetrahydrofuran studied by K-shell electron energy loss spectroscopy and *ab initio* calculations".

Affiche présentée au colloque "X08 21rst International Conference on X-Ray and Inner Shell Processes", Paris, France, 22-27 juin 2008 ;
Affiche présentée au colloque "XI^{ème} Rencontre des Chimistes Théoriciens Francophones ", Dinard, France, 30 juin-4 juillet 2008.
Affiche présentée au colloque "PAMO/JSM 2008 ", Villeneuve d'Ascq, France, 7-9 juillet 2008.

- **COMMUNICATIONS ORALES**

1. J-M. Robbe, J-P. Flament, D. Duflot :"Dissociation of the ethyne dication $C_2H_2^{++}$".

Communication orale présentée au colloque "Inner shell excitation and soft X-rays induced dynamics of isolated molecules : Experiment and Theory", Lisbonne, Portugal, 10-11 septembre 1992.

2. D. Duflot, J-M. Robbe, J-P. Flament : "Dissociation of the $C_2H_2^{++}$ dication".

Communication orale présentée au colloque "Spectroscopic and dynamic study of core excited molecules by impact and photon absorption", Wimereux, France, 21-22 octobre 1993.

3. J-M. Robbe, H. Lavendy, J-P. Flament, D. Duflot : "Application des méthodes de la chimie quantique à l'étude de problèmes de spectroscopie moléculaire".

Conférence donnée à la réunion du groupe de contact "PhLAM-LCPM", Université Libre de Bruxelles (ULB), Belgique, 3 Avril 1998.

4. D. Duflot, J-P. Flament, C. Hannay, M-J. Hubin-Franskin : "Etude *ab initio* de l'excitation en couche interne de composés cycliques".

Communication orale présentée au colloque "6ème Réunion des Chimistes Théoriciens Français", Villeneuve d'Ascq, France, 13-16 Octobre 1998.

5. D. Duflot, J-P. Flament, M-J. Hubin-Franskin : "Etude théorique et expérimentale de l'excitation en couche interne du benzène".

Communication orale présentée à la réunion du groupe de contact "PhLAM-LCPM", Villeneuve d'Ascq, France, 19 Mars 1999.

6. D. Duflot, J-P. Flament, C. Hannay, J. Heinesch, M-J. Hubin-Franskin : "Etude théorique et expérimentale de l'excitation en couche interne de composés cycliques".

Conférence invitée (1h) à la Réunion du groupe de contact FNRS "Atomes, Molécules et Radiation", Liège, Belgique, 25 octobre 1999.

7. D. Duflot, J-P. Flament : "Etude *ab initio* du spectre d'excitation en couche interne de molécules hydrocarbonées".

Communication orale présentée à la réunion "Journée calcul numérique intensif en chimie et en physique", Villeneuve d'Ascq, France, 6 mars 2003.

8. D. Duflot, J-P. Flament : "*Ab initio* study of core excited biomolecules".

Communication orale présentée à la réunion du COST-RADAM, Bruxelles, Belgique, 30 octobre 2004.

9. D. Duflot, J-P. Flament : "*Ab initio* study of core excited molecules".

Communication orale présentée au colloque "Radiation damage in biomolecules, RADAM06", Groningen, Pays-Bas, 6 juin-10 juin 2006.

10. D. Duflot, J-P. Flament : "*Ab initio* simulation of K-shell spectra of small molecules"

Communication orale présentée au workshop ACTINET 2007 "How can we improve coupling theoretical chemistry with X-ray absorption spectroscopy?", Avignon, 11-12 Octobre 2007.

- **SEMINAIRES**

1. D. Duflot : "Méthodes *ab initio* : principes et applications à l'étude des dications et à l'excitation de couches internes".

Séminaire donné au Laboratoire de Spectroscopie d'Electrons Diffusés de l'Université de Liège, 15 juin 1995.

2. J-P. Flament, D. Duflot : "Excitation en couche interne".

Séminaire donné au DCMR, Ecole Polytechnique, Palaiseau, France, 5 mai 2003.

3. D. Duflot, J-P. Flament : "Etats excités de cœur. Spectres ISEELS. Etude *ab initio*".

Séminaire donné à l'IRSAMC, Université Paul Sabatier, Toulouse, France, 21 janvier 2007.

ANNEXE:

ARTICLES

Article 1

Ab initio study of the acetylene and vinylidene dications fragmentation

D. Duflot, J-M. Robbe, and J-P. Flament
Laboratoire de Dynamique Moléculaire et Photonique, URA CNRS 779, Université des Sciences et Technologies de Lille, UFR de Physique, 59655 Villeneuve d'Ascq Cedex, France

(Received 25 July 1994; accepted 26 September 1994)

The $C_2H_2^{++}$ fragmentation processes have been studied using the complete active space self-consistent field method followed by a multireference perturbative configuration interaction, in order to interpret recent charge separation spectroscopy experiments. For two-body processes, the calculated appearance thresholds of the C_2H^+/H^+ and CH^+/CH^+ fragment pairs are in good agreement with the experimental data. It is shown that the $C_2H_2^{++} \rightarrow CH^+ + CH^+$ dissociation occurs with an important rotation of the CH^+ ions. The presence of the CH_2^+ ion is explained by a preliminary isomerization of acetylene to vinylidene dication. This reaction has been studied for the lowest lying states of $C_2H_2^{++}$ ($^3\Sigma_g^-$ and $^1\Delta_g$) and compared with other acetylenic ions isomerizations (C_2H_2, $C_2H_2^+$, $C_2H_2^-$). For three-body processes, the calculations are consistent with the mechanisms proposed by the experimentalists. © *1995 American Institute of Physics.*

I. INTRODUCTION

As it is one of the smallest stable polyatomic dication, the $C_2H_2^{++}$ ion has been the subject of numerous experimental[1–11] and theoretical[12–16] works. It has been first observed in the mass spectrum of acetylene,[1–5] before being studied by means of Auger spectroscopy,[6,7] double charge transfer[8–10] and coincidence spectroscopies.[11] From the theoretical point of view, the $C_2H_2^{++}$ dication has been studied using self-consistent-field (SCF),[11] semiempirical methods[12–15] and fourth-order Möller–Plesset (MP4)[16] calculations. To date, the most precise work concerns the Auger spectrum, which was calculated with Green functions methods.[17,18]

In a previous paper,[19] we have reported preliminary results of the first large configuration interaction (CI) study of the acetylene dication, together with the results obtained by photoelectron–photoion–photoion coincidence (PEPIPICO) spectroscopy. For energies of the incident photons greater than the appearance threshold of the double ionization reaction (31.7 ± 0.1 eV), monocations and neutral fragments are produced via two-body and three-body processes:[19,20]

$$C_2H_2^{++} \rightarrow C_2H^+ + H^+ \quad 34.0 \pm 0.2 \text{ eV}, \tag{1}$$

$$C_2H_2^{++} \rightarrow CH_2^+ + C^+ \quad 34.0 \pm 0.2 \text{ eV}, \tag{2}$$

$$C_2H_2^{++} \rightarrow CH^+ + CH^+ \quad 34.5 \pm 0.2 \text{ eV}, \tag{3}$$

$$C_2H_2^{++} \rightarrow C_2^+ + H + H^+ \quad 38.0 \pm 0.4 \text{ eV}, \tag{4}$$

$$C_2H_2^{++} \rightarrow C^+ + H + CH^+ \quad 38.0 \pm 0.4 \text{ eV}, \tag{5}$$

$$C_2H_2^{++} \rightarrow C + H^+ + CH^+ \quad 40.0 \pm 0.4 \text{ eV}. \tag{6}$$

In the present work, we present a complete set of theoretical results in order to interpret the PEPIPICO measurements. This paper is divided into the following sections: Section II describes the methods used to calculate the geometries and energies of the studied molecules; Sec. III gives the main results for the three lowest electronic states of $C_2H_2^{++}$; Sec. IV deals with two-body processes while Sec. V is devoted to three-body processes; finally, in Sec. VI some conclusions are given.

II. COMPUTATIONAL METHOD

The Gaussian atomic orbital (AO) basis set used in the present study consisted of the TZP basis set taken from Dunning,[21] i.e. $(5s1p)/[3s1p]$ for hydrogen and $(11s6p1d)/[5s3p1d]$ for carbon ($\alpha_d = 0.72$), leading to a total of 52 basis functions for $C_2H_2^{++}$. All energy calculations and geometry optimizations were carried out at the complete active space SCF (CASSCF) level[22] with the HONDO8 program package[23] using analytic gradients. In the valence active space, the $1s$ carbon orbitals were kept frozen. For example, the active space for $C_2H_2^{++}$ contained 8 electrons in 10 molecular orbitals (MO's). A similar procedure was used when studying the products of dissociation (C_2H^+, CH^+, CH_2^+, C_2^+).

Transition state structures were located also at the CASSCF level using the Cerjan and Miller method[24,25] implemented on HONDO8. The nature of the saddle points has been verified by diagonalization of the Hessian matrix calculated by means of finite differences. Unscaled eigenvalues of this matrix were used to calculate zero-point vibrational energies (ZPEs) using the harmonic oscillator approximation.

In order to take into account the effect of dynamical correlation, configuration interaction (CI) calculations were performed at the CASSCF optimized geometries using the two-class version of the CIPSI program[26] and its diagrammatic version.[27] In this method, a reduced CI matrix, so called the *S* space and containing the dominant configurations (contribution to the energy greater than a threshold value of typically 0.01) is constructed iteratively and diagonalized. The effect of all other configurations is treated by second order perturbative theory, using the Möller–Plesset partition of the Hamiltonian.[28] In the present study, we found that a *S* space of about 450 Slater determinants was sufficient to obtain high-quality zeroth-order wave functions. The size

TABLE I. Calculated energies of the molecular states involved in the fragmentation of the $C_2H_2^{++}$ dication.

		State	E_{MCSCF} (a.u.)	E_{CIPSI} (a.u.)	Norm[a]	ΔE_{MCSCF}	ΔE_{CIPSI}
C_2H_2	**1**	$^1\Sigma_g^+$	−76.978 422	−77.164 819	0.024	0.00	0.00
$C_2H_2^{++}$	**2a**	$^3\Sigma_g^-$	−75.904 086	−76.016 613	0.034	29.23	31.24
	2b	$^1\Delta_g$	−75.870 257	−75.990 011	0.025	30.15	31.96
	2c	$^1\Sigma_g^+$	−75.854 548	−75.975 735	0.028	30.58	32.34
TS[b]	**3**	$^3\Sigma^-$	−75.787 827	−75.909 856	0.024	32.40	34.15
C_2H^+	**4a**	$^3\Pi$	−75.893 223	−76.032 198	0.037	29.53	30.82
	4b	$^3\Sigma^-$	−75.869 630	−76.004 089	0.038	30.17	31.58
TS[b]	**5**	^1A_g	−75.778 129	−75.882 078	0.019	32.66	34.91
CH^+	**6a**	$^1\Sigma^+$	−37.972 727	−38.015 673	0.015		
	6b	$^3\Pi$	−37.927 741	−37.977 314	0.018		
TS[b]	**7a**	$^3A''$	−75.823 313	−75.934 279	0.027	31.43	33.48
	7b	$^1A'$	−75.776 183	−75.885 889	0.023	32.71	34.80
	7c	^1A	−75.785 748	−75.898 759	0.029	32.45	34.45
H_2CC^{++}	**8a**	$^3B_1$	−75.843 213	−75.957 981	0.026	30.89	32.84
	8b	$^1A_1$	−75.837 940	−75.950 308	0.014	31.03	33.05
	8c	$2\ ^1A_1$	−75.737 433	−75.859 017	0.055	33.77	35.53
TS[b]	**9a**	$^3B_1$	−75.777 306	−75.893 696	0.019	32.68	34.59
	9b	$^1A_1$	−75.804 905	−75.921 521	0.019	31.93	33.83
CH_2^+	**10a**	$^2A_1$	−38.631 053	−38.690 211	0.013		
	10b	$^2B_1(^2\Pi)$	−38.574 233	−38.684 264	0.016		
	10c	$^2B_2$	−38.520 052	−38.574 233	0.015		
C_2^+	**11a**	$^4\Sigma_g^-$	−75.225 307	−75.363 523	0.023		
	11b	$^2\Pi_u$	−75.219 529	−75.325 162	0.033		
C^+		^2P		−37.378 557	0.002		
C		^3P		−37.782 232	0.002		

[a]Norm of the perturbation correction to the CIPSI wave function.
[b]Transition state.

of the perturbative space P was about 5 to 6 million determinants and the norm of the correction to the wave function was less than 5.5% (see Table I).

The CASSCF optimized geometries of the various ions studied in the present work are displayed in Fig. 1 and the corresponding energies are given in Table I. In order to permit comparisons with experimental work, all the energies are expressed with respect to the neutral acetylene ground state $^1\Sigma_g^+$, whose CIPSI energy was calculated to be −77.164 819 a.u. (Table I). The calculated harmonic vibrational frequencies for each species are given in Tables II–IV. Except for neutral acetylene, no experimental determinations are available. However, comparison of the predicted C_2H_2 frequencies with experimental values given by Herzberg[29] shows a good agreement, deviations being less than 8% in all cases. A similar accuracy may be expected for other species.

III. $C_2H_2^{++}$ DICATION

The ground state configuration of the $C_2H_2^{++}$ dication is obtained by removing two π electrons from the well-known configuration of neutral acetylene:

$$1\sigma_g^2 1\sigma_u^2 2\sigma_g^2 2\sigma_u^2 3\sigma_g^2 1\pi_u^2. \quad (7)$$

This configuration leads to the three lowest lying linear states of $C_2H_2^{++}$, $^3\Sigma_g^-$(**2a**), $^1\Delta_g$(**2b**) and $^1\Sigma_g^+$(**2c**) (see Fig. 1). As previously shown by Pople and co-workers,[16] the ground state is the $^3\Sigma_g^-$.

The calculated equilibrium geometries of the ground states of both C_2H_2 and $C_2H_2^{++}$ are compared with previous works in Table V. The calculated bond lengths for neutral acetylene (R_{CC}=1.216 Å and R_{CH}=1.062 Å) are close to the experimental ones[29] (R_{CC}=1.203 Å and R_{CH}=1.060 Å). As mentioned earlier,[19] these distances are slightly overestimated, as usually observed in CASSCF calculations.

For $C_2H_2^{++}$, there is no experimental determination available. The CASSCF CC bond length (1.344 Å) is found to be much longer than the neutral one, and close to the ethylene experimental CC distance (1.339 Å[29]). This is not surprising, since the two removed π electrons lead to an ethylenic-type double bond. The CH bond length (1.137 Å) is much longer than in the neutral case and quasi-identical to the isolated CH^+ bond length [1.138 Å, see (**6b**) in Fig. 1]. This is consistent with a Mulliken population analysis[30] (CASSCF level) which shows a +0.5 charge on each hydrogen and carbon atom, similar to that obtained in isolated CH^+.

Concerning the $^1\Delta_g$ and $^1\Sigma_g^+$ excited states, we observe that the CH bond length seems unaffected by the change of symmetry, whereas the CC bond length slightly increases when going from $^3\Sigma_g^-$ to $^1\Delta_g$ and to $^1\Sigma_g^+$ states. The same behavior has been found in B_2H_2,[31,32] which is isovalent to $C_2H_2^{++}$. Moreover, the calculated energies with respect to the ground state (0.72 eV and 1.10 eV for $^1\Delta_g$ and $^1\Sigma_g^+$, respectively) are almost identical to that calculated in B_2H_2 (0.72 eV and 1.14 eV[32]).

IV. TWO-BODY PROCESSES

Among the three two-body processes described in the introduction, two of them are direct fragmentations while the third supposes a previous isomerization to occur.

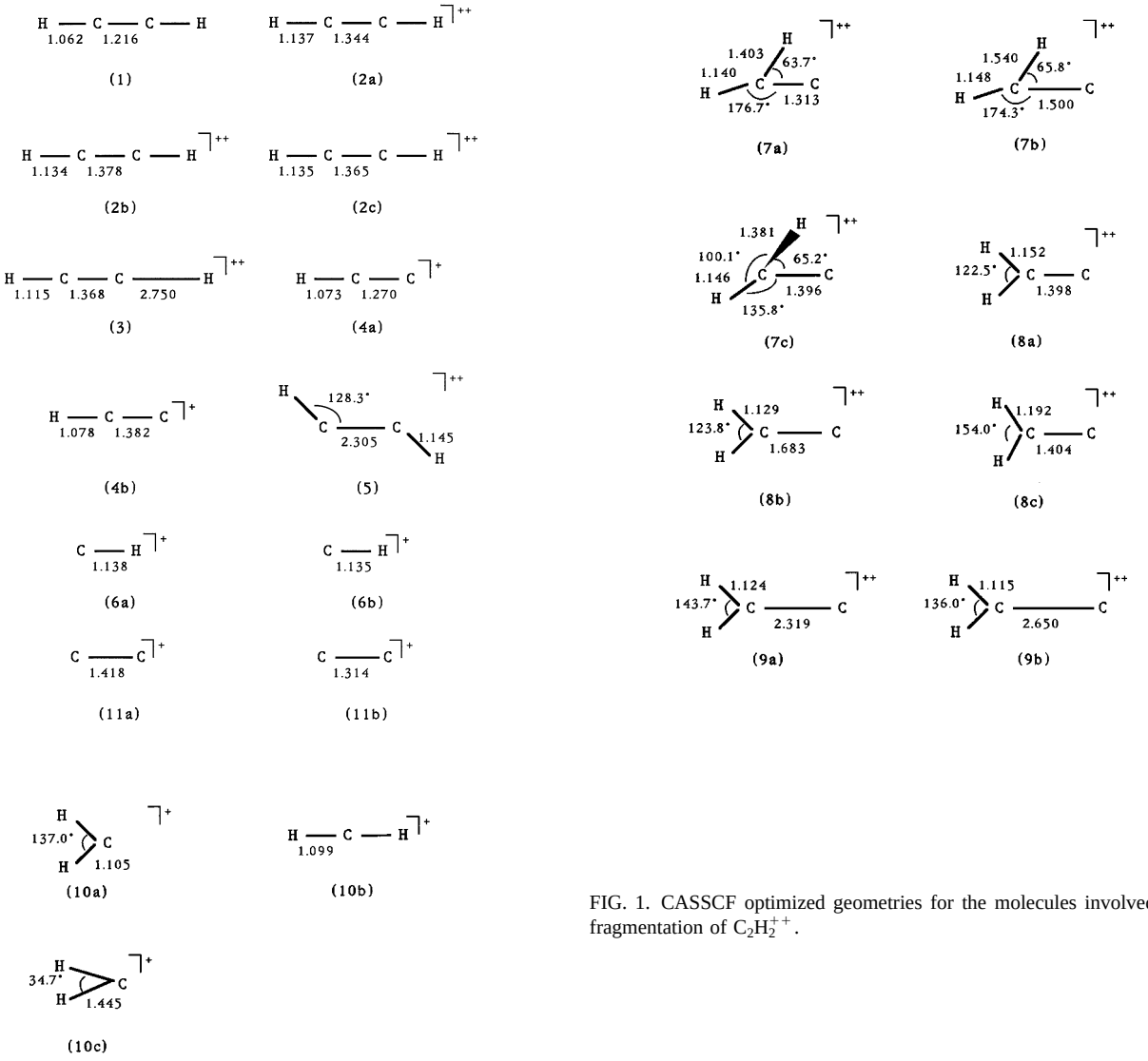

FIG. 1. CASSCF optimized geometries for the molecules involved in the fragmentation of $C_2H_2^{++}$.

A. The $C_2H_2^{++} \rightarrow C_2H^+ + H^+$ direct dissociation

In our previous work,[19] this deprotonation reaction was studied assuming a linear geometry by optimizing the $^3\Sigma_g^-$ CC bond length and the other CH bond length for chosen values of the CH breaking bond (see Fig. 4 of Ref. 19). In that configuration, we predicted an activation barrier of 34.3 eV in good agreement with the experimental value (34.0 $\pm$0.2 eV[19]). A more precise search of the corresponding transition state leads to the following geometry [(**3**) in Fig. 1]: R_{CC}=1.368 Å, R_{CH}=1.115 Å, R_{CH}=2.750 Å), which com-

TABLE II. Harmonic vibrational frequencies (cm^{-1}) for the ground state of C_2H_2 and the three lowest lying states of $C_2H_2^{++}$.

Assignment	C_2H_2[a] $^1\Sigma_g^+$	$C_2H_2^{++}$ $^3\Sigma_g^-$	$^1\Delta_g$	$^1\Sigma_g^+$
CH asym. stretch	3512 (3372)	2863	2827	2823
CH sym. stretch	3446 (3295)	2753	2770	2773
CC stretch	1977 (1973)	1546	1457	1407
CCH bend	672 (729)	652	704	759
CCH bend	588 (612)	646	665	654
ZPE (kcal/mol)	16.38 (16.19)	13.95	14.00	14.05
ZPE (eV)	0.710 (0.702)	0.605	0.607	0.609

[a]The experimental values taken from Ref. 19 are given in parentheses.

TABLE III. Harmonic vibrational frequencies (cm^{-1}) for the transition states involved in the $C_2H^+ + H^+(^3\Sigma^-)$ and $CH^+ + CH^+(^1A_g)$ dissociations.

Assignment	$^3\Sigma^-$
CH stretch	$i642$
CCH bend	230
CCH bend	422
CC stretch	1485
CH stretch	2997
ZPE (kcal/mol)	8.27
ZPE (eV)	0.359
	^1A_g
CC stretch	$i603$
Out of plane	518
CH sym. stretch	543
CH asym. stretch	850
HCC sym. bend	2755
HCC asym. bend	2758
ZPE (kcal/mol)	10.61
ZPE (eV)	0.460

pares well with that obtained by Pople[16] at HF/6-31G* level (R_{CC}=1.331 Å, R_{CH}=1.091 Å, R_{CH}=2.707 Å). Calculation of harmonic frequencies (Table III), confirmed the nature of this transition state, since we found one imaginary frequency ($i642$ cm^{-1}) along the CH stretch.

The theoretical appearance threshold of the pair C_2H^+/H^+ is now calculated to be 33.90 eV (after ZPE correction), in very good agreement with the experimental value (34.0±0.2 eV[19,20]) but significatively above the result of Pople (33.57 eV with ZPE correction) obtained at the MP4/6-31G** level.[16]

TABLE IV. Harmonic vibrational frequencies (cm^{-1}) for molecular states involved in the production of the CH_2^+ ion.

Assignment	Triplet states	Singlet states
	(**8a**)	(**8b**)
HCH rock	610	790
Out of plane	967	1037
HCH bend	1128	1321
CC stretch	1186	648
CH sym. stretch	2576	2791
CH asym. stretch	2653	2931
ZPE (kcal/mol)	13.04	13.61
ZPE (eV)	0.565	0.590
	(**7a**)	(**7b**)
$C_2C_1H_3$ bend[a]	$i682$	705
Out of plane	834	$i655$
HCH bend	920	1000
CC stretch	1423	1134
C_1H_3 stretch	1736	1765
C_2H_4 stretch	2778	2678
ZPE (kcal/mol)	11.00	10.41
ZPE (eV)	0.477	0.451
	(**9a**)	(**9b**)
CC stretch	$i466$	$i547$
HCH rock	476	584
Out of plane	900	1026
HCH bend	1014	1199
CH sym. stretch	2793	2838
CH asym. stretch	3021	2975
ZPE (kcal/mol)	11.73	12.32
ZPE (eV)	0.508	0.534

[a]C_2 is the vinylidene terminal carbon atom and H_3 is the migrating hydrogen atom.

B. The $C_2H_2^{++} \rightarrow CH^+ + CH^+$ direct dissociation

As for the deprotonation reaction, we imposed in previous work[19] a linear configuration for this symmetric dissociation by optimizing the $^3\Sigma_g^-$ CH bond length for increasing values of the CC breaking bond. The relevant potential curves for the determination of the appearance threshold are shown in Fig. 2. Due to symmetry rules, the $^3\Sigma_g^-$ and $^1\Delta_g$ states of $C_2H_2^{++}$ dissociate into CH^+ fragments in their first excited state ($^3\Pi$), while the $^1\Sigma_g^+$ excited state of $C_2H_2^{++}$ dissociates into CH^+ fragments in their ground $^1\Sigma^+$ state. This feature can be explained by valence bond considerations on the MO's occupation in both $^1\Sigma^+$ and $^3\Pi$ states of CH^+ (Fig. 3). In $^3\Pi$, the p_z electron of the carbon atoms is located in a σ lone pair, the other in a π-type orbital. This configuration favors the formation of σ and π CC bonds when the two fragments approach each other and explain why the lowest states of $C_2H_2^{++}$ are $^3\Sigma_g^-$ and $^1\Delta_g$. The barrier corresponding to the $^3\Sigma_g^-$ state is 37.10 eV with $R_{CC}\approx$2.6 Å, well above the experimental threshold, since the cross section presents a first onset at 34.5 eV.[20]

If we now consider the orbitals of the $^1\Sigma^+$ state of CH^+ (Fig. 3), we see that the σ lone pair is doubly occupied, leading to a repulsive interaction as soon as the CC distance decreases, although this configuration is more stable at large CC separations. This repulsive character appears clearly in Fig. 2, by following the diabatic state constructed with the two lowest $^1\Sigma_g^+$ states of $C_2H_2^{++}$. In fact, these two states present an avoided crossing and this lowers the activation barrier to 36.36 eV, with $R_{CC}\approx$2.2 Å. Still, there remains a difference of about 2 eV between the experimental and the theoretical result. Two explanations for this discrepancy may be proposed:

(a) The experimental value is difficult to determine precisely, because of the presence of another signal in the same zone of the PEPIPICO spectrum. This signal is a metastable trail coming from the fragmentation of $C_2H_2^{++}$ into C_2H^+ and H^+ with a lifetime of 80 ns.[19,20] By taking this effect into account, Thissen[20] has proposed a new appearance threshold around 35.5 eV.

(b) The calculations were made in a linearly constrained geometry, but it is possible that the dissociation takes place with a rotation of the CH^+ fragments, leading to a lower activation barrier.

In order to test this last hypothesis, it is necessary to optimize a bent singlet transition state. However, examination of Fig. 2 shows that the topology of the potential energy surfaces in the region $R_{CC}\approx$2.2 Å is very complicated. First, there is the avoided crossing between the two lowest $^1\Sigma_g^+$ states. Moreover, as soon as the molecule is bent, the $^1\Delta_g$ and $^1\Sigma_g^+$ states belong to the same irreducible representation of the symmetry group and cannot cross anymore, leading to a conical intersection,[33] precisely in the $R_{CC}\approx$2.2 Å region. For these reasons, we did not employ the Cerjan and Miller

TABLE V. Comparison of calculated equilibrium distances of C_2H_2 and $C_2H_2^{++}$ with previous works.

	This work CASSCF TZP	Ref. 14 MINDO3	Ref. 15 MNDO	Ref. 16 HF 6-31G*	Ref. 42 CISD TZ+2P	Ref. 29 Expt
C_2H_2 $X\ ^1\Sigma_g^+$						
R(C–H) (Å)	1.062			1.057	1.058	1.060
R(C–C) (Å)	1.216			1.185	1.195	1.203
$C_2H_2^{++}$ $X\ ^3\Sigma_g^-$						
R(C–H) (Å)	1.137	1.110	1.096	1.113		
R(C–C) (Å)	1.344	1.346	1.380	1.308		

procedure to locate this singlet transition state, but rather we calculated a minimum energy path along the CC stretch coordinate, by optimizing the geometry for increasing values of the CC distance.

The resulting geometry is a trans bent C_{2h} structure [(**5**) in Fig. 1] with ^1A_g symmetry. Calculation of harmonic frequencies confirms the nature of this state, since there is only one imaginary frequency, along the CC stretch mode ($i603$ cm^{-1}, see Table III). The CC bond length (2.305 Å) is slightly increased with respect to the linear case (2.2 Å). Examination of the evolution of the HCC angle along the reaction path shows a large variation as soon as the CC distance is increased (R_{CC}=1.3 Å→1.5 Å) whereas the variation is less important around the transition state geometry. These features confirm that the dissociation of $C_2H_2^{++}$ into $CH^+ + CH^+$ takes place with an important rotation of the CH^+ fragments.

From an energetic point of view, the theoretical appearance threshold is now calculated to be 34.56 eV (after ZPE correction), which is 1.8 eV below the value obtained in linear geometry. This result is close to the measured value of 34.5 eV but far below the corrected value of 35.5 eV proposed by Thissen.[20] Information about the energetics of this dissociation pathway and the $C_2H_2^{++}\rightarrow C_2H^+ + H^+$ reaction are summarized in Fig. 4.

C. The $C_2H_2^{++}\rightarrow CH_2^+ + C^+$ indirect dissociation

The presence of the CH_2^+ fragment in the dissociation products indicates that the $C_2H_2^{++}$ dication undergoes before dissociating an isomerization reaction, leading to the vinylidene dication H_2CC^{++}:

$$C_2H_2^{++}\rightarrow H_2CC^{++}\rightarrow CH_2^+ + C^+. \tag{8}$$

We have studied the $C_2H_2^{++}\rightarrow H_2CC^{++}$ isomerization reactions for the two ($^3\Sigma_g^-$ and $^1\Delta_g$) lowest lying states of $C_2H_2^{++}$. Following the ground triplet surface, one passes from the linear $^3\Sigma_g^-$ state of $C_2H_2^{++}$(**2a**) to the $^3B_1$ state of H_2CC^{++}(**8a**) through a $^3A''$ transition state (**7a**). The $^3B_1$ ground state of the vinylidene dication has the following configuration:

$$1a_1^2 2a_1^2 3a_1^2 4a_1^2 1b_2^2 5a_1^1 1b_1^1. \tag{9}$$

The two first a_1 MO's are the $1s$ carbon core orbitals; $3a_1$ represents the σ_{CC} bond, $4a_1$ and $1b_2$ MO's are the CH bonds; the $5a_1$ MO is a sp-type lone pair centered on the terminal carbon atom; the $1b_1$ MO (HOMO) is the out of

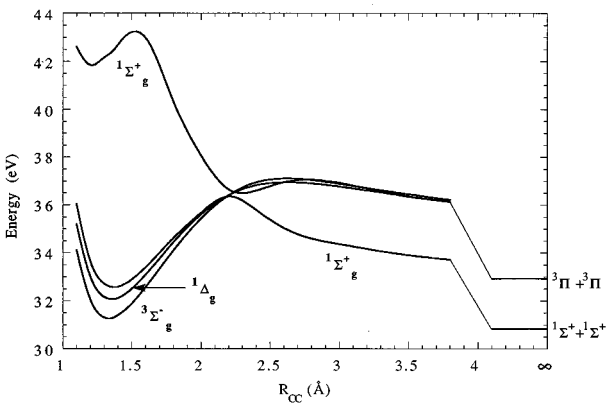

FIG. 2. Potential energy curves relevant for the determination of the activation barrier during $C_2H_2^{++}\rightarrow CH^+ + CH^+$ colinear dissociation.

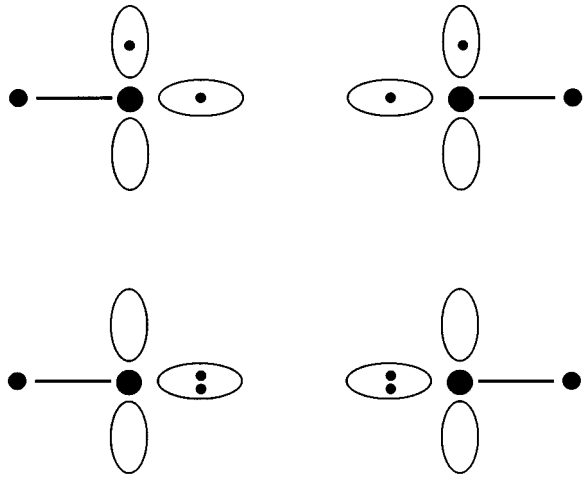

FIG. 3. Schematic representation of the interaction between two CH^+ fragments in $^3\Pi$ (upper panel) and $^1\Sigma^+$ (lower panel) molecular states.

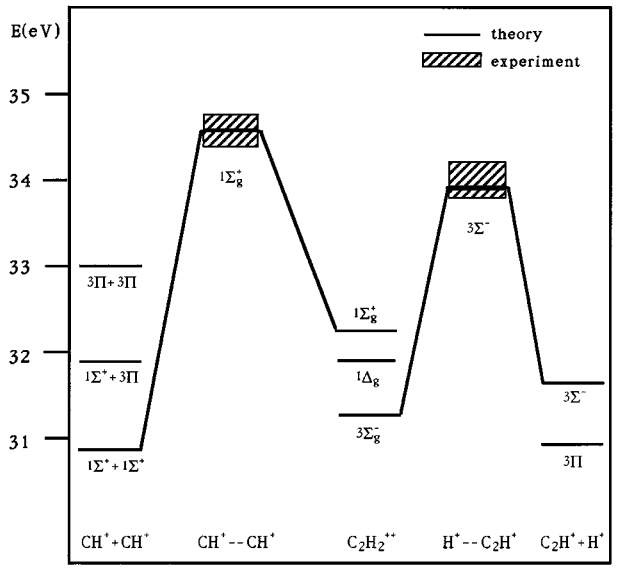

FIG. 4. Energy diagram for $C_2H_2^{++} \rightarrow C_2H^+ + H^+$ and $C_2H_2^{++} \rightarrow CH^+ + CH^+$ dissociations.

plane π_{CC} bond. Moreover, the LUMO ($2b_2$) is an in-plane p-type nonbonding orbital located essentially on the terminal carbon atom.

The corresponding geometry (**8a**) is given in Fig. 1 (see also Table VI). The CC bond length (1.398 Å) is slightly greater than the $C_2H_2^{++}$ value (1.344 Å) since there remains only one electron in the π_{CC} MO (bond order of 1.5 instead of 2) and tends to approach the CC single bond length of ethane (1.536 Å[29]). The $^3A''$ isomerization transition state (**7a**) is found to be planar with the configuration:

$$1a'^2 2a'^2 3a'^2 4a'^2 5a'^2 6a'^1 1a''^1. \quad (10)$$

The geometry of this state is very similar to that obtained in the case of the $^3A''$ transition state of acetylene–vinylidene monocations isomerization[34–37] (see Table VI), except the large nonmigrating CH bond length (1.140 Å). In particular, the CC bond length (1.316 Å) is identical to the CC bond length in $C_2H_2^+$ obtained by Hamilton and Schaefer at the TZ2P/CISD level[37] (1.316 Å), since in both cases the bond index is 1.5 (Table VI). Moreover, the calculated activation barrier (12.7 kcal/mol after ZPE correction) is also close to the $C_2H_2^+$ case (≈10 kcal/mol[37]). This resemblance is not surprising, since these two molecules only differ by the occupation of the $5a_1$ lone pair, which does not participate to the reaction. However, the value of the isomerization barrier is significantly above the barrier of the neutral species (≈2 kcal/mol), which has been extensively studied in the past years.[35,38–44]

We now turn to the first excited singlet surface which correlates the linear $^1\Delta_g$ state of $C_2H_2^{++}$(**2b**) to the $^1A_1$ state of H_2CC^{++}(**8b**) with the following configuration:

$$1a_1^2 2a_1^2 3a_1^2 4a_1^2 1b_2^2 5a_1^2. \quad (11)$$

The $1b_1$ MO is unoccupied and the CC bond is thus a σ_{CC} single one. Effectively, the CC bond length is very large [1.683 Å, see (**8b**)], being even greater than the ethane one (1.536 Å[29]). This feature is also reflected by the unusually weak CC stretch vibrational frequency (648 cm^{-1}, see Table IV). The CH distance and the HCH angle are not very different from the ground state case.

TABLE VI. Characteristics of the acetylene–vinylidene isomerization for C_2H_2 family ions.

	$C_2H_2^-$ Ref. 35[a]	C_2H_2 Ref. 42[b]	C_2H_2 Refs. 47,48[b]	$C_2H_2^+$ Ref. 37[b]	$C_2H_2^{++}$ this work		
Acetylene	^2B_u	$^1\Sigma^+_g$	$^3B_2$	$^2\Pi_u$	$^3\Sigma^-_g$	$^1\Delta_g$	$^1\Sigma^+_g$
R(C–C) (Å)	1.308	1.195	1.327	1.242	1.344	1.365	1.378
R(C–H) (Å)	1.082	1.058	1.083	1.078	1.137	1.135	1.134
HCC angle (°)	118	180	128	180	180	180	180
Bond index	2.5	3	2	2.5	2	2	2
Vinylidene	$^2B_2$	$^1A_1$	$^3B_2$	$^2B_1$	$^3B_1$	$^1A_1$	$2\ ^1A_1$
R(C–C) (Å)	1.352	1.296	1.312	1.385	1.398	1.683	1.404
R(C–H) (Å)	1.098	1.079	1.081	1.096	1.152	1.129	1.192
HCH angle (°)	124	120	118	120	122	124	154
Bond index	2	2	2	1.5	1.5	1	1.5
Transition state	^2A	$^1A'$	^3A	$^2A''$	$^3A''$	^1A	
$R(C_1C_2)$ (Å)	1.384	1.244	1.410	1.316	1.313	1.396	
$R(C_1H_3)$ (Å)	1.413	1.410	1.389	1.404	1.403	1.381	
$R(C_1H_4)$ (Å)	1.145	1.065	1.099	1.088	1.140	1.146	
$H_3C_1C_2$ angle (°)	61	53	59	56	64	65	
$H_4C_1C_2$ angle (°)	116	179	122	176	177	136	
$H_4C_1C_2H_3$ angle (°)	108	0	115	0	0	100	
Bond index	1.5	2	1.5	1.5	1.5	1.5	
Barrier (kcal/mol)	53	2	48	10	13	29	

[a]MP2/6-31G*//UHF/4-31G calculations.
[b]TZ+2P/CISD calculations.

A search for a planar transition state led to a $^1A'$ state with the geometry given in (**7b**). However, analysis of the calculated vibrational frequencies revealed the presence of two imaginary frequencies, the first ($i1184$ cm^{-1}) corresponding as expected to the motion of the migrating hydrogen, and the other ($i705$ cm^{-1}) to a HCCH torsional motion. This C_{s^-} symmetry structure has then a Hessian index of two, and the real saddle point (index of one) has thus a C_1 symmetry.

The structure of this transition ^1A state is shown in Fig. 1 (**7c**) and is compared with previous studies on acetylenic family ions (C_2H_2, $C_2H_2^+$, $C_2H_2^-$) in Table VI. It appears that the calculated geometry is very similar to those obtained in the isomerization of the ^2B_u ground state of $C_2H_2^-$ (Ref. 35) and the $^3B_2$ excited state of C_2H_2.[45–48] In the three cases, the migrating hydrogen has a quasiperpendicular position to the other atoms plane. Moreover, the ZPE corrected barrier for isomerization (29.0 kcal/mol, instead of 35.7 kcal/mol with the planar transition state) is much higher than for the ground state case (12.7 kcal/mol). Thus, the isomerization of the acetylenic ions can be divided into two classes: for $^1\Sigma_g^+$ (C_2H_2), $^2\Pi_u$ ($C_2H_2^+$) and $^3\Sigma_g^-$ ($C_2H_2^{++}$), the transition state is planar with a low activation barrier (2, 10, and 13 kcal/mol, respectively), whereas for ^2B_u ($C_2H_2^-$), $^3B_2$ (C_2H_2) and $^1\Delta_g$ ($C_2H_2^{++}$), the transition state is nonplanar with a high activation barrier (53, 48, and 29 kcal/mol, respectively). Two explanations have been proposed in order to explain these differences.

When the $2b_2$ in-plane p-type MO is occupied, the repulsive interaction with the migrating hydrogen atom makes the in-plane isomerization a very high-energy pathway, above the out-of-plane migration. This effect has already been invoked in the case of $C_2H_2^-$ (Ref. 35) and the $^3B_2$ excited state of C_2H_2.[48] However, this explanation does not hold for the dication, since Eq. (11) shows that the $2b_2$ MO is unoccupied.

(a) In the case of neutral C_2H_2, there is a small energy difference between the two lowest triplet states, $^3B_2$ and $^3A_2$ (0.56 eV[46]). As first noticed by Harding,[49] there is an avoided crossing between the two surfaces in C_1 symmetry, leading to a lowering of the activation barrier of the $^3B_2$ state via the C_1-symmetry path with respect to the planar C_{s^-} symmetry path.

(b) In order to check this possibility, we optimized the geometry of the second $^1A_1$ state of H_2CC^{++}(**8c**). It appears that this state lies at an energy of 35.5 eV, 2.5 eV above the first singlet state. The corresponding transition state must have an energy well above the first one and thus there is no avoided crossing between these two states. Unfortunately, it was not possible to optimize with HONDO8 the geometry of this second transition state and we have no explanation for the nonplanar structure of the first singlet transition state.

Once the vinylidene dication has been formed, the CH_2^+ ion is obtained by breaking the CC bond. The geometries of the transition states corresponding to the lowest triplet and singlet dissociation are shown in Fig. 1 (**9a**, **9b**). From the energetic point of view, examination of Fig. 5 shows that the $H_2CC^{++}\rightarrow CH_2^+ + C^+$ singlet transition state is below the triplet one by about 0.8 eV. The figure indicates also clearly

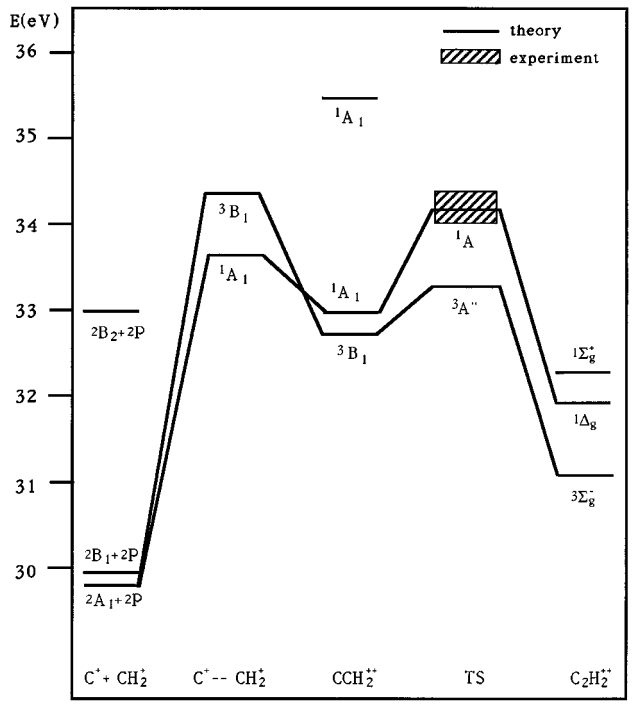

FIG. 5. Energy diagram for $C_2H_2^{++}\rightarrow H_2CC^{++}\rightarrow CH_2^+ + C^+$ dissociation.

that the theoretical appearance threshold is due to the singlet $C_2H_2^{++}\rightarrow H_2CC^{++}$ isomerization and is calculated to be 34.19 eV (after ZPE correction), in very good agreement with experimental data (34.0 ± 0.2 eV[19,20]). However, the triplet activation barrier (34.39 eV) is very close and we conclude that both states (triplet and singlet) are involved in the production of CH_2^+.

V. THREE-BODY PROCESSES

Interpretation of PEPIPICO spectra for three-body processes is much more difficult than for two-body processes.[50] In the case of $C_2H_2^{++}$, several possible mechanisms have been proposed to explain the presence of the observed ion pairs.[19]

A. The $C_2H_2^{++}\rightarrow C_2^+ + H + H^+$ dissociation

Analysis of experimental data suggests a secondary dissociation of C_2H^+ into $C_2^+ + H$:[19]

$$C_2H_2^{++}\rightarrow C_2H^+ + H^+ \rightarrow C_2^+ + H + H^+. \quad (12)$$

The cross section becomes linear at 39.5 eV.[19] Monte Carlo simulations show that the kinetic energy release (KER) during primary charge separation is 4 eV at 40.8 eV.[19] *Ab initio* calculations on the dissociation of the two lowest lying states of C_2H^+ give the following results:

$$C_2H^+(^3\Sigma^-)\rightarrow C_2^+(^4\Sigma_g^-) + H(^2S) \quad 35.41 \text{ eV}, \quad (13)$$

$$C_2H^+(^3\Pi)\rightarrow C_2^+(^2\Pi_u) + H(^2S) \quad 36.45 \text{ eV}. \quad (14)$$

Taking into account the KER, we obtain a theoretical appearance threshold of 39.4 eV, in very good agreement with the experimental value of 39.5 eV. The C_2^+ ion is thus formed in its $^4\Sigma_g^-$ ground state.

B. The $C_2H_2^{++} \rightarrow C^+ + CH^+ + H$ dissociation

Analysis of experimental data suggests a secondary dissociation of CH^+ to explain the presence of the C^+/CH^+ pair:[19]

$$C_2H_2^{++} \rightarrow CH^+ + CH^+ \rightarrow C^+ + CH^+ + H. \quad (15)$$

The appearance threshold is found to be 38.0 ± 0.4 eV with a linear part beginning at 40.0 ± 0.5 eV and the KER is 4.4 ± 0.7 eV at 40.8 eV.[19] *Ab initio* calculations lead to the following energies:

$$CH^+(^1\Sigma^+) + CH^+(^1\Sigma^+) \rightarrow CH^+(^1\Sigma^+) + C^+(^2P) + H \quad 34.58 \text{ eV}, \quad (16a)$$

$$CH^+(^1\Sigma^+) + CH^+(^3\Pi) \rightarrow CH^+(^1\Sigma^+) + C^+(^2P) + H \quad 34.58 \text{ eV}, \quad (16b)$$

$$CH^+(^1\Sigma^+) + CH^+(^3\Pi) \rightarrow CH^+(^3\Pi) + C^+(^2P) + H \quad 35.62 \text{ eV}, \quad (16c)$$

$$CH^+(^3\Pi) + CH^+(^3\Pi) \rightarrow CH^+(^3\Pi) + C^+(^2P) + H \quad 35.62 \text{ eV}. \quad (16d)$$

Adding 4.4 ± 0.7 eV to 34.58 eV leads to a theoretical appearance threshold of 39.0 ± 0.7 eV which is close to the experimental result of 40.0 ± 0.5 eV. Thus, the CH^+ ion is in its ground $^1\Sigma^+$ state when dissociating.

C. The $C_2H_2^{++} \rightarrow CH^+ + H^+ + C$ dissociation

The experimental appearance threshold is found to be 40.0 ± 0.4 eV and the cross section becomes linear at 42 eV. Several hypotheses have been proposed by the experimentalists to explain the presence of the CH^+/H^+ pair.[19]

(a) Slow secondary dissociation of a CH^+ ion:

$$C_2H_2^{++} \rightarrow CH^+ + CH^+ \rightarrow C + CH^+ + H^+. \quad (17)$$

(b) Slow secondary dissociation of a C_2H^+ ion:

$$C_2H_2^{++} \rightarrow C_2H^+ + H^+ \rightarrow C + CH^+ + H^+. \quad (18)$$

(c) Fast dissociation (20 fs) of a primary CH^+ ion in the Coulombic repulsion zone of the other CH^+ [reaction identical to (17)]. This hypothesis seems to be the best one.

In the two first cases, the kinetic energy release is about 7 eV, whereas in the last case the KER is about 5 eV. *Ab initio* calculations for the dissociation of C_2H^+ give the following results:

$$C_2H^+(^3\Sigma^-) \rightarrow CH^+(^1\Sigma^+) + C(^3P) \quad 37.19 \text{ eV}, \quad (19a)$$

$$C_2H^+(^3\Pi) \rightarrow CH^+(^1\Sigma^+) + C(^3P) \quad 37.19 \text{ eV}. \quad (19b)$$

For hypotheses (a) and (c), previous works[51,52] showed that the lowest state of CH^+ which can dissociate into $C + H^+$ is a $^3\Sigma^-$:

$$CH^+(^3\Sigma^-) + CH^+(^1\Sigma^+) \rightarrow CH^+(^1\Sigma^+) + C(^3P) + H^+ \quad 37.19 \text{ eV}. \quad (20)$$

Thus, calculations cannot determine directly whether the process occurs by dissociation of C_2H^+ or of CH^+. However, a kinetic energy release of 5 eV [case (c)] leads to a theoretical threshold of 42.2 eV in good agreement with the experimental one (42 eV), whilst a kinetic energy release of 7 eV leads to a too high energy of 44.2. We can conclude that our calculations confirm the (c) hypothesis.

VI. CONCLUSION

High level *ab initio* calculations have been performed in order to interpret coincidence spectroscopy experiments on the $C_2H_2^{++}$ dication. For two-body processes, the theoretical appearance thresholds for ion pairs are in very good agreement with the experimental ones. The dissociation of $C_2H_2^{++}$ into $C_2H^+ + H^+$ occurs in colinear geometry whilst the dissociation into $CH^+ + CH^+$ takes place with an important rotation of the fragments. The CH_2^+ ion is produced after a preliminary isomerization of acetylene into vinylidene. This reaction has been studied for the lowest triplet and singlet states of $C_2H_2^{++}$. For triplet state, the saddle point is planar and the activation barrier is low, whereas for singlet surface, the saddle point is nonplanar and the activation barrier is high. For three-body processes, the mechanisms proposed earlier[19] are now confirmed by our calculations.

ACKNOWLEDGMENTS

The authors wish to acknowledge a particular debt to Dr. Jacques Delwiche (University of Liège) for general criticism and specific suggestions during the composition of this manuscript. They acknowledge also the CNRS (Mathematical and Physical Science Department) and the Ministère de la Recherche et de l'Enseignement Supérieur for a generous allocation of computer time on the 3090 IBM at CIRCE (Orsay). This work has also been supported by a EEC grant (SCIENCE program).

[1] J. H. Beynon, A. Mathias, and A. E. Williams, Org. Mass. Spectrom. **5**, 303 (1971).
[2] T. Ast, J. H. Beynon, and R. G. Cooks, Org. Mass. Spectrom. **6**, 749 (1972).
[3] B. E. Jones, L. E. Abbey, H. L. Chatham, A. W. Hanner, L. A. Teleshevsky, E. M. Burgess, and T. F. Moran, Org. Mass. Spectrom. **17**, 10 (1982).
[4] B. P. Mathur, L. E. Abbey, E. M. Burgess, and T. F. Moran, Org. Mass. Spectrom. **15**, 312 (1980).
[5] J. R. Appling, B. E. Jones, L. E. Abbey, D. E. Bostwick, and T. F. Moran, Org. Mass. Spectrom. **18**, 282 (1983).
[6] R. R. Rye, T. E. Madey, J. E. Houston, and P. H. Holloway, J. Chem. Phys. **69**, 1504 (1978).
[7] M. Thompson, P. A. Hewitt, and D. S. Wooliscroft, Anal. Chem. **48**, 1336 (1976).
[8] J. Appel, J. Durup, F. C. Fehsenfeld, and P. G. Fournier, J. Phys. B **7**, 406 (1974).
[9] S. R. Andrews, F. M. Harris, and D. E. Parry, Chem. Phys. **166**, 69 (1992).
[10] J. H. D. Eland, S. D. Price, J. C. Cheney, P. Lablanquie, I. Nenner, and P. G. Fournier, Philos. Trans. R. Soc. London Ser. A **324**, 247 (1986).
[11] J. H. D. Eland, F. S. Wort, P. Lablanquie, and I. Nenner, Z. Phys. D **4**, 31 (1986).
[12] A. W. Hanner, L. E. Abbey, D. E. Bostwick, E. M. Burgess, and T. F. Moran, Org. Mass. Spectrom. **17**, 19 (1982).

[13] G. W. Burdick, G. C. Shields, J. R. Appling, and T. F. Moran, Int. J. Mass. Spectrosc. Ion Proc. **64**, 315 (1985).
[14] J. R. Appling and T. F. Moran, Chem. Phys. Lett. **118**, 188 (1985).
[15] G. C. Shields and T. F. Moran, Theor. Chim. Acta **69**, 147 (1986).
[16] J. A. Pople, M. J. Frisch, K. Raghavachari, and P. v. R. Schleyer, J. Comp. Chem. **3**, 468 (1982).
[17] C-M. Liegener, Chem. Phys. **92**, 97 (1985).
[18] E. M-L. Ohrendorf, F. Tarantelli, and L. S. Cederbaum, J. Chem. Phys. **92**, 2984 (1990).
[19] R. Thissen, J. Delwiche, J-M. Robbe, D. Duflot, J-P. Flament, and J. H. D. Eland, J. Chem. Phys. **99**, 6590 (1993).
[20] R. Thissen, Ph.D. thesis, Université de Liège, Belgium, 1993.
[21] T. H. Dunning, J. Chem. Phys. **55**, 716 (1971); **55**, 3958 (1971).
[22] B. O. Roos, Adv. Chem. Phys. **69**, 399 (1987).
[23] M. Dupuis, A. Farazdel, S. P. Karna, and S. A. Maluendes, in *Modern Techniques of Computational Chemistry*, edited by E. Clementi (ESCOM, Leyden, 1990).
[24] C. J. Cerjan and W. H. Miller, J. Chem. Phys. **75**, 2800 (1981).
[25] J. Simons, P. Jørgensen, H. Taylor, and J. Ozment, J. Phys. Chem. **87**, 2745 (1983).
[26] B. Huron, J-P. Malrieu, and P. Rancurel, J. Chem. Phys. **58**, 5745 (1973).
[27] R. Cimiraglia, J. Chem. Phys. **83**, 1746 (1985); R. Cimiraglia and M. Persico, J. Comp. Chem. **8**, 39 (1987).
[28] C. Möller and M. S. Plesset, Phys. Rev. **46**, 618 (1934).
[29] K. P. Huber and G. Herzberg, *Molecular Spectra and Molecular Structure, Vol. III. Electronic Spectra and Electronic Structure of Polyatomic Molecules* (Van Nostrand, New York, 1979).
[30] R. S. Mulliken, J. Chem. Phys. **23**, 1833 (1955).
[31] J. D. Dill, P. v. R. Schleyer, and J. A. Pople, J. Am. Chem. Soc. **97**, 3402 (1975).
[32] C. Jouany, J. C. Barthelat, and J. P. Daudey, Chem. Phys. Lett. **136**, 52 (1987).
[33] C. Petrongolo, J. Chem. Phys. **89**, 1297 (1988).
[34] P. Rosmus, P. Botschwina, and J. P. Maier, Chem. Phys. Lett. **84**, 71 (1981).
[35] G. Frenking, Chem. Phys. Lett. **100**, 484 (1983).
[36] J. Baker, Chem. Phys. Lett. **159**, 447 (1989).
[37] T. P. Hamilton and H. F. Schaefer III, J. Phys. Chem. **93**, 7560 (1989).
[38] J. H. Davis, W. A. Goddard III, and L. B. Harding, J. Am. Chem. Soc. **99**, 2919 (1977).
[39] C. E. Dykstra and H. F. Schaefer III, J. Am. Chem. Soc. **100**, 1378 (1978).
[40] R. Krishnan, M. J. Frisch, J. A. Pople, and P. v. R. Schleyer, Chem. Phys. Lett. **79**, 408 (1981).
[41] T. Carrington, L. M. Hubbard, H. F. Schaefer III, and W. H. Miller, J. Chem. Phys. **80**, 4347 (1984).
[42] M. M. Gallo, T. P. Hamilton, and H. F. Schaefer III, J. Am. Chem. Soc. **112**, 8714 (1990).
[43] B. J. Smith, R. Smernik, and L. Radom, Chem. Phys. Lett. **188**, 589 (1992).
[44] Ph. Halvick, D. Liotard, and J. C. Rayez, Chem. Phys. **177**, 69 (1993).
[45] M. P. Conrad and H. F. Schaefer III, J. Am. Chem. Soc. **100**, 7820 (1978).
[46] Y. Osamura and H. F. Schaefer III, Chem. Phys. Lett. **79**, 412 (1981).
[47] Y. Yamaguchi, G. Vacek, and H. F. Schaefer III, Theor. Chim. Acta **82**, 1 (1993).
[48] G. Vacek, J. R. Thomas, B. J. DeLeeuw, Y. Yamaguchi, and H. F. Schaefer III, J. Chem. Phys. **98**, 4766 (1993).
[49] L. B. Harding, J. Am. Chem. Soc. **103**, 7469 (1981).
[50] J. H. D. Eland, Mol. Phys. **61**, 725 (1987).
[51] H. Sun and K. F. Freed, Chem. Phys. Lett. **78**, 531 (1981).
[52] A. J. Lorquet, J. C. Lorquet, H. Wankenne, J. Momigny, and H. Lefebvre-Brion, J. Chem. Phys. **55**, 4053 (1971).

Article 2

Stability of the CH_3Cl dication

D. Duflot, J-M. Robbe, and J-P. Flament
Laboratoire de Dynamique Moléculaire et Photonique, URA CNRS 779, Université des Sciences et Technologies de Lille, UFR de Physique, 59655 Villeneuve d'Ascq Cedex, France

(Received 28 June 1995; accepted 19 September 1995)

The chloromethane cation and dication have been studied using the complete active space self-consistent field method followed by a multireference perturbative configuration interaction. The ^2E ground state of CH_3Cl^+ presents a weak Jahn–Teller distortion, the $^2A'$ and $^2A''$ components being separated by only 3.4 kcal/mol with very similar geometries. Both states are equilibrium structures. Contrary to previous calculations, the lowest singlet and triplet states of CH_3Cl^{++} are calculated to be stable. While the $^3A_2$ state keeps the neutral C_{3v} symmetry, the ^1E singlet state shows a large Jahn–Teller effect, with a splitting of 32.7 kcal/mol in favor of the $^1A'$ state, which is the ground state of the molecule. The planar $^1A'$ state of CH_2ClH^{++} is found to be the most stable isomer, lying 41.4 kcal/mol below the corresponding state of CH_3Cl^{++}. The $^3A''$ state, which lies 22.59 kcal/mol above the $^1A'$ state, has a nonplanar C_s-symmetry geometry. Finally, the CH_3Cl^{++} $(^1A')\rightarrow CH_2ClH^{++}$ $(^1A')$ isomerization takes place via a C_1-symmetry transition state, with an energy barrier of 32.85 kcal/mol. © *1995 American Institute of Physics.*

I. INTRODUCTION

In the past few years, interest in the study of dicationic species has largely increased, due to progresses in experimental and theoretical methods (for a recent review of both aspects, see Ref. 1). As a member of the methyl compounds CH_3–X family, the chloromethane dication has been the subject of several experimental studies,[2–5] using double charge transfer[2] and coincidence spectroscopy.[3–5] The most striking result of these works is probably the presence of the H_3^+ ion among the fragmentation products.[4,5]

From the theoretical point of view, the only work of which we are aware concerning the dissociation of CH_3Cl^{++} is part of the general study of ylides dications by Yates and co-workers[6] at the MP3/6-31G*//UHF/6-31G* level. Their main conclusions were that the singlet and triplet states of CH_3Cl^{++} are unstable, while the singlet conventional isomer CH_2ClH^{++} is stable and can dissociate into $H^+ + CH_2Cl^+$ and $CH_2^+ + HCl^+$ through energy barriers.

As a first step in the theoretical interpretation of the chloromethane dication fragmentation processes, we have reinvestigated the question of the stability of CH_3Cl^{++}, using large scale quantum mechanical methods. This paper is organized as follows. Section II describes the methods used to calculate the geometries and energies of the studied molecules; Sec. III gives the results obtained successively for CH_3Cl, CH_3Cl^+, CH_3Cl^{++}, CH_2ClH^{++}, and for the $CH_3Cl^{++}\rightarrow CH_2ClH^{++}$ isomerization reaction; finally, in Sec. IV some conclusions are given.

II. COMPUTATIONAL METHOD

The computational method employed in the present study is very close to that previously used in our work on the acetylene dication dissociations,[7,8] with a few minor differences. In order to reduce the size of the calculations, the $1s$ and $1s2s2p$ shells of the carbon and chlorine atoms were described with the compact effective potentials (CEP) of Stevens and co-workers.[9] The Gaussian atomic orbital (AO) basis set consisted of the TZP basis set given by Stevens,[9] i.e., $(4sp)/[3sp]$ for carbon and chlorine, augmented with d-type polarization functions ($\alpha_C=0.75$ and $\alpha_{Cl}=0.55$). A TZP basis set from Dunning[10] was also used for the hydrogen atom, i.e., $(5s)/[3s]$ with a p-type polarization function ($\alpha_H=1.0$). The total size of the basis set was thus 54 AO's. All energy calculations and geometry optimizations were carried out at the self-consistent-field (SCF) and the MCSCF (multiconfigurational SCF) levels[11] with the HONDO8 program package[12] using analytic gradients. The MCSCF space was obtained by following the CASSCF (complete active space SCF) method.[13] Thus, the active space for CH_3Cl^{++} contained 12 electrons in 11 molecular orbitals (MO's).

Transition-state structures were located also at both SCF and CASSCF levels. It was found that the Cerjan and Miller method[14,15] implemented in HONDO8 was not efficient for this purpose when beginning far from the saddle point geometry. Therefore, we employed a step by step procedure: We calculated a minimum energy path along the reaction coordinate, by optimizing the geometry for fixed values of this coordinate. The nature of the singular points of the potential energy surfaces was verified by diagonalization of the Hessian matrix calculated by means of finite differences at SCF and CASSCF levels. In a few cases (especially open shells systems), the size of the CI matrix was beyond the capability of HONDO8. Thus the active space was reduced by freezing the occupation of the first MO. This orbital corresponds to the chlorine $3s$ shell, which remains quasiunaffected in all the studied geometries. The change in the CASSCF energy was about a few milli-Hartrees but the Hessian matrix should not be modified significatively. Unscaled eigenvalues of this Hessian matrix were used to calculate zero-point vibrational energies (ZPE's) using the rigid harmonic oscillator approximation.

In order to take into account the effect of dynamical correlation, configuration interaction (CI) calculations were performed at the CASSCF optimized geometries using the two-class version of the CIPSI program[16] and its diagram-

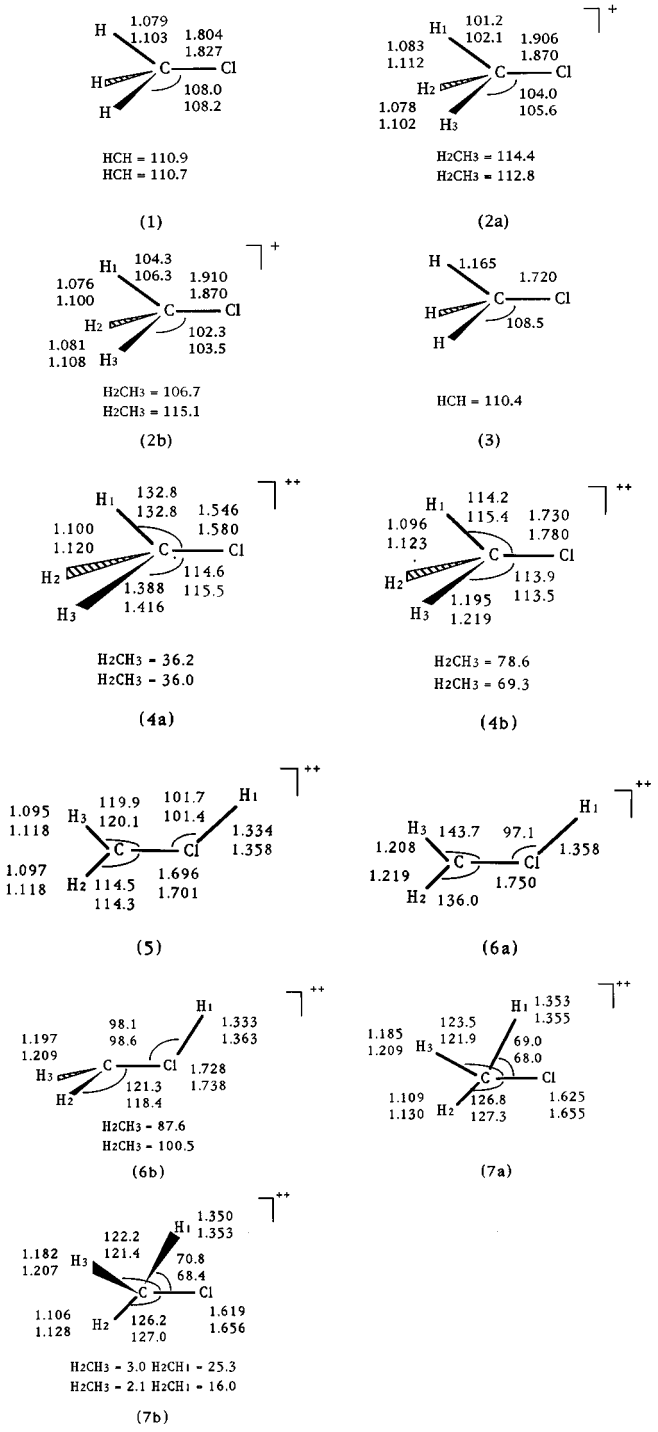

FIG. 1. Optimized geometries of the structures studied in the present work. The upper values are the SCF results (when existing), the lower values indicates the CASSCF results.

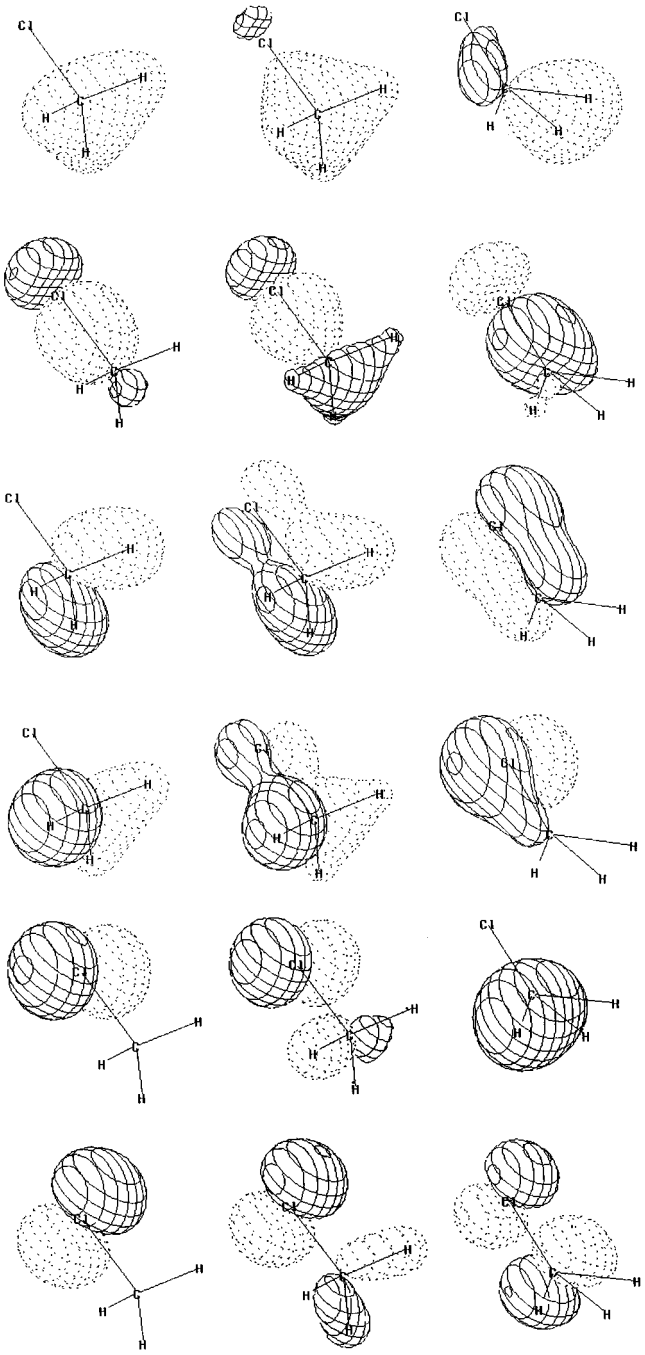

FIG. 2. Shape of the CASSCF MO's in CH_3Cl ($^1A_1$) (left column), CH_3Cl^{++} ($^3A_2$) (center column), and CH_3Cl^{++} ($^1A'$) (right column): $2a_1(2a')$, $3a_1(3a')$, $1e(4a',1a'')$, and $2e$ $(5a',2a'')$.

matic version.[17] In this method, a reduced CI matrix, called the *S* space and containing the dominant configurations (contribution to the wave function greater than a threshold value of typically 0.01) is constructed iteratively and diagonalized. The effect of all other configurations is treated by second order perturbative theory, using the Möller–Plesset partition of the Hamiltonian.[18] In the present study, we found that a *S* space of about 1500 Slater determinants was sufficient to obtain high-quality zeroth-order wave functions. The size of the perturbative space *P* was about 10 million determinants and the norm of the correction to the wave function was less than 4.5% (see Table I) in all cases. Our best level of calculation thus corresponds to the CIPSI energies corrected with CASSCF ZPE's.

The SCF and CASSCF optimized geometries of the structures studied in the present work are displayed in Fig. 1 and the corresponding absolute energies are given in Table I. The relative energies with respect to the $^1A'$ ground state of CH_3Cl^{++} are shown in Table II.

TABLE I. Calculated absolute energies of the optimized geometries.

		State	Nature[a]	E_{SCF} (a.u.)	E_{CASSCF} (a.u.)	E_{CIPSI} (a.u.)	Norm[b]
CH_3Cl	1	$^1A_1$	0	−21.927 841	−22.014 432	−22.247 343	0.027
CH_3Cl^+	2a	$^2A'$	0	−21.547 146	−21.632 409	−21.843 796	0.028
	2b	$^2A''$	0	−21.547 125	−21.632 361	−21.843 786	0.028
CH_3Cl^{++}	3	$^3A_2$	0	c	−20.936 983	−21.129 397	0.045
CH_3Cl^{++}	4a	$^1A'$	0	−20.846 992	−20.980 933	−21.159 529	0.025
	4b	$^1A''$	1	−20.833 555	−20.915 250	−21.103 035	0.033
CH_2ClH^{++}	5	$^1A'$	0	−20.945 090	−21.052 072	−21.229 535	0.027
CH_2ClH^{++}	6a	$^3A''$	2	c	−20.866 254	−21.057 764	0.041
	6b	$^3A''$	0	−20.814 508	−20.899 047	−21.089 305	0.042
CH_2–H–Cl^{++}	7a	$^1A'$	2	−20.818 617	−20.951 346	−21.105 069	0.022
	7b	^1A	1	−20.818 938	−20.951 461	−21.104 938	0.022

[a]Nature of the state: the number of imaginary vibrational frequencies is indicated.
[b]Norm of the perturbation correction to the CIPSI wave function.
[c]Dissociative state.

III. RESULTS AND DISCUSSION

A. The neutral CH_3Cl

The ground state $^1A_1$ configuration of the neutral CH_3Cl [(1) in Fig. 1] is given by

$$^1A_1 \quad 1a_1^2 2a_1^2 1e^4 3a_1^2 2e^4. \tag{1}$$

The $1a_1$ MO is the $3s$ AO of the chlorine atom and remains unchanged in the molecule. The $2a_1$ MO is the $\sigma(CH_3)$ bond constructed with the $2s$(C) and the three $1s$(H) AO's. The doubly degenerate $1e$ MO corresponds to the two $\pi(CH_3)$ bonds constructed with the $2p_x$ and $2p_y$ carbon AO's. The $3a_1$ MO is the σ(CCl) bond and finally, the doubly degenerate highest occupied molecular orbitals (HOMO's) $2e$ are composed of the two $3p_x$ and $3p_y$ lone pairs located on the chlorine atom (see the first column of Fig. 2).

Our optimized SCF and CASSCF geometries are compared with previous works in Table III. For bond angles, there is an excellent agreement between theoretical and experimental determinations, since all the HCCl and HCH values are within a range of less than 1°. All the SCF C–H bond distances[6,19,20] are overestimated by about 0.005 Å with respect to experiments,[21,22] whereas the deviation is much greater (≈0.02 Å) for our CASSCF result. For C–Cl distance, the theoretical results are usually too large, especially in our CASSCF calculation and that of Benassi and co-workers,[23] where the discrepancy is 0.04–0.05 Å. This is not surprising, since the CASSCF method is well known to overestimate bond distances.

The calculated harmonic vibrational frequencies are compared with previous theoretical[19,20] and experimental[22,24–27] works in Table IV. As usually observed, it appears that all SCF calculations give values overestimated by about 10% with respect to experiments. The discrepancies are slightly less (<8%) in MP2 treatment[19] but the agreement is much better in our CASSCF calculations, deviations being less than 4%. A similar accuracy may be expected for the ionic structures, for which no other data are available.

B. The CH_3Cl^+ monocation

The CH_3Cl^+ cation configuration is obtained from CH_3Cl by removing one electron from the $2e$ HOMO:

$$1a_1^2 2a_1^2 1e^4 3a_1^2 2e^3. \tag{2}$$

This configuration leads to the ^2E lowest lying state of CH_3Cl^+, which is doubly degenerate. In this case, the Jahn–Teller theorem[28] states that the molecule will distort to two C_s states, where the degeneracy will be removed [these two states are respectively denoted (2a) and (2b) in Fig. 1]:

$$^2A' \quad 1a'^2 2a'^2 3a'^2 1a''^2 4a'^2 5a'^1 2a''^2, \tag{3a}$$

TABLE II. Relative energies (kcal/mol) of the chloromethane dication structures at various levels of calculation.

		State	Nature[a]	ΔE_{SCF}	$\Delta E_{SCF}+ZPE_{SCF}$	ΔE_{CASSCF}	$\Delta E_{CASSCF}+ZPE_{CASSCF}$	ΔE_{CIPSI}	$\Delta E_{CIPSI}+ZPE_{CASSCF}$
CH_3Cl^{++}	3	$^3A_2$	0	b	b	27.58	26.20	18.57	17.19
CH_3Cl^{++}	4a	$^1A'$	0	0.00	0.00	0.00	0.00	0.00	0.00
	4b	$^1A''$	1	8.43	8.14	41.22	39.43	34.45	32.66
CH_2ClH^{++}	5	$^1A'$	0	−61.56	−59.01	−44.64	−42.13	−43.90	−41.39
CH_2ClH^{++}	6a	$^3A''$	2	b	b	71.96	67.82	63.86	59.72
	6b	$^3A''$	0	20.38	18.12	23.80	21.23	25.16	22.59
CH_2–H–Cl^{++}	7a	$^1A'$	2	17.80	15.29	18.57	16.58	34.17	32.18
	7b	^1A	1	17.60	15.80	18.49	16.83	34.51	32.85

[a]Nature of the state: The number of imaginary vibrational frequencies is indicated.
[b]Dissociative state.

TABLE III. Comparison of calculated equilibrium distances of CH_3Cl ($^1A_1$) with previous works.

	Method	Basis	R(C–Cl) (Å)	R(C–H) (Å)	HCCL (°)	HCH (°)
This work	SCF	ECP/TZP	1.804	1.079	108.0	110.9
	CASSCF	ECP/TZP	1.827	1.103	108.2	110.7
Reference 19	SCF	4-31G*	1.779	1.078	108.7	110.3
	SCF	DZP	1.791	1.079	108.3	110.6
	MP2	DZP	1.786	1.088	108.8	110.2
Reference 6	SCF	3-21G*	1.806	1.076	108.1	
	SCF	6-31G*	1.785	1.078	108.5	
	MP2	6-31G*	1.778	1.088	108.9	
Reference 20	SCF	ECP/DZP	1.777	1.078	108.5	110.5
Reference 23	CASSCF	6-31G*	1.816	1.078	108.1	
Reference 21	Expt.		1.778	1.086	108.2	110.7
Reference 22	Expt.		1.776	1.085	108.5	110.3

$$^2A'' \quad 1a'^2 2a'^2 3a'^2 1a''^2 4a'^2 5a'^2 2a''^1. \tag{3b}$$

The equilibrium geometries of these two states are compared with previous theoretical[29,30] studies in Table V. The distances and bond angles are in good agreement with the notable exceptions of R(C–Cl) and the H_2CH_3 angle. The C–Cl distance show large variations (1.76→1.97 Å) depending on the method used for its determination. By comparison with our neutral species results, we think that our CASSCF value could be overestimated by about 0.05 Å due to the combined use of ECP and CAS methods. Concerning the H_2CH_3 angle, the result of Yates[29] are surprisingly greater by 10–20 ° with respect to our own work and that of Flores and co-workers.[30]

Moreover, examination of Table V reveals that the $^2A'$ and $^2A''$ have very similar geometries, as well as the same absolute energies given in Table I. This feature has been explained by Glidewell[31] in terms of the degree of localization of the $2e$ HOMO in the neutral: the greater the localization, the smaller the Jahn–Teller distortion. Figure 2 clearly shows that the $2e$ MO's are actually concentrated on the chlorine atom in the neutral. No noticeable change in the shape of the same MO's in the cation is visible. The small Jahn–Teller distortion is also reflected in the vibrational frequencies of the two states (Table VI): Several couples of values are quasidegenerate.

Inspection of Table VI shows that the $^2A'$ state is a minimum of the potential energy surface at both SCF and CASSCF levels. Concerning the $^2A''$ state, SCF calculations reveal the presence of one imaginary mode ($i629$ cm^{-1}) corresponding to an asymmetric bending of the H_2CCl and H_3CCl angles. This state is thus a transition state, in agreement with the UHF/3-21G* calculations of Yates.[31] However, the situation changes dramatically at the CASSCF level: while the other modes are comparable with their SCF counterparts, the imaginary frequency becomes now real, with a value of 709 cm^{-1}. The $^2A''$ state is thus a minimum at CASSCF level.

From the energetic point of view, the Jahn–Teller splitting $\Delta E = E(^2A') - E(^2A'')$ comes from the differences in ZPE corrections: ΔE(SCF)=1.89 kcal/mol and ΔE(CASSCF+CIPSI)=3.43 kcal/mol in favor of the $^2A''$ state. This small gap is another consequence of the similarity of the two states.

C. The CH_3Cl^{++} dication

The CH_3Cl^{++} dication configuration is obtained from CH_3Cl by removing two electrons from the $2e$ HOMO:

$$1a_1^2 2a_1^2 1e^4 3a_1^2 2e^2. \tag{4}$$

Of course, the situation where the two positive charges are located on the chlorine atom is not the most stable one: at equilibrium geometries, the CH_3 fragment plays the role of an electron donor and chlorine that of an acceptor, leading to important rearrangements of the charge repartition.

The configuration given in Eq. (4) leads to the three lowest lying states of CH_3Cl^{++}, $^3A_2$ and ^1E (doubly degen-

TABLE IV. Calculated harmonic frequencies (cm^{-1}) of neutral CH_3Cl compared with previous works.

	Refs. 21,22,24–27	This work		Ref. 19			Ref. 20
	Expt.	SCF ECP/TZP	CASSCF ECP/TZP	SCF 4-31G*	SCF DZP	MP2 DZP	SCF ECP/DZP
ν_i (cm^{-1})	3039.29[a]	3303	3078	3360.4	3376.6	3283.1	3371
	2950.20	3199	2971	3256.8	3253.1	3147.7	3268
	1452.18[a]	1606	1506	1636.5	1604.0	1521.6	1630
	1354.88	1507	1409	1551.4	1552.0	1447.7	1540
	1018.07[a]	1115	1038	1141.3	1116.7	1058.3	1142
	732.85	763	720	783.5	778.3	772.7	793
ZPE (kcal/mol)	22.95	25.04	23.36	25.54	25.41	24.44	25.57

[a]Degenerate value.

TABLE V. Comparison of calculated equilibrium distances of CH_3Cl^+ ($^1A'$ and $^1A''$) with previous works.

	Method	Basis	R(C–Cl) (Å)	R(C–H_1) (Å)	H_1CCl (°)	R(C–H_{23}) (Å)	H_{23}CCl (°)	H_2CH_3 (°)
CH_3Cl^+ ($^1A'$)								
This work	SCF	ECP/TZP	1.906	1.083	101.2	1.078	104.0	114.4
	CASSCF	ECP/TZP	1.870	1.112	102.1	1.102	105.6	112.8
Reference 30	MP2	6-31G**	1.764	1.100	103.3	1.085	108.4	
Reference 6	SCF	3-21G*	1.964	1.080	101.5	1.075	115.5	116.7
	SCF	6-31G*	1.869	1.082	102.5	1.080	119.1	115.8
	MP2	6-31G*	1.765	1.086	103.5	1.090	126.7	115.7
CH_3Cl^+ ($^1A''$)								
This work	SCF	ECP/TZP	1.910	1.076	104.3	1.081	102.3	106.7
	CASSCF	ECP/TZP	1.870	1.100	106.3	1.108	103.5	115.1
Reference 6	SCF	3-21G*	1.965	1.074	103.5	1.078	112.6	114.2
	SCF	6-31G*	1.869	1.075	105.5	1.080	114.8	112.6
	MP2	6-31G*	1.765	1.086	109.3	1.099	117.3	107.7

erate). In a previous work, Yates and co-workers[6] found that the $^3A_2$ state was not stable and dissociated spontaneously into $CH_3^+ + Cl^+$ at the RHF/3-21G* and 6-31G* levels. Indeed, our own SCF calculations confirm this behavior. However, the same optimization performed at the CASSCF level converges towards the C_{3v} structure (3) shown in Fig. 1, which is a minimum of the potential energy surface after its vibrational frequencies, which are all real (Table VII). This result shows that inclusion of correlation effects is necessary to calculate the geometry of this triplet state.

Due to the Jahn–Teller theorem,[28] the ^1E state will distort to two nondegenerate $^1A'$ and $^1A''$ states:

$$^1A' \quad 1a'^2 2a'^2 3a'^2 1a''^2 4a'^2 5a'^2, \tag{5a}$$

$$^1A'' \quad 1a'^2 2a'^2 3a'^2 1a''^2 4a'^2 5a'^1 2a''^1. \tag{5b}$$

The optimized geometries of these states are shown in Fig. 1 [(4a) and (4b) respectively]. Examination of the vibrational frequencies (Table VII) indicates that the $^1A'$ state is an energy minimum at both SCF and CASSCF levels. This result is in contradiction with the calculation of Yates and co-workers[6] who found that it dissociates spontaneously in $CH_3^+ + Cl^+$ at the RHF/3-21G* and 6-31G* levels. This indicates that the 3-21G* and 6-31G* basis are not large enough to describe properly this singlet state at the SCF level.

For the $^1A''$ state, the vibrational frequencies are all real at the SCF level, the lower mode (713 cm^{-1}) corresponding to the C–Cl stretching (Table VII). This state is thus an energy minimum at the SCF level. However, the same calculation performed at the CASSCF level gives a rather different result: the lowest real value (645 cm^{-1}) is again the C–Cl stretching frequency, but there is now one imaginary mode (i490 cm^{-1}), corresponding to the H_2CCl and H_3CCl asymmetric bending movement. In SCF calculations, the same mode had a real value of 1122 cm^{-1} (Table VII). We conclude that this state is a saddle point between two $^1A''$ equivalent forms.

The comparison between the geometries of the $^3A_2$ (3) and $^1A'$ (4a) states of CH_3Cl^{++} and the $^1A_1$ state of CH_3Cl shows large variations, especially in C–H and C–Cl bond lengths (Fig. 1). At the CASSCF level, the C–Cl distance ranges from 1.827 Å in CH_3Cl ($^1A_1$) to 1.780 Å in CH_3Cl^{++}

TABLE VI. Calculated harmonic frequencies (cm^{-1}) of the $^2A'$ and $^2A''$ states of CH_3Cl^+.

		State	ν (SCF)	ν (CASSCF)	ZPE (SCF)	ZPE (CASSCF)
CH_3Cl^+	2a	$^2A'$	3401	3032	24.50	21.43
			3349	3022		
			3219	2890		
			1538	1336		
			1527	1331		
			1466	1383		
			1101	775		
			1091	773		
			443	451		
	2b	$^2A''$	3396	3130	22.61	17.89
			3218	2995		
			3216	2941		
			1535	1433		
			1464	1374		
			1459	1353		
			1092	1037		
			436	538		
			i629	709		

TABLE VII. Calculated harmonic frequencies (cm^{-1}) of the states of CH_3Cl^{++}.

		State	ν (SCF)	ν (CASSCF)	ZPE (SCF)	ZPE (CASSCF)
CH_3Cl^{++}	3	$^3A_2$		2402		16.70
				2359[a]		
				1059		
				816[a]		
				638[a]		
				598		
CH_3Cl^{++}	4a	$^1A'$	3214	3091	19.37	18.08
			3144	2953		
			1540	1409		
			1249	1121		
			1230	1060		
			1112	969		
			987	867		
			855	800		
			219	377		
	4b	$^1A''$	3042	2928	19.08	16.29
			2545	2335		
			1949	1990		
			1412	1313		
			1122	$i490$		
			878	862		
			824	766		
			770	533		
			713	645		

[a]Degenerate value.

($^3A_2$) and 1.580 Å in CH_3Cl^{++} ($^1A'$). This latter value, which is very short and corresponds to a double C–Cl bond, has already been observed in substituted methylene dications.[32–35] In particular, R(C–Cl)=1.459 Å at MP2/6-31G* level in $HCCl^{++}$.[35] This feature has been explained[35] by a conjugative interaction between the dicationic carbon atom (electron acceptor) and the chlorine atom (electron donor). As previously pointed out by Ruhl and co-workers,[4] the situation is the same in CH_3Cl^{++} but in the reverse direction, since the CH_3Cl HOMO is located on chlorine: the CH_3 fragment plays the role of the donor, the chlorine atom, that of the acceptor.

In fact, examination of the CASSCF atomic charges after a Mulliken population analysis[36] shows that the electron transfer comes mainly from the hydrogen atoms. In the case of the $^3A_2$ state, the chlorine atom has a charge of +1.1, the carbon atom −0.3 and each hydrogen +0.4. For the $^1A'$ state, the results are the following. Only +0.8 on chlorine, +0.2 on carbon, +0.4 on H_1, and +0.3 on each H_2 and H_3. Thus, the charges are separated as much as possible in the dication. This conclusion was already deduced by Ruhl and co-workers,[4] from the analysis of the kinetic energy release during the fragmentation of CH_3Cl^{++}.

The increasing of the C–Cl bond strength in dication may be visualized on the shape of the occupied MO's (Fig. 2). In CH_3Cl ($^1A_1$), the $1e$ MO is purely localized on the CH_3 fragment. In CH_3Cl^{++} ($^3A_2$), these MO's are slightly delocalized on chlorine, increasing the electron density between C and Cl and reducing the C–Cl distance. On the other hand, the $2e$ MO's, which are chlorine lone pairs in the neutral are slightly delocalized on the CH_3 group, with an antibonding character. In CH_3Cl^{++} ($^1A'$), the delocalization is even more pronounced, especially for the $2a''$ MO which can be viewed as a π(CCl) bond. Of course, the delocalization of the MO's between the chlorine atome and the CH_3 fragment is responsible of the electron transfer.

Concerning the C–H bonds, it is easy to predict that they should be weakened because of the loss of electrons on the methyl fragment. Indeed, the C–H distance in CH_3Cl^{++} ($^3A_2$) is 1.165 Å at the CASSCF level instead of 1.103 Å in neutral CH_3Cl ($^1A_1$). The effect is more spectacular in CH_3Cl^{++} ($^1A'$); whereas the C–H_1 distance is close to the neutral one (1.100 Å instead of 1.103 Å), the C–H_2 and C–H_3 bonds are very long: 1.416 Å. The CASSCF Mulliken atomic charges[36] show the presence of 1.3 electrons on the H_2H_3 group. The H_2H_3 distance (0.874 Å) approaches the experimental H_2 internuclear distance [0.741 Å (Ref. 37)]. This structure may thus be viewed as a H_2 molecule weakly bounded to a $HCCl^{++}$ dication. The situation is reflected in

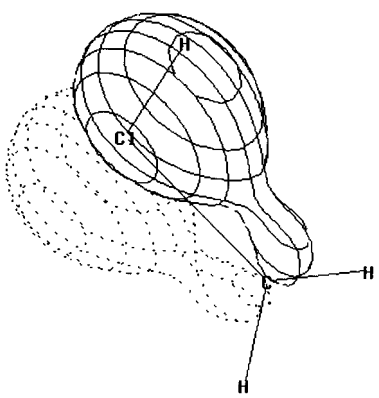

FIG. 3. Shape of the $1a''$ MO in CH_2ClH^{++}, showing the slight C–Cl strengthening effect.

TABLE VIII. Comparison of calculated equilibrium distances of CH_2ClH^{++} ($^1A'$) with previous works.

	Method	Basis	R(C–Cl) (Å)	R(Cl–H_1) (Å)	H_1ClC (°)	R(C–H_2) (Å)	H_2CCl (°)	R(C–H_3) (Å)	H_3CCl (°)
This work	SCF	ECP/TZP	1.696	1.334	101.7	1.097	114.5	1.095	119.9
	CASSCF	ECP/TZP	1.701	1.358	101.4	1.118	114.3	1.118	120.1
Ref. 6	SCF	3-21G*	1.671	1.317	101.9	1.093	115.5	1.091	121.1
	SCF	6-31G*	1.673	1.313	102.6	1.093	115.1	1.091	120.5

the shape of the MO's (Fig. 2): the $2a'$ MO, which corresponds to the $2a_1$ MO of the neutral, is now concentrated on the H_2 and H_3 atoms with, however, a noticeable density of electrons between the C and Cl atoms.

Finally, it is clear from Table II that the ground state of CH_3Cl^{++} is the $^1A'$ state, which lies 18.91 kcal/mol below the $^3A_2$ state at the CASSCF level and 17.19 kcal/mol at the CIPSI level. The Jahn–Teller splitting $\Delta E = E(^1A'') - E(^1A')$ shows large variations between SCF and CI calculations: ΔE(SCF)=8.14 kcal/mol, ΔE(CASSCF)=39.43, and ΔE(CIPSI)=32.66 kcal/mol.

D. The CH_2ClH^{++} dication

As previously shown by Yates and co-workers,[6] the singlet state $^1A'$ of the methylenechloronium dication CH_2ClH^{++} [(5) in Fig. 1] is planar with the following configuration:

$$1A' \quad 1a'^2 2a'^2 3a'^2 4a'^2 5a'^2 1a''^2. \tag{6}$$

The $1a''$ HOMO is an out of plane orbital essentially composed of the p chlorine AO, with however a small component on the carbon p AO (see Fig. 3). This small binding explains why the C–Cl distance (1.701 Å at CASSCF level) is slightly shorter than a C–Cl single bond value [1.720 Å for the $^3A_2$ state of CH_3Cl^{++}, compare (3) and (5) in Fig. 1].

Our calculated SCF and CASSCF equilibrium geometries are compared with those of Yates and co-workers in Table VIII. The SCF values are in good agreement, except for the C–Cl which is slightly greater in our work (1.696 Å instead of 1.673 Å). Once more, the CASSCF bond distances are systematically overestimated. Examination of the harmonic frequencies (see Table IX) clearly shows without any ambiguity that this structure is a minimum of the potential energy surface at both SCF and CASSCF levels.

Geometry optimization at the SCF level shows that the lowest triplet state of CH_2ClH^{++} is unstable. The same calculation performed in planar geometry at the CASSCF level converges to the geometry denoted (6a) in Fig. 1, which lies 59.72 kcal/mol above the singlet state at CIPSI level (Table II). The calculation of the vibrational frequencies (Table IX) indicates that this $^3A''$ state is a saddle point with two imaginary modes, corresponding both to out of plane movements

TABLE IX. Calculated harmonic frequencies (cm^{-1}) of the states of CH_2ClH^{++}.

		State	ν (SCF)	ν (CASSCF)	ZPE (SCF)	ZPE (CASSCF)
CH_2ClH^{++}	5	$^1A'$	3263	3054	21.92	20.59
			3101	2899		
			2614	2423		
			1514	1407		
			1254	1147		
			1177	1101		
			928	875		
			844	811		
			637	690		
CH_2ClH^{++}	6a	$^3A''$		2440		13.94
				2415		
				1786		
				987		
				900		
				735		
				488		
				i605		
				i830		
CH_2ClH^{++}	6b	$^3A''$	2611	2409	17.11	15.51
			2557	2316		
			1928	1864		
			1139	958		
			993	791		
			862	729		
			781	720		
			754	641		
			346	423		

TABLE X. Calculated harmonic frequencies (cm^{-1}) of the transition states for $CH_3Cl^{++} \rightarrow CH_2ClH^{++}$ isomerization.

		State	ν (SCF)	ν (CASSCF)	ZPE (SCF)	ZPE (CASSCF)
CH_2-H-Cl^{++}	7a	$^1A'$	3031	2853	16.86	16.09
			2502	2348		
			1636	1666		
			1594	1509		
			1056	982		
			1006	950		
			968	947		
			i166	i16		
			i1911	i1684		
	7b	^1A	3068	2862	17.57	16.42
			2523	2338		
			1627	1673		
			1579	1489		
			1092	976		
			1039	953		
			996	949		
			369	241		
			i1823	i1632		

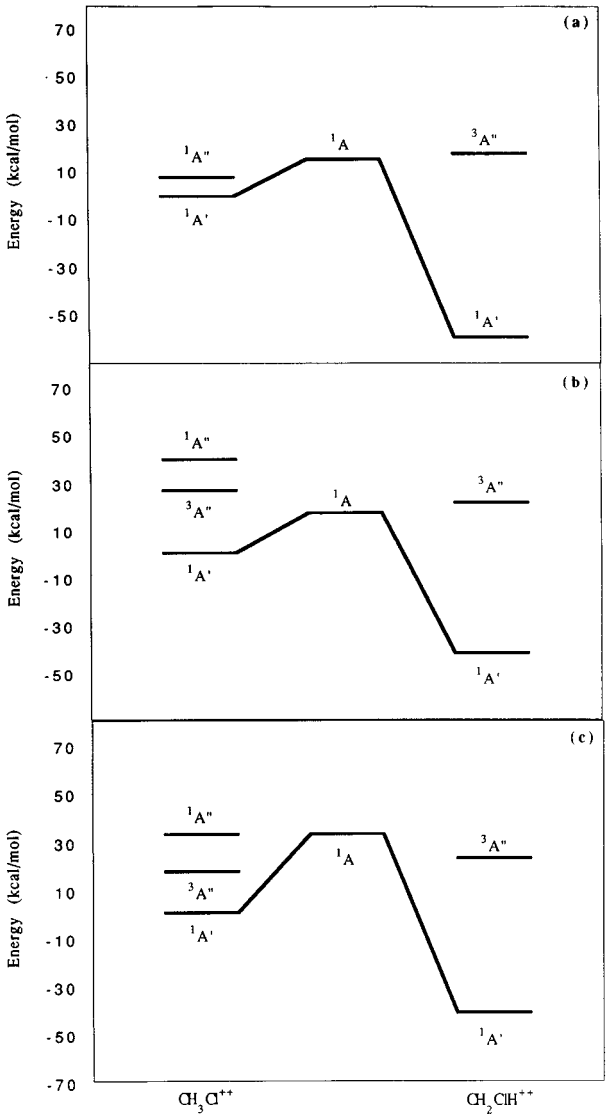

FIG. 4. Energy diagram of the lowest states of the chloromethane dication: (a) SCF level; (b) CASSCF level; (c) CIPSI level.

of the three hydrogen atoms. Another possible geometry for this triplet state is a nonplanar C_s-symmetric structure. Indeed, this form is found to be stable, at both SCF and CASSCF levels [(6b) in Fig. 1], lying 22.59 kcal/mol above the $^1A'$ state (Table II). The calculation of vibrational frequencies (Table IX) shows that this state corresponds to a true minimum.

Table II also shows that the $^1A'$ state of methylenechloronium CH_2ClH^{++} is the most stable isomer of the chloromethane dication, lying 34.83 kcal/mol below the $^1A'$ state of CH_3Cl^{++} at the SCF level, 42.13 kcal/mol at the CASSCF level and 41.39 kcal/mol at the CIPSI level.

E. The $CH_3Cl^{++} \rightarrow CH_2ClH^{++}$ isomerization

This sub-section is devoted to the determination of the transition state connecting the CH_3Cl^{++} and CH_2ClH^{++} isomers. For singlet states, a planar C_s-symmetric structure was searched by decreasing the $CClH_1$ angle of the methylenechloronium isomer, at both SCF and CASSCF levels. This procedure led to the (7a) geometries shown in Fig. 1. It is noticeable that the SCF and CASSCF are very close to each other, contrary to what happens for the other geometries studied in the present work. However, the calculation of vibrational frequencies shows the presence of two imaginary frequencies (Table X): the first one corresponding as expected to the in-plane $CClH_1$ bending mode (i1911 cm^{-1} at SCF level and i1684 cm^{-1} at the CASSCF level), the second one to the displacement of the H_1 migrating atom out of the plane of the molecule. This second mode is very low, especially at the CASSCF level (i166 cm^{-1} at the SCF level and only i16 cm^{-1} at the CASSCF level, respectively). These small values indicate that the true transition state does not differ very much from the planar structure.

Indeed, the ^1A transition state is found to have the structure denoted (7b) in Fig. 1, which is very similar to the planar one. At the SCF level, the H_1CCl plane forms an angle of 25.3° with the H_2CCl plane chosen as the reference,

whereas the H_3 atom is slightly (3°) out of this plane. At the CASSCF level, the H_1 torsion angle is reduced to 16°. The planar and nonplanar geometries have nearly the same energies (Table I). Finally, the energy barrier for the $CH_3Cl^{++}(^1A')\rightarrow CH_2ClH^{++}(^1A')$ isomerization is calculated to be 15.80 kcal/mol at the SCF level, 16.83 kcal/mol at the CASSCF level, and 32.85 kcal/mol at the CIPSI level (Table II).

In the case of the triplet states, the transition state might be obtained for example by reducing the H_1CCl angle of the structure (6b). However, a careful step by step search did not succeed in locating this structure. As soon as the angle reached the value of 67°, the molecule dissociated along the CCl mode. This behavior is due to a strong mixing between the H_1CCl bending mode and the CCl stretching mode, as confirmed by a calculation of the harmonic frequencies. Thus, it was not possible to determine the transition state of the triplet isomerization reaction.

IV. CONCLUSION

To summarize, the main conclusions of the present work are the following (see also Fig. 4).

(i) The ^2E ground state of the CH_3Cl^+ cation presents a weak Jahn–Teller effect, the two components $^2A'$ and $^2A''$ being quasidegenerate with quasiidentical geometries.

(ii) The lowest triplet and singlet state of CH_3Cl^{++} are both equilibrium structures. The singlet state is distorted because of the Jahn–Teller effect into $^1A'$ and $^1A''$ states, the former being the ground state of the molecule, the latter being a transition state. The Jahn–Teller splitting between the two components is calculated to be 32.7 kcal/mol. On the other hand, the $^3A_2$ state keeps the C_{3v} symmetry of the neutral molecule, and lies 17.19 kcal/mol above the ground state.

(iii) The $^1A'$ state of the methylenechloronium CH_2ClH^{++} is the lowest stable isomer of the chloromethane dication, lying 41.39 kcal/mol below the $CH_3Cl^{++}(^1A')$ state.

(iv) The $CH_3Cl^{++}(^1A')\rightarrow CH_2ClH^{++}(^1A')$ isomerization reaction has an energy barrier of 32.85 kcal/mol, the transition state having a nearly planar geometry. It was not possible to determine the triplet transition state.

(v) Our calculations on CH_3Cl^{++} rule out some of the previous conclusions of Yates and co-workers,[6] obtained at the standard HF/6-31G* level. Thus, the prediction of these authors about the unstability of the $CH_3–X^{++}$ compounds with $X=NH_2$, OH, and F is also questionable. Moreover, the present study shows large discrepancies between SCF and CASSCF results, even with large basis sets (Fig. 4). For these reasons, the stability of $CH_3–X$ dications should be re-investigated using accurate methods, including large basis sets and correlation effects.

ACKNOWLEDGMENTS

The authors acknowledge the CNRS (Mathematical and Physical Science Department) and the Ministère de l'Enseignement Supérieur et de la Recherche for a generous allocation of computer time on the IBM RISC6000 at IDRIS (Orsay). This work has also been supported by a European Economic Community (EEC) grant (SCIENCE program).

[1] D. Mathur, Phys. Rep. **225**, 193 (1993).
[2] W. J. Griffiths and F. M. Harris, Int. J. Mass Spectrom. Ion Proc. **89**, 125 (1989).
[3] B. P. Tsai and J. H. D. Eland, Int. J. Mass Spectrom. Ion Phys. **36**, 143 (1980).
[4] E. Rhul, S. D. Price, S. Leach, and J. H. D. Eland, Int. J. Mass Spectrom. Ion Proc. **97**, 175 (1990).
[5] R. Thissen (unpublished).
[6] B. F. Yates, W. J. Bouma, and L. Radom, J. Am. Chem. Soc. **108**, 6545 (1986).
[7] R. Thissen, J. Delwiche, J-M. Robbe, D. Duflot, J-P. Flament, and J. H. D. Eland, J. Chem. Phys. **99**, 6590 (1993).
[8] D. Duflot, J-M. Robbe, and J-P. Flament, J. Chem. Phys. **102**, 355 (1995).
[9] W. J. Stevens, H. Basch, and M. Krauss, J. Chem. Phys. **81**, 6026 (1984).
[10] T. H. Dunning, J. Chem. Phys. **55**, 716, 3958 (1971).
[11] R. Shepard, Adv. Chem. Phys. **69**, 63 (1987).
[12] M. Dupuis, A. Farazdel, S. P. Karna, and S. A. Maluendes, in *Modern Techniques of Computational Chemistry*, edited by E. Clementi (ESCOM, Leyden, 1990).
[13] B. O. Roos, Adv. Chem. Phys. **69**, 399 (1987).
[14] C. J. Cerjan and W. H. Miller, J. Chem. Phys. **75**, 2800 (1981).
[15] J. Simons, P. Jørgensen, H. Taylor, and J. Ozment, J. Phys. Chem. **87**, 2745 (1983).
[16] B. Huron, J-P. Malrieu, and P. Rancurel, J. Chem. Phys. **58**, 5745 (1973).
[17] R. Cimiraglia, J. Chem. Phys. **83**, 1746 (1985); R. Cimiraglia and M. Persico, J. Comp. Chem. **8**, 39 (1987).
[18] C. Möller and M. S. Plesset, Phys. Rev. **46**, 618 (1934).
[19] S. Kondo, Y. Koga, and T. Nakanaga, J. Chem. Phys. **81**, 1951 (1984).
[20] W. Schneider and W. Thiel, J. Chem. Phys. **86**, 923 (1987).
[21] M. D. Harmony, V. W. Laurie, R. L. Kuezkowski, R. H. Schwendemann, D. A. Ramsay, F. J. Lovas, W. J. Lafferty, and A. G. Maki, J. Phys. Chem. Ref. Data **8**, 619 (1979).
[22] P. Jensen, S. Brodersen, and G. Guelachvili, J. Mol. Spectrosc. **88**, 378 (1981).
[23] R. Benassi, F. Bernardi, A. Bottoni, M. A. Robb, and F. Taddei, Chem. Phys. Lett. **161**, 79 (1989).
[24] N. Bensari-Zizi and C. Alamichel, Mol. Phys. **43**, 1255 (1981).
[25] M. Morillon-Chapey, G. Gulelachvili, and P. Jensen, Can. J. Phys. **62**, 247 (1984).
[26] N. Bensari-Zizi and C. Alamichel, J. Phys. (Paris) **42**, 209 (1981).
[27] G. Wlodarczak, F. Herlemont, J. Demaison, A. Fayt, and J. G. Lahaye, J. Mol. Spectrosc. **112**, 401 (1985).
[28] H. Jahn and E. Teller, Proc. R. Soc. London, Ser. A **161**, 220 (1937).
[29] B. F. Yates, W. J. Bouma, and L. Radom, J. Am. Chem. Soc. **109**, 2250 (1987).
[30] J. R. Flores, C. Barrientos, and A. Largo, J. Phys. Chem. **98**, 1090 (1994).
[31] C. Glidewell, Inorg. Chim. Acta, **64**, *L*59 (1982).
[32] W. J. Bouma and L. Radom, J. Am. Chem. Soc. **105**, 5484 (1983).
[33] K. Lammertsma, M. Brazaghi, G. A. Olah, J. A. Pople, A. J. Kos, and P. v. R. Schleyer, J. Am. Chem. Soc. **105**, 5252 (1983).
[34] W. Koch and G. Frenking, Chem. Phys. Lett. **114**, 178 (1985).
[35] M. W. Wong, B. F. Yates, R. H. Nobes, and L. Radom, J. Am. Chem. Soc. **109**, 3181 (1987).
[36] R. S. Mulliken, J. Chem. Phys. **23**, 1833 (1955).
[37] K. P. Huber and G. Herzberg, *Molecular Spectra and Molecular Structure, Vol. IV. Constants of Diatomic Molecules* (Van Nostrand, New York, 1979).

Article 3

ELSEVIER

International Journal of Mass Spectrometry and Ion Processes 171 (1997) 215–230

International Journal of Mass Spectrometry and Ion Processes

Ab initio study of the chloromethane dication fragmentation

Denis Duflot*, Jean-Michel Robbe, Jean-Pierre Flament

Laboratoire de Dynamique Moléculaire et Photonique, URA CNRS 779, Centre d'Etudes et de Recherches Lasers et Applications, Université des Sciences et Technologies de Lille, UFR de Physique, 59655 Villeneuve d'Ascq Cedex, France

Received 7 May 1997; revised 20 June 1997; accepted 6 July 1997

Abstract

The chloromethane dication dissociation pathways have been studied using the complete active space self-consistent field (CASSCF) method followed by a multi-reference perturbative configuration interaction (CI). The vertical double ionization energy is calculated to be 31.64 eV for the first singlet state and 30.69 eV for the first triplet state, the latter value being close to the experimental determination of 31.5 ± 0.5 eV. For most two-body dissociation processes, the appearance thresholds of the ion pairs observed in coincidence experiments are in good agreement with the results of the calculations. In the case of the CCl^+/H_3^+ pair, the dissociation is indirect and comes from the ionization of a Rydberg excited state of the CH_3Cl^+ monocation. For three-body processes, the uncertainties of the available experimental results and the large number of possible dissociation channels do not allow identification uniquely of the involved mechanisms in most cases. © 1997 Elsevier Science B.V.

Keywords: Configuration interaction; Chloromethane; Dications; Fragmentation

1. Introduction

In a previous paper [1], we used large scale ab initio techniques to study the stability of the two lowest states of the CH_3Cl^{2+} dication. We found that the $^3A_2$ and $^1A'$ states were stable, contrary to the calculations performed at Hartree–Fock level with a 6-31G* basis set by Yates and co-workers [2]. While the $^3A_2$ state keeps the C_{3v} character of the neutral species, the $^1A'$ state is distorted because of an important Jahn–Teller effect [3,4]. In the present work, we present a theoretical interpretation of the available experimental data on the fragmentation of CH_3Cl^{2+}.

The CH_3Cl^{2+} fragmentation has been the subject of only a few experimental studies. Some years ago, Monce and co-workers [5,6] observed the CH_3^+ and Cl^+ fragments after bombarding neutral CH_3Cl with 1 MeV H^+, He^+ and O^+ projectiles. The authors deduced from coincidence measurements that these fragments came from the dissociation of a CH_3Cl^{2+} precursor. More recently, Ruhl and co-workers [7] used the PEPIPICO method (photoelectron-photoion-photoion coincidence) [8] to obtain the relative abundance and the kinetic energy release (KER) of each ion pair at an excitation energy of 40.8 eV. The PEPICO method (photoeelectron-photoion coincidence) combined with synchrotron radiation has also been used to study the excitation of the Cl(2p) shell [9,10] and to obtain the appearance thresholds of the fragmentation products at low energies [11]. The main

* Tel: 00 33 3 20 43 66 96; Fax: 00 33 3 20 43 40 85; E-mail: duflot@lsm350.univ-lille1.fr

PII S0168-1176(97)00123-7

Table 1
Summary of experimental results on the fragmentation of the CH_3Cl^{2+} dication

Products	Neutral	Threshold[a] (eV)	Intensity[b] (% pairs at 40.8 eV)	KER[b] (40.8 eV)
Two-body processes				
$CCl^+ + H_3^+$	—	30.0 ± 0.5	6	3.4 ± 1.0
$CH_2Cl^+ + H^+$	—	31.0 ± 0.5	13	5.2 ± 2.0
$HCCl^+ + H_2^+$	—	31.5 ± 0.5	2	2.8 ± 1.0
$HCCl^{2+}$	H_2	≥ 32.0	0	—
$CH_2^+ + HCl^+$	—	32.0 ± 1.0	0	—
CH_2Cl^{2+}	H	32.0 ± 1.0	0	—
$CH_3^+ + Cl^+$	—	32.5 ± 0.5	61	5.4 ± 1.0
Three-body processes				
$HCCl^+ + H^+$	H	35.0 ± 0.5	4	3.6 ± 2.0
$CCl^+ + H^+$	H_2	35.0 ± 0.5	3	3.6 ± 2.0
$CH_2^+ + Cl^+$	H	35.5 ± 1.0	9	4.3 ± 1.0
$CCl^+ + H_2^+$	H	36.0 ± 0.5	0	—
$CH_2^+ + H^+$	Cl	37.5 ± 1.0	2	3.6 ± 2.0

[a] Ref. [11]. [b] Ref. [7].

results of refs. [7] and [11] are summarized in Table 1.

This paper is divided into the following sections: in Section 2, we describe the methods used to calculate the geometries and energies of the studied molecules; in Section 3 we discuss the double ionization of CH_3Cl; Section 4 deals with two-body processes while Section 5 is devoted to three-body processes; finally, in Section 6 some conclusions are given.

2. Computational method

The computational method used in the present study has already been employed in our previous work [1] on the stability of CH_3Cl^{2+} and is only briefly summarized. We used the compact effective potentials (CEP) of Stevens and co-workers [12], with the corresponding TZP basis set, i.e. (4spld)/[3spld] for carbon and chlorine. The hydrogen atom was described with the (5slp)/[3slp] TZP basis set from Dunning [13]. All energy calculations and geometry optimizations for both equilibrium structures and transition states were carried out at the complete active space SCF (CASSCF) level [14] with the HONDO95.3 program package [15]. Harmonic vibrational frequencies and zero-point energies (ZPEs) were also calculated at the CASSCF level. As already stated in our previous paper [1], the Cerjan and Miller method [16,17] implemented in HONDO95.3 is not efficient for locating transition states and we employed a step by step procedure by freezing the reaction coordinate and optimizing the other ones. This method is sometimes called 'distinguished reaction coordinate'.

The effect of dynamical correlation was included via a multi-reference second-order Moller–Plesset perturbative calculation as implemented in the two-class version of the CIPSI program [18] and its diagrammatic version [19,20]. The size of the zeroth-order wave function was about 2000 Slater determinants and the norm of the correction to the wave function was less than 6.4% in all cases.

The CASSCF optimized geometries of the various molecules studied in the present work are displayed in Fig. 1 for CH_3Cl structures. The geometries of dissociation fragments are not reported here and are available upon request. The corresponding energies are given in Tables 2 and 3. In order to allow comparisons with experimental work (Table 1), all energies are expressed with respect to the neutral chloromethane ground

Table 2
Calculated energies of the molecular structures involved in the fragmentation of the CH_3Cl^{2+} dication

		N^a	State	E_{CASSCF} (au)	E_{CIPSI} (au)	Norm[b]	ΔE_{CASSCF} (eV)	ΔE_{CIPSI} (eV)	ΔE_{CIPSI} + ZPE (eV)
CH_3Cl	**1**	0	$^1A_1$	−22.014432	−22.2473343	0.027	0.00	0.00	0.00
CH_3Cl^+	**2**	0	$^2A''$	−21.632361	−21.843796	0.028	10.40	10.98	10.74
CH_3Cl^{2+}	**3a**	0	$^1A'$	−20.980933	−21.159529	0.028	28.12	29.60	29.37
	3b	0	$^3A_2$	−20.936983	−21.129397	0.045	29.32	30.42	29.96
CH_3^+–Cl^+	**4a**	1	$^1A'$	−20.863262	−21.034041	0.041	31.32	33.01	30.40
	4b	1	$^3A_2$	−20.934805	−21.122848	0.037	29.38	30.60	32.70
CCl^+–H_2–H^+	**5**	1	$^1A'$	−20.855639	−21.033560	0.019	31.53	33.03	32.44
CH_2Cl^{2+}–H	**6**	1	$^3A''$	−20.886589	−21.047200	0.037	30.69	32.66	32.25
CH_2^+–H–Cl^+	**7**	1	^1A	−20.951461	−21.104938	0.022	28.92	31.09	30.79
CH_2ClH^{2+}	**8a**	0	$^1A'$	−21.052072	−21.229535	0.027	26.19	27.69	27.57
	8b	0	$^3A''$	−20.904015	21.089305	0.042	30.21	31.51	31.17
CH_2Cl^+–H^+	**9**	1	$^1A'$	−20.964672	−21.142091	0.027	28.56	30.07	29.76
$HCCl^{2+}$–H_2	**10**	1	$^1A'$	−20.968970	−21.133044	0.024	28.44	30.32	29.97
$HCCl^+$–H_2^+	**11**	3	$^3A''$	−20.815466	−20.992872	0.042	32.62	34.13	33.65
CH_3Cl^{2+}	**12**	1	$^1A'$	−20.977745	−21.133879	0.026	28.21	30.30	30.05
CH_3Cl^{2+}	**13**	1	$^1A_1$	−20.950340	−21.151181	0.023	28.95	29.55	29.28
CH_3Cl^{2+}	**14**	2	$^1\Sigma^+$	−20.969384	−21.140081	0.020	28.44	30.13	29.75
CCl^+–H_3^+	**15**	3	$^1\Sigma^+$	−20.959715	−21.135042	0.020	28.70	30.27	29.77
CH_2^+–HCl^+	**16**	1	$^1A'$	−20.961979	−21.139923	0.029	28.64	30.13	29.75

[a] Number of imaginary frequencies.
[b] Norm of the perturbation correction to the CIPSI wave function.

Table 3
Calculated energies of the fragments appearing in the dissociation of the CH_3Cl^{2+} dication

		State	E_{CASSCF} (au)	E_{CIPSI} (au)	Norm[a]	ZPE (eV)
CH_2Cl^{2+}	**17**	$^2B_1$	−20.386364	−20.560163	0.020	0.58
CH_2^+–Cl^+	**18**	$^2B_1$	−20.303912	−20.477894	0.016	0.51
$HCCl^{2+}$–H	**19**	$^2A'$	−20.312068	−20.465670	0.016	0.36
CH_2Cl^+	**20**	$^1A_1$	−21.079928	−21.276078	0.021	0.67
$HCCl^{2+}$	**21**	$^1\Sigma^+$	−19.811618	−19.963756	0.016	0.35
H^+–CCl^+	**22**	$^1\Sigma^+$	−19.702783	−19.865249	0.014	0.11
$HCCl^+$	**23**	$^2A'$	−20.408476	−20.593239	0.030	0.32
CH_3^+	**24**	$^1A'_1$	−6.925925	−6.996467	0.002	0.84
CH_2^+	**25**	$^2A_1$	−6.238666	−6.297844	0.001	0.44
CCl^+	**26**	$^1\Sigma^+$	−19.812753	−19.988587	0.018	0.07
HCl^+	**27a**	$^2\Pi$	−14.862829	−14.992339	0.003	0.16
	27b	$^2\Sigma^+$	−14.721608	−14.853978	0.002	0.17
H_3^+	**28**	$^1A'_1$	−1.332855	−1.337310[b]		0.56
H_2	**29**	$^1\Sigma_g^+$		−1.167437[b]		0.27
H_2^+	**30**	$^2\Sigma_g^+$		−0.600084[b]		0.15
Cl^+	**31a**	^3P	−14.215823	−14.335546	0.001	
	31b	^1D	−14.149629	−14.273332	0.001	
Cl	**32**	^2P	−14.649503	−14.789370	0.001	

[a] Norm of the perturbation correction to the CIPSI wave function.
[b] Full CI result.

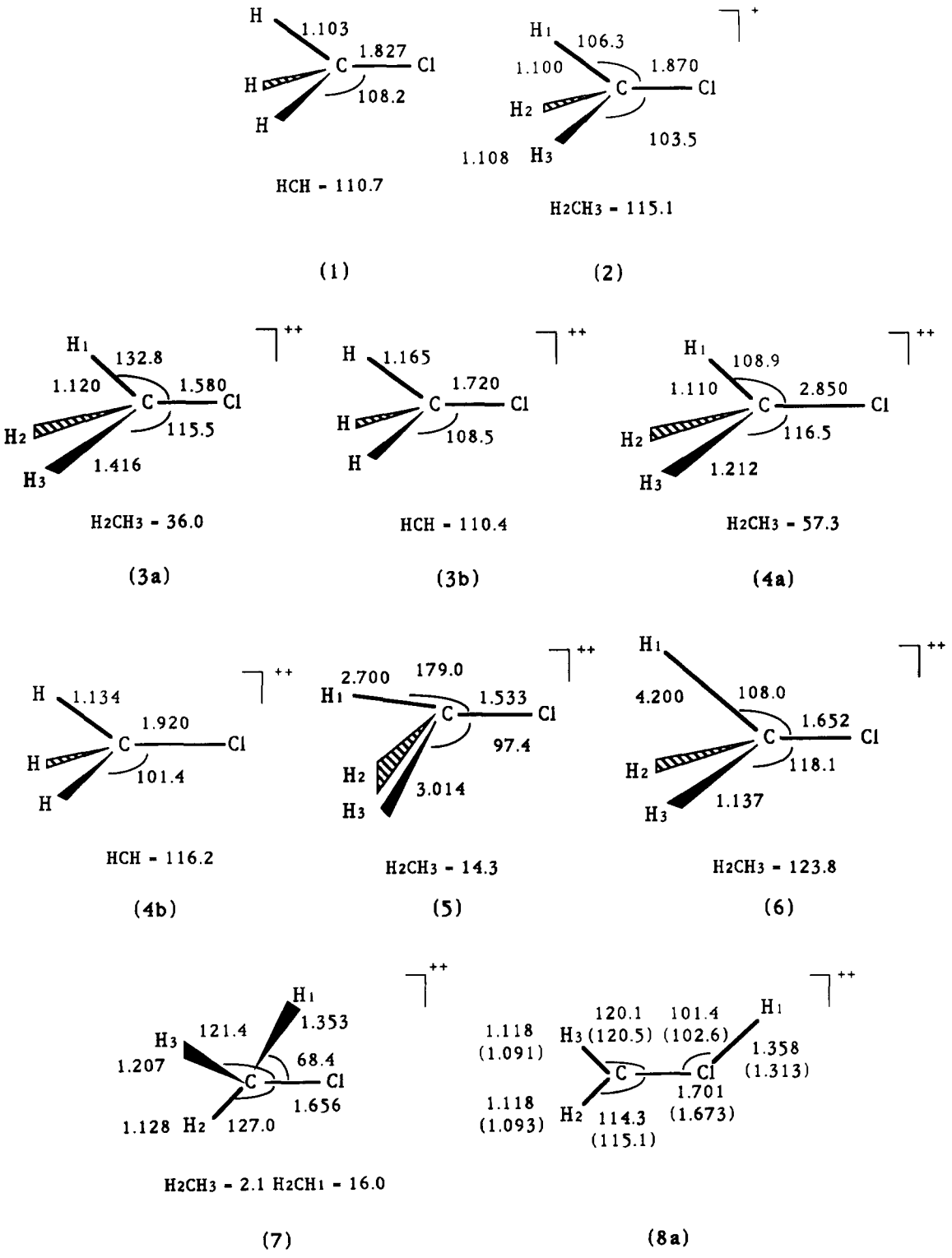

Fig. 1. CASSCF optimized geometrics for the molecules involved in the fragmentation of CH_3Cl^{2+} (when available, the geometries of ref. [2] are given in parentheses).

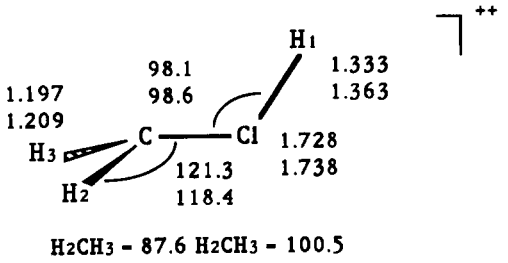

H_2CH_3 - 87.6 H_2CH_3 - 100.5

(8b)

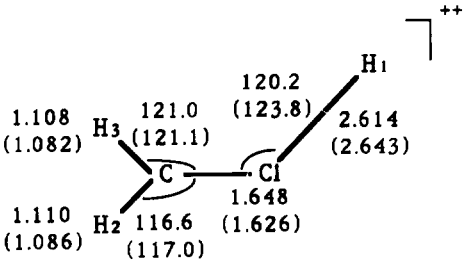

(9)

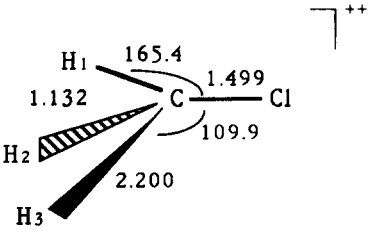

H_2CH_3 - 20.4

(10)

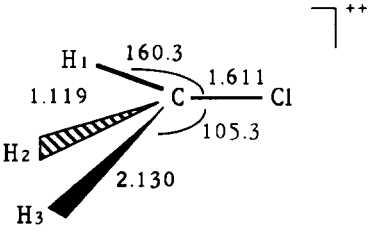

H_2CH_3 - 26.7

(11)

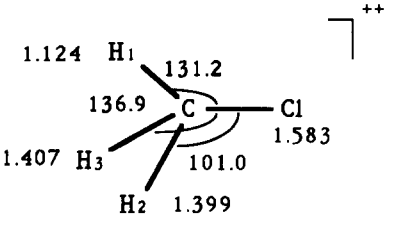

(12)

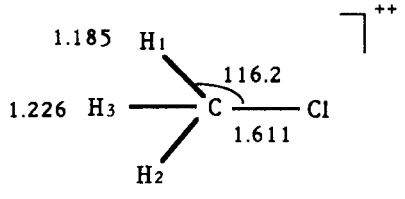

(13)

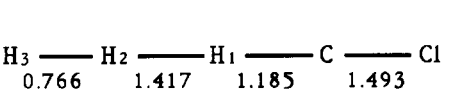

(14)

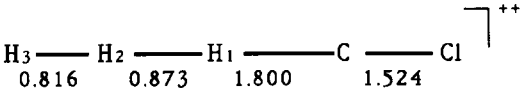

(15)

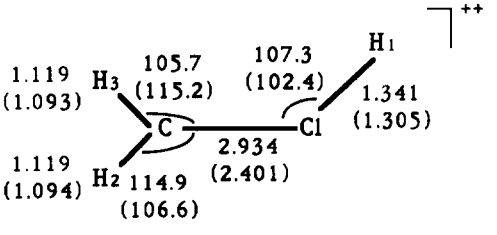

(16)

Fig. 1. (*continued*)

state $^1A_1$, whose CIPSI energy was calculated to be −22.247 343 au (Table 2), after zero-point energy (ZPE) correction. The detailed calculated harmonic vibrational frequencies for each species are available upon request.

3. Double ionization of CH_3Cl

To our knowledge, the only determination of the double ionization threshold of CH_3Cl has been done using the double charge transfer (DCT) method [21]:

$$OH^+(^3\Sigma^-) + CH_3Cl \rightarrow OH^-(^1\Sigma^+) + CH_3Cl^{2+} \quad (1)$$

Following the spin conservation rules which seem to hold in DCT spectrometry [22], the use of OH^+ as collider implies that only triplet states of CH_3Cl^{2+} can be observed. In ref. [21], two peaks were observed at 31.5 ± 0.5 eV and 33.5 ± 0.5 eV.

The calculated vertical ionization spectrum of CH_3Cl is shown in Table 4. The ionization energy is the calculated CIPSI energy difference between the neutral $^1A_1$ state and the dication states at the CASSCF geometry of $CH_3Cl(^1A_1)$. The single ionization threshold is calculated to be 11.03 eV, which is close to the recommended value [23] of 11.22 eV. The results for dicationic states were obtained with the CASSCF orbitals of the CH_3Cl^{2+} first singlet state at the equilibrium geometry of the neutral molecule (structure **1** in Fig. 1). For the $^3A_2$ CH_3Cl^{2+} first triplet state, the agreement with experiment is correct: our value of 30.69 eV is slightly below the measured value of 31.5 ± 0.5 eV. The agreement for the second peak at 33.5 ± 0.5 eV is better, since there are three triplet states lying in the 33–34 eV range, at 33.2, 33.40 and 33.47 eV, respectively (Table 4). In order to test the influence of the starting MOs employed, we also calculated the energy of the first $^3A_2$ state, using its own CASSCF orbitals. The norm of the perturbative correction was then

Table 4
Calculated vertical spectra of the CH_3Cl^{2+} and CH_3Cl^+

	State	Dominant configurations	E_{CIPSI} (au)	Norm[a]	ΔE_{CIPSI}
CH_3Cl	$^1A_1$	$0.93\|1a_1^2 2a_1^2 1e^4 3a_1^2 2e^4\|$	−22.247343	0.030	0.00
CH_3Cl^+	^2E	$0.92\|1a_1^2 2a_1^2 1e^4 3a_1^2 2e^3\|$	−21.842107	0.028	11.03
CH_3Cl^{2+}	$^3A_2$	$0.92\|1a_1^2 2a_1^2 1e^4 3a_1^2 2e^2\|$	−21.119331	0.051	30.69
	^1E	$0.86\|1a_1^2 2a_1^2 1e^4 3a_1^2 2e^2\|$	−21.084602	0.056	31.64
	$^1A_1$	$0.77\|1a_1^2 2a_1^2 1e^4 3a_1^2 2e^2\|$	−21.065642	0.059	32.15
		$0.09\|1a_1^2 2a_1^2 1e^3 3a_1^2 2e^3\|$			
	$^1A_2$	$0.90\|1a_1^2 2a_1^2 1e^3 3a_1^2 2e^3\|$	−21.028446	0.062	33.17
	^3E	$0.87\|1a_1^2 2a_1^2 1e^3 3a_1^2 2e^3\|$	−21.022856	0.061	33.32
	$^3A_1$	$0.90\|1a_1^2 2a_1^2 1e^3 3a_1^2 2e^3\|$	−21.019944	0.060	33.40
	^3E	$0.85\|1a_1^2 2a_1^2 1e^4 3a_1^2 2e^3\|$	−21.017363	0.062	33.47
	$^3A_2$	$0.80\|1a_1^2 2a_1^2 1e^3 3a_1^2 2e^3\|$	−20.991679	0.061	34.17
	^1E	$0.86\|1a_1^2 2a_1^2 1e^4 3a_1^2 2e^3\|$	−20.972629	0.064	34.69
	^1E	$0.71\|1a_1^2 2a_1^2 1e^3 3a_1^2 2e^3\|$	−20.951093	0.058	35.27
		$0.09\|1a_1^2 2a_1^2 1e^2 3a_1^2 2e^4\|$			
	$^1A_1$	$0.65\|1a_1^2 2a_1^2 1e^3 3a_1^2 2e^3\|$	−20.918135	0.062	36.17
		$0.13\|1a_1^2 2a_1^2 1e^4 3a_1^2 2e^2\|$			
		$0.09\|1a_1^2 2a_1^2 1e^2 3a_1^2 2e^4\|$			
CH_3Cl^+	$^2A''$	$0.92\|1a'^2 2a'^2 3a'^2 1a''^2 4a'^2 5a'^2 2a''^1\|$	−21.843786	0.028	0.00
CH_3Cl^{2+}	$^3A''$	$0.92\|1a'^2 2a'^2 3a'^2 1a''^2 4a'^2 5a'^2 2a''^1\|$	−21.124619	0.038	19.57
	$^1A''$	$0.89\|1a'^2 2a'^2 3a'^2 1a''^2 4a'^2 5a'^2 2a''^1\|$	−21.084516	0.038	20.66
	$^1A'$	$0.85\|1a'^2 2a'^2 3a'^2 1a''^2 4a'^2 5a'^2\|$	−21.081736	0.033	20.74

[a] Norm of the perturbation correction to the CIPSI wave function.

0.041 instead of 0.051, but the energy remained almost unchanged (30.60 eV).

A discrepancy between experimental and theoretical ionization energies is commonly observed for various molecules and methods (see ref. [24] and references cited therein for some examples). Among others, a typical case is $C_2H_2^{2+}$: while the DCT value [25] of 32.7 ± 0.3 eV is above the coincidence value at 31.7 eV [24,26], the calculated threshold is 31.35 eV using the Green function method [27] and 32.0 eV [26] using the CIPSI program as in the present work. However, the same CIPSI program gave ionization values about 1 eV too low in the case of CO_2^{2+}, OCS^{2+} and CS_2^{2+} [28], when compared with experimental determinations [29]. The same behavior is observed in the present case for CH_3Cl^{2+}. Clearly, new experiments and calculations to study the double ionization of CH_3Cl^{2+} are needed to examine more closely this problem.

Another remarkable feature in Table 1 is the lack of CH_3Cl^{2+} signal in both experiments in refs. [7,11]. This could indicate that the double ionization threshold of CH_3Cl^{2+} is above the lowest energy barrier for direct dissociation of the dication (in the present case, the CCl^+/H_3^+ fragment pair at 30.0 ± 0.5 eV). However, as discussed below in Section 4.5, it is possible that the CCl^+/H_3^+ pair comes from the dissociation of an excited state of CH_3Cl^+ and it is thus not possible to conclude without ambiguity.

The CH_3Cl^{2+} dication may also be obtained by single ionization of the monocation CH_3Cl^+. The experimental determinations are 20.2 ± 0.5 eV (DCT) [21] and 18.16 ± 0.03 eV (charge stripping) [30]. The result obtained at MP3/6-31G**// UHF/6-31G* level by Yates and co-workers [2] is 21.5 eV. The low value obtained in charge stripping experiment was explained by an excitation to a Rydberg excited state of the monocation with ejection of an electron, followed by an isomerization to the more stable CH_2ClH^{2+} geometry, as already proposed [30] for CH_3F. Thus, the CH_3Cl^{2+} isomer would not be produced in charge stripping experiments.

The three lowest states of the vertical spectrum of CH_3Cl^+ are displayed in Table 4. We used the geometry of the $^2A''$ state (structure **2** in Fig. 1), which was found [1] to be the ground state of CH_3Cl^+ by only 0.15 eV, due to a very weak Jahn–Teller splitting. The $^3A''$ value at 19.57 eV is slightly below the DCT determination [21] at 20.2 ± 0.5 eV. The $^1A'$ value at 20.74 eV is also below the theoretical result of Yates and co-workers [2] at 21.5 eV. However, these values are well above the charge stripping value of 18.16 ± 0.03 eV. Although it is not possible to discuss here the implication of a Rydberg state, it seems clear that the CH_3Cl^{2+} isomer is not produced in this type of experiment.

4. Two-body processes

4.1. $CH_3Cl^{2+} \rightarrow CH_3^+ + Cl^+$

This dissociation pathway is the most important observed in the PEPIPICO experiments of Ruhl and co-workers [7] since the CH_3^+/Cl^+ pair represents 61% of the fragment products with a kinetic energy release (KER) of 5.4 ± 1.0 eV (Table 1). In order to study this dissociation channel, the C–Cl distance of the equilibrium structures of the $^1A'$ and $^3A_2$ lowest states of CH_3Cl^{2+} was progressively increased to obtain the geometry of the corresponding transition states. The results are shown in Fig. 1 (**4a** and **4b** for $^1A_2$ states, respectively) for the geometries and in Table 2 for the energies. Using the calculated ZPE corrections leads to the following activation barriers for the two reactions:

$$CH_3Cl^{2+}(^1A') \rightarrow CH_3 - -Cl^{2+}(^1A') \rightarrow CH_3^+(^1A_1') + Cl^+(^1D) \quad 32.70\ \text{eV} \tag{2}$$

$$CH_3Cl^{2+}(^3A_2) \rightarrow CH_3 - -Cl^{2+}(^3A_2) \rightarrow CH_3^+(^1A_1') + Cl^+(^3P) \quad 30.40\ \text{eV} \tag{3}$$

It should be noticed that the $^1A'$ ground state of CH_3Cl^{2+} dissociates into the ^1D first excited state of chlorine ion while the $^3A_2$ CH_3Cl^{2+} excited state correlates to the ^3P Cl^+ ground state. Another interesting feature is the large difference between the barrier heights of the two reactions with respect to the equilibrium structures: 3.33 eV for Eq. (2) and only 0.44 eV for Eq. (3). However, this is not surprising since the $^1A'$ and $^3A_2$ states have very different geometries, as already discussed in our previous paper [1] (see also **3a** and **3b** in Fig. 1): the CCl bond length in the $^1A'$ state (1.580 Å) is much shorter than in the $^3A_2$ state (1.720 Å), because the 1a″ MO has a very pronounced π(CCl) character [1]. Thus, one has to break a double bond to produce the CH_3^+/Cl^+ pair from the singlet state and only a single bond for the triplet state.

These results allow us to predict the appearance threshold of the CH_3^+ and Cl^+ fragments in coincidence experiments as shown in Fig. 2. From this figure, it is clear that the appearance threshold for the $^1A'$ is 32.70 eV, while that of the $^3A_2$ state is governed by the double ionization energy, i.e. 30.69 eV. The first value is in good agreement with the experimental one at 32.5 ± 0.5 eV (Table 1), which indicates that the singlet state fragmentation is observed. Thus, we conclude that the triplet state must follow another dissociation channel.

By using the theoretical energy values and ZPE corrections for CH_3^+ and Cl^+, it is also possible to calculate the KER of the dissociation reactions. The obtained results are 6.38 eV for Eq. (2) and 5.96 eV for Eq. (3). Both values are in the experimental range (5.4 ± 1.0 eV) and it is not possible to discriminate between the two processes. After bombarding neutral CH_3Cl with 1 MeV atomic ions, Monce and co-workers [5,6] observed the CH_3^+/Cl^+ fragments, with a KER of 6.6 ± 0.1 eV. This result is close to the value obtained for the $^1A'$ ground state of CH_3Cl^{2+} (6.38 eV).

4.2. $CH_3Cl^{2+} \rightarrow CH_2Cl^+ + H^+$

This dissociation pathway is the second most important one observed in the PEPIPICO experiments of Ruhl and co-workers [7] with 13% of the fragment products and a measured KER of 5.2 ± 2.0 eV (Table 1). To produce the CH_2Cl^+/H^+ pair, we calculated the transition state geometries obtained by removing one H atom from the equilibrium geometries of the $^1A'$ and $^3A_2$ states of CH_3Cl^{2+}. This led to the **5** and **6**

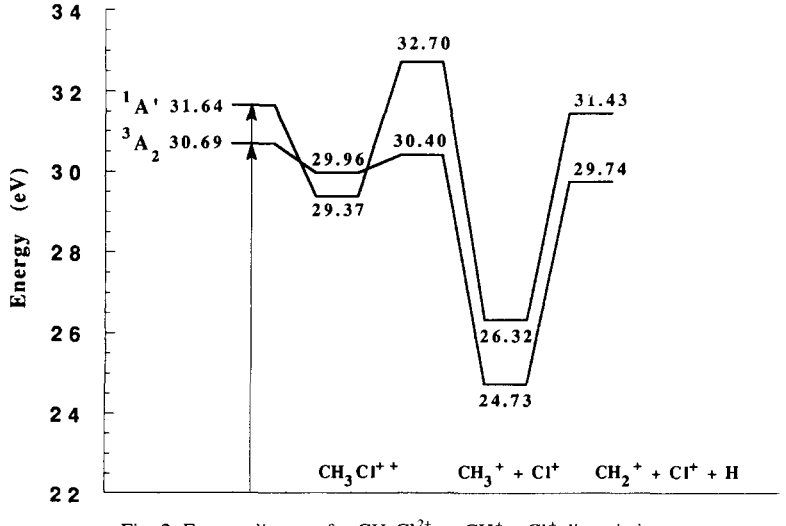

Fig. 2. Energy diagram for $CH_3Cl^{2+} \rightarrow CH_3^+ + Cl^+$ dissociation.

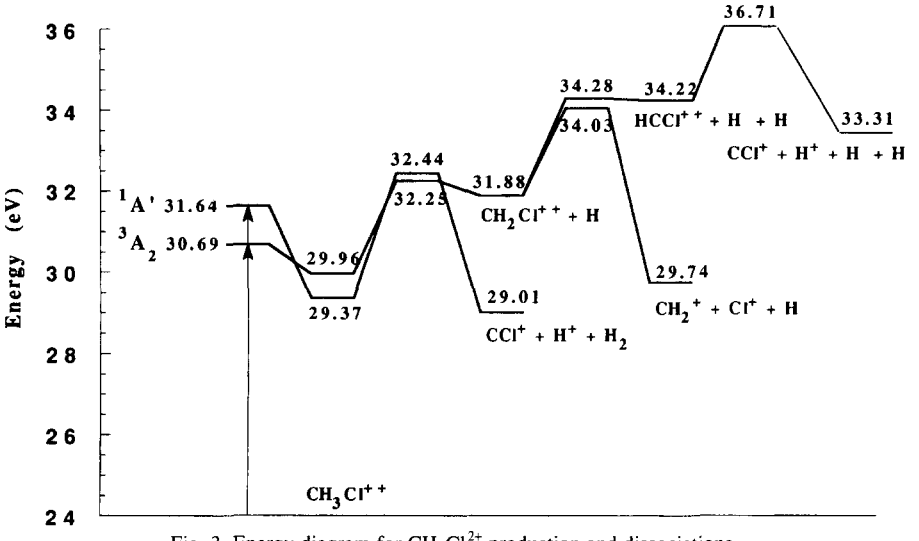

Fig. 3. Energy diagram for CH_2Cl^{2+} production and dissociations.

structures shown in Fig. 1, respectively. Mulliken population analysis [31] showed that the reactions were in fact (see Fig. 3):

$$CH_3Cl^{2+}(^1A') \rightarrow CCl^+ - - H_2 - - H^+(^1A')$$
$$\rightarrow CCl^+(^1\Sigma^+) + H_2(^1\Sigma_g^+) + H^+ \quad 32.44\ \text{eV} \quad (4)$$

$$CH_3Cl^{2+}(^3A_2) \rightarrow CH_2Cl - - H^{2+}(^3A_2)$$
$$\rightarrow CH_2Cl^{2+}(^2B_1) + H(^2S) \quad 32.25\ \text{eV} \quad (5)$$

Eq. (4) corresponds to the direct dissociation of $CH_3Cl^{2+}(^1A')$ in the three $CCl^+/H_2/H^+$ fragments (three-body process, discussed in Section 5). The CH_2Cl^{2+} dication produced in Eq. (5) is not found in the experiments of ref. [7] but is present as a very weak signal in ref. [11] at 32.0 ± 1.0 eV (Table 1). This value is in very good agreement with the calculated one at 32.25 eV. The predicted KER would then be very low (0.37 eV). It is probable that most of the CH_2Cl^{2+} dication

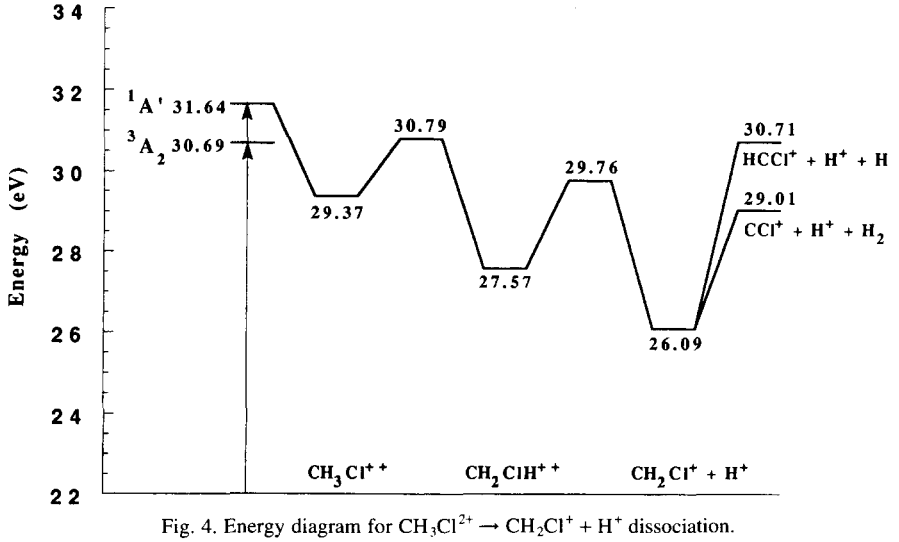

Fig. 4. Energy diagram for $CH_3Cl^{2+} \rightarrow CH_2Cl^+ + H^+$ dissociation.

dissociates spontaneously. Thus, it is clear that the CH_2Cl^+/H^+ pair cannot be obtained by eqns (4) and (5). Another possibility is to break the H–Cl bond of the methylechloronium dication CH_2ClH^{2+} (structure **8a** in Fig. 1) after a preliminary isomerization of CH_3Cl^{2+} (structure **7** in Fig. 1). The isomerization reaction has been studied in our previous paper [1] for the $^1A'$ state only, since the triplet transition state was found to dissociate along the C–Cl coordinate. For this reason, the non-planar $^3A''$ state of CH_2ClH^{2+} (structure **8b** in Fig. 1), which lies 31.17 eV above the energy reference was not considered in the present study. The resulting dissociation pathway as displayed in Fig. 4 is the following:

$$CH_3Cl^{2+}(^1A') \rightarrow CH_2^+ - -H - -Cl^+(^1A) \rightarrow CH_2ClH^{2+}(^1A') \quad 30.79\ eV \tag{6}$$

$$CH_2ClH^{2+}(^1A') \rightarrow CH_2Cl - -H^{2+}(^1A') \rightarrow CH_2Cl^+(^1A_1) + H^+ \quad 29.76\ eV \tag{7}$$

Eq. (7) has already been studied theoretically by Yates and co-workers [2] at MP3/6-31G**// RHF/6-31G* level. The geometry of their transition state is shown in parentheses in Fig. 1 (structure **9**). The agreement between the two calculations is rather good. The isomerization energy of 2.19 eV is close to the previous value of 2.08 eV [2]. The fragments are 1.48 eV below CH_2ClH^{2+}, which is very similar to the result of ref. [2] (1.53 eV).

Finally, it is clear from Fig. 4 that the theoretical appearance threshold is given by the vertical ionization energy of the singlet state, i.e. 31.64 eV. This result is slightly higher than the experimental threshold at 31.0 ± 0.5 eV (Table 1). The calculated KER is 5.55 eV, in good agreement with the experimental value of 5.2 ± 2.0 eV (Table 1).

4.3. $CH_3Cl^{2+} \rightarrow HCCl^{2+} + H_2$

The $HCCl^{2+}$ dication is not detected in the PEPIPICO experiments of ref. [7] but is present in the PEPICO ones [11] as a very weak signal. The appearance threshold is difficult to determine and is at least 32.0 eV (Table 1). It is important to notice that coincidence experiments do not detect neutral fragments. Hence, the $HCCl^{2+}$ ion could correspond to a three-body dissociation with production of two separate H atoms. However, the geometry of the $^1A'$ state of CH_3Cl^{2+} (structure **3a** in Fig. 1) suggests that this state is a weakly bound complex of H_2 with $HCCl^{2+}$. Thus it should be easier to produce the H_2 molecule, as revealed by our calculations: the structure of the corresponding transition state (**10**) is shown in Fig. 1 and the dissociation pathway in Fig. 5, which shows that the height of the energy barrier is only 0.6 eV:

$$CH_3Cl^{2+}(^1A') \rightarrow HCCl^{2+} - -H_2(^1A') \rightarrow HCCl^{2+}(^1\Sigma^+) + H_2(^1\Sigma_g^+) \quad 29.97\ eV \tag{8}$$

The theoretical appearance threshold is governed by the ionization energy of the singlet state, i.e. 31.64 eV, in good agreement with the experimental value at 32.0 eV.

4.4. $CH_3Cl^{2+} \rightarrow HCCl^+ + H_2^+$

The $HCCl^+/H_2^+$ ion pair is the weakest two-body process observed in PEPIPICO experiments [7], with 2% of the final fragments and a KER of 2.8 ± 1.0 eV (Table 1). From the theoretical point of view, these fragments may be obtained by removing two H atoms from the $^3A_2$ C_{3v}-symmetric state of CH_3Cl^{2+} (Fig. 5):

$$CHCl^{2+}(^3A_2) \rightarrow HCCl^+ - -H_2^+(^3A'') \rightarrow HCCl^+(^2A') + H_2^+(^2\Sigma_g^+) \quad 33.65\ eV \tag{9}$$

The geometry of the corresponding $^3A''$ transition state is shown in Fig. 1 (structure **11**). However, the calculation of the harmonic vibrational frequencies gave three imaginary modes, the largest one (i1358 cm^{-1}) corresponding to the movement of the one H atom out of the symmetry plane of the molecule. Curiously, the CH_2/CH_3 symmetric stretching mode, which is the reaction coordinate, is very low (i139 cm^{-1}). The i195 cm^{-1}

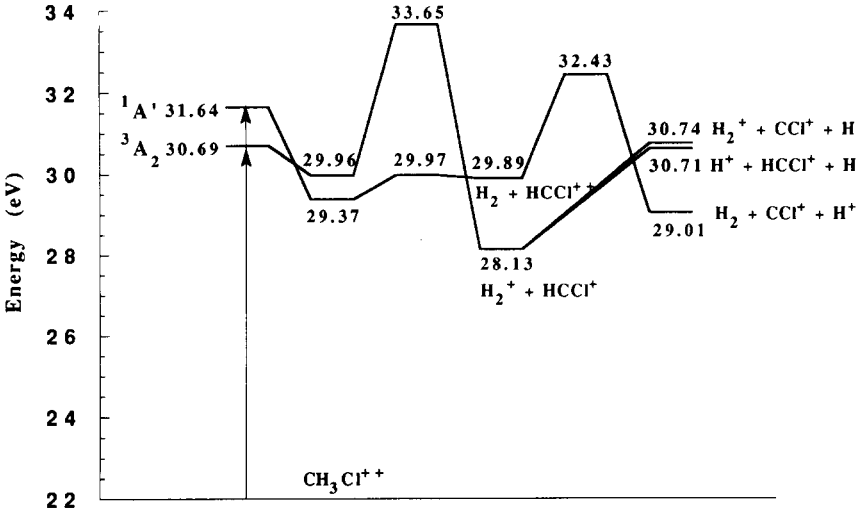

Fig. 5. Energy diagram for $CH_3Cl^{2+} \rightarrow HCCl^{+*} + H_2$ production and dissociations.

mode is the antisymmetric stretching. This indicates that the true transition has no symmetry at all. In order to find its geometry, we performed test calculations with a configuration space reduced to quadri-excitations. Unfortunately, we were not able to locate this particular point of the triplet potential energy surface. Thus, we can only say that the appearance threshold for this pair is below 33.65 eV and the KER is below 5.52 eV. These values are consistent with the experimental ones.

4.5. $CH_3Cl^{2+} \rightarrow CCl^+ + H_3^+$

The production of H_3^+ is the most surprising process occurring in the fragmentation of CH_3–X^{2+} compounds [7,10]. Indeed, it requires the breaking of the three CH bonds and the formation of new H–H bonds. In the case of CH_3Cl^{2+}, it represents 6% of the final products [7], which is rather important, with a KER of 3.4 ± 1.0 eV and a very low appearance threshold [11] of 30.0 ± 0.5 eV (Table 1).

The formation mechanism of H_3^+ is unknown. In the case of methylamine [10], experiments with deuterated species proved that the H_3^+ ion came from the methyl group rather than the amine one. Thissen [10] proposed that the formation of the dication leads to the formation of an H_2 molecule weakly bound to the carbon atom. The dissociation of this structure would give the $H_2/HCNH_2^{2+}$ fragment pair and, owing to the large protonic affinity of H_2 (4 eV), the possible formation of H_3^+ and CNH_2^+. Thus, such a mechanism might also occur in the case of CH_3Cl^{2+}, since, as already seen, the ground $^1A'$ state is a weakly bound complex of H_2 and $HCCl^{2+}$.

In order to test this hypothesis and explain the presence of H_3^+, it is necessary to determine the geometry of a possible transition state between CH_3Cl^{2+} and $CCl^+H_3^+$. This is a difficult task since this geometry cannot be simply guessed, contrarily to other mechanisms studied in the present work. The usual method consists of examining the shape of the normal modes of the molecule. Because of a too large computational cost, we limited the search to the $^1A'$ state of CH_3Cl^{2+}, for which we made SCF test calculations before the CASSCF ones. Indeed, the $^3A_2$ state is not stable at SCF level [1].

The CASSCF harmonic frequencies of $CH_3Cl^{2+}(^1A')$ are very similar to the SCF ones (see ref. [1]): the two lowest ones (377 and 800 cm^{-1} correspond to the rotation of the weakly bound H_2H_3 group, leading to the (**12**) C_s-symmetric planar geometry shown in Fig. 1.

Obviously, this structure has one imaginary frequency (i326 cm^{-1}) which is the out-of-plane rotation of the H_2H_3 group. By increasing the H_2CCl angle, we obtained the (**13**) C_{2v}-symmetric planar structure shown in Fig. 1, which also has one imaginary frequency (i1356 cm^{-1}) corresponding to the in-plane H_2CCl bending mode. By increasing order, the next frequencies of $CH_3Cl^{2+}(^1A')$ are the following: the 867 cm^{-1} mode is the movement of H_1 out of the symmetry plane of CH_3Cl^{2+}, the 969 cm^{-1} mode is the CH_3CH_4 symmetric stretch with its anti-symmetric counterpart at 1121 cm^{-1}; the 1060 cm^{-1} frequency corresponds to the CCl stretch. The 1409 cm^{-1} mode seems more interesting, since it corresponds to a simultaneous increase of the three HCCl angles. However, SCF calculations failed to locate any stable geometry. Finally, the 2953 cm^{-1} mode is the CH_1 stretching and the 3091 cm^{-1} mode is the H_2CH_3 bending mode.

Thus, it does not seem possible to produce the H_3^+ ion by following the normal modes of the $^1A'$ state of CH_3Cl^{2+}. However, while exploring the potential energy surface of this state, we found that the linear $^1\Sigma^+$ structure depicted in Fig. 1 (structure **14**) was stable at both SCF and CASSCF levels. Analysis of its vibrational frequencies shows that this structure is a saddle point with a doubly degenerated imaginary mode (i269 cm^{-1}) corresponding to the rotation of the H_2H_3 group. The most surprising result is that it lies at 29.75 eV, i.e. 0.38 eV above the equilibrium geometry. It is then possible to produce the H_3^+/CCl^+ pair by increasing the CH_1 bond length (structure **15** in Fig. 1):

$$CH_3Cl^{2+}(^1\Sigma^+) \rightarrow CCl^+ - - H_3^+(^1\Sigma^+) \rightarrow CCl^+(^1\Sigma^+) + H_3^+(^1A_1') \quad 29.77\ eV \tag{10}$$

Of course, the structure **15** is not, strictly speaking, a transition state, but it appears that it is rather easy to obtain the H_3^+ ion from $CH_3Cl^{2+}(^1A')$. Tentative calculations to find a true transition state by rotating the H_2H_3 group in **14** failed or led to **13**.

The whole dissociation pathway is displayed in Fig. 6. From this figure, the appearance threshold is governed by the singlet ionization energy at 31.64 eV, well above the experimental one at 30.0 ± 0.5 eV. Similarly, the predicted KER is 5.55 eV which is larger than the experimental value of 3.4 ± 1.0 eV. Because of these large discrepancies, we suggest that the presence of the H_3^+ ion is not due to a direct dissociation of CH_3Cl^{2+} as given in Eq. (10) but rather to the

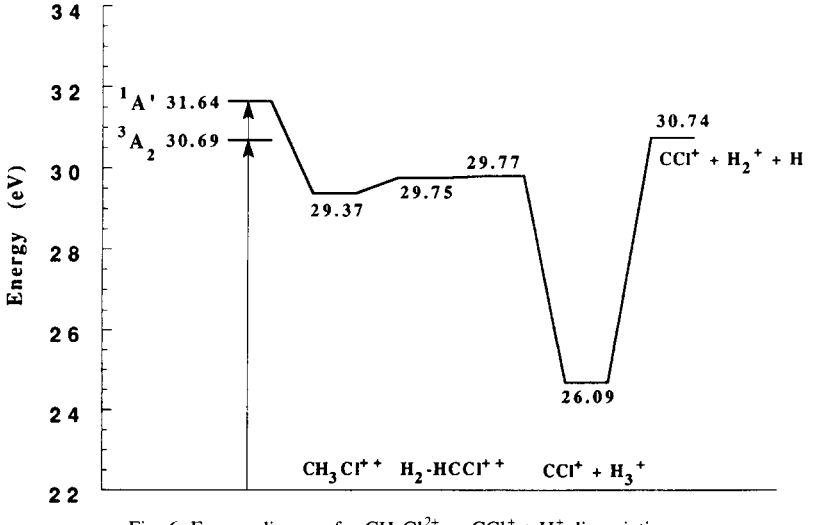

Fig. 6. Energy diagram for $CH_3Cl^{2+} \rightarrow CCl^+ + H_3^+$ dissociation.

ionization of a Rydberg excited state of the monocation. This would explain the fact that the appearance threshold of the CCl^+/H_3^+ pair is lower than the double ionization energy. Such a mechanism was observed for the first time without ambiguity in the case of H_2O^{2+} fragmentation [32]. More recently, the analysis of the KER distributions (KERD) showed a significant contribution of the indirect processes in the case of CO, O_2 and NO dications at an excitation energy of 40.8 eV, owing to the autoionization of the oxygen atom [33].

Concerning CH_3Cl^{2+}, another possibility is the implication of the triplet state, which was not considered here, on condition that its ionization threshold is close to the calculated value of 30.69 eV, rather than the experimental one.

4.6. $CH_3Cl^{2+} \rightarrow CH_2^+ + HCl^+$

The CH_2^+/HCl^+ pair can be obtained through dissociation of the CH_2ClH^{2+} after preliminary isomerization of CH_3Cl^{2+} via Eq. (6):

$$\begin{aligned} CH_2ClH^{2+}(^1A') &\rightarrow CH_2 - -ClH^{2+}(^1A') \\ &\rightarrow CH_2^+(^2A_1) + HCl^+(^2\Pi) \quad 29.75\ eV \end{aligned} \tag{11}$$

The geometry of the transition state (**16**) is shown in Fig. 1, with the values of Yates and co-workers [2] in parentheses. It is remarkable that the C–Cl distance is more than 0.5 Å greater in our calculation. The isomerization barriers are also different: 2.18 eV instead of 2.48 eV given in ref. [2]. The two fragments are 1.94 eV below CH_2ClH^{2+} (1.66 eV in ref. [2]).

The whole dissociation pathway is shown in Fig. 7, from which we deduce a theoretical appearance threshold of the ion pair of 31.64 eV in good agreement with the experimental value of 32.0 ± 1.0 eV (Table 1). The predicted KER is 6.00 eV. However, this pair is not present in the PEPIPICO spectrum of Ruhl and co-workers [7].

5. Three-body processes

Interpretation of PEPIPICO spectra for three-body processes is much more difficult than for two-body processes [34]. In our previous study [26,35] of the fragmentation of $C_2H_2^{2+}$, we explained that ab initio calculations alone do not allow determination of the precise mechanisms of the fragmentations processes, because it is necessary to add the theoretical energy of the products to the measured KER to obtain an estimation of the appearance threshold. In the case of

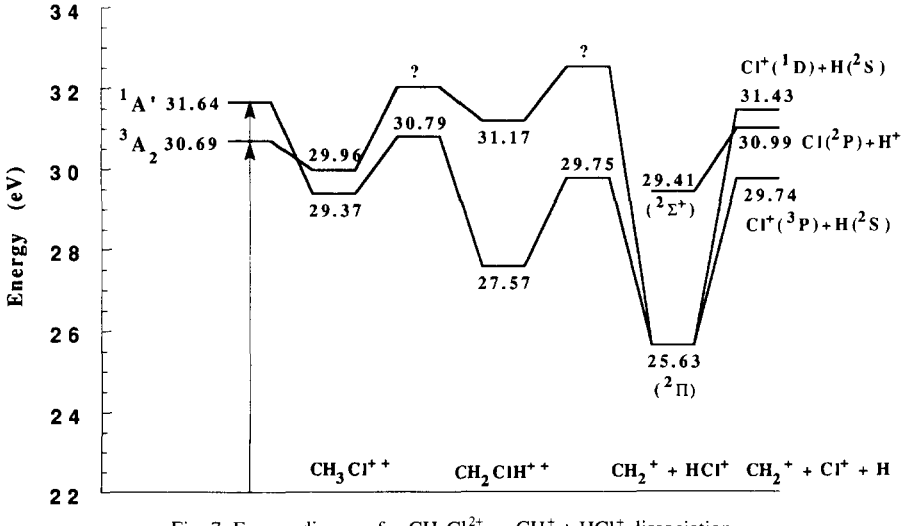

Fig. 7. Energy diagram for $CH_3Cl^{2+} \rightarrow CH_2^+ + HCl^+$ dissociation.

CH_3Cl^{2+}, the situation is even more complex, because of the large number of possible dissociation channels and the low precision of the KER measurements (Table 1).

5.1. $CH_3Cl^{2+} \rightarrow CH_2^+ + Cl^+ + H$

This dissociation pathway is the most important three-body process observed in ref. [7], since the CH_2^+/Cl^+ ion pair represents 9% of the observed products with a KER of 4.3 ± 1.0 eV (Table 1). From the coincidence peak slope, it was deduced that the H atom was formed by decay of CH_3^+. From the theoretical point of view, these fragments can be obtained in different ways:

$$CH_3^+(^1A_1') + Cl^+(^1D) \rightarrow CH_2^+(^1A_1') + Cl^+(^1D) + H(^2S) \quad (12)$$

$$CH_3^+(^1A_1') + Cl^+(^3P) \rightarrow CH_2^+(^1A'_1) + Cl^+(^3P) + H(^2S) \quad (13)$$

$$CH_2^+(^2A_1) + HCl^+(^2\Pi) \rightarrow CH_2^+(^2A_1) + Cl^+(^1D) + H(^2S) \quad (14)$$

$$CH_2Cl^{2+}(^2B_1) + H(^2S) \rightarrow CH_2^+ - -Cl^+(^2B_1) + H(^2S) \rightarrow CH_2(^2A_1) + Cl^+(^1D) + H(^2S) \quad (15)$$

Eqs. (12) and (13) are depicted in Fig. 2. We can predict an appearance threshold of about 34.0 ± 1.0 eV for the triplet state and 35.7 ± 1.0 eV for the singlet one. Both values are consistent with the experimental one at 35–36 eV (Table 1). Eq. (14) is shown in Fig. 7 for the singlet state, with a theoretical threshold of 35.7 ± 1.0 eV. Finally, Eq. (15), which is a 'deferred charge separation' [32], presents two energy barriers (Fig. 6), the higher one at 34.03 eV, leading to a predicted threshold of 38.3 ± 1.0 eV, which is obviously too high. The calculations cannot discriminate between the eqns (12)–(14) processes, but the last one Eq. (15) is excluded by experiments [7].

5.2. $CH_3Cl^{2+} \rightarrow HCCl^+ + H + H^+$

The $HCCl^+/H^+$ ion pair represents 4% of the final products in ref. [7] with a KER of 3.6 ± 2.0 eV (Table 1). The slope of the experimental peak does not allow identification of the mechanism of the fragmentations. There are only two possibilities (Figs. 4 and 5):

$$CH_2Cl + (^1A_1) + H^+ \rightarrow HCCl^+(^2A') + H(^2S) + H^+ \quad (16)$$

$$HCCl^+(^2A') + H_2^+(^2\Sigma_g^+) \rightarrow HCCl^+(^2A') + H(^2S) + H^+ \quad (17)$$

The appearance threshold is predicted to be 34.3 ± 2.0 eV, in good agreement with the measured one at 35.0 ± 0.5 eV (Table 1). However, it is not possible to decide which of the two processes occurs in the fragmentation. Quite unexpectedly, the $CH_2Cl^{2+}(^2B_1)$ dication dissociates in the following way (Fig. 3):

$$CH_2Cl^{2+}(^2B_1) + H(^2S) \rightarrow HCCl^{2+}(^1\Sigma^+) + H(^2S) + H(^2S) + H(^2S) \quad 34.03\ eV \quad (18)$$

5.3. $CH_3Cl^{2+} \rightarrow H^+ + CCl^+ + H_2$

The CCl^+/H^+ ion pair represents 3% of the fragments observed in ref. [7] with a KER of 3.6 ± 2.0 eV (Table 1). Its origin remained ambiguous. Assuming that the two H atoms form a molecule, the first possible dissociation pathway is the 'instantaneous explosion' [32] already shown in Eq. (4) of Section 4.2 (Fig. 3). However, the predicted appearance threshold is 32.44 eV, which is below the measured one at 35.5 ± 0.5 eV (Table 1). Other possible channels are the following (Figs. 4 and 5, respectively):

$$CH_2Cl^+(^1A_1) + H^+ \rightarrow CCl^+(^1\Sigma^+) + H^+ + H_2(^1\Sigma_g^+) \quad (19)$$

$$HCCl^{2+}(^1\Sigma^+) + H_2(^1\Sigma_g^+) \rightarrow CCl^+(^1\Sigma^+) + H^+ + H_2(^1\Sigma_g^+) \quad (20)$$

For both processes, the predicted appearance threshold is 32.6 ± 2.0 eV, which is below the experimental one at 35.0 ± 0.5 eV (Table 1). It is also possible to produce two separate H atoms, after production of $HCCl^{2+}$ via Eq. (18), in the following manner (Fig. 3):

$$HCCl^{2+}(^1\Sigma^+) + H(^2S) + H(^2S) \rightarrow H^+ + CCl^+(^1\Sigma^+) + H(^2S) + H(^2S) \quad 36.71\ eV \quad (21)$$

Thus, we have the very remarkable series of deferred charge separations for the $^3A_2$ state of CH_3Cl^{2+}: $CH_3Cl^{2+} \rightarrow CH_2Cl^{2+} \rightarrow HCCl^{2+} \rightarrow H^+ + CCl^+$. For Eq. (21), the predicted appearance threshold is 36.71 eV, which is above the experimental one, although the calculated KER of 3.4 eV is close to the measured one.

5.4. $CH_3Cl^{2+} \rightarrow H + CCl^+ + H_2^+$

The CCl^+/H_2^+ ion pair is not detected in the PEPIPICO experiments of ref. [7] but is present in the PEPICO ones [11] with an appearance threshold of 36.0 ± 0.5 eV (Table 1). The possible dissociation pathways are the following (Figs. 5 and 6):

$$HCCl + (^2A') + H_2^+(^2\Sigma_g^+) \rightarrow H(^2S) + CCl^+(^1\Sigma^+) + H_2(^2\Sigma_g^+) \quad (22)$$

$$CCl^+(^1\Sigma^+) + H_3^+(^1A_1') \rightarrow H(^2S) + CCl^+(^1\Sigma^+)H_2^+(^2\Sigma_g^+) \quad (23)$$

The calculated energy of the final fragments (30.74 eV) combined with the measured appearance threshold gives a predicted KER of 5.26 ± 0.5 eV.

5.5. $CH_3Cl^{2+} \rightarrow CH_2^+ + H^+ + Cl$

The CH_2^+/H^+ ion pair represents 2% of the fragments observed in ref. [7] with a KER of 3.6 ± 2.0 eV (Table 1). The coincidence peak slope indicates without ambiguity that the Cl atom is formed by decay of HCl^+ into $H^+ + Cl$. Since the $^2\Pi$ ground state of HCl^+, which correlates to the $^1A'$ and $^3A''$ lowest states of CH_2ClH^{2+}, dissociates into $H + Cl^+$ as shown in Eq. (14), this ion pair must come from an excited state of HCl^+. A possible candidate is the first one, i.e the $^2\Sigma^+$ state. The dissociation pathway is the following, after isomerization to produce CH_2ClH^{2+} (Fig. 7):

$$CH_2^+(^2A_1) + HCl^+(^2\Sigma^+) \rightarrow CH_2^+(^2A_1) + H^+ + Cl(^2P) \quad (24)$$

In this case, the final products have an energy of 30.99 eV, and the predicted appearance threshold is about 34.6 ± 2.0 eV, which is below the experimental one at 37.5 ± 1.0 eV (Table 1). Because of the large uncertainties, it is not possible to give more precise information on the origin of this ion pair.

6. Conclusion

In this paper, we have used large scale ab initio calculations to study the fragmentation processes of the chloromethane dication. This study was made difficult for several reasons.

Except the CH_3^+/Cl^+ and CH_2Cl^+/H^+ dissociation pathways representing 74% of the total intensity, all other channels contribute individually to less than 10%, especially the three-body processes.

All two-body dissociations occur in a very small energy range centered around 31 eV and the uncertainties of the available experiments do not allow a good discrimination between the processes.

Nevertheless, our calculations have explained most of the two-body thresholds by a direct dissociation of the lowest singlet and triplet states of CH_3Cl^{2+}, taking into account the experimental uncertainties. It appears that the production of

the H_3^+ ion is due to an indirect process, involving the ionization of a Rydberg excited state of the monocation. For three-body processes, the large uncertainty on the measured KER and the number of possible channels does not allow us to determine precisely the fragmentation pathway in most cases. More precise experiments, combined with dynamical calculations (using RRKM theory for example) are needed to understand in detail the fragmentation of CH_3Cl^{2+}. Another problem is the calculation of the double ionization threshold of molecules.

From the computational point of view, the present work shows that the study of the $CH_3–X^{2+}$ dication family represents a challenge for ab initio calculations. The marginal stability of the species requires the use of extended basis sets combined with correlated methods, as already shown [1]. The use of the CASSCF method is well suited for studying dissociation processes. However, as illustrated in the present paper, the computational cost does not allow us to explore fully the potential energy surfaces of the molecule. It does not seem possible to apply this method to larger $CH_3–X^{2+}$ dications, such as methylamine or methanol [7]. The problem is then to find a good compromise between accuracy and computational time.

Acknowledgements

We are very grateful to Dr Roland Thissen for providing us with his unpublished experimental results and for reading carefully this manuscript. The Laboratoire de Dynamique Moléculaire et Photonique is 'Unité de Recherche Associée au CNRS'. The Centre d'Etudes et de Recherches Lasers et Applications (CERLA) is supported by the Fonds Européen de Développement Economique des Régions. The authors acknowledge the CNRS (Mathematical and Physical Science Department) and the Ministère chargé de la Recherche for a generous allocation of computer time on the IBM RISC 6000 at IDRIS (Orsay).

References

[1] D. Duflot, J-M. Robbe, J-P. Flament, J. Chem. Phys. 103 (1995) 10571.
[2] B.F. Yates, W.J. Bouma, L. Radom, J. Am. Chem. Soc 108 (1986) 6545.
[3] H. Jahn, E. Teller, Proc. R. Soc. London, Ser. A 161 (1937) 220.
[4] M.J. Riley, A. Furlan, Chem. Phys. 210 (1996) 389.
[5] M.N. Monce, A.K. Edwards, R.M. Wood, F.M. Steuer, A.V. Shah, P. Tabor, J. Chem. Phys. 74 (1981) 2860.
[6] M.N. Monce, A.K. Edwards, R.M. Wood, F.M. Steuer, A.V. Shah, J. Chem. Phys. 78 (1983) 597.
[7] E. Ruhl, S.D. Price, S. Leach, J.H.D. Eland, Int. J. Mass Spectrom. Ion Process. 97 (1990) 175.
[8] F.S. Wort, R.N. Royds, J.H.D. Eland, J. Electron Spectrosc. Relat. Phenom. 41 (1986) 297.
[9] R. Thissen, Ph.D. Thesis, University of Liège, Belgium, 1993.
[10] R. Thissen, M. Simon, M.-J. Hubin-Franskin, J. Chem. Phys. 101 (1994) 7548.
[11] R. Thissen, unpublished results.
[12] W.J. Stevens, H. Basch, M. Krauss, J. Chem. Phys. 81 (1984) 6026.
[13] T.H. Dunning, J. Chem. Phys., 55 (1971) 716, 3958.
[14] B.O. Roos, Adv. Chem. Phys. 69 (1987) 399.
[15] M. Dupuis, A. Marquez, E.R. Davidson, HONDO95.3 from CHEM-Station, IBM Corporation, Neighborhood Road, Kingston, NY 12401, 1995.
[16] C.J. Cerjan, W.H. Miller, J. Chem. Phys. 75 (1981) 2800.
[17] J. Simons, P. Jørgensen, H. Taylor, J. Ozment, J. Chem. Phys. 87 (1983) 2745.
[18] B. Huron, J-P. Malrieu, P. Rancurel, J. Chem. Phys. 58 (1973) 5745.
[19] R. Cimiraglia, J. Chem. Phys. 83 (1985) 1746.
[20] R. Cimiraglia, M. Persico, J. Comput. Chem. 8 (1987) 39.
[21] W.J. Griffiths, F.M. Harris, Rapid Commun. Mass Spectrom. 2 (1988) 91.
[22] F.M. Harris, Int. J. Mass Spectrom. Ion Process. 120 (1992) 1.
[23] S.G. Lias, J.E. Bartmess, J.F. Liebman, J.L. Holmes, R.D. Levin, W.G. Mallard, J. Phys. Chem. Ref. Data, Suppl., 17 (1988).
[24] R.I. Hall, L. Avaldi, G. Dawber, A.G. McConkey, M.A. McDonald, G.C. King, Chem. Phys. 187 (1994) 125.
[25] S.R. Andrews, F.M. Harris, D.E. Parry, Chem. Phys. 166 (1992) 69.
[26] E.M.-L. Ohrendorf, F. Tarantelli, L.S. Cederbaum, J. Chem. Phys. 92 (1990) 2984.
[27] R. Thissen, J. Delwiche, J-M. Robbe, D. Duflot, J-P. Flament, J.H.D. Eland, J. Chem. Phys. 99 (1993) 6590.
[28] P. Millie, I. Nenner, P. Archirel, P. Lablanquie, P. Fournier, J.H.D. Eland, J. Chem. Phys. 84 (1986) 1259.
[29] M.L. Langford, F.M. Harris, C.J. Reid, J.A. Ballantine, D.E. Parry, Chem. Phys. 149 (1991) 445.
[30] F. Maquin, D. Stahl, A. Sawaryn, P.v.R. Schleyer, W. Koch, G. Frenking, H. Schwartz, J. Chem. Soc., Chem. Commun., 504 (1985).
[31] R.S. Mulliken, J. Chem. Phys. 23 (1955) 1833.
[32] D. Winkoun, G. Dujardin, L. Hellner, M.J. Besnard, J. Phys. B 21 (1985) 1385.
[33] S. Hsieh, J.H.D. Eland, J. Phys. B 29 (1996) 5795.
[34] J.H.D. Eland, Mol. Phys. 61 (1987) 725.
[35] D. Duflot, J-M. Robbe, J-P. Flament, J. Chem. Phys. 102 (1995) 355.

Article 4

Available online at www.sciencedirect.com
SCIENCE DIRECT®
Chemical Physics 288 (2003) 95–104
Chemical Physics
www.elsevier.com/locate/chemphys

Thiazyl chloride: an experimental and theoretical study of the valence shell HeI photoelectron spectrum

D. Duflot[a], N. Chabert[a], J.-P. Flament[a], J.-M. Robbe[a], I.C. Walker[b], J.H. Cameron[b], A. Giuliani[c], M.-J. Hubin-Franskin[c], J. Delwiche[d,*]

[a] *Laboratoire de Physique des Lasers, Atomes et Molécules (PhLAM), UMR CNRS 8523, Centre d'Études et de Recherches Lasers et Applications (CERLA), Université des Sciences et Technologies de Lille, F-59655 Villeneuve d'Ascq Cedex, France*
[b] *Department of Chemistry, Heriot-Watt University, Riccarton, Edinburgh EH14 4AS, UK*
[c] *Laboratoire de Spectroscopie d'Électrons Diffusés, Département de Chimie, Institut de Chimie B6c, Université de Liège, Sart Tilman, B4000 Liège 1, Belgium*
[d] *Thermodynamique et Spectroscopie, Département de Chimie, Institut de Chimie B6c, Université de Liège, Sart Tilman, B4000 Liège 1, Belgium*

Received 8 March 2002; in final form 21 October 2002

Abstract

High level (CASSCF-MRCI) ab initio calculations are used to investigate the structural, electronic and vibrational properties of the electronic ground state of thiazyl chloride (NSCl) and of the low-lying electronic states of $NSCl^+$. A new high resolution HeI photoelectron spectrum of NSCl has been recorded in the 10–16 eV energy region. From the results of the calculations, the first band is assigned to the $(1)^2A'$ state of $NSCl^+$. The second one corresponds to the $(2)^2A'$ and $(1)^2A''$ states which are quasi-degenerate. Despite the high resolution, the two first bands show no vibrational fine structure. For the first one, Franck–Condon analysis shows that it is due to the overlapping of two vibrational progressions involving the S–Cl stretching and the NSCl bending modes. In the case of the second band, it is explained by the highly repulsive character of the potential energy surfaces of two states of $NSCl^+$ in the Franck–Condon region of the neutral molecule. For the third band, which shows vibrational peaks, the calculation of Franck–Condon factors permits the determination of the adiabatic ionisation energy of the $(3)^2A'$ electronic state of $NSCl^+$ at 13.798 eV. Finally, the fourth band, which is due to three different ionic states with vibrational progressions, is too complicated to be assigned quantitatively.

PACS: 31.14.Ar; 33.60.Cv; 33.20.Tp

1. Introduction

Thiazyl chloride is the S-analogue of nitrosyl chloride, NOCl. At room temperature, it exists as a solid trimer, $N_3S_3Cl_3$, in equilibrium with the

* Corresponding author. Tel.: +32-4-3663435; fax: +32-4-3662941.
E-mail address: jdelwiche@ulg.ac.be (J. Delwiche).

0301-0104/03/$ - see front matter © 2003 Published by Elsevier Science B.V.
doi:10.1016/S0301-0104(02)00966-7

gaseous monomer. The trimer is a six-membered $(NS)_3$ ring having all the chlorine atoms on the same side of the ring. The monomer, characterised by both microwave spectroscopy [1] and electron diffraction [2], is a bent molecule (point group C_s) whose geometry is given in Table 1. Its infrared spectrum is known [3] (Table 2). Consistent with the tabulated data, the S–Cl bond is relatively weak (shared electron number = 0.60, compared with 2.14 for the N–S bond [4]) and photolysis of NSCl in the near UV generates a chlorine atom and an NS radical. However, there is little available information on the electronic states of NSCl. The HeI photoelectron spectrum (PES) was first reported by Cowan et al. [5] some years ago. It showed four unstructured bands between about 10.5 and 15 eV ionisation energy. These were assigned to five ionisations from comparison with the PES of thiazyl fluoride (NSF) together with the results of semi-empirical extended Hückel type calculations. Subsequently, De Kock et al. [6] published HeI and HeII spectra along with a NeI spectrum. In the last, the third and fourth ionisation bands showed fine structure suggesting excitation of the bend vibration, ν_2 (band 3) and the ν_1 stretch vibration (band 4) but the data were complicated by the doublet nature of the NeI source. A fifth ionisation was also reported. Cationic states were assigned using relative intensity differences between the HeI and HeII spectra and CNDO/2 calculations. Like Cowan et al., De Kock et al. [6] proposed two closely spaced ionisations within the second band, as did Allaf et al. from ab initio computations [7]. All of the above workers concur that the first cationic state is $^2A'$ followed by $^2A''$–$^2A'$ but thereafter, the state ordering is confused. It should be noticed that all previous theoretical studies applied Koopmans' theorem to assign the experimental bands.

As part of an investigation into the electronic structure of NSCl, we have carried out a high level ab initio theoretical study of the neutral ground state molecule and its low-lying cationic states, $NSCl^+$. We have also re-measured the HeI photoelectron spectrum, with energy resolution superior to that previously obtained; the spectrum is analysed using the results of the computations.

Table 1
Equilibrium geometries of the electronic ground state of $\tilde{X}^1A'$ of NSCl, at different levels of calculations

	RHF	RHF	CASSCF	CASSCF	CASSCF MRCI	CASSCF MRCI(D)	CASSCF MRCI(D)	RHF[a]	CPF[a]	CPF[a]	Exp.[b]	Exp.[c]
	cc-pVTZ	cc-pVQZ	cc-pVTZ	cc-pVQZ	cc-pVTZ	cc-pVTZ	cc-pVQZ	TZ + 2P	TZ + 2P	TZ + 3P	MW	X-ray
R_{NS} (Å)	1.432	1.425	1.468	1.461	1.470	1.464	1.455	1.444	1.488	1.487	1.450 ± 0.0001	1.448 ± 0.003
R_{SCl} (Å)	2.128	2.121	2.239	2.229	2.203	2.194	2.176	2.140	2.190	2.168	2.161 ± 0.0001	2.159 ± 0.003
$\theta_{(NSCl)}$ (°)	114.47	114.77	117.31	117.48	117.48	117.34	117.45	114.4	(117.7)	(117.7)	117.42 ± 0.05	117.5 ± 1.0

[a] Ref. [4].
[b] Ref. [1].
[c] Ref. [2].

Table 2
Vibrational wavenumbers[a] (cm^{-1}) of the electronic ground state $\tilde{X}^1A'$ of NSCl

	RHF cc-pVTZ	RHF cc-pVQZ	CASSCF cc-pVTZ	CASSCF cc-pVQZ	CASSCF MRCI cc-pVTZ	CASSCF MRCI(D) cc-pVTZ	CASSCF MRCI(D) cc-pVQZ	Exp.[b]	Exp.[c]	Exp.[d]
ω_1 (stretch NS)	1415.8	1429.0	1323.8	1332.4	1313.9	1351.9	1364.7			
ω_2 (bend NSCl)	314.0	318.5	267.1	268.1	272.1	276.8	281.3			
ω_3 (stretch SCl)	472.0	471.1	391.7	396.5	416.3	422.1	424.8			
ZPE	1101.8	1109.3	991.3	998.5	1001.2	1025.4	1035.4			
v_1 (stretch NS)	1394.7	1406.9	1308.4	1315.9	1297.6	1335.2	1351.9	1324.5 ± 1	1327.3	1326
v_2 (bend NSCl)	313.9	317.8	267.2	265.0	271.9	272.7	281.5	271.6 ± 1	267.4	
v_3 (stretch SCl)	470.6	464.6	379.1	400.6	405.1	422.3	431.6	414.8 ± 1	403.75	414
ZPE	1099.0	1094.7	987.8	990.8	997.1	1022.0	1035.1	1005.4	999.2	

[a] ω_1, ω_2, and ω_3 correspond to the harmonic vibrations, while v_1, v_2, and v_3 correspond to the anharmonic vibrations.
[b] Ref. [3].
[c] Ref. [27].
[d] Ref. [7].

2. Computational details

All the ab initio calculations in this paper were carried out with the MOLPRO program package [8]. Two Gaussian atomic orbital basis sets, taken from Dunning [9], were used: the cc-pVTZ (98 basis functions) and the cc-pVQZ (173 basis functions) basis sets.

The molecular orbitals (MOs) were optimised at the RHF and CASSCF [10–12] levels. In the latter case, the active space consists of the $n = 2$ shell for the N atom and the $n = 3$ shell for the S and Cl atoms, the inner shells being kept inactive. Thus, for the $\tilde{X}^1A'$ ground state of NSCl, the active space consists in 9 a′ MOs, 3 a″ MOs with 18 active electrons, leading to 8029 CSFs. For $NSCl^+$, there are 17 active electrons and the size of the active spaces are much larger (28,503 CSFs for $^2A'$ states and 28,125 CSFs for $^2A''$ states). In order to take into account the effect of dynamical correlation, multi-reference configuration interaction (MRCI) [13,14] calculations were performed, using the CASSCF MOs as starting orbitals. We recall that this method generates *all* single (S) and double (D) excitations from the configurations state functions (CSFs) of the active space. This leads to CI dimensions too large for our present computational possibilities, especially for $NSCl^+$. For example the MRCI space for the $^2A'$ states of $NSCl^+$ contains about 3×10^9 CSFs. To reduce the size of the calculations, the standard method is to generate the excitations from a sub-space of the active space, consisting of the CSFs whose weight in the wave function is greater than a given threshold (typically 0.01). This criterion, however, is somewhat arbitrary and cannot be used for the calculation of potential energy curves. To avoid this problem, we used the excitation degree of the CAS CSFs as the selection parameter. For example, in the case of the $\tilde{X}^1A'$ ground state of NSCl, the active space contains the HF closed shell reference configuration plus all single, double, triple... up to hexa excitations from the occupied orbitals to the empty ones. With the cc-pVQZ basis set, the resulting MRCI space contains about 5 millions of contracted CSFs. If we impose that only the closed shell HF configuration plus all the single and double excitations (which correspond to 219 CSFs among the 8029 of the full CAS) are generators of the MRCI space, the size of this space is reduced to about 1.8 million of uncontracted CSFs. When a similar procedure is applied to the case of $NSCl^+$ states (open shell HF configurations), the reduction of the MRCI space is even more drastic, and the calculations become feasible for our present computational possibilities. In the following, this type of MRCI calculations will be designed as MRCI(D).

In order to determine the equilibrium geometry of the $\tilde{X}^1A'$ ground state of NSCl, a grid of 35

points centred on the experimental geometry was generated. The resulting energies (calculated at RHF, CASSCF and MRCI levels) were then fitted by a fourth-degree polynomial, using the SURFIT program [15]. The resulting surfaces were then converted to quadratic force fields in internal and dimensionless coordinates using *l*-tensor algebra [16] as implemented in SURFIT. The program uses perturbation theory to obtain the harmonic and anharmonic wavenumbers.

A well known problem arising in the calculation of transition energies is the choice of the orbitals for the description of the initial and final states. Here, for the calculations of the electronic states of $NSCl^+$, three types of CASSCF MOs were employed: the NSCl ground state MOs, state-averaged (SA) MOs for the four lowest-lying states of $NSCl^+$ (for each irreducible representation A′ and A″) and state-optimised MOs for each ionic state.

Finally, in order to interpret the vibrational structure of the spectral bands, Franck–Condon factors calculations were carried out, using our local implementation [17,18] of the method proposed by Cederbaum and Domcke [19]. This model requires the determination of the gradient (the κ matrix) and the Hessian (the γ matrix) of the ionisation energy E_v at the neutral geometry:

$$\kappa_i = 2^{-1/2}\left(\frac{\partial E_v}{\partial Q_i}\right)_0, \quad \gamma_{ij} = \frac{1}{4}\left(\frac{\partial^2 E_v}{\partial Q_i \partial Q_j}\right)_0.$$

In the present work, the quadratic coupling matrix γ was neglected and only the κ matrix was computed (linear coupling approximation) at the CASSCF/cc-pVQZ level.

3. Experimental

3.1. Sample preparation

The trimer of thiazyl chloride $N_3S_3Cl_3$ was made using the method described by Jolly and Maguire [20]. This is a two-step synthesis. First, disulfurdichloride, S_2Cl_2, reacts with ammonium chloride, NH_4Cl producing $S_3N_2Cl_2$ which then reacts with chlorine, Cl_2, to give the solid product, $S_3N_3Cl_3$.

$$4S_2Cl_2 + 2NH_4Cl \rightarrow S_3N_2Cl_2 + 8HCl + 5S$$

$$3S_3N_2Cl_2 + 3Cl_2 \rightarrow 2N_3S_3Cl_3 + 3SCl_2$$

The preparation was carried out in small batches, using 1/10th of the quantities recommended in the original recipe. Consequently, the first reaction step was completed in about 3 h (rather than 10–12 h) and the intermediate $S_3N_2Cl_2$ was chlorinated directly. At stages when moist air had to be excluded, oxygen-free nitrogen was flowed through the system. The final batches of product were stored in air-tight sample bottles. Portions were transferred, as required, to a sample tube that was connected directly to the ionisation chamber of the photoelectron spectrometer. Rapid heating under vacuum to 70 °C released the monomer.

3.2. Photoelectron spectrometer

The HeI photoelectron spectra were recorded using an hemispherical energy analyser described elsewhere [21]. The resolution was set to 20 meV, measured as the full width at half height of the $^2P_{3/2}$ peak of the argon HeI photoelectron spectrum.

The resolution was further increased by deconvolution using a procedure described by van Cittert [22] and modified by Allen and Grimm [23]. The energy axis was calibrated with reference to HCl and N_2, present as impurities in some of the spectra, using the values given by Kimura [24]. The spectra have been corrected for the transmission of the electron optics.

4. Results and discussion

4.1. The electronic ground state $\tilde{X}^1A'$ of the neutral molecule

At the Hartree–Fock level, the electronic configuration of the $\tilde{X}^1A'$ ground state is

$$[\text{core}]1a'^2 2a'^2 3a'^2 4a'^2 5a'^2 1a''^2 6a'^2 2a''^2 7a'$$

The experimental equilibrium geometry was determined by microwave spectroscopy [1] and X-ray diffraction [2] (see Table 1). The two sets of values agree well with each other. At the theoret-

ical level, the only ab initio determination is that of Ehrhardt and Ahlrichs [25], using the coupled pair functional (CPF) method [26] but with the NSCl angle kept frozen to 117.7° (Table 1). This study emphasised the importance of polarization functions (especially g AOs) for a good description of the NSCl bond lengths.

Our own calculated geometries using the cc-pVTZ and cc-pVQZ basis sets are presented in Table 1. As expected for these methods, the RHF bond lengths are underestimated while the CASSCF ones are overestimated. In particular, the S–Cl bond length is too large at cc-pVQZ/CASSCF level by 0.07 Å. The full MRCI and MRCI(D) calculations using the cc-pVTZ basis set slightly improve the result with a S–Cl bond length around 2.2 Å, which is too large by ≈0.04 Å. Finally, the cc-pVQZ/MRCI(D) calculations give the best results, with a remaining discrepancy between theory and experiment of 0.015 Å for R_{SCl}.

The vibrational wavenumbers of NSCl have also been determined, using infrared spectroscopy in the gas phase by Müller et al. [3] and in argon matrices by Peake and Downs [27] (see Table 2). The three modes correspond, respectively, to the N–S stretching mode (ν_1), to the N–S–Cl bending mode (ν_2) and to the S–Cl stretching mode (ν_3). The calculated wavenumbers, obtained at RHF, CASSCF and MRCI(D) levels with both basis sets are given in Table 2. Several well known trends can be observed, such that the 10% overestimation of the RHF values. The harmonic wavenumbers are too high in most cases and the inclusion of anharmonicity improves the situation. The basis set effects are less important than for the geometries, the difference between the cc-pVTZ and cc-pVQZ being less than 10 cm^{-1} in most cases. Among the three modes, the bending and S–Cl stretching values are very close to the experimental ones. For these two modes, anharmonic effects seem to be weak since at all levels of theory, the differences between the ω and the ν values are negligible. The MRCI(D) results seem to give slightly poorer results, since the anharmonic values remain above the experimental ones. This tends to indicate that the restrictions of MRCI(D) method described above slightly affect the topology of the potential well around the equilibrium geometry.

4.2. The ionic states

4.2.1. Photoelectron spectrum

The HeI photoelectron spectrum is displayed in Fig. 1. We note that bands 1 and 2 are structureless with FWHM of about 0.18 and 0.46 eV, respectively. Concerning the second band, the results of the calculations described below show that it is the superposition of two displaced peaks with the same FWHM. The result of the fitting of this band by two identical Gaussian functions is displayed in Fig. 2. The energy spacing is 0.224 eV and the FWHM is 0.27 eV. Band 3 shows a vibrational progression, with a wavenumber of about 290 cm^{-1} (0.036 eV) consistent with excitation of the bending vibration ν_2, which has a wavenumber of 271.6 cm^{-1} (0.034 eV) in the ground state

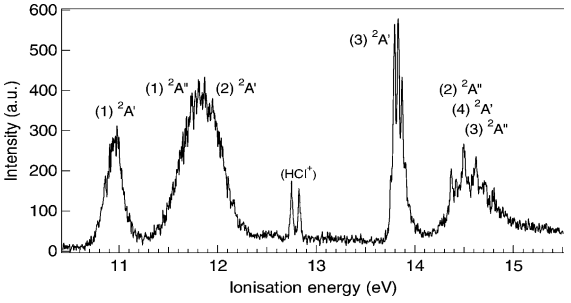

Fig. 1. The HeI photoelectron spectrum of NSCl.

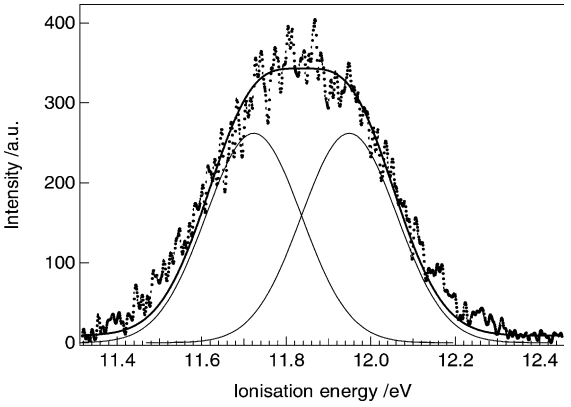

Fig. 2. Results of the fitting of the second peak of the experimental spectrum by two identical displaced Gaussians functions.

Table 3
Calculated vertical ionisation energies of NSCl (eV)

	This work							
	Neutral MOs[a]	SA MOs[a]	Optimised MOs	Exp.	Exp.[b]	Exp.[c]	HF[d]	EH[e]
$(1)^2A'$	10.670	10.346	10.362	10.953	10.96	10.95 (1)	11.27 (7a′)	11.69 (7a′)
$(1)^2A''$	11.679	11.239	11.227	11.725	11.80	11.82 (2)	12.48 (2a″)	12.89 (6a′)
$(2)^2A'$	12.075	11.237	11.153	11.949			12.71 (6a′)	13.04 (2a″)
$(3)^2A'$	14.012	13.474	13.394	13.834	13.77	13.83 (2)	15.92 (1a″)	14.33 (5a′)
$(2)^2A''$	14.587	14.349	13.958	14.499	14.46	14.49 (1)	16.19 (5a′)	15.25 (4a′)
$(4)^2A'$	14.703	14.254	14.202				17.25 (4a′)	
$(3)^2A''$	14.777	14.016	14.404					
$(4)^2A''$	16.291	14.874	15.042					

[a] MRCI(D) values obtained at the calculated MRCI(D)/cc-pVQZ equilibrium geometry of NSCl (see Table 1) and corrected of the ZPE (1035.1 cm^{-1} or 0.128 eV, Table 2).
[b] Ref. [5].
[c] Ref. [6].
[d] Koopmans MOs energies from [7].
[e] Extended Hückel calculations from [5].

neutral molecule. De Kock et al. [6] identified a similar progression in the NeI spectrum, citing a wavenumber of 250 ± 30 cm^{-1} (0.031 ± 0.04 eV). In band 4 vibrational intervals of about 1049 cm^{-1} (0.13 eV) and 403 cm^{-1} (0.05 eV) may be identified; these could relate to excitation of the two stretching vibrations v_1 and v_3 (1325 cm^{-1} or 0.164 eV and 415 cm^{-1} or 0.0514 eV, in the neutral ground state, respectively). However, as will be shown later, this band is complex and its analysis in terms of a single ionisation is simplistic.

4.2.2. Vertical ionisation energies

In Table 3, the vertical ionisation energies calculated at the cc-pVQZ/CASSCF-MRCI(D) level, using the three different types of MOs are reported, as well as the results of previous calculations, based on Koopmans' theorem [5,7]. The present experimental values have been determined in the following way: for the first band, the ionisation potential is taken as the maximum of the band. The two values given for the second band are extracted for the fit by two Gaussian functions. For the third and fourth bands, the values reported in Table 3 are those of the most intense vibrational peaks.

The comparison between the three sets of calculations and the experiment shows that the theoretical results are underestimated, in most cases by several tenths of eV. The use of the neutral MOs seems to give values closer to the experimental ones, but this is an artefact: since the NSCl MOs are not the best choice for the description of $NSCl^+$ states, the calculated energies are too high. Nevertheless, all the calculations agree to assign without ambiguity the first band to the $(1)^2A'$, the second one to the $(1)^2A''$ and $(2)^2A'$ states and the third one to the $(3)^2A'$ state. These results are in agreement with the Koopmans values [5,7], except that Allaf et al. [7] assigned the third band to a A'' state. Concerning the fourth band, one can only say that it is due to several electronic states. According to the theoretical results, there are four states in the 14–15 eV energy region corresponding to this band.

Another problem concerns the ordering and the energy splitting of the $(1)^2A''$ and $(2)^2A'$ states responsible for the second band. The three types of calculations give contradictory results: the neutral MOs give 0.4 eV, which seems too high; SA calculations give quasi-degenerate values while optimised MOs lead to $\Delta E = 0.074$ eV. Relying on this latter value, which is the closest to the splitting deduced from the fit of the experimental band (0.224 eV), the ordering of the states would be $(2)^2A'$ and $(1)^2A''$.

4.2.3. Detailed investigation of the three first bands of the photoelectron spectrum

Despite the good energy resolution used to record the experimental HeI photoelectron

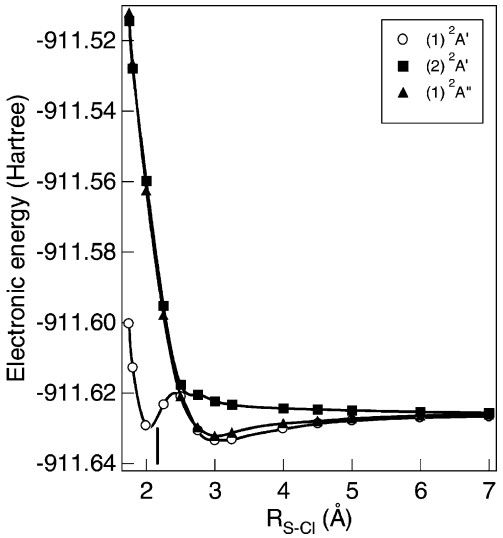

Fig. 3. Calculated potential energy curves of the lowest lying states of $NSCl^+$ (see text for details).

spectrum, no vibrational feature is observed for the two first bands of the spectrum while well resolved vibational structure is observed in the third band. In order to ascertain the reasons for such behaviour, we explored the topology of the potential energy surfaces of the lowest lying $(1)^2A'$, $(1)^2A''$ and $(3)^2A'$ states of $NSCl^+$, which correlates to the $NS^+(X^1\Sigma^+) + Cl(^2P)$ fragments (using the cc-pVTZ basis set). To do this, we optimised (at CASSCF level) the R_{NS} and $\theta_{(NSCl)}$ coordinates for different (frozen) values of R_{SCl} for the lowest lying state $(1)^2A'$ of $NSCl^+$; then, at these geometries, the SA-MRCI(D) energies of the three states were recalculated. The results of these calculations are reported in Fig. 3. In addition, a full geometry optimisation of the lowest lying states of $NSCl^+$ was performed at the CASSCF/cc-pVQZ level. A Mulliken population analysis was also carried out. The bond orders, which are not available in MOLPRO, were obtained with the HONDO package [29]. The results of these calculations are given in Table 4.

Concerning the $(1)^2A'$ state, which is responsible of the first band, the potential energy curve (Fig. 3) presents two minima, the lowest lying around 3.3 Å and the secondary one around 2.0 Å. Indeed, geometry optimisations found the equilibrium geometries indicated in the two first columns of Table 4. In the following, this secondary minimum will be denoted as (1a) to distinguish it from the lowest lying one (1b). Since (1a) takes place in the Franck–Condon zone of the neutral molecule (around 2.2 Å, vertical line in Fig. 3), one should expect the presence of vibrational features in the first band. In order to explain its absence, we have calculated the Franck–Condon factors for this state, using the force constant matrix of NSCl ($\tilde{X}^1A'$) and the κ matrix of $NSCl^+$ ($(1a)^2A'$) obtained at the cc-pVQZ/CASSCF level. The simulated band is in good agreement with the experimental one as shown in Fig. 4. In fact, this band involves excitation of both the S–Cl stretching and the bending modes, which are very close as shown in Table 2. The absence of fine structure is due to the overlapping of two vibra-

Table 4
Calculated properties (CASSCF/cc-pVQZ) of the lowest lying electronic states of $NSCl^+$

	$NSCl^+$				NSCl	NSCl[a]	NSCl[b]
	$(1a)^2A'$	$(1b)^2A'$	$(1)^2A''$	$(3)^2A'$	$\tilde{X}^1A'$	$\tilde{X}^1A'$	$\tilde{X}^1A'$
R_{NS} (Å)	1.524	1.447	1.447	1.470	1.461	1.444	1.450 ± 0.0001
R_{SCl} (Å)	2.046	3.342	3.342	2.171	2.229	2.140	2.161 ± 0.0001
θ_{NSCl} (°)	108.03	118.68	118.07	111.72	117.51	114.4	117.42 ± 0.05
Q_N	+0.01	+0.03	+0.03	+0.06	−0.27	−0.37	
Q_S	+0.82	+0.93	+0.93	+0.87	+0.63	+0.73	
Q_{Cl}	+0.17	+0.04	+0.04	+0.07	−0.36	−0.36	
σ_{NS}	1.83	2.53	2.53	1.88	2.34	2.14	
σ_{SCl}	1.02	0.01	0.01	0.89	0.72	0.60	
σ_{NCl}	0.07	0.06	0.06	0.19	0.15		

[a] HF/TZ + 2P from [4].
[b] Ref. [1].

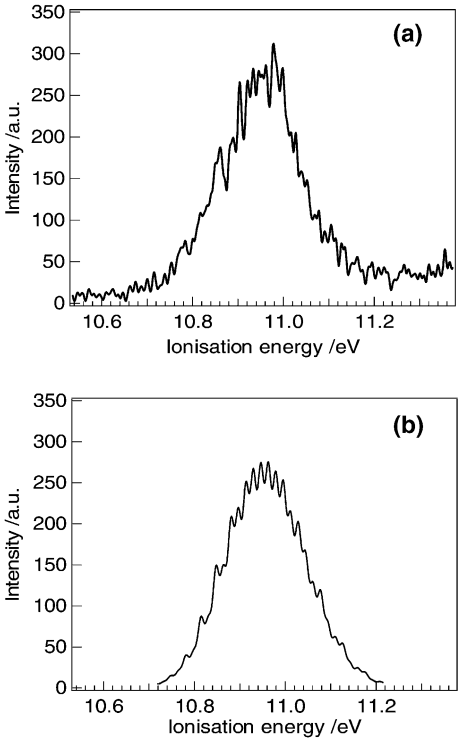

Fig. 4. First electronic band of the HeI photoelectron spectrum of NSCl. (a) Experimental curve. (b) Calculated curve (the energy maximum is set to the experimental value).

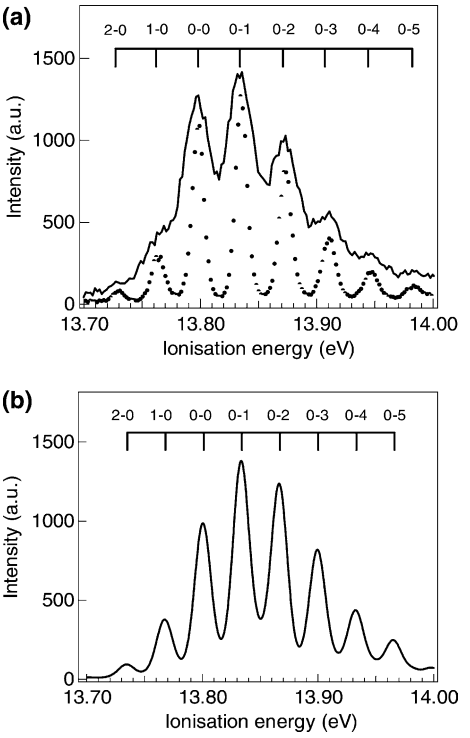

Fig. 5. Third electronic band of the HeI photoelectron spectrum of NSCl. (a) Experimental curve and (dots) deconvoluted curve (×0.4). (b) Calculated curve (the energy of the most intense peak is set to the experimental value).

tional progressions. Moreover, it should be noticed that our calculations do not take into account the tunnelling effect through the potential energy barrier occurring around 2.5 Å (Fig. 3). This should increase the width of the vibrational peaks, at least on the high energy side of the band, and contribute to the absence of fine features.

For the second band, assigned to the $(2)^2A'$ and the $(1)^2A''$ states of $NSCl^+$, inspection of Fig. 3 shows that, in the Franck–Condon zone of the neutral ground state, their potential energy curves are highly repulsive (the $(2)^2A'$ is in fact dissociative) and well above the dissociation asymptote. Furthermore, the $(2)^2A'$ and $(1)^2A''$ potential energy curves have the same slope. After the reflection principle [28], it is possible to estimate from this slope the width of the spectral bands. The resulting value (0.35 eV) is consistent with the value obtained in the fitting of the second experimental band (0.27 eV) as shown in Fig. 2. The repulsive character of potential energy curves explains the absence of vibrational structure in the spectrum for this band.

The situation is somewhat different for the third band of the photoelectron spectrum, corresponding to the $(3)^2A'$ state whose geometry and charge properties are very close to the one of the neutral ground state, as shown in Table 4. By comparison with the wavenumber values in NSCl (Table 2), we can attribute the observed vibrational features in this band of the photoelectron spectrum to ν_2, the bending vibration mode. Another indication is the fact that the main difference between the geometries of the $NSCl^+$ $(3)^2A'$ state and the neutral ground state is the $\theta_{(NSCl)}$ angle (Table 4).

In order to assign precisely the experimental peaks, we have calculated the Franck–Condon factors for this state, using the same method as for the first band. The calculated shape of this third

band is shown in Fig. 5(b) and can be compared to the experiment shown in Fig. 5(a). Despite the simplicity of the model, the overall agreement with the experimental spectrum is good, the main discrepancy being the relative intensity of the third and fifth peaks. According to these calculations, the two first peaks observed correspond to hot band type transitions from the $(0,\ v_2'' = 1, 2,\ 0)$ levels of the $\tilde{X}^1A'$ ground state of NSCl to the $(0,0,0)$ level of the $(3)^2A'$ electronic state of $NSCl^+$. All the following observed peaks correspond to transitions from the $(0,0,0)$ vibrational level of NSCl to the $(0,v_2',0)$ levels of the ionic state. This gives a value of 13.798 ± 0.002 eV for the adiabatic formation of the $(3)^2A'$ electronic state of $NSCl^+$. Moreover, the model predicts that the intensity ratio of the $(v_2'' = 1 \rightarrow v_2' = 0)$ and the $(v_2'' = 0 \rightarrow v_2' = 1)$ transition should match the Boltzmann factor $exp(-v_2/kT)$, i.e., about 0.27 in the present case. This value is in good agreement with the one (around 0.26) deduced form the experimental band shown in Fig. 5(a).

In addition to the geometries, Table 4 shows the Mulliken populations and bond orders of the lowest lying states of $NSCl^+$. For all the structures, the positive charge is located on the sulphur atom. The (1a) and $(3)^2A'$ states, whose geometries are rather close to the neutral one, the charge properties and bond orders are also similar to those of NSCl. On the other hand, the $(1b)^2A'$ and $(1)^2A''$ states of $NSCl^+$ are nearly indistinguishable. These states are very weakly bound complexes between the Cl atom and a NS^+ ion. The A'–A'' splitting is due to the removal of the electron from the in-plane and out-of-plane π orbital which constitutes the HOMO of the neutral NS molecule.

Finally, for the fourth band, one can only say that it is very difficult to perform a detailed theoretical study, as this would require the determination of the ionisation energies, the absolute electronic ionisation intensities and the vibrational wavenumbers of at least three highly excited states.

5. Conclusions

In the present paper, we have reinvestigated the HeI photoelectron spectrum of NSCl, combining a high resolution spectrum, large scale (CASSCF-MRCI) ab initio methods, and Franck–Condon factors calculations. For the three first bands of the spectrum, the theoretical results provide assignments that improve on those from previous semi-empirical calculations. Geometry optimisations of the lowest lying states of $NSCl^+$ and Franck–Condon analysis are used to explain the vibrational structure (or its absence) in the three first bands. In particular, the theoretical simulation of the vibrational progression observed in the third band reveals the presence of hot bands and leads to the conclusion that the adiabatic ionisation energy of the $(3)^2A'$ electronic state of $NSCl^+$ is 13.798 eV.

Acknowledgements

The Laboratoire de Physique des Lasers, Atomes et Molécules (PhLAM) is a ''Unité Mixte de Recherche du CNRS'' of France. The Centre d'Études et de Recherches Lasers et Applications (CERLA) is supported by the Ministère chargé de la Recherche, the Région Nord/Pas-de-Calais of France, and the Fonds Européen de Développement des Régions (FEDER). M.J.H.F. acknowledges the Fonds National de la Recherche Scientifique for a research position. ICW is grateful to the Fonds National de la Recherche Scientifique for funding her stay if the Liège laboratories. The authors thank the referee for very useful suggestions.

References

[1] T. Beppu, E. Hirota, Y. Morino, J. Mol. Spectrosc. 36 (1970) 386;
S. Mizumoto, J. Izumi, T. Beppu, E. Hirota, Bull. Chem. Soc. Jpn. 45 (1972) 786.
[2] W.C. Emken, K. Hedberg, J. Chem. Phys. 58 (1973) 2195.
[3] A. Müller, N. Mohan, S.J. Cyvin, N. Weinstock, O. Glemser, J. Mol. Spectrosc. 59 (1976) 161.
[4] C. Ehrhardt, R. Ahlrichs, Chem. Phys. 108 (1986) 417.
[5] D.O. Cowan, R. Gleiter, O. Glemser, E. Heilbronner, Helv. Chim. Acta 55 (1972) 2418.
[6] D.L. De Kock, M.A. Shehfeh, D.R. Lloyd, P.J. Roberts, J. Chem. Soc. Faraday II 72 (1976) 807.

[7] A.W. Allaf, G.Y. Matti, R.J. Suffolk, J.D. Watts, J. Electron Spectrosc. Rel. Phenom. 48 (1989) 411.
[8] MOLPRO (version 2000.1) is a package of ab initio programs written by H.-J. Werner and P.J. Knowles with contributions from R.D. Amos, A. Bernhardsson, A. Berning, P. Celani, D.L. Cooper, M.J.O. Deegan, A.J. Dobbyn, F. Eckert, C. Hampel, G. Hetzer, T. Korona, R. Lindh, A.W. Lloyd, S.J. McNicholas, F.R. Manby, W. Meyer, M.E. Mura, A. Nicklass, P. Palmieri, R. Pitzer, G. Rauhut, M. Schütz, H. Stoll, A.J. Stone, R. Tarroni, and T. Thorsteinsson. Available from: http://www.tc.bham.ac.uk/molpro.
[9] T.H. Dunning, J. Chem. Phys. 90 (1989) 1007.
[10] H.-J. Werner, P.J. Knowles, J. Chem. Phys. 82 (1985) 5053.
[11] P.J. Knowles, H.-J. Werner, Chem. Phys. Lett. 115 (1985) 259.
[12] H.-J. Werner, Adv. Chem. Phys. 69 (1987) 1.
[13] H.-J. Werner, P.J. Knowles, J. Chem. Phys. 89 (1988) 5803.
[14] H.-J. Werner, P.J. Knowles, Chem. Phys. Lett. 145 (1988) 514.
[15] J. Senekowitsch, Ph.D. Thesis, University of Frankfurt, 1988.
[16] A.R. Hoy, I.M. Mills, G. Strey, Mol. Phys. 24 (1972) 1265.
[17] J.-P. Flament, Ph.D. Thesis, Université de Paris-Sud, Centre d'Orsay (1981).
[18] J.-P. Dognon, C. Pouchan, A. Dargelos, J.-P. Flament, Chem. Phys. Lett. 109 (1984) 492.
[19] L.S. Cederbaum, W. Domcke, Adv. Chem. Phys. 36 (1977) 205.
[20] W.L. Jolly, K.D. Maguire, Inorg. Synth. 9 (1967) 102.
[21] J. Delwiche, P. Natalis, J. Momigny, J.E. Collin, J. Electron Spectrosc. Relat. Phenom. 1 (1972) 219.
[22] P.H. van Cittert, Z. Phys. 69 (1931) 298.
[23] J.D. Allen Jr., F.A. Grimm, Chem. Phys. Lett. 66 (1979) 72.
[24] K. Kimura, S. Katsumata, Y. Achiba, T. Yamazaki, S. Iwata, Handbook of HeI Photoelectron Spectra of Fundamental Organic Molecules, Halsted Press, New York, 1981.
[25] C. Ehrhardt, R. Ahlrichs, J. Chem. Phys. 82 (1985) 890.
[26] R. Ahlrichs, P. Scharf, C. Ehrhardt, Chem. Phys. 108 (1986) 417.
[27] S.C. Peake, A.J. Downs, J. Chem. Soc. (Dalton) (1974) 859.
[28] R. Schinke, Photodissociation Dynamics, Section 6.1, Cambridge Monographs on Atomic, Molecular and Chemical Physics 1, Cambridge University Press, 1993.
[29] M. Dupuis, F. Johnston, A. Marquez, HONDO95.3 from CHEM-Station, IBM Corporation, Neighborhood Road, Kingston, NY, 12401, USA, 1995.

Article 5

Available online at www.sciencedirect.com
SCIENCE DIRECT®
Chemical Physics 324 (2006) 339–349
Chemical Physics
www.elsevier.com/locate/chemphys

Acetic acid electronic state spectroscopy by high-resolution vacuum ultraviolet photo-absorption, electron impact, He(I) photoelectron spectroscopy and ab initio calculations

P. Limão-Vieira [a,b,*], A. Giuliani [c,d], J. Delwiche [e], R. Parafita [a], R. Mota [a], D. Duflot [f], J.-P Flament [f], E. Drage [b], P. Cahillane [b], N.J. Mason [b], S.V. Hoffmann [g], M.-J. Hubin-Franskin [c]

[a] *Laboratório de Colisões Atómicas e Moleculares, Departamento de Física, CEFITEC, FCT-Universidade Nova de Lisboa, Quinta da Torre, 2829-516 Caparica, Portugal*
[b] *Centre of Molecular and Optical Sciences, Department of Physics and Astronomy, The Open University, Walton Hall, Milton Keynes MK7 6AA, UK*
[c] *Laboratoire de Spectroscopie d'Electrons Diffusés, Université de Liège, Institut de Chimie-Bât. B6C, B-4000 Liège, Belgium*
[d] *Laboratoire de Spectrometrie de Masse, Institut de Chimie des Substances Naturelles, CNRS, Avenue de la Terrasse, F-91198, Gif-sur-Yvette Cedex, France*
[e] *Laboratoire de Thermodynamique et Spectroscopie, Université de Liège, Institut de Chimie-Bât. B6C, B-4000 Liège, Belgium*
[f] *Laboratoire de Physique des Lasers, Atomes et Molécules (PhLAM), UMR CNRS 8523, Centre d'Etudes et de Recherches Lasers et Applications (CERLA, FR CNRS 2416), Université des Sciences et Technologies de Lille, F-59655 Villeneuve d'Ascq Cedex, France*
[g] *Institute for Storage Ring Facilities, University of Aarhus, Ny Munkegade, DK-8000, Aarhus C, Denmark*

Received 22 June 2005; accepted 31 October 2005
Available online 1 December 2005

Abstract

Electronic state spectroscopy of CH_3COOH has been investigated using Vacuum UltraViolet (VUV) photo-absorption spectroscopy in the energy range 3.5–10.6 eV. The availability of a high-resolution photon beam (~0.075 nm) has allowed detailed analysis of the vibrational progressions and allowed us to propose, for the first time, new assignments for several Rydberg series. Excited states located in the 10–14 eV region have been studied for the first time. The VUV photo-absorption spectrum is compared with the electron energy loss spectrum (EELS) recorded in dipolar transition mode (100 eV incident energy, ~0° scattering angle) in the 5.0–14 eV energy loss range. A He(I) photoelectron spectrum has also been recorded from 10.5 to 13 eV and compared to earlier low resolution works. A new value of (10.657 ± 0.002) eV for the ground ionic state adiabatic ionisation energy is proposed. All spectra presented in this paper represent the highest resolution data yet reported for acetic acid. New ab initio calculations help in the assignment of the spectral bands.

Keywords: Radiation damage; Photoabsorption; VUV spectrsocopy; Synchrotron radiation; Electronic and vibrational excitation; Ionisation; TDDFT calculations

1. Introduction

Acetic acid (CH_3COOH), commonly known as vinegar, is produced in the human body as a result of alcohol degradation after consumption of alcoholic beverages. It plays an important role in the metabolism processes of most forms of life and results naturally from the action of certain bacteria in foods or liquids containing sugars or ethanol.

Despite the fact that, after formic acid (HCOOH), acetic acid is the simplest organic acid, and is a major component of biological molecules, there are few studies of its electronic state spectroscopy. In this paper, we are particularly interested on its electronic state spectroscopy by means of VUV photo-absorption, as an important route to understand the effects of direct energy deposition by radiation that can lead to damage. It is now generally accepted that

* Corresponding author. Tel.: + 351 21 294 85 76; fax: + 351 21 294 85 49.
E-mail address: plimaovieira@fct.unl.pt (P. Limão-Vieira).

0301-0104/$ - see front matter © 2005 Elsevier B.V. All rights reserved.
doi:10.1016/j.chemphys.2005.10.032

the interaction of ionising radiation with living cells leads to secondary electron emissions, as the most abundant species. These ballistic electrons, with energies of a few tenths of eV (3–20 eV) can efficiently induce single and double strand breaks in supercoiled DNA, e.g. [1].

More recently dissociative electron attachment (DEA) to acetic acid has been reported in the energy range between 0 and 13 eV [2], with the energy dependence of the partial cross section for nine fragment ions being measured. Barnes and Simpson [3] reported detailed correlations among electronic transitions for carbonyl and for carboxyl species and assignments for the observed bands. Basch and co-workers [4] performed an extensive experimental study on the electronic state spectroscopy of isoelectronic amides, acids and acyl fluorides in both gas and condensed phases, supported by Hartree–Fock calculations. Bell and co-workers [5] reported VUV spectra of formic and acetic acids, revealing Rydberg series, allowing the lowest ionisation value to be determined.

Low resolution spectra of the lowest lying electronic states have been studied by Ari et al. [6] by electron impact under pseudo-optical interaction conditions. Ab initio calculations of the vibrational properties of acetic acid monomers and dimers have been reported recently by Burneau et al. [7]. He(I) and He(II) photoelectron spectra of carboxyl acids and esters, unsaturated compounds with planar-skeleton structure and monomers and dimmers of acetic acid and trifluoroacetic acids, have been studied [8–10].

However for acetic acid, as far as we know, no calculations have been reported in the literature. In the present paper, we present extensive new, high resolution, quantitative data on the electronic state spectroscopy of acetic acid. VUV photo-absorption, electron energy loss and He(I) photoelectron spectra are reported and analysed. All the data have been analysed and assigned with the help of ab initio calculations.

2. Brief summary of the structure and properties of CH_3COOH

Acetic acid in its electronic ground state has C_s symmetry [11]. The symmetry species available to a C_s molecule are A′ and A″. The molecule has 18 modes of vibration in its neutral ground state, classified in the symmetry type as $\Gamma_{vib} = 12A' + 6A''$ [11]. Its structure shown in Fig. 1 from our present work (see Section 4), corresponds to the lowest energy spatial configuration, with calculated geometry parameters listed in Table 1. Using this geometry, the electronic calculated configuration of the $^1A'$ ground state of CH_3COOH is: (a) inner orbitals $(1a')^2$ $(2a')^2$ $(3a')^2$ $(4a')^2$ $(5a')^2$ $(6a')^2$; (b) valence orbitals $(7a')^2$ $(8a')^2$ $(9a')^2$ $(10a')^2$ $(1a'')^2$ $(11a')^2$ $(12a')^2$ $(2a'')^2$ $(3a'')^2$ $(13a'^2)$.

The highest occupied molecular orbital in the neutral ground state is localized on the oxygen atom of the carbonyl group (C═O) with n_O (13a′) character [10], while the lowest unoccupied molecular orbital is the π* carbonyl group antibonding orbital [3]. This is also confirmed by the present ab initio calculations.

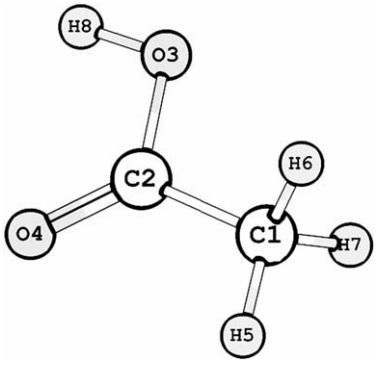

Fig. 1. Ground state structure of CH_3COOH.

Table 1
Calculated geometry of acetic acid compared with previous works bond lengths in Å and angles in (°)

	Ion ($^2A'$)	Ground state				
	PBE0[a]	PBE0[a]	B3LYP[b]	MP2[c]	MP2[d]	Exp.[e]
	6-311G**	6-311G**	6-311++G**	6-31G*	cc-pVDZ	
C_1–C_2	1.4812	1.4977	1.5056	1.500	1.508	1.520
C_2–O_3	1.2780	1.3476	1.3596	1.361	1.361	1.364
C_2═O_4	1.2491	1.2005	1.2127	1.217	1.214	1.214
C_1–H_5	1.0914	1.0924	1.0943	1.0921		
C_1–H_6	1.0974	1.0877	1.0893	1.0883		1.102
O_3–H_8	0.9753	0.9657	0.9724	0.979	0.974	(0.97)
O_3–C_2═O_4	123.0	122.5	122.2	122.6	122.9	122.8
O_3–C_2–C_1	120.6	126.1	126.1	126.4	126.2	126.6
C_2–O_3–H_8	114.9	106.0	107.0	105.5	104.5	107.0

[a] This work.
[b] Ref. [7].
[c] Ref. [28].
[d] Ref. [29].
[e] Ref. [30].

The lowest ionisation energy remains a subject of debate with several values having been obtained, varying between 10.30 and 10.87 eV [3,8–10].

3. Experimental

3.1. VUV photo-absorption

High-resolution VUV photo-absorption spectra of acetic acid were measured at the UV1 beam line using the ASTRID synchrotron facility in the University of Aarhus, Denmark (Fig. 2). The experimental apparatus has been described in detail previously [12]. Synchrotron radiation passes through a static gas sample and a photomultiplier is used to measure the transmitted light intensity. The incident wavelength is selected using a toroidal dispersion grating with 2000 lines/mm providing a resolution of ~0.075 nm. In order to prevent any absorption by air contributing to the spectrum, and for wavelengths below 200 nm, a He gas flow is maintained through the small gap between the photomultiplier and the exit window of the gas cell. The minimum and maximum wavelengths between which scans are performed, 115–320 nm (10.8–3.9 eV), are determined by the windows of the gas cell (LiF entrance and CaF_2 exit) and the grating, respectively. The sample pressure is measured using a capacitance manometer (Baratron) and to ensure that the data was free of any saturation effects [13], the cross-section was measured over the pressure range 0.015–0.750 Torr, with typical attenuations of less than 10%. The synchrotron beam ring current is monitored throughout the collection of each spectrum and a background scan recorded with the cell evacuated. Absolute photo-absorption cross sections are then obtained using the Beer–Lambert attenuation law:

$$I_t = I_0 \exp(-n\sigma x),$$

where I_t is the radiation intensity transmitted through the gas sample, I_0 is that through the evacuated cell, n the molecular number density of the sample gas, σ the absolute photo-absorption cross section, and x the absorption path length (25 cm). The accuracy of the cross-section is estimated to be ±5%.

3.2. High resolution electron energy loss spectroscopy (HREELS)

The instrument used at the Université de Liège, Belgium (VG-SEELS 400) has been described in detail elsewhere [14]. An electrostatic electron energy monochromator defines a narrow energy spread about the mean incident electron energy and a three element lens focuses the electrons into the collision region. The electron beam intersects the effusive gas beam, which flows through a hypodermic needle, at 90°. The working pressure is $\sim 1 \times 10^{-5}$ mbar. The analyser system is also an electrostatic energy analyser [14] with the scattered electron signal detected by an electron multiplier of the continuous dynode type. Both electron energy selectors work in the constant pass-energy mode. Spectra were recorded for energy losses between 5.0 and 14 eV at step intervals of 10 meV. The electron energy loss scale was calibrated to the "elastic peak". The resolution, measured as the FWHM of the elastically scattered electron peak, was about 40 meV. The apparatus was used with relatively high incident energy electrons (100 eV) and a small scattering angle ($\theta \approx 0°$), such that electric dipole interaction conditions apply and the electron energy loss spectrum is comparable with the photo-absorption spectrum. The inelastic scattered intensity was converted to a relative differential oscillator strength distribution, using a method developed previously [15]. The derived VUV cross section was normalized at 8.86 eV from the VUV photo-absorption value of 10.381 Mbarn to obtain absolute cross section values, a method shown to be reliable in previous work [16]. Comparison of the HREELS cross section values with those recorded using the synchrotron source thus provide a test

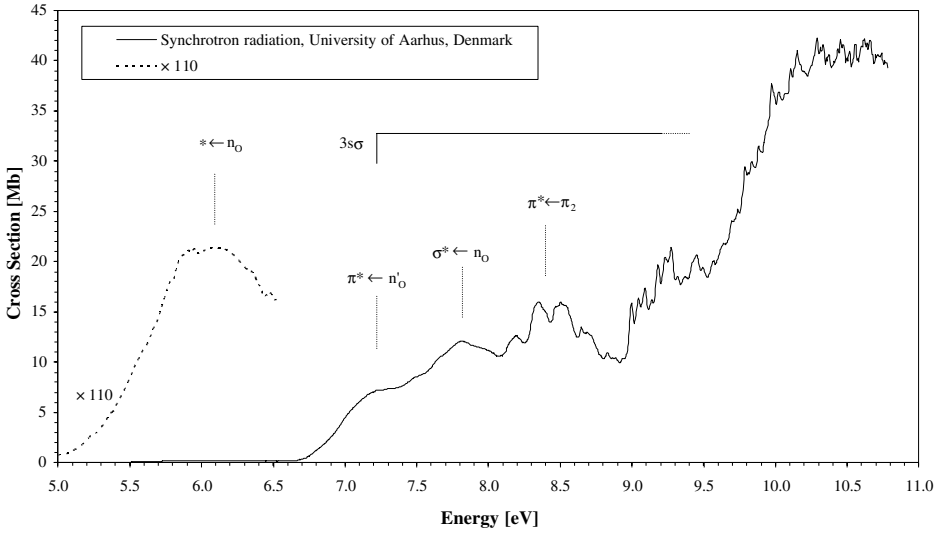

Fig. 2. High resolution VUV photo-absorption spectrum of CH_3COOH including vibrational series, valence excitations and Rydberg transitions.

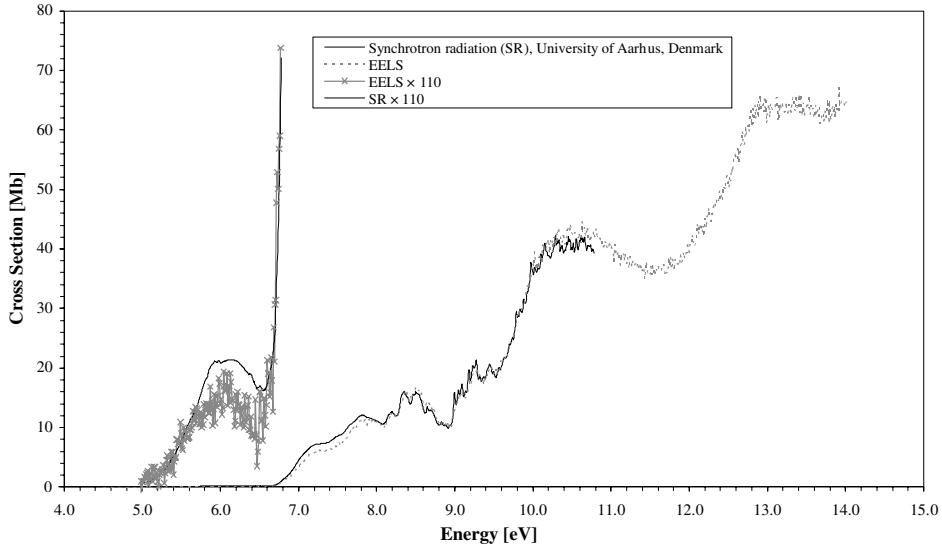

Fig. 3. Acetic acid electron energy loss spectrum (EELS) in the energy region 4.0–15.0 eV.

for any systematic errors in the optical values arising from the line saturation effect and second order light from the light source and beam line. These were found to be negligible in this work. The present HREELS spectrum is shown in Fig. 3.

3.3. Photoelectron spectroscopy

He(I) (21.22 eV) photoelectron spectra of CH_3COOH were recorded at the Université de Liège, Belgium (Fig. 4). The experimental set-up has been described in detail elsewhere [17]. Briefly, the spectrometer consists of a 180° cylindrical electrostatic analyser with a mean radius of 5 cm. The analyser is used in constant energy pass mode and is fitted with a continuous dynode electron multiplier. Incident photons are produced by a dc discharge in a two-stage differentially pumped lamp. The energy scale is calibrated using the $^2P_{3/2}$ (12.130 eV) and $^2P_{1/2}$ (13.436 eV) xenon peaks [18] and the spectra are corrected for the transmission function of the apparatus. The resolution of the present spectrum is measured from the FWHM of the Xe peaks to be 16 meV, in the presence of CH_3COOH. The accuracy of the energy scale is estimated to be ±2 meV. The photoelectron spectrum presented in this paper is the sum of 132 individual spectra. This procedure allows us obtain a good signal-to-noise ration while keeping the pressure in the spectrometer at a very low level ($<2\times10^{-6}$ mbar), minimizing the presence of dimers.

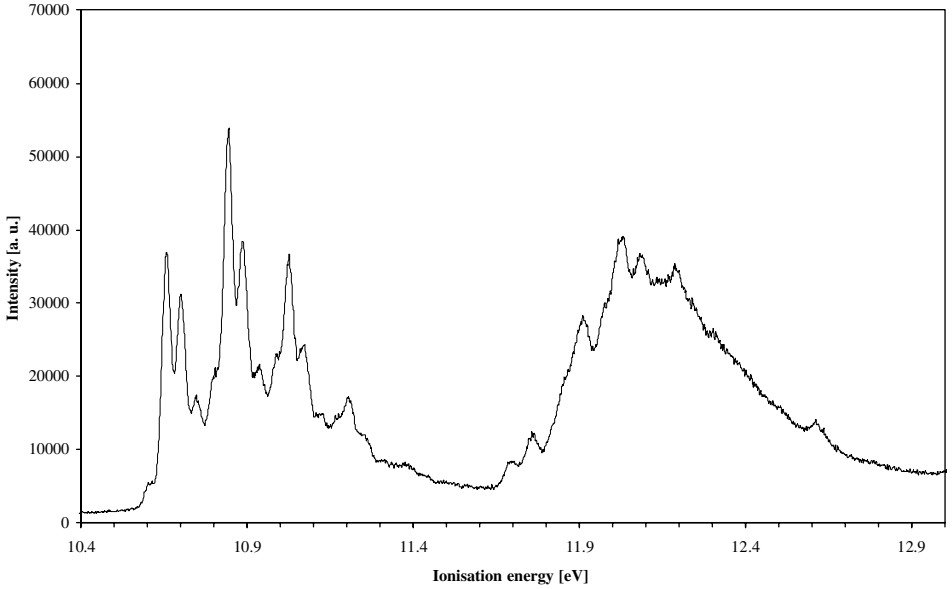

Fig. 4. He(I) photoelectron spectrum of CH_3COOH.

3.4. Acetic acid sample

The liquid sample used in the VUV measurements was purchased from Merck, with a purity of 100%, while for PES and HREEELS experiments the sample was purchased from VEL (Leuven, Belgium) and is quoted as having a minimum purity of 99.8%. The sample was degassed by a repeated freeze–pump–thaw cycle in the three different set of experiments.

4. Computational methods

It is well known that the calculation of electronic spectra of small organic molecules is a difficult task. The use of state-of-the art ab initio methods, despite the large computational cost, may give poor agreement when compared to experiment (see e.g. [19] and references cited therein for the well known case of furan). In the case of acrolein, which is rather similar to acetic acid, Aquilante et al. [20] have shown that TDDFT calculations using the PBE0 functional [21,22] give results in good agreement with more costly calculations (i.e., MS-CASPT2), even for Rydberg states.

In the present work, in order to help in the assignment of the measured spectra, we have used the same method: the geometry was optimised at the DFT/PBE0/6-311G** level, and the electronic spectrum was calculated at the TDDFT//PBE0/6-311++G** level. All the calculations were performed with the Gaussian 03 package [23]. The energies of ionic states were obtained using a restricted open-shell method. Results are shown in Tables 1 and 2. Vibrational frequencies for the lowest ionic configuration have been calculated and the values obtained are very close to those of the ground state, except for the C=O stretching. Since the electron being removed comes from the oxygen lone pair, the neutral and ionic geometries are almost identical, with the exception of the C=O bond length (see Section 6). Therefore assignments in PES spectrum were made taking into account this consideration.

5. Results and discussion

The absolute high resolution VUV photo-absorption spectrum of acetic acid is shown in Fig. 2 from 5.0 to 10.6 eV, extending roughly 1 eV higher in energy than previously reported data [3–5]. Fine structures in both the 8.5 eV and in the 9.3 eV regions are better resolved. In addition, absorption in the 10 eV region is observed for the first time. The observed absorption bands can be classified as members of Rydberg series and molecular valence transitions of the type ($\pi^* \leftarrow n_O$), ($\sigma^* \leftarrow n_O$) and ($\pi^* \leftarrow \pi$). For the low-energy range ($\sim$8 eV) we suggest mixed valence-Rydberg character with the bands having characteristics of both types of transitions, in agreement with previous work [3,4].

Since the experiments have been performed at room temperature, one cannot discard the possibility of dimer formation. However, comparing the present cross sectional data with that of Barnes and Simpson [3], there is no clear

Table 2
Calculated vertical excitation energies (TDDFT/PBE0/6-311++G**) (eV) and oscillator strengths and experimental transition energies of acetic acid for the present work

Orbital character	Calculated		Experimental		Transition between electronic states
	E (eV)	f	E (eV)	Cross section (Mb)	
$n_O \rightarrow 1\pi^*$	5.926	0.0007	6.093	0.193	$1\ ^1A'' \leftarrow 1\ ^1A'$
$n'_O \rightarrow \pi^*$	–	–	7.217	7.175	$2\ ^1A' \leftarrow 1\ ^1A'$
$n_O \rightarrow 3s\sigma/\sigma^*(O–H)$	7.000	0.0495	7.217/7.817	7.175/12.106	$3\ ^1A' \leftarrow 1\ ^1A'$
$n_O \rightarrow 3p\sigma$	7.730	0.0018			
$2\pi \rightarrow 3s\sigma/\sigma^*(O–H)$	8.106	0.0021			
$n_O \rightarrow 3p\pi$	8.404	0.0002			
$n_O \rightarrow 3p\sigma$	8.491	0.0023	8.151	12.086	
$2\pi \rightarrow 1\pi^*$	8.685	0.1719	8.349	16.021	$4\ ^1A' \leftarrow 1\ ^1A'$
$n_O \rightarrow 3d\sigma$	8.847	0.0028			
$2\pi \rightarrow 3s\sigma/\sigma^*(O–H)$	8.906	0.0001			
$n_O \rightarrow 3d\sigma$	9.387	0.0522	8.820	10.750	
$\sigma(O–H) \rightarrow 1\pi^*$	9.426	0.0000			
$n_O \rightarrow 3d\pi$	9.585	0.0098			
$2\pi \rightarrow 3p\pi$	9.735	0.0022			
$2\pi \rightarrow 3p\sigma$	9.781	0.0101			
$n_O \rightarrow 3d\sigma$	9.973	0.0112			
$1\pi \rightarrow 3s\sigma/\sigma^*(O–H)$	9.986	0.0084			
$1\pi \rightarrow 1\pi^*$	10.021	0.1476	10.289	42.273	
$n_O \rightarrow 3d\pi$	10.026	0.0070			
$\sigma(CH_3) \rightarrow 1\pi^*$	10.059	0.0042			
$2\pi \rightarrow 3d\sigma$	10.105	0.0093			
$\sigma(O–H) \rightarrow 3s\sigma/\sigma^*(O–H)$	10.150	0.1401			
$IE_v\ (^2A')$[a]	10.671		10.844	–	
$IE_v\ (^2A'')$[a]	12.044		12.028	–	

[a] 6-311G** values.

evidence that dimers contribute to the present spectra, especially because the relative intensities of the structures observed around 7.217 and 7.817 eV are in good agreement with the work reported by them for monomers.

A high resolution electron energy loss spectrum (HREELS) was recorded at an incident electron energy of 100 eV and at small scattering angle $\theta \approx 0°$ (Fig. 3). The HREELS is recorded from 5.0 to 14 eV and shows several fine features unresolved in the previous work of Ari and Güven [6]. Our EELS measurements are a mirror of most of the structure observed in the present VUV photo-absorption (Fig. 2).

The present high resolution He(I) photoelectron spectra has a much higher resolution (Figs. 4 and 5) than in previous reported work [10,24–26], and allows a new value for the adiabatic ionisation energy to be recommended, (10.657 ± 0.002) eV.

The results of the calculations are presented in Table 2. The values are compared to the experimental measured energies and there is an excellent agreement between both sets.

5.1. Valence states and transitions of CH_3COOH

Using the analysis of Barnes and Simpson [3] we have assigned the first four absorption bands observed at ~6.093, 7.217, 7.817 and 8.349 eV to $(\pi^* \leftarrow n_O)$ (forbidden and predominantly in plane, perpendicular to the C–O line), $(\pi* \leftarrow n'_O)$ (out of plane), $(3s\sigma \leftarrow n_O)$ and $(\sigma^* \leftarrow n_O)$ (in plane, perpendicular to the C–O line) and $(\pi^* \leftarrow \pi)$ (in plane, parallel to the C–O line), respectively. Given that the third band can be due to charge transfer from the hydroxyl, a second $(\pi^* \leftarrow \pi)$ transition due to a pure carbonyl transition might occur [3]. We shall come back to this issue later.

The VUV photo-absorption spectrum has been previously measured [3–5,29] and the first band has been identified as the transition from the non-bonding n_O on the oxygen atom lone pair of the carbonyl group to the first π antibonding MO $(\pi^* \leftarrow n_O)$, with a maximum value of ~0.083 Mb [29]. In the present measurement we report this band with a maximum cross section of 0.193 Mb at 6.093 eV (Fig. 2) as being due to the $1^1A'' \leftarrow 1^1A'$ transition (Table 2).

The second band centred at 7.217 eV, with a cross sectional value of 7.175 Mb, has been assigned to the $(\pi* \leftarrow n'_O)$ transition [3], where n'_O is the oxygen lone pair electrons for the O atom of OH.

The third band peaking at 7.817 eV in our spectrum with a local maximum cross section of 12.106 Mb, was initially reported at 7.749 eV, with a cross sectional value of 6.976 Mb [29], considerably lower than in the present high resolution measurement. The band was assigned to the first $(\pi \rightarrow \pi^*)$ transition band of the C=O bond. Nagakura et al. [27] suggest that this band, as in similar cases in other carboxylic acids and esters containing a carbonyl group (C=O) and a hydroxyl (OH) or alkoxyl group (OR, R being a radical), may be due to the contribution of the intramolecular charge transfer between the electron donor (OH) and the electron acceptor (C=O). Our present calculations on the vertical excitation energies (Table 2) do not support the $(\pi^* \leftarrow \pi)$ assignment but a $(\sigma^*_{O-H} \leftarrow n_O)$ transition in agreement with Barnes and Simpson [3]. Moreover, there is a mixed valence/Rydberg character for the first 3s Rydberg series and, in agreement with [3], we propose that this is also due to a $(3s\sigma_{O-H} \leftarrow n_O)$.

The fourth valence band at 8.349 eV, with a local cross sectional value of 16.021 Mb, has been identified as the $(\pi^* \leftarrow \pi)$ as is found in other compounds containing a car-

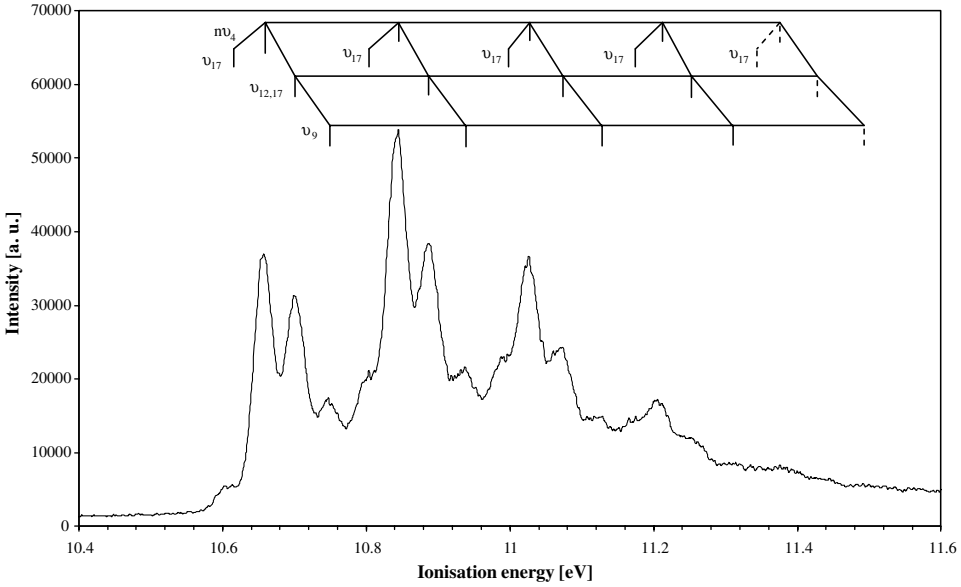

Fig. 5. The first photoelectron band of CH_3COOH, assigned to ionisation from the $n_O(13a')$ orbital.

boxyl group at ~8.3 eV [3]. Its position is in good agreement with our calculations, predicting such transition at 8.687 eV and a probable $\sigma^*(CH_3) \leftarrow n_O$ mixing character. This structured band has been referred to as a transition involving considerable admixture of the HO– or CH_3O– oxygen π orbital in the originating π orbital [3], the latter being the most probable (see Table 2).

5.1.1. The 7.3–9.0 eV energy region

This energy region is displayed in detail in Fig. 6 and the assignments are in Table 3. It exhibits considerable vibrational structure mainly due to the activation of the ν_6, CH_3 symmetric deformation mode on the ($\sigma^*_{O-H} \leftarrow n_O$) and ($\pi^* \leftarrow \pi$) transitions. In the ($\sigma^*_{O-H} \leftarrow n_O$) transition, the vibrational excitation assignments are proposed for the first time, while in the ($\pi^* \leftarrow \pi$) transition, it has been reported before [5], and is attributed to progressions and combinations of C–O stretching mode, ν_8 to ν_6. The (0–0) transition lying 8.192 eV is a result of the excitation to an anti-bonding orbital of the π MO and the vibrational progressions associated with it are represented in Table 3. Our present calculated vertical excitation energies (see Table 2) suggest another contribution to this band, mainly due to a ($\sigma^*_{CH3} \leftarrow n_O$). The structure/shoulder at 8.713 eV is here tentatively assigned as a combination of $3\nu_6 + 1\nu_{12}$ (Table 3) and the features at 8.151 and 8.828 eV assigned as members of Rydberg series (see Section 6.1).

5.1.2. The 8.9–10.8 eV energy region

This energy region is displayed in detail in Fig. 7 and the assignments are given in Table 4, showing rich vibrational excitation. At least four transition bands have been identified in the present data and a fifth is proposed coupled with the 7s Rydberg transition converging to the lowest ionisation energy (IE). These bands are all Rydberg in character (see Section 6.1) [5].

Table 3
Vibrational assignments in the 7.3–9.0 eV absorption band of CH_3COOH

This work				Previous work [5], energy (eV)
Energy (eV)	Assignment	ΔE (ν_6) (eV)	ΔE (ν_8) (eV)	
7.487	ν_{00}	–	–	–
7.653	ν_6	0.166	–	–
7.817	$2\nu_6$	0.164	–	–
7.978	$3\nu_6$	0.161	–	–
8.192	ν_{00}	–	–	8.159
8.349	ν_6	0.157	–	8.308
8.501	$2\nu_6$	0.152	–	8.470
8.646	$3\nu_6$	0.145	–	8.653
8.713	$3\nu_6 + 1\nu_{12}$	–	–	8.836
8.824	$4\nu_6$	0.178	–	–
8.321 (?)	ν_8	–	0.129	–
8.466	$2\nu_8$	–	0.145	–
8.604 (?)	$3\nu_8$	–	0.138	–
8.750 (?)	$4\nu_8$	–	0.146	–
8.885	$5\nu_8$	–	0.135	–
8.397	$\nu_6 + \nu_8$	–	–	–
8.542	$2\nu_6 + \nu_8$	–	0.145	–
8.689	$3\nu_6 + \nu_8$	–	0.147	–
8.713	$3\nu_6 + \nu_{12}$	–	–	–
8.866	$4\nu_6 + \nu_8$	–	0.177	–

Assignment within bracket (?) means uncertainty.

The first (0–0) transition lying at 8.997 eV is rich in vibrational progressions. The features between 8.9 and 9.5 eV are attributed to combinations of C=O stretching, ν_4, with CCO deformation, ν_{12}, and CH_3 rocking, ν_9, modes. The excitation of these modes is also observed in the lowest ionic energy region (Fig. 5). As far as ν_{12} is concerned, another possible assignment should be considered – ν_{17}, instead. In fact, due to the similar energy value for the

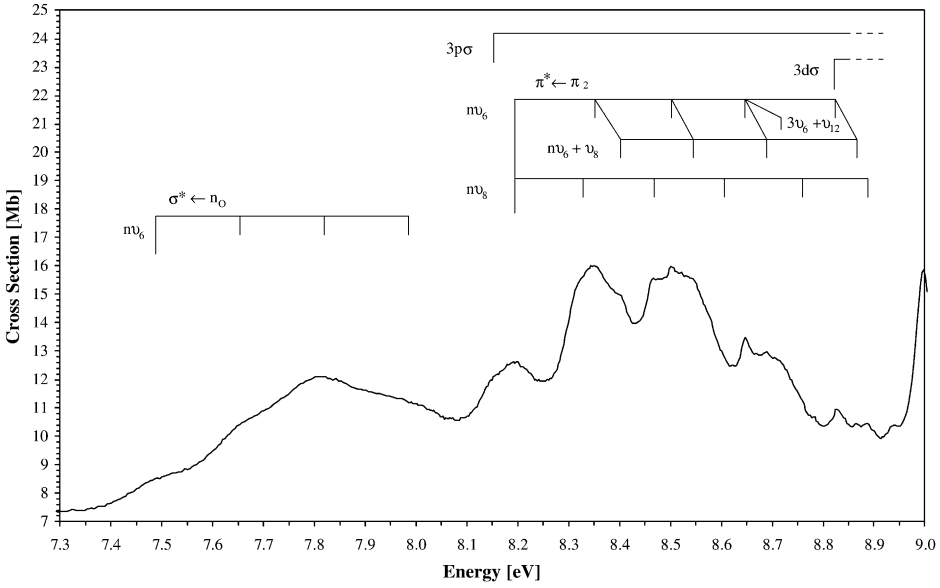

Fig. 6. Vibrational progressions in the 7.3–9.0 eV absorption band of CH_3COOH.

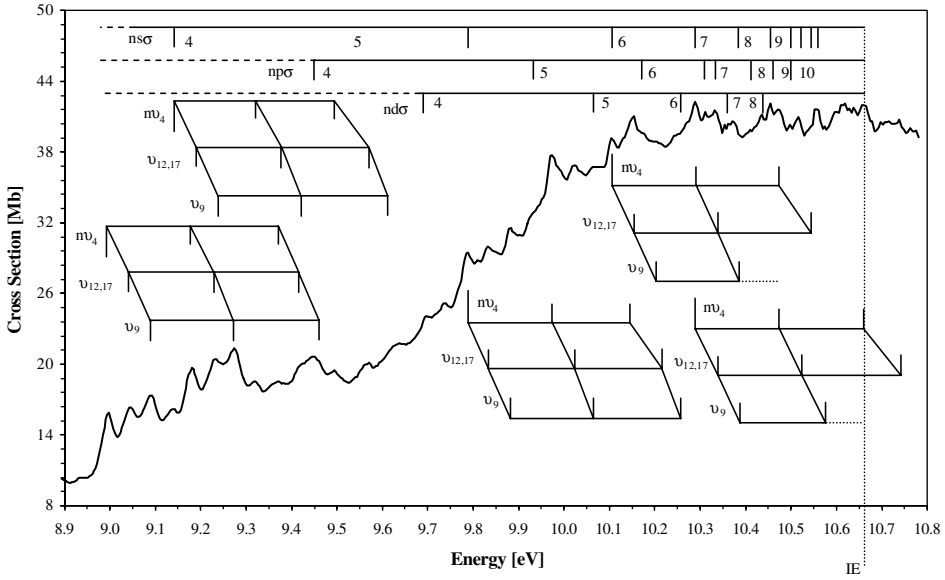

Fig. 7. Vibrational progressions in the 8.9–10.8 eV absorption band of CH_3COOH.

activation of such modes, we propose a $\nu_{12,17}$ notation instead. The feature at 8.942 eV is tentatively assigned to a hot band of the ν_{17} C–O torsion mode from the (0–0) transition.

The second, third and fourth transition bands associated with the 4s, 5s and 6s Rydberg series, the (0–0) transitions lie at 9.137 eV, 9.790 and 10.105 eV, respectively (Table 4). In all of them the vibrational spacing is similar to the one found in the lowest ionic state. The assignments of the vibrational excitation within the fourth band become difficult due to overlap in the observed structures. The feature at 9.736 eV is also tentatively assigned to a hot band of the ν_{17} C–O torsion mode from the 9.790 eV (0–0) transition.

The fifth last band, due to a calculated $1\pi^* \leftarrow 1\pi$ transition (Table 2), with its (0–0) lying at 10.289 eV in the same energy range of the 7s Rydberg series has been assigned in terms of same vibrational modes as in the previous four bands (Table 4). Structures at 10.472 and 10.656 eV are part of a broad non-symmetric peaks which can explain the fact that there must be an overlap with other electronic states; actually for the former structure, we have the proximity of 7p Rydberg series, for the latter the fact that it lies on the lowest ionisation energy threshold and therefore mixes with this ionic state.

6. He(I) photoelectron

The photoelectron spectrum of acetic acid has been reported by several authors with different values for the adiabatic [24–26] and the vertical ionisation energy having been derived [9,10]. In contrast to all other methods, photoelectron spectroscopy often gives both adiabatic and vertical ionisation energies, the former tend to be weak whenever there is a large change in equilibrium molecular geometry on ionisation [18]. Since the shape of the observed lowest ionic band for acetic acid (Figs. 4 and 5) clearly shows the point of maximum intensity at 10.843 eV, corresponding to the vertical ionisation energy, the intense feature at 10.657 eV is attributed to the adiabatic ionisation energy. In fact, the present calculations in Table 1 for both ground and lowest ionic states, show that there is no significant change in geometry. In the present experiment, we suggest values of (10.657 ± 0.002) and (10.843 ± 0.002) eV, respectively (Fig. 4).

The first band, corresponding to the ionic electronic ground state of acetic acid, is shown in Fig. 5. The fine structure in this energy band is resolved here for the first time and proposed to be mainly due to the activation of ν_4 C=O stretching coupled with $\nu_{12,17}$ CCO deformation and/or C–O torsion, and ν_9 CH_3 rocking modes with mean energies of 0.180, 0.042, and 0.098 eV (Table 5), respectively. Another excitation mode is also reported and tentatively assigned to hot bands, with an energy spacing of 0.041 eV, corresponding to molecules with the ν_{17} C–O torsion mode being populated. Table 6 shows the calculated vibrational frequencies for both ground and lowest ionic states.

The calculated vertical IE's are 10.671 and 12.044 eV for A′ and A″ ionic states (Table 2) and the optimised geometry of the A′ ion is shown in the first column of Table 1. The methyl group is not rotating and the largest variations in the ionic state with respect to the ground state concern C_2–O_3 and C_2=O_4 lengths as well as O_3–C_2–C_1 and C_2–O_3–H_8 bending modes (see Fig. 1 for atoms' key). Therefore the most intense vibration peaks in the photoelectron band should involve these modes, which are in good agreement with the experimental values found.

6.1. Rydberg series converging to the lowest ionic ground state

The cross-section above 8 eV consists of a series of sharp peaks superimposed on a background up to the lowest ioni-

Table 4
Vibrational assignments in the 8.9–10.8 eV absorption band of CH_3COOH

This work		Previous work [5], energy (eV)
Energy (eV)	Assignment	
First band		
8.997	v_{00}	9.004
9.043	$v_{12,17}$	9.048
9.090	$v_{12,17} + 1v_9$	9.096
–	–	9.140
9.181	v_4	9.182
9.232	$v_4 + 1v_{12,17}$	9.232
9.273	$v_4 + 1v_{12,17} + 1v_9$	9.279
9.371	$2v_4$	–
9.418	$2v_4 + 1v_{12,17}$	–
9.461	$2v_4 + 1v_{12,17} + 1v_9$	–
Second band		
9.140	v_{00} ($4sa' \leftarrow 13a'$)	–
9.191 (s)	$v_{12,17}$	–
9.239 (s)	$v_{12,17} + 1v_9$	–
9.319	v_4	–
9.378 (s)	$v_4 + 1v_{12,17}$	–
9.421	$v_4 + 1v_{12,17} + 1v_9$	–
9.423	$2v_4$	–
9.570	$2v_4 + 1v_{12,17}$	–
9.608 (s)	$2v_4 + 1v_{12,17} + 1v_9$	–
Third band		
9.786	v_{00}	9.791
9.832	$v_{12,17}$	–
9.883	$v_{12,17} + 1v_9$	9.886
9.975	v_4	9.975
10.023	$v_4 + 1v_{12,17}$	–
10.064	$v_4 + 1v_{12,17} + 1v_9$	–
10.146 (s)	$2v_4$	–
10.213 (d)	$2v_4 + 1v_{12,17}$	–
10.255 (d)	$2v_4 + 1v_{12,17} + 1v_9$	–
Fourth band		
10.105	v_{00}	–
10.154	$v_{12,17}$	–
10.200 (d)	$v_{12,17} + 1v_9$	–
10.289	v_4	–
10.341 (s)	$v_4 + 1v_{12,17}$	10.343
10.384	$v_4 + 1v_{12,17} + 1v_9$	–
10.472	$2v_4$	10.463
10.543 (s)	$2v_4 + 1v_{12,17}$	10.526
Fifth band		
10.289	v_{00}	
10.332 (s)	$v_{12,17}$	
10.380	$v_{12,17} + 1v_9$	
10.472	v_4	
10.521 (s)	$v_4 + 1v_{12,17}$	
10.574	$v_4 + 1v_{12,17} + 1v_9$	
10.656	$2v_4$	
10.739 (?)	$2v_4 + 1v_{12,17}$	

Assignment within bracket (?) means uncertainty.
(s) means peak shoulder.
(d) means diffuse structure.

sation energy (IE), 10.657 eV. Fig. 2 shows the absorption spectrum between 5.0 and 11 eV revealing Rydberg structures. The peak positions, E_n, must fit the Rydberg peak positions formula: $E_n = E_i - R/(n-\delta)^2$, where E_i is the ionisation energy (adiabatic value, $E_i =$ 10.657 eV), n is the principal quantum number of the Rydberg orbital of energy E_n, R is one Rydberg and δ the quantum defect resulting from the penetration of the Rydberg orbital into the core.

Table 5
Energy positions and vibrational analysis of features observed in the first photoelectron band of CH_3COOH

Peak energy (eV)	Analysis
10.608	v_{17}
10.657	v_{00}, adiabatic IE
10.700	$v_{12,17}$
10.747	$v_{12,17} + v_9$
10.801	v_{17}
10.843	v_4, vertical IE
10.886	$v_4 + v_{12,17}$
10.936	$v_4 + v_{12,17} + v_9$
10.988	v_{17}
11.026	$2v_4$
11.070	$2v_4 + v_{12,17}$
11.122	$2v_4 + v_{12,17} + v_9$
11.170	v_{17}
11.207	$3v_4$
11.250	$3v_4 + v_{12,17}$
11.305	$3v_4 + v_{12,17} + v_9$
11.336	v_{17}
11.375 (d)	$4v_4$
11.424 (d)	$4v_4 + v_{12,17}$
11.491 (d)	$4v_4 + v_{12,17} + v_9$

(d) means diffuse peak/structure.

6.1.1. The ns σ Rydberg series

The low intensity feature located at 7.217 eV, is proposed to belong to the Rydberg transition ($3s\sigma \leftarrow n_O$ ($13a'$)) state [10], of $n = 3$ term series with a quantum defect $\delta = 1.01$ (Table 7). Basch et al. [4] have reported an extensive study on the first Rydberg state in amides and carboxylic acids, finding them to be completely structureless, since it may lie on an upper state that is not bound. Actually, one observes that the 3s transition is broader than the others in the spectrum, which can be attributed to interaction with an underlying dissociative valence state. In fact, the dissociative electron attachment studies of Märk and co-workers [2] show a resonance for O^- and OH^- production threshold at ~7.5 eV.

The Rydberg series members, 4, 5 and 6 are accompanied by the vibrational excitation of v_4, $v_{12,17}$ and v_9 modes. The peak at 10.498 eV (Fig. 7) is interpreted as an $n = 10$ term, with a calculated quantum defect $\delta =$ 0.75, slightly lower than for the other members. This is probably due to the fact that this peak is quite broad and therefore may have contributions on the excitation of another Rydberg state, a 10p. The higher members of this series for which relative intensity decreases, are hidden by transitions due to the excitation to other Rydberg series. It is also noteworthy that there is an overlap in this energy region with the vibrational excitation modes v_4, $v_{12,17}$ and v_9.

Table 6
Calculated vibrational energies for both ground and lowest ionic states of CH_3COOH (energies in eV)

		Experiment[a]	Assignment	Ground state[b]	Ion[b]
a′	ν_1	0.444	OH str	0.473	0.459
a′	ν_2	0.378	CH_3 d-str	0.396	0.392
a′	ν_3	0.365	CH_3 s-str	0.381	0.376
a′	ν_4	0.222	C=O str	0.233	0.200
a′	ν_5	0.177	CH_3 d-deform	0.182	0.179
a′	ν_6	0.171	CH_3 s-deform	0.176	0.171
a′	ν_7	0.157	OH bend	0.167	0.159
a′	ν_8	0.147	C–O str	0.153	0.150
a′	ν_9	0.123	CH_3 rock	0.124	0.122
a′	ν_{10}	0.105	CC str	0.110	0.110
a′	ν_{11}	0.081	OCO deform	0.074	0.058
a′	ν_{12}	0.072	CCO deform	0.053	0.045
a″	ν_{13}	0.372	CH_3 d-str	0.390	0.387
a″	ν_{14}	0.177	CH_3 d-deform	0.182	0.178
a″	ν_{15}	0.130	CH_3 rock	0.132	0.123
a″	ν_{16}	0.080	C=O op-bend	0.085	0.083
a″	ν_{17}	0.066	C–O torsion	0.068	0.068
a″	ν_{18}	0.012	CH_3 torsion	0.010	0.014

[a] Ref. [11].
[b] This work (PBE0/6-311G**).

Table 7
Energy values, quantum defect and assignment of the nsσ Rydberg series converging to the ionic ground state (energies in eV)

Energy	Quantum defect	Assignment
7.217	1.01	3s
9.137	1.01	4s
9.790	0.96	5s
10.105	1.04	6s
10.289	0.92	7s
10.380 (s)	0.99	8s
10.454	0.82	9s
10.498 (?)	0.75	10s
10.521 (s)	1.00	11s
10.543 (s)	1.08	12s
10.561 (?)	1.09	13s

Assignment within bracket (?) means uncertainty.
(s) means peak shoulder.

Table 8
Energy values, quantum defect and assignment of the npσ Rydberg series converging to the ionic electronic ground state (energies in eV)

Energy	Quantum defect	Assignment
8.151	0.67	3p
9.450	0.64	4p
9.931	0.67	5p
10.175	0.69	6p
10.311	0.73	7p
10.332	0.53	
10.410	0.58	8p
10.458 (?) (s)	0.73	9p
10.498	0.75	10p

Assignment within bracket (?) means uncertainty.
(s) means peak shoulder.

6.1.2. The npσ Rydberg series

The first member of a *np* series has been assigned to the 8.151 eV (Table 8) with a quantum defect of $\delta = 0.67$. The second and third terms of the series are observed at 9.450 and 9.931 eV, respectively, both with a quantum defect of $\sim\delta = 0.65$. The peak at 10.458 eV is interpreted as a peak shoulder, $n = 9$ term with a calculated quantum defect $\delta = 0.73$.

Table 9
Energy values, quantum defect and assignment of the ndσ Rydberg series converging to the ionic electronic ground state (energies in eV)

Energy	Quantum defect	Assignment
8.828	0.27	3d
9.693	0.25	4d
10.064 (?)	0.21	5d
10.251 (?)	0.21	6d
10.362	0.21	7d
10.436	0.16	8d

Assignment within bracket (?) means uncertainty.

6.1.3. The ndσ Rydberg series

The last observed series starting at 8.828 eV (Fig. 7, Table 9) has been assigned as $n = 3$ term of an *nd* series. The second and third terms of the series lie at 9.693 and 10.064 eV, with quantum defects $\delta = 0.25$ and 0.21, respectively; the latter term is a diffuse structure and lying close to the previously tentatively assigned $5s\sigma + 1\nu_4 + 1\nu_{12,17} + \nu_9$. The peak at 10.436 eV is here assigned as a $n = 8$ term. It is an asymmetric structure and as previously reported, the higher members of this series for which relative intensity decreases, are hidden by transitions due to the excitation of other Rydberg series states and/or vibrational excitations.

7. Conclusions

The present results are found to be in good agreement with previous data [1–4]. Under pseudo-optical conditions,

the electron energy loss spectrum [4] is in good agreement with VUV spectra. The present cross sectional data, especially at ~204 nm, 6.093 eV, is slightly higher that the work of Nagakura et al. [27] with our local maximum of 0.193 Mb twice that of Nagakura.

In the present high resolution data new features are observed in both the valence and Rydberg spectra. Fine structure observed in the photo-absorption spectra has been assigned to specific vibrational modes.

Ab initio calculations on the vertical excitation energies and oscillator strengths, helped in the assignment of the spectral transitions. The theoretical results are in good agreement with the experimental data.

Acknowledgements

P.L.V. acknowledges the honorary research fellow position at University College London, the visiting fellow position at CEMOS, The Open University, UK, and together with M.-J. H.-F. the financial support from the Portuguese-Belgian joint collaboration. The Patrimoine of the University of Liège, the Fonds National de la Recherche Scientifique and the Fonds de la Recherche Fondamentale Collective of Belgium have supported this research. M.-J. H.-F. wishes to acknowledge the Fonds de la Recherche Scientifique for position. R.P. acknowledges the financial support from the EIPAM network, ESF, for the short term scientific mission to Liège, Belgium. P.L.V. and N.J.M. acknowledge the support from the British Council for the Portuguese-English joint collaboration. The authors acknowledge the beam time at the ISA synchrotron facility, University of Aarhus, Denmark, and the support from the European Commission for access to research infrastructure action of the improving human potential programme. Some of this work form part of the EU network programme EPIC, HPRN-CT-2002-00179. The ''PhLAM'' is ''Unité Mixte de Recherche du CNRS''. The ''Centre d'Études et de Recherches Lasers et Applications'' (CERLA, FR CNRS 2416) is supported by the ''Ministère chargé de la Recherche'', the ''Région Nord/Pas-de-Calais'' and the ''Fonds Européen de Développement Économique des Régions'' (FEDER).

References

[1] B. Boudaïffa, P. Cloutier, D. Hunting, M.A. Huels, L. Sanche, Science 287 (2000) 1658.
[2] W. Sailer, A. Pelc, M. Probst, J. Limtrakul, P. Scheier, E. Illenberger, T.D. Märk, Chem. Phys. Lett. 378 (2003) 250.
[3] E.E. Barnes, W.T. Simpson, J. Chem. Phys. 39 (1963) 670.
[4] H. Basch, M.B. Robin, N.A. Kuebler, J. Chem. Phys. 49 (1968) 5007.
[5] S. Bell, T.L. Ng, A.D. Walsh, J. Chem. Soc. Trans. II 1 (1975) 393.
[6] T. Ari, M. Haluk Güven, J. Electron Spectrosc. Rel. Phenom. 106 (2000) 29.
[7] A. Burneau, F. Génin, F. Quilès, Phys. Chem. Chem. Phys. 2 (2000) 5020.
[8] U. Mölder, I. Koppel, P. Burk, R. Pikver, Int. J. Quantum Chem. 62 (1997) 303.
[9] K. Kimura, S. Katsumata, T. Yamazaki, H. Wakabayashi, J. Elect. Spectrosc. Relat. Phenom. 6 (1975) 41.
[10] F. Carnovale, T.H. Gan, J.B. Peel, J. Electron Spectrosc. Relat. Phenom. 20 (1980) 53.
[11] T. ShimanouchiTables of Molecular Vibrational Frequencies Consolidated, vol. I, National Bureau of Standards, 1972, p. 1.
[12] www.isa.au.dk/SR/UV1/uv1.html.
[13] N.J. Mason, J.M. Gingell, J.A. Davis, H. Zhao, I.C. Walker, M.R.F. Siggel, J. Phys. B 29 (1996) 3075.
[14] F. Motte-Tollet, M.-J. Hubin-Franskin, J.E. Collin, J. Chem. Phys. 97 (1992) 7314.
[15] R.H. Huebner, R.J. Celotta, S.R. Mielczarek, C.E. Kuyatt, J. Chem. Phys. 59 (1973) 5434.
[16] A. Giuliani, J. Delwiche, S.V. Hoffmann, P. Limão-Vieira, N.J. Mason, M.-J. Hubin-Franskin, J. Chem. Phys. 119 (2003) 3670.
[17] J. Delwiche, P. Natalis, J. Momigny, J.E. Collin, J. Electron Spec. Relat. Phenom. 1 (1972) 219.
[18] J.H.D. Eland, Photoelectron Spectroscopy, Butterworths, London, 1984.
[19] E.V. Gromov, A.B. Trofimov, N.M. Vitkovskaya, J. Schirmer, H. Köppel, J. Chem. Phys. 119 (2003) 737.
[20] F. Aquilante, V. Barone, B.O. Roos, J. Chem. Phys. 119 (2003) 12323.
[21] J.P. Perdew, M. Ernzerhof, K. Burke, J. Chem. Phys. 105 (1996) 9982.
[22] C. Adamo, V. Barone, J. Chem. Phys. 110 (1999) 6158.
[23] M.J. Frisch et al., Gaussian 03, Revision B.05, Gaussian, Inc., Wallingford, CT, 2003.
[24] K. Watanabe, J. Chem. Phys. 26 (1957) 542.
[25] D.J. Knowles, A.J.C. Nicholson, J. Chem. Phys. 60 (1974) 1180.
[26] U. Mölder, I. Koppel, P. Burk, R. Pikver, Int. J. Quantum Chem. 62 (1997) 303.
[27] S. Nagakura, K. Kaya, H. Tsubomura, J. Mol. Spectrosc. 13 (1964) 1.
[28] L. Turi, J.J. Dannenberg, J. Phys. Chem. 97 (1993) 12197.
[29] J.L. Derissen, J. Mol. Struct. 7 (1971) 67.
[30] W.-H. Fang, R.-Z. Liu, X. Zheng, D.L. Phillips, J. Org. Chem. 67 (2002) 8407.

Article 6

PHYSICAL REVIEW A **76**, 032509 (2007)

Perfluorocyclobutane electronic state spectroscopy by high-resolution vacuum ultraviolet photoabsorption, electron impact, He I photoelectron spectroscopy, and *ab initio* calculations

P. Limão-Vieira,[1,2,*] E. Vasekova,[2] A. Giuliani,[3,4] J. M. C. Lourenço,[1] P. M. Santos,[5] D. Duflot,[6] S. V. Hoffmann,[7] N. J. Mason,[2] J. Delwiche,[3] and M.-J. Hubin-Franskin[3]

[1]*Laboratório de Colisões Atómicas e Moleculares, Departamento de Física, CEFITEC, Universidade Nova de Lisboa, P-2829-516 Caparica, Portugal*

[2]*Centre of Molecular and Optical Sciences, Department of Physics and Astronomy, The Open University, Walton Hall, Milton Keynes MK7 6AA, United Kingdom*

[3]*Laboratoire de Spectroscopie d'Électrons diffusés, Université de Liège, Institut de Chimie-Bât. B6c, B-4000 Liège 1, Belgium*

[4]*DISCO beamline, Synchrotron SOLEIL, BP 48, L'Orme des Merisiers, 91192 Gif-sur-Yvette CEDEX, France and Cepia, Institut National de la Recherche Agronomique, BP 71627, F-44316, Nantes, France*

[5]*Instituto de Telecomunicações, IST, Avenida Rovisco Pais, P-1049-001 Lisboa, Portugal*

[6]*Laboratoire de Physique des Lasers, Atomes et Molécules (PhLAM), UMR CNRS 8523, Centre d'Études et de Recherches Lasers et Applications CERLA, (CNRS 2416), Université des Sciences et Technologies de Lille, F-59655 Villeneuve d'Ascq Cedex, France*

[7]*Institute for Storage Ring Facilities, University of Aarhus, Ny Munkegade DK-8000, Århus C, Denmark*

(Received 3 July 2007; published 24 September 2007)

The electronic state spectroscopy of perfluorocyclobutane (c-C_4F_8) has been investigated using high resolution vacuum ultraviolet (vuv) photoabsorption spectroscopy in the energy range 6.0–11 eV. The electron energy loss spectrum (EELS) was also recorded in the nonelectric dipolar interaction mode (100 eV incident energy, 10° scattering angle) over the 8–14 eV energy-loss range and the excited states in the 11–14 eV spectral region have been observed. An He I photoelectron spectrum recorded between 11.0 and 19.8 eV is compared with earlier lower resolution results. This has allowed us to derive a more precise value of 12.291 ± 0.002 eV for the ground neutral state vertical ionization energy. All spectra presented in this paper represent the highest resolution data yet reported for perfluorocyclobutane, to the best of our knowledge. *Ab initio* calculations have been performed for helping in the assignment of the spectral bands for both neutral excited states and ionic states.

DOI: 10.1103/PhysRevA.76.032509 PACS number(s): 33.20.−t, 33.60.Cv, 33.70.Ca, 31.15.Ar

I. INTRODUCTION

Perfluorocyclobutane, c-C_4F_8, is widely used for many diverse technologies from gaseous dielectric devices to retinal detachment surgery. Recently it has been used as a feed gas for SiO_2 reactive ion etching in the semiconductor industry being cited as a potential replacement of the traditional plasma processing molecules [1], e.g., CF_4, SF_5CF_3, and SF_6. However, c-C_4F_8 has a high global warming potential (GWP) of 8700 [2] and a long atmospheric lifetime depending on the sink mechanism in the upper atmosphere (the estimated lifetime due to photolysis and electron interactions being 1400 and 3200 years, respectively [2,3]). Determining the GWP and lifetime of any atmospheric molecule requires both knowledge of the electronic state spectroscopy and the absolute photoabsorption cross section in the visible and vacuum ultraviolet (vuv) region of the spectrum [4]. As part of a larger project to investigate the electronic state spectroscopy of several plasma processing molecules and to evaluate their role in global warming in the Earth's atmosphere, we have recorded a high-resolution vuv photoabsorption spectrum of c-C_4F_8. As far as we are aware, no other spectra have been reported in the literature. These results are compared with an electron energy-loss spectrum.

In contrast to the paucity of data for photon absorption there have been several studies of electron interactions with c-C_4F_8. Christophorou and Olthoff [1] assembled a detailed compilation of recommended electron collision cross sections and transport-coefficient data for c-C_4F_8 that has been updated by (i) Winstead and McKoy [5], who calculated absolute cross sections for elastic and inelastic collisions of low-energy electrons using the Schwinger multichannel (SMC) method and (ii) experimentally derived absolute cross sections for elastic scattering and vibrational excitation by Jelisavcic *et al.* [6]. Miller *et al.* [7] have recently reported measurements on rate constants for electron attachment and thermal detachment to c-C_4F_8; they also performed Gaussian-3 second-order Moller-Plesset perturbation theory G3(MP2) and density-functional theory (DFT) calculations for ground state neutral geometry and information on efficiency of electron attachment. Energy-loss spectra in these experiments and excitation energies derived by theory are used to help assign the major bands in the photoabsorption spectra. Further information is derived from a high-resolution photoelectron spectrum which is used to identify the position of Rydberg states in the vuv spectrum.

The vuv absolute photoabsorption cross section spectrum has been used to derive the photolysis lifetime of c-C_4F_8 in the terrestrial atmosphere.

*Corresponding author. Present address: Laboratório de Colisões Atómicas e Moleculares, Departamento de Física, CEFITEC, Universidade Nova de Lisboa, P-2829-516 Caparica, Portugal. Fax: +351—21 294 85 49; plimaovieira@fct.unl.pt

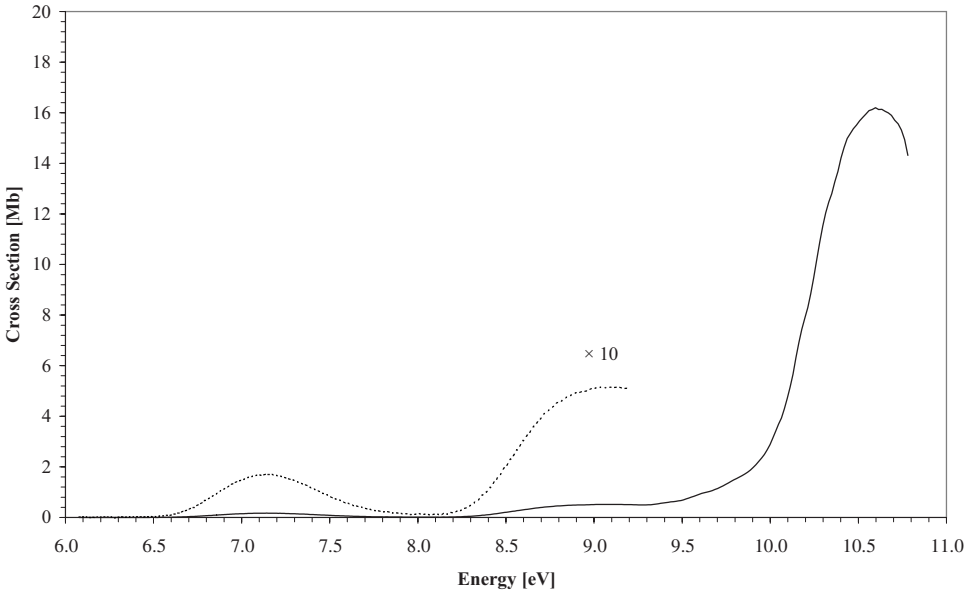

FIG. 1. High resolution vuv photoabsorption spectrum of c-C_4F_8 recorded using Aarhus synchrotron facility in the 6.0–10.8 eV energy range.

II. EXPERIMENTAL SECTION

In order to study the spectroscopy of c-C_4F_8 we used a range of different techniques: vuv photoabsorption using a synchrotron source, which provides data on optical allowed transitions, high-resolution electron-energy-loss spectroscopy (HREELS), which allows forbidden as well as allowed transitions to be monitored, and photoelectron spectrum (PES) to determine the ionization energies.

A. vuv photoabsorption

The present high-resolution vuv photoabsorption measurements (Figs. 1 and 2) were performed using the ASTRID-UV1 beam line at the Institute for Storage Ring Facilities (ISA), University of Aarhus, Denmark. A detailed description of the apparatus can be found elsewhere [8], so only a brief description will be given here. A toroidal dispersion grating is used to select the synchrotron radiation with a full width at half maximum (FWHM) wavelength resolution of approximately 0.075 nm. The synchrotron radiation passes through the gas sample stored in a gas cell maintained at room temperature. A photomultiplier is used to detect the transmitted light. For wavelengths below 200 nm a flow of He gas is flushed through the small gap between the photomultiplier and the exit window of the gas cell to prevent any absorption by air contributing to the spectrum. A LiF entrance window acts as an edge filter for higher order radiation restricting the photoabsorption measures to below 10.8 eV (115 nm). The grating itself provides a maximum wavelength (lower energy limit) of 320 nm (3.9 eV). The sample pressure is measured by a Baratron capacitance gauge. To avoid any saturation effects sample pressures were chosen such that the transmitted flux was $>10\%$ of the incident flux.

Gas transmission results are compared to a background scan recorded with an evacuated cell. Absolute photoabsorp-

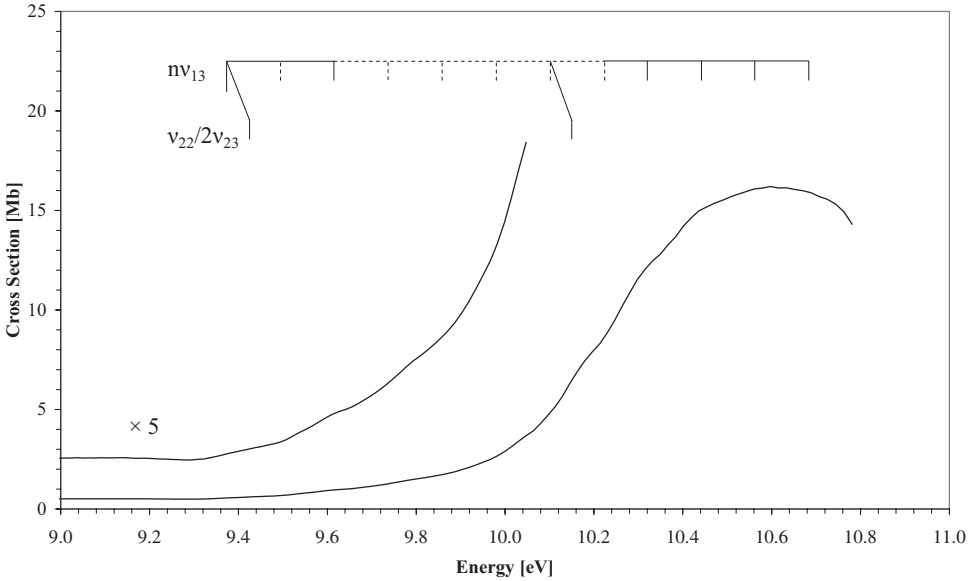

FIG. 2. High resolution vuv photoabsorption spectrum of c-C_4F_8 showing weak vibrational progressions in the 9.0–10.8 eV energy range.

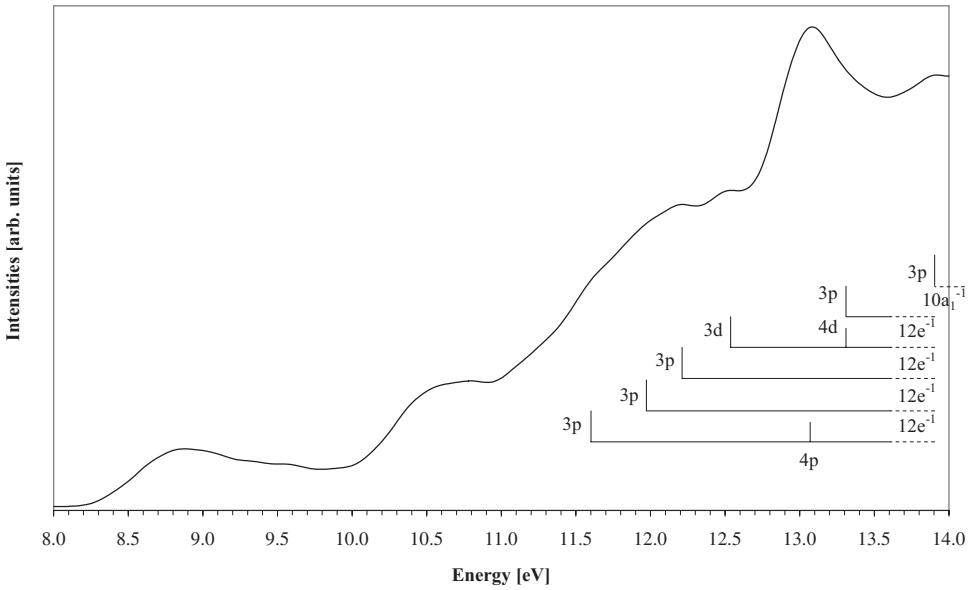

FIG. 3. Electron-energy-loss spectrum of c-C_4F_8 recorded at the University of Liège in the 8.0–14.0 eV energy region in the nonelectric dipolar interaction conditions (100 eV incident energy, 10° scattering angle).

tion cross sections may then be calculated using the Beer-Lambert law:

$$I_t = I_0 \exp(-n\sigma x),$$

where I_t is the intensity of the light transmitted through the gas sample, I_0 is that through the evacuated cell, n is the molecular number density of the sample gas, σ is the absolute photoabsorption cross section, and x is the absorption path length (25 cm). The accuracy of the absolute cross section is estimated to be better than ±5%.

B. High-resolution electron-energy-loss spectroscopy

The instrument used at the Université de Liège, Belgium (VG-SEELS 400) has been described in detail elsewhere [9]. An electrostatic electron energy monochromator defines a narrow energy spread about the mean incident electron energy and a three element lens focuses the electrons into the collision region. The electron beam intersects the effusive gas beam, which flows through a hypodermic needle, at 90°. The working pressure is $\sim 1.5 \times 10^{-5}$ mbar. The analyzer system is also an electrostatic energy analyzer [9] with the scattered electron signal detected by an electron multiplier of the continuous dynode type. Both electron energy selectors work in the constant pass-energy mode. Spectra were recorded for energy losses between 8.0 and 14 eV at step intervals of 10 meV. The electron-energy-loss scale was calibrated to the "elastic scattering peak." The resolution, measured as the FWHM of the elastically scattered electron peak, was about 40 meV. The apparatus was used with relatively high incident energy electrons (100 eV) and a small scattering angle ($\theta = 10°$), such that nonelectric dipole interaction conditions apply. The present HREEL spectrum is shown in Fig. 3.

C. Photoelectron spectroscopy

He I (21.22 eV) photoelectron spectra of c-C_4F_8 were recorded at the Université de Liège, Belgium (Fig. 4). The experimental setup has been described in detail elsewhere [10]. Briefly, the spectrometer consists of a 180° hemispherical electrostatic analyzer with a mean radius of 5 cm. The analyzer is used in constant energy pass mode and is fitted with a continuous dynode electron multiplier. Incident photons are produced by a dc discharge in a two-stage differentially pumped lamp. The energy scale was calibrated using the $^2P_{3/2}$ (12.130 eV) and $^2P_{1/2}$ (13.436 eV) xenon peaks [11] for the low ionization energy part of the spectrum (up to 15.420 eV) and the $^2P_{3/2}$ (15.759 eV) and $^2P_{1/2}$ (15.937 eV) argon peaks [12] for the upper part. The spectra are corrected for the transmission function of the apparatus. The resolution of the present spectrum is measured from the FWHM of the Ar peaks to be 20 meV, in the presence of c-C_4F_8. The accuracy of the energy scale is estimated to be ±2 meV. The photoelectron spectrum presented in this paper is the sum of 20 individual spectra. This procedure allowed us to obtain a good signal-to-noise ratio while keeping the pressure in the spectrometer at a very low level ($<2 \times 10^{-6}$ mbar).

D. Perfluorocyclobutane sample

The gas sample used in the vuv measurements was purchased from Fluorochem, with a minimum purity of 99%, while for photoelectron spectroscopy (PES) and HREELS experiments the sample was purchased from ABCR with a quoted 99% purity.

III. COMPUTATIONAL SECTION

To complement and help to interpret our experimental results, we performed *ab initio* calculations to determine vertical excitation energies of the electronic states and the lowest ionization energies.

It is well known that the calculation of electronic spectra, even for small organic molecules, is a difficult task (see Ref. [13] for a recent review). Because of its low computational cost, the time-dependent density-functional theory (TDDFT) method has recently become a very popular method [14] and

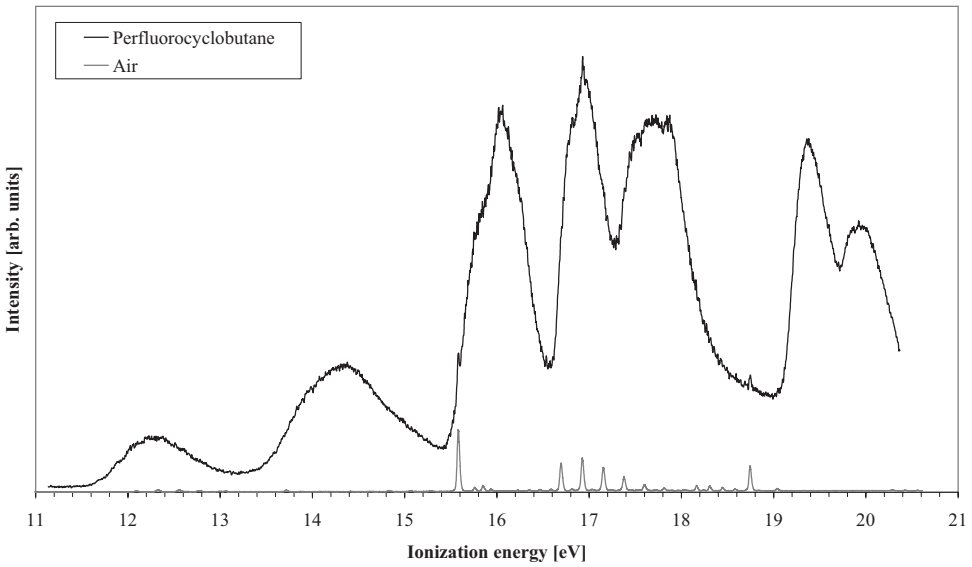

FIG. 4. He I photoelectron spectra of c-C_4F_8 and air which is present as a contaminant in very small amounts (see text), recorded at the University of Liège.

in the case of the acrolein molecule, the PBE0 functional of [15,16] was shown to give results in good agreement with more costly calculations [i.e., multiple scattering-complete-active-space second-order perturbation theory (MS-CASPT2]. Therefore, the same method was employed in the present work: the geometry was optimized at the DFT/PBE0/6–311G** level (Table I) and the electronic excitation spectrum was calculated at the TDDFT//PBE0/6–311++G** level (Table II). These calculations were performed with the GAUSSIAN 03 package [17]. However, it is also well known [13,14] that TDDFT presents problems with the description of certain types of electronic states, including Rydberg states. Thus, the lowest lying excited states were also computed at the CCS, CC2 [18], and CCSD [19] levels (second-order approximate coupled cluster single, double and single and double excitations level, respectively) with the DALTON program [20] (Table III). The geometry was optimized at the second-order Moller-Plesset correlation-consistent polarization valence double ζ (MP2 cc-pVDZ) level and then diffuse functions $(5s,5p,5d)$ taken from Kaufmann *et al.* [21] were added at the center of the molecule (cc-pVDZ+R basis set). These calculations were performed in the C_{2v} group, which is the largest Abelian subgroup of D_{2d}. Finally, the lowest ionization energies of c-C_4F_8 were obtained with the same geometry and basis set (Table IV) at the RCCSD {single-configuration [spin restricted (R)] coupled-cluster approach including single and double} [22], RCCSD(T) {single-configuration [spin restricted (R)] coupled-cluster approach including single and double and a perturbative estimate of triple excitations} [23], and MR-AQCC (multireference averaged quadratic coupled cluster) [24] levels, using the MOLPRO package [25]. For the MR-AQCC calculations, the reference space was limited to the ROHF (restricted open Hartree-Fock) determinant of the first ionic state of each symmetry.

IV. RESULTS AND DISCUSSION

A. Structure and properties of c-C_4F_8

The calculated geometry is shown in Fig. 5(a) and the corresponding parameters are listed in Table I. Using this

TABLE I. Calculated geometry of c-C_4F_8 compared with previous works (bond lengths in Å and angles in degrees).

	Cation ($^2B_1$) PBE0[a] 6–311 G**	Ground state PBE0[a] 6–311 G**	MP2[a] cc-pVDZ	G3(MP2)[b]	B3LYP[c] 6–31 G*	MP2[c] 6–31 G*	Experiment[d]	Anion (^2A_u) G3(MP2)[b]
C-C	1.6398	1.5611	1.5587	1.550	1.566	1.552	1.566±0.008	1.489
C-F_1	1.2973	1.3345	1.3462	1.350	1.346	1.353	1.333±0.002	1.489
C-F_2	1.2901	1.3287	1.3367	1.340	1.340	1.342	1.333±0.002	1.489
CCC	88.1	89.4	88.5		89.4	88.6	89.3±0.3	
F_1CC	111.4	112.2	111.3		112.1	110.9		
F_2CC	115.4	115.7	116.8		115.5	116.9		
F_1CF_2	113.0	110.4	110.6		110.7	111.0	109.9±0.3	
CCCC	20.7	12.0	18.2	17.1	10.5	17.7	17.4	

[a]This work.
[b]Reference [7].
[c]Reference [27].
[d]Reference [34].

TABLE II. Calculated vertical excitation energies (TDDFT/PBE0/6–311++G**//PBE0/6–311 G**) of c-C_4F_8 (eV) and oscillator strengths of the lowest lying states.

Symmetry	Energy[a] (eV)	f	Main character	Experiment[b] (eV)
$^1A_2$	6.695	—	$3b_1 \rightarrow \sigma^*$(C-F)/$\pi$(C-C)($b_2$)	7.142
$^1B_1$	8.404	—	$3b_1 \rightarrow 3s(a_1)$	9.143
^1E	8.597	0.0005	$12e \rightarrow 3p(e)$	—
^1E	9.717	0.0007	$3b_1 \rightarrow 3p(e)$	—
$^1B_2$	9.992	0.0008	$10a_1 \rightarrow \sigma^*$(C-F)/$\pi$(C-C)($b_2$)	—
^1E	10.065	0.0176	$12e \rightarrow 3s(a_1)$	—
^1E	10.104	0.0311	$11e \rightarrow \sigma^*$(C-F)/π(C-C)(b_2)	10.597
$^1A_2$	10.275	—	$2b_1 \rightarrow \sigma^*$(C-F)/$3p\pi(b_2)$	—
$^1A_2$	10.509	—	$3b_1 \rightarrow 3p\pi(b_2)$	—
$^1A_1$	10.676	—	$9b_2 \rightarrow \sigma^*$(C-F)/$\pi$(C-C)($b_2$)	—
$^1A_2$	10.885	—	$3b_1 \rightarrow 3d(b_2)$	—
^1E	10.892	0.0049	$10e \rightarrow \sigma^*$(C-F)/π(C-C)(b_2)	10.597
^1E	10.970	0.0014	$3b_1 \rightarrow 3d(e)$	10.597
$^1A_1$	10.970	—	$3b_1 \rightarrow 3d(b_1)$	—
$^1B_1$	10.987	—	$3b_1 \rightarrow 3d(a_1)$	—
$^1B_2$	11.267	0.0357	$9a_1 \rightarrow \sigma^*$(C-F)/$\pi$(C-C)($b_2$)	—
$^1B_1$	11.277	—	$1a_2 \rightarrow \sigma^*$(C-F)/$\pi$(C-C)($b_2$)	—
			$+2a_2 \rightarrow \sigma^*$(C-F)/$\pi$(C-C)($b_2$)	—
$^1A_1$	11.335	—	$10a_1 \rightarrow 3s(a_1)$	—
$^1B_1$	11.347	—	$1a_2 \rightarrow \sigma^*$(C-F)/$\pi$(C-C)($b_2$)	—
			$+2a_2 \rightarrow \sigma^*$(C-F)/$\pi$(C-C)($b_2$)	—
$^1A_1$	11.394	—	$12e \rightarrow 3p(e)$	—
			$+3b_1 \rightarrow 4s(a_1)$	—
$^1A_2$	11.414	—	$12e \rightarrow 3p$(e)	—
$^1B_2$	11.420	0.0024	$12e \rightarrow 3p$(e)	—
^1E	11.477	<0.0001	$11e \rightarrow 3s(a_1)$	—
$^1B_1$	11.478	—	$12e \rightarrow 3p(e)$	—
$^1B_1$	11.486	—	$3b_1 \rightarrow 4p(e)$	—
			$+12e \rightarrow 3p(e)$	—
^1E	11.530	0.1439	$3b_1 \rightarrow 4p(e)$	—
Ion[a] ($^2B_1$)	11.653	—	—	—

[a]PBE0/6–311 G** value.
[b]This work.

geometry, the calculated electron configuration of the $\tilde{X}\ ^1A_1$ ground state of c-C_4F_8 is

(a) core 1s orbitals $1a_1^2\ 1e^4\ 1b_2^2\ 2b_2^2\ 2e^4\ 2a_1^2\ 3a_1^2\ 3e^4\ 3b_2^2$;
(b) σ(C-F) orbitals $4a_1^2\ 4e^4\ 4b_2^2\ 5b_2^2\ 5e^4\ 5a_1^2$;
(c) σ(CC) orbitals $6a_1^2\ 6e^4\ 6b_2^2$;
(d) p(F) lone pairs $7a_1^2\ 7b_2^2\ 1b_1^2\ 7e^4\ 8e^4\ 8a_1^2\ 9e^4\ 8b_2^2\ 1a_2^2\ 2a_2^2\ 9a_1^2\ 10e^4\ 9b_2^2\ 2b_1^2\ 11e^4\ 10a_1^2\ 12e^4$;
(e) σ(C-C)/p(F) lone pair $3b_1^2$.

The highest occupied molecular orbital (HOMO) in the neutral ground state is localized on the fluorine lone pair electrons with σ(C-C)/$n_F(3b_1)$ mixing character as shown in Fig. 5(b), using the MOLDEN software [26].

The lowest unoccupied molecular orbital (LUMO) is the σ^*[C-F($10b_2$)] orbital, with a slightly π(C-C) bonding character [Fig. 5(c)]. A few vertical ionization energy values for c-C_4F_8 have been reported by Christophorou and Olthoff [1] for the $3b_1^{-1}$ orbital in reasonable agreement with our present high-resolution He I photoelectron spectrum (see Sec. IV E). Excitation of a $3b_1$ electron may also lead to Rydberg state members of series converging to the ionic ground electronic state.

The ground state geometry calculated with the two methods (PBE0 and MP2) is compared with previous works in Table I. Bond lengths at PBE0 level are in better agreement with experiment than MP2 values. On the other hand, the MP2 ring-puckering angle [see Fig. 5(a)] of 18.2° is closer to experiment (17.4°) than the PBE0 result of 12.0°. The first column of Table I shows the optimized geometry of the first cationic state ($3b_1^{-1}$ ionization). The increase of C-C bond length when compared to the neutral molecule is consistent with the C-C bonding nature of the HOMO as displayed in Fig. 5: removal of an electron from the HOMO weakens the

TABLE III. (a) Calculated vertical excitation energies (CC/cc-pVDZ+R//MP2/cc-pVDZ) of c-C_4F_8 (eV), oscillator strengths of the lowest lying states and present experimental vuv and EELS data (see discussion in text); (b) tentative assignments for the 11–14 eV EELS band.

(a)

	CCS E (eV)	f_L	CC2[a] E (eV)	f_L	CCSD[a] E (eV)	f_L	Main character[a,b]	Experiment[a] vuv	(eV) EELS
$^1A_2$	9.09	—	7.37	—	7.73	—	$3b_1 \rightarrow \sigma^*$(C-F)/$\pi$(C-C)($b_2$)	7.142	—
—	—	—	—	—	—	—	—	—	8.880
$^1B_1$	10.94	—	8.54	—	9.04	—	$3b_1 \rightarrow 3s(a_1)$	9.143	9.000
^1E	11.43	0.0030	9.49	0.0010	9.87	0.0008	$3b_1 \rightarrow \sigma^*$(C-F)/$\pi$(C-C)($b_2$)	—	9.520
^1E	11.88	<0.0001	9.40	0.0052	9.98	0.0033	$3b_1 \rightarrow 3p(e)$	—	9.520
$^1A_2$	12.19	—	9.62	—	10.24	—	$3b_1 \rightarrow 3p\pi(b_2)$	—	—
$^1B_1$	12.42	—	9.94	—	10.57	—	$3b_1 \rightarrow 3d(a_1)$	—	—
$^1A_1$	12.56	<0.0001	10.01	<0.0001	10.66	<0.0001	$3b_1 \rightarrow 3d(b_1)$	10.597	10.780
$^1A_2$	12.63	—	10.05	—	10.71	—	$3b_1 \rightarrow 3d(b_2)$	—	—
^1E	12.68	0.0005	10.08	<0.0001	10.74	<0.0001	$3b_1 \rightarrow 3d(e)$	—	—
^1E	12.80	0.0466	10.29	0.0025	10.87	0.0223	$12e \rightarrow 4s(a_1)+3b_1 \rightarrow 4p(e)$	10.597	10.780

(b)

This work EELS (eV)	Tentative assignment	Ionization energy limit (eV)	Quantum defect
11.300	—	—	—
11.660	3p	14.336	0.75
11.980	3p	14.336	0.60
12.220	3p	14.336	0.47
12.540	3d	14.336	0.25
13.080	4p	14.336	0.71
13.320	4d/3p	14.336/16.055	0.34/0.77
13.920	3p	16.055	0.48

[a]This work.
[b]From CCS wave functions.

C-C bond and increases its bond length. It is also interesting to compare the ground state geometry with that of the anion molecule c-$C_4F_8^-$, calculated by Miller *et al.* [7], which has the peculiarity of having a planar carbon ring and symmetry (D_{4h}) higher than the neutral species. The lengthening of the C-F bonds and shortening of the C-C bonds in the anion with respect to the neutral is fully consistent with the σ^*(C-F) and π(C-C) character of the LUMO.

TABLE IV. Calculated and experimental He I photoelectron ionization energies of c-C_4F_8 (values in eV).

Configuration	RCCSD[a]	RCCSD(T)[a]	MR-AQCC[a]	OVGF[b]	Experiment[a]
$3b_1^{-1}$	12.086	11.763	12.123	12.1	12.291
$12e^{-1}$	14.047	13.687	14.016	14.0	14.336
$11e^{-1}$			15.979		16.055
$10a_1^{-1}$	16.237	15.628	15.986		16.055
$2b_1^{-1}$			16.572		16.946
$9b_2^{-1}$			16.594		16.946
$10e^{-1}$			16.923		16.946
$2a_2^{-1}$			17.345		17.524/17.692
$9e^{-1}$			17.600		17.692/17.848
$8e^{-1}$			19.914		19.932

[a]This work.
[b]Reference [30]. Values obtained at the MP2/6–311 G+(d,p) geometry.

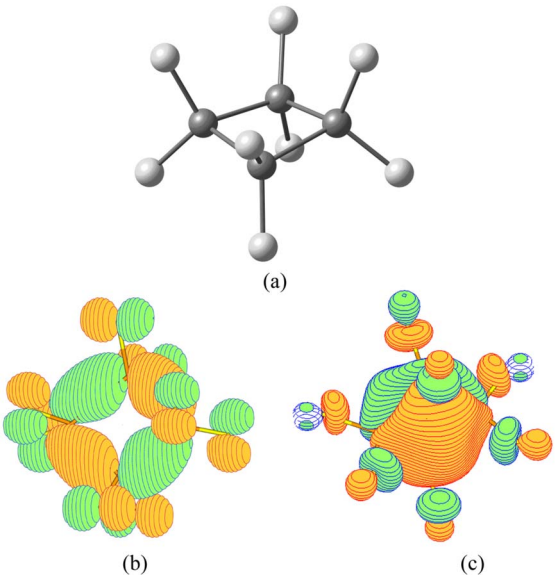

FIG. 5. (Color online) (a) Ground-state structure of c-C_4F_8; (b) highest occupied molecular orbital (HOMO) of c-C_4F_8; (c) lowest unoccupied molecular orbital (LUMO) of c-C_4F_8.

In its ground neutral electronic state c-C_4F_8 has D_{2d} symmetry, with 23 modes of vibration [6]. In the present high-resolution absorption spectrum, very weak vibrational modes with mean excitation energies of 0.120 and 0.046 eV were observed. Comparing these values with vibrational energies of the ground state [27], these have been tentatively assigned (Table V) by comparison with the unfluorinated analog c-C_4H_8 [28], to the $\nu_{13}(b_2)$ CF_2 symmetric stretching (0.152 eV) and the $\nu_{22}(e)$ CF_2 wagging (0.055 eV) or $2\nu_{23}(e)$ ring deformation (0.048 eV) modes, respectively.

The calculated transition energies, oscillator strengths, and the main character of the wave function are shown in Tables II (TDDFT results) and III (CC results). Due to the high symmetry of the molecule, many transitions are electric-dipole forbidden. The comparison between the two tables shows several patterns which are well known in the calculations of electronic spectra [13,14]: the CCS (or CIS) values give too large energies and this method has no quantitative accuracy. There are also differences of several tenths of an eV between TDDFT and both CC values and it seems that the CCSD values are larger than CC2 by about 0.5 eV. Except for transitions to the LUMO, which has valence character, the TDDFT method is expected to give overestimated results for Rydberg transitions. A possible hierarchy of the

TABLE V. Calculated vibrational energies for both ground and lowest ionic states of c-C_4F_8 (energies in eV).

D_{2d} species	Calculation: neutral ground state[a]	Experiment[b] (IR spectroscopy)	Experiment[b] (Raman spectroscopy)	Calculation: ionic ground state[a]
a_1	0.182	—	0.178	0.178
	0.162	—	0.175	0.172
	0.089	—	0.087	0.090
	0.076	—	0.075	0.071
	0.046	—	0.045	0.044
	0.005	—	—	0.007
a_2	0.110	—	—	0.102
	0.027	—	—	0.025
b_1	0.127	—	0.125	0.118
	0.034	—	0.032	0.032
	0.032	—	—	0.028
b_2	0.162	0.160	0.160	0.174
	0.157	0.152	0.152	0.161
	0.083	0.082	0.082	0.084
	0.043	0.043	0.044	0.044
	0.024	0.035	—	0.022
e	0.169	0.166	0.166	0.169
	0.155	0.154	—	0.145
	0.122	0.119	—	0.078
	0.071	0.071	—	0.055
	0.055	0.055	0.054	0.037
	0.035	—	0.034	0.031
	0.023	0.024	0.024	0.017

[a]This work (PBE0/6–311 G**).
[b]Reference [28].

TABLE VI. Vibrational assignments in the 9.0–11.0 eV absorption band of c-C_4F_8. Assignment within brackets (?) means uncertainty; (d) means diffuse structure.

This work Energy (eV)	Assignment	$\Delta E(\nu_{13})$ (eV)	$\Delta E(\nu_{21}/2\ \nu_{23})$ (eV)
9.372	ν_{00}	—	—
9.421	$1\nu_{22}/1\nu_{23}$	—	0.049
9.493 (d)	$1\nu_{13}$(?)	—	—
9.611	$2\nu_{13}$	0.118	—
9.740 (d)	$3\nu_{13}$(?)	—	—
9.856 (d)	$4\nu_{13}$(?)	—	—
9.983 (d)	$5\nu_{13}$(?)	—	—
10.104 (d)	$6\nu_{13}$(?)	—	—
10.146	$6\nu_{13}+1\nu_{22}/1\nu_{23}$	—	0.042
10.213 (d)	$7\nu_{13}$(?)	—	—
10.315	$8\nu_{13}$	0.102	—
10.436	$9\nu_{13}$	0.121	—
10.561	$10\nu_{13}$	0.125	—
10.688	$11\nu_{13}$	0.127	—

present calculations could thus be CCS < TDDFT < CC_2 < CCSD.

B. Neutral excited states

The high-resolution absolute vuv photoabsorption spectrum of perfluorocyclobutane recorded between 6.0 and 11.0 eV using the Aarhus synchrotron facility is shown in Figs. 1 and 2.

Three absorption bands centered at 7.142, 9.143, and 10.597 eV may be identified as transitions from the $\tilde{X}\,^1A_1$ neutral ground state to the $^2A_1$, $^1B_1$, and $^1A_1$ states, respectively (Tables II and III). All bands are quite broad (Fig. 1) suggesting rapid dissociation into neutral radicals with only diffuse, not very well resolved, structure being observed in the latter (Table VI) and reported here. The transitions involved for each band have been assigned to $10b_2$: $^1A_2 \leftarrow 3b_1$: $\tilde{X}\,^1A_1$ [5], $3s \leftarrow 3b_1(^1B_1 \leftarrow \tilde{X}\,^1A_1)$, and $3d \leftarrow 3b_1(^1A_1 \leftarrow \tilde{X}\,^1A_1)$, respectively (Table III). Following the assignment proposed by Winstead and McKoy [5] for the first, weak absorption feature, it was attributed to the excitation of an electron from the HOMO centered on the fluorine lone pair (n) to the LUMO of C-F($10b_2$) σ^* antibonding character. A transition into the singlet A_2 state is symmetry disfavored by the forbidden dipole-electric transition and reinforced by the very weak magnitude observed in the present spectra (the local maximum cross sectional value is 0.171 Mb). However, and due to the fact that c-C_4F_8 shows two reflection planes containing the symmetry axis, the forward and backward excitation cross sections in the electron interaction are reduced but not entirely suppressed as stated in Ref. [5]. Symmetry disfavored by forbidden dipole-electric transitions is also remarkable for the B_1 state with a low cross sectional value of 0.515 Mb. The present calculations, reported in Tables II and III, for the two lowest absorption bands are in good agreement with the assignments proposed previously. As far as the assignment of the third band is concerned, the calculations show a mixing of several Rydberg transitions $(3p, 3d, \ldots)$. However, and due to the broad nature of this band, a predictable transition to a σ^*(C-F) antibonding orbital with a high oscillator strength value may be possible (Table II).

C. Vibrational excitation in the energy range 9.0–11.0 eV

The vuv spectrum in this energy region is a broad continuum (Figs. 1 and 2) with two maxima lying at 9.143 eV (0.515 Mb) and 10.597 eV (16.201 Mb), respectively. However superimposed upon these is a weak structure which may be ascribed to Rydberg character (see Rydberg series section). The band also exhibits an extended poorly defined progression which may be ascribed to the CF_2 symmetric stretching, $\nu_{13}(b_2)$ and the CF_2 wagging, $\nu_{22}(e)$ or ring deformation, $2\nu_{23}(e)$ modes (Table VI). Recently, for the neutral ground state, Jelisavcic *et al.* [6] have observed by electron impact that due to the limited resolution (50 meV) available in their experiments, most of the low-energy modes could not be resolved from the elastic peak as well as some of the high-energy modes and their overtones. However, the ~120 meV structure observed ($\Delta\nu_{13}$) is reinforced by the IR presence at ~120 and 157 meV, which we also report in the calculation results of Table V (0.161 eV). Due to the difficulty in assigning a vibrational mode to the mean excitation energy of 0.046 eV, we have decided to label the weak excitation series starting at 9.421 eV as $\nu_{22}/2\nu_{23}$. $\Delta\nu_{22}$ and $\Delta 2\nu_{23}$ are almost in the ratio 1:2, and therefore the normal mode description of vibrations for the lowest lying excitations may be related to possible strong Fermi resonance.

D. Rydberg series

The cross section above 9 eV consists of two large maxima assigned also to Rydberg structure progressing up to the lowest ionization limit, 12.291 eV (Fig. 3). The peak positions, E_n, must fit the Rydberg formula: $E_n = E_i - R/(n-\delta)^2$, where E_i is the ionization energy, n is the principal quantum number of the Rydberg orbital of energy E_n, R is one Rydberg, and δ is the quantum defect resulting from the penetration of the Rydberg orbital into the core. The two bands at 9.143 and 10.597 eV (Fig. 1) have been identified to correspond to the $3s \leftarrow 3b_1(^1B_1 \leftarrow \tilde{X}\,^1A_1)$ and $3d \leftarrow 1b_1(^1A_1 \leftarrow \tilde{X}\,^1A_1)$ Rydberg transitions, with quantum defects δ of 0.92 and 0.17, respectively. A comparison of the calculated vertical excitation energies in Table III with the present vuv photoabsorption and electron-energy-loss (EEL) features shows some tentative assignments for the structure observed. The electron-energy-loss weak shoulder feature at 11.300 eV remains unassigned. The relative intensity of the spectral bands in the EEL spectrum is different from those in the optical absorption due to the fact that symmetry forbidden transitions are expected to be excited in interaction conditions prevailing in the EEL spectrum.

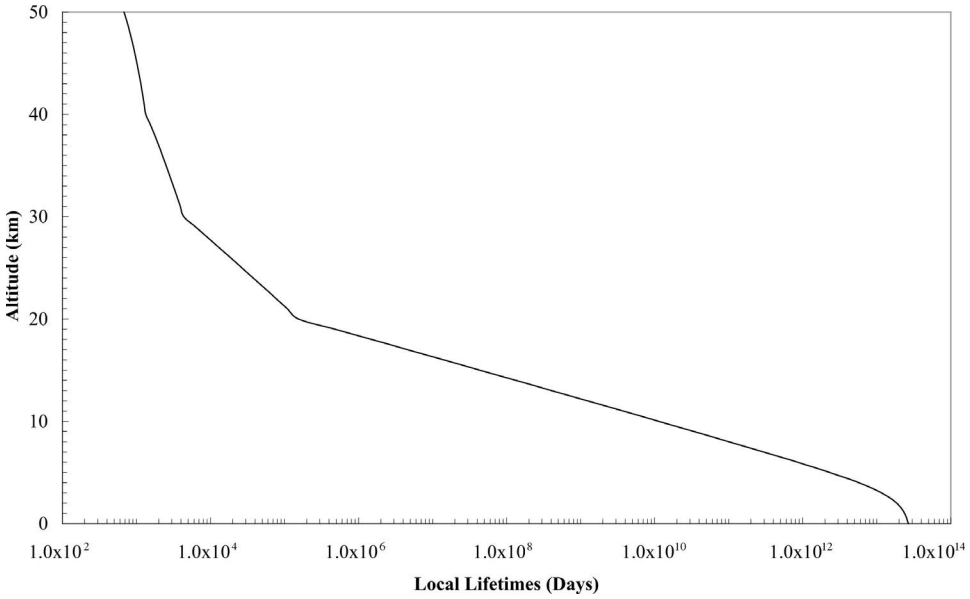

FIG. 6. The local lifetime of perfluorocyclobutane between 0 and 50 km obtained from its vuv photoabsorption spectrum shown in Fig. 1.

E. Ionic states

Figure 4 shows the bands associated with the ionic states of c-C_4F_8. The sample contains a small contamination of air, but this does not affect the assignment of the c-C_4F_8 features since the narrow lines due to N_2 can be readily identified. Since there is no vibrational structure associated with the ionic states, the contamination does not affect our assignment of the weak vibrational pattern observed in the vuv spectra or the ionization energy limits for the assigned Rydberg series. The energy positions of the observed features are summarized in Table IV. The shape of the observed lowest ionic band for c-$C_4F_8^+$(Fig. 4) is quite broad and structureless, the maximum intensity at (12.291 ± 0.002) eV corresponds to the vertical ionization energy. The onset of ionization is measured at (11.60 ± 0.05) eV in good agreement with the value determined by Jarvis *et al.* [29] and Parkes *et al.* [30] in their study of perfluorocyclobutane by the threshold photoelectron-photoion coincidence method. Photoelectron spectroscopy gives both the adiabatic (a very probable value) and vertical ionization energies, the values of which tend to differ significantly whenever there is a large change in equilibrium molecular geometry on ionization [12]. The absence of vibrational structure in the first electronic band of the photoelectron spectrum is due to the very fast decomposition of the c-C_4F_8+molecular producing $C_3F_5^+ + CF_3$ as shown by Jarvis *et al.* [29] and Parkes *et al.* [30].

The results of the present calculations, shown in Table IV, agree very well with the experimental values obtained for the electronic bands of the photoelectron spectrum, especially for the AQCC method and contrary to the CCSD(T) energies which were found to be too low. Moreover, the TDDFT/PBE0 value of 11.653 eV (Table II) is also underestimated. According to Table IV, the first band is unambiguously assigned to the $3b_1^{-1}$ state and the second band to the $12e^{-1}$ state. The asymmetry of the third band, which can be clearly seen in Fig. 4 is due to the presence of two nearly degenerate ionic states ($11e^{-1}$ and $10a_1^{-1}$) in this region. At higher energies, the situation is less clear because of the large number of states, as shown in Table IV. It should be noted that due to convergence problems, it was not possible to calculate higher lying A_1 states with the MR-AQCC method. The high density of ionic states may be connected to the fact that the highest occupied MO's in c-C_4F_8 are essentially lone pairs with very similar energies. The present results are consistent with the outer valence Green's function (OVGF) calculations of Parkes *et al.* [30] (see Fig. 4 in Ref. [30]), although these authors only provide the first two ionization energies. The absence of structures at 12.8 and 14.8 eV in the present photoelectron spectrum (PES) is explained by the fact that these structures observed in the threshold photoelectron spectroscopy (TPES) spectrum [30] of c-C_4F_8 are due to Rydberg states that autoionize, as already suggested by Parkes *et al.* These authors report that at that time there was no PES available the present results fulfill that gap and support their predictions.

V. PHOTOLYSIS RATES AND LOCAL LIFETIMES

The present cross section values can be used to model the atmospheric destruction of c-C_4F_8 by uv photolysis as a function of altitude. Details of the program are presented in a previous publication by Limão-Vieira *et al.* [31]. Photolysis rates at a given wavelength were calculated as the product of the solar actinic flux [32] and the molecular photoabsorption cross section at 1 km altitude steps from the surface up to the stratopause (50 km). At each altitude a total photolysis rate may then be calculated by summing over the individual photolysis rates for that altitude. The reciprocal of the total photolysis rate for a given altitude gives the local photolysis lifetime at that altitude, i.e., the time taken for the molecule to photodissociate at the altitude assuming that the solar flux remains constant. The local lifetimes shown in Fig. 6 assume that the quantum yield for dissociation is unity. The results show that the local photolysis lifetime of c-C_4F_8 varies from about 400 years at 20 km to a few days at 40–50 km. Therefore, it indicates that perfluorocyclobutane will be stable to

photolysis in the troposphere but can be broken up reasonably at higher altitudes. We have recently reported a high-resolution Fourier transform infrared (FTIR) spectra [33] showing a strong infrared absorption cross section in the wavelength region of the Earth's atmospheric window (800–1300 cm^{-1}), such that a long tropospheric lifetime may lead to significant global warming potential of 8500 times that of CO_2. However, the atmospheric lifetime of c-C_4F_8 can be significantly reduced by electron interactions, according to Morris *et al.* [3].

VI. CONCLUSIONS

The present results are experimental data on the spectroscopy of perfluorocyclobutane in the 6.0–11.0 eV energy region. In the high-resolution data features are observed. Weak fine structure observed in the 9 eV photoabsorption band has been assigned to specific vibrational modes.

Ab initio calculations on the vertical excitation energies and oscillator strengths were used in the assignment of the spectral transitions. The theoretical results are in good agreement with the experimental data for both neutral excited states and ionic states.

The measured photoabsorption cross sections have been used to derive the local lifetime in the Earth's atmosphere (0–50 km) showing that perfluorocyclobutane may have a long residence time in the lower atmosphere.

ACKNOWLEDGMENTS

P.L.V. acknowledges support from University College London, CEMOS, The Open University, UK, and together with M.-J.H.-F. the financial support from the Portuguese-Belgian joint collaboration. The Patrimoine of the University of Liège, the Fonds de la Recherche Scientifique (FRS-FNRS), and the Fonds de la Recherche Fondamentale Collective of Belgium have supported this research. M.-J.H.-F. wishes to acknowledge the Fonds de la Recherche Scientifique. P.L.V. and N.J.M. acknowledge the support from the British Council for the Portuguese-English joint collaboration. The authors wish to acknowledge the beam time at the ISA synchrotron facility, University of Aarhus, Denmark, and the support from the European Commission for access to research infrastructure action of the improving human potential program. The "PhLAM" is "Unité Mixte de Recherche du CNRS." The "Centre d'Études et de Recherches Lasers et Applications" (CERLA, FR CNRS 2416) is supported by the "Ministère chargé de la Recherche," the "Région Nord/Pas-de-Calais," and the "Fonds Européen de Développement Économique des Régions" (FEDER).

[1] L. G. Christophorou and J. K. Olthoff, J. Phys. Chem. Ref. Data **30**, 449 (2001).
[2] J. T. Houghton, L. G. M. Filho, B. A. Callander, N. Harris, A. Kattenberg, and K. Maskell, *Climate Change 1995* (Cambridge University Press, New York, 1996).
[3] R. A. Morris, T. M. Miller, A. A. Viaggiano, J. F. Paulson, S. Solomon, and G. Reid, J. Geophys. Res. **100**, 1287 (1995).
[4] N. J. Mason, A. Dawes, R. Mukerji, E. A. Drage, E. Vasekova, S. M. Webb, and P. Limão-Vieira, J. Phys. B **38**, S893 (2005).
[5] C. Winstead and V. McKoy, J. Chem. Phys. **114**, 7407 (2001).
[6] M. Jelisavcic, R. Panajotovic, M. Kitajima, M. Hoshino, H. Tanaka, and S. J. Buckman, J. Chem. Phys. **121**, 5272 (2004).
[7] T. M. Miller, J. F. Friedman, and A. A. Viggiano, J. Chem. Phys. **120**, 7024 (2004).
[8] S. Eden, P. Limão-Vieira, S. V. Hoffmann, and N. J. Mason, Chem. Phys. **323**, 313 (2006).
[9] F. Motte-Tollet, M.-J. Hubin-Franskin, and J. E. Collin, J. Chem. Phys. **97**, 7314 (1992).
[10] J. Delwiche, P. Natalis, J. Momigny, and J. E. Collin, J. Electron Spectrosc. Relat. Phenom. **1**, 219 (1972).
[11] L. Minnhagen, J. Opt. Soc. Am. **63**, 1185 (1973).
[12] J. H. D. Eland, *Photoelectron Spectroscopy* (Butterworths, London, 1994).
[13] L. Serrano-Andres and M. Merchan, J. Mol. Struct.: THEOCHEM **729**, 99 (2005).
[14] A. Dreuw and M. Head-Gordon, Chem. Rev. (Washington, D.C.) **105**, 4009 (2005).
[15] F. Aquilante, V. Barone, and B. O. Roos, J. Chem. Phys. **119**, 12323 (2003).
[16] C. Adamo and V. Barone, J. Chem. Phys. **110**, 6158 (1999).
[17] M. J. Frisch *et al.*, GAUSSIAN 03, Revision D.01. Gaussian, Inc., Wallingford, CT, 2004.
[18] O. Christiansen, H. Koch, and P. Jorgensen, Chem. Phys. Lett. **243**, 409 (1995).
[19] O. Christiansen, H. Koch, and P. Jorgensen, J. Chem. Phys. **105**, 1451 (1996).
[20] DALTON, a molecular electronic structure program, Release 2.0 (2005), see http://www.kjemi.uio.no/software/dalton/dalton.html
[21] K. Kaufmann, W. Baumeister, and M. Jungen, J. Phys. B **22**, 2223 (1998).
[22] P. J. Knowles, C. Hampel, and H.-J. Werner, J. Chem. Phys. **99**, 5219 (1993).
[23] J. D. Watts, J. Gauss, and R. J. Bartlett, J. Chem. Phys. **98**, 8718 (1993).
[24] P. G. Szalay and R. J. Bartlett, Chem. Phys. Lett. **214**, 481 (1993).
[25] MOLPRO, a package of *ab initio* programs designed by H.-J. Werner and P. J. Knowles, Version 2002.1, R. D. Amos *et al.*
[26] G. Schaftenaar and J. H. Noordik, J. Comput.-Aided Mol. Des. **14**, 123 (2000).
[27] G. Fisher, R. L. Purchase, and D. M. Smith, J. Mol. Struct. **405**, 159 (1997).
[28] C. Mao, C. Nie, and Z. Zhu, Spectrochim. Acta, Part A **27**, 1093 (1998).
[29] G. K. Jarvis, K. J. Boyle, C. Mayhew, and R. P. Tuckett, J. Phys. Chem. A **102**, 3230 (1998).
[30] M. A. Parkes, S. Ali, R. P. Tuckettt, V. A. Mikhailov, and C. A.

Mayhew, Phys. Chem. Chem. Phys. **8**, 3643 (2006).
[31] P. Limão-Vieira, S. Eden, P. A. Kendall, N. J. Mason, and S. V. Hoffmann, Chem. Phys. Lett. **364**, 535 (2002).
[32] Evaluation number 12, NASA, Jet Propulsion Laboratory, JPL Publication 97-4, 1997 (unpublished).
[33] E. Vasekova, E. A. Drage, K. M. Smith, and N. J. Mason, J. Quant. Spectrosc. Radiat. Transf. **102**, 418 (2006).
[34] C. H. Chang, R. F. Porter, and S. H. Bauer, J. Mol. Struct. **7**, 89 (1971).

Article 7

Electronic State Spectroscopy of c-C_5F_8 Explored by Photoabsorption, Electron Impact, Photoelectron Spectroscopies and Ab Initio Calculations

P. Limão-Vieira,*,†,‡ D. Duflot,§ A. Giuliani,||,&,⊥ E. Vasekova,‡ J. M. C. Lourenço,† P. M. Santos,# S. V. Hoffmann,▽ N. J. Mason,‡ J. Delwiche,|| and M.-J. Hubin-Franskin||

Laboratório de Colisões Atómicas e Moleculares, Departamento de Física, CEFITEC, Universidade Nova de Lisboa, P-2829-516 Caparica, Portugal, Centre of Molecular and Optical Sciences, Department of Physics and Astronomy, The Open University, Walton Hall, Milton Keynes, MK7 6AA, U.K., Laboratoire de Physique des Lasers, Atomes et Molécules (PhLAM), UMR CNRS 8523, Centre d'Études et de Recherches Lasers et Applications (CERLA, FR CNRS 2416), Université des Sciences et Technologies de Lille, F-59655 Villeneuve d'Ascq Cedex, France, Laboratoire de Spectroscopie d'Électrons Diffusés, Université de Liège, Institut de Chimie-Bât. B6c B-4000 Liège 1, Belgium, DISCO Beamline, Synchrotron SOLEIL, BP 48, L'Orme des Merisiers, 91192 Gif-sur-Yvette CEDEX, France and Cepia, Institut National de la Recherche Agronomique, BP 71627, F-44316, France, Instituto de Telecomunicações, IST, Avenida Rovisco Pais, P-1049-001 Lisboa, Portugal, and Institute for Storage Ring Facilities, University of Aarhus, Ny Munkegade, DK-8000, Aarhus C, Denmark

Received: November 12, 2007

The electronic transitions and resonance-enhanced vibrational excitations of octafluorocyclopentene (c-C_5F_8) have been investigated using high-resolution photoabsorption spectroscopy in the energy range 6−11 eV. In addition, the high-resolution electron energy loss spectrum (HREELS) was recorded under the electric dipolar excitation conditions (100 eV incident energy, ∼0° scattering angle) over the 5−14 eV energy loss range. A He(I) photoelectron spectrum (PES) has also been recorded between 11 and 20 eV, allowing us to derive a more precise value of (11.288 ± 0.002) eV for the ground neutral state adiabatic ionization energy. All spectra presented in this paper represent the first and highest resolution data yet reported for octafluorocyclopentene. Ab initio calculations have been performed for helping in the assignment of the spectral bands for both neutral excited states and ionic states.

1. Introduction

As part of an international effort to reduce the emission of atmospheric pollutants that may lead to global warming the Kyoto Protocol and its amendments have been developed to phase out the use of several anthropogenic gases by 2010, including several species arising from the plasma processing industries. Therefore, in order to meet the requirements of the Kyoto Protocol, industry has been seeking alternative gases that will both operate in current plasma reactors and maintain high performance of current feed gases (e.g., SF_6 and CF_4). Octafluorocyclopentene, c-C_5F_8, is among the fluorocarbons suggested as a candidate to replace the traditional feed gases used in the semiconductor industry to prepare silicon wafers for SiO_2 reactive ion etching.[1] Surface reactions induced by c-C_5F_8 plasmas have been studied on silicon dioxide and silicon nitride substrates using an inductively coupled plasma source, revealing larger etching selectivity and polymerization than in a more conventional c-C_4F_8 plasma.[2] However, before c-C_5F_8 can be widely adopted it must be shown to have little (or no) environmental impact.

To compute the global warming potential (GWP) and lifetime of any atmospheric molecule, one requires both knowledge of the electronic state spectroscopy and the absolute photoabsorption cross-sectional values in the visible and vacuum ultraviolet (VUV) region of the electromagnetic spectrum.[3] As part of a larger project to investigate the electronic state spectroscopy of several plasma processing molecules and to evaluate their role in global warming in the earth's atmosphere (see, e.g., ref 4), we have, therefore, recorded high-resolution VUV photoabsorption, electron energy loss, and photoelectron spectra (PESs) of c-C_5F_8. As far as we are aware, no other spectra have been reported in the literature. Indeed, a review of the literature reveals little experimental data for c-C_5F_8, these being limited to some measurements of the electron attachment line shapes and cross sections at ultralow electron energies.[5] Recent studies on the ionization cross sections of Jiao et al.[6] on cation−molecule reactions and Parkes et al.[7] on threshold photoelectron−photoion coincidence spectroscopy with a He(I) PES obtained with a lower resolution that in the present work have been reported. Quantum chemical studies via configuration interaction scheme (CIS) with the Hartree−Fock method[8] and ab initio calculations on the dissociative attachment resonance energies with comparisons to electron attachment mass spectrometric measurements[9] have also been discussed in a recent

* Corresponding author. Mailing address: Laboratório de Colisões Atómicas e Moleculares, Departamento de Física, CEFITEC, Universidade Nova de Lisboa, P-2829-516 Caparica, Portugal. E-mail address: plimaovieira@fct.unl.pt. Tel: +351-21 294 85 76. Fax: + 351-21 294 85 49.
† Universidade Nova de Lisboa.
‡ The Open University.
§ Université des Sciences et Technologies de Lille.
|| Université de Liège.
& DISCO Beamline, Synchrotron SOLEIL.
⊥ Institut National de la Recherche Agronomique.
Instituto de Telecomunicações, IST.
▽ University of Aarhus.

10.1021/jp7107939 CCC: $40.75
Published on Web 03/11/2008

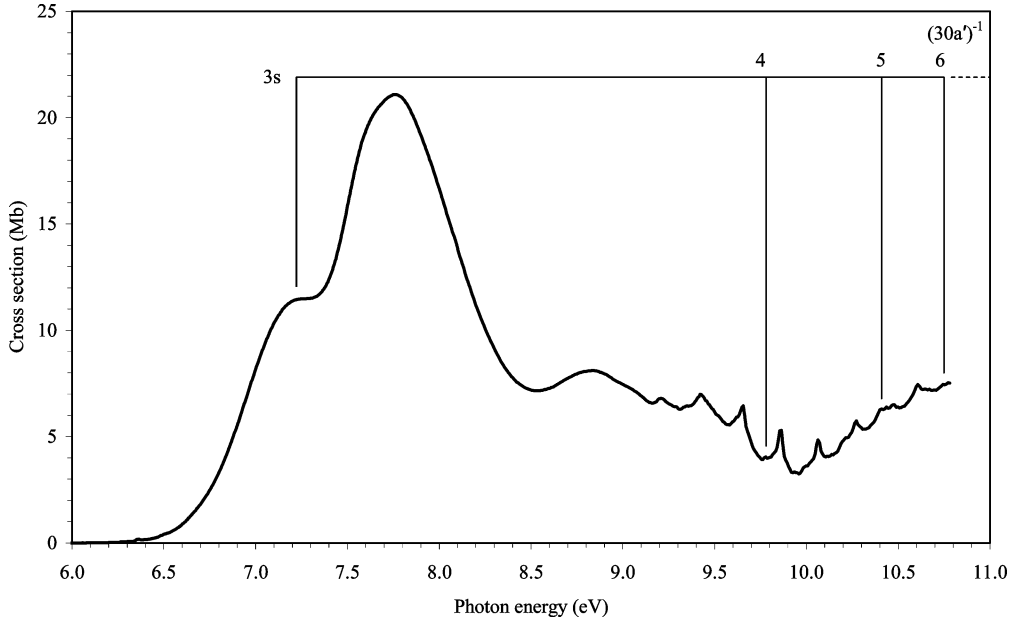

Figure 1. High-resolution VUV photoabsorption spectrum of c-C_5F_8, recorded using the Århus synchrotron facility, showing valence and Rydberg states in the 6−11 eV energy range.

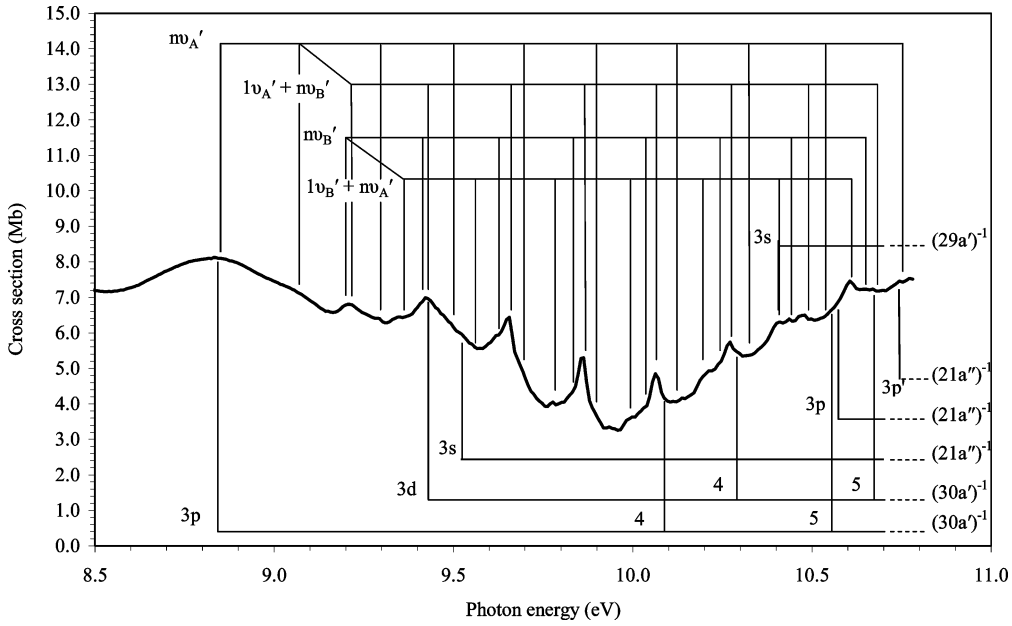

Figure 2. High-resolution VUV photoabsorption spectrum of c-C_5F_8, recorded using the Århus synchrotron radiation facility, showing valence and Rydberg states and vibrational progressions in the 8.5−11.0 eV energy range.

work, but the former has proven to disagree with our present calculations (see Computational Method section).

Electron energy loss spectra in the present experiments and excitation energies derived from theory are used to help assign the major bands in the photoabsorption spectra. Further information is derived from a high-resolution PES, which is used to help in the identification of Rydberg states in the VUV spectrum.

The VUV absolute photoabsorption cross section of c-C_5F_8 reported in this paper is used to derive its photolysis lifetime in the earth's atmosphere and compared to other candidates for replacement in the plasma industry.

2. Experimental Section

The electronic states of octafluorocyclopentene (c-C_5F_8) spectroscopy has been studied using a range of different experimental techniques, including (1) VUV photoabsorption using a synchrotron radiation source, which provides data on optical allowed transitions, (2) high-resolution electron energy loss spectroscopy (HREELS) in electric dipolar interaction conditions, which allow only optically allowed transitions to be monitored, and (3) He(I) photoelectron spectroscopy (PES) to determine the ionization energies. HREELS was used in order to increase the energy range studied, the VUV absorption curve being limited in energy by the transmission limit of the entrance window of the photoabsorption cell (see below).

2.1. VUV Photoabsorption. The high-resolution VUV photoabsorption measurements (Figures 1 and 2) were performed using the ASTRID−UV1 beam line at the Institute for Storage Ring Facilities (ISA), University of Aarhus, Denmark. A detailed description of the apparatus can be found elsewhere,[10] so only

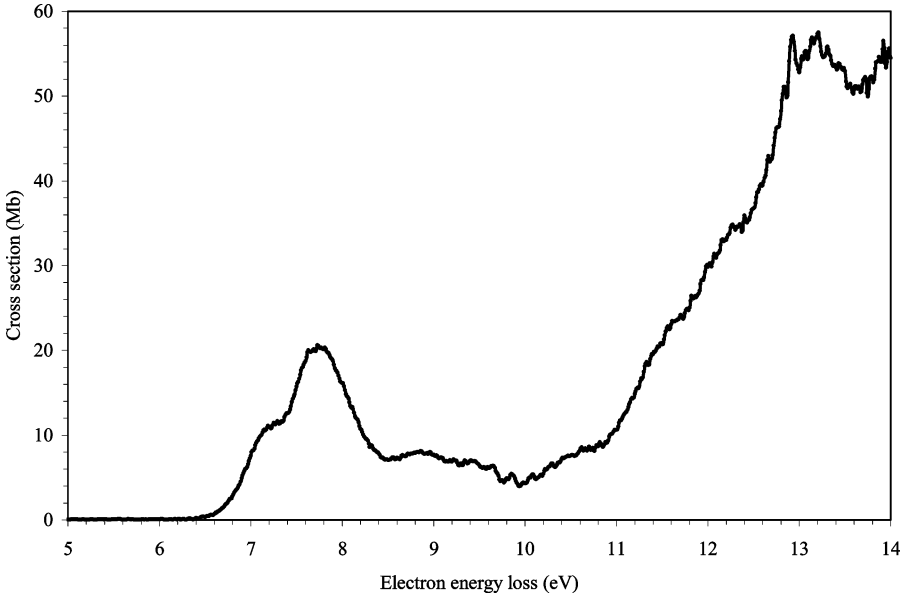

Figure 3. Electron energy loss spectrum of c-C_5F_8 recorded at the University of Liège in the 5−14 eV energy region in electric dipolar interaction conditions (100 eV incident energy, ≈ 0° scattering angle).

a brief description will be given here. A toroidal dispersion grating is used to select the synchrotron radiation with a full width at half-maximum (fwhm) wavelength resolution of approximately 0.075 nm. The synchrotron radiation passes through the static gas sample at room temperature. A photomultiplier is used to detect the transmitted light. For wavelengths below 200 nm, a flow of He gas is flushed through the small gap between the photomultiplier and the exit window of the gas cell to prevent any absorption by air contributing to the spectrum. A LiF entrance window acts as an edge filter for higher-order radiation, restricting the photoabsorption measures to below 10.8 eV (115 nm). The grating itself provides a maximum wavelength (lower energy limit) of 320 nm (3.9 eV). The sample pressure is measured by a Baratron capacitance gauge. To avoid any saturation effects, sample pressures were chosen such that the transmitted flux was >10% of the incident flux.

Gas transmission results are compared to a background scan recorded with an evacuated cell. Absolute photoabsorption cross sections may then be calculated using the Beer−Lambert law:

$$I_t = I_0 \exp(-n\sigma x)$$

where I_t is the intensity of the light transmitted through the gas sample, I_0 is that through the evacuated cell, n is the molecular number density of the sample gas, σ is the absolute photoabsorption cross section, and x is the absorption path length (25 cm). The accuracy of the absolute cross section is estimated to be better than ±5%.

2.2. High-Resolution Electron Energy Loss Spectroscopy. The instrument used at the Université de Liège, Belgium (VG-SEELS 400) has been described in detail elsewhere.[11] An electrostatic electron energy monochromator defines a narrow energy spread about the mean incident electron energy, and a three element lens focuses the electrons into the collision region. The electron beam intersects the effusive gas beam, which flows through a hypodermic needle, at 90°. The working pressure in the chamber with target gas is ∼1.5×10^{-5} mbar. The analyzer system is also an electrostatic energy analyzer[12] with the scattered electron signal detected by an electron multiplier of the continuous dynode type. Both electron energy selectors work in the constant pass-energy mode. Spectra were recorded for energy losses between 5.0 and 14 eV at step intervals of 10 meV. The electron energy loss scale was calibrated to the "elastic scattering peak". The resolution, measured as the fwhm of the elastically scattered electron peak was about 40 meV. The apparatus was used with relatively high incident energy electrons (100 eV) and a quite small scattering angle ($\theta \approx 0°$), such that strictly electric dipole interaction conditions apply. The derived VUV cross section was normalized at 8.57 eV from our VUV photoabsorption value of 7.203 Mbar to obtain absolute cross section values, a method shown to be reliable in previous works (see, e.g., ref 12). Comparison of the HREELS cross section values with those recorded using the synchrotron radiation source thus provides a test for any systematic errors in the optical values arising from the line saturation effect and second-order light from the light source and beam line. These were found to be negligible in this work. The present HREELS spectrum is shown in Figure 3.

2.3. Photoelectron Spectroscopy. He(I) (21.22 eV) photoelectron spectra of c-C_5F_8 (Figure 4) were taken at the Université de Liège, Belgium. The apparatus has been described in detail previously.[13] Briefly, the spectrometer consists of a 180° cylindrical electrostatic analyzer with a mean radius of 5 cm. The analyzer is used in constant energy pass mode. The incident photons are produced by a D.C. discharge in a two-stage differentially pumped lamp. The energy scale was calibrated using argon lines using the values $^2P_{3/2}$ = 15.760 eV and $^2P_{1/2}$ = 15.937 eV),[14,15] and the resolution of the present spectrum is measured from the fwhm of the Ar peaks to be 20 meV, in presence of c-C_5F_8. The position of the first peak in the first electronic band of the c-C_5F_8 PES was determined by making use of a least-square fitting with a Gaussian curve. Repeated tests in our laboratory have shown that this procedure is not very sensitive to the choice of the limits used for the fitting, and so the uncertainty of the position of a peak maximum is more or less one energy interval between two successive experimental points, giving, in the case of the c-C_5F_8 PES, an uncertainty of ±0.002 eV. The same procedure was used for

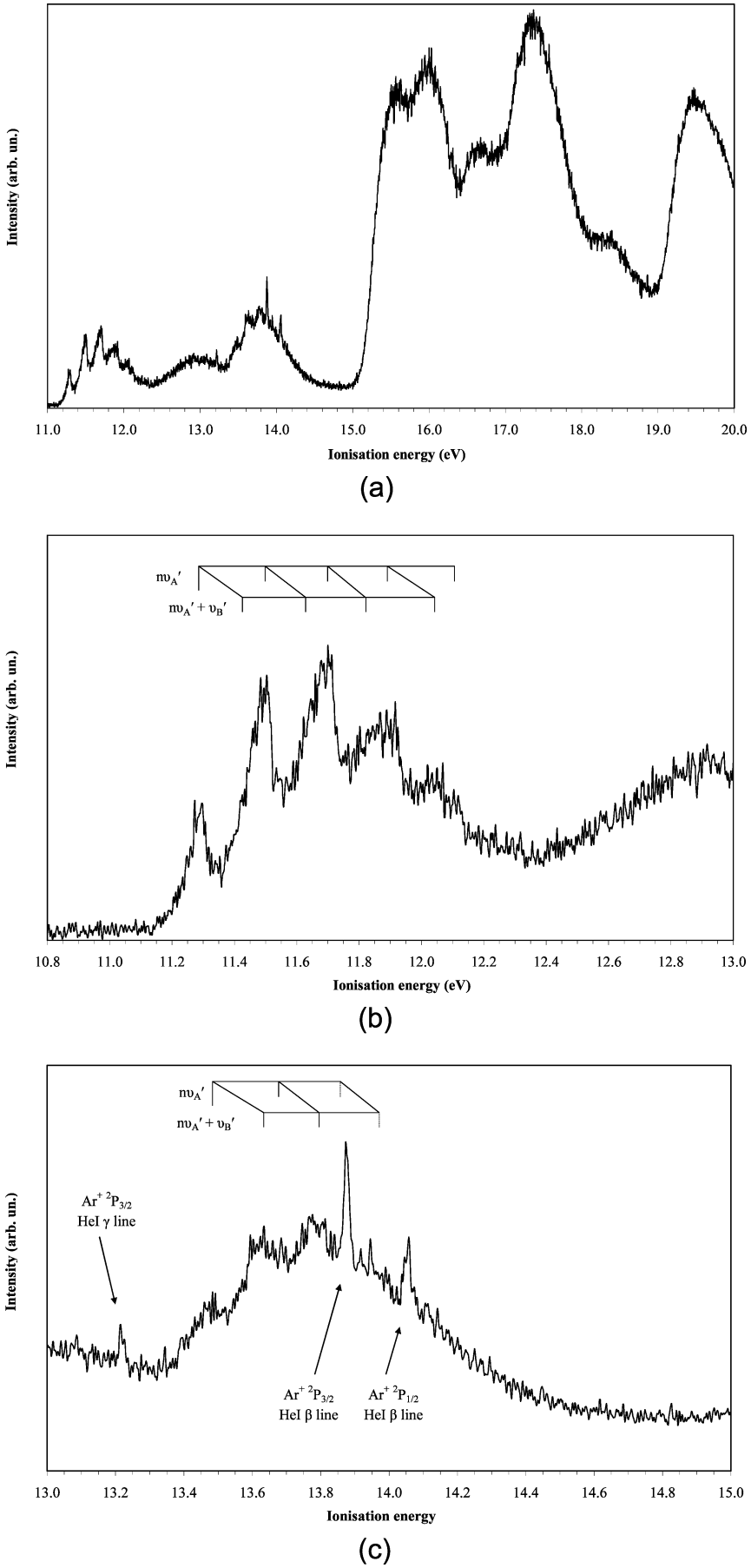

Figure 4. He(I) photoelectron spectra of c-C_5F_8 recorded at the University of Liège (a) in the 11−20 eV energy region, (b) in the 10.8−13.0 eV energy region, and (c) in the 13.0−15.0 eV energy region (see discussion in text).

all the energy values quoted in the paper. The intensities in the spectrum were corrected for the transmission of the analyzing system. The spectrum presented in Figure 4 consists of two parts, with the high-energy region (>15 eV) being recorded without Argon in order to avoid the strong signal due to the presence of the rare gas. The Ar lines shown in the lower energy part of the spectrum are due to Ar features produced by the He(I)β and γ lines, respectively. The PES presented in this paper is the sum of 22 individual spectra. This procedure allowed us to obtain a good signal-to-noise ratio while keeping the pressure in the spectrometer at a very low level ($<5 \times 10^{-6}$ mbar).

Octafluorocyclopentane Sample. The gas sample used in the VUV measurements was purchased from Fluorochem, with a minimum purity of 99%, while for PES and HREELS experiments, the sample was purchased from ABCR with a quoted 99.8% purity.

3. Computational Details

We performed ab initio calculations to determine vertical excitation energies of the electronic states and the lowest ionization energies. As recently reviewed,[16] the calculation of electronic spectra, especially for molecules with a large number of electrons, remains a difficult task. Because of its low computational cost, the time-dependent density functional theory (TDDFT) method has recently become a very popular method[16] and, in the case of the acrolein molecule, was shown to give results in good agreement with more costly calculations (i.e., MS-CASPT2), using the PBE0 functional.[17,18] Therefore, the same method was employed in the present work: the geometry of c-C_5F_8 was optimized at the DFT/PBE0/6-311G** level, and the electronic excitation spectrum was calculated at the TDDFT//PBE0/6-311++G** level. These calculations were performed with the Gaussian 03 package.[19] However, it is also well-known[16,20] that TDDFT has difficulties describing certain types of electronic states, such as Rydberg states. Thus, the lowest lying excited states of c-C_5F_8 were also computed at the EOM-CCSD[21] level with the MOLPRO program.[22] The geometry was optimized at the MP2/cc-pVDZ level with Gaussian, and then diffuse functions (5s, 5p, 5d) taken from Kaufmann et al.[23] were added at the center of the molecule (cc-pVDZ+R basis set). Finally, the lowest ionization energies of c-C_5F_8 were obtained with Gaussian at the UPBE0 level, and at the RCCSD[24] and RCCSD(T) levels[25] with MOLPRO. The ROVGF method[26,27] implemented in Gaussian was also used to obtain the ionization energies using both PBE/6-311G** and MP2/cc-pVDZ geometries.

Two different methods were used to determine the difference between the vertical and adiabatic energies for the lowest ionic states: (a) the vertical ionization energy is simply the difference between the ground state and the ionic state at the neutral equilibrium geometry, while the adiabatic value is given by the difference of the energies (corrected by the zero-point vibrational energy (ZPVE) correction) obtained at both neutral and ionic equilibrium geometries; (b) to use Franck−Condon analysis to obtain the energy difference between the vertical excitation and the position of the 0−0 vibrational band. This analysis was performed in the frame of the Domcke−Cederbaum model,[28] which simply requires the frequencies of the ground state, and the first- and second-order derivatives, with respect to the normal coordinates, of the ion energy, at the geometry of the ground state.

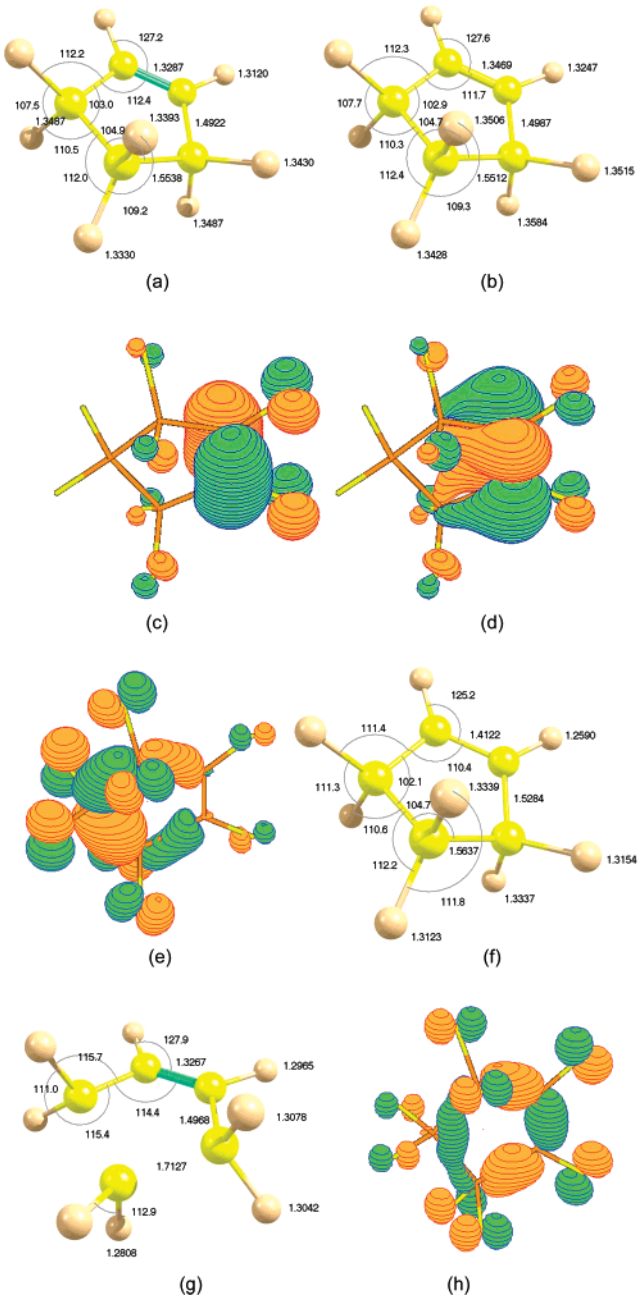

Figure 5. Ground state structure of c-C_5F_8 calculated by (a) the PBE0/6-311G** method, (b) the MP2/cc-pVDZ method, (c) the HOMO (30a′) of c-C_5F_8, (d) the LUMO (22a″) of c-C_5F_8, and (e) the SHOMO (21a″). Ionic states structures (PBE0/6-311G**) of (f) the ^{2}A′ state, (g) the ^{2}A″ state, and (h) HOMO-2, 29a′.

4. Results and Discussion

4.1 Structure and Properties of c-C_5F_8. The calculated geometries in Figure 5a,b show the results from the two calculation methods employed, PBE0/-6311G** and MP2/cc-pVDZ, respectively. To the best of our knowledge, there are no experimental values for the ground state geometry of c-C_5F_8, but our results are very similar to those obtained by Fischer and Cao[29] at the HF, MP2, and B3LYP levels using the 6-31G* basis set.

The calculated electron configuration of the $\tilde{X}^1$A′ ground state of c-C_5F_8 is

(a) core F 1s orbitals $1a''^2\ 1a'^2\ 2a'^2\ 3a'^2\ 2a''^2\ 4a'^2\ 3a''^2\ 5a'^2$

(b) core C 1s orbitals $6a'^2\ 4a''^2\ 7a'^2\ 8a'^2\ 5a''^2$

TABLE 1: Calculated Vertical Excitation Energies (TDDFT/PBE0/6-311++G//PBE0/6-311G**) of the Lowest Lying States of c-C_5F_8 (eV), Oscillator Strengths, and VUV Experimental Data**

symmetry	E (eV)	f_L	HOMO, 30a′ (π)	SHOMO, 21a″ σ(C−C)/n(F)	HOMO-2, 29a″ n(F)	other	exp. (eV)
$\tilde{X}$ ^{1}A′	0.000	ground state					
2 ^{1}A′	7.138	0.0126	$\pi\rightarrow$3s/ σ*(C−F)				7.221
3 ^{1}A′	7.369	0.0020		σ (C−C)/n(F) $\rightarrow\pi$*			
1 ^{1}A″	7.428	0.3064	$\pi\rightarrow\pi$*				7.754
2 ^{1}A″	7.778	0.0047			n(F) $\rightarrow\pi$*		
4 ^{1}A′	8.540	0.0972	$\pi\rightarrow\sigma$*(C−F)				[a]
3 ^{1}A″	8.584	0.0056		σ (C−C)/n(F)$\rightarrow$ 3s/ σ*(C−F)			
4 ^{1}A″	9.072	0.0039		σ (C−C)/n(F) $\rightarrow\sigma$*(C−F)			
5 ^{1}A′	9.120	0.0016			n(F) $\rightarrow$ 3s/ σ*(C−F)		9.523
5 ^{1}A″	9.123	0.0006	$\pi\rightarrow$ 3p				
6 ^{1}A′	9.203	0.0013	$\pi\rightarrow$ 3p				8.837
7 ^{1}A′	9.580	0.0029				n(F) $\rightarrow\pi$*	
6 ^{1}A″	9.626	0.0011				n(F) $\rightarrow\pi$*	
8 ^{1}A′	9.651	0.0004				n(F) $\rightarrow\pi$* + $\pi\rightarrow$ 3d	
9 ^{1}A′	9.728	0.0175				n(F) $\rightarrow\pi$* + $\pi\rightarrow$ 3p + $\pi\rightarrow$ 3d	[a]
10 ^{1}A′	9.747	0.0073				π 3p + $\pi\rightarrow$ 3d + n(F) $\rightarrow\pi$*	9.421
7 ^{1}A″	9.929	<0.0001				n(F) $\rightarrow\pi$*	
11 ^{1}A′	10.023	0.0039			n(F) $\rightarrow\sigma$*(C−F)		
12 ^{1}A′	10.100	0.0186				n(F) $\rightarrow\pi$*	
8 ^{1}A″	10.113	0.0014				n(F) $\rightarrow\pi$*	
9 ^{1}A″	10.223	0.0068		σ (C−C)/n(F) $\rightarrow$ 3p			
10 ^{1}A″	10.279	<0.0001	$\pi\rightarrow$ 3d				
13 ^{1}A′	10.362	0.0042		σ (C−C)/n(F) $\rightarrow$3p			
14 ^{1}A′	10.432	0.0023	$\pi\rightarrow$3d				
11 ^{1}A″	10.521	0.0012				n(F) $\rightarrow\pi$*	
15 ^{1}A′	10.608	0.0059				n(F) $\rightarrow\pi$* +$\pi\rightarrow$ 3d	
16 ^{1}A′	10.624	0.0358				π* 3d + n(F) $\rightarrow\pi$*	[a]
12 ^{1}A″	10.703	0.0039				n(F) $\rightarrow$ 3s/ σ*(C−F)	
17 ^{1}A′	10.721	0.0134				n(F) $\rightarrow$ 3s/ σ*(C−F) + π* $\rightarrow$ 3d	[a]
13 ^{1}A″	10.721	0.0121				n(F) $\rightarrow$ 3s/ σ*(C−F) + n(F) (HOMO^{-2}) $\rightarrow$ 3p	
18 ^{1}A′	10.735	0.0003				n(F) $\rightarrow$ 3s/ σ*(C−F) + $\pi\rightarrow$ 4p	
14 ^{1}A″	10.794	0.0023	$\pi\rightarrow$ 3d				
19 ^{1}A′	10.931	0.0001			n(F) $\rightarrow$ 3p		
15 ^{1}A″	10.957	0.0040	$\pi\rightarrow$ 4s				
16 ^{1}A″	11.001	0.0122		σ (C−C)/n(F) $\rightarrow$ 3p			10.570
20 ^{1}A′	11.012	0.0117				n(F) $\rightarrow\pi$*	
17 ^{1}A″	11.040	0.0001				n(F) $\rightarrow\pi$* + n(F) $\rightarrow$ 3s/ σ*(C−F)	
18 ^{1}A″	11.081	0.0182			n(F) $\rightarrow$ 3p		
21 ^{1}A′	11.088	0.0022	$\pi\rightarrow$ 4p				
19 ^{1}A″	11.131	0.0057		σ (C−C)/n(F) $\rightarrow$ 3d			
22 ^{1}A′	11.161	0.0156				n(F) $\rightarrow$ 3s/ σ*(C−F) + n(F) $\rightarrow\pi$*	10.401

[a] See discussion in text.

(c) σ(CF) orbitals 9a′^{2} 6a″^{2} 10a′^{2} 11a′^{2} 7a″^{2} 12a′^{2} 8a″^{2} 13a′^{2}

(d) σ(CC) orbitals 14a′^{2} 15a′^{2} 9a″^{2} 16a′^{2} 10a″^{2}

(e) n(F) lone pairs 17a′^{2} 18a′^{2} 11a″^{2} 19a′^{2} 12a″^{2} 20a′^{2} 13a″^{2} 21a′^{2} 22a′^{2} 14a″^{2} 15a″^{2} 23a′^{2} 24a′^{2} 16a″^{2} 17a″^{2} 25a′^{2} 26a′^{2} 18a″^{2} 27a′^{2} 19a″^{2} 20a″^{2} 28a′^{2} 29a′^{2} 21a″^{2}

(f) π(C=C)/n(F) lone pair 30a′^{2}.

The highest occupied molecular orbital (HOMO) in the neutral ground state, 30a′, represented in Figure 5c with the MOLDEN software,[30] is calculated to be mainly π(C=C) and only partial F lone pair character. The lowest unoccupied molecular orbital (LUMO) is essentially the π*(C=C) (22a″) orbital (Figure 5d) with a slight bonding π character with the adjacent carbon atoms, as in butadiene. The second highest occupied MO (SHOMO) has an important σ(C−C) bonding character mixed with F lone pair contribution (Figure 5e). This is also the case for several lower lying MO's, so that the distinction between σ(C−C) and n(F) may be somewhat arbitrary.

In its ground neutral electronic state, c-C_5F_8 has C_s symmetry with 33 modes of vibration. In the present high resolution absorption spectrum, for some excited electronic states, resonant vibrational modes with mean excitation energies of 0.219 and 0.148 eV were observed (see Figure 1). In the absence of any experimental data on the excitation energies for the vibrational modes of c-C_5F_8 in the literature, we have labeled these features ν_A′ and ν_B′, respectively, and identified them on the basis of our PES (see section 4.5) as being mainly due to contributions of the C=C stretching and C−C stretching modes. The calculated transition energies, oscillator strengths and the main character of the wave function are shown in Tables 1 (TDDFT results) and 2 (EOM-CCSD results). Most calculated transitions have very low intensities, because of their Rydberg character. There are rather large differences between the two sets of results. It is well-known[16,20] that TDDFT methods do not accurately describe Rydberg states. These differences are more surprising for valence states since, as detailed in a recent review,[31] the EOM-CCSD method is very accurate for the description of electronic spectra of small molecules. However, in the case of c-C_5F_8, it is possible that the limitation to di-excitations in the CCSD model is insufficient, due to the large number of electrons. It should be noted that a recent study on fluoroethylenes,[32] using the SAC-CI method, also found discrepancies of several tenths of an electron volt, even for the $\pi-\pi$* transition.

TABLE 2: Calculated Vertical Excitation Energies (EOM-CCSD/cc-pVDZ + R//MP2/cc-pVDZ) of the Lowest Lying States of c-C_5F_8 (eV), Oscillator Strengths, and VUV Experimental Data

symmetry	E (eV)	f_L	⟨r2⟩	HOMO, 30a′ (π)	SHOMO, 21a″ σ (C−C)/n(F)	HOMO^{-2}, 29a″ n(F)	exp. (eV)
$\tilde{X}$ ^{1}A′	0.000	ground state	158				
2 ^{1}A′	7.569	0.0183	175	$\pi \rightarrow$ 3s/π*(C−F)			7.221
1 ^{1}A″	8.119	0.3503	158	$\pi \rightarrow \pi$*			7.754
2 ^{1}A″	8.615	0.0066	156			n(F) $\rightarrow \pi$*	[a]
3 ^{1}A′	8.664	0.0019	158		σ (C−C)/n(F) $\rightarrow \pi$*		
4 ^{1}A′	9.374	0.0152	227	$\pi \rightarrow$ 3p			8.837
3 ^{1}A″	9.441	<0.0001	237	$\pi \rightarrow$ 3p			
4 ^{1}A″	9.533	0.0029	183		σ (C−C)/n(F) $\rightarrow$ 3s/ σ *(C−F)		9.523
5 ^{1}A′	9.536	0.0010	248	$\pi \rightarrow \sigma$ *(C−F)			
6 ^{1}A′	9.705	0.0024	252	$\pi \rightarrow$ 3p			
7 ^{1}A′	9.840	0.0004	179			n(F) $\rightarrow$ 3s/ σ *(C−F)	
8 ^{1}A′	9.933	0.0857	203	$\pi \rightarrow \sigma$ *(C−F)			10.570
5 ^{1}A″	10.005	0.0029	167		σ (C−C)/n(F) $\rightarrow \sigma$ *(C−F)		
9 ^{1}A′	10.133	0.0070	304	$\pi \rightarrow$ 3d			9.421
6 ^{1}A″	10.271	<0.0001	323	$\pi \rightarrow$ 3d			
7 ^{1}A″	10.283	0.0004	334	$\pi \rightarrow$ 3d			
10 ^{1}A′	10.309	<0.0001	338	$\pi \rightarrow$ 3d			
11 ^{1}A′	10.398	0.0071	338	$\pi \rightarrow$ 3d			
8 ^{1}A″	10.465	<0.0001	462	$\pi \rightarrow$ 4p			
12 ^{1}A′	10.470	0.0006	482	$\pi \rightarrow$ 4s			
13 ^{1}A′	10.548	0.0076	497	$\pi \rightarrow$ 4p			
14 ^{1}A′	10.595	0.0010	544	$\pi \rightarrow$ 4p			
9 ^{1}A″	10.698	0.0004	235		σ (C−C)/n(F) $\rightarrow$ 3p		
10 ^{1}A″	10.849	<0.0001	658	$\pi \rightarrow$ 4d			
11 ^{1}A″	10.887	<0.0001	607	$\pi \rightarrow$ 4d			
12 ^{1}A″	10.942	0.0024	307		σ (C−C)/n(F) $\rightarrow$ 3p		10.570

[a] See discussion in text.

TABLE 3: Vibrational Assignments in the 8.5−11.0 eV Absorption Band of c-C_5F_8[a]

energy[b]	assignment	$\Delta E1$ (ν_A′)	ΔE (ν_B′)	energy[b]	assignment	ΔE (ν_A′)	ΔE (ν_B′)
8.837	ν_{00}			9.191 [s]	ν_{00}		
9.056 [d]	ν_A′	0.219		9.350 [w]	ν_B′		0.159
9.204	ν_A′ + ν_B′		0.148	9.407 [s]	ν_A′	0.216	
9.287	2ν_A′	0.231		9.552 [s]	ν_B′ + ν_A′		
9.421	ν_A′ + 2ν_B′	0.217		9.619 [s]	2ν_A′	0.212	
9.493 [s]	3ν_A′	0.206		9.778	ν_B′ + 2ν_A′	0.205	
9.656	νA′ + 3ν_B′	0.235		9.824 [s]	3ν_A′	0.205	
9.686 [s]	4ν_A′	0.193		9.983 [s]	ν_B′ + 3ν_A′	0.205	
9.864	ν_A′ + 4ν_B′	0.208		10.031	4ν_A′	0.207	
9.895	5ν_A′	0.209		10.188 [s]	ν_B′ + 4ν_A′	0.205	
10.064	ν_A′ + 5ν_B′	0.200		10.238	5ν_A′	0.207	
10.113 [w]	6ν_A′	0.218		10.410	ν_B′ + 5ν_A′	0.222	
10.272	ν_A′ + 6ν_B′	0.208		10.436 [w]	6ν_A′	0.198	
10.315 [d]	7ν_A′	0.202		10.606	ν_B′ + 6ν_A′	0.196	
10.481	ν_A′ + 7ν_B′	0.209		10.643 [d]	7ν_A′	0.207	
10.525 [d]	8ν_A′	0.210					
10.670 [w]	ν1′ + 8ν_B′	0.189					
10.744 [w]	9ν_A′	0.219					

[a] This work (energies are in eV). [b] [d] = diffuse structure; [s] = shoulder; [w] = weak feature.

4.2. Neutral Excited States. The high-resolution absolute VUV photoabsorption spectrum of c-C_5F_8 was recorded between 6.0 and 11.0 eV using the Aarhus Synchrotron Facility and is shown in Figure 1. Four absorption bands centered at 7.221, 7.754, 8.837, and 9.523 eV, respectively, are observed. All bands are quite broad (Figure 1), suggesting rapid dissociation into neutral radicals, with fine structure being observed in the latter (Figure 2 and Table 3) and reported here for the first time. According to the present calculations (Tables 1 and 2), the first band is due to a Rydberg/valence $\pi \rightarrow$ 3s/σ*(C−F) A′ transition. It is noteworthy that the TDDFT value (7.221 eV) is in better agreement with experiment than the EOM-CCSD result (7.569 eV). The second band, which is the most intense, corresponds to the $\pi \rightarrow \pi$* A″ transition. When compared to the measured value of 7.754 eV, the TDDFT result is slightly underestimated (7.428 eV), while the EOM-CCSD value is too high (8.119 eV).

The situation is much less clear for the third band at 8.837 eV, since there are large discrepancies between the two sets of calculations: while TDDFT predicts an intense ($f = 0.0972$) $\pi \rightarrow \sigma$*(C−F) A′ transition to occur at 8.540 eV, the EOM-CCSD counterpart is calculated at much higher energy (9.993 eV). According to EOM-CCSD, the only possible candidate could be the $\pi \rightarrow$ 3p transition calculated at 9.372 eV, but its intensity is rather low (0.0152). Both methods also predict numerous transitions in this energy range, arising mainly from the HOMO and the SHOMO, but their intensities are very weak as a result of their Rydberg nature. The fact that the SHOMO σ(C−C)/n(F) $\rightarrow \pi$* transition is weak may be rationalized by the fact that these MO's have densities on opposite parts of the molecule (Figure 5).

The background level is relatively high in the 8.5−10 eV energy region; therefore there might be a contribution from an

TABLE 4: Calculated Vibrational Energies for Both Neutral Ground and Lowest Ionic States of c-C_5F_8 (Energies Are in cm^{-1})

C_S modes	calculation: neutral ground state[a]	experiment[b]	calculation: ionic $^2A'$ state[a]	calculation: ionic $^2A''$ state[a]
a′	1841	1770	1711	1856
	1417	1386	1402	1420
	1361	1327	1363	1415
	1248	1219	1268	1315
	1207	1180	1259	1283
	1172	1144	1195	1171
	1031	1008	1032	929
	682	663	687	691
	639	617	637	656
	623	603	579	590
	512	499	470	465
	437	430	411	422
	351	347	359	328
	312	312	299	272
	248	252	248	247
	219	234	187	200
	175	187	150	173
	41	-	59	52
a″	1428	1389	1539	1431
	1323	1300	1346	1305
	1181	1211	1222	1282
	1136	1106	1086	1045
	1007	985	1018	828
	874	889	859	738
	715	721	739	648
	608	627	608	473
	451	444	438	417
	418	419	376	376
	313	312	286	284
	271	274	260	275
	258	252	225	211
	245	234	195	127
	99	100	75	i129

[a] This work (PBE0/6-311G**). [b] See reference 35.

underlying σ^* dissociative state in this region. Indeed, the calculations predict a σ^* state at 9.536, as shown in Table 2. This state is therefore very likely dissociative.

4.3. Vibrational Excitation in the Energy Range 8.5−11.0 eV. The VUV spectrum in this energy region (Figure 2) is characterized by a fine structure pattern coupled with the Rydberg series (see next section). Two transitions have been assigned to 8.837 (8.115 Mb) and 9.191 eV (6.733 Mb) in Table 3. These proposed progressions have been identified by calculations, using the Domcke−Cederbaum[28] procedure described above, as being the C═C stretching and C−C stretching modes, with mean energies of 0.219 and 0.148 eV, and labeled as (ν_A') and (ν_B'), respectively. Mode A′ is the 1770 cm^{-1} (0.232 eV) (C═C stretch nature as confirmed by theory) reported in Table 4, while mode B′ could be the 1185 (0.148 eV) and/or 1144 cm^{-1} (0.142 eV) modes (C−C stretch).

4.4. Rydberg Series. The cross section above 7 eV shows contributions from several assigned Rydberg structures (Figures 1 and 2), members of series converging to the three lowest ionization limits at 11.288, 12.944, and 13.791 eV, respectively (Figure 4), and mainly due to the promotion of a fluorine lone pair electron.

The peak positions, E_n, must fit the Rydberg formula: $E_n = E_i - R/(n - \delta)^2$, where E_i is the ionization energy, n is the principal quantum number of the Rydberg orbital of energy E_n, R is the Rydberg constant, and δ is the quantum defect resulting from the penetration of the Rydberg orbital into the core.

TABLE 5: Energy Values, Quantum Defect, and Assignment of the Rydberg Series Converging to the Ionic Electronic Ground State, $(30a')^{-1}$ (Energies Are in eV)

energy	quantum defect	assignment	ΔE (ν_A')
7.221	1.17	3s	
9.747[a]	1.03	4s	
10.410[b]	1.06	5s	
10.744	1.00	6s	
8.837	0.64	3p	
10.080	0.64	4p	
10.550	0.70	5p	
10.820	0.61	6p	
11.040		6p + $1\nu_A'$	0.220
11.230		6p + $2\nu_A'$	0.190
11.390[a]		6p + $3\nu_A'$	0.160
11.610		6p + $4\nu_A'$	0.220
11.820		6p + $5\nu_A'$	0.210
9.421	0.30	3d	
10.289	0.31	4d	
10.670	0.31	5d	

[a] Peak shoulder. [b] Broad feature.

Vibrational excitation associated with some Rydberg states are presented in detail in Tables 5, 6, and 7. However, in order to avoid congestion in the Rydberg series, we have not labeled them in the figures. The two modes being excited are those already reported for the valence excitation in the 8.5−10.0 eV energy region.

4.4.1. Rydberg Series Converging to the Lowest Electronic Ionic Ground State 30 a'^{-1}. The origin of three Rydberg series at 7.221, 8.837, and 9.421 eV have been identified to correspond to the 3s, 3p, and 3d transitions, with quantum defects δ of 1.17, 0.64, and 0.30, respectively (Table 5). The 3s member has a slightly high quantum defect for an s series, but that seems reasonable because of the mixing valence/Rydberg character. A comparison of the calculated vertical excitation energies in Tables 1 and 2 with the present VUV photoabsorption and EELS features (Figures 1 and 3) show some tentative assignments for the observed structure.

4.4.2. Rydberg Series Converging to the First Electronic Excited Ionic State 21 a''^{-1}. The first member of the lowest energy series (Table 6, Figure 2) observed converging to the first ionic electronic excited-state has been assigned to the fluorine lone pair electrons (n(F) → 3s) lying at 9.523 eV with a quantum defect of $\delta = 1.00$. There are three other series: np, np′, and nd, with their first terms being assigned to $n = 3$ at 10.570, 10.744, and 11.330 eV, with quantum defects $\delta = 0.61$, 0.51 and 0.10, respectively. The $n = 5$ at 12.270 eV and $n = 3$ at 11.330 eV are broad features and may also contain contributions from 4s and 3p′, respectively, both converging to the second electronic ionic excited state.

4.4.3. Rydberg Series Converging to the Second Excited Ionic State 29a'^{-1}. The first term of five series has been assigned to converge to the ionic energy 13.791 eV (Table 7, Figures 1 and 2). The energy position of the ns, np, np′, np″, and nd, lying at 10.401, 11.330, 11.450, 11.770, and 12.220 eV corresponds to quantum defects $\delta = 0.99$, 0.65, 0.59, 0.41 and 0.09, respectively. There are several features at 13.070, 13.210, and 13.390 eV that could also be members of different series converging to higher energy levels that can be explained by the broadness of the peaks observed, as shown in the EEL spectrum in the 13−14 eV region.

4.5. Ionic States. Figure 4 shows the bands associated with the ionic states of c-C_5F_8. The energy positions of the observed features are summarized in Table 8. The shape of the lowest

TABLE 6: Energy Values, Quantum Defect, and Assignment of the Rydberg Series Converging to the Ionic Electronic First Excited State, $(21a'')^{-1}$ (Energies Are in eV)

energy	quantum defect	assignment	ΔE (ν_A')	energy	quantum defect	assignment	ΔE (ν_A')
9.523[a]	1.00	3s		12.270[b]	0.51	5p′	
11.430[a]	1.00	4s		12.490	0.53	6p′	
11.610		4s + 1ν_A'	0.180				
12.110[a]	0.96	5s		12.840	0.56	12p′	
				13.030		12p′ + 1ν_A'	0.190
10.570[a]	0.61	3p					
11.700	0.69	4p		11.330	0.10	3d	
12.230[a]	0.64	5p		11.530		3d′ + 1ν_A'	0.200
12.400		5p + 1ν_A'	0.170	11.700		3d′ + 2ν_A'	0.170
12.580		5p + 2ν_A'		11.860		3d′ + 3ν_A'	0.160
				12.020		3d′ + 4ν_A'	0.160
12.750	0.62	9p		12.190		3d′ + 5ν_A'	0.170
				12.350		3d′ + 6ν_A'	0.160
10.744	0.51	3p′		12.540		3d′ + 7ν_A'	0.190
11.820	0.52	4p′		12.070	0.06	4d	
11.990		4p′ + 1ν_A'	0.170	12.400	0.00	5d	
12.160		4p′ + 2ν_A'	0.170				
12.320		4p′ + 3ν_A'	0.160	12.660	0.08	7d	

[a] Peak shoulder. [b] Broad feature.

TABLE 7: Energy Values, Quantum Defect, and Assignment of the Rydberg Series Converging to the Ionic Electronic Second Excited State, $(29a')^{-1}$ (Energies Are in eV)

energy	quantum defect	assignment	ΔE (ν_A')	energy	quantum defect	assignment	ΔE (ν_A')
10.401	0.99	3s		12.720[a]	0.44	4p″	
12.270	1.00	4s		13.140	0.43	5p″	
12.930	1.03	5s		13.340 (sh)	0.51	6p″	
13.210	1.16	6s					
13.390	1.17	7s		13.560	0.33	8p″	
11.330	0.65	3p		12.220 (sh)	0.06	3d	
12.580	0.65	4p					
13.070	0.66	5p		13.210	0.16	5d	
13.310	0.68	6p		13.390	0.17	6d	
13.490		6p + 1ν_A'	0.180	13.560		6d + 1ν_A'	0.170
				13.720		6d + 2ν_A'	0.160
11.450	0.59	3p′		13.870		6d + 2ν_A' + 1ν_B'	
12.620 (sh)	0.59	4p′		13.920		6d + 3ν_A'	0.200
13.070	0.65	5p′					
13.340 (s)	0.51	6p′		13.620	0.08	9d	
13.460 (s)	0.59	7p′		13.790		9d + 1ν_A'	0.170
				13.980		9d + 2ν_A'	0.190
11.770	0.41	3p″		13.650	0.18	10d	
11.940		3p″ + 1ν_B'	0.170				

[a] Peak shoulder

energy ionic band (Figure 4b) is quite broad, and superimposed on it there is a fine structure, whose maximum intensity lies at 11.696 ± 0.002 eV, corresponding to the vertical ionization energy. This value is compared to the calculations in Table 8. Despite their computational cost, the RCCSD and RCCSD(T) results are too low by ~1 eV. The UPBE0 method is better (11.374 eV), but the best results are obtained with the ROVGF method, especially with the cc-pVDZ basis set (11.776 eV).

Photoelectron spectroscopy can give both the adiabatic (or at least the most probable value of it) and the vertical ionization energies, the values of which tend to differ significantly whenever there is a large change in equilibrium molecular geometry on ionization.[14] In order to obtain the theoretical adiabatic ionization energy, the geometry of the $30a'^{-1}$ state was optimized at the UPBE0/6-311G** level, as shown in Figure 5f. As shown in the third column of Table 4, the calculated frequencies prove that this geometry corresponds to a true minimum. The main difference with the neutral geometry is a larger C═C bond due to the weakening of the π MO (+0.1 Å). After zero-point energy (ZPE) correction, the calculated adiabatic energy is predicted to be 10.832 eV, which is too low, but the theoretical difference between vertical and adiabatic energies (0.541 eV) is close to the observed one (0.488 eV). Interestingly, the same quantity is calculated to be 0.54 eV using the Domcke−Cederbaum vibrational analysis.

The vibrational pattern found in this band (Table 9) has been assigned to the excitation of the C═C stretching (ν_A') and to a contribution of the C−C stretching (ν_B') modes, with mean energies of 0.200 and 0.140 eV, respectively. The threshold for c-$C_5F_8^+$ has been quoted to be (11.6 ± 0.7) eV,[6] in good agreement with the maximum position of the present first ionic band. The shape of this first ionic band suggests that the parent ion must have a short lifetime.

The absence of vibrational structure in the second electronic band of the PES centered at 12.944 eV (which is very close to the calculated ROVGF/cc-pVDZ value of 13.047 eV) could be due to a very fast decomposition of the c-$C_5F_8^+$ molecular ion, although the ionization measurements of Jiao et al.[6] do not report

TABLE 8: Calculated and Experimental He(I) Photoelectron Ionization Energies of c-C_5F_8 (Energies Are in eV)

configuration	(U)PBE0[a]	ROVGF[a]	ROVGF[b]	RCCSD[b]	RCCSD(T)[b]	exp.[c]
30 a′ $^{-1}$	11.374	11.938	11.776	10.594	10.534	11.696
21 a″ $^{-1}$	12.354	13.177	13.047	12.178	11.826	12.944
29 a′ $^{-1}$		13.968	13.812			13.791
28 a′ $^{-1}$		15.686	15.872			15.59
20 a″ $^{-1}$		15.707	15.538			15.59
19 a″ $^{-1}$		15.847	15.482			15.59
27 a′ $^{-1}$		15.962	15.573			15.59
18 a″ $^{-1}$		16.142	16.001			15.98
26 a′ $^{-1}$		16.178	15.910			15.98
25 a′ $^{-1}$		16.641	16.407			16.67
17 a″ $^{-1}$		16.916	16.703			16.67
16 a″ $^{-1}$		17.151	16.882			16.67
24 a′ $^{-1}$		17.345	17.094			17.37
15 a″ $^{-1}$		17.428	17.192			17.37
23 a′ $^{-1}$		17.432	17.229			17.37
14 a″ $^{-1}$		17.721	17.463			17.37
22 a′ $^{-1}$		18.399	18.113			18.38
21 a′ $^{-1}$		19.541	19.287			19.51
13 a″ $^{-1}$		19.765	19.533			19.51
12 a″ $^{-1}$		19.940	19.679			19.51
20 a′ $^{-1}$		19.978	19.718			19.51

[a] This work. Values obtained at the PBE0/-6311G** geometry. [b] This work. Values obtained at the MP2/cc-pVDZ geometry. [c] This work.

TABLE 9: Energy Positions and Vibrational Analysis of Features Observed in the Photoelectron Bands of c-C_5F_8[a]

energy (eV)[b]	analysis	ΔE (ν_A') (eV)	ΔE (ν_B') (eV)
11.288	ν_{00}, adiabatic IE_1		
11.431 (?)	$\nu_{B'}$		0.143
11.499	$1\nu_{A'}$	0.211	
11.631 (?)	$1\nu_{A'} + \nu_{B'}$		0.132
11.696	$2\nu_{A'}$, vertical IE_1	0.197	
11.822 (?)	$2\nu_{A'} + \nu_{B'}$		0.126
11.892	$3\nu_{A'}$	0.196	
12.037 (?)	$3\nu_{A'} + \nu_{B'}$		0.145
12.107	$4\nu_{A'}$	0.215	
12.944	vertical IE_2		
13.482	ν_{00}, adiabatic IE_3		
13.636	$\nu_{B'}$		0.154
13.685	$\nu_{A'}$	0.203	
13.791	$1\nu_{A'} + \nu_{A'}$		0.155
13.857 (?)	$2\nu_{A'}$	0.172	
13.972 (?)	$2\nu_{A'} + \nu_{B'}$		0.181
15.59	vertical IE_4		
15.98	vertical IE_5		
16.67	vertical IE_6		
17.37	vertical IE_7		
18.38	vertical IE_8		
19.51	vertical IE_9		

[a] Uncertainties of the values given are ±0.002 eV for IE_1−IE_3 and ±0.02 eV for IE_4−IE_9. [b] (?) means uncertainty to peak/structure position.

any fragmentation yield in this energy region. In order to test this hypothesis, the geometry of the 21a″$^{-1}$, i.e., the SHOMO^{-1}, ionic state was optimized at the UPBE0/6-311G** level (Figure 5g). This state appears to be stable, with a lengthening of the C−C bonds consistent with the shape of the SHOMO (Figure 5e). However, the calculated vibrational modes (last column of Table 4) indicate that this structure is a saddle point with an a″ imaginary frequency, corresponding to the deformation of the carbon ring. Removing the C_s constraint during the optimization leads to the ^{2}A′ (HOMO^{-1}) ionic state, so it is impossible to obtain the geometry of the ^{2}A″ state. Nonetheless, the calculations prove without ambiguity that this state is stable, and the absence of apparent vibrational fine structure could be due to numerous overlapping vibration peaks.

The third ionic band centered at 13.791 eV (Figure 4c) also shows some evidence of excitation of the two vibrational (ν_A') and (ν_B') modes (Table 9). This value is in excellent agreement with the ROVGF/cc-pVDZ calculated value at 13.812 eV. The calculations also show that this band has to be assigned to the (29a′)$^{-1}$, i.e., the HOMO-2 state. The appearance threshold of the fragment ion $C_4F_6^+$ has been reported at (14.2 ± 0.7) eV,[6] which can be closely related to the nature of this ionic band. In fact, the background level is relatively high, suggesting a transition into a repulsive energy surface of the molecular ion leading to dissociation. The calculations are not able to test this hypothesis, but the delocalized character of the 29a′ MO (Figure 5h) does not seem to indicate a fragmentation into $C_4F_6^+ + CF_2$.

The other bands' positions, at higher energies, are listed in Table 9. According to the ROVGF calculations, their high intensity and absence of vibrational structure might be explained by the overlap of ionization bands of the quasi-degenerate lower lying (mainly lone pairs) MO's of the molecule.

The present PES also shows a few extra sharp features between 13.2 and 14.2 eV bands that are due to the Ar^+ calibration $^2P_{3/2}$ He(I)γ line and the $^2P_{3/2}$, $^2P_{1/2}$ He(I)β line, respectively. These features have been shown not to interfere with the observed patterns.

4.6. Photolysis Rates and Local Lifetimes. The absolute cross section values of c-C_5F_8 can be used to model its atmospheric destruction by UV photolysis as a function of altitude. Details of the program are presented in a previous publication by Limão-Vieira et al.[33] Photolysis rates at a given wavelength were calculated as the product of the solar actinic flux,[34] and the molecular photoabsorption cross section at 1 km altitude steps from the surface up to the stratopause (50 km). At each altitude, a total photolysis rate may then be calculated by summing over the individual photolysis rates for that altitude. The reciprocal of the total photolysis rate for a given altitude gives the local photolysis lifetime at that altitude, i.e., the time taken for the molecule to photodissociate at the altitude, assuming that the solar flux remains constant. The local lifetimes and the photolysis rates are shown in Figure 6, where, for the former, we assume that the quantum yield for dissociation is

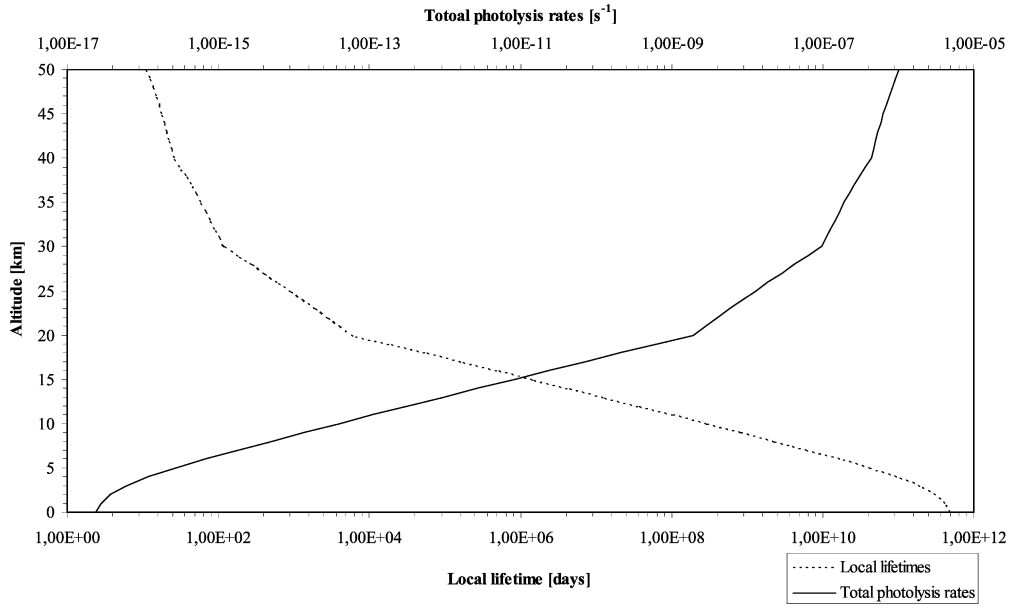

Figure 6. The local lifetime of c-C_5F_8 between 0 and 50 km obtained from its photoabsorption spectrum (Figure 1).

unity. The results show that the local photolysis lifetime of c-C_5F_8 varies from about 17 years at 20 km to a few days at 40−50 km. Therefore, it indicates that c-C_5F_8 will be stable to photolysis in the troposphere but can be broken up reasonably at higher altitudes. We have recently reported high-resolution Fourier transform infrared (FTIR) spectra[35] showing a strong infrared absorption cross section in the wavelength region of the earth's atmospheric window (800−1300 cm^{-1}), such that a long tropospheric lifetime may lead to a GWP of around 60 times that of CO_2 in a 100 years time horizon.

5. Conclusions

The present results are the first comprehensive set of experimental data on the spectroscopy of octafluorocyclopentene (c-C_5F_8) in the 6−14 eV energy region. An electron energy loss spectrum (EELS) was also recorded in the electric dipolar interaction (100 eV incident energy, ∼0° scattering angle) over the 5−14 eV energy loss range. In both spectra a fine structure is observed in the 10 eV energy region that has been assigned to specific vibrational modes. The VUV spectrum shows four absorption bands, centered at 7.221, 7.754, 8.837, and 9.191 eV with cross-sectional values of 11.440, 21.084, 8.116, and 6.733 Mb, respectively.

Ab initio calculations on the vertical excitation energies and oscillator strengths were used in the assignment of the spectral transitions. When compared to experiment the EOM-CCSD method tends to overestimate the excitation energy, while TDDFT values seem to be in better agreement. For ionic states, the ROVGF energies are in very good agreement with experiment, while CC values are too low by about 1 eV.

The measured photoabsorption cross sections have been used to derive the local lifetime in the Earth's atmosphere (0−50 km), showing that octafluorocyclopentene may have a short residence time in the upper atmosphere but a longer residential time in the lower stratosphere, leading to a significant GWP.

References and Notes

(1) Vasekova, E.; Drage, E. A.; Smith, K. M.; Mason, N. J. *J. Quant. Spectrosc. Radiat. Transfer* **2006**, *102*, 418−424.
(2) (a) Motomura, H.; Imai, S.-I.; Tachibana, K. *Thin Solid Films* **2000**, *374*, 243−248; (b) Takahashi, K.; Itoh, A.; Nakamura, T.; Tachibana, K. *Thin Solid Films* **2000**, *374*, 303−310.
(3) Mason, N. J.; Dawes, A.; Mukerji, R.; Drage, E. A.; Vasekova, E.; Webb, S. M.; Limão-Vieira, P. *J. Phys. B* **2005**, *38*, S893−S911.
(4) Limão-Vieira, P.; Vasekova, E.; Giuliani, A.; Lourenço, J. M. C.; Santos, P. M.; Duflot, D.; Hoffmann, S. V.; Mason, N. J.; Delwiche, J.; Hubin-Franskin, M.-J. *Phys. Rev. A* **2007**, *76*, 032509-1−032509-10.
(5) Chutjian, A.; Alajajian, S. H *J. Phys. B* **1985**, *18*, 4159−4167.
(6) Jiao, C. Q.; DeJoseph, C. A., Jr.; Garscadden, A. *J. Phys. D* **2005**, *38*, 1076−1080.
(7) Parkes, M. A.; Ali, S.; Tuckett, R. P.; Mickhailov, V. A.; Mayhew, C. A. *Phys. Chem. Chem. Phys.* **2007**, *9*, 5222−5231.
(8) Nakamura, T.; Motomura, H.; Tachibana, K. *Jpn. J. Appl. Phys.* **2001**, *40*, 847−854.
(9) Nakamura, T.; Tachibana, K. *Appl. Phys. Lett.* **2002**, *80*, 3904−3906.
(10) Eden, S.; Limão-Vieira, P.; Hoffmann, S. V.; Mason, N. J. *Chem. Phys.* **2006**, *323*, 313−333.
(11) Motte-Tollet, F.; Hubin-Franskin, M.-J.; Collin, J. E. *J. Chem. Phys.* **1992**, *97*, 7314−7322.
(12) Giuliani, A.; Delwiche, J.; Hoffmann, S. V.; Limão-Vieira, P.; Mason, N. J.; Hubin-Franskin, M.-J. *J. Chem. Phys.* **2003**, *119*, 3670−3680.
(13) Delwiche, J.; Natalis, P.; Momigny, J.; Collin, J. E. *J. Electron Spectrosc. Relat. Phenom.* **1973**, *1*, 219−225.
(14) Eland, J. H. D. *Photoelectron Spectroscopy*; Butterworth & Co., Ltd.: London, 1984; p 60.
(15) Minnhagen, L. *J. Opt. Soc. Am.* **1973**, *63*, 1185−1198.
(16) Dreuw, A.; Head-Gordon, M. *Chem. Rev.* **2005**, *105*, 4009−4037.
(17) Aquilante, F.; Barone, V.; Roos, B. O. *J. Chem. Phys.* **2003**, *119*, 12323−12334.
(18) Adamo, C.; Barone, V. *J. Chem. Phys.* **1999**, *110*, 6158−6170.
(19) Frisch, M. J.; Trucks, G. W.; Schlegel, H. B.; Scuseria, G. E.; Robb, M. A.; Cheeseman, J. R.; Montgomery, J. A., Jr.; Vreven, T.; Kudin, K. N.; Burant, J. C.; Millam, J. M.; Iyengar, S. S.; Tomasi, J.; Barone, V.; Mennucci, B.; Cossi, M.; Scalmani, G.; Rega, N.; Petersson, G. A.; Nakatsuji, H.; Hada, M.; Ehara, M.; Toyota, K.; Fukuda, R.; Hasegawa, J.; Ishida, M.; Nakajima, T.; Honda, Y.; Kitao, O.; Nakai, H.; Klene, M.; Li, X.; Knox, J. E.; Hratchian, H. P.; Cross, J. B.; Bakken, V.; Adamo, C.; Jaramillo, J.; Gomperts, R.; Stratmann, R. E.; Yazyev, O.; Austin, A. J.; Cammi, R.; Pomelli, C.; Ochterski, J. W.; Ayala, P. Y.; Morokuma, K.; Voth, G. A.; Salvador, P.; Dannenberg, J. J.; Zakrzewski, V. G.; Dapprich, S.; Daniels, A. D.; Strain, M. C.; Farkas, O.; Malick, K. D. Rabuck, A. D.; Raghavachari, K.; Foresman, J. B.; Ortiz, J. V.; Cui, Q.; Baboul, A. G.; Clifford, S.; Cioslowski, J.; Stefanov, B. B.; Liu, G.; Liashenko, A.; Piskorz, P.; Komaromi, I.; Martin, R. L.; Fox, D. J.; Keith, T.; Al-Laham, M. A.; Peng, C. Y.; Nanayakkara, A.; Challacombe, M.; Gill, P. M. W.; Johnson,

B.; Chen, W.; Wong, M. W.; Gonzalez, C.; Pople, J. A. *Gaussian 03*, revision D.01; Gaussian, Inc.: Wallingford, CT, 2004.

(20) Serrano-Andres, L.; Merchan, M. *J. Mol. Struct. (THEOCHEM)* **2005**, *729*, 99−108.

(21) Hampel, C.; Peterson, K.; Werner, H.-J. *Chem. Phys. Lett*. **1992**, *190*, 1−12.

(22) Werner H.-J.; Knowles, P. J.; Lindh, R.; Manby, F. R.; Schütz, M.; Celani, P.; Korona, T.; Rauhut, G.; Amos, R. D.; Bernhardsson, A.; Berning, A.; Cooper, D. L.; Deegan, M. J. O.; Dobbyn, A. J.; Eckert, F.; Hampel, C.; Hetzer, G.; Lloyd, A. W.; McNicholas, S. J.; Meyer, W.; Mura, M. E.; Nicklass, A.; Palmieri, P.; Pitzer, R.; Schumann, U.; Stoll, H.; Stone, A. J.; Tarroni, R.; Thorsteinsson, T. *MOLPRO*: *A Package of Ab Initio Programmes*, version 2006.1; University College Cardiff Consultants, Ltd.: Cardiff, U.K., 2006 (http://www.molpro.net).

(23) Kaufmann, K.; Baumeister, W.; Jungen, M. *J. Phys. B* **1989**, *22*, 2223−2240.

(24) Knowles, P. J.; Hampel, C. Werner, H.-J. *J. Chem. Phys*. **1993**, *99*, 5219−5227.

(25) Watts, J. D.; Gauss, J.; Bartlett, R. J. *J. Chem. Phys*. **1993**, *98*, 8718−8733.

(26) Ortiz, J. V.; Zakrzewski, V. G.; Dolgounircheva, O. In *Conceptual Perspectives in Quantum Chemistry*; Calais, J.-L., Kryachko, E., Eds.; Kluwer Academic: Norwell, MA, 1997; pp 465−518.

(27) Ortiz, J. V. *J. Chem. Phys*. **1988**, *89*, 6348−6352.

(28) Köppel, H.; Domcke, W.; Cederbaum, L. S. *Adv. Chem. Phys.* **1981**, *57*, 59−246.

(29) Fischer, G.; Cao, X. *J. Phys. Chem. A* **1999**, *103*, 3726−3731.

(30) Schaftenaar, G.; Noordik, J. H. *J. Comput.-Aided Mol. Des.* **2000**, *14*, 123−134.

(31) Bartlett, R. J.; Musial, M. *Rev. Mod. Phys.* **2007**, *79*, 291−352.

(32) Arulmozhiraja, S.; Ehara, M.; Nakatsuji, H. *J. Chem. Phys*. **2007**, *126*, 044306/1−044306/10.

(33) Limão-Vieira, P.; Eden, S.; Kendall, P. A.; Mason, N. J.; Hoffmann, S. V. *Chem. Phys. Lett*. **2002**, *364*, 535−541.

(34) *Chemical Kinetics and Photochemical Data for Use in Stratospheric Modeling*, Evaluation Number 12; JPL Publication 97-4; NASA, Jet Propulsion Laboratory: Pasadena, CA, 1997.

(35) Harris, W. C.; Longshore, C. T. *J. Mol. Struct*. **1973**, *16*, 187−204.

Article 8

Eur. Phys. J. D **51**, 97–108 (2009)
DOI: 10.1140/epjd/e2008-00154-7

THE EUROPEAN PHYSICAL JOURNAL D

Regular article

Electronic states of neutral and ionized tetrahydrofuran studied by VUV spectroscopy and ab initio calculations*

A. Giuliani[1,2,a], P. Limão-Vieira[3,4], D. Duflot[5], A.R. Milosavljevic[6], B.P. Marinkovic[6], S.V. Hoffmann[7], N. Mason[4], J. Delwiche[8], and M.-J. Hubin-Franskin[8]

[1] DISCO beamline, Synchrotron Soleil, L'Orme des Merisiers, Saint-Aubin, 91192 Gif-sur-Yvette, France
[2] Cepia, Institut National de la Recherche Agronomique (INRA), BP 71627, 44316 Nantes Cedex 3, France
[3] Laboratório de Colisões Atómicas e Moleculares, CEFITEC, Departamento de Física, Universidade Nova de Lisboa, 2829-516 Caparica, Portugal
[4] Centre of Molecular and Optical Sciences, Department of Physics and Astronomy, The Open University, Walton Hall, Milton Keynes, MK7 6AA, UK
[5] Laboratoire de Physique des Lasers, Atomes et Molécules (PhLAM), UMR CNRS 8523, Centre d'Études et de Recherches Lasers et Applications (CERLA, FR CNRS 2416), Université des Sciences et Technologies de Lille, 59655 Villeneuve d'Ascq Cedex, France
[6] Laboratory for atomic collision processes, Institute of Physics, Pregrevica 118, 11080 Belgrade, Serbia
[7] Institute for Storage Ring Facilities, University of Aarhus, Ny Munkegade, 8000, Aarhus C, Denmark
[8] Laboratoire de Spectroscopie d'Électrons Diffusés, Université de Liège, Institut de Chimie-Bât. B6c, 4000 Liège 1, Belgium

Received 15 January 2008 / Received in final form 13 May 2008 / Published online 6 August 2008

Abstract. The electronic spectroscopy of isolated tetrahydrofuran (THF) in the gas phase has been investigated using high-resolution photoabsorption spectroscopy in the 5.8–10.6 eV with absolute cross-section measurements derived. In addition, an electron energy loss spectrum was recorded at 100 eV and 10° over the 5−11.4 eV range. The He(I) photoelectron spectrum was also collected to quantify ionisation energies in the 9−16.1 eV spectral region. These experiments are supported by the first high-level ab initio calculations performed on the excited states of the neutral molecule and on the ground state of the positive ion. The excellent agreement between the theoretical results and the measurements allows us to solve several discrepancies concerning the electronic state spectroscopy of THF. The present work reconsiders the question of the lowest energy conformers of the molecule and its population distribution at room temperature.

PACS. 33.20.Ni Vacuum ultraviolet spectra – 33.60.+q Photoelectron spectra – 32.80.Ee Rydberg states 31.15.A- Ab initio calculations

1 Introduction

Tetrahydrofuran (THF) is a five membered heterocyclic ring that is often used as a chemical and molecular model for the (deoxy)ribose ring in nucleic acids. In the past ten years considerable research has been dedicated to the study of the spectroscopy and collisional interactions with biomolecules such as THF – either deposited as thin films or in the gas phase. The motivation for much of this work has been in relation to the study of radiation damage to biomolecules since it is known that a large amount of the energy deposited in biological media by ionising radiation is channelled into biomolecules such as DNA and the lipids forming cellular membranes. In particular ionising radiation liberates large numbers of low energy secondary electrons [1]. These secondary electrons, despite having energies below the ionization threshold, can induce significant amounts of both single and double strand breaks within the cellular DNA [2] in turn providing the origin of mutations or inducing cellular death [3].

Low energy electrons may also excite biomolecular targets through inelastic collisions and populate electronically excited states which may subsequently decay with the production of 'radicals' whose chemical reactivity may strongly influence the local site chemistry. A detailed understanding of the electronic state spectroscopy of the molecular constituents of DNA are therefore necessary if we are to develop a comprehensive understanding of radiation induced damage in DNA at a molecular level. However since the nucleosides and nucleotides comprising DNA are solids at room temperature it has, to date, proven difficult to measure absolute photoabsorption cross sections for these compounds and to date there are only a

* Supplementary information Tables 1–7 are only available in electronic form at http://www.epj.org

[a] e-mail: alexandre.giuliani@synchrotron-soleil.fr

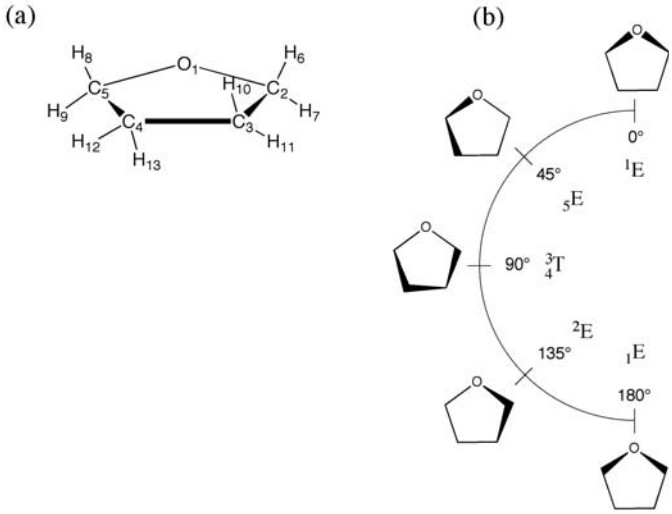

Fig. 1. (a) Structure of THF with atom numbering. (b) Pseudorotation of THF. Half of the cycle of the pseudorotation angle ($\phi = 0$ to 180°) is shown. Picture adapted from references [17] and [25].

few spectroscopic studies of such molecules. THF provides a good analogue for the (deoxy)ribose nucleic acids and therefore in recent years has been the subject of several experimental and theoretical studies [4–15]. However severe discrepancies concerning the spectroscopy of THF remain.

THF is a puckered molecule supporting several internal motions of out-of-plane ring vibrations, called pseudorotation [16]. The molecule may adopt several different conformations, Figure 1, all of which appear to be connected along the pseudorotation path as a function of the pseudorotation angle ϕ. A similar type of ring deformation is known to occur in the nucleosides and nucleotides and is closely related to higher order structure in the nucleic acids like DNA and RNA [17]. The preferred conformation of the isolated molecule in the gas phase is still debated, despite several experimental [18–21] and theoretical studies to clarify the situation [16,21–24]. Recently, Yang at al. suggested that the most populated conformer could be obtained from electron momentum spectroscopy (EMS) [25].

The first study of the electronic state spectroscopy of THF was performed by Picket et al. [26], who measured the VUV photoabsorption spectrum for the first time. This early work reported two electronic transitions at 51 440 cm^{-1} (6.378 eV) and 55 640 cm^{-1} (6.899 eV). Subsequent work by Hernandez [27] confirmed the electronic transitions of Pickett et al. [26]. A vibrational analysis of structure observed in the VUV spectrum was performed and four Rydberg series identified. Subsequently Davidson et al. [28] contested these pioneering investigations. They suggested the lowest energy optically active transition to be the $n \rightarrow 3s$ transition [28] at 6.03 eV. A complex vibrational structure was reported involving multiple excitations and de-excitation of the pseudo-rotation mode with frequencies ranging from 60 to 260 cm^{-1} [28]. Above 6.3 eV the band broadens and a second electronic transition was suggested with vibrational frequencies around 200 cm^{-1}. The presence of such an unexpected transition in this energy region was commented upon by Robin [29]. Tam and Brion have recorded the first electron energy loss spectrum in dipolar excitation conditions of the molecule [30]. Their analysis of the spectral band was based on derived term values. A Rydberg series analysis by Doucet et al. [31] reported a single ns series ($\delta = 0.94$), two np series ($\delta = 0.64$ and 0.52) and a single nd series ($\delta = 0.08$). Their assignment of the $n = 3$ member was in agreement with the previous work, but interestingly, their vibrational analysis of the first spectral band did not involve a second electronic origin. Bremner et al. [32] re-examined the VUV photoabsorption spectrum of THF extending the excitation energy range up to the LiF cut off at 11.8 eV allowing further Rydberg series to be analysed.

In this paper we present a combined theoretical and experimental study of the ground and excited states of both the neutral THF molecule and its cation. We believe that this work represents the highest resolution photoabsorption and photoelectron data currently available. For the first time, the neutral and ionic excited states are studied theoretically using high-level ab initio methods. Through a combination of these theoretical and experimental results we are then able to discuss previous discrepancies concerning the nature of the lowest energy spectral band in the photoabsorption and reassign the broad band features spectrum at higher energies. This, in turn, leads us to address the question of the lowest energy conformers of the molecule and to question the claims of Yang et al. [25] following their EMS study. Hitherto, the electronic spectra of THF recorded at room temperature were interpreted on the basis of a single geometry. We show in the following that a better description of the electronic spectroscopy of the molecule is gained by considering the two lowest energy conformers.

2 Methods

2.1 Photoabsorption spectroscopy

The high-resolution VUV photoabsorption measurements were performed using the ASTRID – UV1 beam line at the Institute for Storage Ring Facilities (ISA), University of Aarhus, Denmark. A detailed description of the apparatus can be found elsewhere [33], so only a brief description will be given here. A toroidal dispersion grating is used to select the synchrotron radiation with a *FWHM* wavelength resolution of approximately 0.075 nm. The synchrotron radiation passes through the static gas sample at room temperature. A photo-multiplier is used to detect the transmitted light. For wavelengths below 200 nm a flow of He gas is flushed through the small gap between the photomultiplier and the exit window of the gas cell to prevent any absorption by air in the VUV range of the spectrum. A LiF entrance window acts as an edge filter for higher order radiation restricting the photoabsorption measures to below 10.8 eV (115 nm). The grating itself provides a maximum wavelength (lower energy limit) of 320 nm (3.9 eV). The sample pressure is measured by

a Baratron capacitance gauge. To avoid any saturation effects sample pressures were chosen such that the transmitted flux was >10% of the incident flux.

Gas transmission results are compared to a background scan recorded with an evacuated cell. Absolute photoabsorption cross sections may then be calculated using the Beer-Lambert law:

$$I_t = I_0 \exp(-n\sigma x),$$

where I_t is the intensity of the light transmitted through the gas sample, I_0 is that through the evacuated cell, n is the molecular number density of the sample gas, σ is the absolute photoabsorption cross section and x is the absorption path length (25 cm). The accuracy of the absolute cross-section is estimated to be better than 5%.

2.2 Photoelectron spectroscopy

He(I) (21.22 eV) photoelectron spectra of THF were recorded at the Université de Liège, Belgium. The apparatus has been described in detail previously [34]. Briefly, the spectrometer consists of a 180° cylindrical electrostatic analyser with a mean radius of 5 cm. The analyser is used in constant energy pass mode. The incident photons are produced by a D.C. discharge in a two-stage differentially pumped lamp. The energy scale was calibrated using argon lines ($^2P_{3/2}$ = 15.760 eV and $^2P_{1/2}$ = 15.937 eV) [35,36] and the resolution of the present spectrum is measured from the full width half maximum of the Ar peaks to be 50 meV, in presence of THF. The intensities in the spectrum were corrected for the transmission of the analyzing system. The data reported here are the sum of many individual spectra. This procedure allows us to obtain a good signal-to-noise ratio while keeping the pressure in the spectrometer at very low level ($< 5 \times 10^{-6}$ mbar). The accuracy of the energy scale is estimated to be ±2 meV.

2.3 Electron energy loss spectroscopy

The electron energy loss spectra of THF have been measured at the Institute of Physics, Belgrade, using a cross beam experimental setup which has been described recently [37]. Briefly, a non-monochromated electron beam produced by an electron gun crosses perpendicularly a molecular beam produced by a non-magnetic stainless steel needle. The scattered electrons are retarded and focused into a double cylindrical mirror energy analyzer (DCMA). After being selected by energy, the electrons are focused by a three-element cylindrical lens into a single channel multiplier, working in a single counting mode. The highest energy resolution was limited by the initial thermal spread of incident electrons to be about 0.5 eV. The accuracy of the incident electron energy was determined to be ±0.4 eV by observing a threshold for He^+ ions yield. The electron gun can be rotated around the gas needle in the range of about −40° to 130°. The uncertainty of the angular scale was found to be better than ±0.5°. The base pressure was about 3×10^{-7} mbar and the operating pressure was about 6×10^{-6} mbar. The electron energy loss measurements were performed in a constant pass energy mode, by ramping the retarding potential at the entrance of DCMA. The calibration of the energy loss scale has been obtained according to the position of the elastic peak. The measurements were performed in conditions that favor dipole-allowed transitions – small scattering angles (10°) and high incident energies (100 eV), such that they may be directly compared with the high-resolution VUV optical measurements.

2.4 The terahydrofuran sample

The gas sample used in all the measurements was purchased from Sigma-Aldrich, with a minimum purity of +99%. The samples have been submitted to repeated freeze-pump-thaw cycles to remove the dissolved gases.

2.5 Ab initio calculations

Ab initio calculations were used to determine vertical excitation energies of the electronic states using the EOM-CCSD [38] implemented in the MOLPRO programme [39]. The equilibrium geometry of the C_2 and C_s conformers is identical to the results of Rayón and Sordo [24] obtained at the MP2 level with the aug-cc-pVDZ basis set. In order to describe Rydberg states, diffuse functions $(5s, 5p, 5d)$ taken from Kaufmann et al. [40] were added at the centre of the molecule. The ionisation energies were obtained with the restricted outer valence Green's function (ROVGF) method [41,42], using the Gaussian03 package [43].

3 Results and discussion

3.1 Neutral ground state

As mentioned in the introduction, the lowest energy structure of the molecule is still the subject of debate. Table 1 summarizes the literature results together with the present findings. According to the microwave spectroscopic studies of Mamleev et al. [20], supported by the recent experimental and theoretical work of Melnik et al. [21], the global minimum is found for the twisted C_2 conformation. These findings are in sharp contrast with the previous results of Engerholm et al. [18] and of Meyer et al. [19], for whom the global minimum is very close to the envelope ${}_5E(C_1)$ conformation. From a theoretical point of view Cadioli et al. [22] using HF and MP2 calculation found C_2, C_1 and C_s in this increasing sequence stability. Han and Kang [23] reported at the HF and MP2 level of theory the twisted C_2 conformations to be the most stable. Melnik et al. [21] carried out MP2/6-31+G(p, d) and B3LYP/6-31+G(p, d) calculations, which gave the twisted C_2 as a global minimum in perfect agreement with their

Table 1. Pseudorotation angle (in degree), symmetry and description of the potential energy surface minima for THF as determined from experiments and theoretical calculations.

	Global minimum			Local minimum		
Experiments	ϕ	Conform.	Symmetry	ϕ	Conform.	Symmetry
MW[a]						
Engerholm et al. [18]	56	$\sim{}_5$E	C_1			
Meyer et al. [19]	52.5	$\sim{}_5$E	C_1			
Mamleev et al. [20]	90	${}^3_4$T	C_2	0, 180	${}_1$E, ^{1}E	C_s
Melnik et al. [21]	90	${}^3_4$T	C_2	0, 180	${}_1$E, ^{1}E	C_s
EMS[b]						
Yang et al. [25]		${}_1$E	C_s			
Theory						
This Work	90	${}^3_4$T	C_2	0, 180	${}_1$E, ^{1}E	C_s
Cadioli et al. [22]	90	${}^3_4$T	C_2	0, 180	${}_1$E, ^{1}E	C_s
Han and Kang [23]	90	${}^3_4$T	C_2	0,180	${}_1$E, ^{1}E	C_s
Wu and Cremer [16]	90	${}^3_4$T	C_2			
Rayón and Sordo [24]	0	${}_1$E	C_s	90	${}^3_4$T	C_2

[a] Microphone spectroscopy. [b] Electron momentum spectroscopy.

experimental results. Wu and Cremer also reported, at the MP2/cc-pVTZ and B3LYP/6-31G(p, d) levels, the twisted ${}_1$E geometry (C_2) to be the global minimum [16] lying ∼0.2 kcal/mol below the C_s geometry. Recently, Rayón and Sordo [24] performed a detailed theoretical study at the MP2/aug-cc-pVTZ including anharmonic ZPE correction and suggested that the envelopes C_s are the global minima structures. The authors estimated the energy difference between C_s and C_2 minima to be 46 cm^{-1} (i.e. 0.13 kcal/mol) at the CCSD(T)//CBS(MP2) level. Surprisingly, this theoretical finding is at variance with every previous result from microwave spectroscopy and from theoretical calculations as seen in Table 1. It is also worth noting that, as previously mentioned by Cadioli et al. [22], results from X-rays [44] and neutron diffraction [45] experiments are consistent with the C_2 geometry, as seen from the values of dihedral angle involving the ring at supplementary information Table 1. Rayón and Sordo [24] have pointed out that the potential energy surface (PES) is nearly flat, which makes the characterisation of geometries as the extrema along the pseudo-rotational coordinate a challenging task. The global shape of the PES was also found to be extremely dependent on the basis set used. Recently, from EMS experiments, Yang et al. [25] have claimed the C_s geometry to be the most populated conformer of THF on the basis on better agreement of calculated orbital momentum distribution for the C_s geometry with the experiment.

We have calculated the ground state geometry at the MP2 level of theory following Rayón and Sordo [24] for the C_{2v}, C_2 and C_s isomers (the C_1 isomer being neglected) using the aug-cc-pVDZ basis set. The results are compared with the available literature data [19,22–24,44,45] at supplementary information, Table 1. At this level, the C_s geometry is a saddle point but with the larger aug-cc-pVTZ basis set C_s and C_2 are minima of the PES. Although the basis set has been found by Rayón and Sordo [24] to have important effects on the nature of the PES extremum, our use of the aug-cc-pVDZ basis set should have little influence on the electronic excitation energies, especially since most excited states are Rydberg in nature. Considering the Rayón and Sordo computed energy separation of 46 cm^{-1} for these two lowest energy conformers, it is very likely that at room temperature both isomers coexist. Indeed, a Boltzmann analysis at 298 K indicates that C_2 and C_s amount to 55.5% and 44.5% of the population, respectively. The C_{2v} geometry is excluded from the Boltzmann population analysis since a consensus has been reached in the literature, for which this geometry is a saddle point [19,22–24,44,45] with two imaginary frequencies. We shall therefore consider in the following discussion the possible spectral signature from the C_s and C_2 conformers of THF.

The electronic configuration of THF in its electronic ground state and in the C_{2v} formalism is: $1a_1^2 1b_1^2 2a_1^2 3a_1^2 2b_1^2 4a_1^2 5a_1^2 3b_1^2 6a_1^2 4b_1^2 1b_2^2 7a_1^2 1a_2^2\, 2b_2^2\, 5b_1^2\, 8a_1^2\, 6b_1^2\, 9a_1^2 2a_2^2 3b_2^2 :\ \widetilde{\mathrm{X}}^1A_1$.

C_{2v} correlates unambiguously to the other lower geometries. In the C_2 point group, the C_{2v} a_1 and a_2 become a and b_1 and b_2 correlate to b. For the C_s geometry, a_1 and b_1 become a' and a_2 and b_2 become a''.

The molecule possesses 33 normal vibrations distributed into two irreducible subgroups 17A+16B in the C_2 point group [22,23,46,47]. The literature data on the normal vibrational mode are shown in supplementary information Table 2 together with the assignments from Lepage et al. [4].

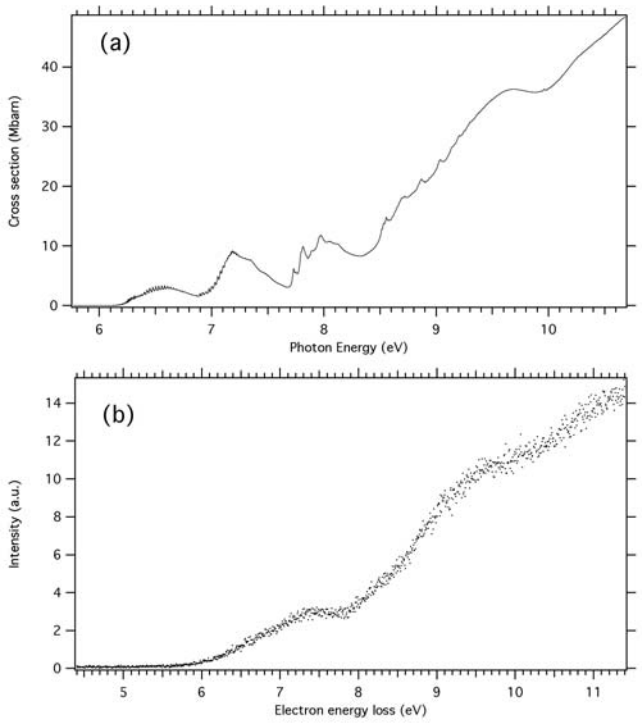

Fig. 2. High-resolution photoabsorption spectrum (a) and electron energy loss spectrum (b) of THF recorded at 100 eV and 10° scattering angle.

3.2 Neutral excited states

Table 2 compares the calculated excited states transition for the two lowest energy geometries of THF, namely C_s and C_2, with the assignments made from the photoabsorption measurements. Figure 2 shows the photoabsorption spectrum recorded between 5.8 eV and 10.7 eV (2a) and the electron energy loss spectra (EELS) up to 11.5 eV (2b). Although measured at lower resolution, the EELS spectra agree well with the photoabsorption data for the band position. Our data also appears to be in very good agreement with the literature data of Davidson et al. [28] and Bremner et al. [32] in both energy position and absolute cross section, although our resolution is better than that of Bremner et al. [32]. The photoabsorption spectrum is composed of a low energy band peaking at 6.6 eV, on which very sharp features are superimposed. At 6.9 eV a second band starts and extending up to 7.7 eV, peaking at 7.15 eV with a local maximum cross section of 12 Mbarn. This band also shows structure on its low energy side. It is followed by a third band up to 8.3 eV on which sharper features are observed. From 8.3 eV, the cross section, superimposed with sharper features, rises almost monotonically up to the end of the present measurements.

3.2.1 Lowest energy excited states

3.2.1.1 The 3s terms of the series converging to the ionic ground electronic state

Figure 3a shows the lowest energy band spanning from 6.04 to 6.88 eV. This spectral region appears extremely structured. As discussed above, the assignments to be given to this band have been much debated in the literature and there is currently no agreement as to its classification. Davidson et al. [28], on the basis of careful vibrational analysis conducted at different sample temperatures, concluded that this band should be assigned to two electronic origins with their associated vibrational progressions. In contrast other authors reported a single electronic transition with heavy hot band structure. This absorption band, centred around 6.5 eV, which corresponds to a term value of 3.25 eV is indicative of a 3s-type Rydberg state. Hence, the presence of two electronic origins was puzzling, as noted by Robin [29].

Our calculations (Tab. 2) predict the lowest energy singlet excited state of the molecule to be the 3s Rydberg state converging to the first ionic limit for every geometry considered. Vertical transition to this excited state is calculated at a noticeable lower energy (6.357 eV) but with half the oscillator strength for the C_2 geometry than for the C_s (6.608 eV). Hence, based on our theoretical results, we assign the first absorption band to the lowest energy transitions for the C_2 and C_s conformers, see Figure 3a. We have placed the $3s(C_2)$ adiabatic transition energy at 6.221 eV in agreement with Davidson et al. [28]. The vibrational assignments are given in supplementary information Table 3. The vibrational structure may be rationalized in terms of a progression of 62.9 cm^{-1} (7.8 meV) corresponding to the excitation of the ring-puckering mode (Tab. 1). We estimate the vertical energy for the $3s(C_2)$ transition to be around 6.3 eV. In agreement with Davidson et al. [28] we find a hot band system involving excitation of ν_{17}, which wavenumber of 250.8 cm^{-1} (31.1 meV) agrees very well with the values reported for the ground state of 286 cm^{-1} (35.5 meV) (see Tab. 3 and also in supplementary information).

The $3s(C_s)$ 0−0 transition is placed at 6.353 eV and appears accompanied by two long and overlapping progressions of 171 cm^{-1} (21.2 meV) and 237 cm^{-1} (29.38 meV) assigned to the ring-puckering modes ν_{33} and ν_{17}, respectively (see Tab. 3 and also in supplementary information). The ν_{33} progression was also reported by Davidson et al. [28] but with no further discussion.

3.2.1.2 The 3p terms of the series converging to the ionic ground electronic state

Figure 3b shows an enlargement of the 6.8 to 8.4 eV band system. Our calculations predict excitations of the 3p members to be mostly responsible for this absorption band, in agreement with the previous work of Bremner et al. [32]. Again, the agreement between theory and experiment is excellent and allows a straightforward interpretation of this spectral region. The calculation predicts the 3p excitation for the C_s geometry at 7.154 eV with an oscillator strength of 0.047, which is very close to the maximum of the absorption band at 7.19 eV. This feature was assigned to excitation of a 3p state by Bremner et al. [32]. The maximum of this band appears structured by less intense and sharp features, which are assigned to

Table 2. Experimental vertical excitation energies (eV) compared to theoretical transition energies (eV) and oscillator strength calculated for the C_2 and C_s conformers of THF.

E	Conformation	Symmetry	f ($\times 10^{-2}$)	$\langle r^2 \rangle$	HOMO[c]	SHOMO[d]	HOMO-2[e]	Exp.
6.357	C_2	B	0.6	111	3s			6.221[a]
6.608	C_s	A′	1.3	108	3s			6.353[a]
6.889	C_2	A	0.04	126	3p			–
7.025	C_2	A	0.02	140	3p			–
7.103	C_2	B	0.2	138	3p			6.898[a]
7.154	C_s	A′	4.7	127	3p			7.142[a]
7.296	C_s	A″	0.3	140	3p			7.300[a]
7.381	C_s	A′	0.7	144	3p			7.350[v]
7.474	C_2	B	0.9	143	3d			7.483[v]
7.713	C_2	A	0.002	170	3d			–
7.715	C_2	B	1.67	184	3d			7.730[a]
7.724	C_s	A′	0.37	143	3d			7.749[a]
7.754	C_2	B	2.07	179	3d			7.813[a]
7.859	C_2	A	0.06	198	3d			–
7.978	C_s	A″	0.28	169	3d			
7.985	C_s	A′	1.5	183	3d			7.867[a]
7.988	C_2	B	0.05	293	4s			–
8.017	C_s	A′	0.72	180	3d			–
8.103	C_s	A′	0.02	196	3d			–
8.144	C_2	A	0.02	372	4p			–
8.188	C_2	B	0.01	369	4p			–
8.194	C_2	A	0.00003	405	4s			–
8.249	C_s	A′	0.18	285	4s			–
8.288	C_2	A	1.12	120		3s		8.3[v]
8.335	C_2	B	0.17	454	4d			8.515[v]
8.405	C_s	A′	0.97	369	4p			8.37[v]
8.422	C_2	B	0.23	558	4d			8.533[v]
8.439	C_2	A	0.002	530	4d			–
8.451	C_s	A″	0.095	393	4p			–
8.457	C_2	B	1.13	558	4d			8.557[v]
8.460	C_s	A′	0.61	345	4p			8.4[v]
8.494	C_s	A′	0.16	170			3s	–
8.496	C_2	A	0.003	598	4d			–
8.545	C_2	B	0.038	770	5s			–
8.584	C_s		0.007	443	4d			–
8.615	C_2	A	0.0008	975	5p			–
8.623	C_2	B	0.0033	907	5p			–
8.635	C_2	A	0.0003	1019	5p			–
8.684	C_s	A″	0.0012	140		3s		–
8.693	C_s	A′	0.40	550	4d			8.652[v]
8.700	C_s	A″	0.12	527	4d			8.695[v]
8.715	C_2	B	0.03	1030	5d			–
8.720	C_s	A″	0.19	555	4d			8.719[v]
8.751	C_s	A′	0.005	591	4d			–
8.760	C_2	B	0.055	1244	5d			–
8.792	C_2	B	0.6	180		3p		8.793[v]
8.800	C_2	A	0.006	839	5d			
8.808	C_s	A′	0.063	752	5s			
8.824	C_2	B	1.11	887	5d			8.875[v]
8.842	C_2	B	0.0265	1546	6s			
8.850	C_2	A	0.0092	835	5d			
8.857	C_2	A	0.00015	1713	6p			
8.861	C_2	A	0.0017	1560	6p			
8.872	C_s	A′	0.322	937	5p			8.888[v]
8.881	C_2	B	0.239	1210	6p			
8.889	C_2	B	0.477	607		3p		8.844[v]

Table 2. Continued.

E	Conformation	Symmetry	f ($\times 10^{-2}$)	$\langle r^2 \rangle$	HOMO[c]	SHOMO[d]	HOMO-2[e]	Exp.
8.899	C_s	A′	0.206	985	$5p$			8.939[v]
8.928	C_2	A	0.028	281	$\sigma*$			–
8.934	C_2	A	0.004	377		$3p$		–
8.965	C_s	A′	0.003	1032	$5d$			–
8.966	C_2	A	0.308	198			$3s$	8.965[v]
9.014	C_s	A′	0.738	519	$5d$			9.024[v]
9.039	C_s	A″	2.43	172			$3p$	9.137[v]
9.040	C_s	A′	0.103	775	$5d$			–
9.064	C_s	A″	0.020	877	$5d$			–
9.081	C_s	A″	0.474	820	$5d$			8.991[v]

[a] Stands for adiiabatic and [v] stands for vertical. [c] HOMO: 9b for C_2 and 12a′ for C_s.
[d] SHOMO: for C_2 and 8a″ for C_s. [e] HOMO-: 10a for C_2 and 11a′ for C_s.

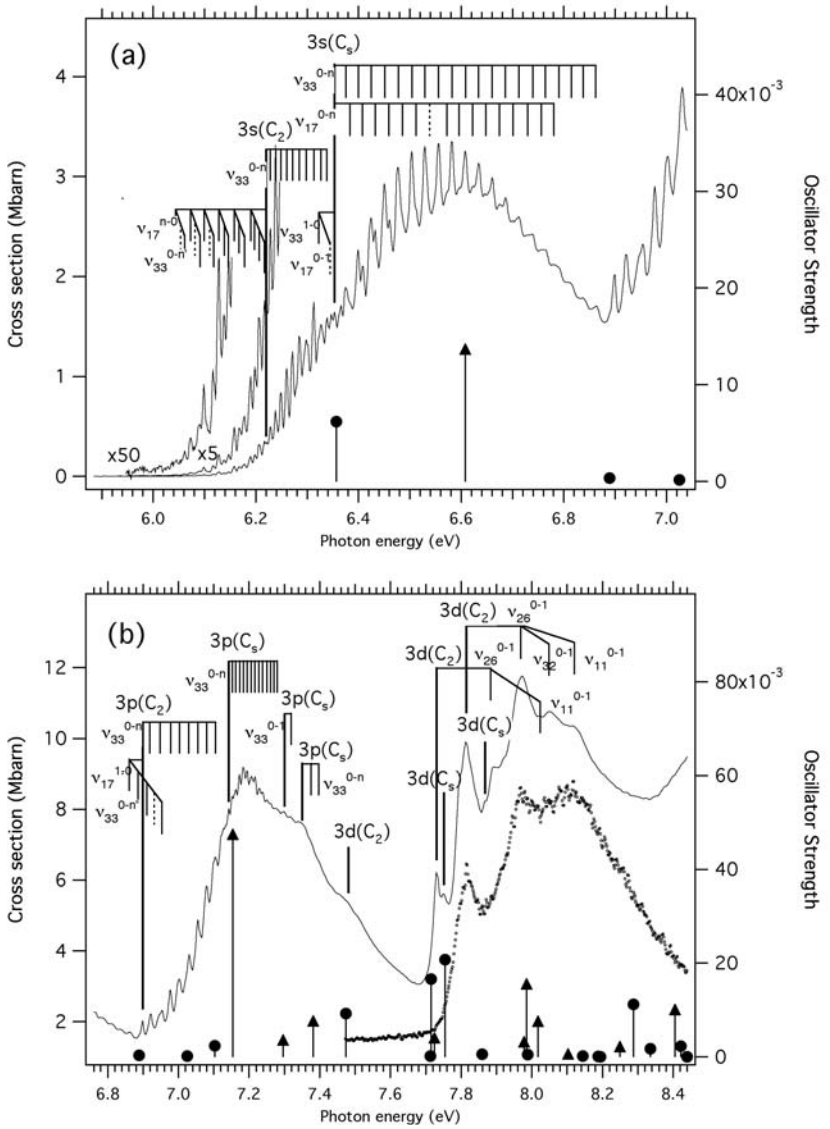

Fig. 3. High-resolution photoabsorption spectrum of THF (full lines) and theoretical calculations (vertical lines). The circles refer to the C_2 geometry and the triangles to the C_s one. (a) Detail of the $3s$ transition region and the associated vibrational progressions. (b) Detail of the $3p$ and $3d$ transitions and associated vibrational progressions. The trace of the first band of the photoelectron spectrum is shown in dots.

Table 3. Comparison of the vibrational progressions found for THF for the neutral electronic ground states, the neutral electronic excited states and the ionic electronic ground state. Wavenumber are those of Table 2 (in cm^{-1}).

	Neutral									Ionic	
Mode	Ground A′/A	$3s(C_2)$ B	$3s(C_s)$ A′	$3p(C_2)$ B	$3p(C_s)$ A′	$3p(C_s)$ A″	$3p(C_s)$ A′	$3d(C_2)$ B	$3d(C_2)$ B	Theory Ground A/B	Exp. Ground A/B
ν_{33}	39.5[a]	62.9	171	183.9	79.8	136.3	185.5				
ν_{17}	286		237								
ν_{26}	1244							1268.7	1296.9	1243.3	1234.0
ν_{32}	591								542.0[b]	570.6	596.8[b]
ν_{11}	1142								1135.6	1042.1	1064.7[b]

[a] Estimation from reference [22]. [b] Deduced from combinations, see text.

vibrational excitation accompanying this electronic transition. Analysis of this fine structure leads us to place the electronic origin at 7.134 eV. We identify a single progression of vibrational modes of 79.8 cm^{-1} (9.9 meV) assigned to ring-puckering vibrations ν_{33}, (Tab. 3 and supplementary information Tab. 4). The two remaining $3p$ transitions for the C_s conformer are expected at slightly higher energy but with lower intensity. The 7.3 eV feature does not fit into the vibrational progression of the first $3p(C_s)$ transition. Hence, it is likely that this peak corresponds to the adiabatic transition of the $3p(C_s)$ transition predicted at 7.296 eV. A single member of a progression involving excitation of a 136.3 cm^{-1} (16.9 meV) mode is also observed (Tab. 3 and supplementary information Tab. 4). On the higher energy side of the absorption band, a poorly resolved feature appears at 7.35 eV. It could arise from the excitation of the third $3p(C_s)$ member calculated at 7.381 eV. This electronic transition is also accompanied by excitation of the ν_{33} mode with 185.5 cm^{-1} (23 meV) (Tab. 3 and supplementary information Tab. 4).

On the low energy side of this absorption band, another structure is observed, which does not fit into the progression associated with the first $3p(C_s)$ transition. As seen in Table 2, the calculation predicts a $3p$ transition for the C_2 conformer at lower energy than the $3p(C_s)$, but with appreciably lower oscillator strength. The two other $3p(C_2)$ transitions are predicted to have negligible oscillator strength. The maximum of this transition may be estimated from the photoabsorption spectrum (Fig. 3b) at 7.03 eV, which fits very well with the theoretical prediction at 7.103 eV for the $3p(C_2)$. We assign the electronic origin of the $3p(C_2)$ transition to the 6.898 eV feature. The progressions identified involve excitation of 183.9 cm^{-1} (22.8 meV) vibrational mode, which we assign to the ring-puckering ν_{33} modes of this excited states. Associated with the electronic origin is a hot band involving excitation of a 277.5 cm^{-1} (34.4 meV) mode, which is consistent with the ν_{17} wavenumber in the ground state (Tab. 3 and supplementary information Tab. 4). Our vibrational assignments for this band are in disagreement with those of Bremner et al. [32]. These authors have looked for a vibrational spacing similar to that observed in the photoelectron spectrum. Indeed, Rydberg states are known to exhibit similar features to the ion to which they converge. We have not followed this procedure in the present case. The computed $\langle r^2 \rangle$ (Tab. 2) for the $3p$ states involved are similar in magnitude to those computed for the $3s$ states for which the vibrational progression are very different from those reported for the ionic ground state (see below). Moreover, the higher resolution of the present data allows us to resolve for the first time fine features on top of the 7.2 eV band (Figs. 2, 3), which were not observed by Bremner et al. [34].

3.2.1.3 The $3d$ terms of the series converging to the ionic ground electronic state

Similar to the $3s$ and $3p$ series, excitation of the first $3d$ members is predicted to occur at a noticeably lower energy for the C_2 conformer than for the C_2. Hence, Table 2 shows that the first $3d(C_2)$ state should be expected on the high-energy side of the $3p$ absorption band. As seen in Figure 3b, a broad feature is observed at 7.483 eV, not well resolved from the underlying background but which agrees with the theoretical value of 7.474 eV for the excitation of the $3d(C_2)$ state. The spectral region extending from 7.40 eV to 8.15 eV is predicted to contain the $3d$ transitions for both conformers, which are computed to account for most of the oscillator strength (Tab. 2). An enlargement of the spectrum shows a congested spectral region with quite sharp features. Two intense features are observed at 7.730 eV and 7.813 eV (Fig. 3b). These values match the predicted transition energies to two $3d(C_2)$ states at 7.715 eV and 7.754 eV. Following Bremner et al. [32], in searching for vibrational progression associated with these origins, it appeared that the shapes of these bands matched the first band of the photoelectron spectrum. The difference with the previous Rydberg states lies in greater $\langle r^2 \rangle$ values, as seen at Table 2. This more diffuse character explains the resemblance of these states with the ionic core. The vibrational assignments are summarized in Table 3 with also supplementary information Table 5.

A feature located at 7.749 eV and poorly resolved from the 7.730 eV peak is assigned to the lowest energy $3d(C_s)$ transition, on the basis of its computed value of 7.724 eV. The remaining $3d(C_s)$ excitations are predicted to be grouped around 8 eV but dominated by an intense excitation. We tentatively assign this excitation to the 7.867 eV feature, appearing as a shoulder on the 7.973 eV peak.

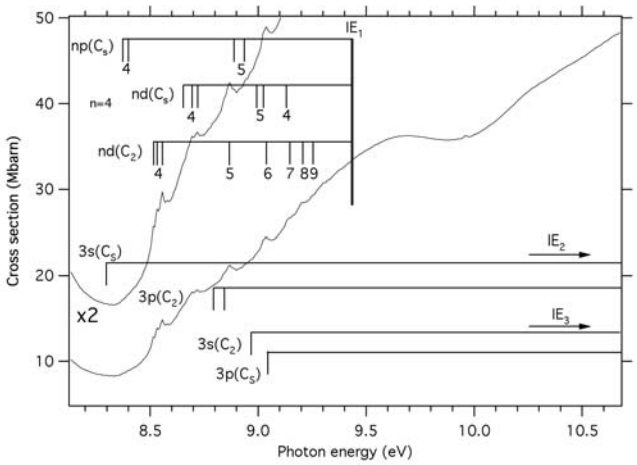

Fig. 4. High-resolution photoabsorption spectrum of THF in the 8.2–10.6 eV showing Rydberg states and vibrational progressions.

3.2.2 Higher excited states

The spectral region spanning from 8.2 to 10.6 eV is shown in Figure 4. Table 4 shows our assignments of features attributable to Rydberg series converging to the first three ionisation limits. We report a single member of the ns series converging to the first ionisation limit for both conformers. The computed oscillator strengths for higher members of the progression are in every case too low to be observed (see Tab. 2). This result is in agreement with Bremner et al. [32]. Interestingly, the calculation predicts more intense np members ($n > 3$) for the C_s isomer. Our assignments follow from that and we report members up to $n = 5$ for the np series of the C_s isomers converging to the first ionic limit. The $n = 4$ members have δ values consistent with np excitations. We tentatively assign $5p$ members on the basis of the calculations, despite quantum defect values not being in perfect agreement with this assignment. Bremner et al. [32] report a single $5p$ member at 8.89 eV. We also report this member at 8.888 eV along with another one at 8.939.

For the C_2 isomer, nd series have been assigned up to $n = 9$, with consistent quantum defects. For the C_s isomer, nd series are reported up to $n = 7$. These assignments, although at variance with the report of Bremner et al. [32] of two $3d$ series, are guided by the theoretical calculations.

Series converging to the second ionisation limit are reported for the C_2 isomer only. In agreement with Bremner et al. [32] and guided by the present calculations, we place a $3s$ series at ∼8.3 eV. Moreover, we report two $3p$ series and a single $3d$ series, for the first time.

The calculation predicts a $3s(C_2)$ and a $3p(C_s)$ converging to the third ionisation limit with noticeable oscillator strength. These members have been respectively assigned to the features at 8.965 eV and 9.037 eV with δ values of 0.870 and 0.655 supporting these assignments.

Table 4. Rydberg series analysis. Energies in eV. Quantum defects are calculated according to the Rydberg formula, see text.

1st ionic limit (EI = 9.433 eV)					
	C_2			C_s	
En		δ	En		δ
	ns			ns	
6.221	3	0.942	6.353	3	0.898
	np			np	
6.8976	3	0.683	7.142	3	0.563
			7.30	3	0.474
			7.350	3	0.444
			8.37	4	0.422
			8.4	4	0.371
			8.888	5	0.004
			8.939	5	–0.248
	nd			nd	
7.483	3	0.359	7.749	3	0.158
7.730	3	0.174	7.867	3	0.052
7.813	3	0.102			
8.515	4	0.149	8.652	4	–0.174
8.533	4	0.119	8.695	4	–0.292
8.557	4	0.060	8.719	4	–0.365
8.875	5	0.062	8.991	5	–0.548
			9.024	5	–0.765
9.037	6	0.141	9.130	6	–0.700
9.143	7	0.146	9.164	7	–0.108
9.211	8	0.16			
9.253	9	0.315			
2nd ionic limit (EI = 11.512 eV)					
	C_2				
En		δ			
	ns				
8.30	3	0.942			
	ns				
8.793	3	0.763			
8.844	3	0.742			
	np				
9.96	3	0.039			
3rd ionic limit (EI = 11.964 eV)					
	C_2			C_s	
En		δ	En		δ
	ns				
8.965	3	0.870			
				np	
			9.037	3	0.655

3.3 Ionic states

The He(I) photoelectron spectrum of THF is shown at Figure 5a. The ionic states have been calculated using the outer valence Green's function (OVGF)/aug-ccp VDZ method. Table 5 shows the results for the C_s and C_2 conformers of the ground electronic state that were considered in this work, and compared with previous theoretical and experimental data. Our experimental results are in good agreement with those of Yang et al. [25], Kimura et al. [48] and Yamauchi et al. [49] where they overlap. Nevertheless, this work reports experimental ionisation energies with

Table 5. Experimental ionisation energies and band assignments for THF.

Theory						Experiment			
This work		Yang et al. [25]				This work	Yang et al. [25]	Kimura et al. [48]	Yamauchi et al. [49]
OVGF/aug-cc-pVDZ		OVGF 6-31G*		SAOP ET-PVQZ		PES[a]	EMS[b]	PES[b]	PES[c]
C_2	C_s	C_2	C_s	C_2	C_s				
9.94 (9b)	9.91 (12a′)	9.38	9.63	10.01 (9b)	10.32 (12a′)	9.718	9.7	9.74	9.67
11.65 (11a)	11.89 (8a″)	11.11	11.36	11.67 (11a)	11.93 (11a′)	11.515	11.9	11.52	11.41
12.20 (10a)	11.65 (11a′)	11.85	11.65	12.11 (10a)	11.97 (8a″)	11.964			11.99
12.43 (8b)	12.26 (7a″)	12.08	11.86	12.51 (8b)	12.40 (7a″)	12.466			12.48
12.62 (9a)	12.30 (10a′)	12.30	12.11	12.75 (9a)	12.72 (6a″)	12.868		12.52	12.90
14.21 (7b)	13.74 (6a″)	14.06	13.69	13.98 (7b)	13.84 (9a′)	14.040	14.1	14.1	14.00
14.82 (6b)	14.49 (9a′)	14.72	14.28	14.48 (8a)	14.23 (5a″)	14.430		14.5	14.45
14.95 (8a)	15.29 (5a″)	14.72	15.13	14.76 (6b)	15.12 (8a′)	15.271		15.4	15.29
16.57 (7a)	16.29 (8a′)	16.54	16.15	16.22 (7a)	15.99 (7a′)	16.246	16.3	16.8	16.70
16.93 (5b)	16.83 (7a′)	16.91	16.66	16.51 (5b)	16.31 (4a″)				16.70
				18.64 (6a)	18.67 (6a′)		19.3	19.5	19.42

[a] He(I) Photoelectron spectroscopy. [b] Electron momentum spectroscopy. [c] Penning ionisation spectroscopy.

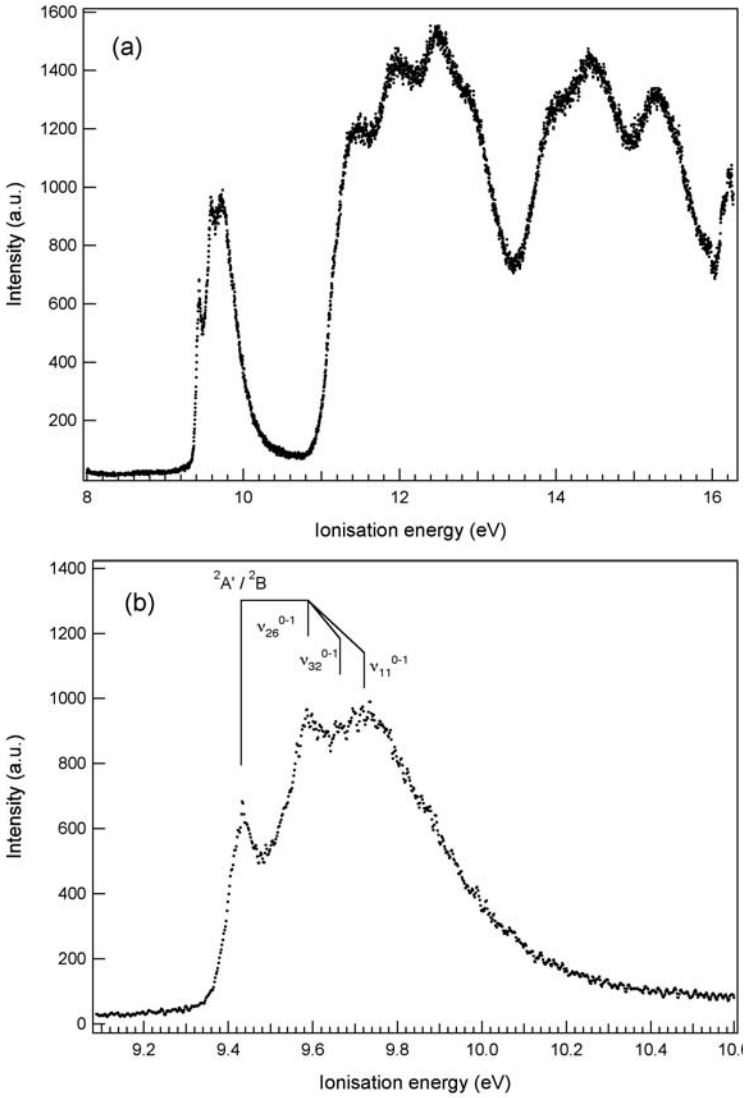

Fig. 5. He(I) photoelectron spectrum of THF (a) in the 8–16 eV energy region, (b) detail of the first band in the 9.1–10.6 eV energy region.

higher precision and the highest level of theoretical description. The ordering of the OVGF ionisation energies is in agreement with those of Yang et al. [25] except for the C_s conformer for which several discrepancies are found.

We have calculated the geometries of the ionic ground states at the UMP2/aug-cc-pVDZ level. It appears that, starting from the C_2 geometry of the ground electronic state, the $\widetilde{X}^2B$ state remains C_2 in nature with all its vibrational frequencies real (see supplementary information Tab. 6). In contrast when the corresponding doublet is considered for the C_s conformer ($\widetilde{X}^2A'$), the calculation converges towards the C_{2v} geometry. The computed vibrational frequencies for C_{2v} give one imaginary A_2 mode (ν_{17}) of 188 cm^{-1} (23.3 meV), which breaks the symmetry towards C_2. Hence, the topology of the ionic ground state potential energy surface is the following: two equivalent C_2 geometries separated by a C_{2v} saddle point giving a barrier of 1093.1 cm^{-1} (calculated with ZPE correction). The geometrical parameters for the C_2 and C_{2v} conformers of the positive ion are given at supplementary information Table 1.

The first band of the photoelectron spectrum, shown at Figure 5b, extends from 9.3 to 10.3 eV. It appears to be composed (with the present 50 meV resolution) of a first feature peaking at 9.433 eV not completely resolved from a broader one on its high energy side. This band contains at least three features at 9.586 eV, 9.66 eV and 9.718 eV, which were not reported by Yang et al. [25]. The adiabatic transition is assigned to 9.433 eV. We assign the 9.586 eV feature to vibrational excitation involving one quantum of mode ν_{26} with 1234 cm^{-1}, which agrees well with the computed value of 1243.3 cm^{-1} (154 meV) for the C_s geometry. This mode also is found combined with ν_{32} and ν_{11} at 596.8 (74 meV) and 1064.7 cm^{-1} (132 meV) at 9.66 eV and 9.718 eV. These wavenumbers are consistent with excitations of reported values for the neutral ground state. Values are gathered in Table 3 and supplementary information Table 7.

According to the theoretical prediction, the ionisation energy of the C_s isomer is lower than that of the C_2 by 34 meV. We cannot resolve at the present experimental resolution two transitions so close in energy. Hence it is very likely that the two electronic origins for the C_2 and C_s isomers are superimposed and both contributes to the 9.433 eV peak.

The energy resolution of the electron momentum spectroscopy of Yang et al. [25] is around 1 eV [50]. This resolution is too poor to allow Yang et al. [25] to resolve the vibrational excitations associated with excitation of the ground ionic state we report. A fortiori, they cannot separate the contribution from the two major conformers of THF, which appear undistinguishable at the present 50 meV resolution.

4 Conclusions

This paper revisits the electronic spectroscopy of THF in the light of the first ab initio calculations ever performed to our knowledge on the excited states of the neutral molecule.

On the basis of the excellent agreement between the calculations and the measurements, we report that the experimental spectrum is composite and contains electronic excitations from both C_s and C_2 conformers of THF. Hence, this provides a solution to previous discrepancies in the literature concerning the nature of the lowest energy transitions for the molecule. The electronic spectrum has been re-examined up to 10.3 eV and new vibrational progression reported for the $3p$ and $3d$ Rydberg states. Higher members of Rydberg series are re-assigned in the light of the calculations.

The lowest energy part of the photoelectron spectrum is reported and an accurate value for the lowest adiabatic ionisation energy is reported. Calculations predict adiabatic transition to the ionic ground state to be separated by 34 meV for the two C_2 and C_s lowest energy conformers of the THF such that the present experimental resolution cannot resolve the separate contribution of the two conformers. Yang et al. [25] have reported experimental orbital momentum distribution for the HOMO of THF and compared these data to simulated distribution for the C_2 and C_s isomers. Since better agreement of the simulated distribution was obtained for the C_s isomer, the authors concluded the most stable conformer of THF to be the C_s one. Our work seems to indicate that both conformers coexist in the gas phase at room temperature and might be observed. Consequently, we question the conclusions of Yang et al. [25] about the reliability of their methodology to provide a new diagnostic for the most populated conformer of THF in the gas phase at room temperature.

We wish to thank the ISA at Aarhus,Denmark for access to the Astrid synchrotron under the EU FP6 programme IA-SFS contract number R113-CT-2004-506008. We also acknowledge support from the ESF EIPAM and ESF COST Action P9 (RADAM). We thank Pr. Jose A. Sordo for providing details on his calculations. A.R.M. and B.P.M. acknowledge the support of the Ministry of Science of Republic of Serbia under Project No. 141011. The "PhLAM" is "Unité Mixte de Recherche du CNRS". The "Centre d'Études et de Recherches Lasers et Applications" (CERLA, FR CNRS 2416) is supported by the "Ministère chargé de la Recherche", the "Région Nord/Pas-de-Calais" and the "Fonds Européen de Développement Économique des Régions" (FEDER). The computations were carried out at the CRI (Centre de Ressources Informatiques), on the IBM computer which is supported by the "Programme de Calcul Intensif et Parallèle" of the "Ministère chargé de la Recherche", the "Région Nord/Pas-de-Calais" and the FEDER. N.J.M. wishes to thank the UK EPSRC for financial support. P.L.V. acknowledges the honorary research fellow position at University College London, the visiting fellow position at CEMOS, The Open University, UK, and together with M.-J.H.-F. the financial support from the Portuguese-Belgian joint collaboration. The Patrimoine of the University of Liège, the Fonds de la Recherche Scientifique (FRS-FNRS) and the Fonds de la Recherche Fondamentale Collective of Belgium have supported this research. M.-J.H.-F. wishes to acknowledge the Fonds de la Recherche Scientifique for position. P.L.V. and N.J.M. acknowledge the support from the British Council for the Portuguese-English joint collaboration.

References

1. L. Sanche, Eur. Phys. J. D **35**, 367 (2005)
2. B. Boudaiffa, P. Cloutier, D. Hunting, M.A. Huels, L. Sanche, Science **287**, 1658 (2000)
3. C. von Sonntag, in *The Chemical Basis for Radiation Biology* (Francis, London, 1987)
4. M. Lepage, S. Letarte, M. Michaud, F. Motte-Tollet, M.-J. Hubin-Franskin, D. Roy, L. Sanche, J. Chem. Phys. **109**, 5980 (1998)
5. D. Antic, L. Parenteau, M. Lepage, L. Sanche, J. Phys. Chem. B **103**, 6611 (1999)
6. D. Antic, L. Parenteau, L. Sanche, J. Phys. Chem. B **104**, 4711 (2000)
7. S.-P. Breton, M. Michaud, C. Jäggle, P. Swiderek, L. Sanche, J. Chem. Phys. **121**, 11240 (2004)
8. A.R. Milosavljevic, A. Giuliani, D. Sevic, M.-J. Hubin-Franskin, B.P. Marinkovic, Eur. Phys. J. D **35**, 411 (2005)
9. A. Zecca, C. Perazzolli, M.J. Brunger, J. Phys. B **38**, 2079 (2005)
10. P. Mozejko, L. Sanche, Radiat. Phys. Chem. **73**, 77 (2005)
11. D. Bouchiha, J.D. Gorfinkiel, L.G. Caron, L. Sanche, J. Phys. B **39**, 975 (2006)
12. C.S. Trevisan, A.E. Orel, T.N. Rescigno, J. Phys. B **39**, L255 (2006)
13. C. Winstead, V. McKoy, J. Chem. Phys. **125**, 074302 (2006)
14. Y.S. Park, H. Cho, L. Parenteau, A.D. Bass, L. Sanche, J. Chem. Phys. **125**, 074714 (2006)
15. P. Sulzer, S. Ptasinska, F. Zappa, B. Mielewska, A.R. Milosavljevic, P. Scheier, T. Mark, J. Chem. Phys. **125**, 044304 (2006)
16. A. Wu, D. Cremer, Int. J. Mol. Sci. **4**, 158 (2003)
17. W. Saenger, in *Principle of Nucleic Acid Structur*e (Springer-Verlag, New York, 1984)
18. G.G. Engerholm, A.C. Luntz, W.D. Gwinn, D.O. Harris, J. Chem. Phys. **50**, 2446 (1969)
19. R. Meyer, J.C. Lopez, J.L. Alonso, S. Melandri, P.G. Favero, W. Caminati, J. Chem. Phys. **111**, 7871 (1999)
20. A.H. Mamleev, L.N. Gunderova, R.V. Galley, J. Struct. Chem. **42**, 365 (2001)
21. D.G. Melnik, S. Gopalakrishnan, T.A. Miller, J. Chem. Phys. **118**, 3589 (2003)
22. B. Cadioli, E. Gallinella, C. Coulombeau, H. Jobic, G. Berthier, J. Phys. Chem. **97**, 7844 (1993)
23. S.J. Han, Y.K. Kang, J. Mol. Struct. Theochem **369**, 157 (1996)
24. V.M. Rayón, J.A. Sordo, J. Chem. Phys. **122**, 204303 (2005)
25. T. Yang, G. Su, C. Ning, J. Deng, F. Wang, S. Zhang, X. Ren, Y. Huang, J. Chem. Phys. **111**, 4927 (2007)
26. L.W. Pickett, N.J. Hoeflich, T.C. Liu, J. Am. Chem. Soc. **73**, 4865 (1951)
27. G.J. Hernandez, J. Chem. Phys. **38**, 2233 (1963)
28. R. Davidson, J. Høg, P.A. Warsop, J.A.B. Whiteside, J. Chem. Soc. Faraday II **68**, 1652 (1972)
29. M.B. Robin, *Higher Excited States of Polyatomic Molecules, Vol. II* (Academic Press, New York and London, 1974)
30. W.-C. Tam, C.E. Brion, J. Electron Spec. Relat. Phenom. **3**, 263 (1974)
31. J. Doucet, P. Sauvegeau, C. Sandorfy, Chem. Phys. Lett. **19**, 316 (1973)
32. L.J. Bremner, M.G. Curtis, I.C. Walker, J. Chem. Soc. Faraday Trans. **87**, 1049 (1991)
33. A. Giuliani, J. Delwiche, S.V. Hoffmann, P. Limão-Vieira, N.J. Mason, M.-J. Hubin-Franskin, J. Chem. Phys. **119**, 3670 (2003)
34. J. Delwiche, P. Natalis, J. Momigny, J.E. Collin, J. Electron Spec. Relat. Phenom. **1**, 219 (1972)
35. *Handbook of Chemistry and Physics*, edited by D.R. Lide (CRC Press, New York, 1992)
36. J.H.D. Eland, in *Photoelectron spectroscopy* (Butterworth & Co Ltd., London, 1984)
37. A.R. Milosavljeviæ, S. Madžunkov, D. Ševiæ, I. Èadež, B.P. Marinkoviæ, J. Phys. B: At. Mol. Opt. Phys. **39**, 609 (2006)
38. C. Hampel, K. Peterson, H.-J. Werner, Chem. Phys. Lett. **190**, 1 (1992)
39. MOLPRO, a package of ab initio programmes, version 2006.1
40. K. Kaufmann, W. Baumeister, M. Jungen, J. Phys. B **22**, 2223 (1989)
41. J.V. Ortiz, V.G. Zakrzewski, O. Dolgounircheva, in *Conceptual Perspectives in Quantum Chemistry*, edited by J.-L. Calais, E. Kryachko (Kluwer Academic, 1997)
42. J. V. Ortiz, J. Chem. Phys. **89**, 6348 (1988)
43. *Gaussian*03, Revision D.01, Gaussian, Inc., Wallingford CT (2004)
44. P. Luger, J. Buschmann, Angew. Chem. **95**, 423 (1983)
45. W.I.F. David, R.M. Ibberson, Acta Crystallogr. C **48**, 301 (1992)
46. E. Gallinella, B. Cadioli, J.-P. Flament, G. Berthier, J. Mol. Struct. Theochem **315**, 137 (1994)
47. Y. Morino, K. Kuchistu, J. Chem. Phys. **20**, 1809 (1952)
48. K. Kimura, S. Katsuwata, Y. Achiba, T. Yamazaki, S. Iwata, in *Handbook of HeI Photoelectron Spectra of fundamental Organic Molecules* (Halsted Press, New York, 1981)
49. M. Yamauchi, H. Yamakado, K. Ohno, J. Phys. Chem. A **101**, 6184 (1997)
50. X.G. Ren, C.G. Ning, J.K. Deng, S.F. Zhang, G.L. Su, F. Huang, G.Q. Li, Rev. Sci. Instrum. **76**, 063103 (2005)

Article 9

JOURNAL OF CHEMICAL PHYSICS VOLUME 109, NUMBER 13 1 OCTOBER 1998

Electronic excitation of gaseous pyrrole and pyrazole by inner-shell electron energy loss spectroscopy

D. Duflot
Laboratoire de Dynamique Moléculaire et Photonique, Centre d'Etudes et de Recherches Lasers et Applications (CERLA), Université des Sciences et Technologies de Lille, F-59655 Villeneuve d'Ascq, France

C. Hannay
Laboratoire de Spectroscopie d'Electrons diffusés, Université de Liège, Institut de Chimie, B6c, B-4000 Liège (Sart Tilman), Belgique

J.-P. Flament
Laboratoire de Dynamique Moléculaire et Photonique, Centre d'Etudes et de Recherches Lasers et Applications (CERLA), Université des Sciences et Technologies de Lille, F-59655 Villeneuve d'Ascq, France

M.-J. Hubin-Franskin
Laboratoire de Spectroscopie d'Electrons diffusés, Université de Liège, Institut de Chimie B6c, B-4000 Liège (Sart Tilman), Belgique

(Received 20 May 1998; accepted 25 June 1998)

The spectroscopy of the unoccupied molecular orbitals of gaseous pyrrole and pyrazole has been studied by electron impact under electric dipole scattering conditions (2 KeV, small angle) and the inner-shell electron energy loss method. The core-excitation spectra have been recorded at the C1*s* and N1*s* edges with 0.2 eV resolution, resolution allowing to observe separately the transitions from the carbon atoms with different chemical environment. *Ab initio* calculations, using the equivalent core model, were performed to help in the interpretation of the spectral features. The spectra are dominated by transitions to the π^* and σ^* molecular orbitals. The calculations confirm that the $3b_1(\pi^*)$ orbital is the lowest-energy unoccupied one in pyrrole. In several cases, the intensity of the Rydberg excitations is enhanced by an important valence σ^* character of the Rydberg orbitals.
 [S0021-9606(98)01237-9]

I. INTRODUCTION

In this work the spectroscopy of the unoccupied molecular orbitals of gaseous pyrrole and pyrazole has been studied by core-electron excitation and the inner-shell electron energy loss method in electric dipole scattering conditions. These heterocyclic molecules (Fig. 1) are of considerable importance for organic/organometallic magnets[1] and inorganic polymers,[2] in biochemistry and also for pesticides.[3] The core-electron excitation at the *K* edges is expected to be strongly localized and is well adapted to study the local electronic properties of groups embodied in complex systems. The electron collisions in electric dipole scattering conditions and the electron energy loss spectroscopy are very well suited to contribute to such investigations.[4–6]

The valence excitation spectrum of pyrrole studied by UV/VUV photoabsorption[7–12] and electron collisions[13] is quite complex, exhibiting broad bands and fine features superimposed to them. It has been interpreted in terms of transitions from the highest occupied molecular orbital (HOMO) to the lowest-energy singlet and triplet excited states.[7–16] The lowest energy unoccupied molecular orbitals (MO) have been calculated by *ab initio* methods[14,17,18] to be the $3b_1$ and $2a_2$ of π^* type and separated by 1.52 eV[14]/1.55 eV[17]/1.93 eV[18] in the neutral ground state in which the molecule belongs to the C_{2v} symmetry point group (planar molecule). The $10a_1$ MO has been predicted[17] to be close to the $3b_1(1\pi^*)$ one. The C1*s* core-electron excitation spectrum[19] measured by electron collisions under electric dipole scattering conditions exhibits an intense feature assigned to the $3b_1(1\pi^*)$ transition and a less intense, not well resolved one located 1.8 eV above the first one and suggested to be due to the $2a_2(2\pi^*)$ excitation. The same information has been provided by the C1*s* NEXAFS spectrum of condensed pyrrole[20] recorded with 0.4 eV bandwidth. At the N1*s* edge, the $2a_2$ MO is optically forbidden and the single band observed both for the gas[19] and solid[20] has been assigned to the transition to the $3b_1(1\pi^*)$ orbital. Few data are available on the σ^* type excitation.

For pyrazole, the information related to the unoccupied molecular orbitals is more fragmentary. The molecule belongs to the C_s symmetry point group. CNDO/2 calculations[21] predict that the lowest-energy unoccupied MOs are $4a''(1\pi^*)$ and $5a''(2\pi^*)$, respectively. The lowest-energy UV absorption band[22,23] has been suggested to be due to the π-π^* type transition by both SCF[24] and CNDO/S calculations.[25] So far as we know, the energy separation of the two lowest-energy unoccupied π^* type MOs is not known.

In this paper, we report new spectroscopic data on the π^* and σ^* type MOs of gaseous pyrrole and pyrazole using the core-electron excitation and the 2 KeV electron collisions in low angular momentum transfer conditions. We have recorded the electron energy loss spectra of pyrrole at the C1*s* and N1*s* edges with a 0.2 eV resolution which is better than

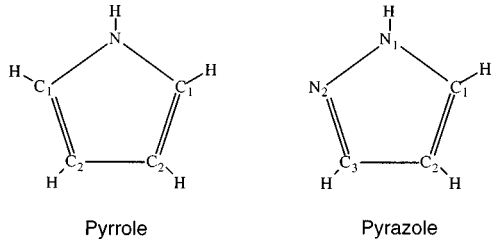

FIG. 1. Schematic drawings of the heterocyclic aromatic molecules pyrrole and pyrazole. The labels C_1, C_2, C_3, and N_1, N_2 indicate the nonequivalent carbon and nitrogen atoms, respectively.

in previous studies[19,26,27] and the same at both edges. We report the electron energy loss spectra of pyrazole at the C1*s* and N1*s* edges with the same 0.2 eV resolution. This is the first time that such spectra of pyrazole have been measured, as far as we know.

In order to help in the assignment of the observed spectral features, *ab initio* calculations have been performed, in the framework of the equivalent core approximation. This simple model allows to calculate easily the term values (TVs) of each electronic transition, which can be compared to the experimental ones.

II. COMPUTATIONAL METHOD

The Gaussian atomic orbitals (AOs) used is the DZP basis set taken from Dunning,[28] i.e., $(10s5p1d)/[3s2p1d]$ for carbon and nitrogen ($\alpha_C=0.75$ and $\alpha_N=0.80$, respectively) and $(4s1p)/[2s1p]$ for hydrogen. One $s(\alpha_s=0.028)$ and one $p(\alpha_p=0.025)$ diffuse orbitals[29] were added at the center of mass of the molecules in order to take into account pure Rydberg and mixed valence-Rydberg orbitals among the core-excited species. Although the intensity of pure Rydberg bands should be negligible, valence-Rydberg bands with enhanced intensity have been obtained in previous calculations on cycloalkanes[30] and benzene.[31]

The ground state geometries of pyrrole and pyrazole were optimized at the self-consistent field (SCF) level with the HONDO95.3 program package,[32] using analytic gradients. The calculations of the core-excited states were performed in the frame of the equivalent core approximation,[33–35] which has proven for small molecules[6] to give reliable information with an accuracy of a few tenths of an eV. In this model, the excitation of a 1*s* electron of an atom of atomic number *Z* is considered to be equivalent to its replacement by an atom of atomic number $Z+1$ in the molecule. Relative energies such as chemical shifts or TVs with respect to core-ionized states are obtained and can be compared to experimental results.

The TVs were calculated using the procedure developed for the SiX_4-type molecules.[36] The TV of the $1s\rightarrow i^*$ excitation (valence or Rydberg) of a given atom is given by:

$$\mathrm{TV}=-\epsilon_{i^*}+P+C, \tag{1}$$

where $-\epsilon_{i^*}$ is the monoelectronic energy of the i^* virtual canonical orbital given in the SCF calculation of the ion (Koopmans' theorem).[37]

The *P* term is due to repolarization effects and was calculated by performing a configuration interaction (CI) in the mono-excited space $S(i^*)$ of each state. Thus for a given $1s\rightarrow i^*$ transition, $S(i^*)$ included all monoexcitations from the occupied valence orbitals to the valence anti-bonding j^* and Rydberg orbitals. The final space *S* was taken as the sum of $S(i^*)$ over the i^* orbitals. It should be noted that the *S* space includes the shake-up excitations (di-excitations of the type $1s\pi\rightarrow\pi^*\pi^*$) which could appear in experimental spectra. The *P* term was obtained as the difference between the CI energy of the i^* state and the SCF energy of the ion.

The calculations showed that the correlation term *C* in (1) was not negligible. In order to evaluate its contribution, the *S* space was used as the zeroth-order wave function for a multireference Moller–Plesset second-order[38] (MP2) calculation, using the diagrammatic version[39] of the CIPSI method.[40] The perturbation space *P* was obtained by taking all mono- and di-excitations of the *S* space into the remaining orbitals and calculating their MP2 contribution to the energy. The correlation term *C* was then given for i^* by the difference between the CIPSI energy and the MP2 energy of the ion.

TABLE I. Calculated geometry. Bond lengths in Å and angles in degrees. Identification of atoms follows Fig. 1.

Pyrrole	SCF[e] DZP	MP2[a] 6-31G*	B3LYP[a] 6-311G (2*df*,*p*)	exp[b]
r(N-C_1)	1.366	1.373	1.370	1.370
r(C_1-C_2)	1.365	1.383	1.373	1.382
r(C_2-C_2)	1.430	1.418	1.421	1.417
r(N-H)	0.992	1.011	1.005	0.996
r(C_1-H_1)	1.071	1.081	1.077	1.076
r(C_2-H_2)	1.071	1.082	1.078	1.077
NC_1C_2	108.2	107.4	107.7	107.7
$C_1C_2C_2$	107.1	107.5	107.4	107.4
HNC_1	125.2	124.9	125.1	125.1
H_1C_1N	121.3	121.2	121.3	121.6
$H_2C_2C_1$	125.9	125.6	125.7	127.1
Pyrazole	**SCF[e] DZP**	**MP2[c] 6-31G****	**B3LYP[c] 6-311G****	**exp[d]**
r(N_1-C_1)	1.332	1.341	1.359	1.359
r(N_1-N_2)	1.345	1.348	1.350	1.349
r(C_1-C_2)	1.369	1.385	1.381	1.372
r(C_2-C_3)	1.418	1.406	1.414	1.416
r(C_3-N_2)	1.306	1.347	1.333	1.331
r(N_1-H)	0.993	1.007	1.008	1.002
r(C_1-H_1)	1.070	1.076	1.080	1.082
r(C_2-H_2)	1.070	1.076	1.079	1.080
r(C_3-H_3)	1.071	1.077	1.082	1.083
$N_1C_1C_2$	106.7	105.7	106.1	106.4
$C_3N_2N_1$	105.2	103.4	103.9	104.1
HN_1C_1	127.8	127.5	127.8	128.5
HN_1N_2	119.5	118.6	118.9	118.4
$H_1C_1N_1$	121.9	121.9	121.9	121.5
$H_2C_2C_1$	127.8	127.0	127.3	127.6
$H_3C_3N_2$	120.1	119.1	119.5	119.3

[a]Reference 41.
[b]Reference 42.
[c]Reference 43.
[d]Reference 44.
[e]This work.

The core binding energies and chemical shifts were calculated at SCF and MP2 levels.

Since in most cases each $1s \rightarrow i^*$ state had a large weight in the zeroth-order configuration, the transition intensities were estimated as the $\langle 1s|\nabla|i^*\rangle^2$ matrix element, the $1s$ orbital taken as the corresponding core-equivalent atom.[36] The intensity of shake-up states was not evaluated.

Except for the N1s excitation in pyrrole, the calculations were done in the C_s symmetry group for the two molecules in the optimized geometry of the ground state, which was kept fixed in all cases. The typical dimension of S space was about 1000 in A'' symmetry and 3000 in A' symmetry.

The SCF optimized geometries are in good agreement with previous theoretical and experimental determinations[41–44] as shown in Table I.

The results of the calculations are given in Sec. IV. Several remarks are common to all the carbon and nitrogen atoms for both molecules. First, the theoretical TVs truncated at the P level in (1) are too small, at least for the first experimental band ($1s \rightarrow \pi^*$). When the correlation term C is included, the situation is better, except for the C1s of pyrrole and N1s of pyrazole, where the discrepancy is 0.5 eV. Second, there is a large number of mixed Rydberg-valence configurations or MOs which have a much larger intensity than the pure Rydberg states and could explain some of the experimental features.

III. EXPERIMENTAL PART

The experiment made use of the VSW electron spectrometer adapted for gas studies and high-energy electron beams[6] and equipped with a homemade position sensitive multi-detector system.[45]

Briefly, the spectrometer consists of an electrostatic 180° electron energy monochromator, a collision chamber, and an electron analyzer of the same type as the monochromator. The incident electrons are accelerated up to 2 KeV and focused into the collision chamber where they are slightly deviated (0.02 rads) by two sets of X-Y plates in order to be in low angular momentum transfer collision conditions. The energy resolution has been 0.2 eV as measured on the elastic peak. The magnetic field is minimized by mumetal layers. The residual pressure is maintained below 1×10^{-8} Torr inside the vacuum vessel by a Cryopumping system. The electron gun and the detector are pumped differentially by two turbomolecular pumps. The whole experiment is under control of an HP 9000/300 computer. Each spectrum is the result of the accumulation of the data from each channel of the detector which removed any detector sensitivity variation.[45]

The electron energy loss scale has been calibrated at the C1s edge with the $1s\sigma^+ \rightarrow \pi^*(v'=0)$ transition in CO at 287.40 eV[46] and at the N1s edge with the $1s\sigma_g^+ \rightarrow \pi^*(v'=0,1)$ bands in N_2[47] (i.e., 401.10 eV: average value of $v'=0$ and 1, the spectral features being not sufficiently resolved within the 0.2 eV resolution). In order to take into account the valence and lower-energy inner-shell excitation cross section, a linear background has been substracted by extrapolating a least-square fit of the pre-edge experimental data points.

The samples were commercial ones from Aldrich with a purity of 98%. They were further purified by repeated freeze–pump–thaw cycles. The CO and N_2 gases used for the energy scale calibration were from UCAR and Air Liquide and of purity of better than 99.999%.

IV. RESULTS AND DISCUSSION

A. Pyrrole

The electronic configuration of pyrrole in its neutral ground state has been calculated to be

$$1a_1^2 1b_2^2 2a_1^2 3a_1^2 2b_2^2 4a_1^2 5a_1^2 3b_2^2 6a_1^2 4b_2^2 7a_1^2 1b_1^2 8a_1^2 4b_2^2 5b_2^2 9a_1^2 2b_1^2 1a_2^2.$$

The $1a_1$, $1b_2$, $2a_1$, $3a_1$, and $2b_2$ MOs are the $1s$ orbitals of the nitrogen and the four carbon atoms. The $1b_1$ MO is the lone pair located on the nitrogen. The $2b_1$ and $1a_2$ (HOMO) MOs are the 1π and 2π ones. Apart from Rydberg MOs, the lowest energy unoccupied MOs are the $3b_1$ LUMO ($1\pi^*$, $\epsilon_i = 4.88$ eV), the $10a_1$ ($\sigma^*_{\text{N-H}}$, $\epsilon_i = 5.81$ eV) and the $2a_2$ ($2\pi^*$, $\epsilon_i = 6.81$ eV) followed by the remaining anti-bonding MOs.

There are two carbon atoms with different chemical environment and their binding energies are separated by 1.0 eV, the lowest one being for C_2[48] (Fig. 1). This ordering and the chemical shift are in very good agreement with our calculations at SCF (1.02 eV) and MP2 (1.06 eV) levels. The same trend is expected for the core-level excitations with the largest TVs for those from C_2. In the following the TVs are given relative to the C_2 limit.

1. Carbon 1s excitation spectrum

The C1s electron energy loss spectrum displayed in Fig. 2 exhibits an intense A peak at 286.45 eV, a weak B band at 288.3 eV, and the broadbands C, D, and E at higher energy. The energy values of the spectral features are listed in Table II. The lowest-energy A peak is complex and partly resolved into three features A', A'', and A''' (inset of Fig. 2).

The spectrum is quite similar to the lower resolution energy loss spectrum published previously[19] and to the NEXAFS spectrum of condensed pyrrole.[20] The fine features are better resolved in our study. The lowest energy A' one is also present in the 0.4 eV resolution NEXAFS spectrum whereas A''' seems to be much less intense or absent in the spectrum of the solid.

The A' and A'' features are separated by 0.56 eV (Table II). They have been suggested to be due to the $1sC_2 \rightarrow 1\pi^*$

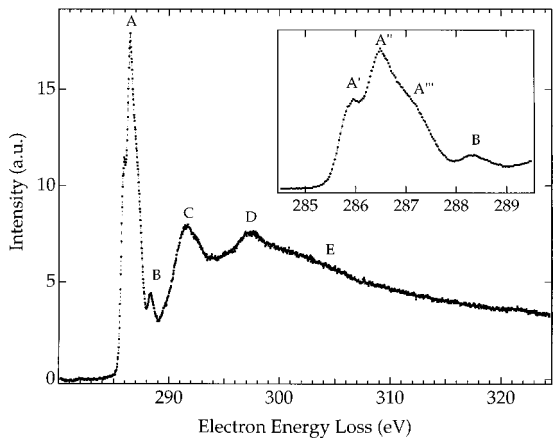

FIG. 2. Electron energy loss spectrum of pyrrole at the carbon *K* edge.

$(3b_1)$ and $1sC_1 \rightarrow 1\pi^*$ $(3b_1)$ transitions.[19,20] This assignment is confirmed by the *ab initio* calculations. Indeed as shown in Table III, the TV calculated for the $1sC_2 \rightarrow 1\pi^*$ transition is 3.46 eV and that calculated for the $1\pi^*$ MO excitation from $1sC_1$ is 2.82 eV. These values are underestimated by about 0.5 eV when compared to experiment but their 0.44 eV splitting is in good agreement with the experimental one (0.56 eV). In addition the calculated intensities (Table III) agree rather well with the relative intensity of features A' and A''.

The transitions to the $2\pi^*$ $(2a_2)$ MO from $1sC_2$ and C_1 have been previously[19] suggested to be in the 288.1 eV band, but not resolved due to the limited resolution. The feature A''' partly resolved in our 0.2 eV resolution spectrum around 287.3 eV indicates that at least one transition is excited with a TV around 2.5 eV. The $1sC_2 \rightarrow 2\pi^*$ transition is calculated to be located in this region, with a TV of 2.14 eV and an intensity lower than for the $1sC_2 \rightarrow 1\pi^*$ (Table III). Moreover, a $1sC_2 \rightarrow 3p\sigma/\sigma^*_{NH}$ Rydberg-valence excitation appears at TV=2.40 eV with a relatively nonnegligible intensity (Table III). These results suggest that these transitions are responsible of the shape of *A* band in the 287 eV region, which is more asymmetric for the gas than in the NEXAFS spectrum. This is consistent with the fact that for the solid, the Rydberg excitation is not present in the spectrum. The transition to the $2\pi^*$ type MO from C_1 is calculated to have a much lower intensity than the corresponding one from C_2 and to be located at much higher energy, 0.52 eV below the C_2 limit (Table III). These results rule out the previous assignment.[19]

The *B* band at 288.3 eV (Table II) corresponds to a TV

TABLE II. Energy values (*E*,eV) of the spectral features in the excitation spectra.

At the C1*s* edge

Pyrrole			Pyrazole	
Spectral feature	This work *E*	Ref. 19 *E*	Spectral feature	This work *E*
A′	285.89	285.6		
A″	286.45	286.3	*A*	286.3
				(286.7)
A‴	(287.3)			(287)
				(287.2)
B	288.3	288.1	*B*	288
				289.2
				(290.2)
C	291.6		*C*	292.3
	(292.5)			(294.8)
	(295)			
D	297.4	296.8	*D*	297.8
E	302	300.5	*E*	301

At the N1*s* edge

Pyrrole				Pyrazole	
Spectral feature	This work *E*	Ref. 19 *E*	Ref. 26 *E*	Spectral feature	This work *E*
A	402.1	402.3	402.3	*A*	400.53
	(402.6)			*B′*	402.60
	(404.6)			*B″*	403.2
	(405.2)	405.9			(405.5)
C	406.8	406.7	407.1	*C*	407.4
	(407.6)				(408)
	(408.4)				
	(410)				
D	413.4	413.4	413.1	*D*	412

( ) not well resolved

TABLE III. Term values (TV,eV) and assignment of the spectral features at the C1*s* edge of pyrrole.

Calculated TV[a]						
$-\epsilon_i^*$[c]	P[c]	C[d]	I[b]	Main Configurations		Exp. TV[f]
2.09	3.10	3.46	169.8	0.89	$1sC_2 \rightarrow 1\pi^*(3b_1)$	3.91
1.61	2.61	2.82	303.6	0.95	$1sC_1 \rightarrow 1\pi^*(3b_1)$	3.35
2.19	2.53	2.75	6.0	0.96	$1sC_2 \rightarrow 3s\sigma$	
1.96	2.23	2.40	14.8	0.97	$1sC_2 \rightarrow 3p\sigma/\sigma^*_{N\text{-}H}$[e]	
0.36	1.36	2.14	34.0	0.90	$1sC_2 \rightarrow 2\pi^*(2a_2)$	2.5
1.33	1.73	2.03	0.2	0.96	$1sC_1 \rightarrow 3p\sigma$	
1.42	1.75	1.90	0.1	0.98	$1sC_2 \rightarrow 3p\sigma$	
1.42	1.55	1.73	20.4	0.91	$1sC_2 \rightarrow 3p\pi/\pi^*$	1.5
0.81	1.07	1.17	6.3	0.97	$1sC_1 \rightarrow 3p\sigma$	
0.50	0.72	0.80	1.9	0.98	$1sC_1 \rightarrow 3s\sigma$	
0.54	0.59	0.71	0.7	0.99	$1sC_1 \rightarrow 3p\pi$	
−1.25	−0.13	0.52	<1.0	0.95	$1sC_1 \rightarrow 2\pi^*(2a_2)$	
−1.19	−0.38	0.28	42.0	0.93	$1sC_2 \rightarrow \sigma^*_{C_2\text{-}H}$	(0.8)
0.00	0.00	0.00			C_2 ion	0.00[f]
−2.15	−1.08	−0.36	19.9	0.89	$1sC_1 \rightarrow \sigma^*_{C_1\text{-}N}$	
−1.86	−0.99	−0.40	8.8	0.92	$1sC_2 \rightarrow \sigma^*_{C_2\text{-}C_2}$	
−2.30	−1.50	−0.91	6.1	0.92	$1sC_2 \rightarrow \sigma^*_{C_1\text{-}N}$	
−1.02	−1.02	−1.06			C_1 ion	−1.0[f]
−2.74	−1.85	−1.17	2.5	0.91	$1sC_1 \rightarrow \sigma^*_{N\text{-}H}$	−1.8
	−4.85	−2.45		0.80	$1sC_1 2\pi \rightarrow 1\pi^* 1\pi^*$	
	−4.44	−2.50		0.76	$1sC_1 1\pi \rightarrow 1\pi^* 1\pi^*$	
	−3.03	−2.59		0.32	$1sC_2 2\pi \rightarrow 1\pi^* 1\pi^*$	(−2.7)
				+0.40	$1sC_2 1\pi \rightarrow 1\pi^* 3p\pi$	
	−3.37	−2.70		0.64	$1sC_2 2\pi \rightarrow 1\pi^* 2\pi^*$	
				+0.17	$1sC_2 2\pi \rightarrow 2\pi^* 3p\pi$	

[a]See text for definition.
[b]Arbitrary units.
[c]With respect to the SCF energy of the ion.
[d]With respect to the MP2 energy of the ion.
[e]Valence-Rydberg mixed MO.
[f]Experimental term values: relative to the $1sC_2$ binding energy 289.8 eV. Ionization energy for C_1: 290.8 eV (Ref. 48).
( ) not well resolved

of 1.50 eV. The excitation of the $3p\pi$ Rydberg orbital from C_2 is predicted with a TV of 1.73 eV and a nonnegligible intensity, about one-tenth of the $1sC_1 \rightarrow 1\pi^*$ band, due to a small valence π^* character of the $3p\pi$ MO (Table III). The calculated TVs are in good agreement with each other and close to the 1.5 eV experimental one for the *B* band. So the observed intensity and TV of the *B* band are consistent with those calculated for the $1sC_2 \rightarrow 3p\pi/\pi^*$. The spectral intensity around 289 eV suggests additional band(s) in this region not completely resolved from *B*. The calculations predict four transitions from $1sC_1$ to $3p\sigma$, $3s\sigma$, and $3p\pi$ and to $2\pi^*$ in this region, just below the C_2 limit, but with negligable intensities and also the $1sC_2 \rightarrow \sigma^*_{C_2\text{-H}}$ excitation, calculated to have TV=0.28 eV, and an observable intensity (Table III). This latter might account for the spectral intensity around 289 eV (TV=0.8 eV).

Above the C_2 ionization edge (289.8 eV), there are two broad bands, *C* at 291.60 eV (TV=−1.8 eV) and *D* at 297.40 eV (TV=−7.6 eV), and a much broader, less intense one *E* at 302 eV (TV=−12.2 eV) (Fig. 2). In addition, on the high-energy side of the *C* band, there are fine features not well resolved around 292.5 eV (TV=−2.7 eV) and 295 eV (TV=−5.2 eV) (Tables II and III). According to the calculations, it is difficult to assign clearly the *C* band with TV=−1.8 eV. Indeed, the calculations do not show any mono-excited state around this value (Table III): above the C_1 limit at −1.0 eV many doubly excited states (shake-up) appear, most of them involving Rydberg orbitals and thus having probably a negligeable intensity. In Table III, are only reported the shake-up states having an important weight on the valence $1\pi^*$ and $2\pi^*$ MOs. Their TVs are grouped around −2.5/−2.7 eV and could be responsible for the fine features observed in this region. At higher energy, the calculations predict other di-excited states with Rydberg MOs up to TV=−3.8 eV but curiously no σ^* resonances. If we return to the *C* band, one possible explanation is that the calculated TVs for the $1sC_1 \rightarrow \sigma^*_{C_1\text{-N}}$, $1sC_2 \rightarrow \sigma^*_{C_2\text{-}C_2}$, and $1sC_2 \rightarrow \sigma^*_{C_1\text{-N}}$ are too low. Their intensities are rather weak but this could be due to the mono-electronic approximation used to calculate them.

The bands *D* and *E* have also been observed previously by Newbury *et al.*[19] at 297.2 eV and 306 eV (Table II) and assigned to σ^*_{CC} and $\sigma^*_{C=C}$ shape resonances. Such high-energy resonances fall outside the range of calculation of this study. The $\sigma^*_{C_1\text{-}C_2}$ MO, which has not been found at lower energy, might be also responsible of the spectral feature in this energy region.

2. Nitrogen 1s excitation spectrum

The N1*s* electron energy loss spectrum displayed in Fig. 3 consists of an intense *A* peak at 402.1 eV and two broad bands *C* and *D* centered at 406.8 and 413.4 eV. It is quite similar to the lower resolution electron energy loss spectrum,[19] the 0.53 eV resolution x-ray absorption spectrum,[26,27] and the NEXAFS spectrum of condensed pyrrole.[20] The energy values of the spectral features are listed in Table II and are in good agreement with previous studies.

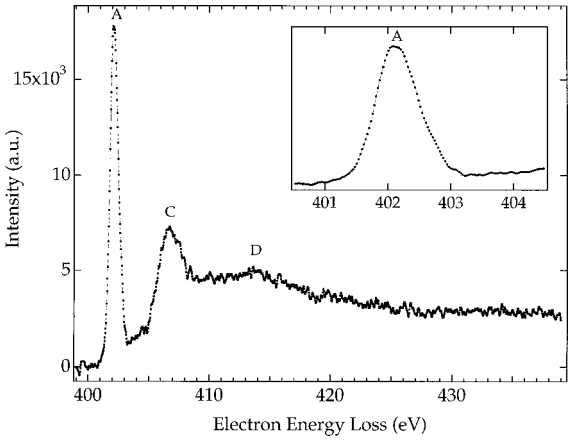

FIG. 3. Electron energy loss spectrum of pyrrole at the nitrogen *K* edge.

The most intense *A* peak at 402.1 eV has been previously suggested to be the $1s \rightarrow 1\pi^*(3b_1)$ transition. This assignment is confirmed by the present calculations which predict a TV of 3.90 eV (Table IV), a value in excellent agreement with the experimental one at 4.0 eV.

The *A* band presents a not well resolved shoulder around 402.6 eV (inset Fig. 3, Table II) (TV=3.5 eV) with an intensity of about one-third of the main peak. This is consistent with the result of the calculations which predict a $1s \rightarrow 3p\sigma/\sigma^*_{N\text{-H}}$ Rydberg-valence excitation at TV=3.85 eV with the correct intensity (Table IV). The strong mixing between the $3p\sigma$ MO and the $\sigma^*_{N\text{-H}}$ one is responsible of the rather high intensity of the Rydberg state, in contrast with the pure Rydberg states predicted at higher energies (Table IV) with negligible intensities.

The weak shoulder at 404.6 eV, not completely resolved on the low-energy side of *C* (Fig. 3), has a TV of 1.5 eV. From Table IV it appears that three Rydberg states with low intensity are calculated around this value. Excitation of these states is consistent with the spectral intensity in the 404.6 eV region. The $1s \rightarrow 2\pi^*$ $(2a_2)$ excitation has a TV of 1.58 eV but it is dipole forbidden. The 405.2 eV feature not well resolved from *C* and also reported previously should be assigned to the $1s \rightarrow \sigma^*_{N\text{-H}}$ (a_1) excitation which has a predicted TV of 1.03 eV and a medium intensity, consistent with the experiment.

The next most intense transitions predicted by the calculations are those to the $\sigma^*_{C_1\text{-H}}$ and $\sigma^*_{C_1\text{-N}}$ MOs. The intensity is expected to be the largest for the $\sigma^*_{C_1\text{-N}}$ and the less for the $\sigma^*_{C_1\text{-H}}$. The calculated TVs of −0.15 and −1.03 eV for the two $1sN \rightarrow \sigma^*_{C_1\text{-H}}$ transitions are consistent with the experimental *C* band at 406.8 eV (TV=−0.7 eV). For the two $1s \rightarrow \sigma^*_{C_1\text{-N}}$ transitions, the calculated TVs of −1.40 and −2.06 eV could explain the two not well resolved bands at TVs of −1.5 and −2.3 eV, respectively (Fig. 3).

At TV=−1.48 eV and higher energies (Table IV), the calculations predict a large number of di-excited states. The $1s1\pi \rightarrow \pi^*\pi^*$ shake-up states appear to be mixed with excitations to the Rydberg $3p\pi$ MO. None of these states should have a noticeable intensity.

The very weak band at 410 eV (Fig. 3, Table II) not well

TABLE IV. Term values (TV,eV) and assignment of the spectral features at the N1*s* edge of pyrrole.[a]

Calculated TV						
$-\epsilon_i^*$	*P*	*C*	*I*	Main Configurations		Exp. TV[c]
2.38	3.07	3.90	133.0	0.94	$1s\rightarrow 1\pi^*(3b_1)$	4.0
2.95	3.36	3.85	44.8	0.96	$1s\rightarrow 3p\sigma/\sigma^*_{\text{N-H}}(a_1)$	(3.5)
1.51	1.57	2.06	3.7	0.96	$1s\rightarrow 3p\pi(b_1)$	
1.62	1.71	1.91	0.5	0.99	$1s\rightarrow 3p\sigma(b_2)$	
1.50	1.65	1.86	3.6	0.99	$1s\rightarrow 3s\sigma(a_1)$	(1.5)
0.47	0.23	1.58	000.0	0.96	$1s\rightarrow 2\pi^*(2a_2)$[b]	
0.27	0.29	1.03	42.3	0.95	$1s\rightarrow\sigma^*_{\text{N-H}}(a_1)$	(0.9)
0.00	0.00	0.00			ion	0.00[c]
−2.03	−1.39	−0.15	78.2	0.95	$1s\rightarrow\sigma^*_{\text{C}_1\text{-H}}(a_1)$	-
−2.27	−1.87	−1.03	38.1	0.97	$1s\rightarrow\sigma^*_{\text{C}_1\text{-H}}(b_2)$	−0.7
−3.58	−3.16	−1.40	185.4	0.97	$1s\rightarrow\sigma^*_{\text{C}_1\text{-N}}(b_2)$	(−1.5)
	−2.27	−1.48		0.50	$1s\ 1\pi\rightarrow(3p\sigma/\sigma^*_{\text{N-H}})1\pi^*$	
				+0.46	$1s\ 2\pi\rightarrow(3p\sigma/\sigma^*_{\text{N-H}})2\pi^*$	
−3.73	−3.35	−2.06	54.9	0.94	$1s\rightarrow\sigma^*_{\text{C}_1\text{-N}}(a_1)$	(−2.3)
	−3.53	−2.39		0.38	$1s\ 1\pi\rightarrow 1\pi^*\ 1\pi^*$	
				+0.24	$1s\ 1\pi\rightarrow 1\pi^*\ 3p\pi$	
				+0.16	$1s\ 1\pi\rightarrow 1\pi^*\ 2\pi^*$	
	−4.37	−2.64		0.33	$1s\ 1\pi\rightarrow 1\pi^*\ 1\pi^*$	
				+0.37	$1s\ 1\pi\rightarrow 1\pi^*\ 3p\pi$	
				+0.16	$1s\ 1\pi\rightarrow 1\pi^*\ 2\pi^*$	
	−3.66	−3.21		0.66	$1s\ 1\pi\rightarrow(3p\sigma/\sigma^*_{\text{N-H}})3s\sigma$	
				+0.29	$1s\ 2\pi\rightarrow 3s\sigma\ 2\pi^*$	
	−3.78	−3.20		0.57	$1s\ 1\pi\rightarrow 1\pi^*\ 3p\sigma$	
				+0.38	$1s\ 2\pi\rightarrow 2\pi^*\ 3p\sigma$	
−4.90	−4.30	−3.41	59.9	0.92	$1s\rightarrow\sigma^*_{\text{C}_1\text{-C}_2}(a_1)$	(−3.9)
−5.00	−4.57	−3.53	41.8	0.96	$1s\rightarrow\sigma^*_{\text{C}_1\text{-C}_2}(b_2)$	
−6.17	−5.59	−4.38	0.3	0.94	$1s\rightarrow\sigma^*_{\text{C}_2\text{-H}}(b_2)$	

[a]See Table III for notations.
[b]Dipole forbidden transition.
[c]Experimental term values: relative to 1*s*N binding energy: 406.1 eV (Ref. 48).
( ) not well resolved

resolved may be due to the $1s\rightarrow\sigma^*_{\text{C}_1\text{-C}_2}$ transitions which are calculated to have TVs of −3.41 eV and −3.53 eV, respectively. Their calculated intensity corresponds to a medium probability. The calculated TVs are rather close to the −3.9 eV roughly estimated experimental one (Table III).

The *D* band centered at 413.4 eV, already reported in a previous work, has not been assigned by the calculations, since it lies at too high an energy. It is probably due to the $1s\rightarrow\sigma^*_{\text{C}_2\text{-C}_2}$ which does not appear at lower energy. This suggestion is in agreement with the previous assignment.[19]

B. Pyrazole

The electronic configuration of pyrazole in its neutral ground state is the following:

$$1a'^2 2a'^2 3a'^2 4a'^2 5a'^2 6a'^2 7a'^2 8a'^2 9a'^2 10a'^2 11a'^2 12a'^2 1a''^2 13a'^2 14a'^2 15a'^2 2a''^2 3a''^2.$$

The first five a' MOs are the 1*s* orbitals of the nitrogen and carbon atoms. The $1a''$, $2a''$, and $3a''$ are the lone pair on the N_2 atom and the π orbitals, respectively (Fig. 1). The lowest-energy unoccupied MOs are calculated to be the $4a''$ (LUMO, $1\pi^*$), $16a'$ ($\sigma^*_{\text{N}_1\text{-H}}$), and $5a''$ ($2\pi^*$).

Pyrazole has its three C atoms and two N atoms with different chemical environment (Fig. 1). The binding energies for the gas, not known as far as we know, were estimated from the solid data.[49,50] In the solid,[49] they have been measured to be separated by 0.8 and 1.6 eV at the C1*s* edge, from the lowest one which is for C_2, the highest one being for C_1 (Fig. 1). These chemical shifts have been calculated for the isolated molecule to be 0.89 (SCF level), 0.56 eV (MP2 level) for the C_2/C_3 binding energies, and 1.45 (SCF level) and 1.19 eV (MP2 level) for the C_2/C_1 energy separation (Table V). At the N1*s* edge, the chemical shift has been calculated to be of 2.06 (SCF level) and 2.11 eV (MP2 level), values agreeing rather well with each other and a little bit higher than the experimental 1.3 eV one for condensed pyrazole.[49] The lowest binding energy is for the N_2 atom

TABLE V. Term values (TV,eV) and assignment of the spectral features at the C1*s* edge of pyrazole.[a]

Calculated TV						Exp.
$-\epsilon_i^*$	P	C	I	Main Configurations		TV[b]
2.54	3.56	4.00	163.9	0.92	$1sC_2 \rightarrow 1\pi^*$	3.9
2.06	3.44	3.81	180.6	0.94	$1sC_3 \rightarrow 1\pi^*$	3.5
2.12	3.19	3.54	211.6	0.94	$1sC_1 \rightarrow 1\pi^*$	3.2
2.47	2.81	3.04	11.3	0.96	$1sC_2 \rightarrow 3s\sigma/\sigma^*_{C_2\text{-}H}$	
0.96	2.22	2.91	40.1	0.71	$1sC_2 \rightarrow 2\pi^*$	3.0
				+0.20	$1sC_2 \rightarrow 3p\pi$	
2.05	2.31	2.48	9.1	0.97	$1sC_2 \rightarrow 3p\sigma/\sigma^*_{N_1\text{-}H}$	
0.18	1.24	2.25	44.0	0.92	$1sC_3 \rightarrow 2\pi^*$	2.2
1.28	1.66	2.25	10.6	0.95	$1sC_3 \rightarrow 3s\sigma/\sigma^*_{C_3\text{-}H}$	
1.20	1.63	2.19	24.4	0.96	$1sC_1 \rightarrow 3s\sigma/\sigma^*_{C_1\text{-}H}$	
1.21	1.48	1.97	12.9	0.97	$1sC_3 \rightarrow 3p\sigma/\sigma^*_{C_3\text{-}H}$	
1.64	1.65	1.89	11.3	0.20	$1sC_2 \rightarrow 2\pi^*$	
				+0.76	$1sC_2 \rightarrow 3p\pi$	
1.39	1.59	1.76	1.4	0.98	$1sC_2 \rightarrow 3p\sigma$	
0.70	0.92	1.36	30.7	0.97	$1sC_3 \rightarrow 3p\sigma/\sigma^*_{C_1\text{-}H/\sigma^*C_2\text{-}H}$	(1.0)
0.78	0.83	1.32	0.7	0.99	$1sC_3 \rightarrow 3p\pi$	
−1.17	0.21	1.09	15.3	0.86	$1sC_1 \rightarrow 2\pi^*$	
0.41	0.67	1.04	0.5	0.97	$1sC_1 \rightarrow 3p\sigma$	
0.01	0.27	0.72	4.5	0.96	$1sC_3 \rightarrow 3p\sigma$	
0.23	0.28	0.70	1.2	0.98	$1sC_1 \rightarrow 3p\pi$	
−1.05	−0.17	0.41	68.6	0.91	$1sC_2 \rightarrow \sigma^*_{C_1\text{-}N_1}/\sigma^*_{N_1\text{-}N_2}$	(0.0)
0.00	0.00	0.00			C_2 ion	0.00[c]
−1.78	−0.93	−0.05	33.6	0.93	$1sC_3 \rightarrow \sigma^*_{C_3\text{-}H}$	
−1.51	−0.72	−0.07	3.8	0.91	$1sC_2 \rightarrow \sigma^*_{C_2\text{-}H}$	
−2.26	−1.28	−0.41	35.5	0.89	$1sC_1 \rightarrow \sigma^*_{C_1\text{-}H}$	
−0.89	−0.89	−0.56			C_3 ion	−0.8[c]
−2.10	−1.39	−0.73	22.1	0.92	$1sC_2 \rightarrow \sigma^*_{C_1\text{-}N_1}$	
−2.83	−1.89	−0.97	76.6	0.91	$1sC_1 \rightarrow \sigma^*_{N_1\text{-}H}$	
−1.45	−1.45	−1.19			C_1 ion	−1.7[c]
−3.19	−2.31	−1.27	8.2	0.92	$1sC_3 \rightarrow \sigma^*_{C_1\text{-}C_2}$	
−4.35	−3.39	−1.62	38.6	0.77	$1sC_3 \rightarrow \sigma^*_{C_1\text{-}C_3}$	
				+0.17	$1sC_3 \rightarrow \sigma^*_{C_3\text{-}N_2}$	
−3.37	−2.57	−1.82	65.6	0.88	$1sC_2 \rightarrow \sigma^*_{C_3\text{-}N_2}$	−2.1
	−3.36	−1.90		0.47	$1sC_1 2\pi \rightarrow 1\pi^* 1\pi^*$	
				+0.31	$1sC_1 1\pi \rightarrow 1\pi^* 1\pi^*$	
	−3.28	−2.35		0.68	$1sC_2 1\pi \rightarrow 1\pi^* 2\pi^*$	
				+0.16	$1sC_2 1\pi \rightarrow 3p\pi 2\pi^*$	
	−4.24	−2.56		0.75	$1sC_2 2\pi \rightarrow 1\pi^* 2\pi^*$	

[a]See Table III for notations.
[b]Experimental TVs: relative to C1s ionization energies deduced from solid state data (Ref. 49) C_2: 285.5 eV; C_3: 286.3 eV; C_1: 287.1; by analogy with imidazole (Ref. 50) the values have been estimated to be shifted 4.7 eV higher for isolated pyrazole than in solid: C_2: 290.2 eV; C_3: 291 eV; C_1: 291.8 eV.
( ) not well resolved

(Fig. 1, Table VI). These trends for the core-electron binding energies are expected to be the same for the excitation energies from the different carbon and nitrogen atoms. In the following the TVs are given relative to the C_2 limit and to the N_2 limit at the C1*s* and N1*s* edges, respectively.

1. Carbon 1s excitation spectrum

The C1*s* electron energy loss spectrum displayed in Fig. 4 consists of an intense *A* peak at 286.30 eV, a much less intense *B* band around 288 eV not completely resolved from *A*, two broadbands *C* and *D* at 292.3 and 297.8 eV, respectively, and a much broader band not well resolved with a maximum of intensity at 301 eV (Table II). It looks like the C1*s* excitation spectrum of pyrrole (Fig. 2), except that *B* and the fine features in *A* are less well separated than for pyrrole. The energy values of the spectral features are given in Table II.

The lowest-energy *A* band exhibits two fine features not well resolved around 286.7 and 287 eV (inset Fig. 4) separated from the main peak by about 0.4 and 0.7 eV, respectively (Table II). The calculations predict that the transition from C_2 to the lowest-energy π^* MO has a term value of 4.00 eV and is separated by about 0.19 eV from the $1sC_3 \rightarrow 1\pi^*$ one, the most intense, and by about 0.46 eV from the $1sC_1 \rightarrow 1\pi^*$ one (Table V). The calculated intensities are roughly the same for the three transitions. The *A* peak and the fine features at 286.7 and 287 eV are thus assigned to the excitation of the $1\pi^*$ MO from C_2, C_3, and C_1, respectively. The experimental TV of 3.9 eV is in very good agreement

TABLE VI. Term values (TV,eV) and assignment of the spectral features at the N1*s* edge of pyrazole.[a]

Calculated TV						
$-\epsilon_{i*}$	*P*	*C*	*I*	Main Configurations		Exp. TV[b]
3.57	4.60	4.77	215.3	0.94	$1sN_2\rightarrow 1\pi^*$	5.27
2.30	2.62	2.88	0.9	0.97	$1sN_2\rightarrow 3p\sigma$	
1.10	2.02	2.24	140.2	0.95	$1sN_1\rightarrow 1\pi^*$	3.2
1.82	2.04	2.15	1.0	0.98	$1sN_2\rightarrow 3s\sigma$	
0.37	1.59	2.11	13.2	0.67	$1sN_2\rightarrow 2\pi^*$	
				+0.23	$1sN_2\rightarrow 3p\pi$	
1.71	1.82	2.10	4.4	0.77	$1sN_2\rightarrow 3p\pi$	
				+0.19	$1sN_2\rightarrow 2\pi^*$	
1.67	1.85	1.99	6.3	0.98	$1sN_2\rightarrow 3p\sigma$	
0.88	1.40	1.80	44.9	0.95	$1sN_1\rightarrow 3p\sigma/\sigma^*_{N_1\text{-}H}$	2.6
−1.04	0.23	1.35	91.5	0.87	$1sN_2\rightarrow \sigma^*_{C_1\text{-}N_1}$	
−0.26	−0.05	0.03	5.9	0.98	$1sN_1\rightarrow 3s\sigma$	
0.00	0.00	0.00			N_2 ion	0.00[b]
−0.36	−0.30	−0.19	0.5	0.99	$1sN_1\rightarrow 2\pi^*$	
−2.04	−0.92	−0.24	0.4	0.88	$1sN_1\rightarrow 3p\pi$	
−0.54	−0.33	−0.25	1.0	0.97	$1sN_1\rightarrow 3p\sigma$	
−2.17	−1.29	−0.59	25.7	0.81	$1sN_2\rightarrow \sigma^*_{C_1\text{-}H}$	(−0.3)
	−2.20	−0.60		0.66	$1sN_21\pi\rightarrow 1\pi^*1\pi^*$	
−2.19	−1.45	−0.83	24.8	0.91	$1sN_1\rightarrow \sigma^*_{N_1\text{-}H}$	
−2.67	−1.70	−0.95	49.6	0.71	$1sN_2\rightarrow \sigma^*_{N_1\text{-}N_2}$	
	−1.76	−1.21		0.73	$1sN_21\pi\rightarrow 1\pi^*3p\sigma$	
−2.06	−2.06	−2.11			N_1 ion	−1.3[b]
−4.27	−3.15	−2.21	131.7	0.79	$1sN_1\rightarrow \sigma^*_{N_1\text{-}C_1}$	−1.2
	−2.60	−2.25		0.81	$1sN_21\pi\rightarrow 1\pi^*3p\pi$	
	−2.92	−2.53		0.83	$1sN_12\pi\rightarrow 2\pi^*3p\sigma$	
−5.18	−4.00	−2.81	244.3	0.79	$1sN_1\rightarrow \sigma^*_{C_2\text{-}C_3}$	−2.2
	−3.72	−2.87		0.70	$1sN_12\pi\rightarrow 1\pi^*1\pi^*$	
	−2.19	−3.11		0.68	$1sN_21\pi\rightarrow 3s\sigma 3p\sigma$	
−4.40	−3.63	−3.15	17.2	0.86	$1sN_1\rightarrow \sigma^*_{C_1\text{-}C_2}$	
	−4.09	−3.97		0.87	$1sN_12\pi\rightarrow 1\pi^*3s\sigma$	
	−4.32	−4.02		0.89	$1sN_12\pi\rightarrow 1\pi^*3p\pi$	

[a]See Table III for notations.

[b]For the experimental TV: N1*s* ionization energies deduced from solid state data. By analogy with imidazole (Ref. 50) the gas values have been estimated to be shifted 4.7 eV at higher energy than in the solid (Ref. 49) (N_2: 401.1 eV, N_1: 402.4 eV): for gas N_2: 405.8 eV; N_1: 407.1 eV.

with the calculated 4.00 eV value. This indicates that the binding energy value of 290.2 eV for C_2 deduced from that measured for pyrazole in thin films[49] is a good one.

According to the calculations (Table V), the transitions to the $2\pi^*$ MO are expected to be less intense than that to the $1\pi^*$ type MO and the electronic configuration of the excited state is mixed with the $3p\pi^*$ Rydberg excitation for carbon C_2. The spectral intensity around 287.2 eV (TV=3.0 eV) (Fig. 4) suggests that at least one additional component is present in the 287.6 eV region between the *A* and *B* bands. It may be due to the transition from C_2 to the $3p\pi/2\pi^*$ orbital (calculated TV=2.91 eV, Table V). This assignment is consistent with the shape of the spectrum in the 287.2 eV region.

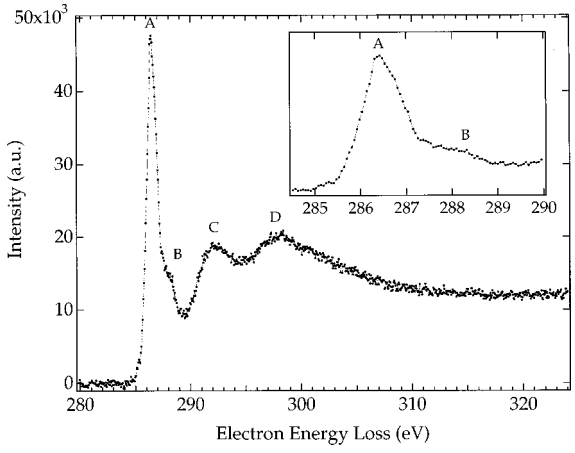

FIG. 4. Electron energy loss spectrum of pyrazole at the carbon *K* edge.

The *B* band centered at 288 eV (TV=2.2 eV) is rather broad and very likely composite. The calculations predict the transitions from C_3 to the $2\pi^*$ MO with a TV of 2.25 eV (Table V) and a nonnegligible intensity, several excitations to Rydberg/$\sigma^*_{C\text{-}H}$ mixed MOs with TVs of 2.25 to 1.97 eV as well as the $1sC_2\rightarrow 3p\pi$ in mixture with $2\pi^*$ transition (TV=1.89 eV). This suggests that in the region of the *B* band, these transitions may be observed and contribute to the spectrum.

The *B* and *C* bands are not completely resolved from each other with a feature at 289.2 eV (TV=1.0 eV) (Fig. 4). This suggests that at least one excitation band is present in this region. Among many Rydberg excited states with negligible intensities, the calculations predict two possible transitions around this TV: the $1sC_3\rightarrow 3p\sigma/\sigma^*_{C_1\text{-}H}/\sigma^*_{C_2\text{-}H}$

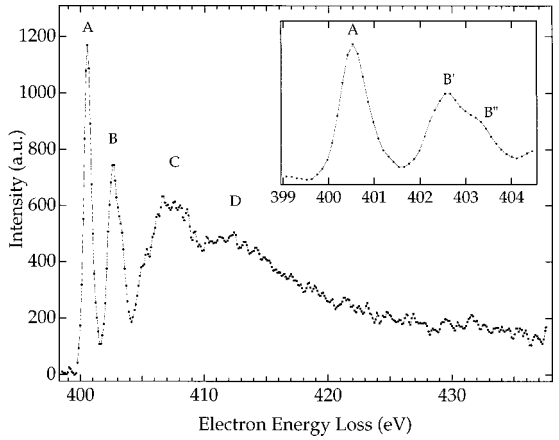

FIG. 5. Electron energy loss spectrum of pyrazole at the nitrogen *K* edge.

(TV=1.36 eV) one and the $1sC_1 \rightarrow 2\pi^*$ one (TV=1.09 eV). Thus we suggest that in the 289.2 eV region, these transitions are excited and are located too close in energy to be resolved within the 0.2 eV energy resolution.

The fine feature around 290.2 eV, not well resolved from *C* comes from the $1sC_2 \rightarrow \sigma^*_{C_1\text{-}N_1}/\sigma^*_{N_1\text{-}N_2}$ excitation, as the TV of 0.0 eV is consistent with the calculated one at 0.41 eV and the intensity is expected to be medium (Table V). In the same region, the calculations predict also the transitions $1sC_3 \rightarrow \sigma^*_{C_3\text{-}H}$ and $1sC_1 \rightarrow \sigma^*_{C_1\text{-}H}$ with lower intensity (Table V).

At higher energy, the intense *C* band (TV=−2.1 eV) may be explained by a group of σ^* resonances which are calculated to have close TVs (see Table V). The most intense ones are the $1sC_1 \rightarrow \sigma^*_{N_1\text{-}H}$ (TV=−0.97 eV) and the $1sC_2 \rightarrow \sigma^*_{C_3\text{-}N_2}$ (TV=−1.82 eV). All these transitions contribute to the *C* band.

Above this energy value, the calculations predict a large number of doubly excited states, most of them involving Rydberg MOs and thus should have very low intensities, as already obtained in pyrrole. In Table V are only indicated the transitions involving valence π^* MOs. They do not seem to match any noticeable spectral feature.

The experimental spectrum presents two broadbands at 297.8 and 301 eV (Table II) which appear at roughly the same energy as in pyrrole, 297.4 and 302 eV, respectively. This energy range falls outside that available by the calculations.

2. Nitrogen 1s excitation spectrum

The N1*s* electron energy loss spectrum shown in Fig. 5 exhibits two intense sharp peaks *A* and *B* at 400.53 and 402.6 eV. At higher energy, there are at least two broadbands *C* and *D* with maximum of intensity at 407.4 eV and 412 eV, respectively. The energy values of the spectral features are given in Table II.

The lowest-energy *A* band at 400.53 eV corresponds to a transition with a TV of 5.27 eV (Table VI). According to the calculations, the lowest-energy and most intense transition is expected to be $1sN_2 \rightarrow 1\pi^*$ with a TV of 4.77 eV (Table VI). This value is 0.5 eV lower than the experimental one. This trend has also been observed at the C1*s* edge excitation spectrum of pyrazole. The *A* band is thus assigned to the $1sN_2 \rightarrow 1\pi^*$ transition as its intensity and TV are consistent with calculations.

The *B* band located at 402.60 eV (or B' in the expanded view of the *A* and *B* regions shown in the inset of Fig. 5) must be due to a transition with a TV of 3.2 eV and lower probability than for the $1sN_2 \rightarrow 1\pi^*$ one. As shown in Table VI, the $1sN_1 \rightarrow 1\pi^*$ transition is calculated to be separated by 2.53 eV from the $1sN_2 \rightarrow 1\pi^*$ one. The B' feature is separated from *A* by 2.07 eV in the spectrum. This suggests that the $1sN_1 \rightarrow 1\pi^*$ transition is located at 402.6 eV, although the calculated TV for this band is too small (2.21 eV instead of 3.2 eV in the spectrum). This assignment is confirmed by the intensity of the B' band which is consistent with that provided by the calculations (two-thirds of the $1sN_2 \rightarrow 1\pi^*$ band) (Table VI).

On the high-energy side of *B* (inset Fig. 5), there is a feature B'' around 403.2 eV only partly resolved from B'. This indicates the excitation of an electronic state with TV of 2.6 eV and lower probability than those involving the $1\pi^*$ MO excited from the $1sN_2$ and $1sN_1$ orbitals. The calculations locate the $1sN_1 \rightarrow 3p\sigma/\sigma^*_{N_1\text{-}H}$ at about 3 eV above the $1sN_2 \rightarrow 1\pi^*$ transition, which is close to the experimental 2.67 eV value. The intensity is expected to be less than half that of the $1sN_2 \rightarrow 1\pi^*$ band (B'). This suggests that the feature B'' is due to the excitation to $3p\sigma/\sigma^*_{N_1\text{-}H}$ from the $1sN_1$ orbital. It is also possible that the $1sN_2 \rightarrow \sigma^*_{C_1\text{-}N_1}$ transition, which is close to the previous one, contributes to this band (Table VI). The $1sN_2 \rightarrow 2\pi^*$ transition is also expected to be excited in this energy region, but with a weaker intensity due to its strong mixing with the $1sN_2 \rightarrow 3p\pi$ transition. It may contribute to the *B* band in between the B' and B'' features and responsible of the fact B'' is not well resolved from B' despite the 0.2 eV resolution. The excitation of the $2\pi^*$ MO from the N_1 core orbital is calculated to be located around the $N_2 1s$ ionization edge (TV=−0.19 eV) and to have a very low probability (Table VI).

The *C* band has a maximum of intensity rather broad and centered at 407.4 eV. This suggests that it may consist of at least two subbands of roughly the same intensity around 407 (TV=−1.2 eV) and 408 eV (TV=−2.2 eV), respectively. According to the calculations, several transitions are expected to be excited in the same energy region, the most intense ones being the $1sN_2 \rightarrow \sigma^*_{C_2\text{-}C_3}$ and $1sN_1 \rightarrow \sigma^*_{N_1\text{-}C_1}$ separated by 0.60 eV (Table VI). This energy difference is consistent with subbands around 407 and 408 eV. This suggests that these transitions contribute to the *C* band. On the low-energy side, there is at least one fine feature at 405.5 eV, not well resolved which may be due to the $1sN_2 \rightarrow \sigma^*_{N_1\text{-}N_2}$ (−0.95 eV) or $1sN_1 \rightarrow \sigma^*_{N_1\text{-}H}$ (−0.83 eV) or $1sN_2 \rightarrow \sigma^*_{C_1\text{-}H}$ (−0.59 eV) calculated to be of lower intensity than that of the other two transitions at higher energy (Table VI). The results of the calculations are consistent with the energy location of the 405.5 eV shoulder and its intensity within the uncertainty on the ionization energies.

Between the *C* and *D* bands, the calculations predict

among some doubly excited states involving Rydberg MOs, the $1sN_1 \rightarrow \sigma^*_{C_1\text{-}C_2}$ transition, with a rather weak intensity and a TV of -3.15 eV (Table VI). It may be not resolved from *C* on its high-energy side. The *D* band with TV$=-5.18$ eV is beyond the calculated states. It could be assigned to the $1sN_2 \rightarrow \sigma^*_{C_1\text{-}N_2}$ transition which is expected to have a strong intensity and does not appear at lower energies.

V. CONCLUSIONS

The inner-shell electron energy loss spectra of pyrrole and pyrazole have been recorded at the C1*s* and N1*s* edges with 0.2 eV resolution, resolution better than in the previous studies of pyrrole, allowing to resolve the transitions from the atoms with different chemical environment. *Ab initio* calculations using the equivalent core model have been performed within the Koopmans approximation, but also taking into account the polarization and correlation effects which have been shown to be not negligible. They have provided the TVs with a few tenths of an eV of accuracy.

For pyrrole the C1*s* excitation spectrum is dominated by the transition to the $1\pi^*$ valence orbital, confirmed to be $3b_1$, with the largest intensity on C_1. The $2\pi^*$ calculated to be 1.4 eV above the $1\pi^*$ with the largest intensity on C_2 is responsible of a weaker band which may also include some contribution from the transition to the $3p\sigma/\sigma^*_{N\text{-}H}$ MO. The excitation of the $3p\pi/\pi^*$ mixed Rydberg-valence MO is responsible of a low intensity band located 1.0 eV above the $1\pi^*$ excitation from C_2. At the N1*s* edge the main peak is due to the transition to the $1\pi^*$ $(3b_1)$, the transition to the $2\pi^*$ orbital being dipole forbidden, but predicted to be located 1.4 eV above the first one. In agreement with the calculations the excitation of the $3p\sigma/\sigma^*_{N\text{-}H}$ mixed Rydberg-valence MO is observed close to the $1s \rightarrow \pi^*$ band, with significant intensity.

For pyrazole, at the C1*s* edge the spectrum is dominated by the transitions to the $1\pi^*$ orbital, with roughly the same intensity on the three C atoms, but the lowest one on C_1. The second π^* MO predicted at 1.56 eV above the $1sC_3 \rightarrow \pi^*$ band, with the largest intensity on C_3 is responsible of a weaker spectral feature. In the same region Rydberg-valence states are also close to the $3s\sigma/\sigma^*_{C\text{-}H}$. At the N1*s* edge the transitions to the two π^* are dipole allowed, the lowest-energy one being responsible of the main peak, the largest intensity being for N_2. They are separated by 2.43 eV according to the calculations. The intensity of the second one is strongly reduced compared to the excitations to the lowest-energy one. The transition from $1sN_1$ to the $3p\sigma/\sigma^*_{N_1\text{-}H}$ mixed MO is observed 0.6 eV above that to the $1\pi^*$ one from N_2 with a TV and intensity in good agreement with the calculations. The excitation of the σ^*_{CN} lowest energy is close to this one with nonnegligible intensity.

For both molecules the calculations predict, at both edges, several doubly excited states responsible of fine features above the ionization limits.

ACKNOWLEDGMENTS

The Laboratoire de Dynamique Moléculaire et Photonique is ''Unité de Recherche Associée au CNRS.'' The Center d'Etudes et de Recherches Lasers et Applications (CERLA) is supported by the ''Ministère chargé de la Recherche,'' the ''Région Nord/Pas-de-Calais,'' and the ''Fonds Européen de Développement Economique des Régions.'' This work has been supported by the European Community (Science program). The belgian team acknowledges the financial support of the ''Patrimoine de l'Université de Liège'' and the ''Actions de Recherche Concertée de la Direction générale de la Recherche Scientifique, Communauté française (94/99-175).'' M.J.H.F. is grateful to the FNRS for the research position. The technical assistance of Jacques Heinesch is highly acknowledged.

[1] O. Khan, *Molecular Magnetism* (VCH Publishers, New York, 1993).
[2] *Inorganic Materials*, edited by D. W. Bruce and D. O'Hare (Wiley, New York, 1992).
[3] A. D. Baker, D. Betteridge, N. R. Kemp, and R. E. Kirby, Anal. Chem. **42**, 1064 (1970).
[4] C. E. Brion, Comments At. Mol. Phys. **16**, 249 (1985).
[5] C. E. Brion and A. Hamnett, Adv. Chem. Phys. **XLV**, 3 (1981).
[6] M.-J. Hubin-Franskin, H. Aouni, D. Duflot, F. Motte-Tollet, C. Hannay, L. F. A. Feirreira, and G. Tourillon, J. Chem. Phys. **106**, 35 (1997).
[7] G. Scheibe and H. Grieneisen, Z. Phys. Chem. (Munich) **25**, 52 (1934).
[8] W. C. Price and A. D. Walsh, Proc. R. Soc. London, Ser. A **179**, 206 (1941).
[9] G. Milazzo, Spectrochim. Acta **2**, 254 (1942); Gazz. Chim. Ital. **83**, 787 (1953).
[10] L. W. Pickett, M. E. Corning, G. M. Wieder, D. A. Semenov, and J. M. Buckley, J. Am. Chem. Soc. **75**, 1618 (1953).
[11] P. A. Mullen and M. K. Orloff, J. Chem. Phys. **51**, 2276 (1969).
[12] M. Bavia, F. Bertinelli, C. Taliani, and C. Zauli, Mol. Phys. **31**, 479 (1976).
[13] W. M. Flicker, O. A. Mosher, and A. Kuppermann, J. Chem. Phys. **64**, 1315 (1976).
[14] W. Butscher and K.-H. Thunemann, Chem. Phys. Lett. **57**, 224 (1978).
[15] K. Tanaka, T. Nomura, T. Noro, H. Tatewaki, T. Takada, H. Kashiwagi, F. Sasaki, and K. Ohno, J. Chem. Phys. **67**, 5738 (1977).
[16] H. Nakano, T. Tsuneda, T. Hashimoto, and K. Hirao, J. Chem. Phys. **104**, 2315 (1996).
[17] W. von Niessen, L. S. Cederbaum, and G. H. F. Diercksen, J. Am. Chem. Soc. **98**, 2066 (1976).
[18] D. C. Rawlings, E. R. Davidson, and M. Gouterman, Int. J. Quantum Chem. **XXVI**, 237 (1984).
[19] D. C. Newbury, I. Ishii, and A. P. Hitchcock, Can. J. Chem. **64**, 1145 (1986).
[20] M. Mauerer, P. Zebisch, M. Weinelt, and H.-P. Steinrück, J. Chem. Phys. **99**, 3343 (1993).
[21] G. Distefano, M. Guerra, D. Jones, and A. Modelli, Spectrochim. Acta **38A**, 85 (1982).
[22] D. Dal Monte, A. Mangini, and R. Passerini, Gazz. Chim. Ital. **86**, 797 (1965).
[23] J. Elguero, R. Jacquier, and H. C. N. Tien Duc, Bull. Soc. Chim. Fr. **12**, 3744 (1966).
[24] I. L. Finar, J. Chem. Soc. 725 (1968).
[25] J. Del Bene and H. H. Jaffé, J. Chem. Phys. **48**, 4050 (1968).
[26] A. A. Pavlychev, K. H. Hallmeier, C. Hennig, L. Hennig, and R. Szargan, Chem. Phys. **201**, 547 (1995).
[27] C. Hennig, K. H. Hallmeier, A. Bach, S. Bender, R. Franke, J. Hormes, and R. Szargan, Spectrochim. Acta **52A**, 1079 (1996).
[28] T. H. Dunning, J. Chem. Phys. **55**, 716 (1971); **55**, 3958 (1971).
[29] T. H. Dunning and P. J. Hay, *Methods of Electronic Structure Theory*, edited by H. F. Schaeffer III (Plenum, New York, 1977), Vol. 3.
[30] A. P. Hitchcock, D. C. Newbury, I. Ishii, J. Stöhr, J. A. Horsley, R. D. Redwing, A. L. Johnson, and F. Sette, J. Chem. Phys. **85**, 4849 (1985).
[31] W. H. E. Schwarz, T. C. Chang, U. Seeger, and K. H. Wang, Chem. Phys. **117**, 73 (1987).

[32] M. Dupuis, F. Johnston, and A. Marquez, ''HONDO95.3 from CHEMStation'' (1995) IBM Corporation, Neighborhood Road, Kingston, NY, 12401.
[33] W. L. Jolly and D. N. Hendrickson, J. Am. Chem. Soc. **92**, 1863 (1970).
[34] J. M. Hollander and W. L. Jolly, Acc. Chem. Res. **3**, 193 (1970).
[35] W. H. E. Schwarz, Angew. Chem. Int. Ed. Engl. **13**, 454 (1974).
[36] S. Bodeur, P. Millié, and I. Nenner, Phys. Rev. A **41**, 252 (1990).
[37] T. Koopmans, Physica (The Hague) **1**, 104 (1933).
[38] C. Möller and M. S. Plesset, Phys. Rev. **46**, 618 (1934).
[39] R. Cimiraglia, J. Chem. Phys. **83**, 1746 (1985); R. Cimiraglia and M. Persico, J. Comput. Chem. **8**, 39 (1987).
[40] B. Huron, J-P. Malrieu, and P. Rancurel, J. Chem. Phys. **58**, 5745 (1973).
[41] S. Y. Lee and B. H. Boo, J. Phys. Chem. **100**, 15073 (1996).
[42] L. Nygaad, J. T. Nielsen, J. Kirchleiner, G. Maltesen, J. Rastrup-Andersen, and S. O. Sorensen, J. Mol. Struct. **3**, 491 (1969).
[43] A. L. Llamas-Saiz, C. Foces-Foces, O. Mó, M. Yáñez, E. Elguero, and J. Elguero, J. Comput. Chem. **16**, 263 (1995).
[44] L. Nygaad, D. Christen, J. T. Nielsen, E. J. Pedersen, O. Snerling, E. Vestergaard, and G. O. Sorensen, J. Mol. Struct. **22**, 401 (1974).
[45] C. Hannay, J. Heinesch, U. Kleyens, and M.-J. Hubin-Franskin, Meas. Sci. Technol. **6**, 1140 (1995).
[46] M. Tronc, G. C. King, R. C. Bradford, and F. H. Read, J. Phys. B **9**, L555 (1976).
[47] R. N. S. Sodhi and C. E. Brion, J. Electron Spectrosc. Relat. Phenom. **34**, 363 (1984).
[48] A. A. Bakke, H. W. Chen, and W. J. Jolly, J. Electron Spectrosc. Relat. Phenom. **20**, 333 (1980).
[49] D. T. Clark and D. M. J. Lilley, Chem. Phys. **9**, 234 (1971).
[50] E. Apen, A. P. Hitchock, and J. L. Gland, J. Phys. Chem. **97**, 6859 (1993).

Article 10

JOURNAL OF CHEMICAL PHYSICS VOLUME 110, NUMBER 12 22 MARCH 1999

The core excitation of pyridine and pyridazine: An electron spectroscopy and *ab initio* study

C. Hannay
Laboratoire de Spectroscopie d'Electrons diffusés, Université de Liége, Institut de Chimie, B6c, B-4000 Liège (Sart Tilman), Belgique

D. Duflot[a] and J.-P. Flament
Laboratoire de Physique des Lasers, Atomes et Molécules (PhLAM), UMR CNRS Centre d'Etudes et de Recherches Lasers et Applications (CERLA), Université des Sciences et Technologies de Lille, F-59655 Villeneuve d'Ascq Cedex, France

M.-J. Hubin-Franskin[b]
Laboratoire de Spectroscopie d'Electrons diffusés, Université de Liége, Institut de Chimie, B6c, B-4000 Liège (Sart Tilman), Belgique

(Received 24 July 1998; accepted 17 December 1998)

The carbon and nitrogen *K*-shell excitation spectra of gaseous pyridine and pyridazine were recorded using the electron-energy loss spectroscopy under electric-dipole conditions (2 keV, small angle) with a resolution of 0.2 eV. *Ab initio* Configuration interaction calculations in the frame of the equivalent core model were performed in order to help in the assignment of the spectral features. The spectra are dominated by the transitions to the $1\pi^*$ and σ^* type orbitals. The $C1s$ spectra of both molecules are close to that of benzene: The intensity of Rydberg transitions are enhanced by an important valence σ^*_{C-H} character; the $1s \rightarrow 3\pi^*$ transition is mixed with double excitations and give rise to several states, some of them lying above the ionization thresholds. Finally, the $N1s$ spectra of both molecules are similar to the *s*-triazine one. © *1999 American Institute of Physics.* [S0021-9606(99)30212-9]

I. INTRODUCTION

This paper is devoted to the electronic spectroscopy of isolated pyridine and pyridazine by core-electron excitation and the inner-shell electron-energy loss spectroscopy (ISEELS).

Very little is known on the energy scheme, the nature and the symmetry of the unoccupied molecular orbitals (MOs) in these molecules and on the influence of the replacement of one and/or two CH group(s) in benzene by one and/or two nitrogen atom(s) on the energy splitting of the lowest energy π^* type MOs. Pyridine and pyridazine are very important molecules as they are units in pesticides,[1] in complex systems having magnetic properties[2] and in biochemistry. Their electronic spectroscopic properties is the basis to understand the big systems in which they are embedded.

The previous experimental studies of pyridine were devoted mainly to the negative ion resonances[3–5] and the valence excitation spectra[3,6,7] which are complex, difficult to interpret, and assigned in terms of transitions to the lowest-energy singlet and triplet electronic excited states. *Ab initio* calculations, using high level multireference Configuration interaction (MRCI)[3,8] and Green's functions[9] were performed to interpret these data. By core-electron excitation and the ISEELS method at the $C1s$ and $N1s$ edges,[10] the lowest energy band, assigned to the $3b_1(1\pi^*)$ and $2a_2(2\pi^*)$ MOs excitations (not resolved within the 1.0 eV resolution) is separated by 3.9 eV from a second one, which was suggested to be due to the $4b_1(3\pi^*)$ MO transition. In the $C1s$ photoabsorption spectrum,[11] with an instrumental resolution of about 0.3 eV, the lowest energy band is partly splitted into two features by 0.5 eV. For these latter, no assignment has been given. At the nitrogen *K*-edge the photoabsorption spectrum[11] is completely different from the ISEELS gas-phase spectrum.[10] There are strong discrepancies, both in the reported features and in the energies. Finally, the thin film $N1s$ spectrum reported by Dudde *et al.*[12] is close to the solid and monolayer ones,[10] although all the energies are too large by about 1 eV.

For pyridazine the data are even more fragmentary. The valence excitation spectrum studied by visible-ultraviolet (VUV) photoabsorption[6,13] and by electron impact[5,13] is complex and has been interpreted in terms of transitions to the lowest energy singlet and triplet excited states involving the lowest energy unoccupied molecular orbital (LUMO) and the highest energy occupied molecular orbital (HOMO). The theoretical studies include MR-CI calculations[13] and Green's functions[8] methods. This molecule supports negative ion resonances by low-energy electron attachment.[4,5] As far as we know, for pyridazine, the core excitation method has not been used and the $C1s$ and $N1s$ spectra have not been published until now.

The parent benzene molecule has been the subject of numerous works. The valence photoelectron spectra have been extensively studied (see Refs. 14 and 15, and references

[a]Electronic mail: Denis.Duflot@univ-lille1.fr
[b]Directeur de Recherches FNRS.

therein for previous studies). The core excitation spectra have been recorded experimentally,[10,11,16–22] both in gas phase[10,11,18–21] and adsorbed on surfaces.[10,17,22] The theoretical works mainly employed semiempirical methods.[23–26] To our knowledge, the only *ab initio* studies are the multiconfigurational approach of Ref. 27, and the recent work using the static exchange (STEX) method.[28]

In this work, we present new data on the unoccupied MOs of pyridine and pyridazine by using the core-electron excitation and the electron collisions in low-momentum transfer conditions and at higher resolution (0.2 eV) than previous studies.[10–12] The resolution is kept constant for the whole excitation range and the energy scale is calibrated with high confidence.[29] In order to help in the assignment of the observed spectral features, *ab initio* calculations using the equivalent ionic core virtual orbital model (EICVOM)[30–32] followed by configuration interaction (CI) have been carried out.

II. EXPERIMENT

The inner-shell electron-energy loss spectra have been obtained with a vibrating sample magnetometer (VSW) spectrometer which has been adapted for gas studies and high-energy electron beams and equipped recently with a home-made position sensitive multidetector system in order to improve data collection times. The apparatus and procedure have been described in detail previously.[33,34]

Briefly the spectrometer consists of an electrostatic 180° monochromator operating in the constant pass energy mode, a collision chamber and an electrostatic analyzer identical to the monochromator. The monochromatized incident electrons are accelerated up to 2 keV and focused into the collision chamber using a four-element electron lens. They are slightly deviated (0.02 radians) by two sets of X-Y plates inside the chamber. The scattered electrons are energy analyzed and focused onto the entrance slit of the analyzer by the same kind of lens as that used for acceleration. In the collision conditions of low angular momentum transfer (i.e., at high incident energy and small scattering angle), primarily electronic electric–dipolar transitions are excited.

Inside the vacuum vessel, a residual pressure of less than 1.10^{-8} Torr is maintained by a cryogenic pump and two turbomolecular pumps which are connected to the electron gun and the analyzer, respectively. The magnetic field within the vacuum vessel, the electron energy selectors, and the electron lenses have been minimized by mumetal layers.

The detection system is an assembly of two microchannel plates, a phosphor screen, fiber-optic couplers and an area array coupled charge device (CCD) sensor. A spectrum is composed from the accumulation of the data from each channel of the detector, which removes any detector-sensitivity variation.[33,35]

In order to take into account the valence and lower-energy inner-shell excitation cross section, a linear background is subtracted from the raw spectra by extrapolating a least-square fit of the pre-edge experimental data points. The electron energy loss scale is calibrated at the $C1s$ edge with the $C1s\sigma^{+}\rightarrow\pi^{*}$ ($v'=0$) band[29] in CO at 287.40 eV and at the $N1s$ edge with the $N1s\sigma\hat{g}^{+}\rightarrow\pi^{*}$ ($v'=0$ and $v'=1$) one in N_2 (i.e., 401.10 eV which is the average value of $v'=0$ and of $v'=1$, as the features due to these two transitions are only partly resolved within the 0.2 eV resolution[29]).

The samples are commercial ones from Acros Chimica with a purity better than 99% for pyridine and of 98% for pyridazine. They were used directly without further purification except repetitive freeze–pump–thaw cycles.

III. COMPUTATIONAL METHOD

The computational method is similar to that successfully used in our spectroscopic study of pyrrole and pyrazole.[36] The Gaussian atomic orbitals (AOs) used is the double zeta (DZ) basis set taken from Dunning,[37,38] i.e., $(10s5p1d)/[3s2p1d]$ for carbon and nitrogen and $(4s)/[2s]$ for hydrogen. One polarization d shell was added on the heavy atoms ($\alpha_C=0.75$ and $\alpha_N=0.80$, respectively). One s ($\alpha_s=0.021$) and one p ($\alpha_p=0.017$) diffuse shells were added at the center of mass of the molecules in order to take into account possible $n=3$ Rydberg states among the core-excited states.

The ground-state geometries of pyridine and of pyridazine were optimized at the self-consistent field (SCF) level with the HONDO95.3 program package.[39] The calculations of the core-excited states were performed in the frame of the equivalent core model,[30–32] which has proven for pyrrole and pyrazole[36] to give reliable information on core-excited states with an accuracy of a few tenths of an eV: The excitation of an $1s$ electron of an atom of atomic number Z is considered to be equivalent to its replacement by an atom $Z+1$ in the molecule. This model allows to calculate chemical shifts or term values (TVs) with respect to core-ionized states, which can be compared to experimental results.

The TVs were calculated using the method developed previously by Bodeur *et al.*:[40] The TV corresponding to the $1s\rightarrow i^{*}$ excitation (valence or Rydberg) of a given atom is

$$\mathrm{TV}=-\epsilon_{i^{*}}+\mathcal{P}+\mathcal{C}, \tag{1}$$

where $-\epsilon_{i^{*}}$ is the mono-electronic energy of the i^{*} virtual canonical orbital given in the SCF calculation of the ion (Koopmans' theorem).[41]

The repolarization term $\mathcal{P}$ was calculated by performing a configuration interaction (CI) in the mono-excited space $S(1s\rightarrow i^{*})$, including all mono-excitations from the occupied valence orbitals to the valence anti-bonding and Rydberg orbitals. The final space S was taken as the sum of $S(1s\rightarrow i^{*})$ over the i^{*} orbitals. The $\mathcal{P}$ term was calculated as the difference between the CI energy of the i^{*} state and the SCF energy of the ion.

The term $\mathcal{C}$ was then evaluated by taking the S space as the zeroth-order wave function for a multireference second-order Molter–Plesset (MP2) calculations,[42] using the diagrammatic version[43] of the configuration interaction by perturbation selected iteratively (CIPSI) method.[44] The correlation contribution $\mathcal{C}$ was then given for the i^{*} state by the difference between the CIPSI energy of the state and the MP2 energy of the ion.

Since in most cases the $1s\rightarrow i^{*}$ state had a large weight c_0 on the zeroth-order configuration, the transition intensities were estimated as the $c_0^2\langle 1s|\nabla|i^{*}\rangle^2$ matrix element, the $1s$

TABLE I. Calculated geometries of pyridine and pyridazine compared with previous works (bond lengths in Å and angles in degrees).

Pyridine	SCP[a] DZP	SCP[b] DZ	SCP[b] TZVP	Exp.[c] MW	Exp.[d] MW
$r(N–C_2)$	1.3235	1.3372	1.3182	1.3401	1.3376
$r(C_2–C_3)$	1.3902	1.3945	1.3833	1.3945	1.3938
$r(C_3–C_4)$	1.3882	1.3937	1.3814	1.3944	1.3916
$r(C_2–H)$	1.0762	1.0814	1.0747	1.0843	1.0865
$r(C_3–H)$	1.0744	1.0810	1.0728	1.0805	1.0826
$r(C_4–H)$	1.0753	1.0823	1.0742	1.0773	1.0818
C_2NC_2	117.69	118.72	117.76	116.83	116.94
NC_2C_3	123.66	122.66	123.58	123.90	123.80
$C_2C_3C_4$	118.22	118.58	118.23	118.53	118.53
$C_3C_4C_3$	118.56	118.81	118.62	118.33	118.40
NC_2H	116.21	116.40	116.16	115.90	116.01
C_2C_3H	120.36	120.16	120.30	120.16	120.12
C_3C_4H	120.72	120.59	120.69	120.83	120.80
Pyridazine	SCF[a] DZP	SCF[e] DZ	SCF[e] TZVP	Exp.[f] MW/ED/NMR	
$r(N–N)$	1.3117	1.3319	1.3052	1.3370(21)	
$r(N–C_3)$	1.3132	1.3322	1.3077	1.3379(15)	
$r(C_3–C_4)$	1.3995	1.4010	1.3919	1.4000(9)	
$r(C_4–C_4)$	1.3716	1.3818	1.3646	1.3846(19)	
$r(C_3–H)$	1.0750	1.0796	1.0729	1.0787(20)	
$r(C_4–H)$	1.0744	1.0801	1.0727	1.0707(20)	
NC_3C_4	123.34	122.70	123.28	123.76(7)	
C_3NN	120.03	120.03	120.04	119.38(5)	
NC_3H	115.46	115.49	115.41	114.91(17)	
C_3C_4H	120.82	120.50	120.75	120.67(13)	

[a]This work.
[b]Reference 3.
[c]Reference 45.
[d]References 46 and 47.
[e]Reference 13.
[f]Reference 48.

orbital taken as the corresponding core-equivalent atom. The results are only qualitative and allow to distinguish between strong, medium, and weak intensities. The intensity of doubly excited states (shake up) was not evaluated.

Except for the core excitation of N and C_4 atoms in pyridine, where the C_{2v} group was used, the calculations were done in the C_s symmetry group. The optimized SCF geometry of the ground state of each molecule was kept fixed in all cases. The typical dimension of S space was about 1500 in A'' symmetry and 3500 in A' symmetry.

The SCF optimized geometries of pyridine and pyridazine are given in Table I and are in very good agreement with previous experimental and theoretical studies.[3,13,45–48] The labeling of the nonequivalent atoms is shown in Fig. 1.

The calculated results are shown in Tables II–V. In some cases, it was not possible to calculate states above the ionization thresholds, especially the bands observed at TV≈ -3 eV in the spectra. This is due to the low symmetry of the core ionized species (and the subsequent large computational time), the large number of di-excited states which appear in these energy regions and a bad convergence during the diagonalization of the CI matrix with Davidson's method.[49]

IV. RESULTS AND DISCUSSION

A. Pyridine

The electronic configuration of pyridine in its neutral ground state has been calculated to be

$$1a_1^2 1b_2^2 2a_1^2 3a_1^2 2b_2^2 3b_2^2 4a_1^2 5a_1^2 4b_2^2 5b_2^2 6a_1^2 7a_1^2 6b_2^2 8a_1^2 \times 7b_2^2 9a_1^2 1b_1^2 8b_2^2 10a_1^2 2b_1 1a_2^2.$$

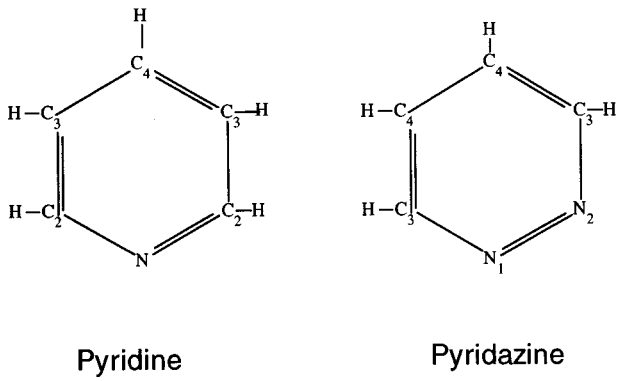

FIG. 1. The pyridine and pyridazine molecules and the labeling of the atoms used throughout the text.

TABLE II. Term values (TV, eV) and assignments of the spectral features at the $C1s$ edge of pyridine.

Calculated TV[a]						
$-\epsilon_{i*}$	$+\mathcal{P}$ [c]	$+\mathcal{C}$ [d]	I[b]		Main configurations	Exp. TV[e]
3.90	5.06	5.45	1.00	0.94	$1sC_4\rightarrow 1\pi^*(3b_1)$	5.10
3.85	5.05	5.42	0.78	0.94	$1sC_3\rightarrow 1\pi^*$	
3.34	4.56	4.94	0.97	0.94	$1sC_2\rightarrow 1\pi^*$	4.68
2.69	3.88	4.47	0.02	0.93	$1sC_2\rightarrow 2\pi^*$	(4.20)
1.93	2.65	4.00	0.00	0.96	$1sC_4\rightarrow 2\pi^*(2a_2)$[f]	
1.80	3.02	3.78	0.02	0.94	$1sC_3\rightarrow 2\pi^*$	(3.70)
2.59	2.94	3.18	0.08	0.97	$1sC_3\rightarrow 3s\sigma/\sigma^*C_3$–H	2.68
2.12	2.46	3.03	0.08	0.96	$1sC_4\rightarrow 3s\sigma/\sigma^*C_4$–H($a_1$)	2.68
1.53	1.87	2.38	0.06	0.96	$1sC_2\rightarrow 3s\sigma/\sigma^*C_2$–H	2.68
1.94	2.12	2.26	0.02	0.98	$1sC_3\rightarrow 3p\sigma$	
1.81	1.85	1.96	<0.01	0.99	$1sC_3\rightarrow 3p\pi$	
1.40	1.46	1.94	<0.01	0.99	$1sC_4\rightarrow 3p\sigma(b_2)$	
1.65	1.81	1.91	<0.01	0.98	$1sC_3\rightarrow 3p\sigma$	
1.10	1.31	1.71	<0.01	0.99	$1sC_2\rightarrow 3p\sigma$	
1.08	1.23	1.70	0.03	0.99	$1sC_4\rightarrow 3p\sigma(a_1)$	
1.26	1.29	1.69	<0.01	0.99	$1sC_4\rightarrow 3p\pi$	
0.83	1.01	1.41	0.01	0.98	$1sC_2\rightarrow 3p\sigma$	
0.90	0.94	1.34	<0.01	0.99	$1sC_2\rightarrow 3p\pi$	
−2.52	−0.04	1.24	0.17	0.59	$1sC_3\rightarrow 3\pi^*$	0.86
				+0.15	$1sC_3 3\pi\rightarrow 1\pi^*1\pi^*$	
				+0.10	$1sC_3 3\pi\rightarrow 1\pi^*2\pi^*$	
−3.09	−0.48	0.95	0.12	0.57	$1sC_4\rightarrow 3\pi^*(4b_1)$	0.86
				+0.28	$1sC_4 3\pi\rightarrow 1\pi^*2\pi^*$	
				+0.11	$1sC_4 3\pi\rightarrow 1\pi^*1\pi^*$	
−3.47	−0.72	0.62	0.12	0.55	$1sC_2\rightarrow 3\pi^*$	0.86
				+0.23	$1sC_2 2\pi\rightarrow 1\pi^*1\pi^*$	
				+0.17	$1sC_2 3\pi\rightarrow 1\pi^*2\pi^*$	
−0.95	−0.09	0.49	0.35	0.92	$1sC_3\rightarrow\sigma^*C_3$–H	0.86
−1.28	−0.44	0.38	0.30	0.92	$1sC_4\rightarrow\sigma^*C_4$–H	0.86
	−1.67	0.16		0.53	$1sC_3 3\pi\rightarrow 1\pi^*1\pi^*$	
				+0.14	$1sC_3 3\pi\rightarrow 1\pi^*2\pi^*$	
				+0.12	$1sC_3 2\pi\rightarrow 2\pi^*2\pi^*$	
0.00	0.00	0.00			C_3 ion	0.00
	−1.90	−0.08		0.40	$1sC_2 2\pi\rightarrow 1\pi^*1\pi^*$	
				0.23	$1sC_2 3\pi\rightarrow 1\pi^*1\pi^*$	
				0.21	$1sC_2 3\pi\rightarrow 1\pi^*2\pi^*$	
	−1.41	−0.12		0.58	$1sC_4 2\pi\rightarrow 1\pi^*1\pi^*$	
				+0.31	$1sC_4 3\pi\rightarrow 1\pi^*2\pi^*$	
	−2.06	−0.15		0.44	$1sC_2 3\pi\rightarrow 1\pi^*1\pi^*$	
				+0.16	$1sC_2 2\pi\rightarrow 1\pi^*2\pi^*$	
				+0.15	$1sC_2 3\pi\rightarrow 1\pi^*2\pi^*$	
−1.96	−1.04	−0.21	0.13	0.91	$1sC_2\rightarrow\sigma^*C_2$–H	
−0.53	−0.53	−0.25			C_4 ion	−0.40
−0.90	−0.90	−0.60			C_2 ion	−0.80
−2.30	−1.32	−0.69	0.31	0.93	$1sC_3\rightarrow\sigma^*C_3$–$C_2/\sigma^*C_3$–$C_4$	−0.64
−2.52	−1.78	−1.16	0.03	0.93	$1sC_3\rightarrow\sigma^*N$–$C_2/\sigma^*C_3$–$C_2$	
−2.58	−2.03	−1.32	0.17	0.95	$1sC_4\rightarrow\sigma^*C_3$–$C_4(a_1)$	(−1.3)
−3.18	−2.73	−1.53	0.01	0.94	$1sC_4\rightarrow\sigma^*C_3$–$C_2(b_2)$	(−1.5)
−5.31	−4.86	−2.95	0.02	0.96	$1sC_4\rightarrow\sigma^*C$–H($b_2$)	
−4.74	−4.41	−3.05	0.52	0.97	$1sC_4\rightarrow\sigma^*C_3$–$C_4(b_2)$	−4.10

[a]See text for definition.
[b]Relative intensity.
[c]$-\epsilon_{i*}+\mathcal{P}$ with respect to the SCF energy of the ion.
[d]$-\epsilon_{i*}+\mathcal{P}+\mathcal{C}$ with respect to the MP2 energy of the ion.
[e]For the experimental term values: $C_3 1s$ ionization energy: 290.2 eV deduced from solid state data (Refs. 10 and 50).
[f]Dipole forbidden transition.

The $1a_1$, $1b_2$, $2a_1$, $3a_1$, $2b_2$, and $3b_2$ MOs are the $1s$ orbitals of the nitrogen atom and the four carbon atoms. The $1b_1$, $2b_1$, and $1a_2$ (HOMO) MOs correspond to the 1π, 2π, and 3π orbitals. The lowest unoccupied MOs are the $3b_1$ ($1\pi^*$, $\epsilon_i=2.95$ eV) and the $2a_2$ (LUMO $2\pi^*$, $\epsilon_i=3.30$ eV). In fact, the degenerate $1\pi^*(e_{2u})$ MO of benzene is splitted into the $3b_1$ and $2a_2$ ones. The $3\pi^*(4b_1)$ MO has an ϵ_i of 8.63 eV. According to the selection rules for the

TABLE III. Term values (TV, eV) and assignments of the spectral features at the $N1s$ edge of pyridine.[a]

Calculated TV						
$-\epsilon_{i*}$	$+\mathcal{P}$	$+\mathcal{C}$	I	Main configurations		Exp. TV[b]
4.41	5.52	5.79	1.00	0.94	$1s\rightarrow 1\pi^*(3b_1)$	6.13
2.46	3.16	4.30	0.00	0.96	$1s\rightarrow 2\pi^*(2a_2)$[c]	
2.28	2.49	2.76	<0.01	0.98	$1s\rightarrow 3s\sigma(a_1)$	
1.91	1.97	2.16	<0.01	0.99	$1s\rightarrow 3p\sigma(b_2)$	
1.85	1.99	2.08	0.02	0.99	$1s\rightarrow 3p\sigma(a_1)$	
1.81	1.84	1.95	<0.01	0.99	$1s\rightarrow 3p\pi(b_1)$	
−2.22	0.27	1.51	0.16	0.53	$1s\rightarrow 3\pi^*(4b_1)$	2.21
				+0.21	$1s2\pi\rightarrow 1\pi^*1\pi^*$	
				+0.23	$1s3\pi\rightarrow 1\pi^*2\pi^*$	
	−1.92	0.05		0.37	$1s3\pi\rightarrow 1\pi^*2\pi^*$	
				+0.53	$1s2\pi\rightarrow 1\pi^*1\pi^*$	
0.00	0.00	0.00			N ion	0.00
−2.22	−3.92	0.00	0.02	0.29	$1s\rightarrow 3\pi^*(4b_1)$	−0.02
				+0.41	$1s3\pi\rightarrow 1\pi^*2\pi^*$	
−1.86	−1.15	−0.05	0.14	0.95	$1s\rightarrow\sigma^*C_2$–N(a_1)	−0.02
−3.03	−2.19	−1.36	0.09	0.96	$1s\rightarrow\sigma^*C_2$–$C_3(b_2)$	−0.02
	−4.33	−1.47		0.70	$1s3\pi\rightarrow 1\pi^*2\pi^*$	
				+0.12	$1s2\pi\rightarrow 1\pi^*1\pi^*$	
−3.03	−2.30	−1.51	0.02	0.93	$1s\rightarrow\sigma^*$C–H(a_1)	
−4.56	−4.13	−2.74	0.58	0.95	$1s\rightarrow\sigma^*C_2$–N(b_2)	−3.42
−4.94	−4.48	−3.31	0.03	0.94	$1s\rightarrow\sigma^*$C–H(b_2)	

[a]See Table II for notations.
[b]For the experimental term values: $N1s$ ionization energy: 404.88 eV for the gas (Ref. 52).
[c]Dipole forbidden transition.

core-excited species, all electronic transitions are optically allowed except $1sC_4\rightarrow 2\pi^*(2a_2)$ and $1sN\rightarrow 2\pi^*(2a_2)$.

For the three carbon atoms with different chemical environment (Fig. 1), the corresponding binding energies for the isolated molecule are not known. However, in the solid state,[50] they are separated by 0.4 eV, with the following order: C_3–C_4–C_2. The calculations predict chemical shifts of 0.53/0.37 eV at SCF level and 0.25/0.35 eV at MP2 level, respectively (Table II). The same trend is expected for the transitions in the neutral core-excited species.

TABLE IV. Term values (TV, eV) and assignments of the spectral features at the $C1s$ edge of pyridazine.[a]

Calculated TV						
$-\epsilon_{i*}$	$+\mathcal{P}$	$+\mathcal{C}$	I	Main configurations		Exp. TV[b]
4.98	6.22	6.42	1.00	0.94	$1sC_4\rightarrow 1\pi^*$	5.87
4.23	5.59	5.83	0.99	0.93	$1sC_3\rightarrow 1\pi^*$	5.33
3.27	4.61	5.07	0.01	0.91	$1sC_3\rightarrow 2\pi^*$	
3.12	4.34	4.94	0.04	0.91	$1sC_4\rightarrow 2\pi^*$	
2.92	3.34	3.55	0.09	0.96	$1sC_4\rightarrow 3s\sigma/\sigma^*C_4$–H	(4.90)
2.30	2.68	2.97	0.08	0.96	$1sC_3\rightarrow 3s\sigma/\sigma^*C_3$–H	(4.30)
1.99	2.19	2.29	0.01	0.98	$1sC_4\rightarrow 3p\sigma$	
−2.06	0.90	2.15	0.13	0.51	$1sC_4\rightarrow 3\pi^*$	2.92
				+0.24	$1sC_43\pi\rightarrow 1\pi^*1\pi^*$	
1.70	1.93	2.15	0.06	0.97	$1sC_3\rightarrow 3p\sigma/\sigma^*C_3$–H	
1.88	1.92	2.04	<0.01	0.99	$1sC_4\rightarrow 3p\pi$	
1.46	1.66	1.78	0.03	0.98	$1sC_4\rightarrow 3p\sigma$	
1.52	1.56	1.77	0.02	0.99	$1sC_3\rightarrow 3p\pi$	
−2.44	0.32	1.53	0.17	0.62	$1sC_3\rightarrow 3\pi^*$	1.63
				+0.19	$1sC_33\pi\rightarrow 1\pi^*2\pi^*$	
				+0.10	$1sC_33\pi\rightarrow 1\pi^*1\pi^*$	
1.18	1.35	1.53	<0.01	0.98	$1sC_3\rightarrow 3p\sigma$	
−0.48	0.39	0.85	0.34	0.91	$1sC_4\rightarrow\sigma^*C_4$–H	−0.16
−1.12	−0.19	0.39	0.28	0.91	$1sC_3\rightarrow\sigma^*C_3$–H	−0.16
0.00	0.00	0.00			C_4 ion	0.00
−1.69	−0.69	−0.10	0.19	0.93	$1sC_4\rightarrow\sigma^*C_3$–$C_4$	−0.16
−0.38	−0.38	−0.29			C_3 ion	−0.60[b]

[a]See Table II for notations.
[b]For the experimental term values: C_41s ionization energy: 290.8 eV deduced from solid-state data (Ref. 50) and taking into account a difference of 4.7 eV between the gas and the solid as for pyridine.

TABLE V. Term values (TV, eV) and assignments of the spectral features at the $N1s$ edge of pyridine.[a]

Calculated TV						
$-\epsilon_{i*}$	$+\mathcal{P}$	$+\mathcal{C}$	I	Main configurations		Exp. TV[b]
5.32	6.60	6.56	1.00	0.93	$1s\rightarrow 1\pi^*$	6.90
3.12	4.50	4.97	0.03	0.89	$1s\rightarrow 2\pi^*$	(6.0)
2.52	2.80	2.95	<0.01	0.98	$1s\rightarrow 3s\sigma$	
2.01	2.20	2.26	0.01	0.98	$1s\rightarrow 3p\sigma$	
−1.78	1.13	2.15	0.11	0.48	$1s\rightarrow 3\pi^*$	2.87
				+0.29	$1s2\pi\rightarrow 1\pi^*1\pi^*$	
				+0.15	$1s3\pi\rightarrow 1\pi^*2\pi^*$	
1.90	1.95	2.04	<0.01	0.99	$1s\rightarrow 3p\pi$	(2.08)
1.65	1.80	1.93	<0.01	0.98	$1s\rightarrow 3p\sigma$	(2.08)
	0.47	1.85		0.76	$1s3\pi\rightarrow 1\pi^*1\pi^*$	(2.08)
−1.59	−0.50	0.37	0.22	0.91	$1s\rightarrow\sigma^*$N–N	0.52
0.00	0.00	0.00			N ion	0.00

[a]See Table II for notations.
[b]For the experimental term values: $N1s$ ionization energy: 405.98 eV deduced from solid-state data (Ref. 50) and taking into account a difference of 4.7 eV between the gas and the solid as for pyridine.

1. Carbon K-shell electron-energy loss spectrum

The electron-energy loss spectrum presented in Fig. 2 is dominated by an intense band A centered at 285.46 eV. At higher energies there are weaker, rather sharp features B to D and broad bands E and F centered at 294.3 and 302.5 eV, respectively. The overall shape is similar to the lower-resolution electron-energy loss spectrum,[10] the features being better resolved, especially those located in the 287–292 eV energy region. The lowest energy band is partly resolved into two intense features A' and A'' at 285.10 (TV=5.10 eV) and 285.52 eV (TV=4.68 eV) are shown in the insert of Fig. 2. The 0.42 eV energy splitting is close to the 0.5 eV reported energy separation value.[11] The energies of the features labeled A' to F have been listed in Table VI and compared with previous works.

The lowest energy intense band A is rather broad with a full width at half maximum (FWHM) of 1.13 eV, much larger than the experimental resolution (0.2 eV), being asymmetric and stretching 1.5 eV above the maximum on the high-energy side. This suggests that the band is composite and contains several subbands in addition to the two partly resolved features A' and A'' separated by 0.42 eV. According to the calculations (Table II), the A' band is to be attributed to the $1sC_4\rightarrow 1\pi^*(3b_1)$ and $1sC_3\rightarrow 1\pi^*$ transitions which are nearly degenerate in energy (TV=5.45, and 5.42 eV, respectively). These calculated TVs are slightly above the experimental one (5.10 eV). The A'' band at 285.52 eV (TV=4.68 eV) is due to the $1sC_2\rightarrow 1\pi^*$ transition calculated at TV=4.94 eV. The subbands A' and A'' are separated by 0.42 eV at both experimental and theoretical levels. The 0.42 eV chemical shift between C_4 and C_2 is very close to the 0.4 eV energy splitting between the binding energies estimated from the solid state $C1s$ data.[50] The chemical shift between C_4 and C_4 is quasi null and is different from the splitting between the binding energies (0.4 eV in favor of C_3) of solid pyridine.[50]

The calculations predict the $1sC_2\rightarrow 2\pi^*$, $1sC_4\rightarrow 2\pi^*(2a_2)$ and $1sC_3\rightarrow 2\pi^*$ transitions to appear at slightly larger energy (Table II). Although these transitions should have very small intensity (the second one being di-

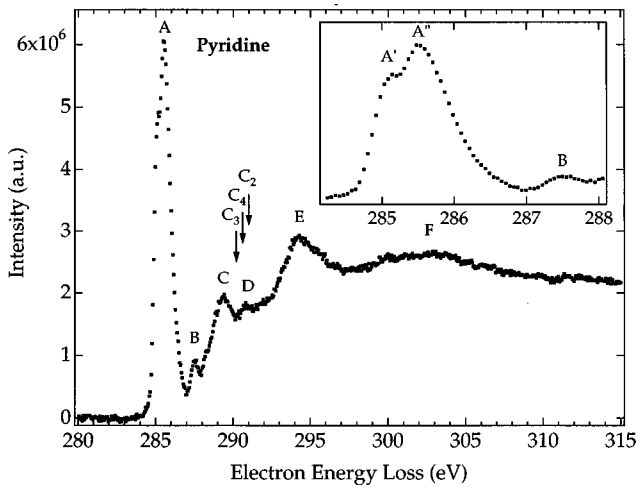

FIG. 2. The electron energy-loss spectrum of pyridine recorded at the carbon K edge with an energy resolution of 0.2 eV. The arrows indicate the locations of the ionization energies (I.E.s) estimated from the XPS measurements in the solid phase. The insert is an expansion of the spectrum in the region of the first features.

TABLE VI. Energy values (E, eV) of the spectral features in the $C1s$ excitation spectrum of pyridine and pyridazine.

	Pyridine				Pyridazine	
Label	This work	Ref. 10 gas	Ref. 10 solid	Ref. 11 gas	Label	This work
A'	285.10	285.3	285.5	285.0	A'	284.93
A''	285.52			285.5	A''	285.47
	(286)					(285.9)
	(286.5)					(286.5)
B	287.52	287.4		287.4	B	287.88
				288.8		
C	289.34	289.2	289.1	289.4	C	289.17
D	290.84	290.8		290.6	D	290.96
	(291.5)					
	(292.0)					
E	294.3	294.2	294.1	294.4	E	294.3
F	302.5	300.1	301.0	302	F	301

pole forbidden), they could contribute to the high-energy tail of the *A* band.

The peak *B* located at 287.52 eV (TV=2.68 eV) is much better resolved in our electron-energy loss spectrum than in the earlier study.[10] The previous assignment[10] was based on the comparison between gaseous pyridine carbon *K*-shell spectrum and the solid one, in which this feature is absent. It was suggested to be due to a Rydberg $3p$ excitation. This feature has also been assigned to a $3s$ state one.[11] This is partly confirmed by our calculations which predict the transition from the three carbon atoms to the $3s\sigma/\sigma^*_{C-H}$ valence-Rydberg mixed MOs at similar energies (Table II). This assignment is consistent with that of the 287.2 eV band observed in benzene, using MC calculations.[27]

The band *C* located at 289.34 eV (TV=0.86 eV) is separated from band *A* by 3.88 eV if we take a mean value of 285.46 eV for this latter. This 3.88 eV value is comparable to the energy separation of the electronic bands due to the $1e_{2u}(1\pi^*)$ and $1b_{2g}(2\pi^*)$ transitions in the core-excited benzene (3.7 eV). This originally led to assign this band to the $1sC\rightarrow 3\pi^*$ transition.[10] However, the calculations give a rather different picture, very similar to that suggested in benzene by MC calculations.[27] As shown in Table II, for the three carbon atoms, the calculated electronic configuration contains only ≈60% on the $1sC\rightarrow 3\pi^*$ transition, the remaining weight involving diexcitations to the $1\pi^*$ and $2\pi^*$ MOs. The calculated TVs for the three atoms are grouped around 1.0 eV and are consistent with the position of the *C* band at TV=0.86 eV.

The very low-intensity feature *D* (TV=−0.64 eV) is better resolved in our spectrum than previously[10] where it has been assigned as continuum onset. It corresponds to the band observed at the same energy of 290.8 eV and at 290.3 eV in the carbon *K*-shell spectrum of *s*-triazine[51] and of benzene,[10] respectively, where it has been assigned to the excitation to a σ^*_{C-H}-type MO in both cases. This is consistent with our calculations on pyridine which place the $1sC_2\rightarrow\sigma^*_{C-H}$ transition at TV=−0.21 eV (Table II). A large number of shake up states involving the $1\pi^*$ and $2\pi^*$ MOs are also present in the same region (Table II).

The *E* band located at 294.3 eV (TV=−1.4 eV) corresponds to the 293.5 eV one in benzene.[10] Unfortunately, because of the low symmetry and a large number of doubly excited states of the type $1s\pi\rightarrow\pi^*$ Ryd., it was not possible to calculate any state in this energy range, except a strong $1sC_4\rightarrow\sigma^*_{C_3-C_4}$ transition at TV=−3.05 eV (Table II), which contributes without ambiguity to the observed feature. The corresponding transitions for C_2 and C_3 should also occur at similar TVs. It should be noted that the monolayer polarization dependence of this band,[10] seems to indicate a σ^* nature. However, by analogy with *ab initio* calculations performed for benzene,[27] it is also possible that excitations containing a $1s\rightarrow 3\pi^*$ character occur in this energy range. Shake up states could also explain the weak fine features appearing at 291.5 eV (TV=−1.3 eV) and 292 eV (TV=−1.8 eV).

The 302.4 eV band (TV=−12.2 eV) is not easy to interpret because there are a large number of σ^* C–C and C–N type orbitals. In the *s*-triazine carbon $1s$ excitation spectrum, it has been assigned to a σ^*_{C-N} type shape resonance.[51] In the 297 to 315 eV region multiple scattering might contribute also at least partly to the spectrum.

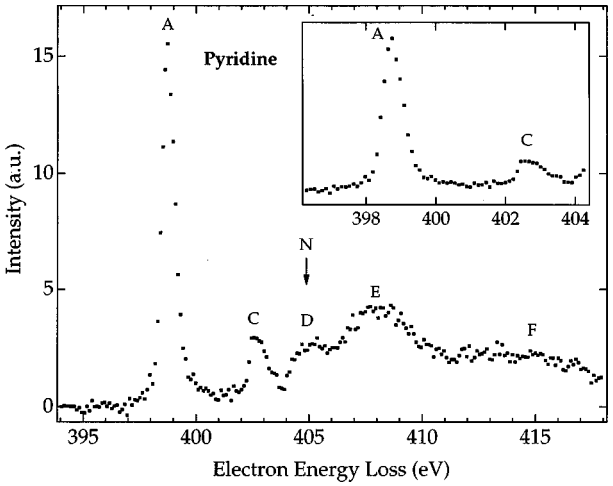

FIG. 3. The electron energy-loss spectrum of pyridine recorded at the nitrogen *K* edge with an energy resolution of 0.2 eV. The arrow indicates the location of the I.E. as determinated by XPS measurements. The insert is an expansion of the spectrum in the region of the first features.

2. Nitrogen K-shell electron-energy loss spectrum

The nitrogen *K*-shell electron-energy loss spectrum of pyridine displayed in Fig. 3 has an overall shape quite similar to the 1 eV resolution electron-energy loss spectrum reported previously.[10] It is dominated by an intense sharp band *A* at 398.76 eV (TV=6.13 eV). At higher energy there is a rather sharp peak *C*, a band *D* not well resolved, and two broad bands *E* and *F* centered at 408.3 and 415 eV, respectively as shown in Fig. 3. The energy positions and those reported previously are listed in Table VII. Our higher resolution results confirm those obtained previously by the ISEELS method both for the overall shape of the $N1s$ excitation spectrum and for the energies of its different features,[10] that the spectrum at the $N1s$ edge[11] is questionable, and that the values reported in Ref. 11 are too low by about 1 eV (because of a calibration error, as suggested in Ref. 51).

The two lowest energy sharp peaks *A* and *C* are separated by 3.92 eV and have relative intensities roughly the same as at the carbon *K* edge. This suggests that they are due

TABLE VII. Energy values (E, eV) of the spectral features in the $N1s$ excitation spectrum of pyridine and pyridazine.

	Pyridine					Pyridazine	
Label	This work gas	Ref. 10 gas	Ref. 10 solid	Ref. 12 solid	Ref. 11 gas	Label	This work
A	398.75	398.8	398.8	399.9	398.6 400.6	*A*	399.08 (400.0)
C	402.67	402.7	403.3	403.8	402.4	*C*	403.11 (403.9)
D	404.91	405.1			404.4	*D*	405.46
E	408.3	408.0	408.0	409.3	407.7	*E*	408.5
F	415	414.3	414.3	417.5	416	*F*	417

to the same transitions. This 3.92 eV energy splitting is a little bit larger than the 3.82 eV corresponding one in the carbon *K* edge spectrum. The nitrogen $1s$ excitation spectrum of *s*-triazine[51] exhibits also two low-energy peaks with roughly the same intensity distribution as in the $N1s$ electron energy loss spectrum of pyridine and separated by 4.1 eV. In the case of *s*-triazine, they have been assigned to the $1sN \rightarrow 1\pi^*(e'')$ and $1sN \rightarrow 2\pi^*(a''2)$ transition, respectively. The band *A* is to be assigned to the $1sN \rightarrow 1\pi^*(3b_1)$ transition. This is confirmed by our calculations (Table III) which give a TV of 5.79 eV.

As shown in Fig. 3, there is a weak and not resolved shoulder around 400 eV (TV=4.9 eV) on the high-energy side of the 398.75 eV band. At TV=4.30 eV, the calculations (Table III) suggest the excitation of the $2\pi^*(2a_2)$ MO, very weak as the transition is symmetry forbidden from the $N1s$ orbital.

According to the calculations, the *C* band (TV=2.21 eV) is explained by the $1sN \rightarrow 3\pi^*(4b_1)$ transition (Table III) with a weight of 53% and mixed with double excitations ($1sN2\pi \rightarrow 1\pi^*1\pi^*$ and $1sN3\pi \rightarrow 1\pi^*2\pi^*$). The same type of excitation prevails also in the $C1s$ spectra of benzene[27] and pyridine as described above. It is probable that the same configuration mixing occurs in *s*-triazine for the peak observed at TV=2.0 eV.[51]

Between 404 and 406 eV (Fig. 3), i.e., around the $N1s$ ionization threshold, there are very likely several fine features of low intensity and not resolved from each other in the *D* band. The calculations predict several states in this region, one of them involving the excitation to the $3\pi^*(4b_1)$ MO with a weight of 29%, and two transitions to the $\sigma^*_{C_2-N}$ and $\sigma^*_{C_2-C_3}$ (Table III). At higher energy, we obtained a large number of di-excited states, most of them involving one Rydberg orbital and which are not displayed in Table III.

The broad features *E* and *F* located at 408.3 eV (TV=−3.42 eV) and 415 eV (TV=−10.12 eV), respectively, are to be attributed to σ^* type shape resonances. In *s*-triazine,[51] two broad bands centered at 409.2 and 415.3 eV have been assigned to σ^*_{C-N} shape resonances. This is confirmed to be the case also for pyridine for the first one by our calculations: The $1sN \rightarrow \sigma^*_{C_2-N}(b_2)$ is predicted to lie at TV=−2.74 eV with a large intensity (Table III).

B. Pyridazine

The electronic configuration of pyridazine in its neutral ground state has been calculated to be

$$1a_1^2 1b_2^2 2b_2^2 2a_1^2 3a_1^2 3b_2^2 4a_1^2 4b_2^2 5a_1^2 5b_2^2 6a_1^2 7a_1^2 8a_1^2 6b_2^2 \times 7b_2^2 9a_1^2 1b_1^2 10a_1^2 8b_2^2 2b_1 1a_2^2.$$

The $1a_1$, $1b_2$, $2b_2$, $2a_1$, $3a_1$, and $3b_2$ MOs are the $1s$ orbitals of the nitrogen atoms and the four carbon atoms. The $1b_1$, $2b_1$, and $1a_2$ (HOMO) MOs correspond to the 1π, 2π, and 3π orbitals. The lowest unoccupied MOs are the $2a_2$ (LUMO $1\pi^*$, ϵ_i=2.33 eV) and the $3b_1$ ($2\pi^*$, ϵ_i=2.95 eV) followed by the remaining anti-bonding MOs. As in pyridine, the degenerate $1\pi^*(e_{2u})$ MO of benzene is splitted into the $3b_1$ and the $2a_2$ ones. For the $3\pi^*(2a_2)$ MO, ϵ_i =8.46 eV. There are no optically forbidden transitions in the core-excited species.

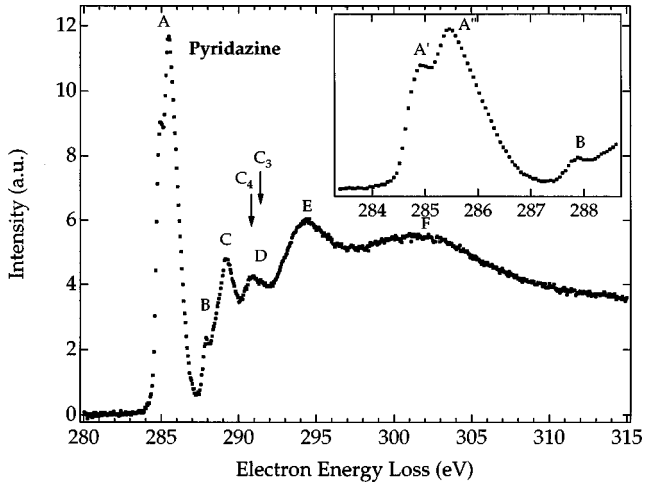

FIG. 4. The electron energy-loss spectrum of pyridazine recorded at the carbon *K* edge with an energy resolution of 0.2 eV. The arrows indicate the locations of the estimated I.E.s deduced from solid state. The insert is an expansion of the spectrum in the region of the first features.

Pyridazine presents two carbon atoms with different chemical environments (Fig. 1). The corresponding binding energies for the isolated molecule have not been measured, as far as we know. However, in the condensed phase[51] they are separated by 0.6 eV from each other, that for C_4 being the lowest one. The calculations predict 0.38 and 0.29 eV at SCF and MP2 levels, respectively for the isolated species (Table IV). The same trend is expected to prevail also in the carbon core-excited molecule.

1. Carbon K-shell electron-energy loss spectrum

The carbon *K*-shell electron-energy loss spectrum of pyridazine is displayed in Fig. 4. It closely resembles to that of pyridine and consists of an intense, sharp peak *A* centered at 285.3 eV, of a second sharp, but less intense band *C* and of the weak features *B* and *D*, noncompletely resolved. At higher energy, there are two broad bands *E* and *F* centered at 294.30 and 301 eV, respectively. The energies of the different features are given in Table VI.

The lowest energy band *A* is broad (FWHM=1.53 eV) and asymmetric on the high-energy side. It is composed of two features partly resolved A' at 284.93 eV (TV=5.87 eV) and A'' at 285.47 eV (TV=5.33 eV, see insert Fig. 4) and seems to contain other contributions responsible of the strong asymmetry above 285.5 eV. The A' and A'' features are separated by 0.54 eV. Their energy difference is a little bit larger than that of the corresponding features observed in the lowest band of pyridine at the carbon *K* edge. In addition their relative intensity distribution is rather similar to that in pyridine. According to the calculations (Table IV), the A' and A'' subbands are assigned to the $1sC_4 \rightarrow 1\pi^*$ and $1sC_3 \rightarrow 1\pi^*$ transitions. The calculated TVs are overestimated by about 0.5 eV, but the experimental chemical shift

of 0.54 eV is correctly reproduced (0.59 eV) by the calculations (Table IV).

The strong asymmetry of the peak *A* on its high-energy side may be due to fine features not resolved around 285.9 eV (TV=4.90 eV) and 286.5 eV (TV=4.30 eV), separated by about 0.6 eV. According to the calculations, the $1sC_3 \rightarrow 2\pi^*$ and $1sC_4 \rightarrow 2\pi^*$ transitions are located at TV=5.07 eV and TV=4.94 eV, respectively (Table IV) and have very low intensities. The $1sC_4 \rightarrow 3s\sigma/\sigma^*_{C_4-H}$ and $1sC_3 \rightarrow 3s\sigma/\sigma^*_{C_3-H}$ transitions are calculated at TV=3.55 eV and TV=2.97 eV, respectively, with larger intensities (Table IV). The transitions to the $2\pi^*$ MO are very likely too weak to be seen in the spectrum. Then, the two features at 285.9 and 286.5 eV may be attributed to the transition to the $3s\sigma/\sigma^*$ MOs from the two carbon atoms, respectively.

The fine feature *B* at 287.88 eV (TV=2.92 eV), not completely resolved from the *C* band, may be attributed to a Rydberg state excitation due to its sharpness and intensity. This is consistent with the calculations which place the $1sC_3 \rightarrow 3p\sigma/\sigma^*_{C_3-H}$ at TV=2.15 eV (Table IV). At the same TV the calculations show the $1sC_4 \rightarrow 3\pi^*$ transition (Table IV) with a weight of 51%, mixed with the $1sC_4 3\pi \rightarrow 1\pi^* 1\pi^*$ double excitation (24%).

The energy difference between the intense band *A* and the second sharp peak *C* (289.17 eV, TV=1.63 eV) of the spectrum (Fig. 3) is about 3.8 eV. This value is very close to the corresponding energy difference in benzene (3.7 eV) and in pyridine (3.8 eV). This suggests that the peak *C* is to be attributed to the transition to $3\pi^*$ mixed with double excitations. Indeed, as shown in Table IV, the $1sC_3 \rightarrow 3\pi^*$ transition, with a weight of 62%, is predicted to occur at TV=1.53 eV.

The low intensity band *D* centered at 290.96 eV (TV=−0.16 eV) might be due to Rydberg state and/or σ^* type MOs excitations. In the benzene $C1s$ excitation spectrum,[10] there is a fine feature at 290.3 eV which has been attributed[22] to the transition to a σ^*_{CH} type MO. For pyridazine, according to the calculations (Table IV), there are several states lying around TV=0.0 eV with rather large intensities and involving the $1sC_4 \rightarrow \sigma^*_{C_4-H}$ (TV=0.85 eV), the $1sC_3 \rightarrow \sigma^*_{C_3-H}$ (TV=0.39 eV) and the $1sC_4 \rightarrow \sigma^*_{C_3-C_4}$ (TV=−0.10 eV) transitions.

At higher energy, the two broad bands *E* and *F* located at 294.3 (TV=−3.5 eV) and 301 eV (TV=−10.2 eV), respectively, are out of the range of the calculations. The comparison with the $C1s$ excitation spectrum of benzene[10] and of pyridine leads to suggest that they are due to the σ^*_{C-C} and/or σ^*_{C-H} and σ^*_{C-N} shape resonances.

2. Nitrogen K-shell electron-energy loss spectrum

The nitrogen *K*-shell electron-energy loss spectrum of pyridazine is displayed in Fig. 5. Its overall shape is similar to that of pyridine (Fig. 3). The spectrum is dominated by an intense sharp peak *A* located at 399.08 eV (TV=6.90 eV). There is a rather sharp, less intense band *C* located at 403.11 eV (TV=2.87 eV), exhibiting a shoulder on its high-energy side. Not well resolved features are observed in the 404.5–407 eV region. At higher energy, the spectrum presents at least two broad bands *E* and *F* centered at 408.5 (TV=−2.52 eV) and 417 eV (TV=−11.02 eV), respectively. The energies values are listed in Table VII and the proposed assignments of the features are given in Table V. It was not possible to calculate any state above the ionization threshold.

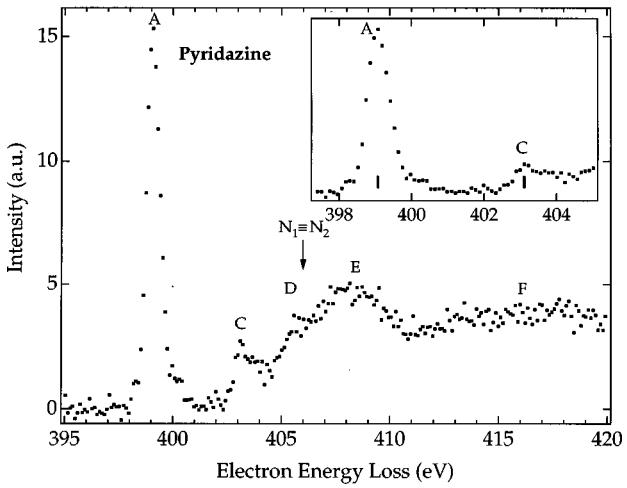

FIG. 5. The electron energy-loss spectrum of pyridazine recorded at the nitrogen *K* edge with an energy resolution of 0.2 eV. The arrow indicates the location of the estimated I.E. deduced from solid state. The insert is an expansion of the spectrum in the region of the first features.

The *A* and *C* bands are separated by 4.03 eV (Table VII). This value is close to the corresponding energy difference in the $N1s$ electron energy loss spectrum of pyridine (3.92 eV) and in the $N1s$ excitation spectrum of *s*-triazine (4.1 eV).[51] This suggests a common assignment for the three molecules. This is confirmed by the calculations: The *A* band is due to the $1sN \rightarrow 1\pi^*$ transition with a calculated TV of 6.56 eV (Table V). The *C* band is then assigned to the $3\pi^*$ transition (also mixed in this case with double excitations), as shown by the calculations. For pyridine, there is no σ^*_{C-H} transition predicted in this energy region.

On the high-energy side of the band *A*, there is a weak band not completely resolved from *A* and located at 400 eV (TV=6.0 eV), separated by 0.9 eV from the 399.08 eV peak. The calculations (Table V) predict the transition to the $2\pi^*$ MO at TV=4.97 eV with a very small intensity. This is consistent with the 400 eV feature whose intensity is weak.

The shoulder of the peak *C* at 403.9 eV (TV=2.08) is probably due to the $3p\pi$ and $3p\sigma$ transitions as shown in Table V, with a possible contribution of the $1s3\pi \rightarrow 1\pi^* 1\pi^*$ di-excitation calculated at TV=1.85 eV. The *D* band located at 405.46 eV (TV=0.52 eV) is due to the transition to the σ^*_{N-N} MO calculated at TV=0.37 eV (Table V).

At higher energy, the broad bands *E* and *F* (Table VII, Fig. 5) correspond very likely to σ^* shape resonances. In pyridine and *s*-triazine[51] $N1s$ excitation spectrua, broad bands are also observed at roughly the same energies and have been assigned to σ^*_{C-N} type shape resonances. For the lowest energy one, this is confirmed by the calculations as described above in pyridine.

V. CONCLUSIONS

In this work, the inner shell electron-energy loss spectra of pyridine and pyridazine have been reported at the $C1s$ and $N1s$ edges with 0.2 eV resolution, allowing to resolve the transitions to the C atoms with different chemical environment. The spectra of pyridazine are reported for the first time. *Ab initio* configuration interaction calculations using the equivalent core model were performed to assign the experimental features.

The shape of the $C1s$ excitation spectra is similar for both molecules and close to that of the benzene parent molecule. The assignments are also similar, as confirmed by the calculations: The first intense band *A* around 285 eV is the $1s\rightarrow 1\pi^*$ transition with a fine structure due to the nonequivalent carbon atoms; the *B* band around 287 eV is a Rydberg transition with its intensity augmented by an important $\sigma^*_{\mathrm{C-H}}$ valence character. It appears that in the core excited species, the $1\pi^*/2\pi^*$ and $1\pi^*/3\pi^*$ splittings are around 1.5 and 4 eV, respectively. A new interesting result is the assignment of the *C* band around 289 eV: In agreement with previous *ab initio* calculations on benzene,[27] this band must be assigned to the $3\pi^*$ transition but mixed with doubly excited configurations. We suggest that the $3\pi^*$ MO participate to several doubly excited states with π^* character above the ionization thresholds.

The $N1s$ excitation spectra for both molecules are similar and look like that of *s*-triazine, the first band *A* at 399 eV being assigned to the $1s\rightarrow 1\pi^*$ transition. As at the $C1s$ edge, the mixing of the $3\pi^*$ transition is also predicted by the calculations. On the other hand, there is no mixed valence character for the Rydberg MOs.

More generally, the present work and our previous study of pyrrole and pyrazole[36] show how high resolution inner-shell spectra may be interpreted successfully with the help of theoretical computations using the simple model of the equivalent core model and large scale CI calculations.

ACKNOWLEDGMENTS

We acknowledge the financial support of the ''Fond National de la Recherche Scientifique (F.N.R.S.) of the Communauté française de Belgique'' and the ''Direction générale de l'Enseignement Supérieur de la Recherche Scientifique (''Actions de Recherche Concertées'')'' and of ''the Patrimoine of the University of Liège.'' This work has also benefited of the support of the European Community by a Laboratory Twinning Contract (Programme ''Science,'' Contract No. SC1-CT90-0475). The Laboratoire de Physique des Lasers, Atomes et Molécules (PhLAM) is ''Unité Mixte de Recherche'' du CNRS. The Centre d'Etudes et de Recherches Lasers et Applications (CERLA) is supported by the Ministère chargé de la Recherche, the Région Nord/Pas-de-Calais and the Fonds Européen de Développement Economique des Régions. M.-J. Hubin-Franskin benefits of the support of the F.N.R.S. for a research position. The authors are grateful to M. Jacques Heinesch for his highly valuable technical assistance.

[1] A. D. Baker, D. Betteridge, N. R. Kemp, and R. E. Kirby, Anal. Chem. **42**, 1064 (1970).
[2] O. Khan, *Molecular Magnetism* (VCH, 1993).
[3] I. C. Walker, M. H. Palmer, and A. Hopkirk, Chem. Phys. **141**, 365 (1989).
[4] I. Nenner and G. J. Schulz, Chem. Phys. **628**, 1750 (1975).
[5] M. N. Pisanias, L. G. Christophorou, J. G. Carter, and D. L. McCorkle, J. Chem. Phys. **58**, 2110 (1973).
[6] A. Bolovinos, P. Tsekeris, J. Philis, E. Pantos, and E. Andritsopoulos, J. Mol. Spectrosc. **103**, 240 (1984).
[7] L. W. Pickett, M. E. Corning, G. M. Wieder, D. A. Semenow, and J. M. Buckley, J. Am. Chem. Soc. **75**, 1618 (1953).
[8] O. Kitao and H. Nakatsuji, J. Chem. Phys. **88**, 4913 (1988).
[9] W. Von Niessen, W. P. Kraemer, and G. H. F. Diercksen, Chem. Phys. **41**, 113 (1979).
[10] J. A. Horsley, J. Stöhr, A. P. Hitchcock, D. C. Newbury, A. L. Johnson, and F. Sette, J. Chem. Phys. **83**, 6099 (1985).
[11] V. N. Akimov, A. S. Vinogradov, A. A. Pavlychev, and V. N. Sivkov, Opt. Spectrosc. **59**, 206 (1985).
[12] R. Dudde, M. L. M. Rocco, E. E. Koch, S. Bernstorff, and W. Eberhardt, J. Chem. Phys. **91**, 20 (1989).
[13] M. H. Palmer and I. C. Walker, Chem. Phys. **157**, 187 (1991).
[14] P. Baltzer, L. Karlsson, B. Wannberg, G. Öhrwall, D. M. P. Holland, M. A. MacDonald, M. A. Hayes, and W. Von Niessen, Chem. Phys. **224**, 95 (1997).
[15] E. E. Rennie, C. A. F. Johnson, J. E. Parker, D. M. P. Holland, D. A. Shaw, and M. A. Hayes, Chem. Phys. **229**, 107 (1998).
[16] A. P. Hitchcock and C. E. Brion, J. Electron Spectrosc. Relat. Phenom. **10**, 317 (1977).
[17] A. C. Liu and C. M. Friend, J. Chem. Phys. **89**, 4396 (1988).
[18] L. J. Medhurst, T. A. Ferrett, P. A. Heimann, D. W. Lindle, S. H. Liu, and D. A. Shirley, J. Chem. Phys. **89**, 6096 (1988).
[19] Y. Ma, F. Sette, G. Meigs, S. Modesti, and C. T. Chen, Phys. Rev. Lett. **63**, 2044 (1989).
[20] Y. Ma, F. Sette, G. Meigs, S. Modesti, and C. T. Chen, Phys. Scr. **41**, 833 (1989).
[21] M. N. Piancastelli, T. A. Ferrett, D. W. Lindle, L. J. Medhurst, P. A. Heinmann, S. H. Liu, and D. A. Shirley, J. Chem. Phys. **90**, 3004 (1989).
[22] D. Menzel, G. Rocker, H.-P. Steinrück, D. Coulman, P. A. Heimann, W. Huber, P. Zebisch, and D. R. Lloyd, J. Chem. Phys. **96**, 1724 (1992).
[23] E. Lindholm and L. Åsbrink, *Lecture Notes in Chemistry*, *vol. 38* (Springer, Berlin, 1985).
[24] T. Yokohama, K. Seki, I. Morisada, K. Edamatsu, and T. Ohta, Phys. Scr. **41**, 189 (1989).
[25] E. Lindholm, L. Åsbrink, and S. Ljunggren, J. Phys. Chem. **95**, 3923 (1991).
[26] A. P. Hitchcock, S. G. Urquhart, and E. G. Rightor, J. Phys. Chem. **96**, 8736 (1992).
[27] W. H. E. Schwarz, T. C. Chang, U. Seeger, and K. H. Wang, Chem. Phys. **117**, 73 (1987).
[28] H. Ågren, O. Vahtras, and V. Carravetta, Chem. Phys. **196**, 47 (1995).
[29] R. N. S. Sodhi and C. E. Brion, J. Electron Spectrosc. Relat. Phenom. **34**, 363 (1984).
[30] W. L. Jolly and D. N. Hendrickson, J. Am. Chem. Soc. **92**, 1863 (1970).
[31] J. M. Hollander and W. L. Jolly, Acc. Chem. Res. **3**, 193 (1970).
[32] W. H. E. Schwartz, Angew. Chem. Int. Ed. Engl. **13**, 454 (1974).
[33] C. Hannay, J. Heinesch, U. Kleyens, and M.-J. Hubin-Franskin, Meas. Sci. Technol. **6**, 1140 (1995).
[34] M.-J. Hubin-Franskin, H. Aouni, D. Duflot, F. Motte-Tollet, C. Hannay, and L. F. Feirrera, J. Chem. Phys. **106**, 35 (1997).
[35] F. Currell and C. M. John, Meas. Sci. Technol. **3**, 1192 (1992).
[36] D. Duflot, C. Hannay, J.-P. Flament, and M.-J. Hubin-Franskin, J. Chem. Phys. **109**, 5308 (1998).
[37] T. H. Dunning, J. Chem. Phys. **55**, 716 (1971); **55**, 3958 (1971).
[38] T. H. Dunning, Jr. and P. J. Hay, *Methods of Electronic Structure Theory*, *Vol. 2*, edited by H. F. Schaeffer, III (Plenum, 1977).
[39] M. Dupuis, F. Johnston, and A. Marquez, ''HONDO95.3 from CHEMStation,'' (1995) IBM Corporation, Neighborhood Road, Kingston, NY, 12401, USA.

[40] S. Bodeur, P. Millié, and I. Nenner, Phys. Rev. A **41**, 252 (1990).
[41] T. Koopmans, Physica (Amsterdam) **1**, 104 (1933).
[42] C. Möller and M. S. Plesset, Phys. Rev. **46**, 618 (1934).
[43] R. Cimiraglia, J. Chem. Phys. **83**, 1746 (1985); R. Cimiraglia and M. Persico, J. Comput. Chem. **8**, 39 (1987).
[44] B. Huron, J-P. Malrieu, and P. Rancurel, J. Chem. Phys. **58**, 5745 (1973).
[45] R. J. Buenker and R. A. Philips, J. Mol. Struct.: THEOCHEM **123**, 291 (1985).
[46] I. Nenner and G. J. Schulz, J. Chem. Phys. **62**, 1747 (1975).
[47] E. Villa, A. Amirav, and E. C. Lim, J. Phys. Chem. **92**, 5393 (1988).
[48] S. Cradock, C. Purves, and D. W. H. Rankin, J. Mol. Struct. **220**, 193 (1990).
[49] E. R. Davidson, J. Comput. Phys. **17**, 87 (1975).
[50] D. T. Clark, R. D. Chambers, D. Kilcast, and W. K. R. Musgrave, J. Chem. Soc., Faraday Trans. 2 **68**, 309 (1972).
[51] E. Apen, A. P. Hitchcock, and J. L. Gland, J. Phys. Chem. **97**, 6859 (1993).
[52] A. A. Bakke, H. W. Chen, and W. L. Jolly, J. Electron Spectrosc. Relat. Phenom. **20**, 333 (1980).

Article 11

ELSEVIER

Journal of Electron Spectroscopy and Related Phenomena 113 (2000) 79–90

JOURNAL OF ELECTRON SPECTROSCOPY and Related Phenomena

www.elsevier.nl/locate/elspec

Re-analysis of the K-shell spectrum of benzene

D. Duflot[a,*], J.-P. Flament[a], J. Heinesch[b], M.-J. Hubin-Franskin[b,1]

[a]*Laboratoire de Physique des Lasers, Atomes et Molécules (PhLAM), UMR CNRS 8523, Centre d'Etudes et de Recherches Lasers et Applications (CERLA), Université des Sciences et Technologies de Lille, F-59655 Villeneuve d'Ascq Cedex, France*

[b]*Laboratoire de Spectroscopie d'Electrons Diffusés, Université de Liège, Institut de Chimie, B6c, B-4000 Liège (Sart Tilman), Belgium*

Received 5 March 2000; received in revised form 27 July 2000; accepted 25 August 2000

Abstract

The carbon K-shell spectrum of gaseous benzene has been recorded by inner-shell electron energy loss spectroscopy (ISEELS) under electric-dipole conditions (2 keV, small angle) with a resolution of 0.17 eV. Ab initio configuration interaction calculations performed in the frame of the equivalent core model have helped in the assignment of the experimental spectrum. They emphasize the importance of the multi-configurational approach and the role of the Rydberg orbitals in the assignment of some features. The band located at 289.09 eV is assigned to Rydberg excitations and a $3\pi^*$ transition mixed with doubly excited configurations, and not to an anti-bonding (C–H) transition as suggested previously. Because of a large 3s/3d character of the (C–H)* orbital, the corresponding peak appears above the ionization threshold. The 293.8 eV band contains in-plane resonances and very likely also several doubly excited states with a $3\pi^*$ contribution.

Keywords: Benzene; Excitation by electron impact; Ab initio calculations; Configuration interaction

1. Introduction

The core excitation spectrum of the benzene molecule has already been the subject of numerous experimental studies, both in gas [1–7] and condensed [3,8–24] phases. Various techniques were employed, including ISEELS [2,3,5], NEXAFS [8–24] and ZKE [6]. Theoretical studies have also been carried out, mainly with semi-empirical methods [3,25–28]. More recently, it has become possible to use ab initio methods, which are expected to give more accurate results. To our knowledge, the only studies of this type are those of Schwarz et al. [29] and the recent work using the STEX (static exchange) method [30–32]. Despite the large amount of studies, the assignment of some features in the spectrum remains ambiguous: the 289.09 eV one has been suggested to be due to the $3\pi^*$ [3,5] but also to the (C–H)* [26,27] transitions and the 293.8 eV one has been assigned to a shape resonance [3,5] and/or doubly excited π^* excitations [29].

The goal of the present paper is to re-analyze the core excitation spectrum of isolated benzene recorded by ISEELS with a resolution of 0.17 eV constant throughout the spectrum. Assignment of the

*Corresponding author. Tel.: +33-3-2043-4980; fax: +33-3-2043-4084.
E-mail address: denis.duflot@univ-lille1.fr (D. Duflot).
[1]Directeur de Recherches FNRS.

0368-2048/00/$ – see front matter
PII: S0368-2048(00)00225-5

observed spectral features has been made by ab initio calculations using the core equivalent model and configuration interaction (CI) calculations. This paper is divided into the following sections: Section 2 describes the experimental set-up; Section 3 deals with the computational method; the results and conclusions are presented in Sections 4 and 5, respectively.

2. Experimental

The inner-shell electron energy loss spectrum has been obtained with a VSW spectrometer which has been adapted for gas studies and high energy electron beams and equipped recently with a home-made position-sensitive multi-detector system in order to improve data collection times. The experimental apparatus and procedure have been described in detail previously [33,34].

Briefly the spectrometer consists of an electrostatic 180° monochromator operating in the constant pass energy mode, a collision chamber and an electrostatic analyzer identical to the monochromator. The monochromatized incident electrons are accelerated up to 2 keV and focused into the collision chamber using a four-element electron lens. The electrons are slightly deviated (0.02 radians) by two sets of $X-Y$ plates inside the collision chamber. The scattered electrons are energy analyzed and focused onto the entrance slit of the analyzer by the same kind of lens as that used for acceleration. In the collision conditions of low angular momentum transfer (i.e. at high incident energy and small scattering angle), primarily electronic electric-dipolar transitions are excited.

Inside the vacuum vessel containing the different parts of the spectrometer, a residual pressure of less than 1×10^{-8} Torr is maintained by a cryogenic pump and two turbomolecular pumps which are connected to the electron gun and the analyzer, respectively. The magnetic field within the vacuum vessel, the electron energy selectors, and the electron lenses have been minimized by mumetal layers.

The detection system consists of an assembly of two microchannel plates, a phosphor screen, fiber-optic couplers and an area array Coupled Charge Device (CCD) sensor. The driving and reading electronics for the detector have been well adapted to the electron-energy loss experiment and to the HP 9000/300 computer which has the whole experiment under control. The spectrum results from the accumulation of the data from each channel of the detector, which removes any detector-sensitivity variation [33,35].

The accelerating and retarding voltages have been delivered by the improved power supplies FUG and VSW 5000, respectively. The voltages were constant to within 10 ppm/°C.

In order to take into account the valence and lower-energy inner-shell excitation cross section, a linear background has been subtracted from the raw spectrum by extrapolating a least-square fit of the pre-edge experimental data points. The electron energy loss scale has been calibrated with the 285.2 eV value for the most intense peak of the benzene spectrum, taken from Ref. [2].

The sample is a commercial one from Merck with a purity better than 99.5%. It was used directly without further purification except repetitive freeze-pump-thaw cycles in order to eliminate air and other volatile impurities of the sample.

3. Computational method

The computational method described in detail elsewhere [36,37] will be briefly summarized. All the calculations were performed in the frame of the equivalent core model [38–40] which is a simple way to obtain term values (TVs) which are directly comparable to the experimental ones [36,37]. The TVs were calculated for a 1sC→i* excitation following the method described in Ref. [41]:

$$\mathrm{TV}(1\mathrm{sC}\rightarrow \mathrm{i}^*) = -\varepsilon_{\mathrm{i}^*} + P + C \qquad (1)$$

where $-\varepsilon_{\mathrm{i}^*}$ is the SCF mono-electronic energy of the i* virtual canonical MO of the $NC_5H_6^+$ ion (Koopmans' theorem). The repolarization term P is obtained via a configuration interaction (CI) in the mono-excited spaces S(1s a→i* j*) for all valence anti-bonding and Rydberg j* orbitals. The correlation term C is evaluated by a multi-reference MP2 calculation [42], using the diagrammatic version [43,44] of the CIPSI method [45]. The intensity of

Table 1
Calculated geometry of benzene compared with previous works (bond lengths in Å and angles in degrees)

	SCF[a] DZP	SCF[b] DZ+P	MP2[b] DZ+P	CCD[c] 6-31G*	CAS(π)[d] DZV	Exp[e] MW
r(C–C)	1.3910	1.386	1.399	1.396	1.406	1.3902
r(C–H)	1.0755	1.079	1.086	1.089	1.073	1.0862

[a] This work.
[b] Ref. [50].
[c] Ref. [51].
[d] Ref. [52].
[e] Ref. [53].

the $1s\rightarrow i^*$ transition is roughly estimated by the $c_o^2\langle 1s|\nabla|i^*\rangle^2$ matrix element.

The Gaussian atomic orbitals (AOs) used are those of Dunning's DZ basis set [46,47] with one d polarization shell on C atoms. The second set of calculations was carried out with an extended basis set including Rydberg orbitals (3s, 3p, 3d, 4s, 4p, 5s, 5p) [48] located at the mass center of the molecule. The exponents of these orbitals were those of the nitrogen atom, as this latter represents the C1s carbon excited atom in the equivalent core model.

The optimized D_{6h} geometry of the SCF ground state of benzene (obtained with the HONDO95.3 program package [49]) is the following: $R_{CC}=$ 1.3910 Å, $R_{CH}=1.0755$ Å. It compares well with experimental and theoretical works [50–53], as shown in Table 1. All the calculations were carried out at this geometry in the C_{2v} point group of $NC_5H_6^+$. In the following, the molecule is placed in the (x, y) plane, the C_2 axis being along the Ox direction; the notation 'C_e' will designate the core excited carbon atom in the molecule.

4. Results and discussion

The SCF electronic configuration of benzene in its neutral ground state $^1A_{1g}$ has been calculated to be:

$$1a_{1g}^2 1e_{1u}^4 1e_{2g}^4 1b_{1u}^2 2a_{1g}^2 2e_{1u}^4 2e_{2g}^4 3a_{1g}^2 2b_{1u}^2 1b_{2u}^2 3e_{1u}^4$$
$$1a_{2u}^2 3e_{2g}^4 1e_{1g}^4$$

The four first MOs are the 1s orbitals of the carbon atoms. The $1a_{2u}$ and $1e_{1g}$ (HOMO) MOs correspond to the 1π, 2π and 3π (degenerate) out-of-plane orbitals. The lowest unoccupied MO (LUMO) is the $1e_{2u}$ (degenerate $1\pi^*$ and $2\pi^*$, $\varepsilon_i=3.48$ eV) followed by the remaining anti-bonding ones. The $3\pi^*$ ($1b_{2g}$) MO lies very much higher in energy ($\varepsilon_i=9.00$ eV). In the C_{2v} symmetry point group of the core excited species, the $1e_{2u}$ generates the $3b_1$ ($1\pi^*$) and the $2a_2$ ($2\pi^*$) MOs, while the $1b_{2g}$ becomes the $4b_1$ ($3\pi^*$) MO. All electronic transitions are optically allowed except $1s\rightarrow 2\pi^*(2a_2)$.

One of the referees insisted on the fact that the σ and π designations, although widely used, were not appropriate for molecules belonging to D_{6h} and C_{2v} groups, especially the σ one, which refers to a localized bond between two atoms. Thus, the in-plane anti-bonding orbitals will be named using their symmetry in the C_{2v} group.

The calculations with the pure DZP valence basis set have helped to locate the position of the resonances expected to be responsible for the absorption above the ionization threshold. The present computational approach, neglecting the coupling between discrete states and the continuum states above ionization threshold, will provide only semi-quantitative results in this region. The calculations with the extended basis set were used to identify and describe accurately the Rydberg bands in the pre-edge energy region. The results of the core excitation spectrum analysis obtained with the valence and Rydberg calculations are presented separately in the following.

4.1. Carbon K-shell electron-energy loss spectrum

The electron-energy loss spectrum is displayed in Fig. 1. The energy values of the features listed in

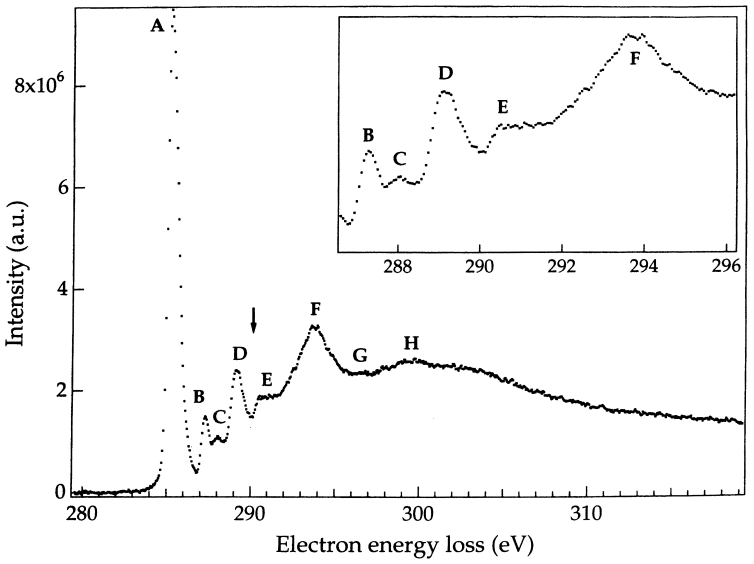

Fig. 1. The electron energy-loss spectrum of benzene recorded at the carbon K edge with an energy resolution of 0.17 eV. The arrow indicates the location of the core ionization threshold. The insert is an expansion of the spectrum in the region around this threshold.

Table 2 are in excellent agreement with the literature data.

The most intense peak A is located at 285.2 eV (TV=5.1 eV). Its asymmetry on the high energy side (Fig. 1), observed once previously [2], has been only partly resolved into fine features in the higher resolution NEXAFS spectrum of condensed benzene [8,9] and assigned to vibrational excitation. The less intense peak B has its maximum at 287.24 eV (TV= 3.06 eV). It appears to be broader than the experimental resolution. It could be due to the overlapping of not well resolved sharp peaks close in energies (Table 2). The presence of the low intensity peak C at 287.9 eV (TV=2.4 eV), reported once previously [2], is confirmed, thanks to the resolution. The maximum of the next band D is at 289.09 eV (TV=1.21 eV). There is some asymmetry on both sides of D, with not well resolved features around 288.9, 289.3 and 289.6 eV (Table 2).

There seems to be a spectral band E of low intensity slightly above the threshold, i.e. at 290.6 eV (TV= −0.3 eV). At higher energy, the spectrum is dominated by broad bands centered at 293.8 eV (F), 296.2 eV (G) and 299.4 eV (H). On the high and low energy sides of band F, there are fine features close in energy and not well resolved (Fig. 1, Table 2).

In order to obtain the experimental TVs from the absolute band energies, the precise knowledge of the ionization threshold is required. The binding energy used is 290.3 eV in most previous studies [1–5]. The value has been confirmed in zero kinetic energy (ZKE) experiments [6] (with an uncertainty of 0.1 eV). It is very close to the value recommended by data tables (290.34 eV [54]), and to the calculated values of 290.35 eV obtained via density functional (DFT) calculations by Hu and Chong [55], and of 290.43 eV obtained with the STEX method [31], respectively. The TVs reported in Table 2 were obtained with a value of 290.3 eV.

4.2. Valence calculations

The first band A at TV=5.1 eV (Table 2) is assigned without ambiguity to the $1s \rightarrow 1e_{2u}$ ($1\pi^*$, $3b_1$) transition, as the calculated TV of 4.89 eV is close to experiment (Table 3). The agreement of the present theoretical value with experiment is much better than for most previous studies (Table 4). The 4.89 eV value is very close to the relativistic DFT calculation at 4.87 eV [55], as detailed in Table 4. This agreement gives confidence on the reliability of

Table 2
Energies, term values (eV) and assignment of the spectral features in the C1s excitation spectrum[a]

	This work		[1]	[2]	[3]	[4]	[5]	[6]	Assignment
	TV[b]	E							
A	5.1	285.2[c]	285.2	285.2	285.2	285.0	285.2	285.2	$1\pi^*(b_1)$
	(4.3)	(286.0)							
	(4.1)	(286.2)							
B	3.06	287.24	287.1	287.2	287.2	287.2	287.2	287.2	$3s\sigma/a_1(C_e–H)^*$
	(2.9)	(287.4)							
	(2.7)	(287.6)							
C	2.4	287.9		288.0				287.9	3p
	(1.9)	(288.4)							
	(1.4)	(288.9)		(288.6)					$3d\sigma/a_1(C_e–H)^*$
D	1.21	289.09	288.9	288.9	288.9	288.8	289.1	289.0	$4s\sigma$
	(1.0)	(289.3)							$4p\sigma$
	(0.7)	(289.6)							$5p\sigma/3\pi^*(b_1)$
									+ doubly excited
E	−0.3	290.6		290.4		290.5			$a_1(C_e–H)^*/(3s\sigma+3d\sigma)$
	(−1.9)	(292.2)		291.3					a_1
F	−3.5	293.8	293.7	293.5	293.5	293.2	293.6	293.5	a_1
	(−3.8)	(294.1)							b_2
	(−4.2)	(294.5)							doubly excited?
	(−4.6)	(294.9)							doubly excited, a_1
G	(−5.9)	(296.2)					299.3	299	b_2
H	−9.1	299.4			300.2	302	302.6	302	

[a] (), not well resolved features.
[b] Ionization energy 290.3 eV (Ref. [6]).
[c] Ref. [2].

the calculated TVs for the bands lying at higher energies.

The electric dipole forbidden transition $1s\rightarrow 1e_{2u}$ ($2\pi^*$, $2a_2$), quadrupole electric allowed, is calculated at TV=3.78 eV (Table 3) leading to a separation of about 1.1 eV from the first band. Quadrupole electric allowed transitions have been observed in several molecules, by electron impact in non-dipolar excitation conditions (large angular momentum transfer, see Ref. [56] and references therein). They are expected to have a very small intensity in our present experimental conditions.

The next calculated value TV=1.54 eV (Table 3) is by far much lower than the experimental TVs measured for B and C bands, and is close to the D band value at 289.09 eV (TV=1.21 eV). This result proves that the bands B and C are due to Rydberg excitations. The assignment of this band D has already been the subject of numerous discussions. It was assigned to the $1s\rightarrow 1b_{2g}$ ($3\pi^*$, $4b_1$) transition, as supported by the angular dependence of the monolayer NEXAFS spectrum and Xα calculations [3]. However, electron attachment experiments [57,58] and multi-configurational ab initio calculations [29] (limited to the π system) showed that the monoelectronic approximation was not adequate to describe this ($3\pi^*$, $4b_1$) state. The CI wave-function was calculated [29] to be 0.35 ($1s\rightarrow 1b_{2g}$) + 0.22 ($1s\ 1e_{1g}\rightarrow 1e^2_{2u}$). This leads to a lowering of the calculated intensity (0.15 instead of 0.42) consistent with experiment (0.2) [3]. On this basis and although the calculated TV was too low (−0.2 eV after Fig. 4 of Ref. [29]), this band was assigned to the $1s\rightarrow 1b_{2g}$ ($3\pi^*$, $4b_1$) transition. Later, it was suggested by Yokoyama et al. [26], using CNDO/S calculations, that the D band was due to the $1b_{2g}$ excitation with a low intensity superimposed with the $a_1(C_e–H)^*$ transition of higher intensity. The $a_1(C_e–H)^*$ assignment has been corroborated by STEX calculations [30].

Our own valence calculations confirm the CNDO/S results [26], in a more precise way: the main peak at 289.09 eV should be assigned to the $a_1(C_e–H)^*$ transition (Table 3). The $1b_{2g}$ ($3\pi^*$, $4b_1$) transition

Table 3
Calculated term values (TV, eV) using valence basis set

Calculated TV[a]			I[b]		Main configurations
$-\varepsilon_{i*}$	$+P$[c]	$+C$[d]			
3.53	4.64	4.89	1.000	0.94	$1s\rightarrow b_1(1\pi^*)$
2.09	2.81	3.78	0.000[e]	0.96	$1s\rightarrow a_2(2\pi^*)$
−0.11	0.90	1.54	0.470	0.94	$1s\rightarrow a_1(C_e–H)^*$
−2.87	−0.55	0.75	0.295	0.57	$1s\rightarrow b_1(3\pi^*)$
				+0.22	$1s\ 3\pi\rightarrow 1\pi^*\ 2\pi^*$
				+0.18	$1s\ 2\pi\rightarrow 1\pi^*\ 1\pi^*$
0.00	0.00	0.00			Ion
	−1.99	−0.41		0.56	$1s\ 2\pi\rightarrow 1\pi^*\ 1\pi^*$
				+0.33	$1s\ 3\pi\rightarrow 1\pi^*\ 2\pi^*$
−2.38	−1.79	−0.60	0.045	0.96	$1s\rightarrow a_1$
−2.87	−4.62	−1.32	0.170	0.33	$1s\rightarrow b_1(3\pi^*)$
				+0.46	$1s\ 3\pi\rightarrow 1\pi^*\ 2\pi^*$
				+0.12	$1s\ 2\pi\rightarrow 1\pi^*\ 1\pi^*$
−2.65	−2.19	−1.33	0.028	0.97	$1s\rightarrow b_2$
−3.09	−2.22	−1.50	0.151	0.90	$1s\rightarrow a_1$
−3.77	−3.31	−2.05	0.010	0.96	$1s\rightarrow b_2$
	−4.96	−2.07	0.026	0.78	$1s\ 3\pi\rightarrow 1\pi^*\ 2\pi^*$
				+0.05	$1s\rightarrow b_1(3\pi^*)$
−4.21	−3.67	−2.55	0.020	0.87	$1s\rightarrow a_1$
	−4.00	−2.66		0.52	$1s\ 2\pi\rightarrow 1\pi^*\ a_1(C_e–H)^*$
				+0.22	$1s\ 3\pi\rightarrow 2\pi^*\ a_1(C_e–H)^*$
				+0.12	$1s\ 1\pi\rightarrow 1\pi^*\ a_1(C_e–H)^*$
	−5.99	−3.09		0.72	$1s\ 1\pi\rightarrow 1\pi^*\ 1\pi^*$
				+0.15	$1s\ 2\pi\rightarrow 1\pi^*\ 3\pi^*$
	−5.05	−3.20		0.72	$1s\ 3\pi\rightarrow 2\pi^*\ a_1(C_e–H)^*$
				+0.26	$1s\ 2\pi\rightarrow 1\pi^*\ a_1(C_e–H)^*$
−4.87	−4.36	−3.36	0.287	0.94	$1s\rightarrow a_1$
−4.85	−4.39	−3.54	0.536	0.91	$1s\rightarrow b_2$
−5.49	−5.02	−3.80	0.016	0.91	$1s\rightarrow b_2$
	−8.49	−4.64		0.56	$1s\ 2\pi\rightarrow 1\pi^*\ 3\pi^*$
				+0.33	$1s\ 3\pi\rightarrow 2\pi^*\ 3\pi^*$
−6.90	−5.94	−4.88	0.178	0.85	$1s\rightarrow a_1$
	−7.92	−5.38		0.62	$1s\ a_1\rightarrow 1\pi^*\ a_1(C_e–H)^*$
				+0.13	$1s\ a_1\rightarrow 1\pi^*\ a_1(C_e–H)^*$
				+0.10	$1s\ a_1\rightarrow 1\pi^*\ a_1(C_e–H)^*$
−7.44	−6.74	−5.49	0.194	0.91	$1s\rightarrow b_2$

[a] See text for definition.
[b] Relative intensity.
[c] $-\varepsilon_{i*}+P$ with respect to the SCF energy of the ion.
[d] $-\varepsilon_{i*}+P+C$ with respect to the MP2 energy of the ion.
[e] Dipole forbidden transition.

Table 4
Calculated TV (eV) of the $1\pi^*$ ($3b_1$) transition compared with previous theoretical works

Exp.	This work			[25] HAM	[3] Xα	[29] EIC	[29] ΔSCF	[29] MC	[29] g-H	[27] CNDO	[26] CNDO/S	[54] DFT	[30,31] STEX
	$-\varepsilon_{i*}$	$+P$	$+C$										
5.1	3.53	4.64	4.89	~4.5	5.5	~3.5	~4.5	~4.6	~5.1	5.4	~7	4.87	3.43

calculated to be mixed with double excitations, in agreement with Ref. [29] but with a calculated TV of 0.75 eV (Table 3) would then be responsible for the asymmetric tail of the D band (Fig. 2). In order to test the accuracy of this calculated TV, more extended calculations were carried out using a larger S space (6500 Slater determinants). The additional configurations were selected with the iterative procedure commonly used in the CIPSI method [45]. The results obtained were not significantly modified (TV=0.69 eV) for the first ($3\pi^*$, $4b_1$) state. However, the inclusion of Rydberg orbitals will partly modify this picture (see Section 4.3 below) for the D band.

In the region of the ionization threshold, the experimental spectrum exhibits a band E of low intensity, at 290.6 eV (TV= −0.3 eV). It was initially assigned to doubly excited states [2], to the ionization continuum [3] and, since it is also present in the high resolution (0.15 eV) spectrum of condensed benzene at the same energy, to several quasi-degenerate in-plane excitations [22]. Our own calculations predict (Table 3) that it is due to a resonance with a TV= −0.60 eV and a rather weak intensity (0.045). The structures between 291 and 292 eV (TV= −0.7 to −1.7 eV) are explained by a second state involving the $1s\rightarrow(3\pi^*, 4b_1)$ (TV= −1.32 eV) and in-plane transitions at TV= −1.33 and −1.50 eV, respectively (Fig. 1, Table 3).

At higher energy, the calculations predict a large number of doubly excited states and resonances, some of the latter having large intensities (Table 3). The two intense in-plane transitions calculated at TV= −3.36 and −3.54 eV are in good agreement with the band F observed at 293.8 eV (TV= −3.5 eV). This assignment is the most commonly proposed [3–5] but is not consistent with some experimental results. Indeed, the polarization dependence of this peak in the condensed phase suggests a double in-plane and out-of-plane character [11,23]. Moreover, in ZKE [6] experiments, the excited state decays primarily through many-electron channels. Based on previous MC calculations [29] predicting the second $1s\rightarrow(3\pi^*, 4b_1)$ state at TV= −4 eV, it has been suggested that F contains both ($3\pi^*$, $4b_1$) (mixed) and in-plane (e_{2g}) excitations. In the present calculations, this second ($3\pi^*$, $4b_1$) state is predicted to lie at TV= −1.32 eV as discussed above. There is a third state calculated at TV= −2.07 eV with a weak ($3\pi^*$, $4b_1$) component (0.05). In the region of F

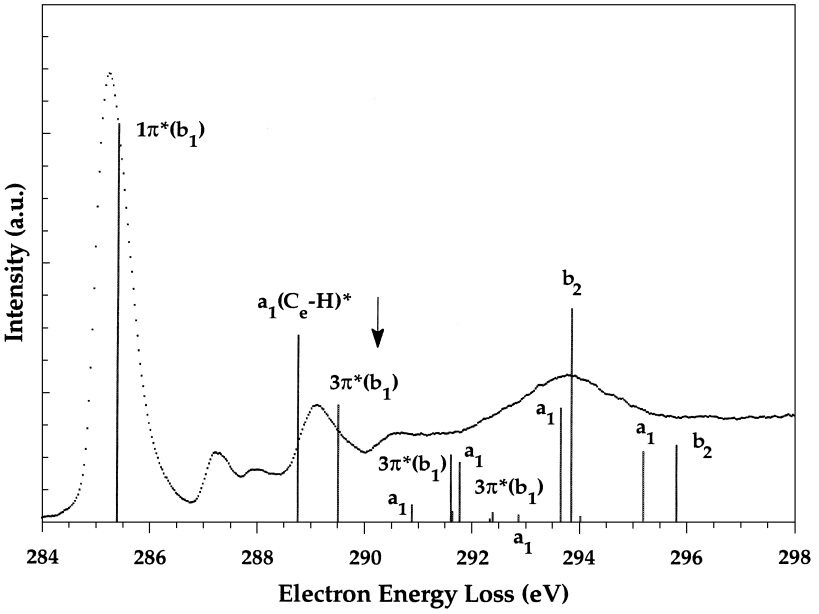

Fig. 2. Comparison of the synthetic spectrum deduced from the pure valence calculations with the experimental one in the 284–298 eV region. The arrow indicates the location of the core ionization threshold.

band, there are several doubly excited out-of-plane states with negligible ($3\pi^*$, $4b_1$) character. The extended calculations with the larger S space slightly modify the results: the second ($3\pi^*$, $4b_1$) state is now located at TV= −1.74 eV with a weight of 0.21, and the third one at TV= −2.65 eV with a weight of 0.16. Thus, the out-of-plane character in the F spectral region deduced from various experiments is due to at least one state with significant ($3\pi^*$, $4b_1$) character mixed with double excitations. It should be noticed as well that the in-plane resonances calculated at TV= −3.36 and −3.54 eV show an ungerade symmetry. Then, in D_{6h} group, the in-plane component of the F band should be assigned to the $4e_{1u}$ transition instead of the $4e_{2g}$ one as commonly suggested [29].

The in-plane transition calculated at TV= −4.88 eV corroborates the feature observed on the high energy side of F at 294.9 (TV= −4.6 eV). Similarly, the in-plane transition predicted at TV= −5.49 eV may be correlated to the not well resolved feature G found around 296.2 eV (TV= −5.9 eV). Finally, the last band H observed around 299.4 eV is beyond the capability of the present calculations. It could be related to the last in-plane (a_{2u}) transition (which is calculated to have an ε_i of 8.7 eV), but this possibility has been recently ruled out by synchrotron experiments [59]: the absence of this feature in the single hole cross-section indicates that it is probably due to satellite effects.

The synthetic spectrum formed by the combination of the calculated TVs and intensities is compared to the experimental one in Fig. 2. The agreement is very good, except in the 286.8–288.5 eV region (bands B and C) where the pure valence calculations do not predict any band.

4.3. Valence-Rydberg calculations

We turn now to the results obtained by adding to the basis set the Rydberg orbitals. For reasons stated above, these calculations were limited to the pre-edge energy range. The calculated TVs are displayed in Table 5. As expected, the results for the two first transitions to the valence $1e_{2u}$ ($1\pi^*$, $3b_1$ and $2\pi^*$, $2a_2$). MOs are not modified significantly.

The second experimental band B at 287.24 eV (Table 2, TV=3.06 eV) is now predicted at TV= 3.07 eV. Both TV and intensity are consistent with experiment (Fig. 1). It was first assigned to the 3s Rydberg transition [2]. However, as already predicted by others [29] and confirmed by our own calculations (Table 5), the 3sσ MO has a strong valence $a_1(C_e–H)^*$ character. This explains why the intensity is about 0.07 that of the first band, which is unusually large for a pure Rydberg excitation. The valence character of this band was also confirmed by Menzel et al. [22]: this band is present in the condensed phase NEXAFS spectrum, where pure Rydberg transitions should be broadened. The asymmetric tail of this band around 287.5 (TV=2.8 eV) does not correspond to any electronic transition in the calculations of Table 5. This suggests vibrational excitation: the fine features not well resolved around 287.4 eV and 287.6 eV (Table 2 and Fig. 1) are separated from the maximum of intensity of B by about 0.16 and 0.36 eV, respectively. These values are close to those reported for the A band in the high resolution NEXAFS spectrum of the solid [8,9] which have been assigned to the C–C non-totally symmetric and C–H stretching modes, respectively [8,9]. They are consistent with the values of these vibrational modes in ground state benzene (0.180–0.200 eV and 0.380 eV [60]).

The third experimental band C at 287.9 eV (TV= 2.4 eV) also present in ZKE spectra [6] has been assigned to the 3p transition [2,6,29]. This band is broader than the experimental resolution and seems to be composed of at least two not well resolved subbands at TV=2.4 and around 1.9 eV, respectively. These two components match the three 3p excitations calculated at TV=2.23, 2.09 and 1.90 eV as indicated in Table 5. The ‘plateau’ appearing in the same energy region in the condensed phase NEXAFS spectrum has been interpreted as the transformation of the Rydberg part of the $3s\sigma/a_1(C_e–H)^*$ MO into a conduction band [22].

According to the valence/Rydberg calculations (Table 5), the D band (TV=1.21 eV) is explained by Rydberg excitations involving the 3d, 4s and 4p shells, with TVs ranging from 1.64 to 0.90 eV. At slightly larger energies (TV≈0.7–0.6 eV) appear the 5s, 5p transitions and the first mixed ($3\pi^*$, $4b_1$) state. The $1s\rightarrow a_1(C_e–H)^*$ excitation is now calculated at TV= −0.55 eV, i.e. above the ionization threshold and at the position of the E band. Examina-

Table 5
Calculated term values (TV, eV) of the C1s core excitation spectrum using valence/Rydberg basis set[a]

Calculated TV			I		Main configurations	Type	$\langle r^2\rangle$[b]
$-\varepsilon_{i*}$	$+P$	$+C$					
3.53	4.71	4.90	1.000	0.93	1s→1π*	b_1	79.3
2.08	2.85	3.79	0.000[c]	0.96	1s→2π*	a_2	79.7
2.54	2.84	3.07	0.068	0.95	1s→3sσ/(C_e–H)*	a_1	146.9
1.93	2.10	2.23	0.039	0.96	1s→3pσ	a_1	191.3
1.86	1.93	2.09	<0.001	0.99	1s→3pσ	b_2	202.8
0.76	1.82	1.90	0.002	0.99	1s→3pπ	b_1	203.2
1.43	1.55	1.64	0.015	0.97	1s→3dσ/(C_e–H)*	a_1	192.8
1.36	1.43	1.52	0.001	0.99	1s→3dσ	b_2	180.8
1.35	1.42	1.50	0.002	0.99	1s→3dσ	a_1	166.0
1.20	1.24	1.28	0.002	0.99	1s→3dπ	b_1	180.6
1.17	1.18	1.24	0.000[c]	0.99	1s→3dπ	a_2	174.6
1.09	1.16	1.24	0.015	0.94	1s→4sσ	a_1	492.5
0.87	0.95	1.00	0.021	0.92	1s→4pσ	a_1	827.7
0.83	0.85	0.94	<0.001	0.99	1s→4pσ	b_2	866.2
0.82	0.84	0.90	0.003	0.99	1s→4pπ	b_1	827.6
0.61	0.66	0.69	0.025	0.94	1s→5pσ	a_1	1048.6
−2.97	−0.51	0.64	0.281	0.57	1s→3π*	b_1	78.4
				+0.23	1s 3π→1π* 2π*		
				+0.17	1s 2π→1π* 1π*		
0.51	0.54	0.64	<0.001	0.99	1s→5pσ	b_2	883.9
0.52	0.54	0.61	0.006	0.99	1s→5pπ	b_1	909.4
0.30	0.43	0.58	<0.001	0.96	1s→5sσ	a_1	367.1
0.00	0.00	0.00			Ion		
−1.88	−1.06	−0.55	0.299	0.90	1s→(C_e–H)*/(3sσ+3dσ)	a_1	124.5
	−1.92	−0.77		0.55	1s 2π→1π* 1π*	b_1	77.7
				+0.32	1s 3π→1π* 2π*		
	−2.59	−1.92		0.54	1s 3π→2π 3pσ	b_2	207.7
				+0.37	1s 2π→1π* 3pσ		

[a] See Table 3 for notations.
[b] Expectation value of the r^2 operator (bohrs^2).
[c] Dipole forbidden transition.

tion of the corresponding MO shows that it has a strong Rydberg character. In order to study the influence of the Rydberg orbitals on the a_1(C_e–H)* MO, test calculations were performed with different sets of diffuse orbitals. The results are detailed in Table 6. It appears that the inclusion of the $n=3$ orbitals, especially the 3s and 3d ones, has a crucial influence on the calculated TV, while the $n=4$ and 5 orbitals are less important. This effect is also visible in the expectation values of the r^2 operator as displayed in the last column of Table 5: $\langle r^2\rangle \approx 125$ au^2 for a_1(C_e–H)*/(3dσ+3sσ), intermediate be-

Table 6
Evolution of the calculated TV (eV) of the 1s→a_1(C_e–H)* transition with the basis set

TV	Valence	3s3p	3s3p 4s4p	3s3p3d	3s3p3d 4s4p	3s3p3d 4s4p 5s5p
$-\varepsilon_{i*}$	−0.11	−1.22	−1.28	−1.81	−1.87	−1.88
$+P$	+0.90	−0.41	−0.44	−0.94	−1.04	−1.06
$+C$	+1.54	+0.22	+0.08	−0.53	−0.53	−0.55

tween the value for the valence π* MOs (≈80 au^2) and the value for the 3p and 3d Rydberg MOs (≈200 au^2). For comparison, the value obtained for the $a_1(C_e–H)$* in the pure valence calculations was ≈90 au^2. Conversely, the $\langle r^2 \rangle$ of 147 au^2 obtained for the $(3d\sigma+3s\sigma)/a_1(C_e–H)$* MO is also intermediate between pure valence and $n=3$ Rydberg MOs. Finally the $3d\sigma_{x^2-y^2}$ transition has a weak $a_1(C_e–H)$* character, reflected in the rather large intensity (0.015) of the transition.

Such a valence-Rydberg mixing of the $a_1(C_e–H)$* MO does not seem to have been noticed in previous theoretical works [25–32], although it was probably implicitly present in Refs. [29,30]. It definitively proves that the C band at 289.09 eV does not come from the $1s \rightarrow a_1(C_e–H)$* transition. The synthetic spectrum formed by the combination of the calculated TVs and intensities is compared to the experimental one in Fig. 3. The agreement is satisfactory, except for the (3π*, $4b_1$) band the intensity of which is too large, due to the crude approximation used to calculate it.

5. Summary and conclusion

The assignment of the K-shell spectrum of benzene is summarized in the last column of Table 2. The present work shows that there is a very good agreement between the inner shell experimental spectrum of benzene and the theoretical spectrum obtained with ab initio configuration interaction calculations using the equivalent core model. These calculations emphasize the importance of multi-configurational methods and the role of Rydberg orbitals in the assignment of the spectral features. The absence of one or two of these requirements in other theoretical studies explains the contradictory assignments proposed in previous works. In particular, it appears that the 289.09 eV band cannot be assigned to the $a_1(C_e–H)$* transition, as commonly suggested: due to an important Rydberg character, this peak is shifted to higher energies. Instead, this band is explained by Rydberg excitations and a (3π*, $4b_1$) state mixed with double excitations. The 'missing weight' of this out-of-plane transition is distributed

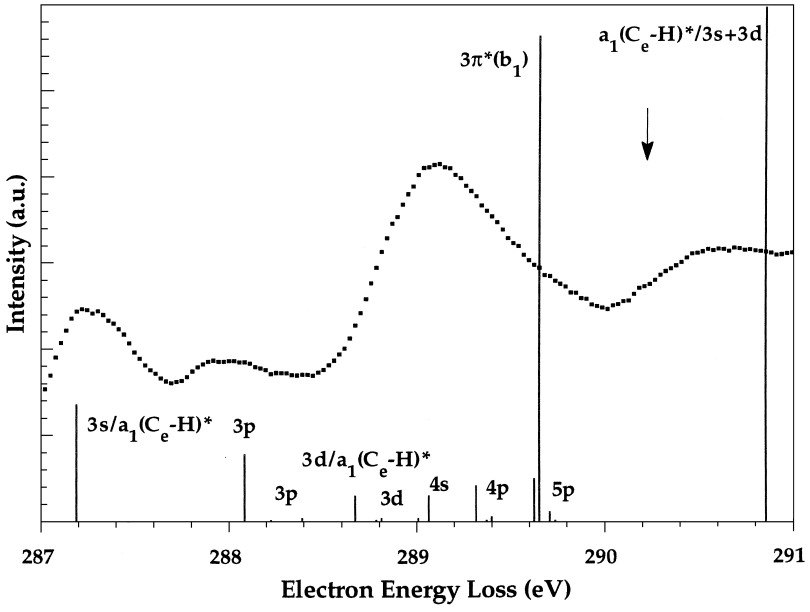

Fig. 3. Comparison of the synthetic spectrum deduced from the Rydberg/valence calculations with the experimental one in the 287–291 eV region. The arrow indicates the location of the core ionization threshold.

among several doubly excited states appearing in the energy region of the 293.8 eV band, in agreement with several experiments on adsorbed benzene.

Acknowledgements

We acknowledge financial support of the 'Fond National de la Recherche Scientifique (F.N.R.S.) of the Communauté française de Belgique' and the 'Direction générale de l'Enseignement Supérieur de la Recherche Scientifique ('Action de Recherche Concertée')' and of 'the Patrimoine of the University of Liège'. M.J.H.F. benefits from an FNRS research position. The Laboratoire de Physique des Lasers, Atomes et Molécules (PhLAM) is 'Unité Mixte de Recherche du CNRS'. The 'Centre d'Etudes et de Recherches Lasers et Applications' (CERLA) is supported by the 'Ministère chargé de la Recherche', the 'Région Nord/Pas-de-Calais' and the 'Fonds Européen de Développement Economique des Régions'.

References

[1] W. Eberhardt, R.-P. Haelbich, M. Iwan, E.E. Koch, C. Kunz, Chem. Phys. Lett. 40 (1976) 180.
[2] A.P. Hitchcock, C.E. Brion, J. Electron Spectrosc. Relat. Phenom. 10 (1977) 317.
[3] J.A. Horsley, J. Stöhr, A.P. Hitchcock, D.C. Newbury, A.L. Johnson, F. Sette, J. Chem. Phys. 83 (1985) 6099.
[4] V.N. Akimov, A.S. Vinogradov, A.A. Pavlychev, V.N. Sivkov, Opt. Spectrosc. (USSR) 59 (1985) 206.
[5] A.P. Hitchcock, P. Fischer, A. Gedanken, M.B. Robin, J. Phys. Chem. 91 (1987) 531.
[6] L.J. Medhurst, T.A. Ferrett, P.A. Heimann, D.W. Lindle, S.H. Liu, D.A. Shirley, J. Chem. Phys. 89 (1988) 6096.
[7] M.N. Piancastelli, T.A. Ferrett, D.W. Lindle, L.J. Medhurst, P.A. Heinmann, S.H. Liu, D.A. Shirley, J. Chem. Phys. 90 (1989) 3004.
[8] Y. Ma, F. Sette, G. Meigs, S. Modesti, C.T. Chen, Phys. Rev. Lett. 63 (1989) 2044.
[9] Y. Ma, F. Sette, G. Meigs, S. Modesti, C.T. Chen, Phys. Scr. 41 (1990) 833.
[10] A.L. Johnson, E.L. Muetterties, J. Stöhr, J. Am. Chem. Soc. 105 (1983) 7183.
[11] M. Bader, J. Haase, K.-H. Frank, C. Ocal, A. Puschmann, J. de Phys. C8 (1986) 491.
[12] P. Yannoulis, R. Dudde, K.-H. Frank, E.E. Koch, Surf. Sci. 189–190 (1987) 519.
[13] A.C. Liu, C.M. Friend, J. Chem. Phys. 89 (1988) 4396.
[14] K.-H. Frank, P. Yannoulis, R. Dudde, E.E. Koch, J. Chem. Phys. 89 (1988) 7569.
[15] A.C. Liu, J. Stöhr, C.M. Friend, Surf. Sci. 235 (1990) 107.
[16] H. Hoffmann, F. Zaera, R.M. Ormerod, R.M. Lampert, L.P. Wang, W.T. Tysoe, Surf. Sci. 232 (1990) 259.
[17] J. Solomon, R.J. Madix, J. Stöhr, Surf. Sci. 255 (1991) 12.
[18] A.C. Liu, J. Stöhr, C.M. Friend, Surf. Sci. 235 (1990) 107.
[19] S. Arminpirooz, L. Baker, J. Haase, Surf. Sci. 244 (1991) L152.
[20] W. Huber, M. Weinelt, P. Zebisch, H.P. Steinrück, Surf. Sci. 253 (1991) 72.
[21] M.G. Ramsey, D. Steinmüller, F.P. Netzer, T. Schedel, A. Santaniello, D.R. Lloyd, Surf. Sci. 251–252 (1991) 979.
[22] D. Menzel, G. Rocker, H.-P. Steinrück, D. Coulman, P.A. Heimann, W. Huber, P. Zebisch, D.R. Lloyd, J. Chem. Phys. 96 (1992) 1724.
[23] M. Weinelt, N. Wassdahl, T. Wiell, O. Karis, J. Hasselström, P. Bennich, A. Nilsson, J. Stöhr, M. Samant, Phys. Rev. B 58 (1998) 7351.
[24] P. Zebisch, M. Stichler, P. Trischberger, M. Weinelt, H.P. Steinrück, Surf. Sci. 396 (1998) 61.
[25] E. Lindholm, L. Åsbrink, in: Lecture Notes in Chemistry, Vol. 38, Springer, Berlin, 1985.
[26] T. Yokohama, K. Seki, I. Morisada, K. Edamatsu, T. Ohta, Phys. Scr. 41 (1989) 189.
[27] E. Lindholm, L. Åsbrink, S. Ljunggren, J. Phys. Chem. 95 (1991) 3923.
[28] A.P. Hitchcock, S.G. Urquhart, E.G. Rightor, J. Phys. Chem. 96 (1992) 8736.
[29] W.H.E. Schwarz, T.C. Chang, U. Seeger, K.H. Wang, Chem. Phys. 117 (1987) 73.
[30] H. Ågren, O. Vahtras, V. Carravetta, Chem. Phys. 196 (1995) 47.
[31] O. Plashkevych, L. Yang, O. Vahtras, H. Ågren, L.G.M. Pettersson, Chem. Phys. 222 (1997) 125.
[32] L.G.M. Pettersson, H. Ågren, Y. Luo, L. Triguero, Surf. Sci. 408 (1998) 1.
[33] C. Hannay, J. Heinesch, U. Kleyens, M.-J. Hubin-Franskin, Measur. Sci. Technol. 6 (1995) 1140.
[34] M.-J. Hubin-Franskin, H. Aouni, D. Duflot, F. Motte-Tollet, C. Hannay, L.F. Feirrera, G. Tourillon, J. Chem. Phys. 106 (1997) 35.
[35] F. Currell, C.M. John, Measur. Sci. Technol. 3 (1992) 1192.
[36] D. Duflot, C. Hannay, J.-P. Flament, M.-J. Hubin-Franskin, J. Chem. Phys. 109 (1998) 5308.
[37] C. Hannay, D. Duflot, J.-P. Flament, M.-J. Hubin-Franskin, J. Chem. Phys. 110 (1999) 5600.
[38] W.L. Jolly, D.N. Hendrickson, J. Am. Chem. Soc. 92 (1970) 1863.
[39] J.M. Hollander, W.L. Jolly, Acc. Chem. Res. 3 (1970) 193.
[40] W.H.E. Schwarz, Angew. Chem. Int. Ed. 13 (1974) 454.
[41] S. Bodeur, P. Millié, I. Nenner, Phys. Rev. A 41 (1990) 252.
[42] C. Möller, M.S. Plesset, Phys. Rev. 46 (1934) 618.
[43] R. Cimiraglia, J. Chem. Phys. 83 (1985) 1746.
[44] R. Cimiraglia, M. Persico, J. Comp. Chem. 8 (1987) 39.

[45] B. Huron, J.-P. Malrieu, P. Rancurel, J. Chem. Phys. 58 (1973) 5745.
[46] T.H. Dunning, J. Chem. Phys. 55 (1971) 716.
[47] T.H. Dunning, J. Chem. Phys. 55 (1971) 3958.
[48] T.H. Dunning, P.J. Hay, in: H.F. Schaeffer III (Ed.), Methods of Electronic Structure Theory, Vol. 3, Plenum Press, 1977.
[49] M. Dupuis, F. Johnston, A. Marquez, HONDO95.3 from CHEM-Station, IBM Corporation, Neighborhood Road, Kingston, NY, 12401, USA, 1995.
[50] S. Irle, H. Lischka, J. Chem. Phys. 103 (1995) 1508.
[51] H. Torii, M. Tasumi, J. Mol. Struct. 352–353 (1995) 465.
[52] P. Norman, H. Ågren, J. Mol. Struct. (Theochem) 401 (1997) 107.
[53] J. Plíva, J.W.C. Johns, L. Goodman, J. Mol. Spectrosc. 148 (1991) 427.
[54] W.L. Jolly, K.D. Bomben, C.J. Eyermann, At. Data Nucl. Data Tables 31 (1984) 433.
[55] C.-H. Hu, D.P. Chong, Chem. Phys. Lett. 262 (1996) 729.
[56] I.G. Eustatiu, T. Tyliszczak, A.P. Hitchcock, Chem. Phys. Lett. 300 (1998) 676.
[57] I. Nenner, G.J. Schulz, J. Chem. Phys. 62 (1975) 1747.
[58] P.D. Burrow, J.A. Michejda, K.D. Jordan, J. Chem. Phys. 86 (1987) 9.
[59] B. Kempgens, H.M. Köppe, A. Kivimäki, M. Neeb, K. Maier, U. Hergenhahn, A.M. Bradshaw, Surf. Sci. 425 (1999) L376.
[60] L. Goodman, A.G. Ozkabak, S.N. Thakur, J. Phys. Chem. 95 (1991) 9044.

Article 12

JOURNAL OF CHEMICAL PHYSICS VOLUME 118, NUMBER 3 15 JANUARY 2003

Core shell excitation of 2-propenal (acrolein) at the O 1*s* and C 1*s* edges: An experimental and *ab initio* study

D. Duflot[a] and J.-P. Flament
Laboratoire de Physique des Lasers, Atomes et Molécules (PhLAM), UMR CNRS 8523, Centre d'Etudes et de Recherches Lasers et Applications (CERLA), Université des Sciences et Technologies de Lille, F-59655 Villeneuve d'Ascq Cedex, France

I. C. Walker
Department of Chemistry, Heriot-Watt University, Riccarton, Edinburgh EH14 4AS, United Kingdom

J. Heinesch and M.-J. Hubin-Franskin[b]
Université de Liège, Laboratoire de Spectroscopie d'Électrons diffusés, Institut de Chimie B6c, Sart Tilman, B4000 Liège 1, Belgium

(Received 8 July 2002; accepted 17 October 2002)

The carbon and oxygen *K*-shell spectra of gaseous 2-propenal (acrolein) have been measured using the inner-shell electron energy loss spectroscopy method. Large scale *ab initio* configuration interaction calculations have been carried out to enable firm assignments of the observed bands. The overall shapes of the spectra are similar to previous low resolution monolayer and multilayer phases NEXAFS spectra recorded by photoabsorption of synchrotron radiation, but the spectral bands are much better resolved than the earlier ones. The spectra are dominated by excitation of π^* type states and by interaction between the C=C and C=O π^* orbitals. © *2003 American Institute of Physics*. [DOI: 10.1063/1.1527924]

I. INTRODUCTION

The 2-propenal molecule ($CH_2=CH-CHO$), commonly named acrolein, is the smallest α,β unsaturated aldehyde. Since the pioneering work of Walsh,[1] it is a prototypal molecule for the study of the π^*(C=C)/π^*(C=O) bond interaction.[2] 2-propenal also plays an important role in various contexts: It is involved in atmospheric chemistry via its reactions with[3] NO_3 and chlorine[4] atoms; its possible detection in interstellar clouds has been recently suggested;[5] the vinylallene/propenal reaction was used as a model system for the study of regio- and stereoselectivity in Diels–Alder reactions.[6] The adsorption and reactivity of 2-propenal on surfaces has also been the subject of various studies, using a large variety of methods.[7–11]

Although a large number of studies have been devoted to the structural and vibrational properties of the ground and first excited states of gas phase 2-propenal,[2,12–16] very little is known about higher excited states. The goal of the present study is to get information on the lowest energy unoccupied molecular orbitals and on the interaction between the C=C and C=O π^* orbitals. The experimental method employed is inner-shell electron energy loss spectroscopy (ISEELS) in electric dipolar excitation conditions. Due to the localization of the 1s orbitals, the ISEELS method has proven to be a powerful tool for the study of higher excited states and their characterization as π^*, σ^*, or Rydberg character.[17,18] The ISEELS spectra of 2-propenal have been recorded at the C 1*s* and O 1*s* edges with a resolution of 0.17 eV, the resolution being the same at both edges. In order to help in the assignment of the observed spectral features, large scale *ab initio* configuration interaction (CI) calculations have been carried out. This paper is divided into the following sections: Section II describes the experimental setup, Sec. III deals with the computational method employed, the results are presented and discussed in Sec. IV, and, finally, in Sec. V some conclusions are given.

II. EXPERIMENT

The inner-shell electron energy loss spectra were obtained with a VSW spectrometer which has been adapted for gas studies and high energy electron beams; it has recently been equipped with a home-made position sensitive multidetector system in order to improve data collection times. The experimental apparatus and procedure have been described in detail previously.[19–21]

Briefly the spectrometer consists of an electrostatic 180° monochromator operating in the constant pass energy mode, a collision chamber, and an electrostatic analyzer identical to the monochromator. The monochromatized incident electrons are accelerated up to 2 keV and focused into the collision chamber using a four-element electron lens. The electrons are slightly deflected (0.02 rad) by two sets of $X-Y$ plates inside the collision chamber. The scattered electrons are energy analyzed and focused onto the entrance slit of the analyzer by a lens similar to that used for acceleration. In the collision conditions of low angular momentum transfer (i.e., high incident energy and small scattering angle), electronic electric-dipolar transitions are primarily excited.

Inside the vacuum vessel containing the different parts of the spectrometer, a residual pressure of less than 1×10^{-8} Torr is maintained by a cryogenic pump and two turbomolecular pumps which are connected to the electron gun

[a]Electronic mail: denis.duflot@univ-lille1.fr
[b]Directeur de recherche F.N.R.S.

and the analyzer regions, respectively. The magnetic field within the vacuum vessel, the electron energy selectors, and the electron lenses have been minimized by mumetal layers.

The detection system consists of an assembly of two microchannel plates, a phosphor screen, fiber-optic couplers, and an area array coupled charge device sensor. The driving and reading electronics for the detector have been adapted to the electron-energy loss experiment and to the HP 9000/300 computer which controls the whole experiment. The spectra result from the accumulation of the data from each channel of the detector, which removes any detector-sensitivity variation.[19,22]

The accelerating and retarding voltages were delivered by improved power supplies FUG and VSW 5000, respectively. The voltages were constant to within 10 ppm/°C.

The spectra have been recorded with 0.048 eV steps. In order to take into account valence and lower-energy inner-shell excitation cross section, a background has been subtracted from the raw spectra by extrapolating a least-squares fit of the pre-edge experimental data points. The electron energy loss scale was calibrated at the C 1*s* edge from the $C\,1s\rightarrow\pi^*\,(\nu'=0)$ band in CO[23] at 287.40 ± 0.02 eV. At the O 1*s* edge, the reference was the $O\,1s\rightarrow\pi^*\,(\nu'=0)$ value for the same molecule[23] at 534.21 ± 0.09 eV. The uncertainty on the measured energies is of 0.07 and 0.13 eV for the C 1*s* and O 1*s* spectra, respectively.

The sample is a commercial one from ACROS with a stated purity of 97.0%. It was used directly without further purification except for repetitive freeze–pump–thaw cycles in order to eliminate air and other volatile impurities in the sample.

III. COMPUTATIONAL METHOD

A well-known problem in the calculation of electronic transition energies is the choice of a common set of molecular orbitals (MOs) for the description of both initial and final states. A common procedure is to use the optimized MOs of the ground state or state-averaged MOs between the ground and excited state(s). Both methods suppose implicitly that the repolarization of the electronic density upon excitation is weak. This hypothesis may be reasonable for valence excitation, but is incorrect in the case of core excitations: the creation of a hole in a 1*s* orbital causes an important relaxation of the electronic density. Thus the ground state MOs are not a good choice for the description of core excited states. Moreover, in the present work, our goal is to describe a large number of excited states (valence and Rydberg). For these reasons, we choose to use the virtual MOs of the core ionized molecule ($C\,1s^{-1}$ or $O\,1s^{-1}$) as a common set for the description of all the core excited states. These MOs are obtained using the restricted open shell Hartree–Fock generalized valence bond (ROHF-GVB) method[24,25] implemented in the GAMESS-US program package.[26]

For a given atom (here three carbons and one oxygen), the absolute core excitation energy is then calculated as follows:[27]

$$E(1s\rightarrow i^*)=E(1s\rightarrow\infty)+\varepsilon_{i^*}+P+C,$$

where ε_{i^*} is the monoelectronic energy of the i^* virtual canonical orbital given in the ROHF-GVB calculation of the core ion (Koopmans' theorem[28]). $E(1s\rightarrow\infty)$ is the core ionization energy, calculated at the second-order Møller–Plesset (MP2) level.

The repolarization term P is calculated by performing a CI in the monoexcited space S including all monoexcitations from the occupied valence orbitals to the virtual orbitals. Using a second quantization formalism, the CI wave function for a core-excited state on a given atom is then

$$\Psi_{\mathrm{CI}}=\sum_{j^*}\left[C_{j^*}+\sum_b\sum_k C_{bk}a_b a_k^+\right]a_{1s}a_{j^*}^+\Psi_{\mathrm{Ref}},$$

where j^* represent the lowest lying (valence antibonding and Rydberg) virtual MOs; b represent the occupied orbitals (excluding the other heavy atom 1*s* ones), and k all the virtual MOs. Ψ_{Ref} is the ground state closed shell configuration using the ROHF ion MOs. The resulting CI matrix is diagonalized using Davidson's method[29] to obtain the lowest lying energies and wave functions.

The correlation term C is evaluated by taking the S space as the zeroth-order wave function for a multireference MP2 calculation, using the three-class diagrammatic version[30] of the CIPSI method.[31] In this three-class procedure, the MP2 energy correction is calculated on a subspace $G\subset S$ to reduce the computational time. G should contain the ''most important'' determinants of S. To recover the result for the full S space, whose computational cost would be prohibitive, we use the extrapolation procedure proposed by Angeli *et al.*[32] Briefly, this consists of selecting several subspaces G_j of increasing sizes such that the weight of the G_j wave function (with respect to the S wave function) must be greater than a given threshold τ_j. In the present work, we used six values for τ_j: 0.998, 0.997, 0.996, 0.995, 0.994, and 0.993. Using the six resulting energies for each state, the exact energy value is extrapolated using a least-squares fit.

The intensity of the electric dipolar transitions is obtained by

$$\mathrm{I}\sim|\langle\Psi_{\mathrm{CI}}|r|\Psi_0\rangle|^2.$$

For technical reasons, it is necessary to employ the same set of MOs to describe the wave functions of the ground state Ψ_0 and the excited states Ψ_{CI}. Since the ROHF-GVB MOs of the core ionized molecule are not the best ones for the description of the ground state, we repolarize them ''backwards'' by performing a CI calculation in the monoexcited space of the ground state:

$$\Psi_0=\sum_b\sum_k\left[C_{\mathrm{Ref}}+C_{bk}a_b a_k^+\right]\Psi_{\mathrm{Ref}}.$$

The calculated intensities are refined by a first-order perturbation calculation. The results show that for most states, the unperturbed and perturbed intensities are very similar. Thus, only the perturbed intensities are reported here. The calculated energies and intensities are then used to create theoretical spectra which can be compared to the experimental ones. The lines are convoluted by Gaussian functions with a full width at half maximum of 0.17 eV.

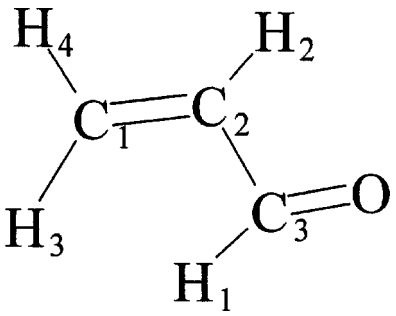

FIG. 1. Labeling of atoms in 2-propenal.

The Gaussian atomic orbitals (AOs) used is the TZP basis set taken from Dunning.[33,34] The exponents of the polarization d AOs are: $\alpha_C = 0.72$ and $\alpha_O = 1.28$. For the calculation of the core-excited states, a set of Rydberg orbitals $(3s, 3p, 3d, 4s, 4p)$ is added on the core-excited atom.[34] We use the exponents of the $(Z+1)$ equivalent of the excited atom (nitrogen for carbon and fluorine for oxygen).

TABLE I. Calculated geometry of 2-propenal compared with previous works (bond lengths in angstroms and angles in degrees).

	RHF[a] TZP	MP2[a] TZP	Expt.[b] MW	Expt.[c] MW	CAS(8,7)[d] cc-pVDZ
C_1-C_2	1.319	1.339	1.345±0.003	1.340	1.360
C_2-C_3	1.479	1.472	1.470±0.003	1.468	1.478
C_3-H_1	1.095	1.104	1.108±0.003	1.113	1.100
C_3-O	1.185	1.218	1.219±0.005	1.214	1.205
C_2-H_2	1.074	1.081	1.084±0.003	1.084	1.083
C_1-H_3	1.076	1.081	1.086±0.005	1.090	1.084
C_1-H_4	1.074	1.078	1.086±0.005	1.080	1.082
$C_1-C_2-C_3$	121.1	120.2	119.8±0.2	120.4	122.0
$C_2-C_3-H_1$	115.2	114.9	115.1±0.2	114.7	116.3
C_2-C_3-O	121.1	124.2	123.3±0.3	124.0	123.2
$C_1-C_2-H_2$	122.4	122.5	122.8±0.2	122.4	121.7
$H_3-C_1-C_2$	121.4	120.8	120.0±0.2	119.7	121.3
$H_4-C_1-C_2$	122.0	122.0	121.5±0.2	122.2	121.6
$C_1-C_2-C_3-O$	180.0	180.0	180.0	180.0	180.0

[a]This work.
[b]Reference 35.
[c]Reference 36.
[d]Reference 15.

IV. RESULTS AND DISCUSSION

The HF electronic configuration of the $^1A'$ neutral ground state of 2-propenal is

$$1a'^2 2a'^2 3a'^2 4a'^2 5a'^2 6a'^2 7a'^2 8a'^2 9a'^2 10a'^2 11a'^2$$
$$12a'^2 1a''^2 13a'^2 2a''^2.$$

The four first MOs are the 1*s* orbitals of the oxygen and carbon atoms. In a qualitative picture, the $1a''(1\pi)$ MO corresponds to the $\pi(C_1C_2)$ bond, while the $2a''(2\pi)$ is the $\pi(C_3O)$ bond (see Fig. 1 for atom labeling). The antibonding MOs are the $3a''(1\pi^*)$ and the $4a''(2\pi^*)$ ones, which are delocalized over the whole molecule, the first one having a bonding C_2C_3 character. All electronic transitions are electric dipole allowed.

The calculated geometries of the ground state of 2-propenal, obtained at the HF and MP2 levels, are compared with previous experimental[35,36] and theoretical[15] determinations in Table I. Only the *s-trans* isomer was considered in the present work, because at room temperature, only 4–5% of the molecule exists in the *s-cis* form.[37] Since the MP2 values are very close to the experimental ones, all the calculations were carried out at this geometry to obtain the vertical excitation energies.

A. Core ionization energies

Bournel *et al.*[10] have measured the core ionization energies of 2-propenal in condensed phases (multilayer and monolayer on Pt surface) using the x-ray photoelectron spectroscopy method. To the best of our knowledge, there is only one gas phase study available.[38] Unfortunately, due to a lack of calibration of absolute energies, only energy differences were reported. The available data are listed in Table II with our calculations for the gas phase at the ΔSCF (self-consistent field) and ΔMP2 levels.

A direct comparison between the calculations results for the gas and the condensed phases values is not easy, because of the influence of the work functions and relaxation effects in the condensed phases (see Sec. 7.4.3 of Ref. 18). On the theoretical side, the ΔSCF method is known to give rather good results mainly because of error cancellations, while ΔMP2 calculations take into account correlation effects. At the carbon edge, both methods show that the chemical shift between C_1 and C_2 is negligible while the C_3 ionization energy is much higher (Table II). The same trends are found for the $1sC \rightarrow 1\pi^*$ excitation energies (see the following). The calculated values of the chemical shift between the C_1/C_2 pair and C_3 (2.82 and 2.34 eV) are in rather good agreement with the gas phase value[38] of 2.6 eV. In the condensed phases,[10] the situation is somewhat different, with a chemical shift of 0.70 eV between C_1 and C_2.

B. Oxygen *K*-shell electron-energy loss spectrum

The electron energy loss spectrum at the O 1*s* edge is shown in Fig. 2(a). The energies of the spectral features are given in Table III where they are compared with the mono- and multilayer NEXAFS spectra.[10] The spectrum is dominated by a strong band labeled *A* and centered at 530.59 eV. The second band *B*, much less intense, is centered at 533.57 eV. It shows fine structure on both low and high energy sides of the maximum intensity. The third band *C* at 535.25 eV is very weak, while the fourth one *D*, at 536.45 eV, is the last feature below the ionization threshold. Above this threshold, there is a very broad band *E* centered at 543.64 eV.

Comparison between the present work and the condensed phase NEXAFS studies (Figs. 17 and 21 of Ref. 10) shows an energy shift of ~2 eV (Table III). This energy difference seems very large, since the deviation between the position of the peaks between adsorbed and gas phase spectra is usually much smaller (see numerous examples in Stöhr's book[18]). Thus we suspect that the energy scale of the condensed phases spectra of Ref. 10 is wrong. Nevertheless, the spectra are very similar. In particular, the *A*, *B*, and *E* bands are present in the condensed molecule spectra, indicating valence-type excitations. Moreover, the intensity depen-

TABLE II. Core ionization energies (eV) of 2-propenal at the O 1*s* and C 1*s* edges.

	Expt.[a]			Expt.[b]			This work[c]		
	Multilayer	Shift	Monolayer/Pt(111)	Shift	Gas	ΔSCF	Shift	ΔMP2	Shift
C_1	290.00	0.00	289.50	0.00	0.0	291.78	0.00	291.48	0.00
C_2	290.70	0.70	290.20	0.70	~0.0	291.69	0.11	291.47	−0.01
C_3	292.90	2.90	292.25	2.75	2.6	294.60	2.82	293.82	2.34
O	537.95		537.00			537.37		538.37	

[a]From Ref. 10. Values corrected from the work functions (4.50 eV for monolayer and 4.95 eV for multilayer).
[b]From Ref. 38. Only chemical shifts are available.
[c]Gas phase values calculated at the TZP/MP2 optimized geometry using the TZP+Rydberg basis sets.

dence of excitation upon the polarization of the synchrotron radiation indicated a π character for *A* and *B* and a σ character for *E*. The theoretical results given in Table IV are consistent with this: The *A* peak, due to the excitation $1sO \rightarrow 1\pi^*$, is calculated to occur at 530.80 eV, in very good agreement with the experimental value of 530.59 eV.

Concerning the *B* band, the calculations predict a second π^* transition at 534.01 eV, a value slightly above the experimental maximum at 533.57 eV. The relative intensities of the *A* and *B* bands in the spectrum are very well reproduced in the computations (Table IV and Fig. 3). The electronic configuration of this (*B*) excited state is complicated, because the $2\pi^*$ MO is mixed with the $3d\pi$ one, and the CI wave function is a combination of several excitations (Table IV). However, the calculated value of $\langle r^2 \rangle$ (59 a.u.^{2}) is close to that of the *A* state (57 a.u.^{2}), showing that it has a valence character. The fine features of the *B* band are not well resolved and spaced by about 0.19 eV or 2×0.19 eV. The only other state computed to lie in this region is that from the $1s \rightarrow 3s\sigma/\sigma^*(C_3-H)$ excitation, calculated energy 535.18 eV. We relate this to the experimental feature at 534.82 eV. It then follows that fine structure on band *B* is vibrational excitation; the spacing (~0.19 eV) is consistent with excitation of C=C/C=O stretch vibrations: according to Ref. 2, the experimental value for the C=C and C=O stretches are 0.20 and 0.21 eV, respectively.

The third band *C* located at 535.25 eV is close to the 534.82 eV maximum and has approximately the same intensity. According to the calculations, this energy range (535–536 eV) contains transitions to $3p\sigma$ and $3p\pi$ states having very small intensities. Thus the existence of this feature is not certain.

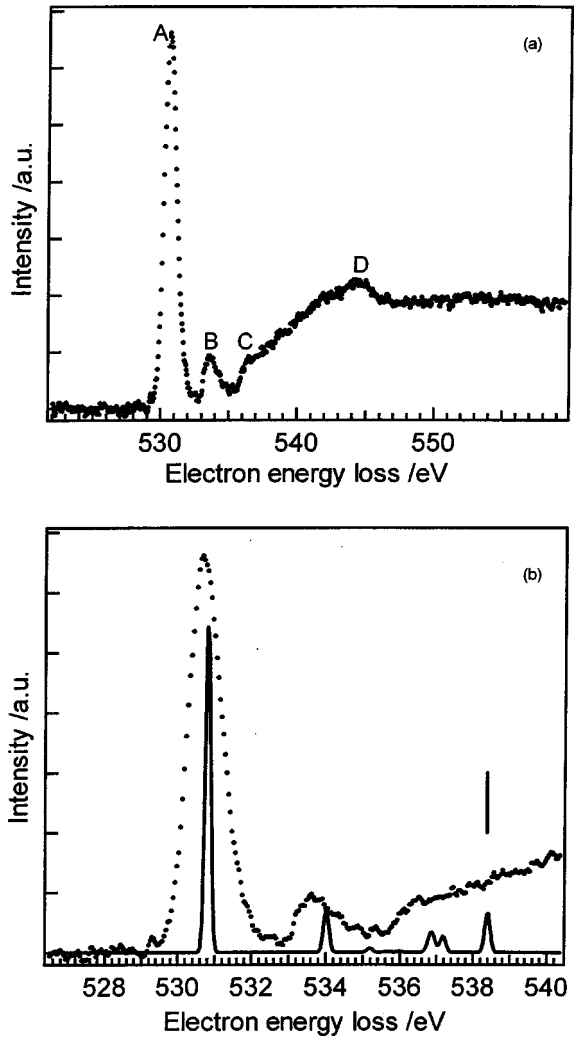

FIG. 2. (a) The electron energy-loss spectrum of 2-propenal recorded at the oxygen *K* edge with an energy resolution of 0.17 eV, steps 48 meV. (b) Comparison between the experimental and the theoretical spectra for the pre-edge region at the oxygen *K* edge. The vertical line indicates the location of the ionization threshold.

TABLE III. Energies (eV) of the spectral features in the gas phase O 1*s* ISEELS spectrum and in the condensed phases NEXAFS spectra.[a]

	This work	Monolayer/Pt(111)[a]	Multilayer[a]	Assignment[a]
A	530.59	532.70	532.85	$1sO \rightarrow 1\pi^*$
	533.19			
B	533.57	535.70	535.70	$1sO \rightarrow 2\pi^*$
	533.86			
	534.29			
	534.82			
C	535.25			
D	536.45			
E	543.64			

[a]Proposed assignments from Ref. 10.

TABLE IV. Calculated energies, relative intensities, and assignments of O 1*s* core excited states of 2-propenal.

State	E(eV)	I		Main configurations	$\langle r^2 \rangle$
$1a''$	530.80	1.000	0.92	$1s \rightarrow 1\pi^*$	57
$2a''$	534.01	0.125	0.34	$1s \rightarrow 2\pi^*/3d\pi$	59
			+0.20	$1s\,2\pi \rightarrow 1\pi^*\,1\pi^*$	
			+0.19	$1s \rightarrow 3p\pi$	
			+0.19	$1s \rightarrow 3d\pi/2\pi^*$	
$1a'$	535.18	0.012	0.95	$1s \rightarrow 3s\sigma/\sigma^*(C_3-H)$	108
$2a'$	535.64	0.003	0.94	$1s \rightarrow 3p\sigma$	121
$3a'$	535.86	<0.001	0.95	$1s \rightarrow 3p\sigma'$	156
$3a''$	535.97	0.004	0.79	$1s \rightarrow 3p\pi$	159
			+0.17	$1s \rightarrow 2\pi^*/3d\pi$	
$4a'$	536.73	0.007	0.95	$1s \rightarrow 3d\sigma$	174
$5a'$	536.82	0.026	0.80	$1s \rightarrow 3d\sigma'$	269
			0.12	$1s \rightarrow 3d\sigma''$	
$6a'$	536.84	0.004	0.81	$1s \rightarrow 3d\sigma''$	246
			0.14	$1s \rightarrow 3d\sigma'$	
$5a''$	536.85	0.002	0.36	$1s \rightarrow 3d\pi'$	233
			+0.30	$1s \rightarrow 2\pi^*/3d\pi$	
			+0.27	$1s \rightarrow 4p\pi$	
$4a''$	536.88	0.008	0.62	$1s \rightarrow 3d\pi'$	188
			+0.20	$1s \rightarrow 3d\pi/2\pi^*$	
			+0.11	$1s \rightarrow 2\pi^*/3d\pi$	
$7a''$	536.89	0.019	0.95	$1s \rightarrow 4p\pi$	267
$7a'$	536.96	0.013	0.91	$1s \rightarrow 4p\sigma$	230
$8a'$	537.16	0.031	0.69	$1s \rightarrow 4p\sigma'$	223
			0.25	$1s \rightarrow 4s\sigma$	
$9a'$	537.18	<0.001	0.72	$1s \rightarrow 4s\sigma$	245
			0.24	$1s \rightarrow 4p\sigma'$	
$6a''$	537.20	0.020	0.25	$1s \rightarrow 3d\pi/2\pi^*$	67
			+0.57	$1s\,2\pi \rightarrow 1\pi^*\,1\pi^*$	
Ion	538.37			$1s \rightarrow \infty$	
$10a'$	538.39	0.122	0.91	$1s \rightarrow \sigma^*(C-H)$	140
$8a''$	539.42	<0.001	0.82	$1s\,2\pi \rightarrow 1\pi^*\,3p\pi$	172
$9a''$	540.12	<0.001	0.61	$1s\,2\pi \rightarrow 1\pi^*\,2\pi^*$	182
			+0.17	$1s\,2\pi \rightarrow 1\pi^*\,4p\pi$	

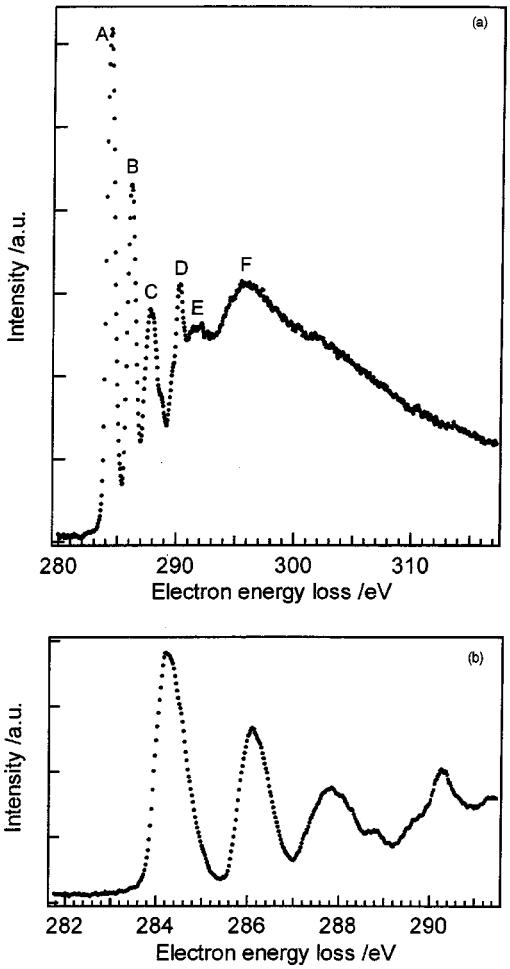

FIG. 3. (a) The electron energy-loss spectrum of 2-propenal recorded at the carbon *K* edge with an energy resolution of 0.17 eV, steps 48 meV. (b) The excitation spectrum in the 281.8–291.6 eV region recorded at a slightly higher resolution and 22 meV steps.

The fourth band *D* at 536.45 eV is assigned to excitation to the 3*d* MOs, with calculated energies between 536.73 and 536.88 eV. At higher energies, the experimental intensity increases quasilinearly. This energy range corresponds to $n > 3$ Rydberg states which accumulate until the ionization threshold (538.37 eV) is reached. The calculations predict two rather intense peaks around this threshold: the first one at 537.20 eV due to a shake up state and the second one at 538.39 eV coming from an excitation to a delocalized $\sigma^*(C-H)$ bond (Table IV). It is interesting to note that the same trends occur in the C 1*s* *K*-shell spectrum of benzene.[39] Moreover, if we assume that the energy of the shake up peak is overestimated, it could contribute to the observed *D* band.

Finally, the last band *E* located at 543.64 eV is beyond the reach of the calculations. Such a broad band is traditionally assigned to a σ^* shape resonance but this attribution remains very controversial, as explained in a recent review.[40]

Except for a slight overestimation of the calculated energies, the agreement between the experimental and theoretical spectra for the pre-edge energy region is good [Fig. 2(b)].

C. Carbon *K*-shell electron-energy loss spectrum

The experimental spectrum at the C 1*s* edge is shown in Fig. 3(a). As for the oxygen edge, the overall shape is similar to the condensed phases NEXAFS spectra[10] but with a much better resolution (0.17 eV compared with 0.80 eV). The energy of the observed bands is detailed in Table V, together with the condensed phases values. The spectrum is dominated by two intense bands, *A* and *B*, centered at 284.19 and 286.10 eV, respectively. The third band *C*, which appeared in the high energy side of band *B* in the low-resolution condensed phases NEXAFS spectra[10] is well resolved in the present work having its maximum at 287.83 eV. According to the photon polarization dependence of the intensity in the condensed phase spectra, these three bands have a π^* character. The *C* band exhibits fine structure especially in the 288.0–289.0 eV region as shown in Fig. 3(b). The next band *D* is centered at 290.25 eV with fine features, not well resolved, at 289.77 and 290.78 eV. It is followed by the *E* band at 291.87 eV. These two peaks (*D* and *E*) match the fourth and fifth peak of the condensed phase NEXAFS spectra which were observed at 289.70 and 291.70 eV, respectively.[10] Because of the slight photon polarization dependence in this energy range, it was suggested that the *D* and *E*

TABLE V. Energies of the spectral features in the gas phase C 1*s* ISEELS spectrum and in the condensed phases NEXAFS spectra.[a]

	This work	Monolayer/Pt(111)[a]	Multilayer[a]	Assignment[a]
A	284.19	285.00	285.00	$1sC_1, C_2 \rightarrow 1\pi^*$
B	286.10	287.00	287.00	$1sC_3 \rightarrow 1\pi^*$
C	287.83	287.85	288.15	$1sC_1, C_2 \rightarrow 2\pi^*$
C′	288.06			
C″	288.29			
C‴	288.72			
D′	289.77			
D	290.25	~290	289.70	$1sC_3 \rightarrow 1\pi^*$ $1sC_1, C_2, C_3 \rightarrow \sigma^*$
D″	290.78			
E	291.87	~291	291.70	$1sC_3 \rightarrow 1\pi^*$ $1sC_1, C_2, C_3 \rightarrow \sigma^*$
F	295.80		>294.00	$1sC_1, C_2, C_3 \rightarrow \sigma^*$

[a]Proposed assignments from Ref. 10.

bands had different (π^* and σ^*) symmetries. Finally, the last very broad band *F* appears at 295.80 eV [Table V, Fig. 3(a)].

The results of the calculations at the carbon edge are presented in Fig. 4 and in Table VI. For clarity, only peaks whose calculated intensity exceeds 2% of the most intense one are reported in Table VI. Thus, a large number of states (mainly Rydberg) do not appear. On the other hand, all the calculated peaks are displayed in Fig. 4, which also allows one to distinguish the contributions of the three carbon atoms.

As anticipated in Ref. 10, the calculations assign the *A* band to $1sC_1$ and $1sC_2$ excitations to the $1\pi^*$ MO, with quasidegenerate energies (284.42 and 284.39 eV, respectively). Similarly, the second band *B* is due to the $1sC_3 \rightarrow 1\pi^*$ excitation, calculated at 286.19 eV (Table VI). The calculated energies for these transitions (Table VI) are in excellent agreement with the experimental values (Table V).

The situation is more complicated in the case of the *C* band. As can be seen in Table VI, the calculations predict a large number of states in the 288 eV energy region, due to excitations of the C_1 and C_2 atoms of mostly $n=3$ Rydberg-type. Those shown in Table VI have relatively high intensities, due to a slight $\sigma^*(C-H)$ and $2\pi^*$ valence character in the 3*s*, 3*p*, and 3*d* MOs. Conversely, the C_1 and C_2 $2\pi^*$ MOs has a diffuse character. Nevertheless, it is clear that the most intense peak is the $1sC_2 \rightarrow 2\pi^*$ excitation, which has a rather mixed CI wave function. This state is predicted at an energy of 287.94 eV, and a relative intensity of 0.323 with respect to the *B* band (Table VI). It is mainly responsible for the *C* band. This assignment is consistent with the π^* character of this band deduced from the photon polarization dependence of the condensed phases NEXAFS spectra.[10] It is also remarkable that the equivalent state for the C_1 atom is predicted at a similar energy (288.03 eV) but with a low intensity (only 0.023, Table VI). The equivalent state for the C_3 atom is calculated at an energy of 288.76 eV with an intensity of 0.123. Excitation of these states and of Rydberg states explains the fine structure observed in the experimental spectrum in the 288–289 eV range. From their $\langle r^2 \rangle$ values (81, 77, and 64 a.u.^{2}, respectively), the three most intense states have valence character.

The next maximum *D* observable in the experimental spectrum is located at 290.25 eV, with weak features at 289.77 and 290.78 eV (Table V). This *D* band corresponds to the fourth peak of the condensed phase NEXAFS spectra,[10] located at 289.70 eV and tentatively assigned to $\sigma^*(C-H \text{ or } C=O/C=C)$ and/or $1sC_3 \rightarrow 2\pi^*$ excitations, due to a weak photon polarization dependence. The calculations show a somewhat different picture: The 290 eV energy range corresponds to the excitation to the 3*d*, 3*p*, and 4*p* Rydberg MOs of the C_1 and C_2 atoms. The most intense of these transitions are shown in Table VI. Moreover, the calculations predict the beginning of the Rydberg series for the C_3 atom, with $1sC_3 \rightarrow 3s\sigma/\sigma^*(C_3-H)$ calculated at 290.24 eV. The most striking result is the intensity of this transition (16.2% of the $1sC_3 \rightarrow 1\pi^*$ peak). This is due to the strong valence character of this MO, reflected by its rather weak $\langle r^2 \rangle$ value of 92 a.u.^{2} We have already studied the importance of such a valence-Rydberg mixing of the $\sigma^*(C-H)$ MO in the case of benzene.[39] We conclude that the *D* peak is mainly due to this transition.

Another question arises from comparison of the relative intensities of the spectral bands between the gas and condensed phases: While the intensity of the *D* band is slightly larger that those of the *C* and *E* ones in the gas phase, it is weaker in the mono- and multilayer cases (compare Fig. 4 in the present work and Figs. 17 and 21 in Ref. 10). As no Rydberg states are expected to contribute to the condensed phase spectra, in these the *D* band arises from a pure $1sC_3 \rightarrow \sigma^*(C_3-H)$ transition; its intensity should be larger than that for $1sC_3 \rightarrow 3s\sigma/\sigma^*(C_3-H)$ which has a diffuse character. A possible explanation could be the presence of the several Rydberg states in the gas phase spectra all contributing to and enhancing the intensity as described earlier.

The *E* band located at 291.87 eV corresponds to the fifth one observed at 291.70 eV in the condensed phases NEXAFS spectra[10] and assigned to $\sigma^*(C-H \text{ or } C=O/C=C)$ and/or $1sC_3 \rightarrow 2\pi^*$ excitations. It is close to the C_1 and C_2 ionization thresholds predicted to occur at 291.48 and 291.47 eV, respectively (Table II). According to the calculations (Table VI), this region corresponds to the 3*p* and 3*d* transitions of C_3, with rather weak intensities accompanied by several excitations of the C_1 and C_2 atoms to σ^* MOs. These σ^* orbitals are delocalized but have mainly a C–H character. The presence of a π^* transition, namely the $1sC_3 \rightarrow 3d\pi/2\pi^*$ one at 291.42 eV, could explain the weak photon polarization dependence of this band in the condensed phases NEXAFS spectra.[10] Its rather large intensity is explained by its valence character ($\langle r^2 \rangle = 105$ a.u.^{2}) due to the $1sC_3\, 2\pi \rightarrow 1\pi^*\, 1\pi^*$ component of the wave function. Conversely, the $1sC_3 \rightarrow 2\pi^*/3d\pi$ state, which has a diffuse character ($\langle r^2 \rangle = 140$ a.u.^{2}), is calculated to occur at 292.35 eV (Table VI).

TABLE VI. Calculated energies, relative intensities, and assignments of C 1*s* core excited states of 2-propenal.

			Main configurations							
State	E(eV)	I	C_1		C_2		C_3		$\langle r^2 \rangle$	Assignment
a''	284.39	0.456		0.90	$1sC_2 \rightarrow 1\pi^*$				68	*A*
a''	284.42	0.675	0.92	$1sC_1 \rightarrow 1\pi^*$					69	*A*
a''	286.19	1.000				0.89	$1sC_3 \rightarrow 1\pi^*$		63	*B*
a'	287.79	0.034	0.95	$1sC_1 \rightarrow 3s\sigma/\sigma^*(C_1-H)$					91	
a'	287.93	0.038			0.95	$1sC_2 \rightarrow 3s\sigma/\sigma^*(C_2-H)$			95	
a''	287.94	0.323			0.48	$1sC_2 \rightarrow 3p\pi/2\pi^*$			81	*C*
					+0.27	$1sC_2 \rightarrow 2\pi^*/3d\pi$				
a''	288.03	0.023	0.32	$1sC_1 \rightarrow 2\pi^*/3d\pi$					77	*C′*
			+0.31	$1sC_1 \rightarrow 3d\pi/2\pi^*$						
			+0.19	$1sC_1 \rightarrow 3p\pi$						
a'	288.29	0.047			0.94	$1sC_2 \rightarrow 3p\sigma/\sigma^*(C_2-H)$			101	*C″*
a''	288.76	0.123					0.27	$1sC_3 \rightarrow 3p\pi/2\pi^*$	64	*C‴*
							+0.25	$1sC_3 \rightarrow 3d\pi/2\pi^*$		
							+0.20	$1sC_3\, 2\pi \rightarrow 1\pi^*\, 1\pi^*$		
							+0.10	$1sC_3 \rightarrow 2\pi^*/3d\pi$		
a''	288.96	0.064	0.77	$1sC_1 \rightarrow 3p\pi$					126	
			+0.13	$1sC_1 \rightarrow 3d\pi/2\pi^*$						
a'	289.63	0.033	0.82	$1sC_1 \rightarrow 3d\sigma'$					151	*D′*
			+0.13	$1sC_1 \rightarrow 3d\sigma''$						
a'	289.74	0.025			0.86	$1sC_2 \rightarrow 3d\sigma''$			190	*D′*
a'	289.86	0.033	0.88	$1sC_1 \rightarrow 4p\sigma$					262	*D′*
a''	289.88	0.027			0.54	$1sC_2 \rightarrow 3d\pi/2\pi^*$			179	*D′*
					+0.16	$1sC_2 \rightarrow 2\pi^*/3d\pi$				
					+0.14	$1sC_2 \rightarrow 4p\pi$				*D′*
					+0.12	$1sC_2 \rightarrow 3d\pi'/2\pi^*$				*D*
a''	290.09	0.029	0.83	$1sC_1 \rightarrow 4p\pi$					286	
a'	290.24	0.162					0.95	$1sC_3 \rightarrow 3s\sigma/\sigma^*(C_3-H)$	92	
a'	290.90	0.021					0.94	$1sC_3 \rightarrow 3p\sigma$	108	
a'	291.14	0.164	0.78	$1sC_1 \rightarrow \sigma_1^*(C_1-H)$					112	
			+0.14	$1sC_1 \rightarrow \sigma_2^*(C_1-H)$						
a'	291.26	0.062			0.77	$1sC_2 \rightarrow \sigma_1^*(C-H)$			105	
					+0.14	$1sC_2 \rightarrow \sigma_2^*(C-H)$				
a'	291.35	0.105	0.77	$1sC_1 \rightarrow \sigma_2^*(C_1-H)$					107	
			+0.14	$1sC_1 \rightarrow \sigma_1^*(C_1-H)$						
a''	291.42	0.063					0.35	$1sC_3 \rightarrow 3d\pi/2\pi^*$	105	
							+0.24	$1sC_3\, 2\pi \rightarrow 1\pi^*\, 1\pi^*$		
	291.47				$1sC_2 \rightarrow \infty$					
	291.48		$1sC_1 \rightarrow \infty$							
a'	291.60	0.028			0.77	$1sC_2 \rightarrow \sigma_2^*(C-H)$			110	
					+0.14	$1sC_2 \rightarrow \sigma_1^*(C-H)$				
a'	291.94	0.050					0.93	$1sC_3 \rightarrow 3d\sigma$	173	*E*
a'	292.00	0.096			0.82	$1sC_2 \rightarrow \sigma_3^*(C-H)$			126	*E*
a''	292.35	0.058					0.67	$1sC_3 \rightarrow 2\pi^*/3d\pi$	140	
							+0.10	$1sC_3\, 2\pi \rightarrow 1\pi^*\, 1\pi^*$		
	293.82							$1sC_3 \rightarrow \infty$		

The last observable band *F* is centered at 295.80 eV. It is also present in the condensed phases NEXAFS spectra,[10] although it is difficult to be precise about its energy. Taking the same precautions as for the O 1*s* edge, we tentatively assign it to a σ^* ''shape resonance.''

The comparison between the pre-edge experimental and convoluted theoretical spectra is shown in Fig. 5. The calculated positions and intensities of the peaks are seen to be in good agreement with experiment.

V. CONCLUSIONS

In this work, the inner shell electron energy loss spectra of gaseous 2-propenal have been measured for the first time at the C 1*s* and O 1*s* edges with 0.17 eV resolution, sufficient to resolve the transitions of the C atoms with different chemical environments. Accompanying *ab initio* configuration interaction calculations using large scale configuration interaction have allowed assignment of the experimental features.

At the O 1*s* edge the spectrum is dominated by excitation of the $1\pi^*$ and $2\pi^*$ states. The calculated energies and intensities of the spectral bands are in good agreement with experiment.

At the C 1*s* edge, the two most intense bands at 284.19 and 286.10 eV are due to the $1sC_{1,2} \rightarrow 1\pi^*$ and $1sC_3 \rightarrow 1\pi^*$ states, the transitions from C_1 and C_2 being calcu-

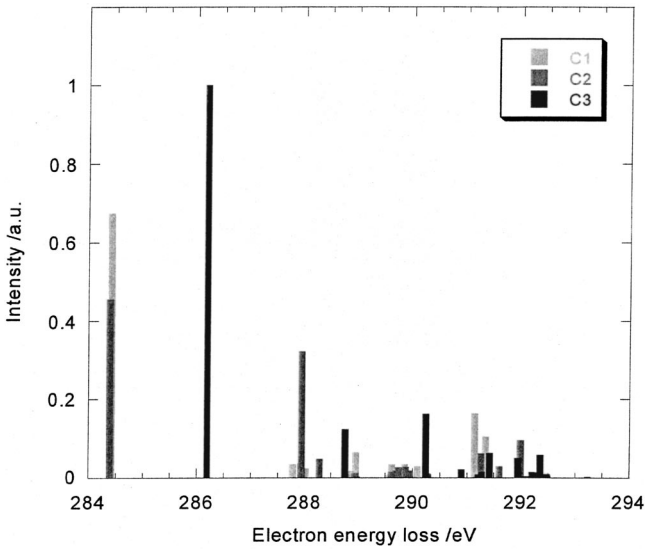

FIG. 4. Calculated *K* edge bar spectra of the three nonequivalent carbon atoms in 2-propenal.

lated to be nearly degenerate. Excitation to the $2\pi^*$ MO from C_1 is observed at 287.94 eV with a calculated intensity much lower than the $1sC_{2s} \rightarrow 2\pi^*$ transition. Excitation to the $2\pi^*$ state from C_3 is also observed but with a lower intensity than those to the $1\pi^*$ state. In the 290.25 eV region the spectral features are due to Rydberg transitions from C_1 and C_2 and to the $3s\sigma/\sigma^*$ (C_3-H) transition from C_3. The experimental spectrum is very well reproduced by the calculations, both for intensities and energies of the spectral features. For calculated binding energies, the same trend is predicted as for the excitation energies, the chemical shift being negligible between C_1 and C_2 and much larger for C_3.

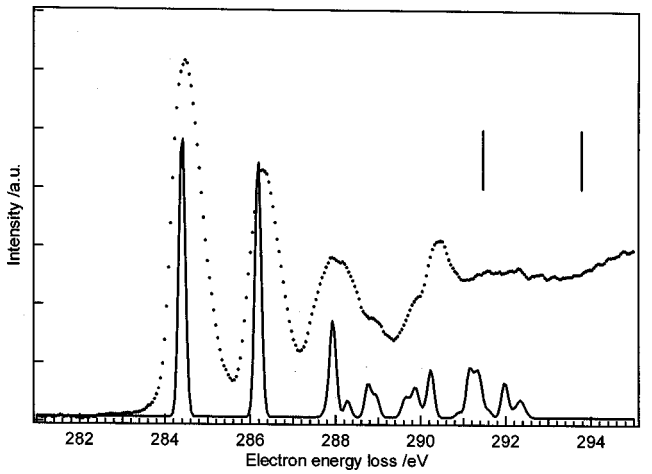

FIG. 5. Comparison between the experimental and the theoretical spectra at the carbon *K* edge. The vertical lines indicate the locations of the ionization thresholds.

ACKNOWLEDGMENTS

The ''Laboratoire de Physique des Lasers, Atomes et Molécules'' (PhLAM) is ''Unité Mixte de Recherche du CNRS.'' The ''Center d'Etudes et de Recherches Lasers et Applications'' (CERLA) is supported by the ''Ministère chargé de la Recherche'', the ''Région Nord/Pas-de-Calais'' and the ''Fonds Européen de Développement Economique des Régions'' (FEDER). Part of the computations was carried out at the CRI (Center de Ressources Informatiques), on the IBM-SP3 computer which is supported by the ''Program de Calcul Intensif et Parallèle'' of the ''Ministère chargé de la Recherche,'' the ''Région Nord/Pas-de-Calais'' and the FEDER. This research has been supported by the Fonds National de la Recherche Scientifique and the Patrimoine of University of Liège. M.-J.H.-F. wishes to acknowledge the Fonds National de la Recherche Scientifique for research position.

[1] A. D. Walsh, Trans. Faraday Soc. **41**, 498 (1945); **42**, 66 (1946).
[2] M. F. Arendt, P. W. Browning, and L. J. Butler, J. Chem. Phys. **103**, 5877 (1995).
[3] C. E. Canosa-Mas, S. Carr, M.D. King, D. E. Shallcross, K. C. Thompson, and R. P. Wayne, Phys. Chem. Chem. Phys. **1**, 4195 (1999).
[4] C. E. Canosa-Mas, E. S. N. Cotter, J. Duffy, K. C. Thompson, and R. P. Wayne, Phys. Chem. Chem. Phys. **3**, 3075 (2001).
[5] J. E. Dickens, W. M. Irvine, A. Nummelin, H. Møllendal, S. Saito, S. Thorwith, A. Hjalmarson, and M. Ohishi, Spectrochim. Acta, Part A **57**, 643 (2001).
[6] J. B. Wright and J. Pranata, J. Mol. Struct.: THEOCHEM **460**, 67 (1999).
[7] M. Akita, N. Osaka, and K. Itoh, Surf. Sci. **405**, 172 (1998).
[8] J. C. de Jesús and F. Zaera, Surf. Sci. **430**, 99 (1999).
[9] J. C. de Jesús and F. Zaera, J. Mol. Catal. A: Chem. **138**, 237 (1999).
[10] F. Bournel, C. Laffon, Ph. Parent, and G. Tourillon, Surf. Sci. **350**, 60 (1996).
[11] F. Bournel, C. Laffon, Ph. Parent, and G. Tourillon, Surf. Sci. **359**, 10 (1996).
[12] C. W. Bock, Y. N. Panchenko, and S. V. Krasnoshchiokov, Chem. Phys. **125**, 63 (1988).
[13] S. Thakur, V. P. Gupta, and B. Ram, Spectrochim. Acta, Part A **53**, 749 (1997).
[14] V. Durier, A. Zanoun, A. Belaidi, and G. Vergoten, J. Mol. Struct. **476**, 271 (1999).
[15] W. H. Fang, J. Am. Chem. Soc. **121**, 8376 (1999).
[16] K. W. Paulisse, T. O. Friday, M. L. Graske, and W. F. Polik, J. Chem. Phys. **113**, 184 (2000).
[17] C. E. Brion, Comments At. Mol. Phys. **16**, 249 (1985).
[18] J. Stöhr, *NEXAFS Spectroscopy*, Springer Series in Surface Science (Springer, Berlin, 1992).
[19] C. Hannay, J. Heinesch, U. Kleyens, and M.-J. Hubin-Franskin, Meas. Sci. Technol. **6**, 1140 (1995).
[20] M.-J. Hubin-Franskin, H. Aouni, D. Duflot, F. Motte-Tollet, C. Hannay, L. F. Feirrera, and G. Tourillon, J. Chem. Phys. **106**, 35 (1997).
[21] M.-J. Hubin-Franskin and J. Heinesch, Nucl. Instrum. Methods Phys. Res. A **477**, 546 (2002).
[22] F. Currell and C. M. John, Meas. Sci. Technol. **3**, 1192 (1992).
[23] R. N. S. Sodhi and C. E. Brion, J. Electron Spectrosc. Relat. Phenom. **34**, 363 (1984).
[24] F. W. Bobrowicz and W. A. Goddard, in *Methods of Electronic Structure Theory*, edited by H. F. Shaefer III (Plenum, New York, 1977), Chap. 4.
[25] G. Chaban, M. W. Schmidt, and M. S. Gordon, Theor. Chem. Acc. **97**, 88 (1997).
[26] M. W. Schmidt, K. K. Baldridge, J.A. Boatz *et al.* J. Comput. Chem. **14**, 1347 (1993).
[27] S. Bodeur, P. Millié, and I. Nenner, Phys. Rev. A **41**, 252 (1990).
[28] T. Koopmans, Physica (Amsterdam) **1**, 104 (1933).
[29] E. R. Davidson, J. Comput. Phys. **17**, 87 (1975).
[30] B. Huron, J-P. Malrieu, and P. Rancurel, J. Chem. Phys. **58**, 5745 (1973); S. Evangelisti, J.-P. Daudey, and J.-P. Malrieu, Chem. Phys. **75**, 91 (1983).

[31] R. Cimiraglia, J. Chem. Phys. **83**, 1746 (1985); R. Cimiraglia and M. Persico, J. Comput. Chem. **8**, 39 (1987); R. Cimiraglia, Int. J. Quantum Chem. **60**, 167 (1996).
[32] C. Angeli, R. Cimiraglia, M. Persico, and A. Toniolo, Theor. Chem. Acc. **98**, 57 (1997).
[33] T. H. Dunning, J. Chem. Phys. **55**, 716 (1971).
[34] T. H.Dunning, Jr. and P. J. Hay, Chapter 1 in Ref. 24, pp 1–27.
[35] E. A. Cherniak and C. C. Costain, J. Chem. Phys. **45**, 104 (1966).
[36] C. Blom, G. Grassi,, and A. Bauder, J. Am. Chem. Soc. **106**, 7427 (1984).
[37] C. E. Blom, R. P. Møller, and Hs. H. Gønthard, Chem. Phys. Lett. **73**, 483 (1980).
[38] G. Distefano, M. Guerra, D. Jones, and A. Modelli, Chem. Phys. **68**, 383 (1982).
[39] D. Duflot, J.-P. Flament, J. Heinesch, and M.-J. Hubin-Franskin, J. Electron Spectrosc. Relat. Phenom. **113**, 79 (2000).
[40] M. N. Piancastelli, J. Electron Spectrosc. Relat. Phenom. **100**, 167 (1999).

Article 13

JOURNAL OF CHEMICAL PHYSICS VOLUME 119, NUMBER 17 1 NOVEMBER 2003

Core shell excitation of furan at the O1*s* and C1*s* edges: An experimental and *ab initio* study

D. Duflot[a] and J.-P. Flament
Laboratoire de Physique des Lasers, Atomes et Molécules (PhLAM), UMR CNRS 8523, Centre d'Etudes et de Recherches Lasers et Applications (CERLA, FR CNRS 2416), Université des Sciences et Technologies de Lille, F-59655 Villeneuve d'Ascq Cedex, France

A. Giuliani, J. Heinesch, and M.-J. Hubin-Franskin[b]
Université de Liège, Laboratoire de Spectroscopie d'Electrons diffusés, Institut de Chimie B6c, Sart Tilman-B4000 Liège 1-Belgium

(Received 4 June 2003; accepted 14 July 2003)

The K-shell spectra of gaseous furan have been measured using the inner-shell electron energy loss spectroscopy (ISEELS) method at the carbon and oxygen thresholds. Large-scale *ab initio* configuration interaction calculations have been carried out in order to help in the assignments of the observed bands. The spectra are close to previous low resolution ones obtained using ISEELS in the gas phase and photoabsorption with the synchrotron radiation in gaseous and condensed phases. The presence of a new feature located at 287.3 eV in the C1*s* spectrum and recently detected by photoabsorption with synchrotron radiation is confirmed. At both edges, the calculations confirm the assignments proposed in earlier experimental works, with the exception of several C1*s* pre-edge features for which a new interpretation is given. © *2003 American Institute of Physics.*
[DOI: 10.1063/1.1606441]

I. INTRODUCTION

The furan molecule C_4H_4O is a member of the five-member heterocyclic C_4H_4X family, comprising also thiophene and pyrrole. This type of molecules constitutes the smallest aromatic species. They are used as building blocks for conducting polymers.[1] They are of basic importance in biochemistry as structural units in several drugs and biologically active molecules such as chlorophyll, vitamin B12, and biotin.[2,3] They are also present in crude petroleum, coal, and biomass resources and because of their various nocuous effects, their removal represents a challenge in petrochemical industry.[4–7] For these reasons, the chemistry of furan on various substrates has been the subject of many works,[8–14] as well as theoretical calculations.

In the gas phase, the spectroscopy of furan has been studied extensively with many experimental techniques.[15–22] and *ab initio* calculations.[23–25] While most of these studies concentrated on the valence region, the core excitation spectroscopy of furan has attracted much less attention. Moreover, most of these studies focused on the core-ionization spectra.[26–28] To the best of our knowledge, the core excitation spectra were measured at both carbon and oxygen edges some time ago by Newberry *et al.*[29] using the electron energy loss spectroscopy (ISEELS) method with a low resolution. Recently, the partial electron yield has been recorded at a much better resolution, but only in the pre-edge region.[30] Two low resolution NEXAFS spectra of condensed (monolayer and multilayer) furan are also available, but only at the carbon edge.[31,32]

Our goal in this paper is to present new core excitation spectra of gaseous furan obtained with the ISEELS method in electric dipolar excitation conditions. The ISEELS spectra of furan have been recorded at the C1*s* and O1*s* edges with a resolution of 0.17 eV, the resolution being the same at both edges. In order to help in the assignment of the observed spectral features, large-scale *ab initio* configuration interaction (CI) calculations have been carried out.

This paper is organized as follows: The experimental setup is described in Sec. II; the computational method is outlined in Sec. III; Sec. IV presents the discussion of the results and some conclusions are given in Sec. V.

II. EXPERIMENT

The inner-shell electron energy loss spectra were obtained with a VSW spectrometer that has been adapted for gas studies and high-energy electron beams and has been equipped with a homemade position-sensitive multidetector system in order to improve data collection times. The experimental apparatus and procedure have been described in detail previously.[33–35]

Briefly, the spectrometer consists of an electrostatic 180° monochromator operating in the constant pass energy mode, a collision chamber, and an electrostatic analyzer identical to the monochromator. The monochromatized incident electrons are accelerated up to 2 keV and focused into the collision chamber using a four-element electron lens. The electrons are slightly deflected (0.02 rad) by two sets of $X-Y$ plates inside the collision chamber. The scattered electrons are energy analyzed and focused onto the entrance slit of the analyzer by a lens similar to that used for acceleration. In the collision conditions of low angular-

[a]Electronic mail: denis.duflot@univ-lillel.fr
[b]Directeur de recherche F.N.R.S.

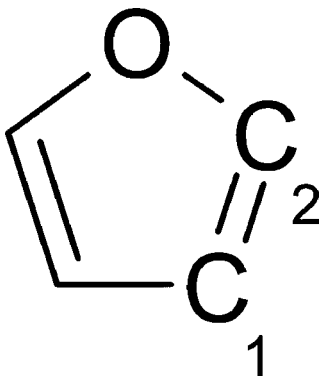

FIG. 1. Labeling of atoms in furan.

momentum transfer (i.e., high-incident energy and small scattering angle), electronic electric–dipolar transitions are primarily excited.

Inside the vacuum vessel, a residual pressure of less than 1×10^{-8} Torr is maintained by a cryogenic pumping system. The electron gun and the analyzer regions are differentially pumped by turbomolecular pumps, respectively.

The detection system consists of an assembly of two microchannel plates, a phosphor screen, fiber-optic couplers, and an area array coupled charge device (CCD) sensor. The driving and reading electronics for the detector have been adapted to the electron-energy loss experiment. The spectra result from the accumulation of the data from each channel of the detector, which removes any detector-sensitivity variation.[4,36]

The accelerating and retarding voltages were constant to within 10 ppm/°C. The spectra have been recorded with 0.04 and 0.020 eV steps.

In order to take into an account valence and lower-energy inner-shell excitation cross section, a background has been subtracted from the raw spectra by extrapolating a least-square fit of the pre-edge experimental data points. The absolute energy scales were determined by calibrating the C1*s* spectrum relative to the $C1s\rightarrow\pi^*(\nu'=0)$ band in CO[37] at 287.40 ± 0.02 eV and the O1*s* spectrum relative to the $O1s\rightarrow\pi^*(\nu'=0)$ value for the same molecule[8] at 534.21 ± 0.09 eV. The spectrum of a mixture of furan and CO was recorded with each gas being let into the collision region through a separate leak to ensure a constant composition mixture. The uncertainty on the measured energies is of 0.06 and 0.13 eV for the C1*s* and O1*s* spectra, respectively.

The sample is a commercial one from ACROS with a stated purity of 99.0%. It was used directly without further purification, except for repetitive freeze–pump–thaw cycles in order to eliminate air and other volatile impurities in the sample.

III. COMPUTATIONAL METHOD

The computational method used has been described in detail elsewhere[38] and will be briefly summarized. The basic assumption[39] is to use the molecular orbitals (MOs) of the core *ionized* molecule (calculated using the ROHF-GVB method implemented in the GAMESS-US package[40]) as a good approximation for the description of the core *excited* states. Thus, the energy corresponding to the $1s\rightarrow i^*$ core excited state may be obtained from the MP2 core ionization energy $E(1s\rightarrow\infty)$ as

$$E(1s\rightarrow i^*)=E(1s\rightarrow\infty)+\epsilon_{i*}+P+C,$$

where ϵ_{i*} is the monoelectronic energy of the i^* MO. The P term represents the residual relaxation of the core ion electron density due to the i^* electron, while the correlation term C takes into account the correlation effects induced by the presence of the i^* electron. P is obtained by performing a configuration interaction (CI) calculation in the monoexcitation space of all the calculated $1s\rightarrow i^*$ states. In order to evaluate the C term, the resulting CI wave functions serve as the zeroth-order space for a multireference MP2 calculation using the three-class diagrammatic CIPSI method.[41,42] In order to reduce the computational time, the extrapolation procedure proposed by Angeli[43] was used with six thresholds between 99.4% and 99.9% of the exact wave functions. Finally, the dipolar electric transition moments with respect to the ground state of the molecule were computed.

At the C1*s* edge, the furan molecule contains two pairs of equivalent carbon atoms (see Fig. 1). For the calculation of the core ionized states, core hole localization has been assumed and the coupling between excitations from different core holes has been neglected. The molecular symmetry has been reduced accordingly from C_{2v} to C_s. This question has been discussed (for the core ions) by Rennie *et al.*,[30] who concluded that the C_2 core holes are probably completely localized while the C_1 holes could be partially delocalized. An accurate treatment of this question requires taking into account vibronic coupling and is beyond the scope of the present calculations.

The Gaussian atomic orbitals (AOs) used is the TZP basis set taken from Dunning.[44,45] For the calculation of the core-excited states, a set of Rydberg orbitals[11] $(3s,3p,3d,4s,4p)$ was added on the core-excited atom.

IV. RESULTS AND DISCUSSION

The calculated HF electronic configuration of the $\tilde{X}\,^1A_1$ neutral ground state of furan is

$$1a_1^2 1b_2^2 2a_1^2 3a_1^2 2b_2^2 4a_1^2 5a_1^2 3b_2^2 4b_2^2 6a_1^2 7a_1^2 1b_1^2 5b_2^2 6b_2^2 8a_1^2 9a_1^2 2b_1^2 1a_2^2.$$

TABLE I. Calculated geometry of furan compared with previous works (bond lengths in Å and angles in degrees).

	RHF[a]	MP2[a]	MP2[b]	MP2[c]	B3LYP[d]	Exp.[e]
	TZP	TZP	cc-pVDZ	DZP	cc-pVTZ	MW
$O-C_2$	1.343	1.362	1.364	1.364	1.361	1.362
$C_1{=}C_2$	1.338	1.366	1.378	1.374	1.354	1.361
C_1-C_1	1.441	1.429	1.436	1.433	1.432	1.430
C_1-H_1	1.068	1.075	1.088	1.078	1.075	1.075
C_2-H_2	1.067	1.073	1.089	1.079	1.076	1.077
C_2-O-C_2	107.3	106.7	106.7	106.9	106.8	106.6
$O-C_2-C_1$	110.7	110.5	110.8	110.5	110.4	110.7
$C_2-C_1-C_1$	105.6	106.1	105.6	106.0	106.2	106.1
$O-C_2-H_2$	116.4	115.8	115.8	115.7	115.9	116.0
$C_2-C_1-H_1$	126.7	126.2	126.3	127.9	127.3	127.8

[a]This work.
[b]Reference 23.
[c]Reference 17.
[d]Reference 48.
[e]Reference 49.

The five first MOs are the $1s$ orbitals of the oxygen and carbon atoms. Qualitatively, the $1b_1$ MO represents the out-of-plane oxygen lone pair while the $2b_1$ and $1a_2$ MOs are the C=C 1π and 2π (HOMO) bonds. Their antibonding counterparts are the $3b_1(1\pi^*)$ MO (LUMO) and the $2a_2(2\pi^*)$ ones. According to the selection rules in the symmetry groups of the core excited species (C_{2v} at the O1s edge and C_s at the C1s one), all electronic transitions are electric dipole allowed, except the $1s(O)\rightarrow a_2$ ones.

The calculated geometries of the ground state of furan, obtained at the HF and MP2 levels, are compared with previous experimental[46] and theoretical[23,47,48] determinations in Table I (a detailed discussion on the calculated geometries of furan may be found in Ref. 48). Since the MP2 values are very close to the experimental ones, all the calculations were carried out at this geometry to obtain the vertical excitation energies.

A. Core ionization energies

The core ionization energies of furan have been measured in several studies, both in gas[26–28] and condensed (monolayer and multilayer) phases.[31,32] The O1s ionization energy was also calculated using *ab initio* methods.[49,50] The results of these earlier studies are compared with our own calculations in Table II. It is well known[51] that the condensed phases values are lowered with respect to the gas phase ones because of the surface work function and relaxation effects. Thus, it is not possible to use the condensed phases values to test the accuracy of the calculations.

In the gas phase, at the C1s edge, the values (Table II) of Chambers and Thomas[27] (290.60 eV for C_1 and 291.81 eV for C_2) are slightly above the two other determinations (290.3 and 291.5 eV from Ref. 26 and 290.32 and 291.59 eV from Ref. 28). Our ΔSCF results (290.94 and 292.10 eV) are overestimated by ≈0.3–0.6 eV for both atoms. Our ΔMP2 values (290.73 and 291.98 eV) are close to those of Chambers and Thomas[27] but still slightly above the two other results by about 0.4 eV. Nevertheless, both the theoretical and experimental results are consistent with a chemical shift of about 1.2 eV in favor of the C_1 atom.

TABLE II. Core ionization energies (eV) of furan.

	C1s			O1s
	C_1	C_2	Shift	
Experiment				
Gas phase[a]	290.3(1)	291.5(1)	1.20(6)	539.4(1)
Gas phase[b]	290.60(6)	291.81(6)	1.22(2)	539.95(4)
Gas phase[c]	290.32(6)	291.59(6)	1.27	
Au thin films[d]	285.6(2)	286.7(2)	1.1	535.8(2)
Ag(110) submonolayer[e]	284.8(3)	286.2(3)	1.4	
Ag(110) monolayer 171 K[e]	284.7(3)	286.1(3)	1.4	
Ag(110) monolayer 135 K[e]	284.8(3)	286.2(3)	1.4	533.8(3)
Multilayer[e]	285.2(3)	286.4(3)	1.2	534.1(3)
Calculations				
TOM[f]				540.2
ΔSCF[g]				539.38
ΔSDCI[g]				539.19
ΔSCF[h]	290.94	292.10	1.16	539.54
ΔMP2[h]	290.73	291.98	1.25	540.44
ΔSDCI[h]				540.83
Δ(SDCI+MP2)[h]				540.11
Δ(SDCI+EN2)[h]				540.11

[a]Reference 26.
[b]Reference 27.
[c]Reference 30.
[d]Reference 28.
[e]Reference 32.
[f]Transition Operator Method (Ref. 50).
[g]Reference 51.
[h]This work. Energies calculated using the TZP+Rydberg basis set at the MP2/TZP optimized geometry.

At the O1s edge, the two experimental determinations differ by ≈0.6 eV (539.4 eV from Ref. 21 and 539.95 eV from Ref. 22, the last column of Table II). Previous *ab initio* calculations[49,50] also predict different values: while the Transition operator method,[50] based on the ΔSCF energy corrected by relaxation effects, leads to 540.2 eV, another study[49] gives 529.38 eV at the ΔSCF and 539.19 eV at the ΔSDCI level. Our own ΔSCF calculation (539.54 eV) is consistent with the lowest value. In this case, our MP2 value (540.44 eV) would be overestimated by about 1 eV, which is rather large. In order to obtain a more reliable estimation of this core ionization energy, additional calculations were carried out at the SDCI level on the ground and core ionized states. The resulting CI wave functions were then perturbed at the MP2 level using the diagrammatic CIPSI method, but without using the extrapolation procedure. The results are shown in the last lines of Table II: The ΔSDCI value is 540.83 eV, i.e., higher than the ΔMP2 value. The Δ(SDCI +MP2) result, which is the most sophisticated one, gives 540.11 eV. Moreover, the use of the Epstein–Nesbet partition[52,53] of the Hamiltonian, instead of the barycentric Møller–Plesset one, gives exactly the same value. In this case, the experimental result at 539.95 eV should be preferred, and our ΔMP2 result would be overestimated by about 0.5 eV. This is consistent with the fact that the calculated core excited energies seem also overestimated by about 0.5 eV when compared to the experimental values, as explained in the next section.

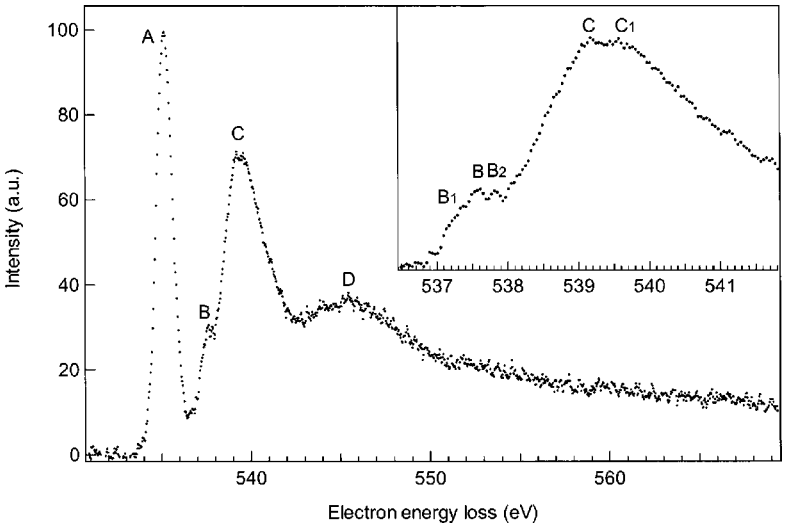

FIG. 2. (a) The electron energy-loss spectrum of furan recorded at the oxygen K edge with an energy resolution of 0.17 eV, steps 40 meV.

B. Oxygen K-shell electron-energy loss spectrum

The O1*s* edge electron energy loss spectrum of furan is shown in Fig. 2, while the energies of the observed bands are indicated in Table III. To the best of our knowledge, the only other available spectrum was published by Newberry *et al.*[29] using the ISEELS method with a resolution of 0.7 eV. Both spectra are similar and the energies of the four main features are close to each other (Table III). However, due to the better resolution (0.17 eV), one can observe some fine features in the second and third peaks (see the inset in Fig. 2). The last column of Table III shows the proposed assignments of Newberry *et al.*[29]

The results of the calculated O1*s* core excited states are presented in Table IV and the corresponding synthetic spectrum is shown in Fig. 3. The comparison between the calculated and measured energies of the most intense peaks shows that the theoretical values present a systematic overestimation of about 0.5 eV as the ionization energy. This implies that the calculated term values (TVs) should be close to the experimental ones.

Concerning the first peak A (located at 535.15 eV), the calculations assign it without ambiguity to the $1s(\mathrm{O}) \rightarrow 1\pi^*(3b_1)$ transition, as proposed by Newberry *et al.*[29] The calculated TV for this band (4.79 eV, Table IV) is in very good agreement with the experimental one (4.80 eV, Table III).

The second band B is centered at 537.57 eV (TV=2.38 eV) and exhibits fine features at 537.2 and 537.81 eV. Based on the TV, Newberry *et al.*[29] assigned it to the $1s(\mathrm{O}) \rightarrow 3p$ transition. This is consistent with our calculations since the three $3p$ transitions are predicted to have TVs of 2.4 eV (Table IV). However, the calculated intensities appear to be very small: 3% of the $1\pi^*$ transition intensity, compared to about 30% in the experimental spectrum. Thus, it is possible that other transitions might contribute to this band. Possible candidates are the two A_2 states (the mixing of $2\pi^*$ and $3d\pi$ excitations), whose calculated TVs are 1.9 eV (Table IV). Since this type of transition is dipole electric forbidden, their presence in the spectrum would be due to a quadrupole excitation, as already suggested by Newberry *et al.*[29] In order to test this hypothesis, we have calculated the quadrupole electric transition intensities for these two states, which were found to be negligible. The O1*s* spectrum of solid furan would clarify the situation. Since this spectrum does not seem to be available, the B region is assigned to Rydberg transitions. A comparison of the results of the calculations with the experiments lead to assign the B1 feature to the transition to $3p\sigma'$, the B band at 537.57 eV to the $3p\sigma$ and the not well-resolved B2 feature to excitation of the $3d\sigma$.

At higher energies, the calculations predict the transitions to $3d$, $4s$, and $4p$ Rydberg transitions, with very small intensities. These states, with higher Rydberg transitions that were not included in the present calculations, contribute to the fine features not well resolved on the low-energy side of the C band (Fig. 2), until the ionization threshold is reached (around 540 eV). The C band appears to be very large (a FWHM of about 2 eV) and the maximum exhibits at least two features located at 539.17 and 539.57 eV (Table III and Fig. 2), corresponding to TVs of 0.78 and 0.38 eV. According to the calculations (Table IV), this band is due to two σ^* transitions, calculated at TVs of 0.65 and 0.39 eV). Although the σ^* MOs involved in these transitions are delocalized over the whole molecule, they correspond to σ^*(C–O) and σ^*(C–C) MOs.

TABLE III. Measured energies and TVs (eV) of the spectral features in the gas phase O1*s* ISEELS spectrum of furan and previous proposed assignments.

	This work	TV	Gas phase[b]	TV[b]	Assignment[b]
A	535.15	4.80	535.3±0.1	4.7	$1\pi^*(3b_1)$
B1	537.2	2.75			
B	537.57	2.38	537.6±0.1	2.4	$3p$ or $2\pi^*(2a_2)$
B2	537.81	2.24			
C	539.17	0.78	539.4±0.1	0.6	σ^*(C–O)
C1	539.57	0.38			
Ion	539.95[a]	0.00	540.0	0.0	
D	545.3	−5.35	545.3±0.1	−5.3	σ^*(C–C)

[a]Reference 27.
[b]Reference 29.

TABLE IV. Calculated energies, TVs, relative intensities, and assignments of O1*s* core excited states of furan.

State	*E* (eV)	TV(eV)	Intensity[a]	Main configurations	$\langle r^2 \rangle$
B_1	535.65	4.79	0.767	0.94 $1s \rightarrow 1\pi^*$	66.7
A_1	537.30	3.14	<0.001	0.97 $1s \rightarrow 3s\sigma$	129.4
B_2	537.98	2.46	0.007	0.98 $1s \rightarrow 3p\sigma'$	167.4
A_1	537.99	2.45	0.023	0.97 $1s \rightarrow 3p\sigma$	164.5
B_1	538.13	2.31	<0.001	0.97 $1s \rightarrow 3p\pi$	168.3
A_1	538.33	2.11	0.013	0.97 $1s \rightarrow 3d\sigma$	145.5
A_2	538.50	1.94	0.000[b]	0.60 $1s \rightarrow 2\pi^*$	111.5
				+0.34 $1s \rightarrow 3d\pi$	
A_2	538.51	1.93	0.000[b]	0.63 $1s \rightarrow 3d\pi$	125.0
				+0.36 $1s \rightarrow 2\pi^*$	
B_2	538.58	1.86	0.005	0.98 $1s \rightarrow 3d\sigma'$	153.6
A_1	538.68	1.76	0.001	0.98 $1s \rightarrow 3d\sigma''$	150.0
B_1	538.92	1.52	<0.001	0.97 $1s \rightarrow 3d\pi'$	168.9
A_1	539.00	1.44	0.002	0.98 $1s \rightarrow 4s\sigma$	254.8
B_2	539.17	1.27	0.009	0.98 $1s \rightarrow 4p\sigma$	267.1
B_1	539.20	1.24	0.001	0.97 $1s \rightarrow 4p\pi$	255.9
A_1	539.32	1.12	0.015	0.97 $1s \rightarrow 4p\sigma'$	189.6
A_1	539.79	0.65	0.296	0.95 $1s \rightarrow \sigma^*$	103.9
B_2	540.05	0.39	1.000	0.89 $1s \rightarrow \sigma^*$	80.6
	540.44			ion	
A_1	540.64	−0.20	0.006	0.95 $1s \rightarrow \sigma^*$	107.7
B_2	541.14	−0.70	0.118	0.91 $1s \rightarrow \sigma^*$	104.9
B_1	541.77	−1.33	0.001	0.59 $1s1\pi \rightarrow 1\pi^*1\pi^*$	78.3
				+0.22 $1s2\pi \rightarrow 1\pi^*2\pi^*$	
A_1	541.91	−1.47	0.012	0.93 $1s \rightarrow \sigma^*$	93.0
B_1	542.03	−1.58	<0.001	0.49 $1s1\pi \rightarrow 1\pi^*3p\sigma'$	170.6
				+0.31 $1s2\pi \rightarrow 3p\pi 2\pi^*$	
B_2	542.30	−1.86	0.054	0.96 $1s \rightarrow \sigma^*$	95.4
A_1	542.69	−2.25	<0.001	0.55 $1s1\pi \rightarrow 1\pi^*3s\sigma$	138.0
				+0.36 $1s2\pi \rightarrow 3s\sigma 2\pi^*$	
B_2	543.24	−2.80	0.052	0.84 $1s \rightarrow \sigma^*$	87.9
B_2	543.42	−2.98	<0.001	0.53 $1s1\pi \rightarrow 1\pi^*3p\sigma'$	183.1
				+0.38 $1s2\pi \rightarrow 3p\sigma' 2\pi^*$	
B_1	543.42	−2.98	0.002	0.96 $1s2\pi \rightarrow 1\pi^*3d\pi$	194.8
B_2	543.95	−3.51	0.001	0.51 $1s1\pi \rightarrow 1\pi^*3d\sigma'$	159.7
				+0.37 $1s2\pi \rightarrow 3d\sigma' 2\pi^*$	
B_1	544.18	−3.74	<0.001	0.50 $1s1\pi \rightarrow 1\pi^*3p\pi$	185.7
				+0.35 $1s2\pi \rightarrow 3d\pi 2\pi^*$	

[a]Relative intensity to the most intense peak.
[b]Forbidden dipole electric transition.

On the high-energy side of the C band, the calculations predict several other σ^* and shake up transitions but these results should be taken carefully, since we do not take into account the influence of the continuum. Finally, the last band D located at 545.3 eV is assigned to a σ^*(C–C) resonance following Newberry *et al.*[29] As pointed out by Piancastelli in a recent paper, possible alternatives for the assignment of the structures observed above the thresholds are doubly excited states (with various decaying processes) and/or satellite thresholds.[54]

C. Carbon K-shell electron-energy loss spectrum

The C1*s* electron energy loss spectrum is shown in Fig. 4 and the energies of the peaks are collected in Table V, together with the results of previous studies. In contrast to the O1*s* threshold, the C1*s* spectrum of furan has been the subject of several studies, both in the gas phase[29,30] and in condensed (monolayer and multilayer) phases with rather low resolutions.[31,32] A high resolution photoabsorption spectrum has been recorded recently by measuring the partial electron yield in the limited energy range of 285–290.2 eV.[30] It exhibits a feature around 287.3 eV not present in previous works. Thanks to the higher resolution, more features are resolved in our spectrum than in the previous ISEELS and NEXAFS spectra and the transition at 287.3 eV is confirmed. The shape of the spectrum is similar to those of these previous studies. The assignments given in the last column of Table V are those of Newburry *et al.*[29] and were followed by all subsequent works.

The results of the calculations are given in Table VI. For clarity, only the transitions with intensity greater than 1% of the most intense one are shown in this table. The resulting synthetic spectrum is compared to the experimental one in Fig. 5. As in the oxygen case, the calculated core excitation energies seem to be overestimated by a few tenths of an eV.

As anticipated by Newburry *et al.*,[29] the first band A, centered at 285.76 eV, is assigned to the $1s(C_1) \rightarrow 1\pi^*(3b_1)$ excitation by the calculations, who place this peak at 286.00 eV (Table VI). Similarly, the second band B (286.64 eV) is assigned to the $1s(C_2) \rightarrow 1\pi^*(3b_1)$ excita-

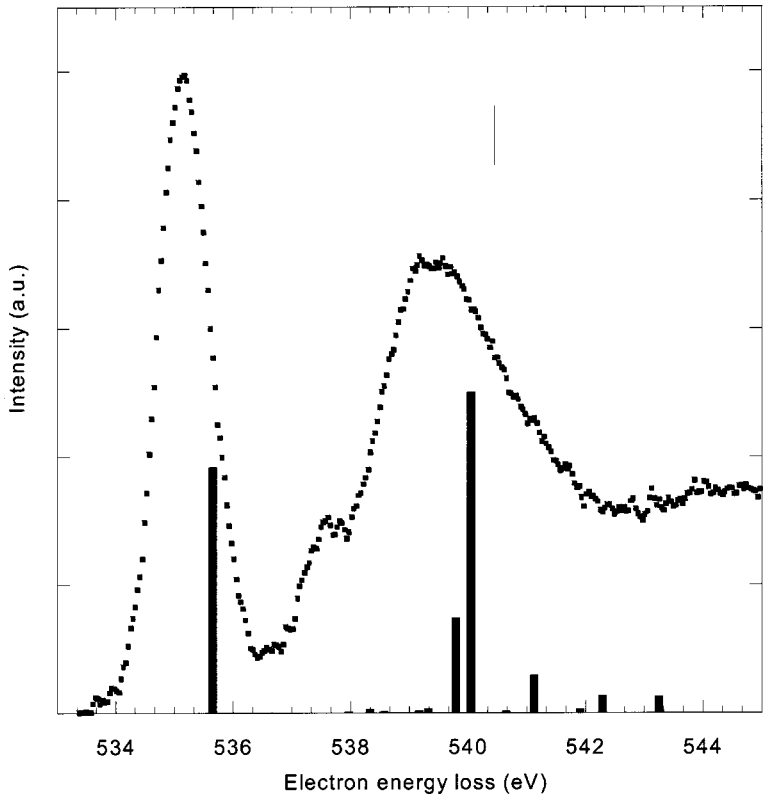

FIG. 3. A comparison between the experimental and the theoretical spectra for the pre-edge region at the oxygen K edge. The vertical line indicates the location of the calculated ionization threshold.

tion, since this transition is calculated to occur at 286.99 eV. The relative intensities of these two peaks, which can be obtained approximately from Fig. 4, is also in good agreement with the theoretical one (about 0.8:1.0). Finally, the calculated TVs for these two bands (4.73 and 4.98 eV) are in very good agreement with the experimental ones (4.56 and 4.95 eV, respectively, obtained with the ionization energies of Ref. 26).

The next spectral feature C, appearing on the high energy side of the B band at an energy of 287.3 eV, was not detected in the previous low resolution spectrum.[29,32] For example, it does not appear in the NEXAFS spectrum of solid furan recorded at a resolution of 0.4 eV (see Fig. 3 of Ref. 32). It was detected for the first time recently by Rennie *et al.*[30] in the partial electron yield (absorption) spectrum of gaseous furan recorded in the pre-edge region (peak "X" in Fig. 2 of Ref. 30). Based on the interpretation of resonant Auger spectra, this feature was tentatively assigned by Rennie *et al.*[30] as a Rydberg transition. Another suggested possibility was a double excitation.

The present calculations (Table VI) confirm the presence of the $1s(C_1) \rightarrow 3s\sigma/\sigma^*(C_1\text{–H})$ transition which occurs at 287.43 eV. The corresponding band (TV=3.31 eV) is very likely responsible for the fact that the C band in not well resolved from the B one. The calculated intensity is rather large for a Rydberg transition, due to the mixed Rydberg-valence character of this state (its $\langle r^2 \rangle$ value is calculated to be 114.1 a.u.^{2}, i.e., intermediate between the $1\pi^*$ and the

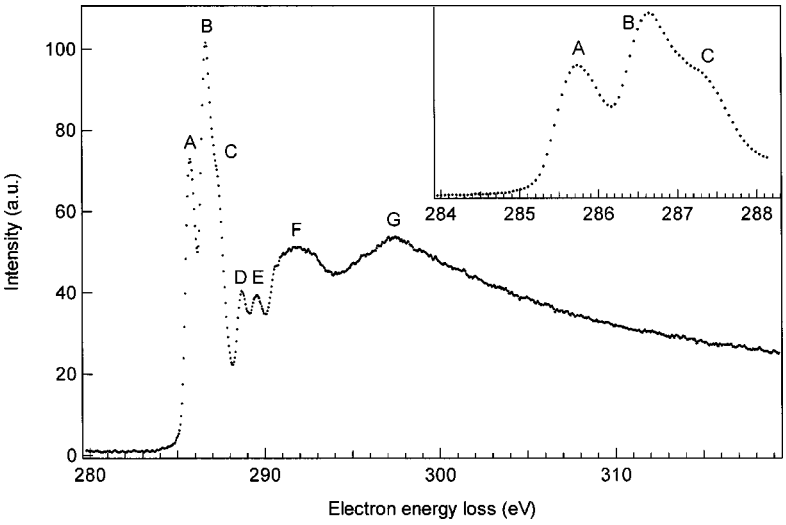

FIG. 4. (a) The electron energy-loss spectrum of furan recorded at the carbon K edge with an energy resolution of 0.17 eV, steps 40 meV. (b) The excitation spectrum in the 281.8–291.6 eV region recorded at a slightly higher resolution and 20 meV steps.

TABLE V. Measured energies (eV) of the spectral features in the C1*s* spectrum and previous proposed assignments.

	ISEELS[a]	ISEELS[b]	NEXAFS[c]	NEXAFS[c]	NEXAFS[c]	NEXAFS[d]		
	Gas	Gas	Submonolayer Ag(110)	Monolayer Ag(110) 171 K	Multilayer	Multilayer	Assignment[b]	
							C_1	C_2
A	285.76	285.6±0.1	285.7	285.9	285.9	285.9±0.8	$1\pi^*(3b_1)$	
B	286.64	286.5±0.1	286.7	287.0	287.0	286.9±0.8		$1\pi^*(3b_1)$
C	287.3							
D	288.66	288.5±0.1	287.8/288.2[e]	288.4/288.7[e]	288.5	288.7±0.8	$2\pi^*(2a_2)$	
D1	289.04							
E1	289.38							
E	289.54	289.3±0.1	289.2/289.5[e]	289.4/289.6[e]	289.7	289.8±0.8		$2\pi^*(2a_2)$
Ion C_1	290.32[f]							
F1	290.67							
F2	291.06							
Ion C_2	291.59[f]							
F	291.81	291.4±0.1	292.5/291.8[e]	292.6/293.4[e]	292.3	292.6±0.8	σ^*(C–O)	
G	297.44	297.0±0.1	298	299	298	297.5±0.8	σ^*(C–C)	

[a]This work.
[b]Reference 29.
[c]Reference 32.
[d]Reference 31.
[e]First value for normal incidence, second for glancing incidence.
[f]Reference 30.

TABLE VI. Calculated energies, TVs, and relative intensities and assignments of C1*s* core excited states of furan.

State	E (eV)	TV (eV)		Intensity		Main configurations			$\langle r^2 \rangle$
		C_1	C_2			C_1		C_2	
A''	286.00	4.73		0.794	0.89	$1sC_1 \rightarrow 1\pi^*$			64.2
A''	286.99		4.98	1.000			0.92	$1sC_2 \rightarrow 1\pi^*$	64.2
A'	287.43	3.31		0.078	0.95	$1sC_1 \rightarrow 3s\sigma/\sigma^*(C_1-H)$			114.1
A''	287.72	3.01		0.365	0.42	$1sC_1 \rightarrow 3d\pi/2\pi^*$			66.8
					+0.36	$1sC_1 \rightarrow 2\pi^*/3d\pi$			
					+0.11	$1sC_1 \rightarrow 4p\pi$			
A'	288.19	2.55		0.030	0.93	$1sC_1 \rightarrow 3p\sigma$			135.3
A''	288.38	2.35		0.012	0.94	$1sC_1 \rightarrow 3p\pi$			148.2
A'	288.72		3.26	0.066			0.95	$1sC_2 \rightarrow 3s\sigma/\sigma^*(C_2-H)$	116.5
A'	288.93	1.80		0.022	0.95	$1sC_1 \rightarrow 3d\sigma$			159.0
A''	289.15		2.82	0.150			0.69	$1sC_2 \rightarrow 2\pi^*$	69.4
							+0.10	$1sC_2 \rightarrow 3p\pi$	
A'	289.21	1.53		0.025	0.94	$1sC_1 \rightarrow 4s\sigma$			279.0
A'	289.34		2.64	0.034			0.95	$1sC_2 \rightarrow 3p\sigma$	133.4
A''	289.45	1.28		0.011	0.65	$1sC_1 \rightarrow 4p\pi$			296.8
					+0.31	$1sC_1 \rightarrow 2\pi^*/3d\pi$			
A'	289.49		2.48	0.010			0.94	$1sC_2 \rightarrow 3p\sigma'$	141.6
A'	289.92		2.06	0.026			0.90	$1sC_2 \rightarrow 3d\sigma$	144.9
A'	290.20		1.77	0.012			0.94	$1sC_2 \rightarrow 3d\sigma''$	148.3
A'	290.46		1.52	0.034			0.93	$1sC_2 \rightarrow 4s\sigma$	282.6
A''	290.47		1.51	0.010			0.92	$1sC_2 \rightarrow 3d\pi'$	168.7
A'	290.47	0.26		0.172	0.83	$1sC_1 \rightarrow \sigma_1^*$			100.3
A'	290.65		1.32	0.021			0.93	$1sC_2 \rightarrow 4p\sigma$	295.9
A''	290.70		1.28	0.020			0.90	$1sC_2 \rightarrow 4p\pi$	293.2
A'	290.72		1.26	0.014			0.90	$1sC_2 \rightarrow 4p\sigma$	224.2
	290.73	0.00				Ion C_1			
A'	290.80	−0.07		0.014	0.63	$1sC_1 \rightarrow \sigma_2^*$			110.7
					+0.22	$1sC_1 \rightarrow \sigma_3^*$			
A'	291.06	−0.32		0.040	0.65	$1sC_1 \rightarrow \sigma_3^*$			115.2
					0.25	$1sC_1 \rightarrow \sigma_2^*$			
A''	291.36	−0.63		0.012	0.36	$1sC_12\pi \rightarrow 1\pi^*2\pi^*/3d\pi$			69.1
					+0.18	$1sC_12\pi \rightarrow 1\pi^*3d\pi/2\pi^*$			
A'	291.50		0.47	0.283			0.70	$1sC_2 \rightarrow \sigma_1'^*$	108.4
							+0.18	$1sC_2 \rightarrow \sigma_2'^*$	
	291.98		0.00					Ion C_2	
A'	292.00		−0.02	0.114			0.72	$1sC_2 \rightarrow \sigma_2'^*$	113.9
							+0.18	$1sC_2 \rightarrow \sigma_1'^*$	
A'	292.36		−0.39	0.024			0.90	$1sC_2 \rightarrow \sigma_3'^*$	109.5

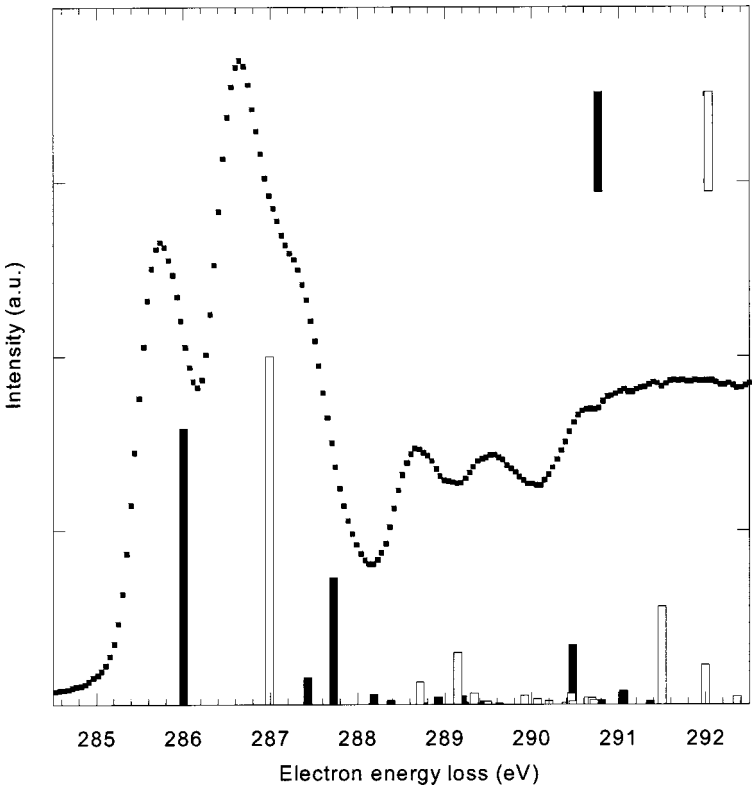

FIG. 5. A comparison between the experimental and the theoretical spectra at the carbon K edge. The vertical lines indicate the locations of the calculated ionization thresholds (black: C_1; white: C_2).

$3p\langle r^2\rangle$ values). However, this intensity is too weak when compared to the observed band, which is almost as intense as the first band A (Fig. 4). In fact, according to the calculations, the C band appears to be due to a π^* transition from the C_1 atom, which is predicted to occur at 287.72 eV (Table VI), with a relative intensity of 36%. The calculated TV of 3.01 eV is in excellent agreement with the experimental one (3.02 eV). The wave function of this state is complex but its $\langle r^2\rangle$ value of 66.8 a.u.^{2}, which is close to those of the $1\pi^*$ transitions (64.2 a.u.^{2}), proves that it is a valence state. Thus, it can be considered as the $1s(C_1)\rightarrow 2\pi^*(2a_2)$ transition.

The next band D in the spectrum is located at 288.66 eV (Table V and Fig. 6). It exhibits a fine feature D1 not well resolved at 289.04 eV. According to the calculations, there are two states predicted in this energy region with significant intensities (the $3d$ transitions of the C_1 atom are also present but their intensities are very low): the $1s(C_2)$ $\rightarrow 3s\sigma/\sigma^*(C_2\text{–H})$ transition (288.72 eV) and the $1s(C_2)$ $\rightarrow 2\pi^*$ one (289.15 eV). The presence of the $3s/\sigma^*$ transition explains why this band does not show the usual polarization dependence of π^* states observed in the monolayer furan NEXAFS spectra (Fig. 6 of Ref. 32).

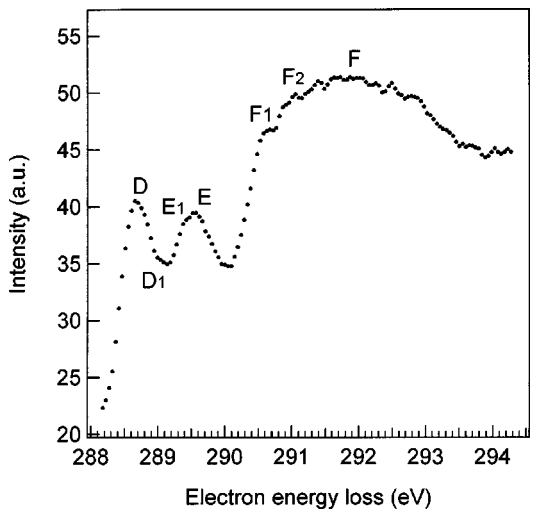

FIG. 6. The C1*s* excitation spectrum in the 288.0–294.6 eV region.

The E band has its maximum at 289.54 eV in the experimental spectrum and also presents a not well-resolved feature at 289.38 eV (Table V and Fig. 6). As for the previous band, a comparison of the monolayer furan NEXAFS spectra at normal and glancing incidences[32] suggested that this band could contain contributions from σ^*(C–H) and/or Rydberg transitions. Taking into account the slight overestimation of the calculated energies, this region corresponds to the excitations of the $1s(C_1)\,4s$ and $4p$ states, as well as the $1s(C_2)\,3p$ and $3d$ ones. The most intense transitions are given in Table VI but the calculated intensities seem to be too weak to account for the intensity of the E band, which is similar to the D one. The next calculated σ^* intense valence transition is calculated to appear at 290.47 eV (Table VI), i.e., close to the C_1 ionization energy and 1 eV above the E band. It seems very unlikely that the calculated energy of the E peak would be so overestimated. To clarify the situation, it would be interesting to obtain a high resolution spectrum of condensed furan in this region.

Our proposed assignments for the bands D and E are in contradiction with those proposed by Newbury *et al.*[29] and followed by all subsequent studies.[30–32] The same situation prevails for the C band for which our assignment differs

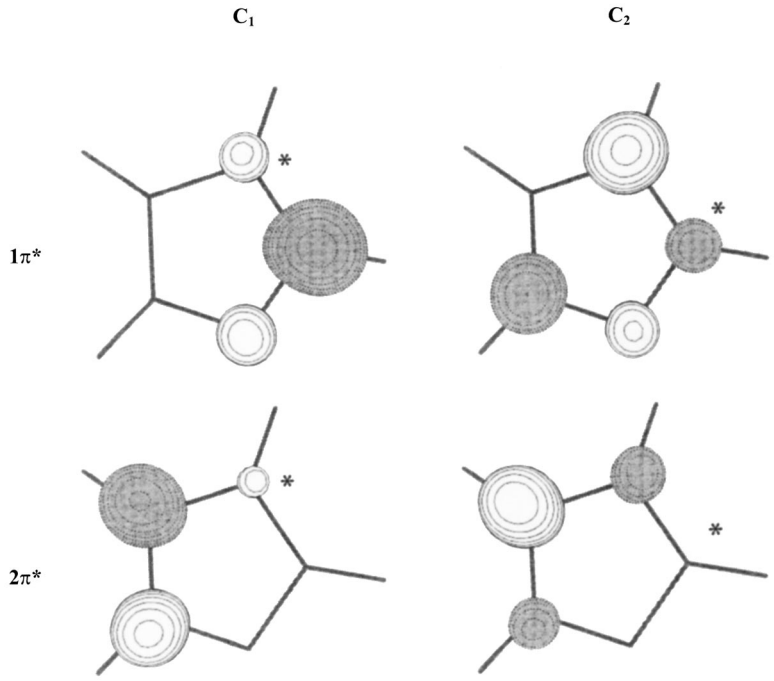

FIG. 7. Natural orbitals of the $1\pi^*$ and $2\pi^*$ transitions of the C_1 and C_2 atoms (the stars indicate the core excited atom).

from that proposed by Rennie *et al.*:[30] the $2a_2$ transitions from C_1 and C_2 atoms were assigned to the D and E bands, because of the similarity of the D–E energy splitting with the A–B one (≈0.9 eV). The relative intensity of these four bands were rationalized by examining the shape of the ground state $3b_1$ and $2a_2$ MOs, although these MOs are not a good description of the core excited states. As stated above, a better choice would be the core ion MOs but an inspection of the wave functions of the π^* core excited states (Table VI) shows a strong mixing of excitations. Nevertheless, as shown by Löwdin,[55] it is possible to construct from these wave functions the so-called ''natural orbitals,'' after diagonalization of the CI density matrix. The resulting MOs, which represent the best approximations of the ''true'' core excited π^* MOs, are displayed in Fig. 7 using the MOLDEN software.[56] They illustrate the breaking of the initial C_{2v} symmetry upon core excitation, assuming a localization of the core holes. The electronic density at the core excited atom is in qualitative agreement with the intensities of the observed bands: The two $1\pi^*$ transitions should have similar and large intensities; the $1s(C_1) \rightarrow 2\pi^*$ intensity should be lower but still rather intense, while finally the $1s(C_2) \rightarrow 2\pi^*$ one should be very weak.

The F band has its maximum at 291.81 eV and thus is located around the C_2 ionization threshold. It exhibits several fine features (Table V and Fig. 6). The calculations predict in this energy region two σ^* transitions from the C_1 atom at 290.80 and 291.06 eV (Table VI) with rather weak intensities. Two other σ^* transitions, much more intense, from the C_2 atom, are predicted slightly above at 291.50 and 292.00 eV.

Finally, the last band G is located at 297.44 eV (Table V and Fig. 5). Since this energy range is beyond the reach of the present calculations, it is tentatively assigned to a σ^* band. As in the O1*s* spectrum, it might also be due to double excitations and/or satellite, but further investigations are needed to clarify this point.[54]

V. CONCLUSION

In this work, the inner shell electron energy loss spectra of gaseous furan have been measured at the C1*s* and O1*s* edges with 0.17 eV resolution. *Ab initio* configuration interaction calculations, using a large-scale configuration interaction have been used to give assignments of the observed features. These calculations are the first ones performed on the core excitation spectra of this molecule.

At the O1*s* edge, the spectrum is dominated by two main bands: The first one assigned to the $1\pi^*$ transition, the second one, centered on the ionization energy and very broad, being due to σ^* transitions. At the C1*s* edge, the better resolution of the present work shows the presence of a new feature on the high-energy side of the second band at 287.3 eV. With the exception of several bands of the C1*s* spectrum, the theoretical calculations confirm the assignments proposed in previous experimental works, which were based on qualitative pictures.

ACKNOWLEDGMENTS

The ''Laboratoire de Physique des Lasers, Atomes et Molécules'' (PhLAM) is ''Unité Mixte de Recherche du CNRS.'' The ''Centre d'Etudes et de Recherches Lasers et Applications'' (CERLA, FR CNRS 2416) is supported by the ''Ministère chargé de la Recherche,'' the ''Région Nord/Pas-de-Calais'', and the ''Fonds Européen de Développement Economique des Régions'' (FEDER). Parts of the computations were carried out at the CRI (Centre de Ressources Informatiques), on the IBM-SP3 computer that is supported by the ''Program de Calcul Intensif et Parallèle'' of the ''Ministère chargé de la Recherche,'' the ''Région Nord/Pas-de-

Calais,'' and the FEDER. This research has been supported by the Fonds National de la Recherche Scientifique and the Patrimoine of Université de Liège. M.-J. Hubin-Franskin wishes to acknowledge the Fonds National de la Recherche Scientifique for a research position.

[1] J. L. Bredäs and R. Silbey, *Conjugated Polymers* (Kluwer, Dordrecht, 1991).
[2] E. Nyulaszi and T. Vespremi, Acta Chim. Hung. **130**, 811 (1993).
[3] C. O. Kappe, S. S. Murphree, and A. Padwa, Tetrahedron **42**, 14179 (1997).
[4] T. E. Caldwell and D. P. Land, Polyhedron **16**, 3197 (1997).
[5] C. D. Cooper, A. D. Williamson, J. C. Miller, and R. N. Compton, J. Chem. Phys. **73**, 1527 (1980).
[6] A. P. Dunlop and F. N. Peters, *The Furans* (Reinhold, New York, 1953).
[7] G. M. Badger, *The Chemistry of Heterocyclic Compounds*, 1st ed. (Academic, New York, 1961).
[8] W. W. Crew and R. J. Madix, J. Am. Chem. Soc. **115**, 729 (1993).
[9] X. Lu, X. Xu, N. Wang, Q. Zhang, and M. C. Lin, J. Phys. Chem. B **105**, 10069 (2001).
[10] T. E. Caldwell and D. P. Land, J. Phys. Chem. B **103**, 7869 (1999).
[11] F. Q. Yan, M. H. Qiao, X. M. Wei, Q. P. Liu, J. F. Deng, and G. Q. Xu, J. Chem. Phys. **111**, 8068 (1999).
[12] R. M. Ormerod, C. J. Baddeley, C. Hardacre, and R. M. Lambert, Surf. Sci. **360**, 1 (1996).
[13] S. Letarte, A. Adnot, and D. Roy, Surf. Sci. **448**, 212 (2000).
[14] M. H. Qiao, F. Q. Yan, W. S. Sim, J. F. Deng, and G. Q. Xu, Surf. Sci. **460**, 67 (2000).
[15] N. Kishimoto, H. Yamakado, and K. Ohno, J. Phys. Chem. **100**, 8204 (1996).
[16] M. Takahashi, K. Otsuka, and Y. Udagawa, Chem. Phys. **227**, 375 (1998).
[17] M. H. Palmer, I. C. Walker, C. C. Ballard, and M. F. Guest, Chem. Phys. **192**, 111 (1995).
[18] E. E. Rennie, C. A. F. Johnson, J. E. Parker, D. M. P. Holland, D. A. Shaw, M. A. McDonald, M. A. Hayes, and L. G. Shpinkova, Chem. Phys. **236**, 365 (1998).
[19] E. E. Rennie, L. Cooper, C. A. F. Johnson, J. E. Parker, R. A. Mackie, L. G. Shpinkova, D. M. P. Holland, D. A. Shaw, and M. A. Hayes, Chem. Phys. **263**, 149 (2001).
[20] D. M. P. Holland, L. Karlsson, and W. von Niessen, J. Electron Spectrosc. Relat. Phenom. **113**, 221 (2001).
[21] A. Giuliani and M.-J. Hubin-Franskin, Int. J. Mass. Spectrom. **205**, 163 (2001).
[22] A. Mellouki, J. Liévin, and M. Herman, Chem. Phys. **271**, 239 (2001).
[23] A. B. Trofimov, H. Köppel, and J. Schirmer, J. Chem. Phys. **109**, 1025 (1998).
[24] O. Christiansen and P. Jørgensen, J. Am. Chem. Soc. **120**, 3423 (1998).
[25] J. Wan, J. Meller, M. Hada, M. Ehara, and H. Nakatsuji, J. Chem. Phys. **113**, 7853 (2000).
[26] U. Gelius, C. J. Allan, G. Johansson, H. Siegbahn, D. A. Allison, and K. Siegbahn, Phys. Scr. **3**, 237 (1971).
[27] S. A. Chambers and T. D. Thomas, J. Chem. Phys. **67**, 2596 (1977).
[28] D. T. Clark and D. M. J. Lilley, Chem. Phys. Lett. **9**, 234 (1971).
[29] D. C. Newberry, I. Ishii, and A. P. Hitchcock, Can. J. Chem. **64**, 1145 (1986).
[30] E. E. Rennie, U. Hergenhahn, O. Kugeler, A. Rüdel, S. Marburger, and A. M. Bradshaw, J. Chem. Phys. **117**, 6524 (2002).
[31] M. Mauerer, P. Zebisch, M. Weinelt, and H.-P. Steinrück, J. Chem. Phys. **99**, 3343 (1993).
[32] J. L. Solomon, R. J. Madix, and J. Stöhr, J. Chem. Phys. **94**, 4012 (1991).
[33] C. Hannay, J. Heinesch, U. Kleyens, and M.-J. Hubin-Franskin, Meas. Sci. Technol. **6**, 1140 (1995).
[34] M.-J. Hubin-Franskin, H. Aouni, D. Duflot, F. Motte-Tollet, L. F. Feirrera, and G. Tourillon, J. Chem. Phys. **106**, 35 (1997).
[35] M.-J. Hubin-Franskin and J. Heinsesch, Nucl. Instrum. Methods Phys. Res. A **477**, 546 (2002).
[36] F. Currell and C. M. John, Meas. Sci. Technol. **3**, 1192 (1992).
[37] R. N. S. Sodhi and C. E. Brion, J. Electron Spectrosc. Relat. Phenom. **34**, 363 (1984).
[38] D. Duflot, J.-P. Flament, I. C. Walker, J. Heinesch, and M.-J. Hubin-Franskin, J. Chem. Phys. **118**, 1137 (2003).
[39] S. Bodeur, P. Millié, and I. Nenner, Phys. Rev. A **41**, 252 (1990).
[40] M. W. Schmidt, K. K. Baldridge, J. A. Boatz, S. T. Elbert, M. S. Gordon, J. J. Jensen, S. Koseki, N. Matsunaga, K. A. Nguyen, S. Su, T. L. Windus, M. Dupuis, and J. A. Montgomery, J. Comput. Chem. **14**, 1347 (1993).
[41] B. Huron, J.-P. Malrieu, and P. Rancurel, J. Chem. Phys. **58**, 5745 (1973).
[42] R. Cimiraglia, Int. J. Quantum Chem. **60**, 167 (1996).
[43] C. Angeli, R. Cimiraglia, M. Persico, and A. Toniolo, Theor. Chem. Acc. **98**, 57 (1997).
[44] T. H. Dunning, Jr., J. Chem. Phys. **55**, 716 (1971).
[45] T. H. Dunning, Jr. and P. J. Hay, in *Methods of Electronic Structure Theory*, edited by H. F. Schaefer III (Plenum, New York, 1997), Vol. 3, Chap. 1, pp. 1–27.
[46] M. D. Harmony, V. W. Laurie, R. L. Kuczkowski, R. H. Schwendeman, D. A. Ramsey, F. J. Lovas, and A. G. Maki, J. Phys. Chem. Ref. Data **8**, 619 (1979).
[47] E. D. Simandiras, N. C. Handy, and R. D. Amos, J. Phys. Chem. **92**, 1739 (1988).
[48] A. A. El-Azhary and H. U. Suter, J. Phys. Chem. **100**, 15056 (1996).
[49] G. De Alti, P. Decleva, and A. Lisini, Chem. Phys. **90**, 231 (1984).
[50] O. Goscinski, M. Hehenberger, B. Roos, and P. Siegbahn, Chem. Phys. Lett. **33**, 427 (1975).
[51] J. Stöhr, *NEXAFS Spectroscopy* (Springer-Verlag, Berlin, 1992), Chap. 7.4.3.
[52] P. S. Epstein, Phys. Rev. **28**, 695 (1926).
[53] R. K. Nesbet, Proc. R. Soc. London, Ser. A **230**, 312,322 (1955); **230**, 312,922 (1955).
[54] M. N. Piancastelli, J. Electron Spectrosc. Relat. Phenom. **100**, 167 (1999).
[55] P.-O. Löwdin, Phys. Rev. **97**, 1474 (1955).
[56] G. Schaftenaar and J. H. Noordik, J. Comput.-Aided Mol. Des. **14**, 123 (2000).

Article 14

Available online at www.sciencedirect.com
SCIENCE DIRECT®
Chemical Physics 310 (2005) 67–75
Chemical Physics
www.elsevier.com/locate/chemphys

Ab initio and experimental study of the K-shell spectra of 2,5-dihydrofuran

D. Duflot [a,*], J.-P. Flament [a], A. Giuliani [b], J. Heinesch [b], M.-J. Hubin-Franskin [b]

[a] *Laboratoire de Physique des Lasers, Atomes et Molécules (PhLAM), UMR CNRS 8523, Centre d'Études et de Recherches Lasers et Applications (CERLA, FR CNRS 2416), Université des Sciences et Technologies de Lille, F-59655 Villeneuve d'Ascq Cedex, France*
[b] *Laboratoire de Spectroscopie d'Électrons diffusés, Institut de Chimie, Université de Liège, B6c Sart Tilman, B4000 Liège 1, Belgium*

Received 2 June 2004; accepted 6 October 2004

Abstract

The K-shell spectra of gaseous 2,5-dihydrofuran at the carbon and oxygen thresholds are reported for the first time. They have been measured using the inner-shell electron energy loss spectroscopy (ISEELS) method. Ab initio Configuration Interaction calculations have been carried out to assign the observed bands. The O1s spectrum is similar to that of tetrahydrofuran and the assignments of the bands are close to those obtained in the case of furan, excepting the furan first π* band. At the C1s edge, the spectrum differs from the furan case, because of the different chemical environment of one of the non-equivalent carbon atoms: due to the presence of hydrogen atoms out of the carbon–oxygen ring plane, several Rydberg core excited states have an important valence character, leading to large intensities in the experimental spectrum.

1. Introduction

The furan molecule C_4H_4O plays an important role in many fields of chemistry and its electronic spectrum has been the subject of many theoretical and experimental studies [1] (and references cited therein). On the other hand, very little is known about the spectroscopy of its derivatives such as 2,5-dihydrofuran (C_4H_6O). Most studies, measuring rotational [2,3] and far infrared [4], have focussed on the determination of the equilibrium geometry of the molecule: the carbon–oxygen ring of the molecule has been shown to be planar, despite the presence of a low energy ring puckering vibration mode [5]. Recently, the infrared and Raman spectra have been recorded and analysed using ab initio methods [6]. While the assignment of the valence electronic spectrum of furan is a largely debated subject [7] (and references therein), the valence spectrum of 2,5-dihydrofuran does not seem to be available. A similar situation occurs for the K shell spectra: while furan has been the subject of several studies both in gaseous [1,8] and condensed [9,10] phases, the only work on 2,5-dihydrofuran concerns monolayers and multilayers probed with the NEXAFS (Near X-ray Absorption Fine Structure) and XPS (X-ray Photoelectron Spectroscopy) methods [10]. This molecule is of importance as model of units in larger systems such as biomolecules. Its physico-chemical behaviour is related to its electronic configuration.

The goal of this paper is to present for the first time the core excitation spectra of gaseous 2,5-dihydrofuran, obtained at the C1s and O1s edges with the ISEELS method in electric dipolar excitation conditions. Due to the strong localisation of the 1s orbitals, the core shell excitation spectroscopy is a powerful tool for the study of excited states and their characterisation as π*, σ* or Rydberg character. In order to help in the assignment of the observed spectral features, large scale ab initio

* Corresponding author. Tel.: +33 3 20 43 49 80; fax: +33 3 20 43 40 84.
E-mail address: denis.duflot@univ-lille.fr (D. Duflot).

0301-0104/$ - see front matter © 2004 Elsevier B.V. All rights reserved.
doi:10.1016/j.chemphys.2004.10.007

Configuration Interaction (CI) calculations have been carried out. This paper is organised as follows: the experimental set up is described in Section 2; the computational method is outlined in Section 3; Section 4 presents the discussion of the results and some conclusions are given in Section 5.

2. Experimental methods

The inner-shell electron energy loss spectra were obtained with a VSW spectrometer which has been adapted for gas studies and high energy electron beams and has been equipped with a home-made position sensitive multi-detector system in order to improve data collection times. The experimental apparatus and procedure have been described in detail previously [11–13].

Briefly the spectrometer consists of an electrostatic 180° monochromator operating in the constant pass energy mode, a collision chamber and an electrostatic analyser identical to the monochromator. The monochromatised incident electrons are accelerated up to 2 keV and focused into the collision chamber using a four-element electron lens. The electrons are slightly deflected (0.02 rad) by two sets of X–Y plates inside the collision chamber. The scattered electrons are energy analysed and focused onto the entrance slit of the analyser by a lens similar to that used for acceleration. The angular resolution of the apparatus has been measured to be $1.074 \pm 0.06 \times 10^{-2}$ rad by measuring the valence excitation spectrum of CO in the 5–150 eV region and normalising the absolute cross-section to that of Chan et al. [14].

In the collision conditions of low angular momentum transfer (i.e., high incident energy and small scattering angle), electronic electric-dipolar transitions are primarily excited.

Inside the vacuum vessel, a residual pressure of less than 1×10^{-8} Torr is maintained by a cryogenic pumping system. The electron gun and the analyser regions are differentially pumped by turbomolecular pumps, respectively.

The detection system consists of an assembly of two microchannel plates, a phosphor screen, fiber-optic couplers and an area array Coupled Charge Device (CCD) sensor. The driving and reading electronics for the detector have been adapted to the electron-energy loss experiment. The spectra result from the accumulation of the data from each channel of the detector, which removes any detector-sensitivity variation [11,15].

The accelerating and retarding voltages were constant to within 10 ppm/°C. The spectra have been recorded with 0.040 and 0.020 eV steps.

In order to take into account valence and lower-energy inner-shell excitation cross-section, a background has been subtracted from the raw spectra by extrapolating a least-square fit of the pre-edge experimental data points. The absolute energy scales were determined by calibrating the C1s spectrum relative to the C1s $\rightarrow \pi^*(v' = 0)$ band in CO [14] at 287.40 ± 0.02 eV and the O1s spectrum relative to the O1s $\rightarrow \pi^*(v' = 0)$ value for the same molecule at 534.21 ± 0.09 eV [16]. The spectrum of a mixture of 2,5-dihydrofuran and CO was recorded with each gas being let into the collision region through a separate leak to ensure of constant composition mixture. The uncertainty on the measured energies is of the order of 0.06 and 0.13 eV for the C1s and O1s spectra, respectively.

The sample is a commercial one from Aldrich with a stated purity of 97.0%. It was used directly without further purification except for repetitive freeze–pump–thaw cycles in order to eliminate air and other volatile impurities in the sample.

3. Computational method

The computational method used in the present work is similar to that used in our studies of the core excitation spectra of acrolein [17] and furan [1] and will be only briefly outlined. First, the energy of the 1s $\rightarrow \infty$ core ion is obtained at the ROHF-GVB (Restricted Open Shell Hartree-Fock Generalised Valence Bond) level with the GAMESS-US program [19]. This energy is improved by an MP2 (second order Møller–Plesset) perturbation. The energy of the 1s $\rightarrow$ i* core excited state is calculated by correcting [18] this core ion energy in the following manner:

$$E(1s \rightarrow i^*) = E(1s \rightarrow \infty) + \varepsilon_i^* + P + C$$

where ε_i^* is the mono-electronic energy of the i* MO. The relaxation term P is obtained via a configuration interaction (CI) calculation in the mono-excited space. The correlation term C is calculated by a multi-reference MP2 calculation with the three-class diagrammatic CIPSI (Configuration Interaction by Perturbation Selected Iteratively) method [20,21]. The computational cost of this latter calculation is reduced by using the extrapolation procedure proposed by Angeli [22]. In the present work, eight thresholds between 99.5% and 96.0% were used. The theoretical dipolar electric intensities are obtained by evaluating the corresponding oscillator strengths (in the length gauge):

$$I = \tfrac{2}{3}\omega |\langle \psi_{CI} | \mathbf{r} | \psi_0 \rangle|^2,$$

where ω is the transition energy, $\mathbf{r}$ the transition moment, both in atomic units. ψ_{CI} and ψ_0 are the excited and ground state wavefunctions, respectively. In 2,5-dihydrofuran, there are two pairs of non-equivalent carbon atoms (see Fig. 1 for labelling). As in our previous study of furan [1], at the carbon edge, core hole localisation has been assumed and the coupling between excita-

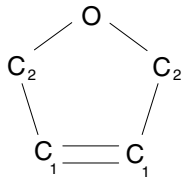

Fig. 1. Labelling of atoms in 2,5-dihydrofuran.

tions from different core holes has been neglected. The molecular symmetry has been reduced accordingly from C_{2v} to C_s. Finally, the Gaussian atomic orbitals (AOs) used is the TZP basis set (triple dzeta plus polarisation) taken from Dunning [23,24]. For the calculation of the core-excited states, a set of Rydberg orbitals (3s, 3p, 3d, 4s, 4p) was added on the core-excited atom [24]. This extended basis set will be designated as TZP + R in the following.

4. Results and discussion

The calculated HF electronic configuration of the $^1A_1$ neutral ground state of 2,5-dihydrofuran is:

$$1a_1^2 1b_2^2 2a_1^2 3a_1^2 2b_2^2 4a_1^2 5a_1^2 3b_2^2 6a_1^2 4b_2^2 7a_1^2 1b_1^2 5b_2^2 1a_2^2 8a_1^2 6b_2^2 9a_1^2 2b_1^2 3b_1^2.$$

The five first MOs (Molecular Orbtials) are the 1s orbitals of the oxygen and carbon atoms. In the present paper, we use the σ/π notation to designate MOs which are symmetrical/antisymmetrical with respect to the ring plane (it is important to keep in mind that this definition is not equivalent to that used for planar molecules such as furan, for example, where σ/π means in-plane/out-of-plane). Qualitatively, the $1b_1$ and $1a_2$ MOs represent the two π(C_2–H) bonds; the σ(C_2–H) are the $6a_1$ and $5b_2$ MOs; the oxygen lone pair is the $2b_1$ MO. Finally, the HOMO $3b_1$ represents the bond between the two C_1 carbon atoms (π($C_1 = C_1$)). The π*($C_1 = C_1$) anti-bonding MO is the LUMO and corresponds to the $2a_2$ Orbital. The $4b_1$ and $3a_2$ MOs correspond to the π*(C_2–H). According to the selection rules in the symmetry groups of the core excited species (C_{2v} at the O1s edge and C_s at the C1s one), all electronic transitions are electric dipole allowed, except the 1s(O) → a_2 transitions.

The calculated geometry of the ground state of 2,5-dihydrofuran, obtained at the MP2 level, is compared with previous experimental and theoretical [2,6,25] determinations in Table 1. Throughout this work, this geometry was employed for the calculation of the core excitations energies (vertical excitation).

4.1. Core ionisation energies

The available experimental core ionisation energies of 2,5-dihydrofuran are displayed in Table 2 and compared with our ΔSCF and ΔMP2 calculations. To the best of our knowledge, these energies have never been measured in the gas phase. Thus, following Solomon et al. [10], the values reported in the first line of this table are those of ethylene (for C_2) and ethanol (for C_1 and O) taken from a compilation [26]. The apparent good agreement with the theoretical values may be explained by the similar chemical environment of the carbon and oxygen atoms in these molecules. According to our previous study of furan [1], the calculated values should be correct within a few tenths of an eV.

Table 2 also shows the condensed (monolayer and multilayer) phases XPS binding energies measured by Solomon et al. [10]. As discussed by Stöhr [27], for adsorbed molecules, the values are well below the gas phase ones, because of the interaction with the substrate, and a

Table 1
Calculated geometry of 2,5-dihydrofuran compared with previous work (bond lengths in Å and angles in degrees)

	RHF[a] (TZP)	MP2[a] (TZP)	B3LYP[b] (6-31G*)	MP2[c] (6-311++G**)	Exp.[d] (ED)	Exp.[e] (MW)
O–C_2	1.4084	1.4317	1.430	1.4308	1.440(2)	1.4293(5)
C_1–C_2	1.5038	1.5003	1.505	1.5036	1.502(3)	1.5013(10)
C_1=C_1	1.3123	1.3332	1.331	1.3388	1.347(4)	1.3443
C_2–H	1.0862	1.0923	1.102	1.0978	1.100(5)	
C_1–H	1.0724	1.0781	1.085	1.0843	1.100(5)	
C_2–O–C_2	111.38	110.02	110.2	110.24	108.3(5)	110.24(9)
O–C_2–C_1	104.60	105.27	105.2	105.28	106.5(4)	105.41(9)
C_2–C_1–C_1	109.71	109.72	109.7	109.60		109.47
O–C_2–H	109.81	109.44	109.7	109.46		
C_2–C_1–H	123.30	123.59		123.72	110.8(9)	
C_1–C_1–H	126.99	126.68	127.0	126.67	134.8(5.6)	
H–C_2–H	107.92	108.27	107.1		107.1(3.5)	
C_2–O–C_2–H	120.74	120.76		120.74		119.55(3)

[a] This work.
[b] Ref. [6] (ED: Electron Diffraction).
[c] Ref. [2].
[d] Ref. [25].
[e] Ref. [2]. Hydrogens parameters fixed to ab initio values (MW: micro-wave).

Table 2
Core ionisation energies (eV) of 2,5-dihydrofuran

	C1s[a]			O1s[a]
	C_1	C_2	Shift[b]	
Experiment				
Gas phase[c]	290.8	292.5	1.7	538.6
Ag(1 1 0) monolayer 160 K[d]	285.1 (289.6)	286.6 (291.1)	1.5	532.8 (537.3)
Multilayer[d]	285.5 (290.0)	287.0 (291.5)	1.5	533.3 (537.8)
Calculations				
ΔSCF[e]	290.84	292.51	1.67	537.72
ΔMP2[e]	290.84	292.27	1.53	538.53

[a] The value in parentheses is obtained by adding the work function (4.5 eV) to the condensed phases results.
[b] Chemical shift (difference between the carbon ionisation energies in eV).
[c] Estimated values from [10] based on the ethylene and ethanol values from [25].
[d] Ref. [10].
[e] This work. Energies calculated using the TZP + R basis set at the MP2/TZP optimised geometry.

direct comparison with our calculations is impossible. Nevertheless, it is possible to estimate the gas phase values from the condensed phases ones by adding the work function (in the case of the Ag(110) surface [28]: 4.5 eV). As can be seen in Table 2, there remains a discrepancy at both edges of about 1 eV due to the interaction of the molecule with the surface. The calculated chemical shift (difference of the ionisation energies between the two carbon atoms having different chemical environments) of about 1.5 eV is comparable to the measured one in the condensed phase [10].

4.2. Oxygen K-shell electron energy loss spectrum

The O1s core excitation spectrum of 2,5-dihydrofuran is displayed in Fig. 2. To the best of our knowledge, it is reported for the first time. There are three main bands, centred at 535.72 eV (band A), 537.27 eV (band B) and 541.15 eV (band C) (Table 3). The latter is above the ionisation threshold. As shown in Table 3, these energies are very close to those of the same bands in the tetrahydrofuran spectrum [29]. The general shape of this spectrum is indeed very similar to that of tetrahydrofuran measured by Newberry et al. at a 0.7 eV resolution (see [29, Fig. 3]), reflecting the fact that the oxygen atom has similar chemical environment in both dihydro and tetrahydro furans. On the other hand, the energies of the corresponding features in the O1s spectrum of furan [1] have higher energies. In tetrahydrofuran [29], Newberry et al. assigned band A to the $1sO \rightarrow \pi^*(C_2\text{–}H)$ transition, band B to a $\sigma^*(C_2\text{–}O)$ transition and band C to a σ^*(ring) transition.

The results of the calculated O1s core excited states of 2,5-dihydrofuran are presented in Table 4. The two first transitions, calculated at 532.95 and 533.53 eV, have A_2 symmetry and are thus forbidden in the dipolar approximation. This is consistent with the absence of any significant feature around 533 eV in the experimental spectrum as can be seen in Fig. 2. Examination of the

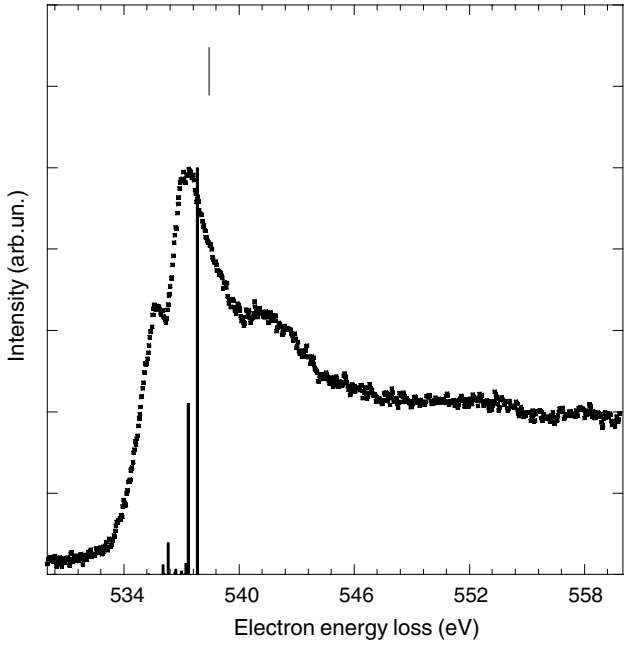

Fig. 2. The electron energy loss spectrum of 2,5-dihydrofuran recorded at the oxygen K edge with an energy resolution of 0.17 eV, steps of 40 meV, compared with the theoretical results. The vertical line indicates the location of the calculated ionisation threshold.

Table 3
Measured energies of the spectral features in the gas phase O1s ISEELS spectrum of 2,5-dihydrofuran compared to those of furan and tetrahydrofuran

	2,5-Dihydrofuran[a]	Tetrahydrofuran[b]	Furan[c]
A	535.72	536.0	537.57
B	537.27	537.4	539.17
C	541.15	541.4	545.3

[a] This work.
[b] Ref. [29].
[c] Ref. [1].

CI wavefunctions shows a strong Rydberg/valence mixing between the $\pi^*(C_1 = C_1)$ and the $3d\pi(a_2)$ MOs. After diagonalisation of the CI density matrix as suggested by

Table 4
Calculated energies, term values (TVs), relative intensities and assignments of O1s core excited states of 2,5-dihydrofuran

State	E (eV)	TV (eV)	Intensity[a]	Main configurations	$\langle r^2 \rangle$
A_2	532.95	5.58	0.000[b]	0.50 1s → 3dπ +0.44 1s → π*(C_1–C_1)	71
A_2	533.53	5.00	0.000[b]	0.52 1s → π*(C_1–C_1) +0.46 1s → 3dπ	164
A_1	535.31	3.23	0.001	0.97 1s → 3sσ/σ*(C_2–H)	128
B_2	536.03	2.50	0.023	0.98 1s → 3pσ	170
A_1	536.08	2.46	0.002	0.97 1s → 3pσ′	167
B_1	536.09	2.44	0.001	0.99 1s → 3pπ	164
A_1	536.32	2.22	0.077	0.93 1s → 3dσ	150
A_2	536.63	1.90	0.000[b]	0.96 1s → π*(C_2–H)	108
A_1	536.68	1.86	0.006	0.95 1s → 3dσ′	153
B_2	536.73	1.81	0.012	0.98 1s → 3dσ″	162
B_1	536.98	1.56	0.008	0.99 1s → 3dπ′	170
A_1	537.05	1.48	0.001	0.95 1s → 4sσ	236
B_1	537.19	1.34	0.002	0.98 1s → 4pπ	268
B_2	537.22	1.31	0.027	0.98 1s → 4pσ	271
A_1	537.34	1.19	<0.001	0.97 1s → 4pσ′	202
A_1	537.37	1.17	0.420	0.93 1s → σ*(C–O)	126
B_2	537.82	0.72	1.000	0.96 1s → σ*(C–O)	83
	538.53	0.00		ion	

[a] Relative intensity to the most intense peak.
[b] Forbidden dipole electric transition.

Löwdin [30], the resulting "natural orbitals" show that the 1sO → π*($C_1 = C_1$) correspond to the first calculated state, while the second is due to the 1sO → 3dπ(a_2) one. This is also confirmed by the respective values of $\langle r^2 \rangle$ (mean value of the r^2 operator) for the two states (71 and 164 a.u.^{2}), as can be seen in the last column of Table 4: the $\langle r^2 \rangle$ of 71 a.u.^{2} for the first state is consistent with a valence character; the rather large value for the second state (164 a.u.^{2}) is characteristic of a Rydberg state. This table also shows that the four other 3d states are calculated at much higher energies (between 536.32 and 536.98 eV). It is remarkable that the valence character of the 3dπ(a_2) state results in an energy lowering of 3 eV. Moreover, the π*(C_2–H) MO, which is also of a_2 symmetry, does not mix with the two others and the corresponding transition is calculated at 536.63 eV (Table 4). A possible rationalisation of these results may be obtained by examining the mono-electronic energies of these MOs in the O1s core ion: the ε_i of the π*(C_1–C_1) and 3dπ(a_2) MOs are −1.54 and −1.34 eV, while the π*(C_2–H) one is much higher (+2.23 eV). A similar Rydberg/valence mixing also occurs in the furan molecule (see [1, Table IV]), between the 3dπ(a_2) and 2π*(a_2) MOs, but the energies of the corresponding transitions remain close to the other 3d ones (between 538.5 and 539.0 eV).

The first band A visible in the experimental spectrum is located at 535.72 eV, on the low energy side of the B band and with a relative intensity of about 66% of the B band. The calculations do not predict any intense transition in this energy region, except for a 3dσ one calculated at 536.32 eV with a relative intensity of 7.7% (Table 4). Other 3p and 3d transitions are predicted in this energy range but their intensities are negligible. The 1s → π*(C_2–H) transition calculated at 536.63 eV is electric-dipole forbidden. Calculation of the quadrupolar electric oscillator strength gives a very small value. It is also possible to assign the A peak to the σ*(C–O) transition which is calculated to occur at 537.37 eV with an intensity of 42%. However, in this case, the calculations would be wrong by more than 1.5 eV, which is unlikely. It should be noticed that the same situation occurs in the O1s spectrum of furan [1]. In the case of tetrahydrofuran, Newberry et al. [29] assigned the corresponding band to the second (B_2) 1s → π*(C_2–H) transition. According to our calculation, this transition has a rather high intensity (28.7%) but is predicted to occur at 539.78 eV, i.e., above the ionisation threshold. Thus, the A band is assigned to $n = 3$ Rydberg transitions. The O1s spectrum of condensed phases would confirm this assignment, since Rydberg transitions do not appear in this type of spectra.

The second band B measured at 537.27 eV is the most intense one (Table 3). The calculations predict $n = 4$ Rydberg transitions in this energy region with very small intensities (Table 4). Since the second 1s → σ*(C–O) is calculated at 537.82 eV with the highest intensity, there is no ambiguity to assign band B to this transition. The third band C located at 541.15 eV is above the ionisation threshold. The calculations predict the remaining σ* transitions to occur in this region. Some of them are relatively intense but a direct comparison with experiment is difficult since the present calculations do not take into account the influence of the continuum.

The theoretical spectrum is also compared with the experimental one in Fig. 2. As in the O1s spectrum of furan (see [1, Fig. 3]), the calculations seem to overestimate the transition energies by a few tenths of an eV.

4.3. Carbon K-shell electron energy loss spectrum

The C1s electron energy loss spectrum of 2,5-dihydrofuran is shown in Fig. 3. A more detailed view of the low energy part of the spectrum is displayed in Fig. 4. The energies of the observed features are given in Table 5 and compared with those from the low resolution ones obtained by Solomon et al. in the condensed

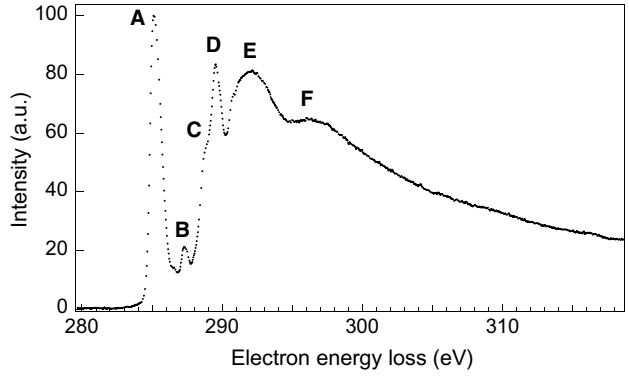

Fig. 3. The electron energy loss spectrum of 2,5-dihydrofuran recorded at the carbon K edge with an energy resolution of 0.17 eV, steps of 40 meV.

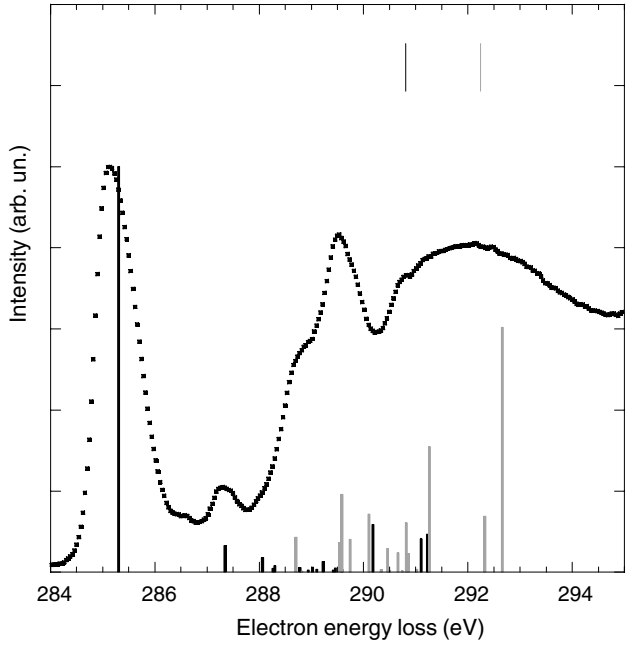

Fig. 4. Comparison between the experimental and the theoretical spectra at the carbon K edge. The vertical lines indicate the locations of the calculated ionisation thresholds (black: C_1; grey: C_2).

Table 5
Measured energies (eV) of the spectral features in the C1s spectrum and previous proposed assignments

	ISEELS[a]	NEXAFS[b]		Assignment[b]
	Gas	Submonolayer Ag(110)	Multilayer	
A	285.14	285.0	285.4	$\pi^*(C_1{=}C_1)$
B	287.30			
B1	287.44			
C	288.68			
C1	289.15			
D	289.50	288.9/289.2[d]	289.6	σ^*(C–H)
D1	289.72			
E1	290.80			
E	292.05	292.1/292.4[d]	292.9	σ^*(C–C, C–O)
F	296.3	298	297	$\sigma^*(C_1{=}C_1)$

[a] This work.
[b] Ref. [10].
[d] First value for normal incidence, second for glancing incidence.

submonolayer and multilayer phases [10]. the overall shape of the gas phase spectrum is in agreement with the thin films ones but the present work reveals more details, due to the better resolution in our experiment, especially in the 286–290 eV region. With the exception of the two first bands, the spectrum is also close to that of tetrahydrofuran recorded by Newberry et al. with a 0.7 eV resolution [29]. On the other hand, the corresponding furan spectrum is somewhat different [1, Fig. 4].

The results of the calculations of the C1s core excited transitions are displayed in Table 6 and the theoretical spectrum is compared with the experimental one in Fig. 4. Not surprisingly, the first band A, which is the most intense of the spectrum, is assigned to the $1sC_1 \rightarrow \pi^*(C_1{=}C_1)$ transition. The calculated energy is 285.32 eV, in very good agreement with the experimental one (285.14 eV). On the high energy side of this band, there is a low intensity feature located at 286.5 eV (Fig. 4). It is difficult to assign this peak, since the calculations do not predict any transition around this energy (Table 6). The $1sC_2 \rightarrow \pi^*(C_1{=}C_1)$ transition is predicted to occur at 288.82 eV. Since the π^* is localised on the C_1 atoms, it is not surprising that its intensity is very low. The triplet $1sC_1 \rightarrow \pi^*(C_1{=}C_1)$ transition should appear below the singlet one and is indeed calculated at 284.87 eV. The energy splitting of 1.34 eV with respect to the first band is too large to be due vibrational excitation of the A band. Since its intensity is also rather small, we assign this feature to the presence of an impurity in the sample. The resolution of the condensed phases spectra [10] is too low to resolve this band in case this peak is present.

The next band B is centred at 287.30 eV and shows a not well resolved feature B1 at 287.44 eV (Table 5). It corresponds to the $1sC_1 \rightarrow 3s\sigma/\sigma^*(C_1{-}H)$ transition, calculated to appear at 287.34 eV. The rather high inten-

Table 6
Calculated energies, term values (TVs) and relative intensities and assignments of C1s core excited states of 2,5-dihydrofuran

State	E (eV)	TV (eV)		Intensity[a]	Main configurations	$\langle r^2 \rangle$
		C_1	C_2			
A″	285.32	5.52		1.000	0.92 $1sC_1 \rightarrow \pi^*(C_1{=}C_1)$	69
A′	287.34	3.50		0.065	0.95 $1sC_1 \rightarrow 3s\sigma/\sigma^*(C_1{-}H)$	114
A′	288.08	2.76		0.036	0.95 $1sC_1 \rightarrow 3p\sigma$	132
A′	288.28	2.56		0.009	0.95 $1sC_1 \rightarrow 3p\sigma'$	137
A′	288.31	2.53		0.016	0.96 $1sC_1 \rightarrow 3p\pi$	141
A′	288.69		3.58	0.086	0.96 $1sC_2 \rightarrow 3s\sigma/\sigma^*(C_2{-}H)$	108
A′	288.80	2.04		0.011	0.94 $1sC_1 \rightarrow 3d\sigma$	150
A′	288.82		3.45	0.002	0.85 $1sC_2 \rightarrow \pi^*(C_1{=}C_1)$	70
A′	288.94	1.90		0.005	0.95 $1sC_1 \rightarrow 3d\sigma'$	172
A′	289.04	1.80		0.012	0.93 $1sC_1 \rightarrow 3d\sigma''$	180
A′	289.09	1.75		0.007	0.97 $1sC_1 \rightarrow 3d\pi$	164
A′	289.22	1.62		0.026	0.95 $1sC_1 \rightarrow 4s\sigma$	264
A′	289.26	1.58		0.005	0.97 $1sC_1 \rightarrow 3d\pi'$	175
A′	289.44	1.40		0.005	0.95 $1sC_1 \rightarrow 4p\sigma$	306
A′	289.47	1.37		0.010	0.97 $1sC_1 \rightarrow 4p\pi$	305
A′	289.55		2.72	0.192	0.97 $1sC_2 \rightarrow 3p\pi/\pi^*(C_2{-}H)$	124
A′	289.56		2.71	0.073	0.65 $1sC_2 \rightarrow 3p\sigma$	124
					$+0.21$ $1sC_2 \rightarrow 3p\sigma'$	
A′	289.58	1.26		0.007	0.93 $1sC_1 \rightarrow 4p\sigma'$	229
A′	289.73		2.54	0.081	0.62 $1sC_2 \rightarrow 3p\sigma'$	141
					$+0.29$ $1sC_2 \rightarrow 3p\sigma$	
A′	290.12		2.15	0.143	0.42 $1sC_2 \rightarrow 3d\sigma$	154
					$+0.31$ $1sC_2 \rightarrow 3d\sigma'$	
A′	290.17	0.67		0.118	0.88 $1sC_1 \rightarrow \sigma_1^*$	105
A′	290.33		1.94	0.006	0.46 $1sC_2 \rightarrow 3d\sigma$	163
					$+0.46$ $1sC_2 \rightarrow 3d\sigma'$	
A″	290.48		1.79	0.058	0.92 $1sC_2 \rightarrow 3d\pi$	180
A′	290.50		1.77	0.004	0.94 $1sC_2 \rightarrow 3d\sigma''$	177
A′	290.68		1.59	0.048	0.85 $1sC_2 \rightarrow 4s\sigma$	258
A″	290.73		1.54	0.003	0.94 $1sC_2 \rightarrow 3d\pi'$	170
A′	290.82		1.45	0.122	0.63 $1sC_2 \rightarrow 4p\sigma$	245
					$+0.11$ $1sC_2 \rightarrow 4p\sigma'$	
	290.84	0.00			Ion C_1	
A″	290.86		1.41	0.046	0.98 $1sC_2 \rightarrow 4p\pi$	296
A′	291.01		1.26	0.007	0.73 $1sC_2 \rightarrow 4p\sigma'$	256
					$+0.20$ $1sC_2 \rightarrow 4p\sigma$	
A′	291.12	−0.28		0.082	0.86 $1sC_1 \rightarrow \sigma_2^*$	106
A′	291.22	−0.38		0.093	0.83 $1sC_1 \rightarrow \sigma_3^*$	119
A′	291.28		0.99	0.309	0.71 $1sC_2 \rightarrow \sigma_1^*$	162
	292.27		0.00		Ion C_2	
A′	292.32		−0.05	0.138	0.79 $1sC_2 \rightarrow \sigma_1^*(C_2{-}H)$	100
A′	292.66		−0.39	0.604	0.95 $1sC_2 \rightarrow \pi_1^*(C_2{-}H)$	119

[a] Relative intensity to the most intense peak.

sity of this peak (6.5% of the first one) is due to the $\sigma^*(C_1{-}H)$ valence character of the $3s\sigma$ MO. It is interesting to note that in the case of furan, this transition is found at exactly the same energy but the corresponding band is hidden by π^* peaks in the experimental spectrum [1]. The B1 feature, measured at 287.44 eV, is located 0.14 eV above the B one. This energy spacing ($\approx$1100 cm^{-1}) suggests excitation of a vibration mode. In order to test this hypothesis, we have simulated the vibrational structure of this band using the method proposed by Domcke and Cederbaum [31,32]. We briefly recall that in its simplest form, this method requires the knowledge of the vibrational frequencies of the ground state (hessian matrix), and the gradient of the energy of the excited state at the ground state geometry (κ matrix). In the present case, the ground state hessian and the κ matrix for the $1sC_1 \rightarrow 3s\sigma/\sigma^*(C_1{-}H)$ core excited state were evaluated at the HF level (ROHF-GVB for the core state). The core hole was also assumed to be localised. Not unexpectedly, the unscaled ground state frequencies appear to be overestimated by $\approx$10% when compared to previous calculated [6] and measured [2,6,3,33] values. The resulting calculated Franck–Condon factors (including hot bands), are displayed in Fig. 5, using a line width of 0.17 eV corresponding to the experimental resolution. The comparison with the experiment also shown in Fig. 5 shows that this very simple model reproduces correctly the envelope of the

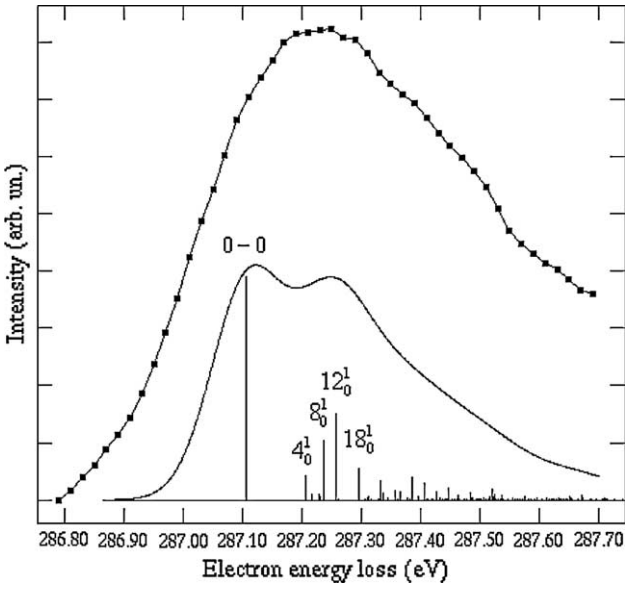

Fig. 5. Comparison between the calculated vibrational structure of the B band and the experimental spectrum. The vertical excitation energy has been set to the experimental value (287.30 eV).

band, especially the two features separated by 0.14 eV. The most intense vibrational transitions are also indicated in Fig. 5: the ν_4 frequency corresponds to the C_2–O–C_2 bending mode, the ν_8 and ν_{12} to the in-plane and out-of-plane C_1–C_1–H bending modes, respectively. The ν_{18} is the H–C_2–H wagging mode. Most of these excitations involves the C_1 atom, i.e., the excited one. This suggests that the differences of geometry between the ground state and the $1sC_1 \rightarrow 3s\sigma/\sigma^*(C_1\text{–H})$ core excited state should be concentrated on the C_1 excited atom. This is confirmed by the calculated ROHF-GVB geometry displayed in Fig. 6 which is close to the ground state one (first column of Table 1). The main difference

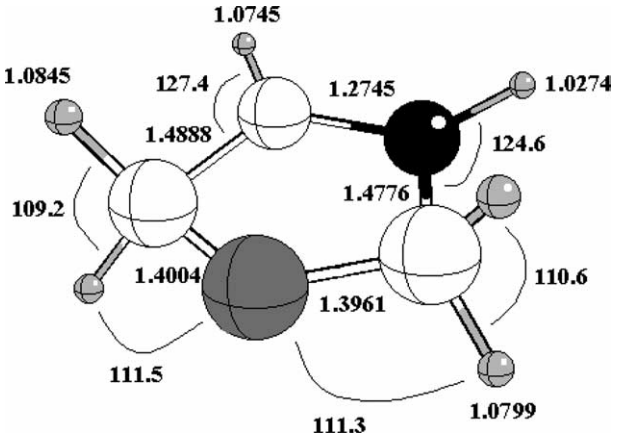

Fig. 6. Calculated geometry (ROHF/TZP + R) of the $1sC_1 \rightarrow 3s\sigma/\sigma^*(C_1\text{–H})$ $^1A'$ core excited state of 2,5-dihydrofuran (bond lengths in Å and angles in degrees). The atom in black is the core excited one.

is the shorter C_1–H bond length (1.0274 Å), typical of a N–H bond, as predicted by the equivalent core approximation. The calculation of the Hessian matrix for this structure showed that it is a true equilibrium geometry since all the frequencies were found to be real.

At higher energies, the measured intensity increases rapidly (Fig. 4) and the next band C at 288.68 eV appears as a shoulder in the low energy side of the D band, centred at 289.50 eV (Table 5). Only the latter appears in the NEXAFS spectra of condensed phases [10]. The polarisation dependence of its intensity led to an assignment of it to a σ*(C–H) transition. The calculations of Table 6 reveal a much more complicated picture. On the 288–290 eV region, the calculations predict Rydberg transitions (3p, 3d, 4s and 4p) from the C_1 atom but with low intensities (Table 6). The rather high intensities of the C and D bands are due to transitions from the C_2 atom: the C peak is assigned to the Rydberg/valence $1sC_2 \rightarrow 3s\sigma/\sigma^*(C_2\text{–H})$ transition with a relative intensity of 8.6%. The D band is due to several transitions to the 3p and 3d orbitals. Their rather large intensities (7.3–19.2%) comes from the $\sigma^*/\pi^*(C_2\text{–H})$ character of these Rydberg MOs and only concern transitions from the C_2 atom. On the other hand, the Rydberg transitions from the C_1 atom have very small intensities (Fig. 4). The large density of calculated intense transitions also explains the presence of fine features such as C1 (289.15 eV) and D1 (289.72 eV) in the experimental spectrum.

The next band E, whose maximum lies at 292.05 eV in the experimental spectrum (Table 5), is located between the two ionisation thresholds. The E1 feature is measured at 290.80 eV and coincides with the calculated C1s ionisation energy, as well as with an intense $1sC_2 \rightarrow 4p\sigma$ transition (Table 6). There is no calculated transition corresponding to the maximum of the E band and this part of the spectrum probably shows the $1sC_1^{-1}$ continuum and possibly the $1sC_2^{-1}$ continuum if the calculated C_2 ionisation is slightly overestimated. This calculated C_2 ionisation threshold is quasi-degenerate with two intense $1sC_2 \rightarrow \sigma^*(C_2\text{–H})$ and $\pi^*(C_2\text{–H})$ transitions. Finally, the last band F measured at 296.3 eV is beyond the reach of the present calculations. It is tentatively assigned to a σ* "shape resonance" but one should keep in mind that this type of assignment is a widely debated question [34].

Fig. 4 shows that the agreement between the experimental spectrum and the synthetic one deduced from the calculations is quite good for both the energies and intensities of the transitions.

5. Conclusion

In this work, we have studied the K-shell electron excitation spectra of gaseous 2,5-dihydrofuran with the

inner shell electron energy loss spectroscopy and ab initio Configuration Interaction calculations. The calculated energies and intensities are in good agreement with the experimental ones and permit the assignment of the observed bands.

At the O1s edge, the spectrum is dominated by one main band, close to the ionisation energy and very broad, assigned to σ* transitions. This band is also present in the furan [1] and tetrahydrofuran [29] spectra.

At the C1s edge, the spectrum differs significatively from the furan case, reflecting the differences in the number and symmetries of the π* MOs between the two molecules. The better resolution of the present work compared to submonolayer and multilayer NEXAFS spectra reveals the presence of new features that were not visible in previous studies on solid 2,5-dihydrofuran. The calculations prove that the two non-equivalent carbon atoms have very different contributions to the experimental spectrum. Indeed, while most of the C_1 Rydberg states have low intensities, as in the furan case, several $n = 3$ and $n = 4$ C_2 Rydberg states have an important valence character. It is very likely that the same phenomenon should occur for both carbon atoms in the C1s spectrum of tetrahydrofuran. Finally, the chemical shift in the C1s neutral excited species is much larger than in the corresponding ionised molecules, suggesting electronic correlation much larger in the C1s excited states than in the ionised ones.

Acknowledgements

The ''Laboratoire de Physique des Lasers, Atomes et Molécules'' (PhLAM) is ''Unité Mixte de Recherche du CNRS''. The ''Centre d'Études et de Recherches Lasers et Applications'' (CERLA, FR CNRS 2416) is supported by the ''Ministère chargé de la Recherche'', the ''Région Nord/Pas-de-Calais'' and the ''Fonds Européen de Développement Économique des Régions'' (FEDER). Parts of the computations were carried out at the CRI (Centre de Ressources Informatiques), on the IBM-SP3 computer that is supported by the ''Programme de Calcul Intensif et Parallèle'' of the ''Ministère chargé de la Recherche'', the ''Région Nord/Pas-de-Calais'' and the FEDER.

This research has been supported by the Fonds National de la Recherche Scientifique and the Patrimoine of University of Liège. M.-J.H.-F. acknowledge the Fonds National de la Recherche Scientifique for research position.

References

[1] D. Duflot, J.-P. Flament, A. Giuliani, J. Heinesch, M.-J. Hubin-Franskin, J. Chem. Phys. 119 (2003) 8946.
[2] S. Melandri, B. Velino, W. Caminati, J. Mol. Struct. 563–564 (2001) 245.
[3] J.C. Lopez, J.L. Alonso, G. Wlodarczak, J. Demaison, J. Mol. Spectrosc. 160 (1994) 158.
[4] L.A. Carreira, R.C. Lord, J. Chem. Phys. 51 (1969) 3225.
[5] T.B. Malloy, L.A. Carreira, J. Chem. Phys. 71 (1979) 2488.
[6] F. Billes, H. Böhlig, M. Ackermann, M. Kudra, J. Mol. Struct. (Theochem) 672 (2004) 1.
[7] E.V. Gromov, A.B. Trofimov, N.M. Vitkoskaya, J. Schirmer, H. Köppel, J. Chem. Phys. 119 (2003) 737.
[8] E.E. Rennie, U. Hergenhahn, O. Kugeler, A. Rüdel, S. Marburger, A.M. Bradshaw, J. Chem. Phys. 117 (2002) 6524.
[9] M. Mauerer, P. Zebisch, M. Weinelt, H.-P. Steinrück, J. Chem. Phys. 99 (1993) 3343.
[10] J.L. Solomon, R.J. Madix, J. Stöhr, J. Chem. Phys. 94 (1991) 4012.
[11] C. Hannay, J. Heinesch, U. Kleyens, M.-J. Hubin-Franskin, Meas. Sci. Technol. 6 (1995) 1140.
[12] M.-J. Hubin-Franskin, H. Aouni, D. Duflot, F. Motte-Tollet, L.F. Ferreira, G. Tourillon, J. Chem. Phys. 106 (1997) 35.
[13] M.-J. Hubin-Franskin, J. Heinesch, Nucl. Instrum. Methods Phys. Res. A 477 (2002) 546.
[14] W.F. Chan, G. Cooper, C.E. Brion, Chem. Phys. 170 (1993) 123.
[15] F. Currell, C.M. John, Meas. Sci. Technol. 3 (1992) 1192.
[16] R.N.S. Sodhi, C.E. Brion, J. Electron Spectrosc. Relat. Phenom. 34 (1984) 363.
[17] D. Duflot, J.-P. Flament, I.C. Walker, J. Heinesch, M.-J. Hubin-Franskin, J. Chem. Phys. 118 (2003) 1137.
[18] S. Bodeur, P. Millié, I. Nenner, Phys. Rev. A41 (1990) 252.
[19] M.W. Schmidt, K.K. Baldridge, J.A. Boatz, S.T. Elbert, M.S. Gordon, J.J. Jensen, S. Koseki, N. Matsunaga, K.A. Nguyen, S. Su, T.L. Windus, M. Dupuis, J.A. Montgomery, J. Comp. Chem. 14 (1993) 1347.
[20] B. Huron, J.-P. Malrieu, P. Rancurel, J. Chem. Phys. 58 (1973) 5745.
[21] R. Cimiraglia, Int. J. Quantum. Chem. 60 (1996) 167.
[22] C. Angeli, R. Cimiraglia, M. Persico, A. Toniolo, Theor. Chem. Acc. 98 (1997) 57.
[23] T.H. Dunning Jr., J. Chem. Phys. 55 (1971) 716.
[24] T.H. Dunning Jr., P.J. Hay, in: H.F. SchaeferIII (Ed.), Methods of Electronic Structure Theory, vol. 3, Plenum Press, New York, 1977, p. 1 (Chapter 1).
[25] K. Takawaga, R.L. Hildebrandt, J. Am. Chem. Soc. 106 (1984) 20.
[26] A.A. Bakke, H.W. Chen, W.L. Jolly, J. Electron Spectrosc. Relat. Phenom. 20 (1980) 333.
[27] J. Stöhr, NEXAFS Spectroscopy, Springer, Berlin, 1992 (Chapter 7.4.3).
[28] A.W. Dweydari, C.H.B. Mee, Phys. Status Solidi A 27 (1975) 223.
[29] D.C. Newberry, I. Ishii, A.P. Hitchcock, Can. J. Chem. 64 (1986) 1145.
[30] P.-O. Löwdin, Phys. Rev. 97 (1955) 1474.
[31] L.S. Cederbaum, W. Domcke, Adv. Chem. Phys. 36 (1977) 205.
[32] J.-P. Dognon, C. Pouchan, A. Dargelos, J.-P. Flament, Chem. Phys. Lett. 109 (1984) 492.
[33] T.D. Klots, W.B. Collier, Spectrochim. Acta 50A (1994) 1725.
[34] M.N. Piancastelli, J. Electron Spectrosc. Relat. Phenom. 100 (1999) 167.

Article 15

PHYSICAL REVIEW A **75**, 052719 (2007)

C 1*s* and N 1*s* core excitation of aniline: Experiment by electron impact and *ab initio* calculations

D. Duflot and J.-P. Flament
Laboratoire de Physique des Lasers, Atomes et Molécules (PhLAM), UMR CNRS 8523, Centre d'Études et de Recherches Lasers et Applications (CERLA, FR CNRS 2416), Université des Sciences et Technologies de Lille, F-59655 Villeneuve d'Ascq Cedex, France

A. Giuliani
DISCO Beamline, SOLEIL Synchrotron, BP 48, L'Orme des Merisiers, 91192 Gif-sur-Yvette Cedex, France and Cepia, Institut National de la Recherche Agronomique, BP 71627, 44316 Nantes Cedex 3, France

J. Heinesch, M. Grogna, and M.-J. Hubin-Franskin
Laboratoire de Spectroscopie d'Électrons diffusés, Université de Liège, Institut de Chimie B6c, B-4000 Liège 1, Belgium

(Received 20 January 2007; revised manuscript received 14 March 2007; published 30 May 2007)

Core shell excitation spectra of aniline at the carbon and nitrogen 1*s* edges have been obtained by inner-shell electron energy-loss spectroscopy recorded under scattering conditions where electric dipolar conditions dominate, with higher resolution than in the previous studies. They are interpreted with the aid of *ab initio* configuration interaction calculations. The spectrum at the C 1*s* edge is dominated by an intense π^* band. The calculated chemical shift due to the different chemical environment at the carbon 1*s* edge calculated is in agreement with the experimental observations within a few tenths of an eV. The transition energies of the most intense bands in the C 1*s* excitation spectrum are discussed at different levels of calculations. In the nitrogen 1*s* excitation spectrum the most intense bands are due to Rydberg-valence transitions involving the σ^*-type molecular orbitals, in agreement with the experiment. This assignment is different from that of extended Hückel molecular orbital calculations. The geometries of the core excited states have been calculated and compared to their equivalent core molecules and benzene.

DOI: 10.1103/PhysRevA.75.052719 PACS number(s): 32.80.Hd, 34.80.Gs

I. INTRODUCTION

One of the most important properties of aniline is to polymerize easily in polyaniline. This polymer is relatively easy to synthesize and can get, under specific conditions, interesting electric conducting properties [1]. This is also involved for the synthesis of molecular systems having potentially large nonlinear optical responses [2].

The physicochemical properties of polyaniline are related at least partly to the π molecular orbitals in the valence bands but also in the empty levels. In a general way these are expected at least for thin films to be predicted to be not too different from the individual molecule constituting the unit.

To our knowledge core excitation spectra of aniline have been reported by only two experimental studies previously, namely x-ray photoabsorption [near-edge x-ray-absorption fine-structure (NEXAFS)] of the condensed multilayer solid [3–5] and inner-shell electron energy-loss spectroscopy (ISEELS) of aniline in gas phase [6]. Calculations of the core excitation spectra have been reported using the extended Hückel molecular orbital (EHMO) method [6], the multiconfiguration self-consistent-field (MCSCF) method for the carbon first π^* transitions [5], and the static exchange (STEX) method [7,8]. In Ref. [7], the assignments of the main features of the spectra were briefly discussed, while in the later work, no detailed discussion was given.

In the present work the electronic structure of aniline, and much more specifically the unoccupied levels, have been investigated by core shell excitation and *ab initio* calculations. Inner-shell electron energy-loss spectroscopy has been used to record the C 1*s* and N 1*s* excitation spectra of aniline. The experimental conditions—high electron impact energy and quite small scattering angle—are such that electron energy-loss spectra are expected to exhibit the same features with quite similar relative intensities to those of the corresponding ones in photoabsorption.

The core excitation spectra have been measured for gaseous aniline with higher energy resolution than in the previous studies. *Ab initio* configuration interaction (CI) calculations have been performed to assist in the spectral assignments and to discuss aspects of the unoccupied molecular-orbital electronic structure.

II. EXPERIMENTAL PART

The inner-shell electron energy-loss spectra were obtained with a Vacuum Science Workshop Ltd. spectrometer which has been adapted for gas studies and high-energy electron beams and has been equipped with a home-made position sensitive multidetector system in order to improve data collection times. The experimental apparatus and procedure have been described in detail previously [9–11].

Briefly the spectrometer consists of an electrostatic 180° monochromator operating in the constant pass energy mode, a collision chamber, and an electrostatic analyzer identical to the monochromator. The monochromatized incident electrons are accelerated up to 2 keV and focused into the collision chamber using a four-element electron lens. The electrons are slightly deflected (0.02 radians) by two sets of *X*-*Y* plates inside the collision chamber. The scattered electrons are energy analyzed and focused onto the entrance slit of the analyzer by a lens similar to that used for acceleration.

In the collision conditions of quite low momentum transfer (i.e., high incident energy and quite small scattering

angle), only electronic electric-dipolar transitions are excited. Inside the vacuum vessel, a residual pressure of less than 1×10^{-8} Torr is maintained by a cryogenic pumping system. The electron gun and the analyzer regions are differentially pumped by turbomolecular pumps, respectively. The spectra have been recorded with 0.040- and 0.020-eV steps.

In order to take into account valence and lower-energy inner-shell excitation cross section, a linear background has been subtracted from the raw spectra by extrapolating a least-square fit of the pre-edge experimental data points.

The absolute energy scale has been calibrated at both edges relative to CO and the C $1s\rightarrow\pi^*$ $(\nu'=0)$ band at 287.40 ± 0.02 eV [12] recording the spectra with 0.01-eV steps and the mean value of 400.99 ± 0.09 eV between the N $1s\rightarrow\pi^*$ $(\nu'=0)$ at 400.88 eV and the N $1s\rightarrow\pi^*$ $(\nu'=1)$ at 401.1 eV [12] recording the spectra with 0.02-eV steps.

The sample has been provided by ACROS Organics with a stated purity better than 99.5%. It was used directly without further purification except for repetitive freeze-pump-thaw cycles in order to eliminate air and other volatile impurities in the sample.

III. COMPUTATIONAL METHOD

Since the computational method used has been described in detail elsewhere [13], it will be briefly outlined. The starting hypothesis [14] is that, due to the important relaxation of the electronic density following the creation of the core hole, the molecular orbitals (MOs) of the core *ionized* molecule are a better approximation for the description of the core *excited* states than the ground state MOs. Formally, the energy of a given $1s\rightarrow\mathrm{i}^*$ core excited state may be obtained by correcting the core ion energy in the following manner:

$$E(1s\rightarrow\mathbf{i}^*)=E(1s\rightarrow\infty)+\varepsilon_{\mathbf{i}^*}+P_{\mathbf{i}^*}+C_{\mathbf{i}^*},$$

where $\varepsilon_{\mathrm{i}^*}$ is the Hartree-Fock monoelectronic energy of the i^* MO. $E(1s\rightarrow\infty)$ is the core ion energy, obtained using the ROHF-GVB method implemented in the GAMESS-US package [15]. The $P_{\mathbf{i}^*}$ and $C_{\mathbf{i}^*}$ terms represent the residual relaxation and valence correlation effects of the i^* electron with respect to the core ion, respectively. The relaxation term is taken into account by performing a configuration interaction (CI) calculation in the monoexcitation space of the lowest-lying core states, obtained by a preliminary diagonalization of the full $1s\rightarrow\mathrm{i}^*$ CI matrix. In order to evaluate the $C_{\mathbf{i}^*}$ term, the calculated CI wave functions serve as the zeroth-order space for a multireference MP2 calculation using the three-class diagrammatic CIPSI method [16,17]. To spare computational time, an extrapolation procedure [18] was employed, using six thresholds between 97.0 and 99.5 % of the exact wave functions. Finally, the dipolar electric transition oscillator strengths with respect to the ground state of the molecule were computed, using the length gauge.

The Gaussian atomic orbitals (AOs) used are the TZP basis set taken from Dunning [19]. For the calculation of the core excited states, a set of Rydberg orbitals $(5s,5p,2d)$ was added to the core excited atom basis set. The first exponents were taken from Dunning and Hay [20] and the last ones were determined in an "even-tempered" manner. In the following, the basis set with diffuse functions will be named "TZP+*R*." The theoretical width of the bands was set to the experimental resolution (0.17 eV) and a Gaussian profile was used in the comparison of the calculations and the experiment.

The aniline molecule contains four chemically nonequivalent carbons and one nitrogen atom (see Fig. 1 for labeling). For the calculation of the core ionized MOs at both edges, core hole localization was assumed and the coupling between excitations from different core holes was neglected.

IV. RESULTS AND DISCUSSION

It is now well known that aniline is nonplanar in its ground electronic state [21,22], the amine group being pyramidally distorted [Fig. 1(a)]. The symmetry point group is therefore C_s, with the symmetry plane corresponding to the (yz) plane using the frame of Fig. 1(a). The energy difference between the planar [Fig. 1(a)] and nonplanar [Fig. 1(c)] conformations is rather small, with proposed values of 524.4 cm^{-1} [23], 454 cm^{-1} [24], and 509.0 cm^{-1} [25]. From the theoretical point of view, this quantity is very sensitive to the basis set and method employed [26,27]. In the present work, the inversion barrier is calculated to be 388 cm^{-1} at the HF level and 710 cm^{-1} at the MP2 level.

In the present work, as in previous theoretical studies of core excited aniline [5,6,8], the planar conformation was used. This geometry reduces the computational cost and allows calculating a larger number of states. Moreover, the high symmetry facilitates the assignment of the core states. The calculation of valence electronic spectrum for nonplanar and planar conformations [28] showed very small differences for the energies and intensities (Fig. 3 of [28]). Therefore for N and C_4 atoms, the calculations were performed in the C_{2v} group of planar aniline. For C_2 and C_3, because of assumed core hole localization, the C_{2v} symmetry was reduced to C_s, but with the symmetry plane being the (xz) plane of Fig. 1. Thus it should be kept in mind that the (xz) symmetry plane used for C_2 and C_3 is in fact perpendicular to the true (yz) symmetry plane of the molecule, resulting in an inversion between A' and A'' irreducible representations.

The use of C_{2v} symmetry also has some consequences on the allowed dipole electric transitions: the $1s(a_1)\rightarrow\pi^*(a_2)$ or $nd(a_2)$ transitions are forbidden while all transitions should be allowed in the nonplanar (C_s) conformation. However, their intensities should be small when compared to other transitions.

The calculated HF electronic configuration of the neutral ground state of aniline for the planar molecule is

$$1a_1^2 2a_1^2 3a_1^2 1b_2^2 2b_2^2 4a_1^2 5a_1^2 6a_1^2 7a_1^2 3b_2^2 8a_1^2 4b_2^2 9a_1^2 \times 10a_1^2 5b_2^2 11a_1^2 12a_1^2 6b_2^2 7b_2^2 1b_1^2 13a_1^2 8b_2^2 2b_1^2 1a_2^2 3b_1^2.$$

The seven first MO's (molecular orbitals) are the $1s$ orbitals of the nitrogen atom and of the six carbon atoms. There are four occupied π-type MO's, namely the $1b_1$, $2b_1$, $1a_2$, and $3b_1$. The $1b_1$ MO corresponds to the nitrogen lone pair, with C_1 and C_2 bonding character; the $2b_1(1\pi)$ MO has

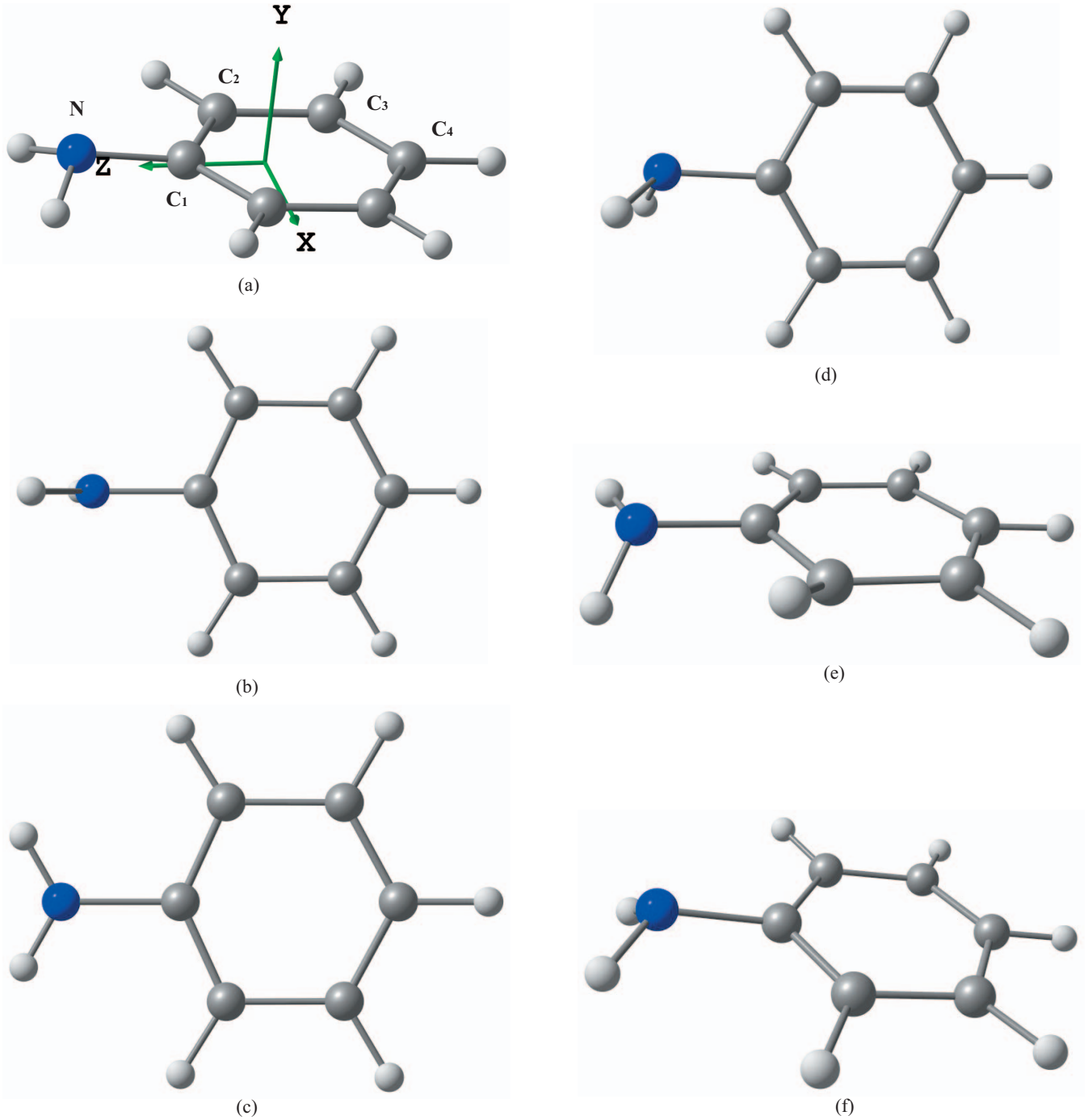

FIG. 1. (Color online) (a) Labeling of atoms in aniline and ground-state geometry. (b)–(f) Possible geometries for core ionized and excited states of aniline and their $Z+1$ equivalent.

C_3-C_4 bonding character, and antibonding with the N lone pair; the $1a_2(2\pi)$ is essentially the $\pi(C_2\text{-}C_3)$ MO and finally, the $3b_1(3\pi,\text{HOMO})$ has C_3-C_4 and C_1-C_2 bonding character, with C_2-C_3 and C_1-N antibonding character. There are three unoccupied π^* MO's: $2a_2$ ($1\pi^*$, lowest unoccupied molecular orbital), $4b_1$ ($2\pi^*$), and $5b_1$ ($3\pi^*$) (see Fig. 8 of Ref. [3]).

The HF and MP2 optimized geometries of the ground state, obtained for both C_{2v} and C_s conformations, are compared with previous experimental [22] and theoretical [29] works in the supplementary data of this paper [30] (see also [27]). The C_s MP2 results agree quite well with the experiment. The pyramidalization of the amine group is usually measured via the ϕ angle between the H-N-H bisector axis and the C_1C_4 axis. Our calculated MP2 ϕ value of 41.41° is slightly larger than the earlier measures (37.5° in [22]), partly due to the fact that in some previous studies, the N, C_1, and C_4 atoms were supposed to be aligned. Other determinations are very close to our calculations: 42.17° in [23], 42° in [24], and 41.7° in [25].

TABLE I. Core ionization energies (eV) of aniline at the N 1*s* and C 1*s* edges.

	ΔSCF[a]	Shift[a]	ΔMP2 (CIPSI)[b]	Shift[b]	ΔMP2 (ZAPT)[b]	Shift[b]	ΔMP2 (RMP)[b]	Shift[b]	ΔSCF[c]	Shift[c]	STEX[d]	Shift[d]	Expt.[e]	Shift[e]
C_1	291.77	2.00	291.52	1.73	291.64	1.74	291.62	1.73	291.77	2.00	291.53	1.92	291.3	1.6
C_2	289.94	0.17	289.99	0.20	290.11	0.21	290.09	0.20	289.96	0.19	289.77	0.16	289.9	0.2
C_3	290.39	0.62	290.13	0.34	290.24	0.34	290.23	0.34	290.41	0.64	290.31	0.70	290.2	0.5
C_4	289.77	0.00	289.79	0.00	289.90	0.00	289.89	0.00	289.77	0.00	289.61	0.00	289.7	0.0
N	405.30		405.47		405.60		405.59		405.30		405.41		405.3	

[a]This work. Gas phase values calculated at the TZP/RHF optimized geometry using the TZP+Rydberg basis set.
[b]This work. Gas phase values calculated at the TZP/MP2 optimized geometry using the TZP+Rydberg basis set.
[c]Reference [8].
[d]Reference [7].
[e]Reference [31].

A. Core ionization energies

The calculated core ionization energies obtained at the ΔMP2 and ΔSCF levels are given in Table I and compared with the ΔSCF results of Carravetta *et al.* [8] and the XPS experimental values [31]. Since in MP2 calculations, several possible definitions of the zero-order Hamiltonian for open-shell systems are possible [32], the ΔMP2 values of the present work were obtained using three different models: RMP [33,34], ZAPT [35,36], and CIPSI. The two ΔSCF are nearly identical because Carravetta *et al.* [8] employed the same basis set as in the present work. While RMP and ZAPT methods are very similar, the CIPSI values are slightly different. All results are within 0.5 eV of the experimental values.

In order to test the influence of using a planar geometry on core energies, the calculations were done in both planar (C_{2v}) and nonplanar (C_s) conformations. As shown in the EPAPS document [30], using the nonplanar geometry affects the core ionization energies by at most 0.18 eV, although the variation is different for each atom. For carbon atoms, the nonplanar absolute energy values are closer to experiment than the planar results. The situation is reversed for nitrogen. Globally, for both geometries, chemical shifts are in good agreement with experiment, while most calculated absolute energies are too large by a few tenths of an eV. A similar trend will be found in the calculation of the core excitation spectra (see next sections). In order to remain consistent with the calculation of the core excited states, the CIPSI values obtained in the planar geometry will be used as a reference in the following.

B. Nitrogen *K*-shell electron energy-loss spectrum

The electron energy-loss spectrum measured experimentally at the N 1*s* edge is displayed in Fig. 2. The lowest energy bands are a little bit better resolved than in previous work [6] thanks to the higher resolution in the present study. The energies are given in Table II and are in excellent agreement with those obtained by Turci *et al.* [6]. Table II gives also the assignments proposed by Turci *et al.* [6]. The results of the calculations are given in Table III. Only the transitions with intensities larger than 1.5% of the most intense band are shown, except for A_2 transitions. As for the core ionization

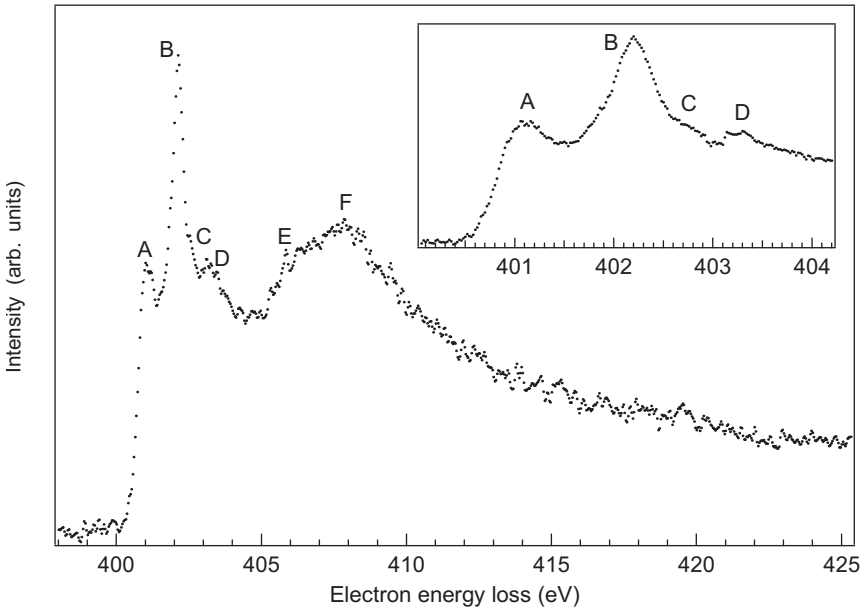

FIG. 2. The electron energy-loss spectrum aniline recorded at the nitrogen *K*-edge with an energy resolution of 0.17 eV, steps of 40 meV. Inset: lowest energy region recorded with 20-meV steps.

TABLE II. Experimental energy values (eV) of the spectral bands in the N 1*s* excitation spectrum of aniline and previous proposed assignments.

Band	*E* (eV)[a]	TV (eV)[b]	*E* (eV)[c]	TV (eV)[c]	Assignment[c]
A	401.1	4.2	400.7	4.6	$3s$
B	402.2	3.1	402.2	3.1	$3p/\pi^*$ (NH_2) $(2\pi^*,4b_1)$
C	402.72	2.58			
D	403.24	2.06	404	1.3	σ^* (NH_2)
E	406.1	−0.8			
F	407.6	−2.3	407.6	−2.3	σ^* (CN)

[a]This work.
[b]This work using ionization energy of Ref. [31].
[c]Reference [6].

energy, the calculated values seem to be overestimated by a few tenths of an eV. This implies that the calculated term values (TV's) should be in better agreement with experiment than the absolute energies. Therefore TV's of Tables II and III will be used for the assignment of the spectrum.

The first band *A* is observed at 401.1 eV (TV=4.2 eV) and is only partly resolved from the most intense one. It was assigned by Turci *et al.* [6] to the N $1s\rightarrow 3s$ transition. Plashkevych *et al.* [7] suggested $p\sigma^*$ (a_1) MO with *s* character. As shown in Table III, the calculations confirm partially this assignment: the N $1s\rightarrow 3s\sigma/\sigma^*$ (NH_2) transition is calculated at 401.49 eV (TV=3.98 eV) but its rather large intensity is due to the important σ^* (NH_2) valence character of the $3s$ Rydberg orbital.

The next band *B* is located at 402.2 eV (TV=3.1 eV) and was assigned to the N $1s\rightarrow 3p/\pi^*$ (NH_2) $(2\pi^*,4b_1)$ transi-

TABLE III. Calculated energies, term values (TV), relative intensities, and assignments of N 1*s* core excited states of aniline.

State	*E* (eV)	TV (eV)	Intensity[a]	Main configurations[b]	$\langle r^2\rangle$
A_1	401.49	3.98	0.114	0.97 N $1s\rightarrow 3s\sigma/\sigma^*$ (NH_2)	133
B_2	402.53	2.94	0.465	0.97 N $1s\rightarrow 3p\sigma/\sigma^*$ (NH_2)	144
A_2	402.60	2.87	0.000[c]	0.45 N $1s\rightarrow 1\pi^*$ $(2a_2)$	86
				+0.43 N $1s\rightarrow 3d\pi$	
B_1	402.61	2.86	0.171	0.54 N $1s\rightarrow 2\pi^*$ $(4b_1)$	89
				+0.24 N $1s\rightarrow 3p\pi$	
				+0.11 N $1s\rightarrow 4p\pi/2\pi^*$	
B_1	403.26	2.21	0.281	0.74 N $1s\rightarrow 3p\pi$	181
				+0.17 N $1s\rightarrow 2\pi^*$ $(4b_1)$	
A_1	403.66	1.81	0.024	0.95 N $1s\rightarrow 4s\sigma$	309
B_2	403.73	1.73	0.086	0.98 N $1s\rightarrow 3d\sigma/\sigma^*$ (NH_2)	244
A_2	403.98	1.49	0.000[c]	0.54 N $1s\rightarrow 3d\pi$	274
				+0.43 N $1s\rightarrow 1\pi^*$ $(2a_2)$	
B_1	403.99	1.47	0.023	0.96 N $1s\rightarrow 3d\pi$	275
B_2	404.09	1.38	0.072	0.98 N $1s\rightarrow 4p\sigma/\sigma^*$ (NH_2)	432
B_1	404.26	1.21	0.098	0.77 N $1s\rightarrow 4p\pi/2\pi^*$ $(4b_1)$	524
A_2	404.52	0.94	0.000[c]	0.90 N $1s\rightarrow 4d\pi$	589
B_1	404.64	0.83	0.036	0.92 N $1s\rightarrow 5p\pi$	985
	405.47	0.00		Ion	
A_1	405.47	0.00	0.123	096 N $1s\rightarrow\sigma^*$ (NH_2)	274
B_2	405.56	−0.09	1.000[d]	0.96 N $1s\rightarrow\sigma^*$ (NH_2)	220
B_1	406.60	−1.13	0.033	0.56 N $1s\rightarrow 3\pi^*$ $(5b_1)$	110
B_2	406.90	−1.43	0.034	0.80 N $1s\rightarrow\sigma^*$ (C_3H)	147

[a]Relative intensity to the most intense band.
[b]Main configuration of the CI wave function.
[c]Dipole-electric forbidden transition.
[d]Absolute calculated oscillator strengths (length gauge): $f_L=0.0199$.

TABLE IV. Quantum defect analysis (energies in eV).

	N		C_1		C_2		C_3		C_4	
	δ_ℓ	IP	δ_ℓ	IP	δ_ℓ	IP	δ_ℓ	IP	δ_ℓ	IP
$ns(a_1)$	1.14	405.42 $ns(a_1)$	0.84	291.41 $ns(a')$	0.97	290.12 $ns(a')$	0.94	290.25 $ns(a_1)$	0.83	289.69
$np(a_1)$	0.56	405.45 $np(a_1)$	0.60	291.47 $np(a')$	0.71	290.07 $np(a')$	0.70	290.21 $np(a_1)$	0.65	289.71
$np(b_2)$	0.84	405.45 $np(b_2)$	0.58	291.42 $np(a')$	0.68	290.14 $np(a')$	0.67	290.27 $np(b_2)$	0.48	289.66
$np(b_1)$	0.48	405.38 $np(b_1)$	0.32	291.40 $np(a'')$	0.35	289.83 $np(a'')$	0.43	290.07 $np(b_1)$	0.33	289.65
CIPSI		405.47		291.52		289.99		290.13		289.79

tion by Turci *et al.* [6] and to a $p\sigma^*$ (b_2) MO by Plashkevych *et al.* [7]. The present calculations of Table III show a much more complex situation, since there are three transitions predicted to have a TV around 2.9 eV. The most intense one, calculated at 402.53 eV (TV=2.94 eV), is due to the N $1s \rightarrow 3p\sigma/\sigma^*$ (NH_2), i.e., an in-plane $3p\sigma$ with an important σ^* (NH_2) valence character. The two other states are nearly degenerate and correspond to transitions to the $1\pi^*$ $(2a_2)$ and $2\pi^*$ $(4b_1)$ MO's. For both states, the CI wave functions appear to be a mixing between π^* and Rydberg MO's ($3d\pi$ for $1\pi^*$ and $3p\pi/4p\pi$ for $2\pi^*$). However, the low values of the $\langle r^2 \rangle$ parameters (86 and 89 a.u.^{2}) prove without ambiguity the two transitions to have a valence character and corresponding to the $1\pi^*$ $(2a_2)$ and $2\pi^*$ $(4b_1)$ transitions. It should also be noticed that if the nonplanar geometry had been used, the A_2 transition would have A'' symmetry while the B_1 transition would be A'. The A_2 transition would then be allowed but its intensity should be weak. Experimentally, the σ/π nature of band *B* could be confirmed by measuring the near-edge x-ray-absorption fine-structure spectra of condensed aniline at glancing and normal incidence [4], as done at the C 1*s* edge [3], or by using the symmetry-resolved method of Shigemasa *et al.* [37].

A shoulder *C* not well resolved on the high-energy side of the most intense band is observed at 402.72 eV (inset of Fig. 2, Table II), corresponding to a TV of 2.58 eV. According to the data of Table IV, it involves excitation to the $3p\pi$ MO, calculated at 403.26 eV (TV=2.30 eV). While the $\langle r^2 \rangle$ value of 181 a.u.^{2} identifies this transition to be of Rydberg character, its unusually high intensity (28.1% of the most intense band) may be explained by a mixing with the N $1s \rightarrow 2\pi^*$ $(4b_1)$ excitation.

The next band *D* has its maximum at 403.24 eV (Table II) with a TV of 2.06 eV and was assigned [6] to the transition to a σ^* (NH_2) state. For TV's below 2 eV, the calculations of Table III predict a large number of transitions, most of them being pure Rydberg states with very low intensities. A few states have larger intensities, because of a mixed Rydberg-valence character of the transition: the N $1s \rightarrow 3d\sigma/\sigma^*$ (NH_2) transition, calculated with a TV of 1.73 eV, could be responsible for the 403.24-eV feature. The N $1s \rightarrow 4p\sigma/\sigma^*$ (NH_2) and N $1s \rightarrow 4p\pi/2\pi^*$ $(4b_1)$ transitions are also rather intense and contribute to the intensity in this energy region.

At higher energies, the Rydberg transitions converge to the continuum onset corresponding to the ionization energy, calculated at 405.47 eV. A simple way to test the accuracy of the calculated Rydberg transitions is to perform a quantum defect analysis using the well-known Rydberg formula:

$$E(1s \rightarrow n\ell) = E(1s \rightarrow \infty) - \frac{R}{(n - \delta_\ell)^2},$$

where *R* is the Rydberg constant, *n* is the principal quantum number, and δ_ℓ is the quantum defect. Table IV shows the results of a fitting procedure using the calculated values of Table III. For *s* and *p* transitions, the fitted ionization potential (IP's), located between 405.38 and 405.45 eV, are close to the experimental value [31] of 405.3 eV and consistent with the CIPSI value of 405.47 eV.

According to the calculations, the two N $1s \rightarrow \sigma^*$ (NH_2) have TV's close to zero and lie at the ionization continuum onset. One of these transitions (B_2 symmetry) has the largest intensity of the whole spectrum. It is highly probable that this proximity to the continuum induces a very short lifetime for these transitions. Consequently, the corresponding bands have probably large full width at half maximum (FWHM) which might explain the flatness of the observed spectrum around 405 eV (Figs. 2 and 3).

The last two bands *E* and *F* can be seen in the experimental spectrum at higher energies (Fig. 2) at 406.1 eV (TV=−0.8 eV) and 407.6 eV (TV=−2.3 eV). Above the ionization threshold, the present calculations may not be quantitatively accurate, since they do not take into account the coupling with the continuum states. According to Table IV, the *E* band could be due to the N $1s \rightarrow 3\pi^*$ and N $1s \rightarrow \sigma^*$ (C_3H) transitions. The N $1s \rightarrow 3\pi^*$ $(5b_1)$ state is strongly mixed with a large number of di-excitations and there is also a doubly excited state with small $3\pi^*$ character calculated at 408.40 eV. A natural population analysis [38] shows without ambiguity that the 406.60-eV transition is essentially monoelectronic. A similar mixing also occurs for the N $1s \rightarrow \sigma^*$ (C_3H) transition. For band *F* there is very likely also a contribution from shape resonances, although this type of assignment has been questioned [39].

In Fig. 3, the experimental spectrum is compared with the calculated one. It should be noticed that all calculated bands have been taken into account, including the low intensity transitions not shown in Table IV. There is good agreement between both sets of data, except from a slight overestimation (~0.5 eV) of the calculated values, as already stated before. It should be noticed that the STEX results of Carravetta *et al.* (Fig. 4 of Ref. [8]) were overestimated by

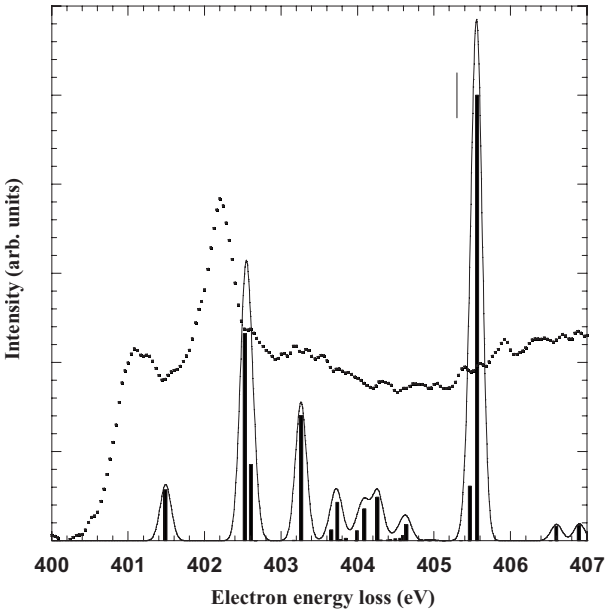

FIG. 3. Comparison between the experimental and the theoretical spectra for the pre-edge region at the nitrogen *K*-edge. The calculated results are convoluted by the experimental profile with 0.17 eV as the bandwidth at half maximum. The vertical lines show the measured ionization threshold.

~1.2 eV with respect to the spectrum of Turci *et al.* [6]. This figure also shows that the 0.17-eV bandwidth used is too narrow to reproduce the observed spectrum, the most part of the broadness of the experimental bands being due to the short lifetimes of the excited species.

C. Carbon *K*-shell electron energy-loss spectrum

The experimental excitation spectrum at the C 1*s* edge is presented in Fig. 4. It is quite similar to that of Turci *et al.* [6], some fine features being better resolved thanks to the higher resolution in the present study. The energy values of the observed spectral bands are given in Table V and are compared to previous studies on gaseous aniline but also on samples condensed on metallic substrates. The table also provides the assignments proposed previously for the gas phase spectra. In Table VI the results of the calculations are given. Only the transitions with intensities larger than 1.5% of the most intense band are shown, except for A_2 transitions. For the assignment of the spectrum, one has to keep in mind that the calculated values are probably slightly overestimated (see Fig. 5). Contrary to the nitrogen case, using TV values is more difficult, because of the four nonequivalent carbon atoms.

The first band *A*, the most intense one, is observed at 285.29 eV (Table V) and is assigned without ambiguity to the excitation of the $2\pi^*$ molecular orbital from C_2 1*s*, C_3 1*s*, and C_4 1*s* which are calculated to be nearly degenerate, respectively, at 285.52, 285.53, and 285.64 eV as shown in Table VI. The largest intensity predicted is for C_3 $1s \rightarrow 2\pi^*$. These results are consistent with the experimental broadness of the spectral band (Fig. 4) which has a FWHM of about 0.9 eV. Table VII compares the present calculations to previous theoretical studies. With the exception of the EHMO values of Turci *et al.* [6], which are underestimated by several eV, all results are slightly too high. Table VIII confirms that C_2 $1s \rightarrow 2\pi^*$ and C_3 $1s \rightarrow 2\pi^*$ transitions are almost perfectly degenerate, because they are less perturbed by the substitution of a hydrogen atom by the amino group when going from benzene to aniline. On the other hand, the chemical shifts are more important for C_4 and of course for C_1. They appear to be smaller than their equivalent in the core ions (Table I).

The band *B* has its maximum of intensity at 286.69 eV and is highly asymmetric on the high-energy side with a not well resolved feature *C* at 286.88 eV as shown in the inset of Fig. 4. Feature *C* is not mentioned by Turci *et al.*, very likely

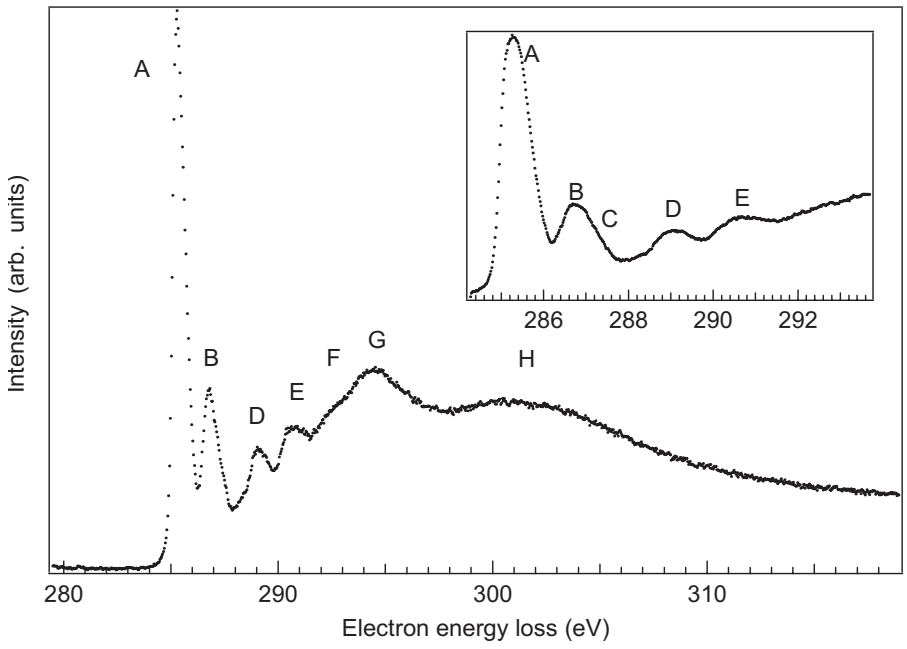

FIG. 4. The electron energy-loss spectrum of aniline recorded at the carbon *K*-edge with an energy resolution of 0.17 eV, steps of 40 meV. Inset: lowest energy region recorded with 20-meV steps.

TABLE V. Experimental energy values (eV) of the spectral bands in the C 1*s* excitation spectrum of aniline and previous proposed assignments.

					Assignments[b]	
Band	*E* (eV)[a] gas	*E* (eV)[b] gas	*E* (eV)[c] solid	*E* (eV)[d] solid	(C-H) C_1, C_2, C_3	(C-N) C_4
A	285.29	285.2	285.4	285.4	$2\pi^*$ $(4b_1)$	
B	286.69	286.7	286.9	286.8		$2\pi^*$ $(4b_1)$
C	286.88					
D	289.11	289.0	288.7		$3\pi^*$ $(5b_1)/3p$	
	(290.2)					
E	290.65	290.5	290.6			$3\pi^*$ $(5b_1)/\sigma^*$ (CNH_2)
F	292.3					
G	294.5	294.5	294.5			$1\sigma^*$
H	301	3.2	303±1.0			$2\sigma^*$

[a]This work.
[b]Reference [6].
[c]Reference [3].
[d]Reference [5].

being not resolved at all in their spectrum. The *B* band has been assigned to the C_4 $1s\rightarrow 2\pi^*$ $(4b_1)$ [6]. The calculations support this assignment, since the C_1 $1s\rightarrow 2\pi^*$ $(4b_1)$ transition is predicted to occur at a slightly higher energy of 287.16 eV (Table VIII). This transition has also the highest intensity of all. The calculations also reveal the presence of many other transitions in this energy region. Some of them, being purely Rydberg, are not shown in Table VI. For C_2, C_3, and C_4, the transitions to the $3s\sigma$ MO are predicted at very close energies (between 286.79 and 287.07 eV). Their relatively high intensity (about 4% of the most intense peak) is due to their σ^* (CH) valence character. The corresponding transition C_1 $1s\rightarrow 3s\sigma/\sigma^*(NH_2)$ (not shown in Table VI) is calculated at 288.48 eV but with a very small intensity (0.3%). The four transitions have nearly identical TV's, around 3 eV.

The calculated transitions to the $1\pi^*$ exhibit the same patterns as the $2\pi^*$ and $3s\sigma$ transitions for the four atoms: the C_2, C_3, and C_4 transitions occur between 285.90 and 286.59 eV, while the C_1 transition is calculated at 287.48 eV. There are, however, differences in the wave functions: for C_1 and C_4, the wave function is purely $1\pi^*$, while for C_2 and C_3, there is a mixing between $1\pi^*$ and $3p\pi$ and $3d\pi$ configurations. This mixing is due to the fact that C_2 and C_3 were calculated in C_s symmetry while C_{2v} symmetry was used for C_1 and C_4. It is also interesting to note that the C_2 and C_3 transitions have very weak intensities. This would tend to confirm that the two A_2 transitions would have also weak intensities in the nonplanar geometry.

The band *D* is observed with a maximum intensity at 289.11 eV. It presents fine features not well resolved on the low-energy side at 288.37 eV and on the high-energy side at 289.43 eV. It has been reported previously [3,6] and assigned to excitation of $3\pi^*$ $(5b_1)$ or $3p$ MO's [6] or possibly σ^* (CH) MO [3] from C_2, C_3, or C_4 atoms. Plashkevych *et al.* [7] noticed that the experimental TV would suggest a $4p$ rather than $3p$ transition in this region. The present calculations show that there are many $n=4$ and 5 Rydberg transitions from C_1, C_2, and C_3 in this energy region. Most of them have very low intensities and are not shown in Table VI. They contribute to the intensity on the low-energy side of the *D* band. In fact, according to the calculations, the *D* band appears to be due to the excitation to the $3\pi^*$ MO form C_2 and C_4 and, to a lesser extent, from C_3 in the low-energy side. As for N and C_4, the wave functions appear to be a mixing between $3\pi^*$ and valence $1s$ $\pi\rightarrow\pi^*$ π^* di-excited configurations. Because of their $\langle r^2\rangle$ value around 90 a.u.^{2}, they clearly have valence character. The configuration mixing might reflect the fact that the $3\pi^*$ virtual MO of the core ion is not the best one to describe the core excitation, but it may also indicate the presence of a true high intensity shake-up state, as we have found recently in the N $1s$ *K* shell of *s*-triazine [40]. This is especially true for C_3, since there are two states (calculated at 288.83 and 289.82 eV) with an important $3\pi^*$ character (19 and 27 %) mixed with di-excitations. In order to define the mono- or di-excited character of this type of states, a natural orbital analysis [38] was performed. The resulting fractional occupation numbers show that for C_2, C_3, and C_4, there are about 1.5 electrons in π^* MO's, corresponding to an intermediate situation between mono- and di-excited states. With a population of 1.8 electrons in π^* and about 0.9 electron removed from the π MO's, the second C_3 $3\pi^*$ state may be viewed as a "true" shake-up state.

The next band *E* is located at 290.65 eV as shown in Fig. 4 and is between the C_2, C_3, C_4 ionization threshold and the C_1 one. Previously it has been assigned to $3\pi^*$ $(5b_1)$ [3,6] or σ^* (CNH_2) [3,6,7] (Table V). The calculations predict an intense transition at 290.88 eV involving the C_1 $1s\rightarrow 3\pi^*$ transition with an important (20%) 2π C_1 $1s\rightarrow 1\pi^*2\pi^*$ character. According to the natural MO's analysis, it may be considered as monoelectronic since there is 1.1 electron in π^* MO's. There are also σ^* and shake-up transitions in this energy range but their intensities are low. The quasidegener-

TABLE VI. Calculated energies, TV's, relative intensities, and assignments at the C 1*s* different core shell of aniline.

State	E (eV)	TV (eV)				Intensity[a]	Main configurations[b]	$\langle r^2 \rangle$
		C_1	C_2	C_3	C_4			
A''	285.52		4.47			0.588	0.91 C_2 $1s \rightarrow 2\pi^*$ $(4b_1)$	90
A''	285.53			4.59		0.803	0.90 C_3 $1s \rightarrow 2\pi^*$ $(4b_1)$	88
B_1	285.64				4.14	0.645	0.89 C_4 $1s \rightarrow 2\pi^*$ $(4b_1)$	88
A_2	285.90				3.89	0.000[c]	0.92 C_4 $1s \rightarrow 1\pi^*$ $(2a_2)$	89
A''	286.59			3.53		0.029	0.58 C_3 $1s \rightarrow 1\pi^*$ $(2a_2)$	90
							+0.13 C_3 $1s \rightarrow 3p\pi$	
A_1	286.79				2.99	0.041	0.95 C_4 $1s \rightarrow 3s\sigma/\sigma^*$ (C_4H)	160
A'	286.84		3.15			0.047	0.97 C_2 $1s \rightarrow 3s\sigma/\sigma^*$ (C_2H)	157
A'	287.07			3.06		0.043	0.96 C_3 $1s \rightarrow 3s\sigma/\sigma^*$ (C_3H)	161
B_1	287.16	4.36				1.000[d]	0.91 C_1 $1s \rightarrow 2\pi^*$ $(4b_1)$	91
A_2	287.48	4.04				0.000[c]	0.92 C_1 $1s \rightarrow 1\pi^*$ $(2a_2)$	92
A_1	287.93				1.85	0.015	0.93 C_4 $1s \rightarrow 3d\sigma$	215
A''	288.03			2.10		0.017	0.82 C_3 $1s \rightarrow 3p\pi$	208
							+0.15 C_3 $1s \rightarrow 1\pi^*$ $(2a_2)$	
B_1	288.28				1.51	0.037	0.98 C_4 $1s \rightarrow 3d\pi$	292
A_2	288.33				1.46	0.000[c]	0.98 C_4 $1s \rightarrow 3d\pi'$	308
A_1	288.39				1.40	0.015	0.94 C_4 $1s \rightarrow 4s\sigma$	550
A'	288.49		1.50			0.019	0.98 C_2 $1s \rightarrow 4s\sigma$	510
A'	288.68			1.44		0.016	0.97 C_3 $1s \rightarrow 4s\sigma$	551
B_1	288.79				0.99	0.040	0.98 C_4 $1s \rightarrow 4d\pi$	604
A''	288.83			1.29		0.064	0.19 C_3 $1s \rightarrow 3\pi^*$ $(5b_1)$	88
							+0.58 3π C_3 $1s \rightarrow 2\pi^*$ $(4b_1)$ $2\pi^*$ $(4b_1)$	
A_2	288.83				0.96	0.000[c]	0.98 C_4 $1s \rightarrow 4d\pi'$	552
A''	288.98			1.14		0.017	0.93 C_3 $1s \rightarrow 4p\pi$	774
A''	289.36		0.63			0.137	0.54 C_2 $1s \rightarrow 3\pi^*$ $(5b_1)$	85
							+0.19 3π C_2 $1s \rightarrow 2\pi^*$ $(4b_1)$ $2\pi^*$ $(4b_1)$	
B_1	289.42				0.36	0.166	0.58 C_4 $1s \rightarrow 3\pi^*$ $(5b_1)$	91
							+0.17 2π C_4 $1s \rightarrow 1\pi^*$ $(2a_2)$ $2\pi^*$ $(4b_1)$	
	289.79				0.00		Ion C_4	
A''	289.82			0.30		0.027	0.27 C_3 $1s \rightarrow 3\pi^*$ $(5b_1)$	95
							+0.20 3π C_3 $1s \rightarrow 2\pi^*$ $(4b_1)$ $2\pi^*$ $(4b_1)$	
							+0.26 3π C_3 $1s \rightarrow 1\pi^*$ $(2a_2)$ $2\pi^*$ $(4b_1)$	
A_2	289.98	1.54				0.000[c]	0.98 C_1 $1s \rightarrow 3d\pi$	274
	289.99		0.00				Ion C_2	
A_1	290.06				−0.27	0.040	0.94 C_4 $1s \rightarrow \sigma^*$ (C_2H)	142
	290.13			0.00			Ion C_3	
A''	290.35		−0.35			0.018	0.30 3π C_2 $1s \rightarrow 2\pi^*$ $(4b_1)$ $2\pi^*$ $(4b_1)$	142
							+0.37 3π C_2 $1s \rightarrow 2\pi^*$ $(4b_1)$ $3p\pi$	
A_2	290.53	0.99				0.000[c]	0.98 C_1 $1s \rightarrow 4d\pi$	576
A''	290.73		−0.74			0.027	0.24 3π C_2 $1s \rightarrow 2\pi^*$ $(4b_1)$ $2\pi^*$ $(4b_1)$	166
							+0.37 3π C_2 $1s \rightarrow 2\pi^*$ $(4b_1)$ $3p\pi$	
B_1	290.88	0.64				0.255	0.56 C_1 $1s \rightarrow 3\pi^*$ $(5b_1)$	103
							+0.20 2π C_1 $1s \rightarrow 1\pi^*$ $(2a_2)$ $2\pi^*$ $(4b_1)$	
B_1	291.37	0.15				0.047	0.54 3π C_1 $1s \rightarrow 2\pi^*$ $(4b_1)$ $2\pi^*$ $(4b_1)$	96
							+0.24 2π C_1 $1s \rightarrow 1\pi^*$ $(2a_2)$ $2\pi^*$ $(4b_1)$	
	291.52	0.00					Ion C_1	
A_1	291.56	−0.04				0.036	0.91 C_1 $1s \rightarrow \sigma^*$ (CH)	159
B_2	291.80				−2.01	0.018	0.95 C_4 $1s \rightarrow \sigma^*$ (C_3H)	125
B_2	291.97	−0.44				0.033	0.93 C_1 $1s \rightarrow \sigma^*$ (NH_2)	121

[a]Relative intensity to the most intense band.
[b]Main configuration of the CI wave function.
[c]Dipole-electric forbidden transition.
[d]Absolute calculated oscillator strengths (length gauge): f_L=0.0525.

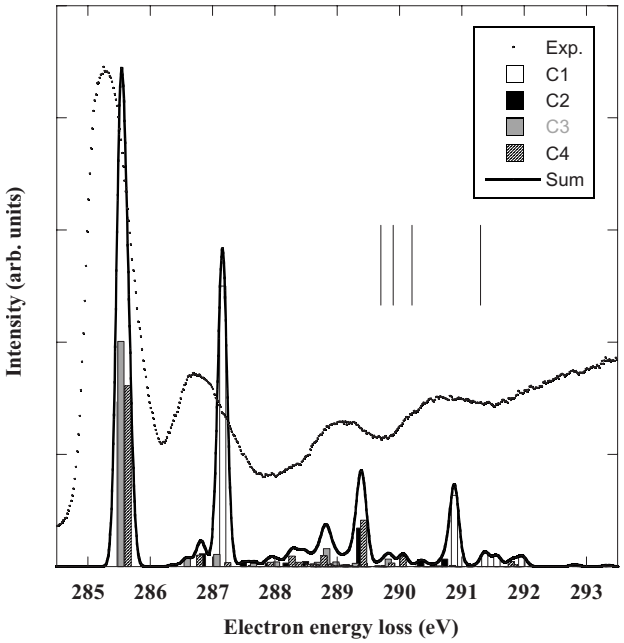

FIG. 5. Comparison between the experimental and the theoretical spectra at the carbon *K*-edge. The calculated results are convoluted by the experimental profile with 0.17 eV as the bandwidth at half maximum and compared to the experimental spectrum. The vertical lines show the measured ionization thresholds.

ate continuum onsets are probably responsible for the large width of this band.

The *F* feature at 292.3 eV appears as a shoulder on band *G*. It is above the C_1 ionization threshold. In this energy region there are several bands with rather small intensities predicted by the calculations, involving σ^* and shake-up transitions. At higher energy as shown in Fig. 4 there are two broad bands with maximum of intensity at 294.5 and 301 eV also reported previously and assigned to σ^* type excitation (Table V). They are tentatively assigned to shape resonances [39].

As shown in Table IV, it is also possible to perform a quantum defect analysis on the Rydberg states of the four carbon atoms. For *s* and *p* transitions, all atoms give very similar δ_ℓ values and the fitted ionization potentials are consistent with the calculated CIPSI value. Finally, Fig. 5 compares the experimental spectrum with the calculated bands. The upper spectrum shows the contributions of all carbon atoms to the spectrum, the result of the calculations being fitted with 0.17-eV FWHM Gaussians. It should be noticed that all calculated bands have been taken into account, including the low intensity transitions not shown in Table VI. There is an excellent agreement for the relative intensities and the calculated energies seem to be slightly overestimated by a few tenths of an eV. In the STEX calculations of Plashkevych *et al.* [Fig. 7(a) of [7]], the calculated spectrum was shifted by 1.52 eV to match the experiment of Turci *et al.* [6].

D. Geometry of core excited aniline

Due to variational collapse of the wave function, geometry optimization of the core states of polyatomic molecules is a difficult task [41–43], especially at the multiconfigurational level. In the case of benzene, Norman and Ågren [44] optimized the geometry of the core ion, the C $1s \rightarrow 1\pi^*$ ($1e_{2u}$) core state, and its equivalent core ($Z+1$) [45], using a double-dzeta quality basis state and an active space limited to π MO's. It was shown that these three states remained planar, in contradiction with early suggestions of a pyramidalized structure [46]. On the whole, the equivalent core approximation geometry and frequencies were very close to the true core results, except for the lowest frequencies ("soft" modes).

In the case of aniline, it is interesting to study how the substitution of a NH_2 group in benzene could affect the geometry of the core excited molecule. These calculations were performed with the GAMESS-US program at the ROHF-GVB level [47], using the TZP+*R* basis set. The nature (minima or saddle points) of the structures was determined by calculating analytically the harmonic frequencies at the same level. The various geometries obtained can be classified in six main types, displayed in Figs. 1(a)–1(f). The results of the calculations are summarized in Table VIII, while the detailed structural parameters are provided in the supplementary data of this paper [30]. Briefly, the changes in bond lengths are consistent with the findings of Norman and Ågren [44] for benzene: the core excited C-H length is shortened to a value close to a N-H bond (about 1.0 Å). Similarly, the core excited N-H bond is shortened to the typical O-H value (about 0.96 Å). When the 1*s* electron is excited to a Rydberg MO with σ^* (C-H) valence character, this shortening is counterbalanced by a slight increase of the bond length. Bond angles

TABLE VII. Transition energies of the most intense bands in carbon 1*s* excitation spectrum at different levels of theory.

	CIPSI[a]	Shift[a]	STEX[b]	Shift[b]	ΔSCF[b]	Shift[b]	Shift[c]	EHMO[d]	Shift[d]	Expt.[a]	Shift[a]
C_1	287.16	1.63	287.23	1.45	287.69	1.46	1.15	282.1	1.15	286.61	1.32
C_2	285.52	−0.01	285.68	0.09	286.31	0.08	0.03	281.0	0.03		≈0.0
C_3	285.53	0.00	285.78	0.00	286.23	0.00	0.00	280.8	0.00	285.29	0.0
C_4	285.64	0.11	285.89	0.11	286.51	0.28	0.29	281.2	0.40		≈0.0

[a]This work.
[b]Reference [8].
[c]MCSCF values from Ref. [5].
[d]Reference [6].

TABLE VIII. Core ionized and excited states of aniline and $Z+1$ equivalent molecules.

	Core			$Z+1$		
	State	Figure	n_i[a]	State	Figure	n_i[a]
Ion C_1	$^2A'$	1(d)	0	$^1A'$	1(d)	0
Ion C_2	$^2A'$	1(c)	0	$^1A'$	1(c)	0
Ion C_3	^2A	1(d)	0	^1A	1(d)	0
Ion C_4	$^2A_1$	1(c)	0	$^1A_1$	1(c)	0
Ion N	$^2A_1$	1(b)	0	$^1A'$	1(d)	0
C_1 $1s\rightarrow 3s\sigma/\sigma^*$ (NH_2)	$^1A'$	1(d)	0	$^2A'$	1(d)	0
C_1 $1s\rightarrow 2\pi^*$ ($4b_1$)	^1A	1(d)[b]	0	^2A	1(d)[b]	0
C_2 $1s\rightarrow 3s\sigma/\sigma^*$ (C_2H)	$^1A'$	1(c)	0	$^2A'$	1(c)	0
C_2 $1s\rightarrow 1\pi^*$ ($2a_2$)	^1A	1(e)	0	^2A	1(e)	0
C_3 $1s\rightarrow 3s\sigma/\sigma^*$ (C_3H)	$^1A'$	1(c)	1	$^2A'$	1(c)	1
C_3 $1s\rightarrow 1\pi^*$ ($2a_2$)	^1A	1(f)	0	^2A	1(f)	0
C_4 $1s\rightarrow 2\pi^*$ ($4b_1$)	$^1B_1$	1(c)	0	$^2B_1$	1(c)	0
C_4 $1s\rightarrow 3p\sigma/\sigma^*$ (CH)	$^1B_2$	1(c)	0	$^2B_2$	1(c)	0
C_4 $1s\rightarrow 3s\sigma/\sigma^*$ (C_4H)	$^1A_1$	1(c)	0	$^2A_1$	1(c)	0
C_4 $1s\rightarrow 1\pi^*$ ($2a_2$)	$^1A''$	1(a)	0	$^2A''$	1(a)	0
N $1s\rightarrow 3s\sigma/\sigma^*$ (NH_2)	$^1A'$	1(d)	0	$^2A'$	1(d)	0
N $1s\rightarrow 3p\sigma$	$^1B_2$	1(b)	0	$^2A''$	1(d)	0
N $1s\rightarrow 3p\pi/\sigma^*$ (NH_2)	$^1B_1$	1(b)	0	$^2B_1$	1(b)	1
N $1s\rightarrow 1\pi^*$ ($2a_2$)	$^1A_2$	1(b)	2	$^2A_2$	1(b)	1

[a]Number of imaginary frequencies.
[b]Slightly distorted from the C_s geometry (C_1-N bond out of ring plane).

generally remain close to 120°. These trends are also valid for the $Z+1$ molecules.

However, as indicated in Table VIII, it appears that most core states do not have the geometry of the ground state [Fig. 1(a)]. Core ions are either planar [C_1, C_4, Fig. 1(c)] or the amino group is rotated by 90° from the ring plane [C_2, C_4, Fig. 1(c)]. For N, there is a discrepancy between the core ion predicted to have the geometry of Fig. 1(b), while the $Z+1$ approximation predicts the geometry shown in Fig. 1(d). Since the rotation of the NH_2 group has the lowest frequency, these results confirm the prediction of Norman and Ågren [44].

For core excited aniline, it was possible to optimize at least two states for each carbon atom. For C_4, which is the farthest from the amino group, and thus similar to benzene, the C_4 $1s\rightarrow 1\pi^*$ ($2a_2$) core state keeps the geometry of the ground state, while the C_4 $1s\rightarrow 2\pi^*$ ($4b_1$) state is planar. On the other hand, for C_2 and C_4, the same transition leads to a pyramidalized structure [Figs. 1(e) and 1(f)]. For C_1, the lowest transition is the π^* ($3b_1$) and corresponds to Fig. 1(d) but with the C_1-N bond slightly out of the ring plane. Most of the Rydberg-σ^* (CH) states are planar. For carbons, there is a perfect agreement between core states and their $Z+1$ equivalent.

For nitrogen, the N $1s\rightarrow 3s\sigma/\sigma^*$ (NH_2) has the geometry of Fig. 1(d), while the two $3p\sigma$ states have the 90° rotated structure of Fig. 1(b). The N $1s\rightarrow 1\pi^*$ ($2a_2$) state could not be found (the planar form had three imaginary frequencies and the nonplanar structures correspond to other transitions) but has probably the Fig. 1(d) geometry. As for the core ion, there are some discrepancies between the core states and their $Z+1$ equivalent concerning the nature of the calculated structures. These discrepancies, which are due to the valence to core penetration neglected in the $Z+1$ approximation [43], would be more important for nitrogen than for carbon, leading to different geometries. Geometry optimizations on species containing both carbon and oxygen atoms [48] show similar trends, while for cyclopropane, the $Z+1$ structures and energies were found to be very close to the core states [43].

V. CONCLUSIONS

The C 1*s* and N 1*s* electron energy-loss spectra have been recorded by electron impact under electric dipole interaction conditions and with higher resolution than previously. Accompanying *ab initio* configuration interaction calculations have been performed in order to propose quite reliable assignments.

The transitions to the lowest energy unoccupied MO's of π^* type from the carbon atoms C_2, C_3, C_4 are nearly degenerate. They are separated by about 1.6 eV from the C_1 $1s\rightarrow 2\pi^*$. This suggests that the carbon atoms C_2, C_3, and C_4 have roughly the same chemical environment and that of C_1 is about 1.6 eV different and shifting the spectral bands at higher energy. At the N 1*s* edge the most intense transitions are due to the strong Rydberg-valence states, involving the σ^*-type unoccupied molecular orbitals.

Some discrepancies between the N 1*s* excited core states and their $Z+1$ equivalent concerning the nature of their equilibrium geometries are observed. It is not the case for the carbons for which there is an excellent agreement between core states and their $Z+1$ equivalent. These differences, being due to the valence to core penetration neglected in the $Z+1$ approximation, seem to be more important for nitrogen than for carbon.

ACKNOWLEDGMENTS

The Laboratoire de Physique des Lasers, Atomes et Molécules (PhLAM) is Unité Mixte de Recherche du CNRS. The Centre d'Études et de Recherches Lasers et Applications (CERLA, FR CNRS 2416) is supported by the Ministère chargé de la Recherche, the Région Nord/Pas-de-Calais, and the Fonds Européen de Développement Économique des Régions (FEDER). Parts of the computations were carried out at the CRI (Centre de Ressources Informatiques), on the IBM-SP computer that is supported by the Programme de Calcul Intensif et Parallèle of the Ministère chargé de la Recherche, the Région Nord/Pas-de-Calais, and the FEDER. This research has been supported by the Fonds National de la Recherche Scientifique and the Patrimoine of University of Liège. The support of the COST action P9 "Radiation Damage in Biomolecular Systems" is also acknowledged.

[1] M. Magnuson *et al.*, J. Chem. Phys. **111**, 4756 (1999).
[2] N. E. Agbor *et al.*, Sens. Actuators B **41**, 137 (1997).
[3] J. L. Solomon, R. J. Madix, and J. Stohr, Surf. Sci. **255**, 12 (1991).
[4] J. Stöhr, *NEXAFS Spectroscopy* (Springer-Verlag, Berlin, 1992).
[5] Y. Luo *et al.*, Phys. Rev. A **52**, 3730 (1995).
[6] C. C. Turci, S. G. Urquhart, and A. P. Hitchcock, Can. J. Chem. **74**, 851 (1996).
[7] O. Plashkevych *et al.*, Chem. Phys. **222**, 125 (1997).
[8] V. Carravetta, O. Plashkevych, and H. Ågren, Chem. Phys. **263**, 231 (2001).
[9] C. Hannay *et al.*, Meas. Sci. Technol. **6**, 1140 (1995).
[10] M.-J. Hubin-Franskin *et al.*, J. Chem. Phys. **106**, 35 (1997).
[11] M.-J. Hubin-Franskin and J. Heinesch, Nucl. Instrum. Methods Phys. Res. A **477**, 546 (2002).
[12] R. N. S. Sodhi and C. E. Brion, J. Electron Spectrosc. Relat. Phenom. **34**, 363 (1984).
[13] D. Duflot *et al.*, J. Chem. Phys. **118**, 1137 (2003).
[14] S. Bodeur, P. Millié, and I. Nenner, Phys. Rev. A **41**, 252 (1990).
[15] M. W. Schmidt *et al.*, J. Comput. Chem. **14**, 1347 (1993).
[16] B. Huron, J. P. Malrieu, and P. Rancurel, J. Chem. Phys. **58**, 5745 (1973).
[17] R. Cimiraglia, J. Chem. Phys. **83**, 1746 (1985).
[18] C. Angeli *et al.*, Theor. Chem. Acc. **98**, 57 (1997).
[19] T. H. Dunning, Jr., J. Chem. Phys. **55**, 716 (1971).
[20] T. H. Dunning, Jr. and P. J. Hay, in *Methods of Electronic Structure Theory*, edited by H. F. Schaefer III (Plenum Press, New York, 1977), Vol. 3, p. 1.
[21] D. G. Lister and J. K. Tyler, Chem. Commun. (London) **6**, 152 (1966).
[22] D. G. Lister *et al.*, J. Mol. Struct. **23**, 253 (1974).
[23] N. W. Larsen, E. L. Hansen, and F. M. Nicolaisen, Chem. Phys. Lett. **43**, 584 (1976).
[24] M. Quack and M. Stockburger, J. Mol. Spectrosc. **43**, 87 (1972).
[25] J. Pyka and M. Kreglewski, J. Mol. Spectrosc. **109**, 207 (1985).
[26] O. Bludský *et al.*, J. Chem. Phys. **105**, 11042 (1996).
[27] M. Alcolea Palafox, J. L. Nunez, and M. Gil, J. Mol. Struct.: THEOCHEM **593**, 101 (2002).
[28] Y. Honda *et al.*, J. Chem. Phys. **117**, 2045 (2002).
[29] P. M. Wojciechowski, W. Zierkiewicz, and D. Michalska, J. Chem. Phys. **118**, 10900 (2003).
[30] See EPAPS Document No. E-PLRAAN-75-069704 for detailed structural and energy information on the ground, core ion, and core excited states of aniline. For more information on EPAPS, see http://www.aip.org/pubservs/epaps.html
[31] T. Ohta, T. Fujikawa, and H. Kuroda, Bull. Chem. Soc. Jpn. **48**, 2017 (1975).
[32] T. D. Crawford, H. F. Schaefer III, and T. J. Lee, J. Chem. Phys. **105**, 1060 (1996).
[33] P. J. Knowles *et al.*, Chem. Phys. Lett. **186**, 130 (1991).
[34] W. J. Lauderdale *et al.* Chem. Phys. Lett. **187**, 21 (1991).
[35] T. J. Lee *et al.* J. Chem. Phys. **100**, 7400 (1994).
[36] T. J. Lee and D. Jayatilaka, Chem. Phys. Lett. **201**, 1 (1993).
[37] E. Shigemasa *et al.*, Phys. Rev. A **66**, 022508 (2002).
[38] P.-O. Löwdin, Phys. Rev. **97**, 1474 (1955).
[39] M. N. Piancastelli, J. Electron Spectrosc. Relat. Phenom. **100**, 167 (1999).
[40] D. Duflot *et al.*, Eur. Phys. J. D **35**, 239 (2005).
[41] S. Shirai, S. Yamamoto, and S.-a. Hyodo, J. Chem. Phys. **121**, 7586 (2004).
[42] A. B. Trofimov *et al.*, J. Chem. Phys. **113**, 6716 (2000).
[43] D. Duflot, S. Zeggari, and J.-P. Flament, Chem. Phys. **327**, 518 (2006).
[44] P. Norman and H. Ågren, J. Mol. Struct.: THEOCHEM **401**, 107 (1997).
[45] W. L. Jolly and D. N. Hendrickson, J. Am. Chem. Soc. **92**, 1863 (1970).
[46] Y. Ma *et al.*, Phys. Rev. Lett. **63**, 2044 (1989).
[47] G. Chaban, M. W. Schmidt, and M. S. Gordon, Theor. Chem. Acc. **97**, 88 (1997).
[48] D. Duflot *et al.* (unpublished).

Article 16

Eur. Phys. J. D **35**, 239–248 (2005)
DOI: 10.1140/epjd/e2005-00193-6

THE EUROPEAN PHYSICAL JOURNAL D

Ab initio and experimental study of the K-shell spectra of *s*-triazine

D. Duflot[1,a], K. Sidhoum[1], J.-P. Flament[1], A. Giuliani[2], J. Heinesch[2], and M.-J. Hubin-Franskin[2,b]

[1] Laboratoire de Physique des Lasers, Atomes et Molécules (PhLAM), UMR CNRS 8523, Centre d'Études et de Recherches Lasers et Applications (CERLA, FR CNRS 2416), Université des Sciences et Technologies de Lille, 59655 Villeneuve d'Ascq Cedex, France

[2] Université de Liège, Laboratoire de Spectroscopie d'Électrons diffusés, Institut de Chimie B6c, Sart Tilman, 4000 Liège 1, Belgium

Received 21 March 2005 / Received in final form 19 May 2005
Published online 26 July 2005 – © EDP Sciences, Società Italiana di Fisica, Springer-Verlag 2005

Abstract. The carbon and nitrogen K-shell spectra of gaseous *s*-triazine have been studied using inner-shell electron energy loss spectroscopy (ISEELS) method. *Ab initio* Configuration Interaction calculations have been carried out in order to assign the observed bands. As in many similar molecules, both spectra are dominated by an intense π^* peak, followed by lower intensity features. At the C1*s* edge, the calculations show that some previous assignments made using an underestimated core ionisation energy of about 2.5 eV have to be revisited. At the nitrogen edge, the calculations predict a high intensity π^* doubly excited state lying below the ionisation threshold, which could be responsible for one the most intense observable bands at 405.32 eV.

PACS. 31.25.Qm Electron correlation calculations for polyatomic molecules – 34.80.Gs Molecular excitation and ionization by electron impact

1 Introduction

The *s*-triazine molecule and its derivatives are a well-known class of herbicides that are used as photosynthesis inhibitors [1]. Their accumulation in waters, due to their intensive use, has transformed them into pollutants [2] and has raised the question of finding an appropriate treatment for their elimination [3]. Among others, it has been suggested to use photodegradation [4]. To this end, a precise knowledge of the low lying electronic states of the molecule is important. A large number of studies have been devoted to this goal, using both theoretical and experimental methods (see Ref. [5] and references cited therein). Among them, core shell spectroscopy has proven to be a powerful tool for the study of excited states and their characterization as valence or Rydberg character. Due to the localization of the 1s orbitals, this method gives information which are complementary to valence spectroscopies which probe delocalised high-lying orbitals [6].

The *s*-triazine molecule has already been studied using the inner-shell electron energy loss spectroscopy (ISEELS) method by Apen et al. [7], who recorded low resolution (FWHM of 0.6 eV) spectra and assigned the spectral bands by comparison with similar molecules, such as pyridine or benzene. Since our previous works on these molecules [8,9] have led to reconsider some assignments, it seems worthwhile to reconsider the core spectra of *s*-triazine.

The goal of the present paper is to present a new ISEELS spectrum of *s*-triazine recorded with a resolution of 0.17 eV. In order to help in the assignment of the observed spectral features, *ab initio* calculations using Configuration Interaction (CI) calculations have been carried out. This paper is divided into the following sections: Section 2 describes the experimental set-up; Section 3 deals with the computational method employed; the results are presented and discussed in Section 4 and finally, in Section 5 some conclusions are given.

2 Experiment

The inner-shell electron energy loss spectra were obtained with a VSW spectrometer which has been adapted for gas studies and high energy electron beams and has been equipped with a home-made position sensitive multi-detector system in order to improve data collection times. The experimental apparatus and procedure have been described in detail previously [10,11].

Briefly the spectrometer consists of an electrostatic 180° monochromator operating in the constant pass energy mode, a collision chamber and an electrostatic

[a] e-mail: denis.duflot@univ-lille1.fr
[b] Directeur de recherche F.N.R.S.

analyser identical to the monochromator. The monochromatised incident electrons are accelerated up to 2 keV and focused into the collision chamber using a four-element electron lens. The electrons are slightly deflected (0.02 radians) by two sets of X-Y plates inside the collision chamber. The scattered electrons are energy analyzed and focused onto the entrance slit of the analyser by a lens similar to that used for acceleration.

In the collision conditions of low momentum transfer (i.e. high incident energy and small scattering angle), electronic electric-dipolar transitions are primarily excited.

Inside the vacuum vessel, a residual pressure of less than 1×10^{-8} Torr is maintained by a cryogenic pumping system. The electron gun and the analyser regions are differentially pumped by turbomolecular pumps respectively.

The detection system consists of an assembly of two microchannel plates, a phosphor screen, fiber-optic couplers and an area array Coupled Charge Device (CCD) sensor. The driving and reading electronics for the detector have been adapted to the electron-energy loss experiment. The spectra result from the accumulation of the data from each channel of the detector, which removes any detector-sensitivity variation [10,12].

The accelerating and retarding voltages were constant to within 10 ppm/°C. The spectra have been recorded with 0.040 eV steps. At the C1s and N1s edges the regions containing fine features not well resolved have been recorded with smaller steps 0.020 eV and 0.010 eV in order to determine more accurately the corresponding energy values.

In order to take into account valence and lower-energy inner-shell excitation cross section, a background has been subtracted from the raw spectra by extrapolating a least-square fit of the pre-edge experimental data points. The absolute energy scales were determined by calibrating the C1s spectrum relative to the C1$s \rightarrow \pi^*$ ($\nu' = 0$) band in CO [13] at 287.40 ± 0.02 eV and the N1s spectrum relative to the N1$s \rightarrow \pi^*$ ($\nu' = 0$ and $\nu' = 1$) band for N_2 (i.e. 401.10 eV which is the average value of $\nu' = 0$ and $\nu' = 1$ as the features due to these transitions are only partly resolved within our 0.17 eV resolution [13]). The spectrum of a mixture of s-triazine and the calibration gas (CO or N_2) was recorded with each gas being let into the collision region through a separate leak to ensure of constant composition mixture. The uncertainty on the measured energies is of the order of 0.06 eV and 0.13 eV for the C1s and N1s spectra, respectively.

The sample is a commercial one from ALDRICH with a stated purity of 97.0%. It was used directly without further purification except for repetitive freeze-pump-thaw cycles in order to eliminate air and other volatile impurities in the sample.

3 Computational method

Since the computational method used has been described in detail elsewhere [14], it will be briefly outlined. The starting hypothesis [15] is that, due to the important relaxation of the electronic density following the creation of the core hole, the molecular orbitals (MO's) of the core *ionised* molecule are a better approximation for the description of the core *excited* states than the ground state MO's. Similarly, the energy of a given $1s \rightarrow i^*$ core excited state may be obtained by correcting the core ion energy in the following manner:

$$E(1s \rightarrow i^*) = E(1s \rightarrow \infty) + \varepsilon_{i*} + P + C$$

where ε_{i^*} is the Hartree-Fock mono-electronic energy of the i^* MO. $E(1s \rightarrow \infty)$ is the MP2 core ion energy, obtained using the ROHF-GVB method implemented in the GAMESS-US package [16]. The P and C terms represent the residual relaxation and valence correlation effects of the i^* electron with respect to the core ion, respectively. P is obtained by performing a configuration interaction (CI) calculation in the mono-excitation space of all the calculated $1s \rightarrow i^*$ states. In order to evaluate the C term, the resulting CI wave-functions serve as the zeroth-order space for a multi-reference MP2 calculation using the three-class diagrammatic CIPSI method [17]. To spare computational time, an extrapolation procedure [18] was employed, using 6 thresholds between 99.4 and 99.9% of the exact wave functions. Finally, the dipolar electric transition oscillator strengths with respect to the ground state of the molecule were computed, using the length gauge.

The s-triazine molecule contains three chemically equivalent carbon and nitrogen atoms. For the calculation of the core ionised MO's at both edges, core hole localisation was assumed and the coupling between excitations from different core holes was neglected. Thus, the molecular symmetry was reduced from D_{3h} to C_{2v}. In the following, the core excited carbon and nitrogen atoms will be noted as C_e and N_e, respectively. Finally, the Gaussian atomic orbitals (AO's) used are the TZP basis set taken from Dunning [19]. For the calculation of the core-excited states, a set of Rydberg orbitals (5s, 5p, 2d) was added at the centre of the molecule. The first exponents were taken from Dunning and Hay [20] and the last ones were determined in an "even-tempered" manner.

Finally, in order to interpret the width of the first band at both edges, Franck-Condon factors calculations were carried out, using the method proposed by Cederbaum and Domcke [21]. Using the linear coupling approximation, this model requires the determination of the gradient (the κ-matrix) of the core excitation energy at the ground state geometry:

$$\kappa_i = 2^{-1/2} \left(\frac{\partial E_v}{\partial Q_i} \right)_0 .$$

The κ-matrix and the unscaled harmonic frequencies of the ground state were evaluated at the HF level. In the present work, the calculations included hot bands as well as combination bands. The theoretical width of the vibrational bands was set to the experimental resolution (0.17 eV) and Gaussian profile was used.

Table 1. Calculated geometry of *s*-triazine compared with previous works (bond lengths in Å and angles in degrees).

	RHF[a]	MP2[a]	CASSCF[b]	B3LYP[b]	RHF[c]	Exp.[d]	Exp.[e]	Exp.[f]
	TZP	TZP	6-31G*	6-31G*	TZVP	ED	Raman	X-ray
r(C-N)	1.3158	1.3372	1.328	1.337	1.3154	1.338(1)	1.338	1.317
r(C-H)	1.0736	1.0810	1.073	1.089	1.0739	1.106(8)	(1.084)[g]	1.045
HCN	117.3	117.0				116.9	116.6	114.8
NCN	125.4	126.0			125.5	126.1	127.0	125.2
CNC	114.6	114.0				113.9(1)	113.2	

[a] This work, [b] Ref. [5], [c] Ref. [25], [d] Ref. [24], [e] Ref. [23], [f] Ref. [22], [g] value fixed arbitrarily.

Table 2. Core ionisation energies (eV) of *s*-triazine.

	C1s	N1s
ΔSCF[a]	294.15	405.70
ΔMP2[a]	293.28	406.14
Experiment[b]	290.6	404.9

[a] This work. Energies calculated using the TZP+Rydberg basis set at the MP2/TZP optimised geometry. [b] Estimated values from reference [7] based on like materials from reference [26].

4 Results and discussion

The HF electronic configuration of the neutral ground state of *s*-triazine is:

$$1e'^4 1a_1'^2 2e'^4 2a_1'^2 3a_1'^2 3e'^4 4e'^4 4a_1'^2 1a_2'^2 1a_2''^2 5e'^4 5a_1'^2 1e''^4 6e'^4.$$

The six first MO's are the 1s orbitals of the nitrogen and carbon atoms. The $1a_2''$ MO is the lowest π orbital (1π). The $1e''$ MO corresponds to the 2π and 3π (degenerate) orbitals. Their anti-bonding counterparts are the $2e''$ and the $2a_2''$ ones, respectively. In the C_{2v} symmetry point group of the core excited species, the $2e''$ MO generates the $3b_1$ ($1\pi^*$) and the $2a_2$ ($2\pi^*$) MO's, while the $2a_2''$ becomes the $4b_1$ ($3\pi^*$) MO. In the D_{3h} symmetry group, corresponding to the true symmetry of the molecule (or a delocalised core hole), the transitions from the $1s(1e')$ MO's to a_1'' and a_2'' MO's are dipole electric forbidden; for the $(1s)1a_1'$ MO, only transitions to a_2'' and e' MO's are dipole electric allowed. In the C_{2v} group, corresponding to the localised picture used for the calculations, all electronic transitions are dipole allowed except $1s \rightarrow 2\pi^*(2a_2)$. The MP2 optimised D_{3h} geometry of the ground state of *s*-triazine compares well with previous experimental [5,22–24] and theoretical works [25], as shown in Table 1. Thus, all the calculations were carried out at this geometry.

The calculated core ionisation energies, obtained at the RHF and MP2 levels, are shown in Table 2. In the absence of any experimental determination of these quantities, Apen et al. [7] used the values of like materials taken from a compilation [26]. Since, according to our previous work [27], the calculated values should be accurate within a few tenths of an eV, it appears that the values of 290.6 eV for the C1s ionisation energy is underestimated by several eV. This will have some consequences on the assignment of the carbon K-shell spectrum (see below). The N1s ionisation energy appears to be also underestimated by about 1 eV.

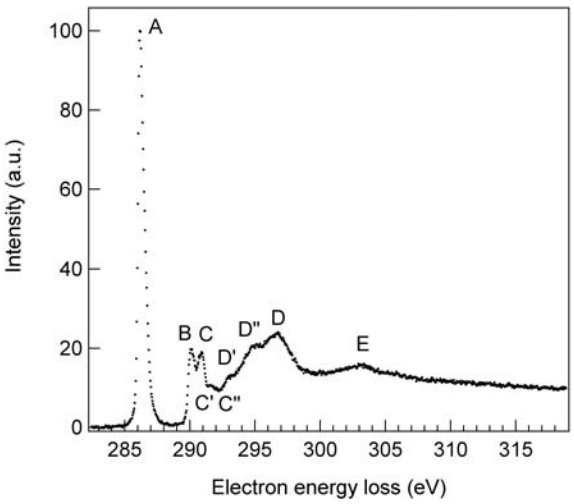

Fig. 1. The electron energy loss spectrum of *s*-triazine recorded at the carbon K edge with an energy resolution of 0.17 eV.

4.1 Carbon K-shell electron-energy loss spectrum

The measured carbon K-shell energy loss spectrum of *s*-triazine is displayed in Figure 1. The spectrum is similar to that obtained by Apen et al. [7] at low resolution (0.6 eV) but the better resolution of the present work allows to distinguish more details. Globally, the energies of the observed bands are in agreement with those of Apen et al. [7], as shown in Table 3. The table also provides the assignments initially proposed in reference [7]. The results of the calculations are given in Table 4.

The first band A is observed at 286.16 eV and is assigned without ambiguity to the $1s \rightarrow 1\pi^*$ ($1e''$, $3b_1$) transition, which is calculated to occur at 286.32 eV (Tab. 4). This band has a FWHM of 0.57 eV, close to the 0.55 eV value reported by Apen et al. [7]. The band is asymmetric in the high energy region, which suggests possible vibrational excitation. The calculated vibrational structure is displayed in Figure 2a. The vertical transition was set to the calculated value of 286.32 eV. Although the calculated width is too small, the asymmetry is correctly reproduced. The vibrational progression is dominated by the 0–0 transition. This peak is followed by four medium

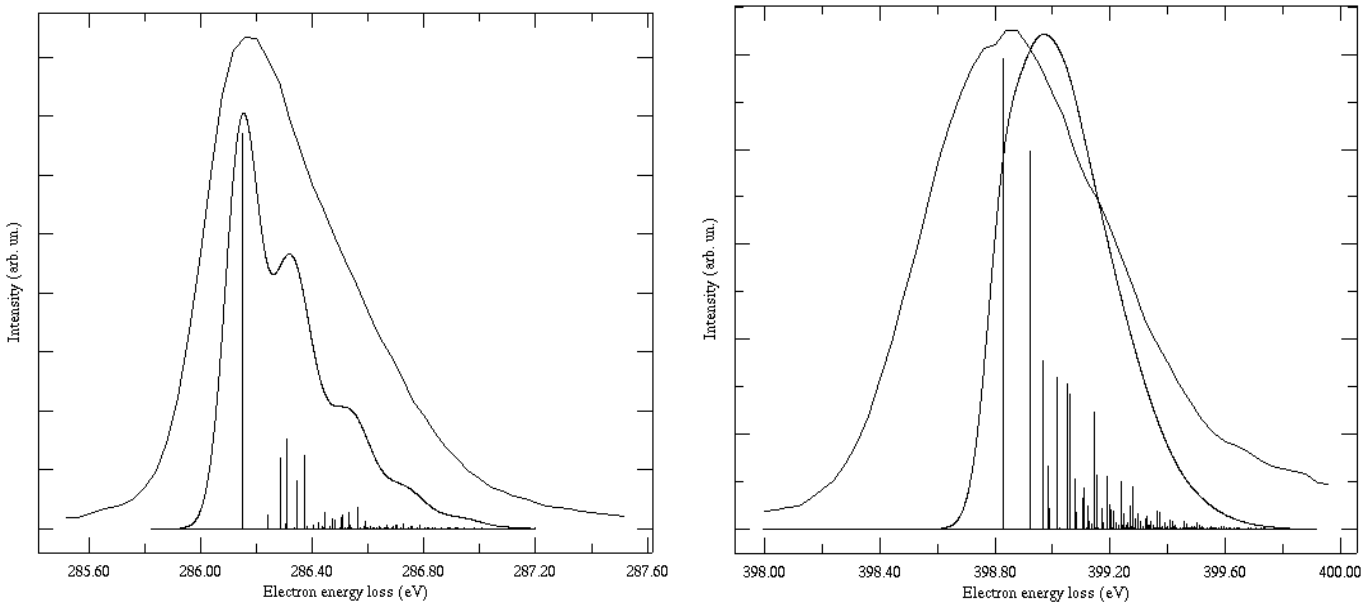

Fig. 2. Calculated vibrational structure of the first bands. (a) C1s edge; (b) N1s edge.

Table 3. Measured energies (eV) of the spectral features in the C1s spectrum and previous proposed assignments.

	E (eV)[a]	E (eV)[b]	Assignment[b]
A	286.16	286.2	$1\pi^*$ $(2e'')$
		287.5	
B	290.09	290.1	$3\pi^*$ $(2a_2'')$
	(290.64)		
C	290.84	290.8	σ^*(C–H)
	(291.22)		
C'	291.58		
C"	292.02	(292)	double excitation
D'	293.08	(293)	double excitation
		(294)	double excitation
D"	295.12		
D	296.66	296.5	σ^*(C–N)
E	303.36	303.0	σ^*(C–N)

[a] This work. Not well resolved features are given in parentheses, [b] Ref. [7].

intensity peaks corresponding to excitation of the carbon-nitrogen ring modes. This suggests that the geometry of the $1s \rightarrow 1\pi^*$ state should be close to the ground state one. This is confirmed by a geometry optimisation of this state (at HF level): the molecule remains planar; the ring is slightly distorted with the C_eN distance reduced to 1.2806 Å.

Apen et al. [7] also reported a low intensity feature at 287.5 eV, without giving any assignment. This feature does not seem to be present in the present spectrum (Fig. 1) but, according to the calculations, the $1s \rightarrow 2\pi^*(1e'', 2a_2)$ dipole electric forbidden transition is predicted to occur at 286.98 eV. However, its calculated electric quadrupole oscillator strength is negligible.

The next band B is observed at 290.09 eV with a not well resolved feature at 290.64 eV (Tab. 3). Apen et al. [7] assigned it to the $1s \rightarrow 3\pi^*(2a_2'', 4b_1)$ transition, by analogy with the pyridine case [28]. However, it has to be assigned to the $1s \rightarrow 3s\sigma/\sigma^*(C_e$–H) which is predicted to occur by the calculations at 289.83 eV (Tab. 4). Its rather large intensity (6.4% of the first peak) is due to the large $\sigma^*(C_e$–H) valence character of the $3s\sigma$ MO. This trend is very frequent in the carbon K-shell spectra of organic molecules [8–27].

The B band is also asymmetric in the high energy side, probably because of vibrational excitation, and overlaps partially with the C band, whose maximum is measured at 290.84 eV with a not well resolved feature at 291.22 eV. This band was assigned by Apen et al. [7] to a $1s \rightarrow \sigma^*$(C–H) transition and was supposed to lie at the continuum onset, assuming a ionisation energy of 290.6 eV. In fact it is mainly due to a $1s \rightarrow 3p\sigma/\sigma^*(C_e$–H) valence-Rydberg transition, calculated at 290.56 eV, and to a rather intense (12.8%) π^* (b_1) transition predicted at 290.73 eV (Tab. 4). Although the calculated wave-function appears to be strongly mixed (Tab. 4), this state is assigned to the $3\pi^*$ transition.

The next energy region of the spectrum between 291 and 293 eV does not present any clear feature, except possible not well resolved structures at C' at 291.58 eV and C" at 292.02 eV. As shown in Table 4, the transitions calculated in this energy range correspond to Rydberg states ($n = 3$–7) and have very small intensities. Two states of particular interest are calculated at 291.83 and 291.85 eV. Their wave-functions are strongly mixed: the first one is dominated by valence di-excitations with a

Table 4. Calculated energies, TV's, relative intensities and assignments of C1s core excited states of *s*-triazine.

State	E(eV)	TV(eV)	Intensity[a]	Main configurations	$\langle r^2 \rangle$
B_1	286.32	6.96	1.000	0.92 $1s \rightarrow 1\pi^*$	79
A_2	286.98	6.30	0.000[b]	0.92 $1s \rightarrow 2\pi^*$	80
A_1	289.83	3.45	0.064	0.95 $1s \rightarrow 3s\sigma/\sigma^*(C_e–H)$	128
B_1	290.45	2.83	0.008	0.74 $1s \rightarrow 3p\pi$	128
				+ 0.12 $1s \rightarrow 3\pi^*$	
A_1	290.56	2.72	0.053	0.94 $1s \rightarrow 3p\sigma/\sigma^*(C_e–H)$	145
B_1	290.73	2.55	0.128	0.35 $1s \rightarrow 3\pi^*$	134
				+ 0.22 $1s \rightarrow 3p\pi$	
				+ 0.11 $1s \rightarrow 3d\pi$	
				+ 0.10 $1s2\pi \rightarrow 1\pi^*1\pi^*$	
B_2	290.88	2.40	<0.001	0.97 $1s \rightarrow 3p\sigma$	195
A_1	291.23	2.06	0.002	0.95 $1s \rightarrow 3d\sigma$'	180
B_2	291.43	1.85	0.004	0.97 $1s \rightarrow 3d\sigma$	200
A_1	291.47	1.82	0.004	0.95 $1s \rightarrow 3d\sigma$	225
B_1	291.51	1.77	<0.001	0.84 $1s \rightarrow 3d\pi$	220
A_2	291.60	1.68	0.000[b]	0.98 $1s \rightarrow 3d\pi$	232
A_1	291.70	1.59	0.017	0.95 $1s \rightarrow 4s\sigma/\sigma^*(C_e–H)$	400
B_1	291.83	1.45	0.010	0.39 $1s2\pi \rightarrow 1\pi^*1\pi^*$	261
				+ 0.36 $1s \rightarrow 4d\pi$	
				+ 0.13 $1s3\pi \rightarrow 1\pi^*2\pi^*$	
B_1	291.85	1.43	0.004	0.58 $1s \rightarrow 4d\pi$	500
				+ 0.14 $1s2\pi \rightarrow 1\pi^*1\pi^*$	
				+ 0.12 $1s3\pi \rightarrow 1\pi^*2\pi^*$	
B_1	291.88	1.41	0.039	0.82 $1s \rightarrow 4p\pi$	463
A_1	291.93	1.35	0.019	0.95 $1s \rightarrow 4p\sigma$	490
B_2	292.02	1.26	0.000	0.96 $1s \rightarrow 4p\sigma$	734
A_1	292.08	1.20	<0.001	0.96 $1s \rightarrow 4d\sigma$	688
B_2	292.14	1.14	0.002	0.97 $1s \rightarrow 4d\sigma$	617
A_1	292.16	1.12	<0.001	0.95 $1s \rightarrow 4d\sigma$'	715
A_2	292.20	1.09	0.000[b]	0.98 $1s \rightarrow 4d\pi$	598
A_1	292.26	1.02	0.010	0.94 $1s \rightarrow 5s\sigma$	966
B_1	292.31	0.97	0.005	0.93 $1s \rightarrow 5p\pi$	1231
B_2	292.34	0.94	<0.001	0.96 $1s \rightarrow 5p\sigma$	1091
A_1	292.35	0.93	0.005	0.86 $1s \rightarrow 5p\sigma$	1058
A_1	292.53	0.75	<0.001	0.89 $1s \rightarrow 6s\sigma$	3555
A_1	292.66	0.62	0.001	0.97 $1s \rightarrow 6p\sigma$	7724
B_2	292.66	0.62	<0.001	0.98 $1s \rightarrow 6p\sigma$	7690
B_1	292.66	0.62	<0.001	0.98 $1s \rightarrow 6p\pi$	7746
A_1	292.77	0.51	<0.001	0.98 $1s \rightarrow 7s\sigma$	>10000
A_1	292.83	0.45	<0.001	0.98 $1s \rightarrow 7p\sigma$	>10000
B_2	292.83	0.45	<0.001	0.98 $1s \rightarrow 7p\sigma$	>10000
B_1	292.83	0.45	<0.001	0.98 $1s \rightarrow 7p\pi$	>10000
A_1	293.07	0.21	0.089	0.94 $1s \rightarrow \sigma^*(C_e–H)$	179
	293.28	0.00		ion	
B_2	293.80	–0.52	0.059	0.94 $1s \rightarrow \sigma^*$(C–N)	129
A_1	293.86	–0.58	0.004	0.95 $1s \rightarrow \sigma^*$(C–N)	125
A_1	294.91	–1.62	<0.001	0.54 $1s\ 2\pi \rightarrow 1\pi^*\ 3s\sigma/\sigma^*(C_e–H)$	134
B_2	294.93	–1.64	0.031	0.95 $1s \rightarrow \sigma^*$	101
A_1	295.50	–2.22	<0.001	0.63 $1s\ 2\pi \rightarrow 3\pi^*\ 3p\sigma/\sigma^*(C_e–H)$	186
B_2	296.12	–2.84	<0.001	0.63 $1s\ 2\pi \rightarrow 1\pi^*\ 3p\sigma$	209

[a] Relative intensity to the most intense peak. The absolute calculated oscillator strength of the first transition is $f = 0.0577$,
[b] forbidden dipole electric transition.

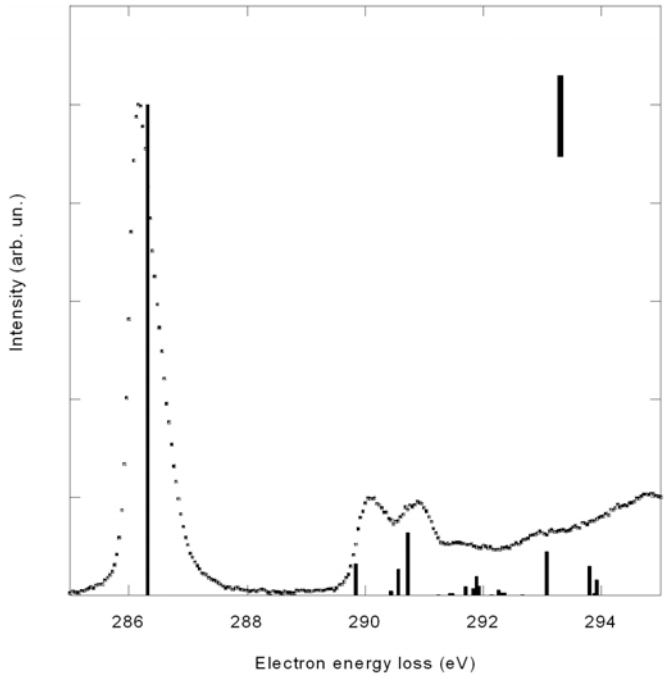

Fig. 3. Comparison of the calculated C1s spectrum with the experimental one. The vertical line indicates the calculated ionisation threshold.

substantial $4d\pi$ character, while the situation is reversed for the second one. The $\langle r^2 \rangle$ values of the first one (261 a.u.^{2}) is too low to assign it to an $n = 4$ Rydberg state. The $\langle r^2 \rangle$ values of the first one (500 a.u.^{2}) is higher and is compatible with an $n = 4$ Rydberg state. Thus, we qualitatively assign the first state to a valence di-excited state and the second to the $4d\pi$ Rydberg transition.

The feature D' observed at 293.08 eV was assigned by Apen et al. [7] to a double excitation state, since it was supposed to lie well above the ionisation threshold. In fact, it should correspond to the continuum onset if the calculated ionisation energy of 293.28 eV is correct. Moreover, the calculations predict the $1s \rightarrow \sigma^*(C_e\text{–H})$ transition to occur at 293.07 eV (Tab. 4) with a rather large intensity (8.9%). Therefore, the calculations confirm that the $\sigma^*(C_e\text{–H})$ transition is quasi-degenerate with the continuum onset, but about 2.5 eV higher than proposed by Apen et al. [7].

The last three features observed in the spectrum (D" at 295.12 eV, D at 296.66 eV and E at 303.36 eV) are above the ionisation threshold (Tab. 3). The calculations of Table 4 predict several states above the edge, including excitations to σ^* orbitals as well as di-excited states. However, these results cannot be considered as quantitative since the influence of the continuum is not taken into account. Moreover, the observed bands are too high in energy to be calculated. These three bands are tentatively assigned to shape resonances but it should be kept in mind that this type of assignment has been questioned [29].

The synthetic spectrum resulting from the calculations is compared with the experimental spectrum in Figure 3.

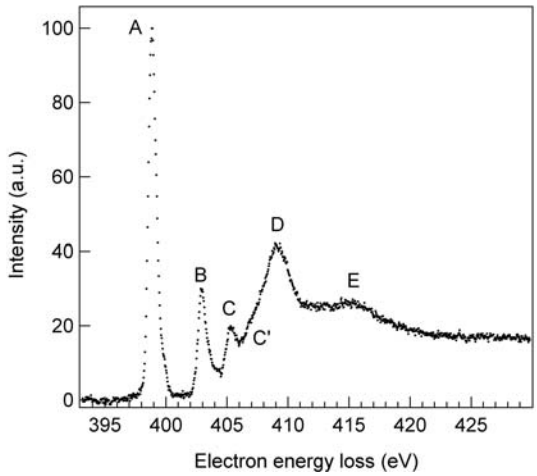

Fig. 4. The electron energy loss spectrum of s-triazine recorded at the nitrogen K edge with an energy resolution of 0.17 eV.

Table 5. Measured energies (eV) of the spectral features in the N1s spectrum and previous proposed assignments.

	E (eV)[a]	E (eV)[b]	E (eV)[c]	Assignment[b]
A	398.84	398.8	399.9	$1\pi^*$ $(2e'')$
	(402.36)			
B	402.92	402.9	404.2	$3\pi^*$ $(2a_2'')$
	(403.24)			
	(403.44)			
	(403.60)			
B'	404.12			
C	405.32	405.5	406.8	double excitation/ continuum onset
C'	406.84			
D	409.10	409.2	409.6	σ^*(C–N)
E	415	415.3	417.5±1	σ^*(C–N)

[a] This work. Not well resolved features are given in parentheses, [b] Ref. [7], [c] Ref. [30].

It appears that the theoretical energies are accurate within a few tenths of an eV.

4.2 Nitrogen K-shell electron-energy loss spectrum

The measured nitrogen K-shell energy loss spectrum of s-triazine is shown in Figure 4 and the energies of the observed bands are given in Table 5. As for the carbon case, the results are in good agreement with those obtained at low resolution by Apen et al. [7]. Table 5 also displays the results obtained by Dudde et al. [30] on condensed thick films of s-triazine. These values appear to be too large by about 1 eV when compared to the two gas phases studies, possibly because of a calibration error as suggested by Apen et al. [7]. The results of the present calculations are given in Table 6.

Table 6. Calculated energies, TV's, relative intensities and assignments of N1*s* core excited states of *s*-triazine.

State	E(eV)	TV(eV)	Intensity[a]	Main configurations	$\langle r^2 \rangle$
B_1	399.05	7.09	1.000	0.91 $1s \rightarrow 1\pi^*$	79
A_2	399.69	6.45	0.000[b]	0.93 $1s \rightarrow 2\pi^*$	80
A_1	402.76	3.38	<0.001	0.97 $1s \rightarrow 3s\sigma$	127
B_1	403.43	2.71	0.093	0.91 $1s \rightarrow 3p\pi$	142
A_1	403.66	2.48	0.020	0.96 $1s \rightarrow 3p\sigma$	176
B_2	403.66	2.48	<0.001	0.98 $1s \rightarrow 3p\sigma$	182
B_1	404.03	2.11	0.116	0.46 $1s \rightarrow 3d\pi$	186
				+ 0.20 $1s \rightarrow 3\pi^*$	
				+ 0.16 $1s \rightarrow 4p\pi$	
A_1	404.06	2.08	0.007	0.95 $1s \rightarrow 3d\sigma$	176
B_1	404.10	2.04	0.152	0.52 $1s \rightarrow 3d\pi$	195
				+ 0.18 $1s \rightarrow 3\pi^*$	
				+ 0.15 $1s \rightarrow 4p\pi$	
A_1	404.28	1.86	0.002	0.95 $1s \rightarrow 3d\sigma$	201
B_2	404.36	1.78	0.005	0.97 $1s \rightarrow 3d\sigma$'	220
A_2	404.45	1.69	0.000[b]	0.98 $1s \rightarrow 3d\pi$	231
A_1	404.58	1.56	<0.001	0.97 $1s \rightarrow 4s\sigma$	423
B_1	404.62	1.52	0.042	0.65 $1s \rightarrow 4p\pi$	513
				+ 0.20 $1s \rightarrow 3\pi^*$	
A_1	404.84	1.30	0.012	0.72 $1s \rightarrow 4p\sigma$	557
				+ 0.20 $1s \rightarrow 4d\sigma$	
B_2	404.86	1.28	<0.001	0.97 $1s \rightarrow 4p\sigma$	628
A_1	404.92	1.22	0.001	0.72 $1s \rightarrow 4d\sigma$	684
				+ 0.24 $1s \rightarrow 3p\sigma$	
A_1	405.00	1.14	0.001	0.93 $1s \rightarrow 4d\sigma$'	624
B_2	405.02	1.12	0.003	0.97 $1s \rightarrow 4d\sigma$	771
B_1	405.04	1.10	0.003	0.97 $1s \rightarrow 4d\pi$	617
A_2	405.05	1.09	0.000[b]	0.98 $1s \rightarrow 4d\pi$	600
A_1	405.12	1.02	<0.001	0.93 $1s \rightarrow 5s\sigma$	875
B_1	405.15	0.99	0.007	0.90 $1s \rightarrow 5p\pi$	1221
B_2	405.20	0.94	0.001	0.97 $1s \rightarrow 5p\sigma$	1036
A_1	405.21	0.93	0.007	0.88 $1s \rightarrow 5p\sigma$	1148
A_1	405.38	0.76	0.001	0.93 $1s \rightarrow 6s\sigma$	3597
B_1	405.51	0.63	<0.001	0.98 $1s \rightarrow 6p\pi$	7745
B_2	405.52	0.62	<0.001	0.98 $1s \rightarrow 6p\sigma$	7693
A_1	405.52	0.62	<0.001	0.98 $1s \rightarrow 6p\sigma$	7728
A_1	405.63	0.51	<0.001	0.99 $1s \rightarrow 7s\sigma$	>10000
B_2	405.69	0.45	<0.001	0.99 $1s \rightarrow 7p\sigma$	>10000
B_1	405.69	0.45	<0.001	0.99 $1s \rightarrow 7p\pi$	>10000
A_1	405.69	0.45	<0.001	0.99 $1s \rightarrow 7p\sigma$	>10000
B_1	405.89	0.25	0.163	0.13 $1s \rightarrow 3\pi^*$	92
				+ 0.52 $1s\ 3\pi \rightarrow 1\pi^*\ 2\pi^*$	
				+ 0.18 $1s\ 2\pi \rightarrow 2\pi^*\ 3p\pi$	
B_1	405.94	0.20	<0.001	0.67 $1s\ 2\pi \rightarrow 1\pi^*\ 1\pi^*$	79
				+ 0.19 $1s\ 3\pi \rightarrow 1\pi^*\ 2\pi^*$	
	406.14	0.00		ion	
A_1	406.26	–0.12	0.025	0.87 $1s \rightarrow \sigma^*$(C–H)	142
B_2	406.71	–0.57	0.132	0.95 $1s \rightarrow \sigma^*$(C–H)	131
A_1	406.72	–0.58	0.017	0.85 $1s \rightarrow \sigma_1^*$	123
B_2	407.87	–1.73	0.078	0.97 $1s \rightarrow \sigma_1^*$	99
B_2	407.89	–1.75	0.038	0.37 $1s \rightarrow \sigma_2^*$	171
				+ 0.50 $1s\ 3\pi \rightarrow 1\pi^*\ 3p\sigma$	
A_1	407.93	–1.79	<0.001	0.80 $1s\ 3\pi \rightarrow 2\pi^*\ 3s\sigma$	138
A_1	408.52	–2.38	0.037	0.55 $1s \rightarrow \sigma_4^*$	149
				+ 0.30 $1s\ 3\pi \rightarrow 3\pi^*\ 3p\sigma$	
B_2	408.57	–2.43	0.067	0.54 $1s \rightarrow \sigma_3^*$	148
				+ 0.33 $1s\ 3\pi \rightarrow 1\pi^*\ 3p\sigma$	
A_1	408.59	–2.45	0.026	0.37 $1s \rightarrow \sigma_4^*$	163
				+ 0.45 $1s\ 3\pi \rightarrow 2\pi^*\ 3p\sigma$	

[a] Relative intensity to the most intense peak. The absolute calculated oscillator strength of the first transition is $f = 0.0294$.
[b] Forbidden dipole electric transition.

As for C1s threshold, the first band A, observed at 398.84 eV with a FWHM of 0.77 eV, corresponds to the N1$s \rightarrow 1\pi^*$ ($2e''$, $3b_1$) transition, calculated at 399.05 eV (Tab. 6). This band is asymmetric in the high energy range and there seems to be a not well resolved feature around 399.9 eV, in the high energy tail of the A band. Its energy seems too large to assign it to vibrational excitation of the A band. This is confirmed by the calculation of the vibrational structure, which is compared to the experiment in Figure 2b. As for the C1s case, the theoretical width is too small but the asymmetry is reproduced. The vibrational structure is also dominated by the 0–0 transition, with excitation of the ring modes. Vibrational excitation appears to be more important than for the C1s case. Optimisation of the geometry of this state at the HF level shows that it remains planar, with an important distortion of the ring: the N_eC is practically unchanged (1.3170 Å), the next CN bonds are shortened (1.2792 Å) and the last NC bonds (where C is opposite to N_e) is increased (1.3307 Å). The CH bonds are unchanged.

The electric dipole forbidden $1s \rightarrow 2\pi^*(1e'', 2a_2)$ transition is calculated at 399.69 eV (Tab. 6). This suggests a possible electric quadrupole transition for the 399.9 eV feature. However, the corresponding calculated oscillator strength was found to be negligible.

The next band B in the spectrum is centred at 402.92 eV with not well resolved fine features at 402.36, 403.24, 403.44 and 403.60 eV (Fig. 4). This band was assigned by Apen et al. [7] to the $1s \rightarrow 3\pi^*$ ($2a_2''$, $4b_1$) transition by analogy with the pyridine case [28]. The results of the calculations given in Table 6 show a more complex situation. Although the predicted energies seem to be slightly overestimated by ∼0.5−1.0 eV, this band may be assigned to three intense transitions, among several low intensity Rydberg transitions. The first one corresponds to the $1s \rightarrow 3p\pi$ transition. Its calculated intensity (9.3%) is unexpectedly high, since there is no N–H* bond which could provide a valence character to the Rydberg transitions and increase the intensity of the band. The two other intense transitions, of B_1 symmetry, are calculated to occur at 404.03 eV and 404.10 eV, with close intensities (11.6 and 15.2%, respectively). Their CI wave-functions are also very similar: about 50% of the $1s \rightarrow 3d\pi$ excitation, with 20% of the $1s \rightarrow 3\pi^*$ and 15% of the $1s \rightarrow 4p\pi$ excitations. Moreover, these two states have also the same $\langle r^2 \rangle$ value (186 and 195 a.u.^{2}). Since the four other 3d transitions are calculated unambiguously to occur in this energy region, it is tempting to assign one of these two states to the $3d\pi$ (B_1) one, while the other would correspond to the $3\pi^*$ transition, which does not appear elsewhere in the calculations. One would therefore expect a low intensity and a large $\langle r^2 \rangle$ value for the Rydberg transition, and the opposite for the valence transition. This is obviously not the case and we have to conclude that it is not possible to label without ambiguity the two states. This is an example of the limit of the mono-electronic description of transitions. It should be reminded that a similar situation occurred at the C1s with the two states calculated at 291.83 and 291.85 eV.

Because of the discrepancy between the calculated transition energies and the maximum of this B band, it is difficult to make a precise assignment. Its asymmetry could indicate that it corresponds to several transitions but could also be due to vibrational excitation. Thus, we tentatively assign the low energy part of this band to the $1s \rightarrow 3p\pi$ transition, while the high energy tail is assigned to the two $1s \rightarrow 3d\pi/3\pi^*$ quasi-degenerate transitions. If this assignment is correct, the calculated intensities are not in agreement with the shape of the band. A possible explanation could be the different lifetimes of these transitions, leading to different widths. However, it is not possible to evaluate these parameters.

The next band C has its maximum at 405.32 eV (Tab. 5) and was assigned by Apen et al. [7] to a double excitation state and the continuum onset. Dudde et al. [30] also proposed a multi-electron state for this feature. The fact that this feature is present in the condensed phase spectrum of Dudde et al. [30] indicates that it cannot be due to Rydberg excitations. The calculations (Tab. 6) predict a large number of low intensity transitions to occur between 404.5 and 406 eV, due to the $n > 3$ Rydberg states, converging to the calculated MP2 ionisation energy (406.14 eV). The energy difference of 0.8 eV could be due to the inaccuracy of the calculations. It is also possible that the continuum onset corresponds to the not-well resolved C' feature, observed at 406.84 eV (Tab. 5). This question could be solved by measuring the core ionisation energy of gaseous s-triazine.

The results of the calculations displayed in Table 6 also confirm the presence of a doubly excited state, calculated at 405.89 eV. Its wave-function is rather complex: $0.13(1s \rightarrow 3\pi^*) + 0.52(1s3\pi \rightarrow 1\pi^*2\pi^*) + 0.18(1s2\pi \rightarrow 2\pi^*3p\pi)$. To clarify the situation, we have used the calculated CI density matrix to obtain the so-called "natural orbitals", as proposed by Löwdin [31]. Such an analysis resulted in four orbitals with an occupation number close to one, confirming the double excitation nature of this state. The calculated $\langle r^2 \rangle$ value of 92 a.u.^{2} shows that it is a valence transition. The most striking result is the calculated intensity: 16.3% of the main peak, which could be sufficient to explain the intensity of the C band if the continuum onset lies at higher energies. A similar high intensity doubly excited state has already been predicted in the K-shell spectrum of benzene [8–32], which is iso-electronic to s-triazine. In the case of benzene, Schwarz et al. [32] placed this state at the continuum onset while our own calculations [8] led us to assign this state to the band observed at 289.09 eV. It is remarkable that the situation is very different at the C1s threshold of s-triazine: the $1s \rightarrow 3\pi^*$ state is mixed mainly with Rydberg excitations and lies well below the ionisation threshold. Another example of doubly excited state is the H_2CO C1s $n \rightarrow \pi^{*2}$ transition predicted to occur just above the C1$s \rightarrow \pi^*$ one with a relative intensity of 0.05% [33]. Doubly excited states around the ionisation threshold have also been predicted in N_2 [34] and their presence has been confirmed experimentally [35]. Triply excited states have also been confirmed [35,36].

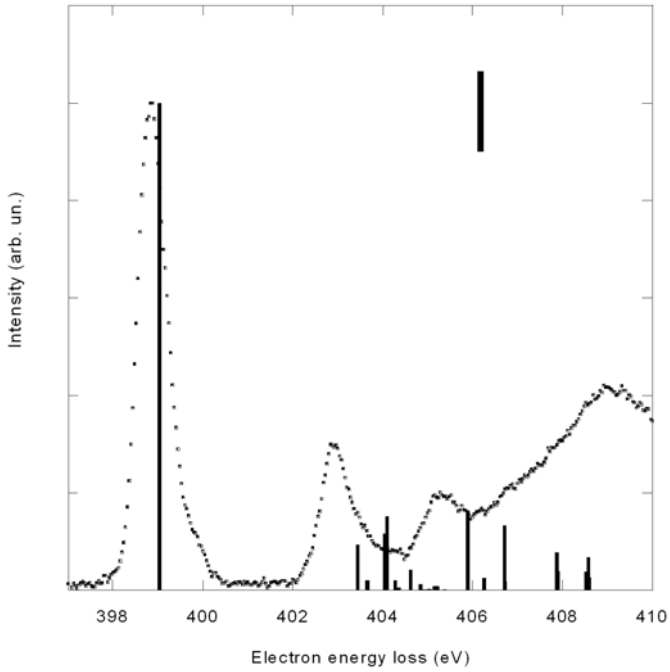

Fig. 5. Comparison of the calculated N1*s* spectrum with the experimental one. The vertical line indicates the calculated ionisation threshold.

The next two bands which can be seen in the experimental spectrum lie at much higher energies (409.10 eV for D and 415 eV for E). As for the C1*s* case, the calculated σ^* and di-excited states shown in Table 6 have only qualitative meaning and are two low in energy. Thus, bands D and E are tentatively assigned to shape resonances. Figure 5 compares the experimental spectrum with the calculated peaks. It appears that the calculations seem to overestimate the core excitation energies by about 0.5 eV.

5 Conclusions

In this work, the inner shell electron energy loss spectra of gaseous *s*-triazine have been measured at the C1*s* and N1*s* edges with 0.17 eV resolution. Accompanying *ab initio* Configuration Interaction calculations using Configuration Interaction have been performed, in order to obtain reliable assignments

At the carbon edge, it appears that the previous assignments of Apen et al. [7] were based on a too low ionisation energy. The present calculations lead to give more precise assignments for some spectral bands and this without ambiguity. At the nitrogen edge, the most important result of the calculations is the presence of an intense doubly excited state predicted to occur below the ionisation threshold, as already observed in the C1*s* spectrum of benzene [8].

At both edges, the calculated wave functions show rather complex patterns, including strong Rydberg-valence character as well as mixing between mono and di-excitations. These results show that in certain cases, a proper description of core electronic transitions requires to go beyond the mono-electronic picture, as done for example in the STEX [37] or GSCF3 [38] approaches. It can be done for example by using Configuration Interaction methods (see for example [14,39], but with a higher computational cost.

The assignments of the K-shell spectra of gaseous *s*-triazine presented in the present work should be useful for the interpretation of core spectra of similar but more complex molecules, such as triazine-based herbicides, either in gas or solid phases. This is of particular importance in the context of soil science, where synchrotron-based spectroscopy has already been used as an analytical technique to detect heterocyclic N compounds [40].

The "Laboratoire de Physique des Lasers, Atomes et Molécules" (PhLAM) is "Unité Mixte de Recherche du CNRS". The "Centre d'Études et de Recherches Lasers et Applications" (CERLA, FR CNRS 2416) is supported by the "Ministère chargé de la Recherche", the "Région Nord/Pas-de-Calais" and the "Fonds Européen de Développement Économique des Régions" (FEDER). Parts of the computations were carried out at the CRI (Centre de Ressources Informatiques), on the IBM-SP3 computer that is supported by the "Programme de Calcul Intensif et Parallèle" of the "Ministère chargé de la Recherche", the "Région Nord/Pas-de-Calais" and the FEDER. This research has been supported by the Fonds National de la Recherche Scientifique and the Patrimoine of University of Liège. M.-J. Hubin-Franskin wishes to acknowledge the Fonds National de la Recherche Scientifique for research position.

References

1. R.T. Meister, C. Sine, *Farm Chemical Handbook* (Meister Publishing Co., Willoughby, OH, 1998)
2. R. Spear, in *Handbook of Pesticide Toxicology*, edited by W.J. Hayes, E.R. Laws (Academic Press, San Diego, 1991)
3. E. Hodgson, P.E. Levi, Environ. Health Perspect. **104**, 97 (1996)
4. H.D. Burrows, M.L. Canle, J.A. Santaballa, J. Photochem. Photobiol. B **67**, 71 (2002)
5. J.M. Oliva, M.E.D.G. Azenha, H.D. Burrows, R. Coimbra, J. Serxio Seixas de Melo, L. Moisés Canle, M. Isabel Fernàndez, J. Arturo Santaballa, L. Serrano-Andrés, Chem. Phys. Chem. **6**, 306 (2005)
6. J. Stöhr, *NEXAFS Spectroscopy* (Springer Verlag, 1992)
7. E. Apen, A. Hitchcock, J. Gland, J. Phys. Chem. **97**, 6859 (1993)
8. D. Duflot, J.-P. Flament, J. Heinesch, M.-J. Hubin-Franskin, J. Electron Spectrosc. Rel. Phen. **113**, 79 (2000)
9. C. Hannay, D. Duflot, J.-P. Flament, M.-J. Hubin-Franskin, J. Chem. Phys. **110**, 5600 (1999)
10. C. Hannay, J. Heinesch, U. Kleyens, M.-J. Hubin-Franskin, Meas. Sci. Technol. **6**, 1140 (1995)
11. M.-J. Hubin-Franskin, H. Aouni, D. Duflot, F. Motte-Tollet, C. Hannay, L.F. Ferreira, G. Tourillon, J. Chem. Phys. **106**, 35 (1997); M.-J. Hubin-Franskin, J. Heinesch, Nucl. Instrum. Meth. Phys. Res. A **477**, 546 (2002)
12. F. Currell, C.M. John, Meas. Sci. Technol. **3**, 1192 (1992)

13. R.N.S. Sodhi, C.E. Brion, J. Electron Spectrosc. Rel. Phen. **34**, 363 (1984)
14. D. Duflot, J.-P. Flament, I.C. Walker, J. Heinesch, M.-J. Hubin-Franskin, J. Chem. Phys. **118**, 1137 (2003)
15. S. Bodeur, P. Millié, I. Nenner, Phys. Rev. A **41**, 252 (1990)
16. M.W. Schmidt, K.K. Baldridge, J.A. Boatz, S.T. Elbert, M.S. Gordon, J.H. Jensen, S. Koseki, N. Matsunaga, K.A. Nguyen, S. Su, T.L. Windus, M. Dupuis, J.A. Montgomery Jr, J. Comp. Chem. **14**, 1347 (1993)
17. B. Huron, J.P. Malrieu, P. Rancurel, J. Chem. Phys. **58**, 5745 (1973); R. Cimiraglia, J. Chem. Phys. **83**, 1746 (1985)
18. C. Angeli, R. Cimiraglia, M. Persico, A. Toniolo, Theor. Chem. Acc. **98**, 57 (1997)
19. T.H. Dunning Jr, J. Chem. Phys. **55**, 716 (1971)
20. T.H. Dunning Jr, P.J. Hay, in *Methods of Electronic Structure Theory*, edited by H.F. Schaefer III (Plenum Press, New York, 1977), Vol. 3, p. 1
21. H. Köppel, W. Domcke, L.S. Cederbaum, Adv. Chem. Phys. **57**, 59 (1984)
22. P.F. Price, E.N. Matsen, W.T. Delany, Acta Cryst. A **34**, 194 (1978)
23. J.E. Lancaster, B.P. Stoicheff, Can. J. Phys. **34**, 1016 (1956)
24. W. Pyckout, I. Callaerts, C. Van Alsenoy, H.J. Geise, A. Almenningen, R. Seip, J. Mol. Struct. **147**, 321 (1986)
25. I.C. Walker, M.H. Palmer, C.A. Ballard, Chem. Phys. **167**, 61 (1992)
26. W.L. Jolly, K.D. Bomben, C.J. Eyerman, At. Data Nucl. Data Tables **31**, 433 (1984)
27. D. Duflot, J.-P. Flament, A. Giuliani, J. Heinesch, M.-J. Hubin-Franskin, J. Chem. Phys. **119**, 8946 (2003)
28. J.A. Horsley, J. Stöhr, A.P. Hitchcock, D.C. Newbury, A.L. Johnson, F.J. Sette, J. Chem. Phys. **83**, 6099 (1985)
29. M.N. Piancastelli, J. Electron Spectrosc. Related Phen. **100**, 167 (1999)
30. R. Dudde, M.L.M. Rocco, E.E. Koch, S. Bernstorff, W. Eberhardt, J. Chem. Phys. **91**, 20 (1989)
31. P.-O. Löwdin, Phys. Rev. **97**, 1474 (1955)
32. W.H.E. Schwarz, T.C. Chang, U. Seeger, K.H. Hwang, Chem. Phys. **117**, 73 (1987)
33. J. Schirmer, A. Barth, F. Tarantelli, Chem. Phys. **122**, 9 (1988); A.B. Trofimov, E.V. Gromov, T.E. Moskovskaya, J. Schirmer, J. Chem. Phys. **113**, 6716 (2000)
34. R. Arneberg, H. Agren, J. Muller, R. Manne, Chem. Phys. Lett. **91**, 362 (1982)
35. E. Shigemasa, T. Gejo, M. Nagasono, T. Hatsui, N. Kosugi, Phys. Rev. A **66**, 022508 (2002)
36. R. Feifel, K. Ueda, A. De Fanis, K. Okada, S. Tanimoto, T. Furuta, H. Shindo, M. Kitajima, H. Tanaka, O. Bjorneholm, L. Karlsson, S. Svensson, S.L. Sorensen, Phys. Rev. A **67**, 032504 (2003)
37. H. Ågren, V. Carravetta, O. Vahtras, L.G.M. Pettersson, Theor. Chem. Acc. **97**, 14 (1997)
38. N. Kosugi, H. Kuroda, Chem. Phys. Lett. **74**, 490 (1980)
39. S. Stranges, M. Alagia, G. Fronzoni, P. Decleva, J. Phys. Chem. A **105**, 3400 (2001)
40. A. Jokic, J.N. Cutler, D.W. Anderson, W.F.L., Can. J. Soil Sci. **84**, 291 (2004)

Article 17

Available online at www.sciencedirect.com
ScienceDirect
Chemical Physics 327 (2006) 518–528
Chemical Physics
www.elsevier.com/locate/chemphys

Ab initio study of core excited cyclopropane

D. Duflot *, S. Zeggari, J.-P. Flament

Laboratoire de Physique des Lasers, Atomes et Molécules (PhLAM), UMR CNRS 8523, Centre d'Etudes et de Recherches Lasers et Applications (CERLA, FR CNRS 2416), Université des Sciences et Technologies de Lille, F-59655 Villeneuve d'Ascq Cedex, France

Received 13 April 2006; accepted 25 May 2006
Available online 16 June 2006

Abstract

Ab initio configuration interaction calculations have been carried out in order to assign the bands observed in the carbon K-shell spectrum of gaseous cyclopropane, measured using the inner-shell electron energy loss spectroscopy (ISEELS) method. Simple Franck–Condon calculations, based on the linear coupling approximation, were performed in order to reproduce the observed vibrational structure. The good agreement between the theoretical and the measured spectra allows to assign precisely most of the peaks. The spectrum is dominated by an intense band, corresponding to the $1s \rightarrow \sigma^*(CC)(1a_2')$ transition, with large vibrational excitation. This is explained by the trimethylenic equilibrium geometry of this core state, very different from the D_{3h} ground state structure. On the other hand, the Rydberg core-excited states and the core ion are only slightly distorted. Finally, the calculated structural and energetic parameters of the NC_2H_6 valence states match well those of the corresponding core states of C_3H_6, illustrating the validity of the equivalent core approximation.

Keywords: Cyclopropane; Core excitation; *Ab initio*; Configuration interaction

1. Introduction

The cyclopropane molecule is the simplest cyclic hydrocarbon. Because of the high ring strain, it is rather different from other saturated alkanes. Therefore, many theoretical and experimental studies have been devoted to various properties of this molecule, such as bonding structure [1], equilibrium geometry [2–4], photodissociation dynamics [5]. The cyclopropane-propene isomerisation has also been the subject of numerous works [6–9]. Electronic excited states have been studied theoretically [10] and with various experimental methods [11–13], the most recent work concerning the vibrational structure of the photoelectron spectrum [14,15]. Among these, the K-shell excitation studies, using electron energy loss (ISEELS) or synchrotron radiation (NEXAFS), has proven to be a useful tool for probing the electronic structure of molecules [16].

The carbon K-shell spectrum of cyclopropane, was recorded using the ISEELS method by Hitchcock et al. [17] with a resolution of 0.7 eV. The same spectrum was recorded later by Sze and Brion [18] with a much better resolution of 0.065 eV. The assignments proposed by these authors were based on MS-Xα calculations from Hitchcock et al. [17], and on comparison with similar molecules. Our own previous works have shown that in some cases, *ab initio* calculations proved that such assignments could be incorrect [19]. The goal of the present paper is the study of the K-shell spectrum of cyclopropane using Configuration Interaction methods. Since the experimental spectrum shows evidence of vibrational excitation, Franck–Condon calculations were also carried out for a few selected states. Indeed, thanks to the apparition of third generation synchrotron sources, vibrational structure has become an important aspect of K-shell studies, both experimentally and theoretically, as recently reviewed by Hergenhan [20] (see also [21] and references therein). However, most of these studies have focussed on core ions, while a large number of states are involved in core excitation spectra.

* Corresponding author. Tel.: +33 3 20 43 49 80; fax: +33 3 20 43 40 84.
E-mail address: denis.duflot@univ-lille1.fr (D. Duflot).

0301-0104/$ - see front matter © 2006 Elsevier B.V. All rights reserved.
doi:10.1016/j.chemphys.2006.05.027

Finally, the geometry of some selected core-excited states of cyclopropane was also examined, as well as the corresponding "$Z+1$" states of NC_2H_6. Geometry optimisation of core states remains a difficult task [22,23], since it is not possible to employ the well-known methods used for valence states (see for example [24] for the difficulties to employ multi-reference methods for core binding energies).

2. Computational method

The computational method used in the present work is similar to that used in our previous study of the core excitation spectra of acrolein [25] and will be only briefly outlined. The basic assumption is that core ion MOs (obtained at the ROHF-GVB level with the GAMESS-US program [26]), are a better starting point than the ground state MOs for the calculation of the core excitation energies. Formally, these $E(1s \rightarrow i^*)$ core excitation energies can be written with respect to the $E(1s \rightarrow \infty)$ core ion energy in the following manner [27,28]:

$$E(1s \rightarrow i^*) = E(1s \rightarrow \infty) + \varepsilon_{i^*} + P_{i^*} + C_{i^*}$$

where ε_{i^*} is the mono-electronic energy of the i^* virtual MO. Therefore, truncating the equation to the ε_{i^*} term corresponds to the well-known Koopmans' theorem. The P_{i^*} term represents the residual relaxation of the core ion electron density due to the i^* electron, while the last term C_{i^*} represents the correlation effects induced by the presence of the i^* electron. In practice, relaxation is taken into account by diagonalisation of a single CI matrix including all mono-excitations with respect to all the $1s \rightarrow i^*$ core excitations. This also allows to describe possible di-excited (shake up) states, in contrast to other methods based on the mono-electronic approximation [19]. The correlation term C_{i^*} is obtained via a multi-reference MP2 calculation with the three-class diagrammatic CIPSI [29,30] method and using the extrapolation procedure proposed by Angeli et al. [31]. In the present work, six thresholds between 99.9% and 99.4% were used. The zero-order wave-functions are the result of the previous CI matrix diagonalisation step. The theoretical dipolar electric intensities are obtained by evaluating the corresponding oscillator strengths (in the length gauge):

$$f_L = \frac{2}{3}\omega|\langle \Psi_{CI}|\mathbf{r}|\Psi_0\rangle|^2$$

where ω is the transition energy, $\mathbf{r}$ is the electric dipole transition moment, both in atomic units. Ψ_{CI} and Ψ_0 are the excited and ground state wave functions, respectively. For these calculations, the full CI wave-functions are used (no extrapolation as for the energy calculations). Moreover, the f_L values were refined by a first-order perturbation calculation, at the expense of a much larger computational time.

Since in C_3H_6, there are three equivalent carbon atoms, the core holes may be represented using a localised or delocalised picture. This question has been the subject of many previous works, for example in ethylene [32]. Schulte and Cederbaum [33] have compared the two representations for the π^* core states of $C_3H_3^+$ and $B_3N_3H_6$, who belong to the same symmetry group D_{3h} as C_3H_6. They showed that the delocalised picture gives core energies in very good agreement with the prediction of the simpler localised model. Moreover, it is well known that localised MOs give better core energies [34]. Thus, in the present work, core hole localisation has been assumed and the coupling between excitations from different core holes has been neglected. Therefore, the molecular symmetry has been reduced from D_{3h} to C_{2v}. According to the selection rules for this latter group, all electronic transitions are optically allowed except $1sC \rightarrow a_2$ ones. The gaussian atomic orbitals (AOs) used is the TZ2P basis set taken from Dunning [35]. For the calculation of the core-excited states, a set of Rydberg orbitals (5s, 5p, 3d) was added at the centre of the molecule. The exponents of the first diffuse AOs are taken from Dunning and Hay [36] and the other ones are obtained in an "even-tempered" manner. In the following, the core-excited atom will be referred as C_e while the extended basis set will be designated as TZ2P + R.

Then, in order to interpret the vibrational structure of the spectral bands, Franck–Condon factors calculations were carried out, using our local implementation [37] of the method proposed by Cederbaum and Domcke [38]. According to this method, the calculation of the Franck–Condon factors requires the determination of the gradient (κ matrix) and the hessian (γ matrix) of the excitation energy E_{ex}, both calculated at the ground state equilibrium geometry:

$$\kappa_i = 2^{-1/2}\left(\frac{\partial E_{ex}}{\partial Q_i}\right)_0 \quad \gamma_{ij} = \frac{1}{4}\left(\frac{\partial^2 E_{ex}}{\partial Q_i \partial Q_j}\right)_0$$

where the linear coupling constants κ_i are non-zero only for totally symmetric modes and the off diagonal element of the γ matrix are responsible of the mode mixing (Duschinsky rotation).

In the present work, the Duschinsky effect is neglected and only the κ matrix was computed (linear coupling approximation). These calculations, as well as geometry optimisation and harmonic frequencies determination, were performed at the ROHF-GVB level, because the more sophisticated methods widely used when dealing with valence states cannot be employed with core states (see for example [22]). The present calculations include hot bands, as well as combination bands. A gaussian profile was used to generate the vibrational spectrum, using a FWHM of 65 meV corresponding to the experimental resolution of Ref. [18].

The ROHF-GVB energies of the optimised core states were improved at the MP2 level in order to obtain adiabatic excitation energies. It is well known that, in MP2 calculations, there are several possible definitions of the zero-order hamiltonian for open-shell systems (see Ref. [39] for a review). Moreover, MP2 calculations cannot be performed on GVB wave-functions in the GAMESS-US package.

Therefore, the MP2 energies were obtained using the CIPSI program, with the sole Hartree–Fock determinant as zero-order space (this is also the method employed for the calculation of the MP2 core ionisation energy). The energies of the optimised geometries were also calculated at the SDCI level. For core states, these calculations were done using the orbital restricted molecular active space (ORMAS) method proposed by Ivanic [40], with the constraint that the 1s orbital remained singly occupied. Both SDCI and ORMAS calculations were done with the GAMESS-US package [26], using direct diagonalisation. In order to test the validity of the equivalent core (or $Z+1$) model, calculations at the same level (i.e. ROHF, MP2 and SDCI) were performed on the NC_2H_6 molecule, which is the $Z+1$ analogue of C_3H_6 (see also Ref. [22]). The maximum size of the CI matrix in the present work was about 2.5 million determinants and the weight of the Hartree–Fock configurations in the CI wave-functions was at least 0.88. Finally, the calculated energies were then corrected for ZPE using unscaled ROHF harmonic frequencies.

3. Results and discussion

The HF electronic configuration of the $\widetilde{X}\,{}^1A_1'$ neutral ground state of cyclopropane is:

$$1a_1'^2\,1e'^4\,2a_1'^2\,2e'^4\,1a_2''^2\,3a_1'^2\,1e''^4\,3e'^4$$

Table 1
Symmetries and energies[a] of cyclopropane MOs

D_{3h}	C_{2v}	ε_i (eV)[a]	
$1a_1'^2$	$1a_1^2$	−305.29	C1s
$1e'^4$	$2a_1^2+1b_1^2$	−305.27	C1s
$2a_1'^2$	$3a_1^2$	−30.91	σ_{CC}
$2e'^4$	$4a_1^2+2b_1^2$	−22.32	σ_{CC}
$1a_2''^2$	$1b_2^2$	−18.27	π_{CH_2}
$3a_1'^2$	$4a_1^2$	−17.17	σ_{CH_2}
$1e''^4$	$1a_2^2+2b_2^2$	−13.98	π_{CH_2}
$3e'^4$	$5a_1^2+3b_1^2$	−11.44	σ_{CH_2}
$4a_1'^0$	$6a_1^0$	4.39	$\sigma^*_{CH_2}$
$4e'^0$	$7a_1^0+4b_1^0$	4.81	$\sigma^*_{CH_2}\sigma^*_{CC}$
$2a_2''^0$	$3b_2^0$	5.05	$\pi^*_{CH_2}$
$1a_2'^0$	$5b_1^0$	7.21	σ^*_{CC}
$2e''^0$	$2a_2^0+4b_2^0$	7.35	$\pi^*_{CH_2}$
$5e'^0$	$8a_1^0+6b_1^0$	7.88	$\sigma^*_{CC}\sigma^*_{CH_2}$

[a] TZ2P/HF geometry.

The symmetry of the occupied and anti-bonding MOs in both D_{3h} and C_{2v} groups are given in Table 1, together with their qualitative shape and their mono-electronic energies. The calculated geometries of the ground state of cyclopropane, obtained at the HF and MP2 levels, are compared with previous experimental [3,4] and theoretical [2] values in Table 2. Since the MP2 values are in good agreement with the experimental ones, all the calculations were carried out at this geometry to obtain the vertical excitation energies.

The energies of the observed features in the C1s spectrum of cyclopropane and the assignments proposed by Sze and Brion [18] are presented in Table 3. The pre-edge

Table 3
Energies, term values and suggested assignments of the bands observed in the K-shell spectrum of cyclopropane from Ref. [18]

Band	E (eV)	TV (eV)	Assignment
1	287.09	3.59	$3s/4a_1'$
2	287.23	3.45	
3	287.33	3.35	
4	287.64	3.04	$3p/2a_2''$
5	287.82	2.86	
6	287.96	2.72	
7	288.10	2.58	
8	288.69	1.99	3d
9	288.78	1.90	
10	288.97	1.71	$1a_2'$
11	289.06	1.62	4s
12	289.18	1.50	
13	289.30	1.38	4p
14	289.57	1.11	4d
15	289.69	0.99	
16	289.97	0.71	5p
17	290.14	0.54	6p
18	290.34	0.34	7p
Ion	290.68[a]	0.00	
19	292.8	−2.1	4e′
20	294.7	−4.0	2e″
21	299.2	−8.5	5e′

[a] From Ref. [42].

Table 2
Calculated geometry of cyclopropane compared with previous works (bond lengths in Å and bond angles in degrees)

	HF[a]	MP2[a]	CCSD(T)[b]	Exp. (r_e)[b]	Exp. (r_e)[c]	Exp. (r_e)[d]
	TZ2P	TZ2P	cc-pVQZ			MW
r(C–C)	1.4971	1.5084	1.5019	1.5030(10)	1.5034(3)	1.5101(23)
r(C–H)	1.0731	1.0785	1.0781	1.0786(10)	1.0775(5)	1.0742(29)
HCH	118.00	117.62	114.81	114.97(10)	115.09(10)	115.85(33)

[a] This work.
[b] Ref. [2].
[c] Ref. [3].
[d] Ref. [4].

part of the measured spectrum is shown in Fig. 1. It is composed of two main bands, showing many not well resolved features. The first band, located between 287.0 and 288.5 eV, was assigned by Sze and Brion [18] to the $1s \rightarrow 3s\sigma/4a_1'$ and $1s \rightarrow 3p\pi/2a_2''$ Rydberg-valence transitions, with vibrational excitation. The next intense band, whose maximum occurs at 288.97 eV, was assigned to a $1a_2'$ "giant resonance" [41]. Unresolved weak features on both side of this band were assigned to Rydberg transitions, based on their term values [18]. Table 3 also reports the C1s core ionisation potential (IP) of 290.68 eV, obtained via XPS measurements [42]. Finally, above the ionisation threshold (not shown in Fig. 1), three broad structures were identified and assigned to shape resonances (Table 3).

3.1. Electronic transitions

The results of the present *ab initio* calculations are shown in Table 4. The predicted core ionisation energy of 290.74 eV, obtained at the ΔMP2 level, is in very good agreement with the experimental one at 290.68 eV. The theoretical purely electronic spectrum is compared graphically with the experimental one of [18] in Fig. 1. From this figure, it appears that the two methods employed for the calculations of intensities give very similar results for most transitions, despite the fact that the perturbative calculations have a much larger computational cost. The main exception concerns the intensity ratio of the two first transitions, which is 25% for the perturbed intensities f_L^p and about 50% without perturbation (f_L^u values). Other discrepancies appear for high-lying Rydberg ($n = 6, 7$) states where the perturbed calculations predict much larger intensities than the unperturbed ones. This figure also shows that some calculated transition energies are slightly overestimated when compared to experiment, but these discrepancies may be due to vibronic effects as discussed below.

The present calculations confirm the proposed assignments for the first band (Table 4): the $1s \rightarrow 3s\sigma/\sigma^*(C_eH_2)(4a_1')$ transition is predicted to occur at 287.24 eV (TV = 3.50 eV), while the $1s \rightarrow 3p\pi/\pi^*(C_eH_2)$-$(2a_2'')$ one is calculated at 287.71 eV (TV = 3.03 eV). The relatively high intensities of these two transitions come from their important valence character, due to a mixing with anti-bonding C_eH_2 MOs. This valence character is reflected not only in the intensities of the transitions but also in the low values of the $\langle r^2 \rangle$ operator (about 90 a.u.^{2} for both wave functions). By contrast, the two other 3pσ transitions, calculated in the same energy range at 287.95 and 288.01 eV, are purely Rydberg and consequently have negligible intensities, as well as slightly higher $\langle r^2 \rangle$ values (100 a.u.^{2}).

The two next features identified in the experimental spectrum by Sze and Brion [18] are located in the low energy tail of the main band at 288.69 and 288.78 eV (Table 3) and assigned to 3d transitions. This is confirmed by the present calculations (Table 4) since the five 3d states are calculated at slightly larger energies (between 288.73 and 289.09 eV). At least two of these transitions (at 289.02 and 289.07 eV, TV = 1.72 and 1.67 eV) have predicted intensities (about 5% of the most intense transition) large enough to explain the observed features. However, the calculations also predict the 4s and 4p Rydberg transitions to also occur in the leading edge of this band. These transitions have small intensities, except for the 4pπ one, predicted to occur at 289.22 eV (TV = 1.51 eV), which is as intense (≈6%) as some 3d transitions. We have already encountered rather intense Rydberg $n = 4$ transitions in our study of the K-shell spectra of 2,5-dihydrofuran [43] : for one of the two non-equivalent C atoms, the presence of H atoms out of the ring plane leads to Rydberg-valence

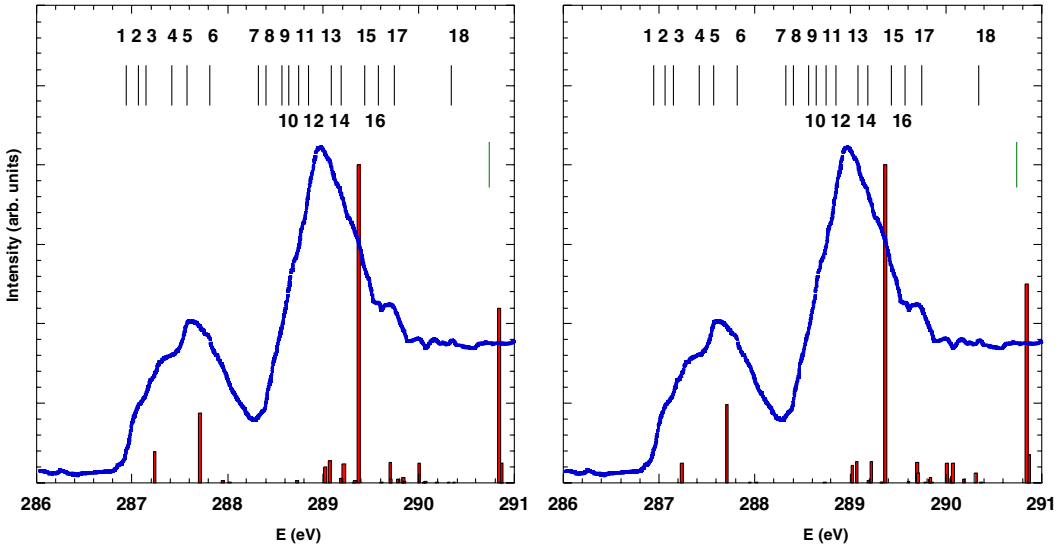

Fig. 1. Comparison between the experimental and the theoretical C1s spectra of cyclopropane (left: unperturbed intensities, right: perturbed intensities). The numbered vertical line indicate the location of the features given in Table 3. The position of the ionisation threshold is also shown.

Table 4
Calculated C1s core excitation energies (eV) and intensities of cyclopropane

State	E (eV)	TV	f_L^{u}[a]	f_L^{p}[a]	Main	Configurations	$\langle r^2 \rangle$
A_1	287.24	3.50	0.096	0.060	0.97	$1s \rightarrow 3s\sigma/\sigma^*(C_eH_2)(4a_1')$	88
B_2	287.71	3.03	0.219	0.244	0.97	$1s \rightarrow 3p\pi/\pi^*(C_eH_2)(2a_2'')$	92
A_1	287.95	2.79	0.006	0.002	0.97	$1s \rightarrow 3p\sigma$	103
B_1	288.01	2.73	<0.001	0.001	0.97	$1s \rightarrow 3p\sigma$	105
A_1	288.73	2.01	0.008	0.001	0.97	$1s \rightarrow 3d\sigma$	150
B_2	289.02	1.72	0.049	0.055	0.98	$1s \rightarrow 3d\pi$	173
A_1	289.07	1.67	0.024	0.021	0.98	$1s \rightarrow 3d\sigma$	183
B_1	289.07	1.67	0.045	0.046	0.98	$1s \rightarrow 3d\sigma$	182
A_2	289.09	1.65	0.000[b]	0.000[b]	0.99	$1s \rightarrow 3d\pi$	189
A_1	289.19	1.55	0.013	0.008	0.98	$1s \rightarrow 4s\sigma$	315
B_2	289.22	1.51	0.059	0.066	0.98	$1s \rightarrow 4p\pi$	310
B_1	289.32	1.42	0.003	0.002	0.97	$1s \rightarrow 4p\sigma$	333
A_1	289.33	1.41	0.006	0.003	0.97	$1s \rightarrow 4p\sigma$	375
B_1	289.37	1.37	1.000[c]	1.000[c]	0.84	$1s \rightarrow \sigma^*(CC)(1a_2', 5b_1)$	292
					+0.08	$1s \rightarrow 4d\sigma$	
A_1	289.61	1.13	0.003	0.004	0.98	$1s \rightarrow 4d\sigma$	651
B_2	289.70	1.04	0.011	0.012	0.98	$1s \rightarrow 4d\pi$	606
B_1	289.70	1.04	0.052	0.052	0.98	$1s \rightarrow 4d\sigma$	597
A_1	289.71	1.03	0.011	0.031	0.98	$1s \rightarrow 4d\sigma$	608
A_2	289.71	1.03	0.000[b]	0.000[b]	0.99	$1s \rightarrow 4d\pi$	606
A_1	289.78	0.96	0.012	0.002	0.94	$1s \rightarrow 5s\sigma$	923
B_2	289.83	0.90	0.011	0.012	0.98	$1s \rightarrow 5p\pi$	1410
B_1	289.84	0.90	0.015	0.015	0.96	$1s \rightarrow 5p\sigma$	1378
A_1	289.85	0.89	0.005	<0.001	0.93	$1s \rightarrow 5p\sigma$	1213
B_1	290.01	0.72	0.060	0.061	0.91	$1s \rightarrow 5d\pi$	2620
A_1	290.05	0.69	<0.001	0.013	0.98	$1s \rightarrow 5d\sigma$	2988
B_2	290.05	0.68	0.001	0.001	0.99	$1s \rightarrow 5d\sigma$	2832
A_2	290.05	0.68	0.000[b]	0.000[b]	0.99	$1s \rightarrow 5d\pi$	2827
A_1	290.06	0.68	0.001	0.017	0.98	$1s \rightarrow 5d\sigma$	2848
A_1	290.07	0.67	0.005	0.060	0.98	$1s \rightarrow 6s\sigma$	3393
A_1	290.19	0.55	<0.001	0.009	0.99	$1s \rightarrow 6p\sigma$	7395
B_2	290.19	0.55	0.001	0.001	0.99	$1s \rightarrow 6p\pi$	7398
B_1	290.19	0.55	0.001	0.001	0.99	$1s \rightarrow 6p\sigma$	7399
A_1	290.31	0.43	<0.001	0.031	0.99	$1s \rightarrow 7s\sigma$	>10,000
A_1	290.37	0.37	<0.001	<0.001	0.99	$1s \rightarrow 7p\sigma$	>10,000
B_2	290.37	0.36	<0.001	<0.001	0.99	$1s \rightarrow 7p\pi$	>10,000
B_1	290.37	0.36	<0.001	<0.001	0.99	$1s \rightarrow 7p\sigma$	>10,000
	290.74[d]					Ion	
B_2	290.84	−0.10	0.549	0.625	0.95	$1s \rightarrow \pi^*(C_eH_2)$	144
A_1	290.87	−0.13	0.061	0.089	0.95	$1s \rightarrow \sigma^*(C_eH_2)$	181
A_1	291.89	−1.15	0.097	0.043	0.77	$1s \rightarrow \sigma^*$	123
					+0.19	$1s \rightarrow \sigma^*$	
B_2	292.17	−1.43	0.239	0.292	0.97	$1s \rightarrow \pi^*(CH_2)$	84
B_1	292.24	−1.50	0.014	0.028	0.95	$1s \rightarrow \sigma^*$	131
B_1	292.67	−1.93	0.047	0.053	0.96	$1s \rightarrow \sigma^*(CH_2)$	73
A_2	292.82	−2.09	0.000[b]	0.000[b]	0.98	$1s \rightarrow \pi^*(CH_2)$	76

[a] Relative oscillator strength to the most intense peak. f_L^{u}: unperturbed calculations, f_L^{p}: first-order perturbed calculations (see text).
[b] Forbidden dipole electric transition.
[c] Absolute calculated oscillator strengths $f = 0.0202$ (unperturbed), $f = 0.0239$ (perturbed).
[d] ΔMP2/TZ2P + R//MP2/TZ2P level.

mixing, not only for the 3s and 3p transitions but also for the 4s and 4p ones. On the other hand, for the second C atom, the hydrogens lie in the ring plane and the $n = 4$ transitions have very low intensities. Similarly, in the furan case [44], these transitions are weak for both carbon atoms. The same qualitative explanation holds for the intensity of the 4pπ transition in C_3H_6, as well as the 4dσ and 5dπ predicted to occur at 289.70 and 290.01 eV (Table 4).

The $1s \rightarrow \sigma^*(CC)(1a_2', 5b_1)$ transition is calculated to occur at 289.37 eV (TV = 1.37 eV), i.e. 0.40 eV above the maximum of the observed band, and has the highest intensity ($f_L \approx 0.02$). As pointed out by Sze and Brion [18], this band may be related to the "giant resonance" discussed by Robin [41] in the C_3H_6 valence absorption spectrum: the cross section shows an extremely intense ($f = 0.7$) band around 82,000 cm^{-1} (10.2 eV), assigned to the $3e'$(d-type) $\rightarrow 1a_2'$(f-type) transition. Similarly, this transition is connected to the resonance observed by Allan [45,46] at 5.5 eV, when studying the vibrational excitation of cyclopropane by low-energy electrons: the analysis of

the angular dependence led to assign unambiguously this resonance to a f-type orbital involving the carbon atoms, i.e. the $1a_2'$ MO, a prediction confirmed by calculations [47].

Above the maximum of this band, Sze and Brion [18] have assigned the not well resolved features as Rydberg transitions, based on their term values (Table 3). The present calculations shown in Table 4 are globally in agreement with the proposed assignments, although it is difficult to be precise. This is especially true for the $n = 4$ Rydberg states, which are quasi-degenerate with the $1s \rightarrow 1a_2'$ transition. Because of the CC anti-bonding character of this orbital, it seems possible that some of the observed features are due to vibrational excitation (see following section).

At higher energies, the Rydberg transitions converge to the continuum onset corresponding to the ionisation energy, calculated at 290.74 eV. The calculated term values of Table 4 are consistent with the assignments of Table 3. A simple way to test the accuracy of the calculated Rydberg transition is to perform a quantum defect analysis using the well-known Rydberg formula:

$$E(1s \rightarrow n\ell) = E(1s \rightarrow \infty) - R/(n - \delta_\ell)^2$$

where R is the Rydberg constant, n is the principal quantum number and δ_ℓ the quantum defect. Table 6 shows the results of a fitting procedure using the calculated values of Table 5. For s and p transitions, the fitted IPs (located between 290.65 and 290.67 eV) are remarkably close to the experimental value of 290.68 eV. For d transitions except the first a_1 one, the calculated IPs are slightly (≈0.1 eV) below the experiment. The s and p δ_ℓ values are also close to those proposed for valence transitions [13].

The calculations also predict that two quasi-degenerate and intense $1s \rightarrow \pi^*(C_eH_2)$ and $\sigma^*(C_eH_2)$ transitions occur at this energy (Table 4). They do not seem to correspond to any observable feature in the spectrum, probably because they are masked by the continuum. Finally, the last calculated transitions shown at the end of Table 4 should not be considered as accurate since our theoretical model does not take into account the effect of the ionisation continuum. However, it should be kept in mind that the assignments [18] of the three band observed at 292.8, 294.7 and 299.2 eV as "shape resonances" has been questioned by Piancastelli [48].

Table 5
Quantum defect analysis

	δ_ℓ	IP	δ_ℓ[a]
ns(a_1)	1.00	290.66	0.9
np(a_1)	0.77	290.67	0.73
np(b_1)	0.74	290.65	
np(b_2)	0.87	290.67	0.65
nd(a_1)	0.35	290.66	
nd(b_1)	−0.04	290.54	
nd(b_2)	0.03	290.56	
nd(a_2)	−0.02	290.57	
nd(a_1)	0.01	290.59	

[a] Valence values from Ref. [13].

3.2. Vibrational structure

Examination of Fig. 1 shows that some of the fine features observed in the experimental spectrum cannot be assigned to pure electronic transitions, especially for the first main band. Since the vibrational structure is not resolved, the linear coupling approximation should be sufficient to obtain some insight in vibration spectrum. However, since the calculations can only be performed at the ROHG-GVB level, only a limited number of transitions were considered. For the first band, the $1s \rightarrow 3s\sigma/\sigma^*(C_eH_2)(4a_1')$ and $1s \rightarrow 3p\pi/\pi^*(C_eH_2)(2a_2'')$ states were kept, the two other 3p transitions having negligible intensities. For the description of the main band, only the $1s \rightarrow 3d\pi(a_2)$ and $1s \rightarrow \sigma^*(CC)(1a_2', 5b_1)$ states were explicitly calculated. The core ion was also considered for comparison.

In Table 6, the calculated ground state harmonic frequencies are compared to the experimental values [49]. As usual, the HF values are about 10% too large while the MP2 results are in better agreement with experiment. However, since the experimental resolution of the ISEELS spectrum is 65 meV (524 cm^{-1}), the use of the HF results will have no effect on the calculated spectrum. In Table 7 are given the elements of the κ matrix for the states considered. It should be kept in mind that in the linear coupling approximation, only totally symmetric vibration modes

Table 6
Calculated harmonic frequencies (cm^{-1}) of the cyclopropane ground state compared with experiment

	Number	Mode	HF[a]	MP2[a]	Exp.[b]
a_1'	ν_1	CH_2 s-stretch	3279	3172	3038
a_1'	ν_2	CH_2 scissor	1653	1542	1479
a_1'	ν_3	Ring stretch	1276	1204	1188
a_1''	ν_4	CH_2 twist	1253	1161	1126
a_2'	ν_5	CH_2 wag	1209	1088	1070
a_2''	ν_6	CH_2 a-stretch	3362	3272	3103
a_2''	ν_7	CH_2 rock	915	876	854
e′	ν_8	CH_2 s-stretch	3265	3161	3025
e′	ν_9	CH_2 scissor	1595	1494	1438
e′	ν_{10}	CH_2 wag	1167	1058	1029
e′	ν_{11}	Ring deform	937	886	866
e″	ν_{12}	CH_2 a-stretch	3338	3250	3082
e″	ν_{13}	CH_2 twist	1314	1217	1188
e″	ν_{14}	CH_2 rock	796	753	739

[a] This work, TZ2P basis set.
[b] Ref. [49].

Table 7
Vibronic coupling constants κ_i (eV/bohr) of core states of cyclopropane

	ν_1	ν_2	ν_3	ν_8	ν_9	ν_{10}	ν_{11}
3sσ(a_1)	0.115	0.003	0.084	0.146	0.057	0.123	0.012
3pπ(b_2)	−0.102	0.014	0.106	−0.163	0.043	−0.127	−0.008
3dπ(a_2)	−0.520	−0.231	−0.417	0.287	−0.125	0.048	−0.093
Ion	−0.520	−0.231	−0.417	0.287	−0.125	0.048	−0.093
$1a_2'(5b_1)$	−0.236	−0.122	−0.186	0.215	−0.040	0.080	−0.042

have non-zero κ values (in the C_{2v} group of the core-excited molecule, corresponding to a_1' and e' in the ground state D_{3h} symmetry). For all states, there are large values, corresponding mostly to CH_2 vibrations. This is not surprising since upon core excitation, the C_e–H bond length is largely reduced (see following section). Another striking feature is the fact that there is no difference between the $3d\pi(a_2)$ and the ion κ values. Therefore, for pure Rydberg states, using the κ matrix of the ion would be a very good approximation.

Fig. 2a–d shows the simulated vibrational structure of the four considered bands, using a FWHM of 65 meV. The three first bands corresponding to $3s\sigma$, $3p\pi$ and $3d\pi$, exhibit similar patterns, due to their common Rydberg character. The most intense peaks are due to ν_{10} (CH_2 wag), ν_3 (ring stretch) and ν_8 (CH_2 symmetric stretch) modes. The situation is somewhat different for the fourth band (Fig. 2d) corresponding to the $\sigma^*(CC)$ excitation, where the ν_3 mode is predominantly excited. The vibrational excitation appears to be more important for this state than for the Rydberg ones. Moreover, Fig. 2d can be compared to the electron impact vibrational excitation of the 5.5 eV resonance found by Allan [45,46] and assigned to the temporary occupation of the a_2'' MO (compare Fig. 2d to Fig. 5 in [46]). It appears that there is at least a qualitative resemblance between the present calculations and Allan's experiments, with a similar excitation of the vibrational modes. On the other hand, for the second resonance at 2.6 eV and assigned by Allan to the $2a_2''$ MO, the agreement between Fig. 2b and Fig. 5 in [46] seems to be worse. These discrepancies are mainly due to the fact that the core orbitals remain fully occupied in Allan's low energy loss spectra while the present calculations explicitly consider a core hole.

Using the results shown in Fig. 2, it is possible to reconstitute the vibrational structure of the whole ISEELS spec-

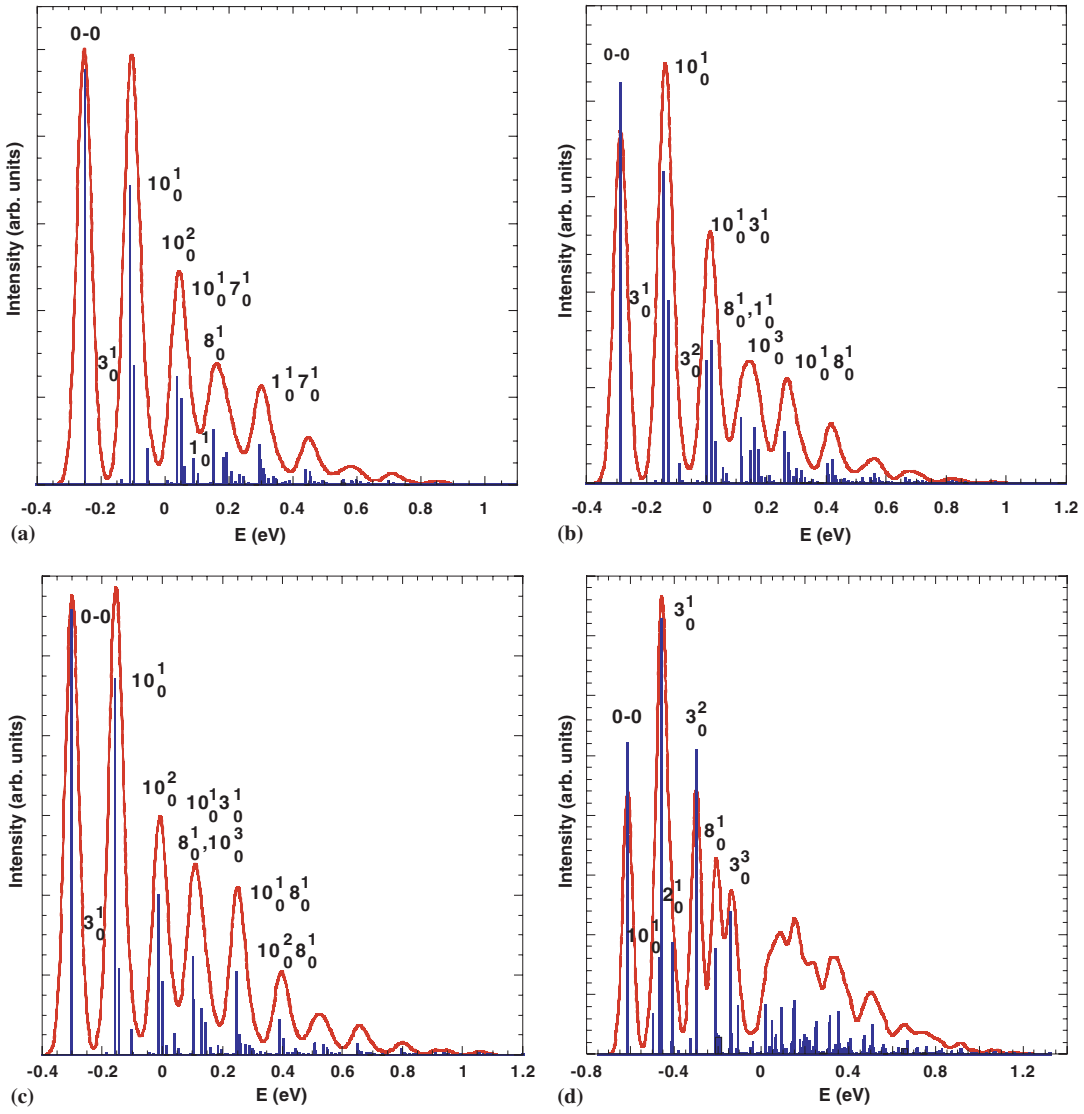

Fig. 2. Calculated vibrational structure of the four main electronic bands (FWHM = 0.065 eV): (a) $3s\sigma/\sigma^*(C_eH_2)$; (b) $3p\pi/\pi^*(C_eH_2)$; (c) $3d\pi a_2$; (d) $\sigma^*(CC)(1a_2', 5b_1)$.

trum. In Fig. 3a, the three explicitly calculated bands are shown with the measured spectrum, using their respective calculated vertical energies and unperturbed intensities (Table 3). Then, the $3d\pi(a_2)$ values were used for the simulation of the 4s, 4p, 4d, 5s, 5p and 5d Rydberg bands (higher Rydberg states have negligible contributions). Fig. 3b shows the sum of all these bands compared to the experiment. Considering the approximations made, the agreement between calculated and experimental spectra is quite satisfactory, since the overall shape of the experimental spectrum is rather well reproduced. The main discrepancies concern the first observed band, because the intensity ratio of the $3s\sigma/3p\pi$ transitions is probably too low. For the most intense observed band, the low energy tail is not well reproduced, perhaps because the 3d transition energies are slightly overestimated. The intensity ratio between this band and the $3p\pi$ band is also correctly reproduced. Moreover, the difference between the calculated σ^*(CC) transition energy (289.37 eV) and the measured one (288.97 eV) is now compensated by the large shift between the 0–0 peak and the vertical excitation value (Fig. 2d). The not well resolved features around this maximum are due to both vibrational excitation of the σ^*(CC) transition and pure Rydberg transitions.

It is now possible to discuss the assignments proposed in Table 3 for the not well resolved features of the spectrum. The two first located at 287.09 and 287.23 eV match perfectly the two first vibrational peaks of the $3s\sigma$ band of Fig. 2a, since $\nu_{10} = 0.14$ eV. On the other hand, the third peak seems too weak to explain feature **3** found at 287.33 eV. In that case, feature **3**, together with features **4**–**7** would be assigned to the $3p\pi$ transition, despite the fact that the **3**–**4** spacing of 0.31 eV is not consistent with ν_{10}. On the other hand, the **4**–**7** spacings (0.18 and 0.14 eV) are in agreement with the excitation of the ν_{10} mode displayed in Fig. 2b.

For the most intense band, it is difficult to tell if the fine features **8**–**18** are due to Rydberg peaks or vibrational excitation or both. For example, the shoulder which can be seen below 290 eV is due to vibrational excitation of the σ^*(CC) transition together with high intensity Rydberg bands. Therefore it does not seem possible to confirm precisely the assignments proposed.

3.3. Geometry of core excited cyclopropane

From the results of the previous section, the important vibrational excitation of the $1s \rightarrow \sigma^*$(CC) state indicates that its equilibrium geometry should be very different from the ground state. In contrast, the three other calculated Rydberg states, which show weaker vibrational excitation, should have geometries close to the ground state, except for the C_e–H bond lengths: by removing one 1s carbon electron, the C_e atom behaves as a nitrogen atom, as stated by the well-known "Equivalent Core" or $Z+1$ model. Consequently, the geometries of the core-excited states of cyclopropane should be similar to the corresponding valence states of NC_2H_6.

This is confirmed by the ROHF optimised geometries of both species shown in Table 8. The calculations of harmonic frequencies (not shown here), proved that all the reported geometries correspond to minima of the potential energy surfaces. For all core-excited states of cyclopropane, the $r(C_e$–H) ranges from 1.0142 to 1.0225 Å to be compared to the ground state value of 1.0731 Å (Table 2). The HC_eH angles are also reduced by a few degrees. For the three considered Rydberg states and for the core ion, the carbon ring is only slightly distorted from the equilateral equilibrium, the CCC angles remaining close to 60°. The situation is completely different for the $1s \rightarrow \sigma^*$(CC) state which exhibits a large opening of the carbon ring, similar to that obtained for the first valence excited state of

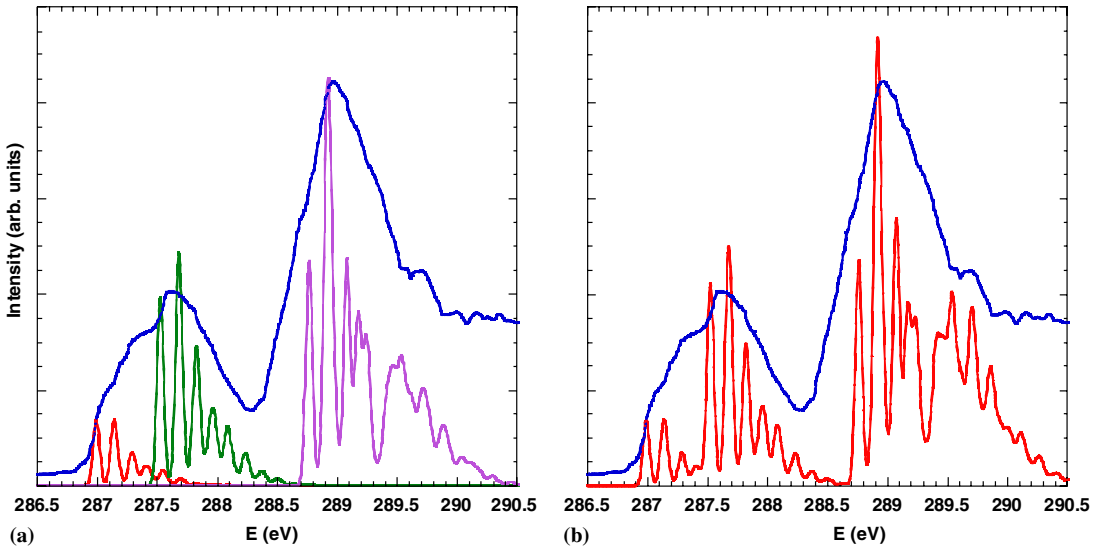

Fig. 3. Comparison of the experimental spectrum with vibrational calculations, using theoretical electronic transitions energies and oscillator strengths: (a) individual electronic bands; (b) total spectrum.

Table 8
Calculated geometry of core-excited states (ROHF-GVB) of cyclopropane and NC_2H_6 (ROHF) (bond lengths in Å and bond angles in degrees)

		r(C–C)	r(C–X)[a]	r(C–H)	r(X–H)[a]	CXC[a]	CCX[a]	HCH	HXH[a]
C_3H_6	$3s\sigma/\sigma^*(C_eH_2)$	1.4621	1.4804	1.0700	1.0225	59.19	60.41	116.48	112.17
	$3p\pi/\pi^*(C_eH_2)$	1.4537	1.4786	1.0733	1.0222	58.89	60.56	116.98	114.33
	$3d\pi(a_2)$	1.4586	1.4952	1.0704	1.0158	58.39	60.81	116.38	113.55
	Ion	1.4569	1.4971	1.0707	1.0158	58.23	60.89	116.25	113.35
	$\sigma^*(CC)(1a_2', 5b_1)$	2.3949	1.4724	1.0740	1.0142	108.83	35.59	116.28	106.26
C_3H_6[b]	$\sigma^*(CC)(1a_2', 5b_1)$	2.506	1.4887	1.088	1.098	114.28	22.9	118.2	102.3
NC_2H_6	$3s\sigma/\sigma^*(NH_2)$	1.4637	1.4722	1.0699	1.0123	59.62	60.19	116.51	112.54
	$3p\pi/\pi^*(NH_2)$	1.4561	1.4676	1.0732	1.0066	59.48	60.26	117.12	114.86
	$3d\pi(a_2)$	1.4609	1.4854	1.0705	0.9994	58.91	60.54	116.50	114.13
	Ion	1.4593	1.4872	1.0708	0.9994	58.76	60.62	116.37	113.91
	$\sigma^*(CC)$ $(5b_1)$	2.3885	1.4677	1.0754	0.9991	108.91	35.54	115.39	106.29

[a] X represents C_e for C_3H_6 and N for NC_2H_6.
[b] Calculated geometry of the first triplet valence excited state of C_3H_6 from [50] (PW91XC/triple dzeta/ADF level).

C_3H_6 by Wang et al. [50], or the geometry of the trimethylene form [9]. However, as shown in Fig. 4, the C_{2v} geometry of this $1s \rightarrow \sigma^*(CC)$ state is rather unusual, because the planes formed by the three methylene groups are perfectly parallel. This is not the case for the valence excited state (compare Fig. 4 to Fig. 2 in [50]) or the trimethylene case [9].

The geometry given in Fig. 4 may also be compared to that suggested by Gadéa et al. [51] in their proposition of an "X-ray induced organic chemistry": using the $Z+1$ model, these authors suggested that upon core excitation, the C_3H_6 molecule would relax to a ring-opened aminoethyl conformation NH_2–CH_2–CH_2. The present calculations show that the N (or C_e) atom would be in a central rather than terminal position. However, it is also possible that the molecule shown in Fig. 4 could undergo an isomerisation to a more stable form, such as a CH_3–C_eH–CH_2 propenic form. We did not try to study this process, which is beyond the scope of the present work, but it should be noted that the cyclopropane–propene isomerisation reaction is complex. The exploration of the potential energy surface [8,9,52,53] has uncovered several minima and saddle points, including trimethylene and propylidene forms [53].

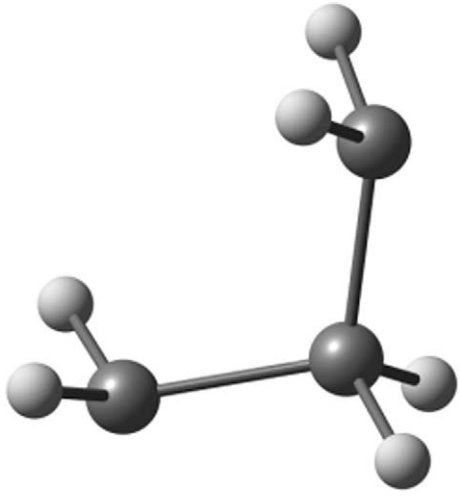

Fig. 4. Calculated ROHF-GVB geometry of $1sC \rightarrow \sigma^*(CC)(1a_2', 5b_1)$ core-excited state of cyclopropane (and corresponding state of NC_2H_6).

In Table 8 are also given the optimised geometries of the NC_2H_6 states. They appear to be very close to their core excited cyclopropane counterparts. This is certainly not surprising for Rydberg states but is true as well for the $\sigma^*(CC)$ state. There are however a few minor quantitative differences, the most important one concerning the N–H bond lengths which are all around 1.0 Å while the C_e–H values are slightly larger.

Table 9 gives the calculated adiabatic energies of the core states of C_3H_6, obtained at ROHF, MP2 and ORMAS levels, while those for NC_2H_6 are given in Table 10. The C_3H_6 MP2 values can be compared to the vertical transition energies of Table 4, but it should be kept in mind that the methods of calculations are slightly different. However, it is clear that for the three Rydberg states and the core ion, the difference between vertical and adiabatic energies are almost negligible, reflecting the weak structural relaxation with respect to the ground state equilibrium geometry. On the other hand, there is a large difference (about 2.4 eV) for the $\sigma^*(CC)$ state. For all states, the energies calculated with the three methods are within a few tenths of an eV, except for the MP2 value of the $\sigma^*(CC)$ state, which seems to be too low.

The calculated core excitation energies in Table 9 cannot be used directly for comparison with the NC_2H_6 case. The only parameters that seem pertinent to do this are the term values (TVs). As can be seen from the three last lines of both Tables 8 and 9, the TVs are similar at HF and MP2 levels, the largest difference being less than 0.4 eV. The differences are larger (up to 1 eV) when comparing ORMAS and SDCI results. Interestingly, the MP2 TV's of the $\sigma^*(CC)$ state of C_3H_6 (−3.80 eV) and its $Z+1$ equivalent in NC_2H_6 (−3.64 eV) seem to be both overestimated when compared to the HF and ORMAS/SDCI values. Thus, one can conclude that the energies and geometries of the valence states of NC_2H_6 are close to those of the "true" core states of cyclopropane, as postulated by the equivalent core model.

Table 9
Calculated adiabatic energies of core excited and ionised states of cyclopropane

	GS	$3s\sigma/\sigma^*(C_eH_2)$	$3p\pi/\pi^*(C_eH_2)$	$3d\pi(a_2)$	$\sigma^*(CC)(1a_2', 5b_1)$	Ion
E_{SCF} (a.u.)	−117.099702	−106.532058	−106.513151	−106.474729	−106.502611	−106.423802
E_{MP2} (a.u.)	−117.623302	−107.066504	−107.047263	−106.998637	−107.076402	−106.947679
E_{ORMAS} (a.u.)	−117.546365	−106.995096	−106.976779	−106.939654	−106.958131	−106.888903
ΔSCF (eV)	0.00	287.56	288.07	289.12	288.36	290.51
ΔMP2 (eV)	0.00	287.27	287.79	289.11	287.00	290.50
ΔORMAS (eV)	0.00	287.11	287.61	288.62	288.12	290.00
ZPE_{SCF} (kcal/mol)	54.0	55.8	56.1	56.8	53.4	56.7
$\Delta SCF + ZPE_{SCF}$ (eV)	0.00	287.64	288.17	289.24	288.34	290.62
$\Delta MP2 + ZPE_{SCF}$ (eV)	0.00	287.34	287.88	289.23	286.97	290.62
$\Delta ORMAS + ZPE_{SCF}$ (eV)	0.00	287.19	287.71	288.74	288.10	290.12
$TV_{SCF} + ZPE_{SCF}$ (eV)		−2.98	−2.46	−1.38	−2.29	0.00
$TV_{MP2} + ZPE_{SCF}$ (eV)		−3.27	−2.73	−1.38	−3.64	0.00
$TV_{ORMAS} + ZPE_{SCF}$ (eV)		−2.93	−2.42	−1.38	−2.03	0.00

Table 10
Calculated adiabatic energies of the NC_2H_6 states

	$3s\sigma/\sigma^*(NH_2)$	$3p\pi/\pi^*(NH_2)$	$3d\pi(a_2)$	$\sigma^*(CC)$ $(5b_1)$	Ion
E_{SCF} (a.u.)	−133.574357	−133.549859	−133.510695	−133.541783	−133.459741
E_{MP2} (a.u.)	−134.133977	−134.104926	−134.054710	−134.104926	−134.136902
E_{SDCI} (a.u.)	−133.923460	−134.021297	−133.975592	−134.031834	−133.923460
TV_{SCF} (eV)	0.00	−3.12	−2.45	−1.39	−2.23
TV_{MP2} (eV)	0.00	−3.59	−2.80	−1.43	−3.67
TV_{SDCI} (eV)	0.00	−3.40	−2.66	−1.42	−2.95
ZPE_{SCF} (kcal/mol)	55.2	56.0	56.6	53.4	56.6
$TV_{SCF} + ZPE_{SCF}$ (eV)	−3.18	−2.48	−1.38	−2.37	0.00
$TV_{MP2} + ZPE_{SCF}$ (eV)	−3.65	−2.82	−1.43	−3.80	0.00
$TV_{SDCI} + ZPE_{SCF}$ (eV)	−3.46	−2.69	−1.42	−3.09	0.00

4. Conclusion

In this work, the inner shell electron energy loss spectrum of gaseous cyclopropane has been interpreted using *ab initio* Configuration Interaction and simple Franck–Condon calculations. Despite the simplicity of the model used, the agreement between the calculated and the experimental spectra is good, especially for the lowest lying bands. At higher energy, the calculations slightly correct the assignments initially proposed by the experimentalists. For all states, including Rydberg ones, taking into account the vibrational excitation appears to be necessary.

However, the main problem is due to the fact that the vibrational structure is not completely resolved in the experiment. In order to improve these results, the use of synchrotron radiation with a resolution lower than 65 meV could provide a better resolved spectrum. Moreover, comparison with the spectrum of the C_3D_6 isotopomer would perhaps allow to distinguish vibrational from purely electronic peaks. In this case, a more refined theoretical model could be needed.

The vibrational excitation observed in the K-shell spectrum is connected to the geometrical relaxation of the molecule upon core excitation. While for the Rydberg and ionic core states, the equilibrium geometry remains close to the ground state one, the $1s \rightarrow \sigma^*(CC)$ has an unusual trimethylenic structure. Finally, comparison with the corresponding states of NC_2H_6 gives similar geometries and energies. In view of the difficulties to study core states geometries at post-Hartree–Fock level [22], these results shows that equivalent core approximation remains useful and can give at least semi-quantitative accuracy.

Acknowledgements

The authors thanks Prof. J. Delwiche (Université de Liège) for his help in the preparation of the manuscript. The PhLAM is ''Unité Mixte de Recherche du CNRS''. The CERLA (FR CNRS 2416) is supported by the ''Ministère chargé de la Recherche'', the ''Région Nord/Pas-de-Calais'' and the ''Fonds Européen de Développement Economique des Régions'' (FEDER). Parts of the computations were carried out at the CRI (Centre de Ressources Informatiques), on the IBM-SP3 computer which is supported by the ''Programme de Calcul Intensif et Parallèle'' of the ''Ministère chargé de la Recherche'', the ''Région Nord/Pas-de-Calais'' and the FEDER. The support of the COST action P9 ''Radiation Damage in Biomolecular Systems'' is acknowledged.

References

[1] P.B. Karadakov, J. Gerratt, D.L. Cooper, M. Raimondi, J. Mol. Struct. (THEOCHEM) 341 (1995) 13.
[2] J. Gauss, D. Cremer, J.F. Stanton, J. Phys. Chem. A 104 (2000) 1319.
[3] D.S. Kummli, H.M. Frey, M. Keller, S. Leutwyler, J. Chem. Phys. 123 (2005) 054308.

[4] Y. Endo, M.C. Chang, E. Hirota, J. Mol. Spectrosc. 126 (1987) 63.
[5] C.C. Wang, Y.T. Lee, J.J. Lin, J. Shu, Y.-Y. Lee, X. Yang, J. Chem. Phys. 117 (2002) 153.
[6] Y. Yamaguchi, H.F. Schaefer III, J.E. Baldwin, Chem. Phys. Lett. 185 (1991) 143.
[7] J.E. Baldwin, T.B. Freedman, Y. Yamaguchi, H.F. Schaefer III, J. Am. Chem. Soc. 118 (1996) 10934.
[8] C. Doubleday, J. Phys. Chem. 100 (1996) 3520.
[9] F. Dubnikova, A. Lifshitz, J. Phys. Chem. A 102 (1998) 3299.
[10] V. Galasso, Chem. Phys. 206 (1996) 289.
[11] W.v. Niessen, M.J. Brunger, E. Weigold, J. Phys. B 27 (1994) 4309.
[12] K. Kameta, K. Muramatsu, S. Machida, N. Kouchi, Y. Hatano, J. Phys. B 32 (1999) 2719.
[13] M. Gingell, N.J. Mason, I.C. Walker, G. Marston, H. Zhao, M.R.F. Siggel, J. Phys. B 32 (1999) 2729.
[14] D.M.P. Holland, L. Karlsson, K. Siegbahn, J. Electron Spectrosc. Relat. Phenom. 125 (2002) 57.
[15] T.S. Venkatesan, S. Mahapatra, L.S. Cederbaum, H. Köppel, J. Phys. Chem. A 108 (2004) 2256.
[16] J. Stöhr, NEXAFS Spectroscopy, Springer, Berlin, 1992.
[17] A.P. Hitchcock, D.C. Newbury, I. Ishii, J. Stohr, J.A. Horsley, R.D. Redwing, A.L. Johnson, F. Sette, J. Chem. Phys. 85 (1986) 4849.
[18] K.H. Sze, C.E. Brion, J. Electron Spectrosc. Relat. Phenom. 57 (1991) 117.
[19] D. Duflot, K. Sidhoum, J.-P. Flament, A. Giuliani, J. Heinesch, M.-J. Hubin-Franskin, Eur. Phys. J. D (2005) 239.
[20] U. Hergenhahn, J. Phys. B 37 (2004) R89.
[21] S. Carniato, R. Taieb, E. Kukk, Y. Luo, B. Brena, J. Chem. Phys. 123 (2005) 214301.
[22] A.B. Trofimov, E.V. Gromov, T.E. Moskovskaya, J. Schirmer, J. Chem. Phys. 113 (2000) 6716.
[23] A.B. Trofimov, T.E. Moskovskaya, E.V. Gromov, H. Köppel, J. Schirmer, Phys. Rev. A 64 (2001) 022504.
[24] S. Shirai, S. Yamamoto, S.-a. Hyodo, J. Chem. Phys. 121 (2004) 7586.
[25] D. Duflot, J.-P. Flament, I.C. Walker, J. Heinesch, M.-J. Hubin-Franskin, J. Chem. Phys. 118 (2003) 1137.
[26] M.W. Schmidt, K.K. Baldridge, J.A. Boatz, S.T. Elbert, M.S. Gordon, J.H. Jensen, S. Koseki, N. Matsunaga, K.A. Nguyen, S. Su, T.L. Windus, M. Dupuis, J.A. Montgomery Jr., J. Comput. Chem. 14 (1993) 1347.
[27] S. Bodeur, P. Millié, I. Nenner, Phys. Rev. A 41 (1990) 252.
[28] S. Carniato, Y. Luo, J. Electron Spectrosc. Relat. Phenom. 142 (2005) 163.
[29] B. Huron, J.P. Malrieu, P. Rancurel, J. Chem. Phys. 58 (1973) 5745.
[30] R. Cimiraglia, J. Chem. Phys. 83 (1985) 1746.
[31] C. Angeli, R. Cimiraglia, M. Persico, A. Toniolo, Theor. Chem. Acc. 98 (1997) 57.
[32] H. Koppel, F.X. Gadéa, G. Klatt, J. Schirmer, L.S. Cederbaum, J. Chem. Phys. 106 (1997) 4415.
[33] H.D. Schulte, L.S. Cederbaum, J. Chem. Phys. 103 (1995) 698.
[34] L.S. Cederbaum, W. Domcke, J. Chem. Phys. 66 (1977) 5084.
[35] T.H. Dunning, J. Chem. Phys. 55 (1971) 716.
[36] T.H. Dunning Jr., P.J. Hay, in: H.F. Schaefer III (Ed.), Methods of Electronic Structure Theory, Plenum Press, New York, 1977, p. 1.
[37] J.-P. Flament: Ph.D. Thesis, Université de Paris-Sud, 1981.
[38] L.S. Cederbaum, W. Domcke, Adv. Chem. Phys. 36 (1977) 59.
[39] T.D. Crawford, H.F. Schaefer III, T.J. Lee, J. Chem. Phys. 105 (1996) 1060.
[40] J. Ivanic, J. Chem. Phys. 119 (2003) 9364.
[41] M.B. Robin, Chem. Phys. Lett. 119 (1985) 33.
[42] W.L. Jolly, K.D. Bomben, C.J. Eyerman, At. Data Nucl. Data Tables 31 (1984) 433.
[43] D. Duflot, J.-P. Flament, A. Giuliani, J. Heinesch, M.-J. Hubin-Franskin, Chem. Phys. 310 (2005) 67.
[44] D. Duflot, J.-P. Flament, A. Giuliani, J. Heinesch, M.-J. Hubin-Franskin, J. Chem. Phys. 119 (2003) 8946.
[45] M. Allan, J. Am. Chem. Soc. 115 (1993) 6418.
[46] M. Allan, L. Andric, J. Chem. Phys. 105 (1996) 3559.
[47] T. Beyer, B.M. Nestmann, B.K. Sarpal, S.D. Peyerimhoff, J. Phys. B 30 (1997) 3431.
[48] M.N. Piancastelli, J. Electron Spectrosc. Relat. Phenom. 100 (1999) 167.
[49] T. Shimanouchi, Tables of Molecular Vibrational Frequencies Consolidated, National Bureau of Standards, 1972.
[50] X. Wang, S. Takami, M. Kubo, A. Miyamoto, Chem. Phys. 279 (2002) 7.
[51] F.X. Gadéa, S. Mathieu, L.S. Cederbaum, J. Mol Struct. (THEOCHEM) 401 (1997) 15.
[52] K.-N. Fan, Z.-H. Li, W.-N. Wang, H.-H. Huang, W. Huang, Chem. Phys. Lett. 277 (1997) 257.
[53] H.F. Bettinger, J.C. Rienstra-Kiracofe, B.C. Hoffman, H.F. Schaefer III, P.v.R. Schleyer, J.E. Baldwin, Chem. Commun. (1999) 1515.

Article 18

International Journal of Mass Spectrometry 277 (2008) 70–78

Contents lists available at ScienceDirect

International Journal of Mass Spectrometry

journal homepage: www.elsevier.com/locate/ijms

Electronic excitation of gaseous acetic acid studied by K-shell electron energy loss spectroscopy and *ab initio* calculations

Denis Duflot[a,*], Jean-Pierre Flament[a], Alexandre Giuliani[b,1], Jacques Heinesch[b], Marie-Jeanne Hubin-Franskin[b,2]

[a] *Laboratoire de Physique des Lasers, Atomes et Molécules (PhLAM), UMR CNRS 8523, Centre d'Études et de Recherches Lasers et Applications (CERLA, FR CNRS 2416), Université des Sciences et Technologies de Lille, F-59655 Villeneuve d'Ascq Cedex, France*

[b] *Université de Liège, Laboratoire de Spectroscopie d'Électrons diffusés, Institut de Chimie B6c, Sart Tilman, B4000 Liège 1, Belgium*

ARTICLE INFO

Article history:
Received 27 March 2008
Received in revised form 7 May 2008
Accepted 7 May 2008
Available online 15 May 2008

Keywords:
Acetic acid
K-shell excitation
Ab initio
Electron excitation

ABSTRACT

Ab initio Configuration Interaction calculations have been carried out in order to assign the bands observed in the carbon and oxygen K-shell spectra of gaseous acetic acid, measured using the inner-shell electron energy loss spectroscopy (ISEELS) method with better energy resolution than in previous studies. The good agreement between the theoretical and the measured spectra allows us to assign precisely most of the peaks, especially for the Rydberg states. Some of them have been shown to have strong valence character. The lowest energy band at the carbon edge is assigned to the transitions $1sC_1 \rightarrow 3p\pi/\sigma^*(C_1–H)$ and $1sC_1 \rightarrow \pi^*(C_2–O_2)$. Simple Franck–Condon calculations, based on the linear coupling approximation, were performed in order to reproduce the vibrational structure observed for the first time in the oxygen and carbon core excited species as well as in the previously measured X-ray photoelectron spectroscopy spectra of the core ionised molecule. Finally, the calculated structural parameters of the core states of acetic acid match well those of the corresponding valence states of their Z + 1 molecules, as predicted by the equivalent core approximation. However, significant differences between the geometry of the $1sC_1 \rightarrow \pi^*(C_2–O_2)$ state and the CH_3NOOH ground state are obtained.

1. Introduction

Acetic acid (CH_3COOH), commonly known as vinegar, is produced in the human body as a result of alcohol oxidation after consumption of alcoholic beverages. It plays an important role in the metabolism processes of most forms of life and results naturally from the action of certain bacteria in foods or liquids containing sugars or ethanol.

Despite the fact that, after formic acid (HCOOH), acetic acid is the simplest organic acid, and is a major component of biological molecules, there are only a very few studies of its electronic states spectroscopy by inner shell excitation . The core ionisation energies have been measured by Naves de Brito et al. [1,2] using XPS methods. To our knowledge core excitation spectra have been reported by only one experimental study previously, namely inner-shell electron energy loss spectroscopy (ISEELS) in gas phase [3]. The energy resolution was about 0.6 eV. More recently, Urquhart and Ade [4] have performed a systematic comparison between measured and *ab initio* C1s,O1s $\rightarrow \pi^*(C_2–O_2)$ transitions energy in a large family of carbonyl compounds, including acetic acid but other transitions were not considered.

In the present work the electronic structure of acetic acid, and much more specifically the unoccupied levels, has been investigated by core shell excitation and *ab initio* calculations. Inner-shell electron energy loss spectroscopy has been used to record the C1s and O1s excitation spectra of acetic acid. The experimental conditions – high electron impact energy and quite small scattering angle – are such that electron energy loss spectra are expected to exhibit the same features with quite similar relative intensities as those of the corresponding ones in photoabsorption.

The goal of the present paper is to present a new ISEELS spectrum of acetic acid recorded with an apparatus resolution of 0.17 eV. In order to help in the assignment of the observed spectral features, *ab initio* calculations using Configuration Interaction (CI) techniques and vibrational analysis have been carried out. This paper is divided into the following sections: Section 2 describes

* Corresponding author. Tel.: +33 3 20 43 49 80; fax: +33 3 20 43 40 84.
E-mail address: denis.duflot@univ-lille1.fr (D. Duflot).

[1] Present address: DISCO Beamline, Synchrotron SOLEIL, BP 48, L'Orme des Merisiers, F-91192 Gif sur Yvette, France, and Cepia, Institut National de la Recherche Agronomique, BP 71627, F-44316 Nantes Cedex 3, France.

[2] Directeur de recherche du FRS-F.N.R.S.

1387-3806/$ – see front matter © 2008 Elsevier B.V. All rights reserved.
doi:10.1016/j.ijms.2008.05.006

the experimental set up; Section 3 deals with the computational method employed; the results are presented and discussed in Section 4 and finally, in Section 5 some conclusions are given.

2. Experimental

The inner-shell electron energy loss spectra were obtained with a Vacuum Science Workshop Ltd. (VSW) spectrometer which has been adapted for gas studies and high energy electron beams and has been equipped with a home-made position sensitive multi-detector system in order to improve data collection times. The experimental apparatus and procedure have been described in detail previously [5–7].

Briefly the spectrometer consists of an electrostatic 180° monochromator operating in the constant pass energy mode, a collision chamber and an electrostatic analyser identical to the monochromator. The monochromatised incident electrons are accelerated up to 2 keV and focused into the collision chamber using a four-element electron lens. The electrons are slightly deflected (0.02 radians) by two sets of *X*–*Y* plates inside the collision chamber. The scattered electrons are energy analysed and focused onto the entrance slit of the analyser by a lens similar to that used for acceleration.

In the collision conditions of low momentum transfer (i.e., high incident energy and small scattering angle), electric-dipolar transitions are primarily excited. Inside the vacuum vessel, a residual pressure of less than 1×10^{-8} mbar is maintained by a cryogenic pumping system. The electron gun and the analyser regions are differentially pumped by turbomolecular pumps respectively. The spectra have been recorded with 0.040 and 0.020 eV steps.

In order to take into account valence and lower energy inner shell excitation cross-section, a linear background has been subtracted from the raw spectra by extrapolating least square fit of the pre-edge experimental data.

The absolute energy scale has been calibrated at both edges relative to CO and the C1s → π* ($\nu' = 0$) band at 287.40 ± 0.02 eV and the O1s → π* transition at 534.21 ± 0.09 eV recording spectra with 0.01 eV steps [8].

The sample of acetic acid was purchased from VEL (Leuven, Belgium) and is quoted as having a minimum purity of 99.8%. It was used directly without further purification except for repetitive freeze–pump–thaw cycles in order to eliminate air and other volatile impurities in the sample.

3. Computational method

The computational method used in the present work is similar to that used in our previous study of the core excitation spectra of acrolein [9] with a few minor differences. The basic assumption is that core ion MO's (obtained at the ROHF-GVB level [10] with the GAMESS-US program [11]), are a better starting point than the ground state MO's for the calculation of the core excitation energies. Formally, these $E(1s \rightarrow i^*)$ core excitation energies may be written with respect to the $E(1s \rightarrow \infty)$ core ion energy in the following manner [12,13]:

$$E(1s \rightarrow i^*) = E(1s \rightarrow \infty) + \varepsilon_{i^*} + P_{i^*} + C_{i^*}$$

where ε_{i^*} is the mono-electronic energy of the i* virtual MO (Koopmans' theorem). The P_{i^*} and C_{i^*} terms represent the residual relaxation and correlation effects of the i* electron with respect to the core ion. In practice, relaxation is taken into account by diagonalisation of a CI matrix. The correlation term C_{i^*} is calculated by a multi-reference MP2 calculation with the three-class diagrammatic CIPSI [14,15] method and using the CI matrix eigenfunctions as zeroth-order wave-functions. In the present work, two types of CI calculations were performed:

(I) a preliminary calculation included all 1s → i* excitations from the core orbital to all virtual MO's. This type of calculations is sometimes called 1h–1p CI [16]. Physically, this means that the electron density of the core state is identical to that of the ion and relaxation is treated perturbatively during the CIPSI step together with correlation.
(II) a larger CI matrix including all mono-excitations with respect to all the 1s → i* core excitations was diagonalized (2h–2p scheme), taking explicitly into account relaxation effects and permitting the description of possible di-excited (shake up) states. In this case, in order to reduce the computational cost of the CIPSI step, the extrapolation procedure proposed by Angeli et al. [17] was employed, with 6 thresholds between 99.9 and 99.4%.

Finally, the theoretical dipolar electric intensities are obtained by evaluating the corresponding oscillator strengths (in the length gauge):

$$f_L = \frac{2}{3}\omega \left| \left\langle \Psi_{CI} \middle| \mathbf{r} \middle| \Psi_0 \right\rangle \right|^2$$

where ω is the transition energy, $\mathbf{r}$ the electric dipole transition moment, both in atomic units. ψ_{CI} and ψ_0 are the CI excited and ground state wave functions, respectively. The Gaussian atomic orbitals (AO's) used are the TZ2P basis set taken from Dunning [18]. The same exponents of the d polarization functions ($\alpha_C = 1.44$, 0.36 and $\alpha_O = 2.56$, 0.64) were used for the Z + 1 (equivalent core) atoms. For core-excited states, a set of Rydberg orbitals (5s, 5p, 3d) was added on the core excited atom. The exponents of the first diffuse AO's are taken from Dunning and Hay [19] and the other ones are obtained in an "even-tempered" manner. In the following, the extended basis set will be designated as TZ2P + R.

Then, in order to simulate the vibrational structure of some of the spectral bands, Franck–Condon factors calculations were carried out, using our local implementation [20,21] of the method proposed by Cederbaum and Domcke [22,23]. In its simplest form (linear coupling approximation), this model describes the potential energy surface of the excited state by the same harmonic oscilla-

Table 1
Core ionisation energies (eV) of acetic acid at the O1s and C1s edges

	C1s			O1s		
	C_1	C_2	Shift	O_1	O_2	Shift
Exp.[a]	291.55	295.38	3.83	540.09	538.29	−1.8
Exp.[b]	291.55(3)	295.35(3)	3.80	540.10(3)	538.31(3)	−1.79
ΔSCF[b]	292.49	296.96	4.47	541.03	538.80	−2.23
ΔSCF (GSCF3)[c]		296.52			537.70	
SA-MCQDPT[d]	288.32	293.02	4.70	532.38	530.31	−2.07
SA-MRMP[d]	288.21	292.36	4.15	530.10	528.98	−1.12
MRMP[d]	291.65	295.90	4.25	540.21	538.69	−1.52
ΔKS[e]	291.51	294.97	3.46	540.24	538.19	−2.05
ΔSCF[f]	292.00	296.39	4.39	540.07	537.87	−2.20
ΔMP2 (RMP)[f]	291.59	295.53	3.94	540.44	538.71	−1.73
ΔMP2 (ZAPT)[f]	291.60	295.55	3.95	540.44	538.71	−1.73
ΔMP2 (CIPSI)[f]	291.45	295.40	3.95	540.35	538.59	−1.76
ΔMP2 (CIPSI) + ZPVE[f]	291.09	295.24	4.15		538.36	

[a] Ref. [32].
[b] Refs. [1,2] (DZP basis set).
[c] Ref. [4].
[d] Ref. [30].
[e] Ref. [31] (Δ(PW86-PW91)/QZ4P//HF/6-31G* result with relativistic correction).
[f] This work. Values calculated at the TZ2P/MP2 optimized geometry using the TZ2P + Rydberg basis set.

tor as the ground state, the only difference being the equilibrium geometry. This model has proven to be satisfactory in the context of inner ionisation and excitation [24–26]. Thus, it is necessary to determine the gradient of the excitation energy E_{ex} at the ground state geometry:

$$\kappa_i = 2^{-1/2}\left(\frac{\partial E_{ex}}{\partial Q_i}\right)_0$$

This κ matrix has non-zero elements only for totally symmetrical modes (a' in the present case). These calculations were performed at the ROHF-GVB level for core states, because the more sophisticated methods widely used when dealing with valence states cannot be employed with core states (see for example Ref. [27]). Similarly, RHF geometry and frequencies were used for the ground state. Anharmonic frequencies were also calculated with the VSCF method [28] on a 40,000 points grid including 3-D couplings, as shown in the supplementary information. However, the anharmonic values could not be used because the Domcke–Cederbaum model is based on harmonic approximation. Therefore, the RHF harmonic frequencies were scaled by a factor of 0.9. The present calculations include hot bands, as well as combination bands, using a temperature of 298 K.

4. Results and discussion

In the following, the four heavy atoms of acetic acid will be labelled as $H_3C_1–C_2{=}O_2–O_1H$. The most stable isomer corresponds to an eclipsed conformation between $C_2{=}O_2$ and one of the $C_1{-}H$ bonds. As shown in the supplementary data, the calculated MP2 geometry are in better agreement with experiment [29] than the HF calculation and therefore, was used to calculate vertical core excitation energies. The electronic configuration is:

$$[1a'^2 2a'^2 3a'^2 4a'^2]5a'^2 6a'^2 7a'^2 8a'^2 9a'^2 10a'^2 1a''^2 11a'^2$$
$$12a'^2 2a''^2 3a''^2 13a'^2$$

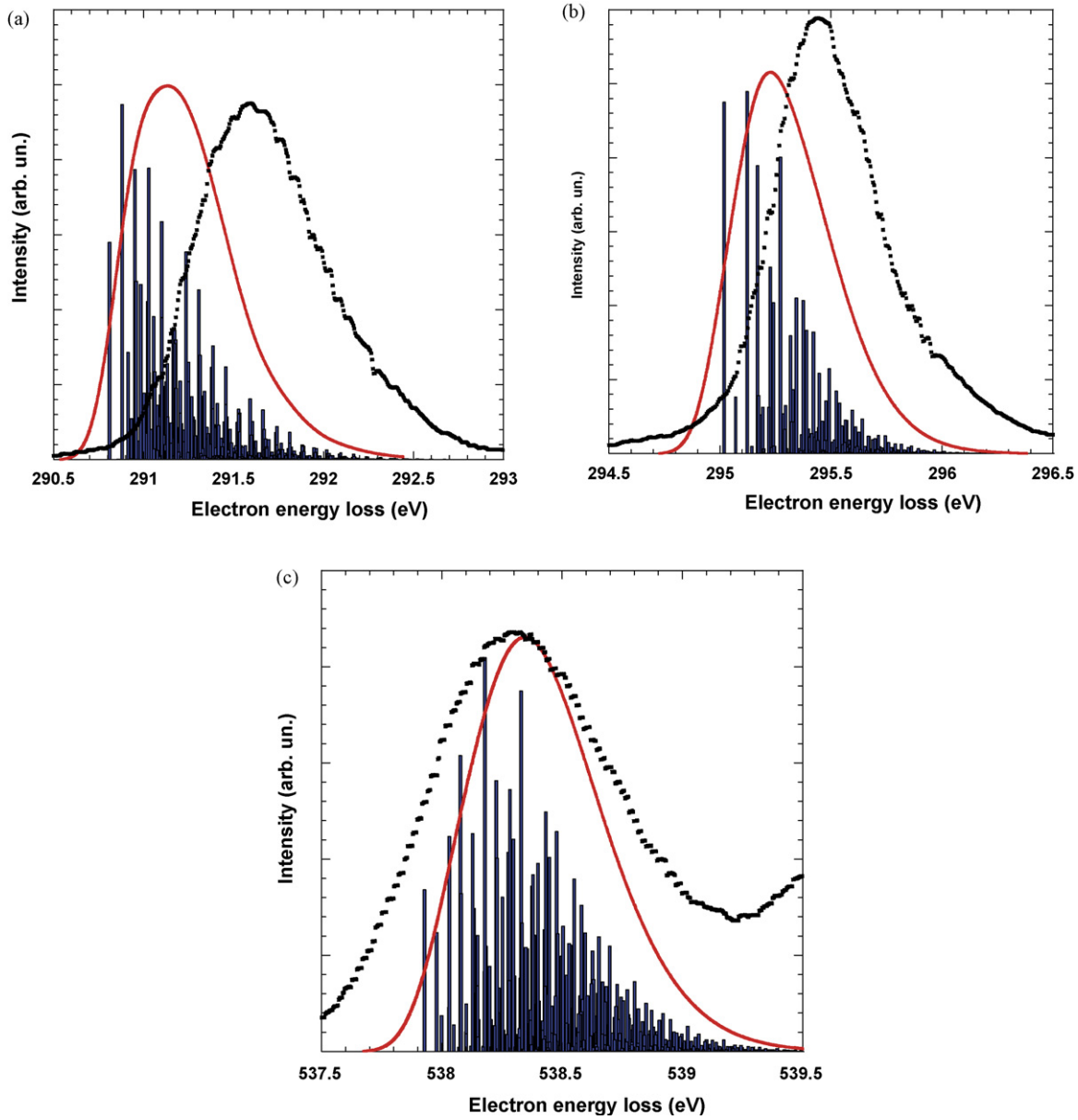

Fig. 1. Comparison of the calculated vibrational structure of the core ions with XPS: (a) C_1, (b) C_2, (c) O_2. Dots: experiment from Ref. [2]; sticks: calculated vibrational transitions; line: total calculated vibration spectrum, using FWHM = 0.25 eV gaussian functions.

where the bracketed MO's correspond to the O_1, O_2, C_2 and C_1 core 1s orbitals, respectively. The HOMO 13a′ is essentially the in-plane O_2 lone pair (the "plane" being defined as $C_1C_2O_1O_2$). The SHOMO 3a″ is the $\pi(C_2–O_2)$ and has an anti-bonding character with the out-of-plane O_1 lone pair. The LUMO corresponds to the $\sigma^*(O_1–H)$ MO, the $\pi^*(C_2–O_2)$ being higher in energy.

4.1. Core ionisation energies

The calculated core ionisation energies are compared with theoretical [2,4,30,31] and experimental [1,32] determinations in Table 1. Since several possible definitions of the zero-order hamiltonian are possible in open-shell MP2 calculations [33], the ΔMP2 values were obtained using three different models: RMP [34,35], ZAPT [36,37], and CIPSI.

Our ΔSCF values are close to the ΔSCF/GSCF3 ones [4]: the C_1 and C_2 energies are too large, while the O_1 values are close to experiment and the O_2 values are too low by ∼1 eV. On the other hand, the ΔSCF values of Naves de Brito et al. [2] are rather different, with a 1.6 eV error for C_2. These authors have discussed in detail the possibility that the zero-point vibrational energy (ZPVE) correction could be responsible of this effect. However, both the present and GSCF3 [4] results suggest basis set effects. At the correlated level, the ΔKS values of Takahata and Chong [31] are in very good agreement with experiment, except for C_2 where the result is too low by ∼0.5 eV. Shirai et al. [30] have shown the complete failure of State-Averaged (SA) multiconfigurational calculations, especially for the oxygen atoms where the calculated values differ by ∼10 eV from experiment.

For the three ΔMP2 methods of the present work, the agreement with experiment is within a few tenths of an eV, especially for carbons. Our mono-reference MP2 results also compare well with the MRMP results of Shirai et al. [30]. All the ΔSCF chemical shifts are also too large, while the MP2 ones are in excellent agreement with experiment. In the following, the CIPSI values will be used in order to be consistent with the core excitation energy calculations.

Concerning possible vibrational effects, Naves de Brito et al. [2] simply subtracted the ground state zero-point energy from their ΔSCF ionisation energies to explain the discrepancies with experiments. They pointed out that a complete normal mode analysis would be necessary to determine the "appropriate fraction" of the ZPVE to be removed. Using the simple vibrational model described in the previous section, such an analysis was done. The results of Fig. 1 show the comparison with the experimental spectra [1,2]. The vibrational structure being not discernible in the XPS spectrum [1,2], a FWHM of 0.25 eV was used for the vibrational bands. It should be noticed that since the O_1 core ion state was found to be dissociative (see Section 4.4), such an analysis is meaningless. This is consistent with the fact that the O1 XPS band has the largest FWHM (1.20 eV) [2] of the four atoms. The shape of the bands is correctly reproduced and the calculated half-widths (0.66 eV for C_1, 0.50 eV for C_2 and 0.66 eV for O_2) are close to the experiment [2] (0.83 eV for C_1 and 0.58 eV for C_2), except for O_2 where the 1.04 eV measured value may be too large because of the overlapping of the O_1 band at high energy. According to the authors [2], these observed widths of the XPS bands are mainly due to spectrometer resolution and vibrational broadening, both effects approximated by a single asymmetric gaussian profile, while lifetime broadening is much smaller. The vibrational analysis also shows that the 0–0 band origin is always below the calculated vertical energy (0.58 eV for C_1, 0.34 eV for C_2 and 0.60 eV for O_2). Moreover, the maximum of the total band does not correspond to the 0–0 transition, because of the numerous vibrational peaks. Assuming the maximum of each band in Fig. 1 should give the "ZPVE-corrected" ionisation energy, the resulting values, given in the last line of Table 1, are very close to experiment for C_2 and O_2, while the C_1 ionisation energy is too large by 0.5 eV. The origin of this discrepancy may come from the fact that we used the calculated CIPSI values for the vertical ionisation energies. As recently reviewed by Carniato and Luo [13], various terms other than ZPVE, may play a role in the calculation of core ionisation energies, leading to an accuracy of a few tenths of an eV. For example, the relativistic correction could slightly alter the calculations. However, according to Takahata and Chong [31], this correction is only 0.05 eV for carbons and 0.20 eV for oxygens.

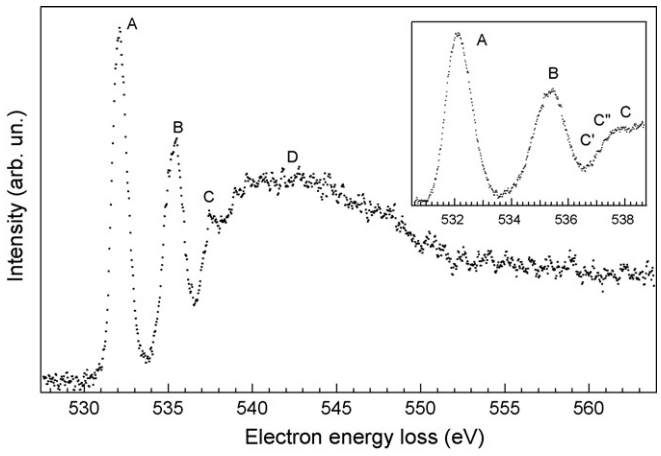

Fig. 2. The electron energy-loss spectrum of acetic acid recorded at the oxygen K edge with an energy resolution of 0.17 eV and 40 meV steps. Insert: The excitation spectrum in the 530.6–538.7 eV region is recorded with 20 meV steps.

4.2. Oxygen K-shell electron-energy loss spectrum

The O1s edge electron energy loss spectrum of acetic acid is shown in Fig. 2, while the energies of the observed bands are indicated in Table 2. To the best of our knowledge, the only other available ISEELS spectrum was published by Robin et al. [3] with a resolution of 0.6 eV. The two spectra are in agreement but the

Table 2
Energies (eV) of the spectral features in the ISEELS spectra

O1s	This work	ISEELS[a]	Assignment[a]	
			O_1	O_2
A	532.10	531.95		$1\pi^*(\pi^*(C_2–O_2))$
B	535.35	535.2	$1\pi^*(\pi^*(C_2–O_2))$	3p
C′	537.04			
C″	537.36			
C	537.90	537.6	$3p/\sigma^*(O_1–H)$	Rydberg
D	541.40	541.4(8)	$\sigma^*(C_1–C_2)$	$\sigma^*(C_2–O_1)$
		543.5(8)	$\sigma^*(C_2–O_1)$	
		546.3(8)	$\sigma C_2{=}O_2)$	

C1s	This work	ISEELS[a]	Assignment[a]	
			C_1	C_2
A	287.8	287.4	3s	
B[b]	288.74	288.69	$3p/\sigma^*(C_1–H)$	$1\pi^*(\pi^*(C_2–O_2))$
C	290.56	290.3	4p	
C′	291.64	291.5		3s
D[c]	293.60	293.4	$\sigma^*(C_1–C_2)$	3p
D′	294.35	294.6		4p
E	297.35	297.3		$\sigma^*(C_1–C_2)$
F	302.7	303.1(5)		$\sigma^*(C_2–O_2)$

[a] Ref. [3].
[b] Band B: on the high energy side a low intensity feature not well resolved at 289.4 eV.
[c] Band D: fine features not well resolved at 293.38 and 293.84 eV.

Table 3
Calculated energies and relative intensities of the O1s core excited states of acetic acid

State	E (eV)	TV (eV)		Intensity[a]	Main configurations		$\langle r^2 \rangle$ (a.u.^{2})
		O_1	O_2		O_1	O_2	
A″	532.29		6.29	1.000[b]		0.92 $1sO_2 \rightarrow \pi^*(C_2–O_2)$	52
A′	534.82		3.77	0.020		0.97 $1sO_2 \rightarrow 3s\sigma$	107
A″	535.52	4.83		0.334	0.92 $1sO_1 \rightarrow \pi^*(C_2–O_2)$		50
A′	535.78	4.56		0.303	0.97 $1sO_1 \rightarrow 3s\sigma/\sigma^*(O_1–H)$		93
A′	535.81		2.78	0.048		0.98 $1sO_2 \rightarrow 3p\sigma$	123
A″	536.09		2.49	0.034		0.98 $1sO_2 \rightarrow 3p\pi$	138
A′	537.20		1.39	0.021		0.98 $1sO_2 \rightarrow 4s\sigma$	440
A″	537.24		1.35	0.027		0.98 $1sO_2 \rightarrow 4p\pi$	387
A′	537.39	2.96		0.113	0.98 $1sO_1 \rightarrow 3p\sigma/\sigma^*(O_1–H)$		101
A″	537.70	2.64		0.072	0.98 $1sO_1 \rightarrow 3p\pi$		123
A′	537.92	2.42		0.033	0.98 $1sO_1 \rightarrow 3p\sigma'$		147
A′	538.35	2.00		0.061	0.97 $1sO_1 \rightarrow 3d\sigma$		225
	538.59[c]		0.00			Ion O_2	
A′	538.91	1.43		0.039	0.98 $1sO_1 \rightarrow 4p\sigma$		423
A″	538.92	1.42		0.036	0.99 $1sO_1 \rightarrow 4p\pi$		356
A′	539.03	1.31		0.022	0.99 $1sO_1 \rightarrow 4p\sigma'$		506
	540.35[c]	0.00			Ion O_1		

[a] Relative oscillator strength to the most intense peak.
[b] Absolute calculated oscillator strength $f = 0.0280$.
[c] ΔMP2(CIPSI)/TZ2P + R//MP2/TZ2P level.

higher resolution of the present work shows some fine features (C, C′ and C″) below the O_2 threshold. The assignments proposed by Robin et al. [3] are also given in Table 2. The spectrum is dominated by two broad bands A and B, centred at 532.10 and 535.35 eV, respectively.

The results of the calculations are shown in Table 3. Only the 2h–2p values with a relative intensity of 2% of the most intense peak are given (the complete table may be found in the supporting information). The spectra derived from the two types of calculations (1h–1p and 2h–2p) are given in Fig. 3a and b (the calculated bands were convoluted using 0.17 eV FWHM gaussian functions). Both CIPSI methods give very similar results. This is not surprising since all calculated core states wave functions are dominated by a single mono-excitation. As proposed earlier [3], the first band A is assigned to the $1sO_2 \rightarrow \pi^*(C_2–O_2)$. The characteristics (energy, Term Value and oscillator strength) of this transition, are compared to experiment in Table 4. The GSCF3 results [4] overestimate the core excitation energy, due to the frozen core approximation used [38]. On the other hand, the present ROHF-GVB energy is underestimated, but the TV is correct. The two CIPSI values, using the 1h–1p and 2h–2p models, give nearly identical results, in much better agreement with experiment. In particular, the calculated absolute oscillator strengths (0.0303 and 0.0280) are in very good agreement with the measured values [3] of 2.9×10^{-2} while the GSCF3 value of 0.0149 are too low.

Table 4
Transition energies, Term Values and oscillator strengths of the two most intense bands at different levels of theory

	$1sO_2 \rightarrow \pi^*(C_2–O_2)$			$1sC_2 \rightarrow \pi^*(C_2–O_2)$		
	E (eV)	TV (eV)	f	E (eV)	TV (eV)	f
GSCF3[a]	533.29	4.40	0.0149	291.37	5.15	0.0715
ROHF-GVB[b]	531.62	6.25		289.41	6.98	
CIPSI (1h–1p)[b]	532.23	6.35	0.0303	288.43	6.96	0.0829
CIPSI (2h–2p)[b]	532.29	6.29	0.0280	288.60	6.80	0.0920
Exp.[c]	532.10	6.21	0.029	288.74	6.61	0.104

[a] Ref. [4].
[b] This work.
[c] This work with Refs. [3,1].

The rather large width of the A band (FWHM ≈ 1.0 eV) suggests the presence of vibrational excitation, although it is not resolved. Another possible cause of broadening for band A could be a small contribution due to O1s transitions from dimerised acetic acid. However, such a contribution would be very unlikely at the pressures used in the present experiment. The results of the vibration calculations are compared to experiment in Fig. 4a. The agreement is rather good and the general shape of this band is well reproduced. Not surprisingly, the structure is mainly due to the $C_2–O_2$ stretching mode (1987 cm^{-1}). Other totally symmetric bending modes are also excited. These results were confirmed by calculating the equilibrium geometry of the $1sO_2 \rightarrow \pi^*(C_2–O_2)$ core excited state at the ROHF-GVB level, as shown in Table 5 and supplementary data. When compared to the RHF ground state geometry, the $C_2–O_2$ bond is weakened and the length increases from 1.1816 to 1.3435 Å, close to the $C_2–O_1$ single bond value. Moreover, the $\pi^*(C_2–O_2)$ HOMO is mainly concentrated on the C_2 atom and has a sp^3 contribution from C_1. This causes the pyramidalisation of the COOH group, with the angles between the four heavy atoms close to 109°, much as in the methyl group. Another peculiarity is the fact that the C_1, C_2, O_1 and H atoms nearly lie in the same plane. Remarkably, the geometry of the ground state of CH_3CFOH, which is the "Z + 1" equivalent of acetic acid, is almost perfectly identical, confirming the equivalent core approximation.

The second band B of the spectrum has its maximum at 535.35 eV and is wider than band A (FWHM ≈ 1.5 eV), suggesting the presence of more than one transition. It was assigned [3] to the $1sO_1 \rightarrow \pi^*(C_2–O_2)$ and $1sO_2 \rightarrow 3p$ Rydberg transitions (Table 2). This is confirmed by the present calculations, since the $1sO_1 \rightarrow \pi^*(C_2–O_2)$ transition is calculated to occur at 535.52 eV with a relative intensity of 33% of the first peak A (Table 3). This rather high intensity may be rationalised by the fact that the $\pi^*(C_2–O_2)$ MO is slightly delocalised on the O_1 atom. The three $1sO_2 \rightarrow 3p$ Rydberg transitions are predicted to occur at 535.81, 536.09 and 536.28 eV, i.e., on the high energy tail of the band, while the $1sO_2 \rightarrow 3s\sigma$ is calculated on the low energy side, at 534.82 eV. However, the calculated intensities for these four transitions are small (<5%) so that their contributions to the B band should be weak. On the other hand, the calculations predict the $1sO_1 \rightarrow 3s\sigma$ transition to occur at 535.78 eV with an intensity of 30% (Table 3). The

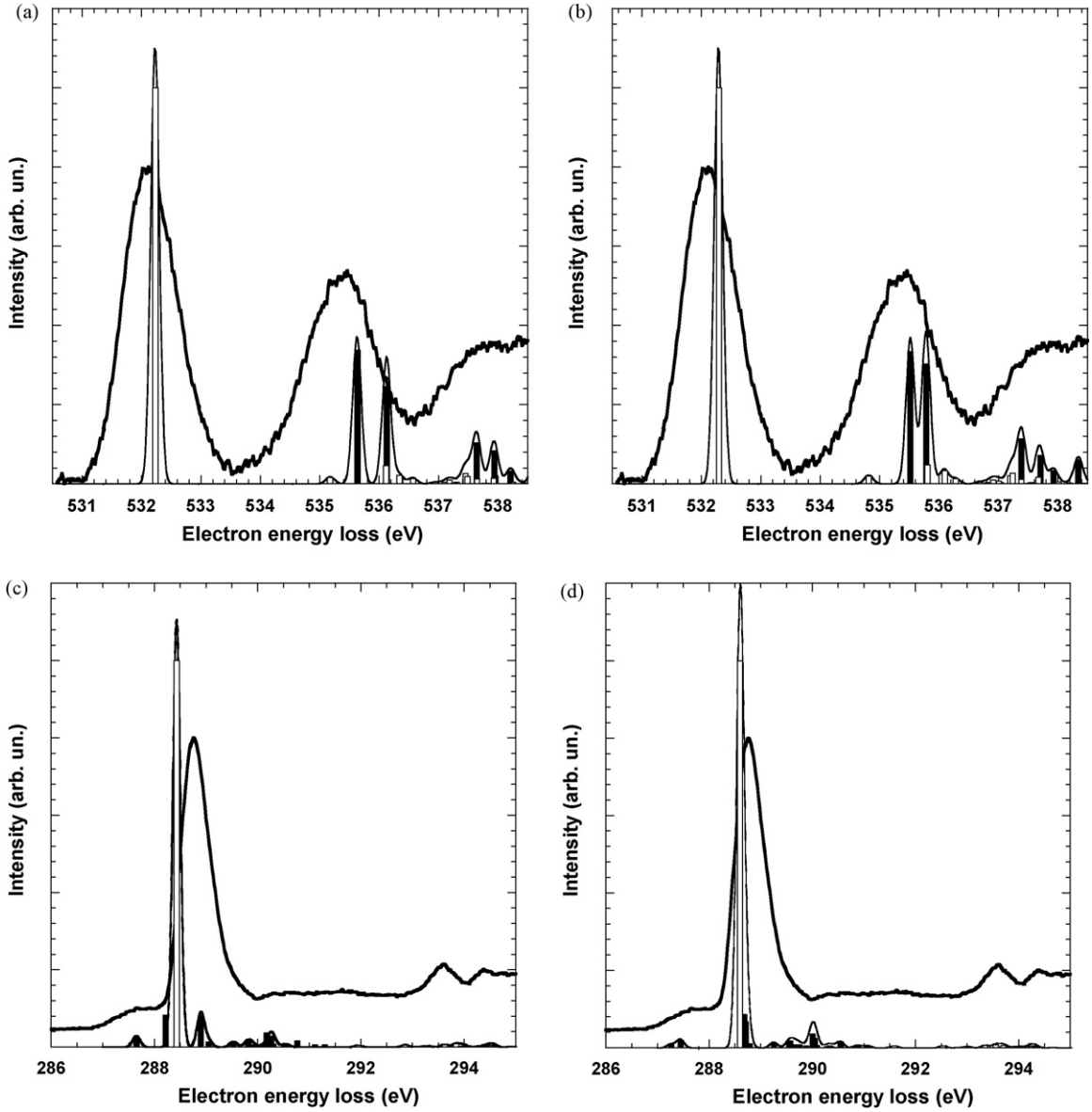

Fig. 3. Comparison between the experimental and the theoretical spectra (FWHM = 0.17 eV) for the pre-edge regions (white: O_1 and C_2, black: O_2 and C_1): (a) O1s 1h–1p calculations, (b) O1s 2h–2p calculations, (c) C1s 1h–1p calculations, (d) C1s 2h–2p calculations.

contrast in the intensities of the 3sσ transitions for the two O atoms may be explained by the important $\sigma^*(O_1–H)$ valence character of the 3sσ MO for O_1. To summarise, the B band is mainly due to the $1sO_1 \rightarrow \pi^*(C_2–O_2)$ and $1sO_1 \rightarrow 3s\sigma/\sigma^*(O_1–H)$ transitions, having very similar energies and intensities, and with minor contributions of O_2 3s and 3p Rydberg transitions.

As for band A, it is possible that vibrational excitation contributes to the width of band B. However, the geometry optimisation of the two $1sO_1$ states (at ROHF-GVB level) showed that both states are unstable (Table 5): the $3s\sigma/\sigma^*(O_1–H)$ state dissociates into $CH_3COO + H$, while the $\pi^*(C_2–O_2)$ state dissociates into $CH_3CO + OH$. For the first state, the $\sigma^*(O_1–H)$ valence character of the 3sσ MO is consistent with the O_1–H bond breaking. For the second state, the breaking of the C_2O_1 bond, rather than the C_2O_2 one, may be due to the delocalised nature of the π* MO on the O_1 atom. The same state of the CH_3COFH Z + 1 equivalent molecule exhibits the same behaviour with an important qualitative difference in the Mulliken charges: the π* states dissociates into $HF^- + CH_3CO^+$ fragments (Table 5). The dissociative nature of these two states proves that the B band of the K-shell spectrum should exhibit a continuum, even at a better resolution.

At higher energy, the observed spectrum does not show any discernible band, since the intensity increases monotonously until the O_2 ionisation threshold is reached around 538.5 eV (Fig. 2). This is consistent with the calculations, predicting the O_2 Rydberg transitions to occur above 536 eV (Table 3). All these transitions are purely Rydberg with very small intensities. They are probably responsible for the weak feature C′ located at 537.04 eV. On the other hand, the C″ feature measured at 537.36 eV corresponds to the $1sO_1 \rightarrow 3p\sigma/\sigma^*(O_1–H)$, calculated at 537.39 eV. As for the 3sσ transition, its high intensity (11%) is due to its important valence character. The C feature at 537.90 eV is assigned to the $1sO_1 \rightarrow 3p\pi$ transition, calculated at 537.70 eV, with a rather high intensity (7%) due to a small valence character.

The next energy region of the spectrum corresponds to the O1 ionisation continuum. Robin et al. [3] distinguished three features

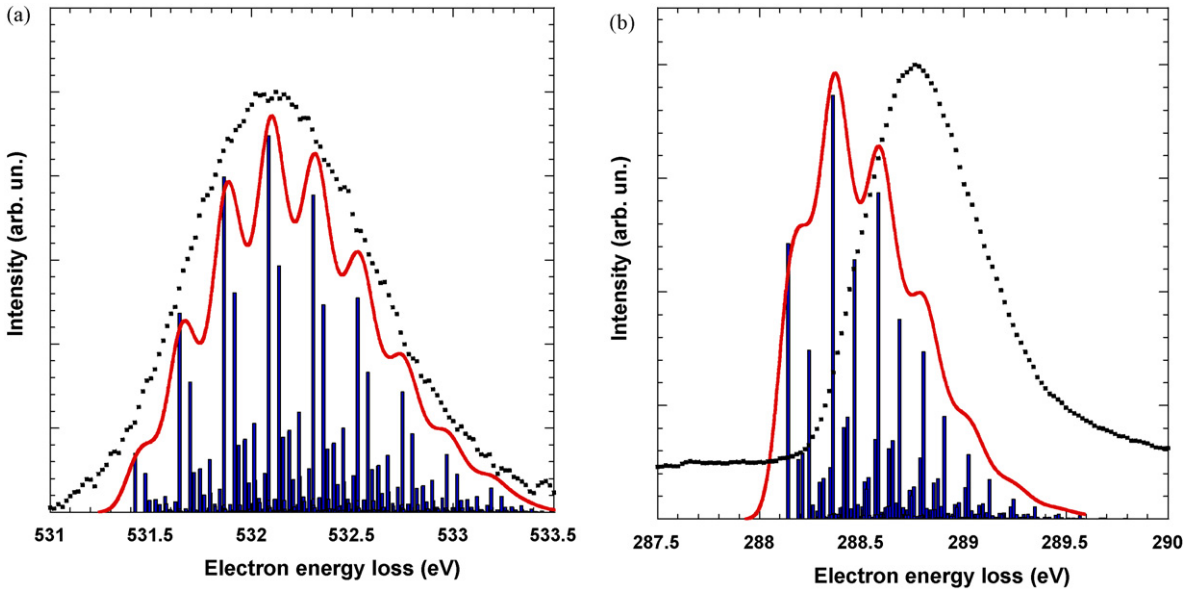

Fig. 4. Calculated vibrational structure (FWHM = 0.17 eV gaussian functions) compared to experiment. (a) Band A, O1s edge, (b) band B, C1s edge.

at 541.4, 543.5 and 546.3 eV (Table 2), assigned to O_1 shape resonances, but only the first one seems to be present in the spectrum of Fig. 3. The calculations reported in Table 3 predict O_1 Rydberg transitions to occur at such energies with weak intensities. However, the present theoretical model does not allow a proper description of transitions beyond the ionisation threshold.

4.3. Carbon K-shell electron-energy loss spectrum

The C1s electron energy loss spectrum is shown in Fig. 5 and the energies of the peaks are collected in Table 2, together with the results of the previous study of Robin et al. [3]. The spectrum is dominated by a strong band B, centred at 288.74 eV, which is highly asymmetric on the high energy side. The A band, which appeared only as weak shoulder in Robin's spectrum, is now clearly discernible at 287.8 eV. Above 290 eV, the spectrum is nearly flat with two weak features C (290.56 eV) and C' (291.64 eV).

The most intense (>1%) calculated transitions (2h–2p level) are displayed in Table 6, while the theoretical spectra obtained at both 1h–1p and 2h–2p levels are compared to the experiment in Fig. 3c and 3d. As in the O1s case, for nearly all calculated core excited states, the CI wave function is dominated by a single mono-excitation (weight >91%). There is however an important exception: the two lowest lying A "C_1 transitions, corresponding to transitions to the $3p\pi/\sigma^*(C_1–H)$ and $\pi^*(C_2–O_2)$ MO's. At the 1h–1p level, these transitions are calculated at the same energy (288.22 and 288.23 eV, respectively), although with different intensities: 8% for $1sC_1 \rightarrow 3p\pi/\sigma^*(C_1–H)$ and less than 0.1% for $1sC_1 \rightarrow \pi^*(C_2–O_2)$. These intensities are consistent with the fact that the $3p\pi$ MO has an important $\sigma^*(C_1–H)$ valence character, while the $\pi^*(C_2–O_2)$ MO

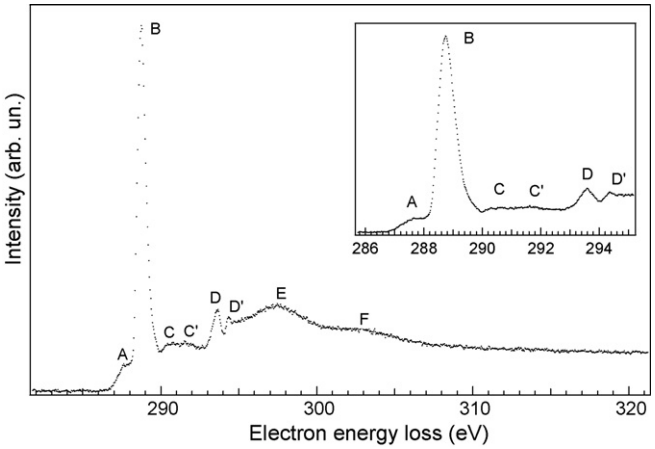

Fig. 5. The electron energy-loss spectrum of acetic acid recorded at the carbon K edge with an energy resolution of 0.17 eV and 40 meV steps. Insert: The excitation spectrum in the 285.8–295.2 eV region recorded with 20 meV steps.

Table 5
Stability of core ionised and excited states of acetic acid and corresponding states of Z + 1 molecules

Acetic acid		Core states	Z + 1 molecule	Valence states		
Ion O_1	$^2A'$	$C_1H_3C_2O_2 + O_1H^+$	CH_3COFH^+	Ion O_1	$^1A'$	$CH_3CO^+ + FH$
Ion O_2	$^2A'$	Stable	CH_3CFOH^+	Ion O_2	$^1A'$	Stable
Ion C_1	$^2A'$	Stable	NH_3COOH^+	Ion C_1	$^1A'$	Stable
Ion C_2	$^2A'$	Stable	CH_3NOOH^+	Ion C_2	$^1A'$	Stable
$1sO_1 \rightarrow \pi^*(C_2–O_2)$	$^1A''$	$C_1H_3C_2O_2 + O_1$ H	CH_3COFH	$\pi^*(C_2–O_2)$	$^2A''$	$CH_3CO^+ + FH^-$
$1sO_1 \rightarrow 3s\sigma/\sigma^*(O_1–H)$	$^1A'$	$C_1H_3C_2O_2O_1 + H$		$3s\sigma/\sigma^*(F–H)$	$^2A'$	$CH_3COF + H$
$1sO_2 \rightarrow \pi^*(C_2–O_2)$	^1A	Stable	CH_3CFOH	$\pi^*(C_2–F)$	^2A	Stable
$1sO_2 \rightarrow 3s\sigma$	$^1A'$	$C_1H_3C_2O_2O_1 + H$		$3s\sigma$	$^2A'$	$CH_3CFO + H$
$1sC_1 \rightarrow 3s\sigma/\sigma^*(C_1–H)$	$^1A'$	Stable	NH_3COOH	$3s\sigma/\sigma^*(N–H)$	$^2A'$	Stable
$1sC_1 \rightarrow \pi^*(C_2–O_2)$		$C_1H_3 + C_2O_2O_1H$		$\pi^*(C_2–O_2)$		$NH_3 + COOH$
$1sC_2 \rightarrow \pi^*(C_2–O_2)$	^1A	Stable	CH_3NOOH	$\pi^*(N–O_2)$	^2A	Stable
$1sC_2 \rightarrow 3s\sigma$	$^1A'$	Stable		$3s\sigma$	$^2A'$	Stable

Table 6
Calculated energies and relative intensities of the C1s core excited states of acetic acid

State	E (eV)	TV (eV)		Intensity[a]	Main configurations		$\langle r^2 \rangle$ (a.u.^{2})
		C_1	C_2		C_1	C_2	
A″	287.27	4.18		0.009	0.39 $1sC_1 \rightarrow 3p\pi/\sigma^*(C_1–H)$ +0.48 $1sC_1 \rightarrow \pi^*(C_2–O_2)$		64
A′	287.45	4.00		0.021	0.98 $1sC_1 \rightarrow 3s\sigma$		82
A″	288.60		6.80	1.000[b]		0.91 $1sC_2 \rightarrow \pi^*(C_2–O_2)$	55
A′	288.68	2.77		0.087	0.98 $1sC_1 \rightarrow 3p\sigma/\sigma^*(C_1–H)$		105
A″	288.71	2.74		0.068	0.58 $1sC_1 \rightarrow 3p\pi/\sigma^*(C_1–H)$ 0.39 $1sC_1 \rightarrow \pi^*(C_2–O_2)$		105
A″	290.01	1.44		0.035	0.96 $1sC_1 \rightarrow 4p\pi$		324
A′	290.05	1.40		0.024	0.98 $1sC_1 \rightarrow 4p\sigma'$		343
	291.45[c]	0.00			Ion C_1		
	295.40[c]		0.00			Ion C_2	

[a] Relative oscillator strength to the most intense peak.
[b] Absolute calculated oscillator strength $f = 0.0920$.
[c] ΔMP2(CIPSI)/TZ2P + R//MP2/TZ2P level.

is mainly localised on C_2 and O_2. At the 2h–2p level (Table 6), the results are somewhat different: the first A" transition is now predicted at 287.27 eV with an intensity of 0.9%, while the second one is calculated at 288.71 eV with an intensity of 6.8%. Thus, the splitting between the two states is now 1.44 eV. For both states, the CI wave functions show a strong mixing between the $1sC_1 \rightarrow 3p\pi/\sigma^*(C_1–H)$ and $1sC_1 \rightarrow \pi^*(C_2–O_2)$ excitations. As shown by Löwdin [39], it is possible to construct from these wave functions the so-called "natural orbitals", after diagonalisation of the CI density matrix. The resulting MO's represent the best approximations of the "true" core excited MO's (see supplementary data). Both transitions appear to be mono-electronic, with 1s and virtual MO's having occupation numbers close to 1. The first transition can be viewed as the $1sC_1 \rightarrow \pi^*(C_2–O_2)$, while the second one is the $1sC_1 \rightarrow 3p\pi/\sigma^*(C_1–H)$ transition. These assignments are consistent with the calculated $\langle r^2 \rangle$ values: 64 a.u.^{2} for the first one, typical of a valence transition and 105 a.u.^{2} for the second one, close to the two other 3p values. Moreover, the fact that the energy of the second transition is close to the two other 3p transitions supports these assignments.

Using these results, it appears that the weak band A observed in the spectrum at 287.8 eV is assigned not only to the $1sC1 \rightarrow 3s\sigma$ transition, as proposed by Robin et al. [3], but also to the $1sC1 \rightarrow \pi^*(C_2–O_2)$, both having low intensities (Table 6). The next band B is assigned mainly to the intense $1sC_2 \rightarrow \pi^*(C_2–O_2)$ transition, with contributions from the $1sC_1 \rightarrow 3p$ transitions calculated at the same energy. In particular, two 3p transitions have non negligible intensities, due to their Rydberg-valence character: the $1sC_1 \rightarrow 3p\sigma/\sigma^*(C_1–H)$ (8.7%) and the $1sC_1 \rightarrow 3p\pi/\sigma^*(C_1–H)$ (6.8%). Together with the 3d states predicted around 289.5 eV, they are responsible of the asymmetry observed on the high energy side of the B band. Another possible cause of the asymmetry may be vibrational excitation. Fig. 4b compares with experiment the vibrational fine structure of the $1sC_2 \rightarrow \pi^*(C_2–O_2)$ transition, calculated at the ROHF-GVB level. It should be kept in mind that the vibration contributions of the $1sC_1$ transitions present in this region are not included. The asymmetry is well reproduced, although the maximum of the calculated band is 0.3 eV below the experimental maximum. This discrepancy is partially due to the difference between the calculated (288.60 eV) and the measured (288.74 eV) vertical ionisation energies.

The parameters of the intense $1sC_2 \rightarrow \pi^*(C_2–O_2)$ transition, obtained using various methods, are shown in Table 4. The behaviour of the different theoretical methods is essentially the same as for the $1sO_2 \rightarrow \pi^*(C_2–O_2)$ transition, the best results being obtained with CIPSI. Because of the mono-electronic nature of this transition, the 1h–1p and 2h–2p are almost identical. The CIPSI calculated absolute oscillator strengths (0.0829 and 0.0920) are in very good agreement with the measured values of 10.4×10^{-2} measured by Robin et al. [3] while the GSCF3 value of 0.0715 is slightly too small.

According to the calculations, the next energy region, between 290 and 291.5 eV, corresponds to Rydberg transitions from the C_1 atom. Most of these transitions are purely Rydberg and have thus very low intensities, with the exception of two 4p transitions predicted at 290 eV whose MO's have a slight valence character and who are responsible for the feature C observed at 290.56 eV. The C′ at 291.64 eV may be due to the C_1 ionisation threshold at 291.45 eV. At higher energies, the calculations predict the C_2 Rydberg transitions to occur. According to Table 2 and Fig. 3d, there seems to be a good agreement between the position of the D (293.60 eV) and D′ (294.35 eV) bands and some of these transitions. However, these results must be considered with caution, because of the possible coupling between the C_1 continuum and the C_2 Rydberg transitions, which has not been taken into account by the calculations. Moreover, these features may also be due to (above threshold) C_1 transitions. Finally, the two last observed features E (297.35 eV) and F (302.7 eV) are assigned to possible shape resonances.

4.4. Geometry of core states of acetic acid

Due to the variational collapse of the core hole wave function, standard correlated methods cannot be employed to optimise the geometry of core excited states, especially for polyatomic molecules. Therefore, the geometry of core states of acetic acid were obtained at the ROHF-GVB level, as implemented in the GAMESS-US package, and compared to their Z + 1 counterparts. The main results are given in Table 5. The case of the 1s $O_2 \rightarrow \pi^*(C_2–O_2)$ transition has already been discussed in detail above. Qualitatively, the Z + 1 approximation gives results identical to the core calculations. The only difference resides in the Mulliken charge repartition for the dissociation products of the O_1 ion and 1s $O_1 \rightarrow \pi^*(C_2–O_2)$ state. Detailed structural information may be found in the supplementary material of this paper. For all the optimised states, the Z + 1 and core angles are identical within 0.1°, except for a few dihedral angles. The bond lengths are also identical within 0.01 Å. This agreement is fully consistent with the results obtained in the case of core excited

cyclopropane [26]. There is however one exception, concerning the 1s $C_2 \rightarrow \pi^*(C_2–O_2)$ state, where the Z + 1 model give results qualitatively different from the core states: while both molecules appear to be pyramidalised at the C_2 atom, the orientation of the O_1–H bond is completely different. One possible explanation would be that both geometries correspond to two different minima of the potential energy surfaces of the two molecules. However, this is not confirmed by the calculations. One has to conclude that in this particular example, the equivalent core model fails to predict the "true" core result. Similar discrepancies have been found in the case of core excited benzene [40] and aniline [41]. The differences seem to involve mainly the lowest frequency modes, such as the O_1–H torsion in acetic acid, or the rotation of the NH_2 group in aniline [41].

The results of Table 5 are also another example of the selectivity of bond breaking upon core excitation, such as in the recent case of $\sigma^*(COCH_3)$ MO of ester thin films [42–44]. The results have been rationalised by calculating the core state energy gradient in the Franck–Condon region of the ground state [45]. Finally, the fragment products of C1s excited acetic acid have been studied experimentally [46,47]. Several dissociation channels involving ion pairs were found and these results may seem contradictory with the calculations shown in Table 5 where core states appear to be stable or giving neutral fragment. There are two possible explanations for this discrepancy: the experimental method cannot detect neutral species. Moreover, the fragments observed are probably due to the valence CH_3COOH^{++} dication which is the results of the Auger decay of the core states.

5. Conclusions

In this work, the core excitation spectra of gaseous acetic acid have been measured and interpreted using *ab initio* Configuration Interaction and simple Franck–Condon calculations based on the linear coupling approximation at both edges. The spectra have been recorded by high energy electron impact in electric dipolar interaction conditions, with a higher resolution than in previous works. The calculations allow a precise assignment of most observed bands and show that most core states are well described by a monoelectronic representation. Vibrational excitation in the first band at the C1s and O1s edges, respectively, have been observed for the first time. This vibrational fine structure looks quite similar to that of the ions observed in the X-ray photoelectron spectrum and both are well reproduced by simple Franck–Condon calculations. Finally, the calculated core states geometries are found to be close to their equivalent core counterparts. Some exceptions occur when low vibrational modes are involved, leading to qualitatively different geometries.

Acknowledgements

The "Laboratoire de Physique des Lasers, Atomes et Molécules" (PhLAM) is "Unité Mixte de Recherche du CNRS". The "Centre d'Études et de Recherches Lasers et Applications" (CERLA, FR CNRS 2416), is supported by the "Ministère chargé de la Recherche", the "Région Nord/Pas-de-Calais" and the "Fonds Européen de Développement Économique des Régions" (FEDER). Part of the computations were carried out at the CRI (Centre de Ressources Informatiques), on the IBM computer which is supported by the "Programme de Calcul Intensif et Parallèle" of the "Ministère chargé de la Recherche", the "Région Nord/Pas-de-Calais" and the FEDER. This research has been supported by the Fonds de la Recherche Scientifique (FRS-FNRS) and the Patrimoine of the Université de Liège. M.-J. Hubin-Franskin wishes to acknowledge the Fonds de la Recherche Scientifique for her research position.

Appendix A. Supplementary data

Supplementary data associated with this article can be found, in the online version, at doi:10.1016/j.ijms.2008.05.006.

References

[1] A. Naves de Brito, M.P. Keane, N. Correia, S. Svensson, U. Gelius, B.J. Lindberg, Surf. Interface Anal. 17 (1991) 94.
[2] A. Naves de Brito, N. Correia, S. Svensson, H. Agren, J. Chem. Phys. 95 (1991) 2965.
[3] M.B. Robin, I. Ishii, R. McLaren, A.P. Hitchcock, J. Electron Spectrosc. Relat. Phenom. 47 (1988) 53.
[4] S.G. Urquhart, H. Ade, J. Phys. Chem. B 106 (2002) 8531.
[5] C. Hannay, J. Heinesch, U. Kleyens, M.-J. Hubin-Franskin, Meas. Sci. Technol. 6 (1995) 1140.
[6] M.-J. Hubin-Franskin, H. Aouni, D. Duflot, F. Motte-Tollet, C. Hannay, L.F. Ferreira, G. Tourillon, J. Chem. Phys. 106 (1997) 35.
[7] M.-J. Hubin-Franskin, J. Heinesch, Nucl. Instrum. Methods A 477 (2002) 546.
[8] R.N.S. Sodhi, C.E. Brion, J. Electron Spectrosc. Relat. Phenom. 34 (1984) 363.
[9] D. Duflot, J.-P. Flament, I.C. Walker, J. Heinesch, M.-J. Hubin-Franskin, J. Chem. Phys. 118 (2003) 1137.
[10] G. Chaban, M.W. Schmidt, M.S. Gordon, Theor. Chem. Acc. 97 (1997) 88.
[11] M.W. Schmidt, K.K. Baldridge, J.A. Boatz, S.T. Elbert, M.S. Gordon, J.H. Jensen, S. Koseki, N. Matsunaga, K.A. Nguyen, S. Su, T.L. Windus, M. Dupuis, J.A. Montgomery Jr., J. Comp. Chem. 14 (1993) 1347.
[12] S. Bodeur, P. Millié, I. Nenner, Phys. Rev. A 41 (1990) 252.
[13] S. Carniato, Y. Luo, J. Electron Spectrosc. Relat. Phenom. 142 (2005) 163.
[14] B. Huron, J.P. Malrieu, P. Rancurel, J. Chem. Phys. 58 (1973) 5745.
[15] R. Cimiraglia, J. Chem. Phys. 83 (1985) 1746.
[16] S. Stranges, M. Alagia, G. Fronzoni, P. Decleva, J. Phys. Chem. A 105 (2001) 3400.
[17] C. Angeli, R. Cimiraglia, M. Persico, A. Toniolo, Theor. Chem. Acc. 98 (1997) 57.
[18] T.H. Dunning, J. Chem. Phys. 55 (1971) 716.
[19] T.H. Dunning Jr., J. Hay, in: H.F. Schaefer III (Ed.), Methods of Electronic Structure Theory, Plenum Press, New York, 1977, p. 1.
[20] J.P. Dognon, C. Pouchan, A. Dargelos, J.P. Flament, Chem. Phys. Lett. 109 (1984) 492.
[21] J.-P. Flament, Ph.D. Thesis, Université de Paris-Sud, 1981.
[22] L.S. Cederbaum, W. Domcke, J. Chem. Phys. 64 (1976) 603.
[23] H. Köppel, W. Domcke, L.S. Cederbaum, Adv. Chem. Phys. 57 (1984) 59.
[24] T.D. Thomas, L.J. Saethre, S.L. Sorensen, S. Svensson, J. Chem. Phys. 109 (1998) 1041.
[25] U. Hergenhahn, J. Phys. B 37 (2004) R89.
[26] D. Duflot, S. Zeggari, J.-P. Flament, Chem. Phys. 327 (2006) 518.
[27] A.B. Trofimov, E.V. Gromov, T.E. Moskovskaya, J. Schirmer, J. Chem. Phys. 113 (2000) 6716.
[28] R.B. Gerber, J.O. Jung, in: P.R. Bunker, P. Jensen (Eds.), Computational Molecular Spectroscopy, Wiley and Sons, Chichester, 2000, p. 365.
[29] J.L. Derissen, J. Mol. Struct. 7 (1971) 67.
[30] S. Shirai, S. Yamamoto, S.-A. Hyodo, J. Chem. Phys. 121 (2004) 7586.
[31] Y. Takahata, D.P. Chong, J. Electron Spectrosc. Relat. Phenom. 133 (2003) 69.
[32] W.L. Jolly, K.D. Bomben, C.J. Eyermann, At. Data Nucl. Data Tables 31 (1984) 433.
[33] T.D. Crawford, H.F. Schaefer III, T.J. Lee, J. Chem. Phys. 105 (1996) 1060.
[34] P.J. Knowles, J.S. Andrews, R.D. Amos, N.C. Handy, J.A. Pople, Chem. Phys. Lett. 186 (1991) 130.
[35] W.J. Lauderdale, J.F. Stanton, J. Gauss, J.D. Watts, R.J. Bartlett, Chem. Phys. Lett. 187 (1991) 21.
[36] T.J. Lee, D. Jayatilaka, Chem. Phys. Lett. 201 (1993) 1.
[37] T.J. Lee, A.P. Rendell, K.G. Dyall, D. Jayatilaka, J. Chem. Phys. 100 (1994) 7400.
[38] W.J. Hunt, I. Goddard, A. William, Chem. Phys. Lett. 3 (1969) 414.
[39] P.-O. Löwdin, Phys. Rev. 97 (1955) 1474.
[40] P. Norman, H. Agren, J. Mol Struct. (THEOCHEM) 401 (1997) 107.
[41] D. Duflot, J.-P. Flament, A. Giuliani, J. Heinesch, M. Grogna, M.-J. Hubin-Franskin, Phys. Rev. A 75 (2007) 052719.
[42] O. Takahashi, K. Tabayashi, S.-I. Wada, R. Sumii, K. Tanaka, M. Odelius, L.G.M. Pettersson, J. Chem. Phys. 124 (2006) 124901.
[43] K. Tanaka, H. Kizaki, R. Sumii, Y. Matsumoto, S. Wada, Radiation Physics and Chemistry, Proceedings of the 20th International Conference on X-ray and Inner-Shell Processes, vol. 75, Melbourne, Australia, July 4–8, 2006, p. 2076.
[44] H. Kizaki, Y. Matsumoto, H. Ban, K. Morishita, S.-i. Wada, K. Tanaka, Surf. Sci. 601 (2007) 3956.
[45] O. Takahashi, T. Matsui, A. Kawano, K. Tabayashi, K. Yamasaki, J. Mol. Struct. (THEOCHEM) 808 (2007) 35.
[46] S. Pilling, A.C.F. Santos, H.M. Boechat-Roberty, Astronom. Astrophys. 449 (2006) 1289.
[47] S. Pilling, H.M. Boechat-Roberty, A.C.F. Santos, G.G.B. de Souza, A. Naves de Brito, J. Electron Spectrosc. Relat. Phenom. 156–158 (2007) 139.